Dynamics of quantum dot lasers subject to optical feedback and external optical injection

vorgelegt von
Diplom-Physiker
Christian Otto
aus Wuppertal

von der Fakultät II – Mathematik und Naturwissenschaften –
der Technischen Universität Berlin

zur Erlangung des akademischen Grades
Doktor der Naturwissenschaften
– Dr. rer. nat. –
genehmigte Dissertation

Promotionsausschuss:

Vorsitzender:	Prof. Dr. Michael Lehmann
Berichter:	Prof. Dr. Eckehard Schöll, PhD
Berichterin:	Priv.-Doz. Dr. Kathy Lüdge
Berichter:	Prof. Dr. Thomas Erneux

Tag der wissenschaftlichen Aussprache: 19. Juni 2013

Berlin 2013
D 83

To Antje

Abstract

In this thesis, I study the complex dynamics of different semiconductor laser structures under optical injection and under external optical feedback.

In the first part of this thesis, I concentrate on nanostructured quantum dot (QD) lasers. Here, the impact of the internal nonlinear carrier dynamics – and thus the impact of the band structure – on the dynamics of these QD lasers is intensively studied. Therefore, a microscopically based rate equation model is used, in which the carrier scattering dynamics between the discrete energy levels of the QDs and the surrounding carrier reservoir is described by Coulomb scattering rates. These rates depend nonlinearly on the carrier densities in the carrier reservoir and thus on the pumping conditions. Further, they strongly depend on the energy spacing between the band edge of the carrier reservoir and the discrete QD levels, which permits to describe different band structures. The impact of the scattering rates on the damping of the relaxation oscillations (ROs) of the solitary laser are discussed in detail. Beside the impact of the band structure, I investigate the dependence of the complex dynamics of a QD laser under optical injection on the pump current and on the phase-amplitude coupling (α-factor). By means of multiscale analysis, analytical approximations are derived for the saddle-node and Hopf bifurcations bordering the region of stable continuous wave emission as well as for a codimension-2 zero-Hopf point acting as organizing center for more complex dynamics, and the minimal injection strength, below which no Hopf instability may occur. Moreover, for the QD laser subject to optical feedback, an analytic expression for the first supercritical Hopf bifurcation marking the boundary for stable continuous wave emission is obtained. The analytic expressions for the bifurcation lines and bifurcation points reveal their dependence on the RO damping, and thus on the band structure, as well as on the α-factor. Further, the possibility to employ the QD laser subject to feedback as an excitable optical unit is discussed. By adding white noise to the dynamic equation for the electric field in the cavity, coherence resonance is observed in the excitable regime, and its dependence on the pump current is studied.

In the second part of this thesis, the response of a passively mode-locked two-section laser to external optical feedback is studied. This type of laser permits to realize compact devices that are well suited for optical telecommunication applications due to their ability to emit trains of short optical pulses with a high repetition frequency of 40 GHz, which is an upcoming IEEE standard. One major drawback of passively mode-locked lasers is their relatively large timing jitter degrading the quality of the pulse stream and thus increasing the bit-error rate. Resonant optical feedback provides an easy-to-handle way of reducing the timing jitter. I analyze the resonances of the inter-pulse interval time and the external delay time, and it is shown that the resonances can be ordered in a Farey-sequence similar to the resonances in externally driven systems, which allows for easy prediction of the laser dynamics. Further, I discuss that the timing jitter can be reduced drastically in the main resonances, where the largest stabilizing effect of the feedback is obtained, which is of relevance for applications.

Zusammenfassung

In der vorliegenden Arbeit untersuche ich die komplexe Dynamik verschiedener Halbleiterlaserstrukturen unter optischer Injektion und optischer Rückkopplung.

In dem ersten Teil der Arbeit stehen nanostrukturierte Quantenpunktlaser im Vordergrund. Hierbei analysiere ich den Einfluss der internen, nichtlinearen Ladungsträgerdynamik von Quantenpunktlasern – und damit der Bandstruktur – auf die Laserdynamik. Dafür wird ein Ratengleichungsmodell verwendet, bei dem der Ladungsträgeraustausch zwischen den diskreten Energieniveaus der Quantenpunkte und dem umgebenden Ladungsträgerreservoir durch mikroskopisch berechnete Coulomb-Streuraten beschrieben wird. Zum einen hängen diese nichtlinear von der Konzentration der Ladungsträger in dem Ladungsträgerreservoir und damit von dem Pumpstrom ab und zum anderen werden sie von dem energetischen Abstand zwischen den Bandkanten des Reservoirs und den Quantenpunktniveaus bestimmt. Letzteres ermöglicht es, den Einfluss unterschiedlicher Bandstrukturen auf die Dämpfung der Relaxationsoszillationen (ROs) des Lasers zu untersuchen. Für den optisch injizierten Quantenpunktlaser betrachte ich neben dem Einfluss der Bandstruktur zudem die Auswirkungen des Pumpstroms sowie der Phasen-Amplitudenkopplung (α-Faktor) auf die komplexe Laserdynamik. Mit Hilfe einer Multiskalenanalyse werden analytische Ausdrücke für die Sattel-Knoten und Hopf-Bifurkationslinien, die den Synchronisationsbereich (Arnoldzunge) begrenzen, hergeleitet. Des Weiteren werden analytische Ausdrücke für den Kodimension-2 Sattel-Knoten-Hopf-Punkt, der ein Organisationszentrum für komplexere Dynamik darstellt, sowie für die Injektionsstärke, unterhalb derer keine Hopf-Bifurkation möglich ist, hergeleitet. Auch für den Laser mit externer Rückkopplung wird ein Ausdruck für die Rückkopplungsstärke, bei der die erste Hopf Instabilität auftritt, abgeleitet. Die Formeln für die Bifurkationslinien und Bifurkationspunkte zeigen deren Abhängigkeit von der Dämpfung der ROs sowie von dem α-Faktor auf. Des Weiteren wird gezeigt, dass der Quantenpunktlaser unter optischer Rückkopplung in einem bestimmten Parameterbereich anregbar ist. Unter dem Einfluss additiven, weißen Rauschens weist das System in diesem Regime Kohärenzresonanz auf, deren Pumpstromabhängigkeit untersucht wird.

In dem zweiten Teil der Arbeit untersuche ich den Einfluss zeitverzögerter optischer Rückkopplung auf passiv modengekoppelte Zweisektionslaser. Diese zeichnen sich durch regelmäßige Pulsemission mit einer hohen Wiederholrate von bis zu 40 GHz aus. Diese entspricht dem nächsten IEEE-Standard und ist daher von besonderem Interesse für die digitale, optische Datenübertragung. Ein gravierender Nachteil dieser Laser ist, dass der zeitliche Abstand aufeinanderfolgender Pulse (timing jitter) relativ großen Fluktuationen unterworfen ist, was zu einer erhöhten Bit-Fehlerrate führt. Optische Rückkopplung stellt eine einfache Möglichkeit dar, den timing jitter zu reduzieren. In der vorliegenden Arbeit wird gezeigt, dass sich zwischen dem zeitlichen Abstand benachbarter Pulse und der Umlaufzeit des Lichts in der externen Kavität ein ähnliches Resonanzverhalten einstellt, wie es von dynamischen Systemen mit externem periodischen Antrieb bekannt ist. Dadurch können die Resonanzen in einer Farey-Folge angeordnet werden, was eine einfache Vorhersage der Laserdynamik ermöglicht. Des Weiteren wird gezeigt, dass innerhalb der Hauptresonanzen die Pulsfolge durch die Rückkopplung stabilisiert wird, wodurch eine deutliche Verringerung des timing jitters bewirkt wird.

CONTENTS

LIST OF TABLES

ACRONYMS

cw	continuous wave
DDE	delay differential equation
ECM	external cavity modes
FML	fundamental mode-locked
FWHM	full-width at half maximum
HML	harmonic mode-locked
LFF	low frequency fluctuations
LK	Lang-Kobayashi
ML	mode-locked
PSD	power spectral density
rms	root-mean-square
rf	radio-frequency
RO	relaxation oscillation
SNIC	saddle-node on an invariant cycle
SNIPER	saddle-node infinite period bifurcation
QD	quantum dot
QP	quasiperiodic
QW	quantum well

CHAPTER

ONE

INTRODUCTION

Nowadays, semiconductor lasers and amplifiers play a key role for many technological applications as for example high bit rate optical communication [KNO00], optical interconnects [KEE03], and electro-optic sampling [REI99]. Further, they are of importance for biomedical applications as, for instance, optical coherence tomography [HUA91].

The first semiconductor lasers were realized in 1962 [HAL62, NAT62, HOL62, QUI62]. These early devices were based on p-n homojunctions, in which p and n doped regions were made out of the same semiconductor material (GaAs). Thus, the band gap on both sides of the junction was the same, and high pump currents and low temperatures were needed to reach inversion. As a consequence, these bulk semiconductor lasers could only be operated at low temperatures, and their lifetimes were too short for applications. The breakthrough of semiconductor lasers as light sources for optical applications came with the introduction of lasers based on a double heterostructure in 1969 by Alferov et al. [ALF69] (see [COL12] for a review). In a double heterostructure, a quantum film of a semiconductor material with a lower band gap is sandwiched between a bulk material with a larger band gap forming a quantum well (QW) [KRO63]. If the quantum film is thinner than the de-Broglie wavelength of the carriers, their energy levels are discretized in a direction vertical to the layer. This confinement of the carriers in one spatial dimension yields a splitting of the energy bands of the bulk semiconductor into energetic sub-bands, which permits lower threshold currents and continuous wave (cw) operation at room temperature [COL12].

However, a further confinement of the carries is possible: in lasers based on quantum wires, the carries are confined in two spatial dimensions, and, eventually, in quantum dot (QD) based semiconductor lasers, the charge carriers are confined in all three spatial dimensions on a length scale smaller than the de-Broglie wavelength [BIM99], i.e, the typical extension of QDs is on the order of 10 nm . Due to this carrier confinement in a QD laser, the optical transition takes places between discrete energy levels broadened to Lorentzians by the finite decay time of the polarization [CHO99]. This permits a further threshold reduction and a higher temperature stability with respect to QW devices [BIM08].

In contrast to the encouraging theoretical predictions [DIN76, ARA82, ASA86a], the first QD lasers based on lattice-matched heterostructures were pulsed lasers operating only at low temperature up to 77 K, and they had unpractical high threshold current densities [HIR94a]. A milestone on the way to commercially successful QD lasers was the discovery of universal self-organization effects, which are known as Stranski-Krastanow growth mode. This growth mode leads to the formation of self-similar, lens shaped QDs admitting to produce QD devices, in which the density of QDs in the active region, i.e., the gain of the device, as well as their optical properties, i.e., their material composition and their size, are easily tunable [BIM95, SHC99, SHC03, SHC07]. Most common are ternary alloys based on the InGaAs/GaAs material system, where the optical transition takes places at $1.3\,\mu$m. This is a local minimum of attenuation, and, at the same time, the dispersion minimum of standard single mode optical fibers making this wavelength range of particular interest for telecommunication applications.

From a dynamical systems point of view, semiconductor lasers are characterized by a time scale separation between the fast photon and the slower carrier subsystem, i.e., they are typical slow-fast systems [ERN10b]. As a consequence, their turn-on dynamics shows damped nonlinear intensity oscillations, which are called relaxation oscillations (ROs). The damping of the ROs is a key point in order to understand the stability properties of the laser subject to external perturbations, for instance, optical feedback or optical injection. QW lasers show pronounced, weakly damped ROs, while the ROs of QD lasers are strongly damped [KUN02, MAL06, ERN07a, LUE09, LUE11a]. As a result, QD lasers display a higher dynamical stability under optical injection [ERN10a, KEL11a, KEL11c, PAU12] and optical feedback [SU03, HUY04, OBR03a, CAR06a, CAR05, CAR06a, GLO12].

In QD devices, the carriers are first injected into a surrounding QW acting as a carrier reservoir, before they scatter into the discrete energy levels of the QDs, between which the optical transition takes place. The carrier scattering rates strongly depend on the energy spacing between the band edge of the QW and the discrete QD levels, i.e., on the band structure of the device. The scattering rates provide (nonlinear) carrier lifetimes of the carriers in the QD levels, which yield additional time scales compared to QW lasers. The energy spacings determine how these time scales compare to the carrier lifetimes in the carrier reservoir and the photon lifetime.

For a small energy spacing, short lifetimes (large scattering rates) are obtained, which are on the same time scale or shorter than the photon lifetime yielding overdamped, very stable devices, which act similar to gas lasers, i.e., typical class A lasers. For large energy spacings, long carrier lifetimes on the order of pico-seconds are obtained, which guarantee a clear time-scale separation between the carrier and the photon subsystem (time-scale of femtoseconds) resulting in weakly damped, less stable lasers, whose dynamics is similar to conventional QW lasers, i.e., typical class B lasers. QD lasers lie in-between these two limiting cases and exhibit typical dynamical features of class B and class A lasers [ERN07a, ERN10a, KEL11c].

One particularity of semiconductor lasers is their high sensitivity to external optical perturbations due to the relatively low reflectivity of their facets [TAR95a]. On the one hand, this may be a disadvantage, because in applications expensive optical isolators are needed to guarantee a stable continuous wave (cw) emission of the laser. On the other hand, from a fundamental physics points of view, semiconductor lasers display, subject to optical injection or optical feedback, a wealth of different dynamical regimes ranging from stable cw emission, over periodical intensity modulations, to chaotic waveforms [TAR98a].

Numerous application arise from optical injection ranging from chirp reduction [OLS85], over a reduction of relative intensity noise [SCH86g, YAB00], and enhanced side-mode suppression [IWA82], to a larger bandwidth under direct optical modulation [JIN06, LAU09a], and the generation of microwave signals [SEO01, CHA07].

Moreover, semiconductor lasers subject to delayed optical feedback are ideal candidates to study the stabilization of steady states and periodic orbits by non-invasive time delayed feedback control [SCH06a, FLU07, DAH07, DAH08b, FIE08, DAH10] (see [SCH07, SCH09a] for an overview). Further, delay synchronization of coupled lasers [HIC11], bubbling in coupled lasers [FLU09, FLU10], and networks of delay coupled lasers [DAH11b, DAH12] are subject of current research (see [SOR13] for a recent review).

This thesis is organized in two parts. Part I deals with QD semiconductor lasers under optical injection and optical feedback. At first, a rate equation model for a QD laser that focuses on a microscopical modeling of the Coulomb carrier scattering dynamics between carrier reservoir and QDs is introduced in Chapter 2. Although microscopically funded, this modeling approach is simple enough to gain analytic insight into the impact of the band structure, the pump current, and the phase-amplitude coupling on the complex dynamics of the QD laser under optical injection and optical feedback. Optical injection is discussed in Chapter 3, and Chapter 4 deals with optical feedback.

In Part II passively mode-locked (ML) QW semiconductor lasers are investigated. Mode-locking of semiconductor lasers is the method of choice to reach short pulse widths at high repetition rates needed to use semiconductor lasers as transmitters in fiber based optical networks [HAU00]. Mode-locking generates an optical pulse comb with repetition rates ($\sim 40\,$GHz [FIO11]) far above the cutoff frequency for direct current modulation ($\sim 10\,$GHz [SUG05]). However, especially passively mode locked lasers have the drawback of a high temporal instability of the pulse stream, which is characterized as timing jitter. Delayed optical feedback from an external fiber loop has turned out to be an effective control method to suppress the timing fluctuations of the pulses [SOL93, MUL06, MER09, AVR09, BRE10, LIN10e, LIN11d, LIN11f, FIO11]. Such a closed-loop control has the advantage that the laser generates its own control signal, which can be modified by tuning the delay time and the strength of the feedback. As a consequence, real-time computation of the control signal can be avoided, which is crucial for ML lasers due to their fast pulse-repetition dynamics. In this thesis, a delay equation model of a passively mode-locked laser [VLA04, VLA05, VLA11] is extended to take into account delayed feedback control. This simple modeling approach delivers insights into the resonance structure of the inter-spike interval time, i.e., the temporal distance of subsequent pulses, and the delay time. Moreover, it is shown how the timing jitter is influenced by this resonance structure.

Eventually, a summary of the results of the thesis and an outlook to possible future investigations of QD lasers subject to optical injection and delayed optical feedback is given in Chapter 6. Moreover, Chapter 6 provides an outlook on possible continuations of the work on passively ML semiconductor lasers subject to optical feedback.

Part I.

Quantum dot laser

TABLE OF SYMBOLS

Table 1.1.: List of corresponding quantities in the three different coordinate systems used in Part I, which are characterized by different scalings of time. (**first column**): physical time t, (**second column**): dimensionless time $t \equiv 2\kappa\tau_{\mathrm{in}}$ that is rescaled with respect to the photon lifetime $(2\kappa)^{-1}$, and (**third column**): dimensionless time $s \equiv 2\sqrt{\kappa \bar{W} N_{\mathrm{ph}}^0}t$.

Meaning	physical time t	time $t' \equiv 2\kappa t$	time $s \equiv 2\sqrt{\kappa \bar{W} N_{\mathrm{ph}}^0}t$
injection/feedback strength	K	$\tilde{k}$, $\tilde{k}_1$	k
of saddle-node bifurcation	–	–	k^{sn}
of Hopf bifurcation	K_H, K_H^{QD}, K_H^{QW}	$\tilde{k}_H$	k_H
of zero-Hopf points	$K^{\mathrm{ZH},1}$, $K^{\mathrm{ZH},2}$	$\tilde{k}^{\mathrm{ZH}}$, $\tilde{k}^{\mathrm{ZH},1}$	–
of critical Hopf point	$K_{H,c}$	$\tilde{k}_{H,c}$	–
frequency detuning	$\Delta\nu_{\mathrm{inj}}$, $\Delta\omega_{\mathrm{inj}}$	$\delta\omega$, $\delta\omega^{\mathrm{s}}$	Δ, Δ_1
of saddle-node bifurcation	–	$\delta\omega_{\pm}^{\mathrm{sn}}$, $\delta\omega_{\pm}^{\mathrm{s,sn}}$	$\Delta_{\pm}^{\mathrm{sn}}$, $\Delta_{1,\pm}^{\mathrm{sn}}$
of Hopf bifurcation	–	$\delta\omega_H$	Δ_H
of zero-Hopf point	$\Delta\nu_{\mathrm{inj}}^{\mathrm{ZH},1}$	$\delta\omega^{\mathrm{ZH},1}$	–
of critical Hopf point	$\Delta\nu_{\mathrm{inj}}^{H,c}$	$\delta\omega_{H,c}$	–
inversion	–	ρ_{inv}, $\rho_{\mathrm{inv},1}$, $\rho_{\mathrm{inv}}^{\mathrm{s}}$	u_+, U_+, $\frac{u_e}{2}$, $\frac{U_e}{2}$
of saddle-node bifurcation	–	$\rho_{\mathrm{inv}}^{\mathrm{sn}}$, $\rho_{\mathrm{inv},\pm}^{\mathrm{s,sn}}$	$\left(\frac{u_e}{2}\right)^{\mathrm{sn}}$
eigenvalues	$\tilde{\sigma}$	σ	λ
RO frequency	ω_{RO}, $\omega_{\mathrm{RO}}^{\mathrm{ref}}$, $\omega_{\mathrm{RO}}^{\mathrm{S}}$, $\omega_{\mathrm{RO}}^{\mathrm{vf}}$, $\omega_{\mathrm{RO}}^{\mathrm{QW}}$	ω^{RO}, ω^{ref}, ω^{S}, $\omega_{1/2}$, ω^{vf}, $\omega_{1/2}^{\mathrm{vf}}$, ω^{QW}	ω_s^{ref}, ω_s^{S}
RO damping	Γ_{RO}, $\Gamma_{\mathrm{RO}}^{\mathrm{ref}}$, $\Gamma_{\mathrm{RO}}^{\mathrm{S}}$, $\Gamma_{\mathrm{RO}}^{\mathrm{vf}}$, $\Gamma_{\mathrm{RO}}^{\mathrm{QW}}$, $\Gamma_{\mathrm{RO}}^{\mathrm{S,QW}}$	Γ^{RO}, Γ^{ref}, Γ^{S}, Γ_1, Γ^{vf}, Γ_1^{vf}, Γ^{QW}, $\Gamma^{\mathrm{S,QW}}$	Γ_1^{ref}, Γ_1^{S}
Hopf frequency	$\omega_{H,t}^{\mathrm{ref}}$, $\omega_{H,t}^{\mathrm{S}}$, $\omega_{H,t}^{\mathrm{vf}}$	ω_H, ω_H^{ref}, ω_H^{S}, ω_H^{vf}	$\omega_{H,s}$, $\omega_{H,s}^{\mathrm{ref}}$, $\omega_{H,s}^{\mathrm{S}}$

CHAPTER

TWO

SOLITARY QUANTUM DOT LASER

2.1. Introduction

In this chapter, the model for the solitary semiconductor QD laser is introduced and its turn-on dynamics is studied. As already discussed in the introduction, one striking difference distinguishing QD from conventional semiconductor QW lasers is their special carrier scattering dynamics between the discrete QD levels and the continuous subbands of the surrounding carrier reservoir [BIM99, RAF11]. For instance, this scattering dynamics is responsible for the strongly damped ROs of QD lasers in comparison to QW lasers [KUN02, ERN07a, LUE09, ERN10a, KEL11c].

Our modeling approach aims to study in detail the dependence of the dynamics of the QD laser on the carrier scattering dynamics. Therefore, a microscopically based rate equation model is introduced that assumes a classical light field, but takes into account microscopically calculated Coulomb scattering rates for the carrier exchange between QD and carrier reservoir as discussed in [MAL06, MAL07, LUE08, LUE09, LUE10] (see [LUE11a] for a concise review). The microscopically calculated Coulomb scattering rates yield nonlinear carrier lifetimes τ_e and τ_h for electrons and holes in the QD levels, which strongly depend on the band structure, i.e., on the size and the material composition of the QDs, as well as on the filling of the carrier reservoir and thus on the pump current [LUE09, LUE10a]. Further, in this microscopic modeling approach it is taken into account that the energetic distances of the QD levels and the band edges of the carrier reservoir are different for electrons and holes, which results in different dynamics for electrons and holes in the QD levels as well as in the carrier reservoir. Therefore, in a hierarchy of semiconductor modeling approaches (see [CHO99] for an overview), the model bridges the gap between simple rate equation models and full quantum-mechanic modeling approaches, which treat also the light field quantum-mechanically and permit to study the photon statistic of the emitted light [SU10, GIE07]. Simpler rate equation models take into account only one carrier type, i.e., the dynamics of electron-hole pairs is modeled. Further, the carrier exchange between QDs and carrier reservoir is, in these models, described by constant carrier lifetimes in the QD levels [GOU07], or by linear in-scattering rates and constant out-scattering rates [OBR04, HUY04].

Our model is kept simple enough to derive analytical expression for RO frequency and damping. Therefore, a variety of effects has been neglected. For instance, a more complex modeling approach has to be chosen if changes in the emission wavelength due to Coulomb enhancement are of interest [CHO05, LIN10, LIN10a, LIN12, LIN12a, LIN12t]. Furthermore, to study ultrafast coherent dynamics on the fs-scale, for example, the gain recovery in QD-based optical amplifiers [GOM09], the dynamics of the microscopic polarization becomes important, which has been eliminated adiabatically in our model. To model the dynamics of the microscopic polarization, semiconductor Bloch equations have to be considered [WEG10, MAJ10, MAJ11, MAJ11a, WIL12c].

This chapter is organized as follows. After an introduction to the QD laser model in Subsection 2.2, the dynamical equations are non-dimensionalized in Subsection 2.3. Then, the turn-on dynamics of the QD laser is studied for different band structures in Subsection 2.4, and in Section 2.5, analytical expressions for the steady states as well as RO frequency and damping of the QD laser are presented for different band structures. These expressions reveal how the damping of the ROs is increased with respect to QW lasers by the carrier lifetimes τ_e and τ_h. Finally, a summary is given in Section 2.6.

2.2. Quantum dot laser model

In this section, the dynamical equations modeling the solitary QD laser are introduced. The QDs are embedded into a two dimensional QW acting as a carrier reservoir. A band structure of the device is depicted in Fig. 2.1. The crucial parameters are the confinement energies ΔE_e and ΔE_h that mark the energy differences between the QD ground state and the band edge of the surrounding QW for electrons and holes, respectively. The QD laser model is based on the model described in [LUE09, LUE10a], which has shown good quantitative agreement with experiments regarding the turn-on behavior and the modulation response of QD lasers [LUE10a]. The nonlinear, coupled, and five-variable rate equation model including the photon number in the cavity N_{ph}, as well as the electron and hole occupation probabilities in the QDs, ρ_e and ρ_h, and the electron and hole densities in the QW, w_e and w_h, respectively, is given by the following equations

$$\frac{dN_{\mathrm{ph}}}{dt} = \left[2\bar{W}Z_a^{QD}(\rho_e+\rho_h-1)-2\kappa\right]N_{\mathrm{ph}} + \beta 2 Z_a^{\mathrm{QD}} W\rho_e\rho_h, \tag{2.1a}$$

$$\frac{d\rho_e}{dt} = S_e^{\mathrm{in}}(1-\rho_e) - S_e^{\mathrm{out}}\rho_e - \bar{W}(\rho_e+\rho_h-1)N_{\mathrm{ph}} - W\rho_e\rho_h, \tag{2.1b}$$

$$\frac{d\rho_h}{dt} = S_h^{\mathrm{in}}(1-\rho_h) - S_h^{\mathrm{out}}\rho_h - \bar{W}(\rho_e+\rho_h-1)N_{\mathrm{ph}} - W\rho_e\rho_h, \tag{2.1c}$$

$$\frac{dw_e}{dt} = \frac{j}{e_0} - 2N^{\mathrm{QD}}\left[S_e^{\mathrm{in}}(1-\rho_e) - S_e^{\mathrm{out}}\rho_e\right] - B^S w_e w_h, \tag{2.1d}$$

$$\frac{dw_h}{dt} = \frac{j}{e_0} - 2N^{\mathrm{QD}}\left[S_h^{\mathrm{in}}(1-\rho_h) - S_h^{\mathrm{out}}\rho_h\right] - B^S w_e w_h. \tag{2.1e}$$

Here, 2κ are the optical intensity losses, which are balanced by the linear gain term $2\bar{W}Z_a^{\mathrm{QD}}(\rho_e+\rho_h-1)$, where $\bar{W}Z_a^{\mathrm{QD}}$ is the linear gain coefficient for the processes of induced emission and absorption. The gain coefficient is proportional first to the Einstein coefficient of induced emission $\bar{W}$ that measures the coherent interaction between the two-level system and the laser mode, and second to the number Z_a^{QD} of lasing QDs inside the waveguide (the factor 2 is due to spin degeneracy). A detailed derivation of $\bar{W}$ may be found in [PAU12, GLO12]. The number of lasing QDs, Z_a^{QD}, is given by $Z_a^{\mathrm{QD}} \equiv a_L A N_a^{\mathrm{QD}}$, where a_L is the number of self-organized QD layers, A is the in-plane area of the QW, and N_a^{QD} is the density per unit area of the active QDs. As a result of the size distribution and of the material composition fluctuations of the QDs, the gain spectrum is inhomogeneously broadened, and only a subgroup (density N_a^{QD}) of all QDs (N^{QD}) matches the mode energies for lasing. The spontaneous emission from one QD is taken into account by the term $W\rho_e\rho_h$, where W is the Einstein coefficient for spontaneous emission. It can be determined by calculating the coherent interaction of a two-level system, i.e., a single QD, with all resonator modes in the framework of the second quantization [CHO99]. Note that the coefficients $\bar{W}$ and W differ by three orders of magnitude. The spontaneous emission factor measuring the probability that a spontaneously emitted photon is emitted into the lasing mode is denoted by β. The spontaneous emission in the QW is incorporated by $B^S w_e w_h$, where B^S is the band-band recombination coefficient. The carriers are first injected into the carrier reservoir with the current density j, and e_0 is the elementary charge. In the lasing regime, where the reservoir carrier densities w_e and w_h are very high, Coulomb scattering, i.e., nonlocal Auger recombination, is the dominant carrier exchange process between reservoir and discrete QD levels, and phonon scattering may be neglected [WET04, WET04a, KUN05c, LOR06]. This is also supported by the modeling of carrier transport in QD structures [WET00, RAC02]. Nevertheless, phonon scattering is taken into account for the intra-band cooling processes in the reservoir. Thus, for the calculation of the Coulomb scattering rates a quasi-equilibrium within the carrier reservoir is assumed, which is realized by fast phonon intra-band scattering. The Coulomb scattering rates are calculated microscopically within the framework of the Boltzmann equation and an orthogonalized plane-wave approach [MAL06, MAL07]. The Coulomb interaction is treated in the second-order Born approximation in the Markov limit up to the second order in the screened Coulomb potential [NIE04, NIL05]. All relevant electron-electron, hole-hole, and mixed processes are included. A detailed discussion of the scattering processes can be found in [MAJ10, LUE11, LUE12]. The nonlinear scattering rates are denoted by S_e^{in} and S_h^{in} for electron and hole capture into the QD

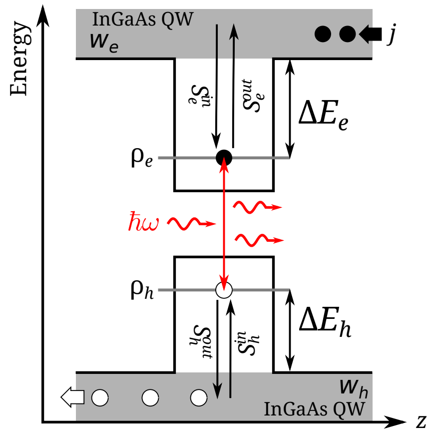

Figure 2.1: Energy diagram of the band structure across a QD. The ground state lasing energy is labeled by $\hbar\omega$. The energetic distances of the QD levels from the band edge of the carrier reservoir (QW) for electrons and holes are marked by ΔE_e and ΔE_h, respectively. The Auger in- and out-scattering rates between QD levels and QW are denoted by $S_{e/h}^{\mathrm{in}}$ and $S_{e/h}^{\mathrm{out}}$, respectively. The occupation probabilities of the QDs are denoted by $\rho_{e/h}$, the reservoir carrier densities are labeled by $w_{e/h}$, and j is the pump current density.

levels and by S_e^{out} and S_h^{out} for carrier escape to the reservoir, respectively (see Fig. 2.1). The scattering rates depend on the reservoir densities w_e and w_h, and are thus pump current dependent.

In thermodynamic equilibrium, there is a detailed balance between in- and out-scattering rates, which allows one to relate the coefficients of in- and out-scattering even away from the thermodynamic equilibrium [SCH87]. The detailed balance relation for in- and out-scattering rates for the quasi-equilibrium then reads [LUE09, LUE10]

$$S_e^{\mathrm{out}}(w_e, w_h) = S_e^{\mathrm{in}}(w_e, w_h) e^{-\frac{\Delta E_e}{k_{\mathrm{bo}}\mathcal{T}}} \left[e^{\frac{w_e}{D_e k_{\mathrm{bo}}\mathcal{T}}} - 1 \right]^{-1}, \tag{2.2a}$$

$$S_h^{\mathrm{out}}(w_e, w_h) = S_h^{\mathrm{in}}(w_e, w_h) e^{-\frac{\Delta E_h}{k_{\mathrm{bo}}\mathcal{T}}} \left[e^{\frac{w_h}{D_h k_{\mathrm{bo}}\mathcal{T}}} - 1 \right]^{-1}. \tag{2.2b}$$

Here, $\Delta E_e \equiv E_e^{\mathrm{QW}} - E_e^{\mathrm{QD}}$ and $\Delta E_h \equiv E_h^{\mathrm{QD}} - E_h^{\mathrm{QW}}$ are the energy differences between the QD levels, E_e^{QD} and E_h^{QD}, and the band edges of the QW, E_e^{QW} and E_h^{QW}, for electrons and holes, respectively. The carrier degeneracy concentrations are given by $D_{e/h} k_{\mathrm{bo}}\mathcal{T}$, where $D_{e/h} \equiv m_{e/h}/(\pi\hbar^2)$ are the 2D densities of state in the carrier reservoir with the effective masses $m_{e/h}$. The temperature is denoted by $\mathcal{T}$ and k_{bo} is Boltzmann's constant. Figure 2.2(a)–(d) depict electron in- and out-scattering rates (S_e^{in} and S_e^{out})

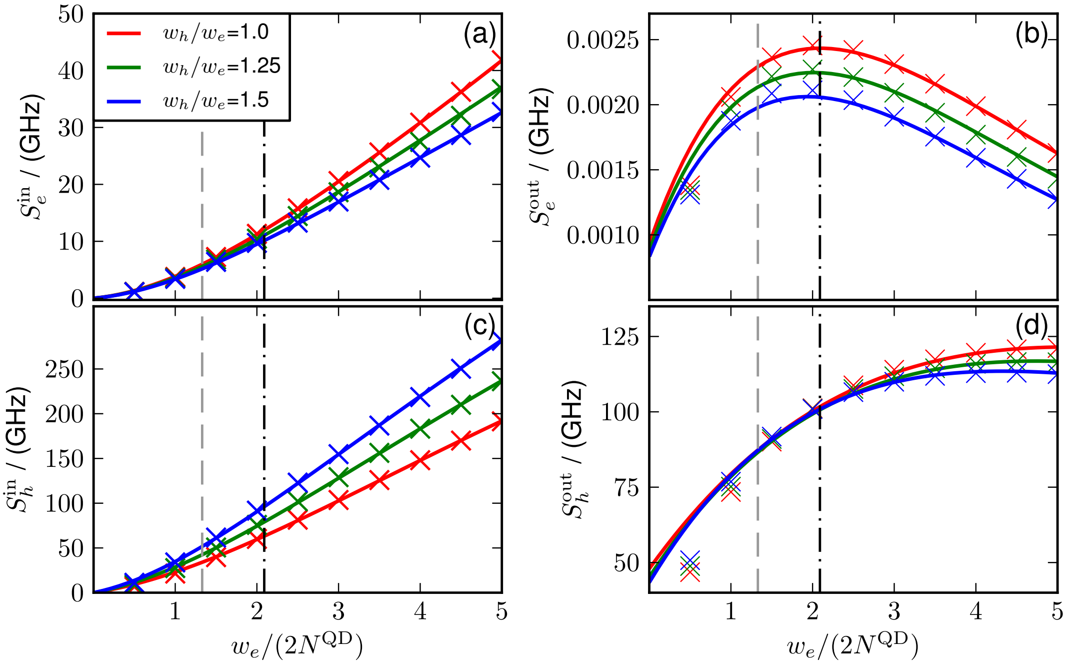

Figure 2.2.: In- and out-scattering rates for electrons (S_e^{in} **(a)** and S_e^{out} **(b)**) and holes (S_h^{in} **(c)** and S_h^{out} **(d)**), respectively, in dependence of the electron density in the carrier reservoir w_e (normalized to $2N^{\mathrm{QD}}$). The energy spacings between the band edges of the carrier reservoir and the discrete energy levels of the QDs are $\Delta E_e = 210\,\mathrm{meV}$ and $\Delta E_h = 50\,\mathrm{meV}$ for electrons and holes, respectively (reference rates). Crosses denote results of microscopic calculations and lines denote fit functions given in Appendix A.0.1. The gray dashed and the dash-dotted black line denote steady state values of w_e for pump current densities of $j = 1.5j_{\mathrm{th}}$ and $j = 3.5j_{\mathrm{th}}$, respectively. j_{th} is the current density at lasing threshold. Different colors denote different ratios w_h/w_e of hole (w_h) and electron (w_e) densities in the carrier reservoir. Parameters as in Table 2.2.

as well as hole in-and out-scattering rates (S_h^{in} and S_h^{out}) in terms of the electron density w_e in the carrier reservoir for three fixed ratios w_h/w_e of hole and electron densities. The energy spacings are $\Delta E_e = 210\,\text{meV}$ and $\Delta E_h = 50\,\text{meV}$ for electron and holes, respectively. Crosses mark microscopically calculated values, while colored lines depict the fit functions given in Appendix A.0.1. Gray dashed and black dash-dotted vertical lines denote the steady state values of w_e close to ($j = 1.5 j_{\text{th}}$) and well above threshold ($j = 3.5 j_{\text{th}}$), where j_{th} denotes the threshold current density. j_{th} is the current density, at which the induced emission starts to dominate the induced absorption and the cavity losses [HAK83a].

Hole in- and out-scattering rates are larger than their electronic counterparts, due to the smaller energetic distances of the QD level of the holes to the band edge of the reservoir. For low reservoir densities, the in-scattering rates increase quadratically with w_e as expected from mass action kinetics.

The carrier lifetimes τ_e and τ_h that result from Coulomb scattering between QDs and carrier reservoir are defined by the nonlinear scattering rates as

$$\tau_e \equiv (S_e^{\text{in}} + S_e^{\text{out}})^{-1} \quad \text{and} \quad \tau_h \equiv (S_h^{\text{in}} + S_h^{\text{out}})^{-1}. \tag{2.3}$$

It is important to note that these lifetimes are not constant but depend on the carrier densities in the surrounding carrier reservoir and thus on the injected pump current. They constitute the additional time scales that distinguishes QD from QW lasers. In the following chapters, their importance for the turn-on dynamics of the laser as well as for its dynamical response to external optical injection and feedback will be discussed. One advantage of QD lasers is that the additional lifetimes τ_e and τ_h can be tuned by the growth conditions and the material composition of the QDs [BIM99], which changes the energy spacings ΔE_e and ΔE_h between the band edge of the carrier reservoir and the QD levels. The energy spacings determine how τ_e and τ_h compare to the carrier lifetimes in the carrier reservoir and the photon lifetime. The pump dependent steady state values of τ_e and τ_h are shown in Fig. 2.3 for three different QD structures, which are compared throughout this work. The different structures are modeled by using three

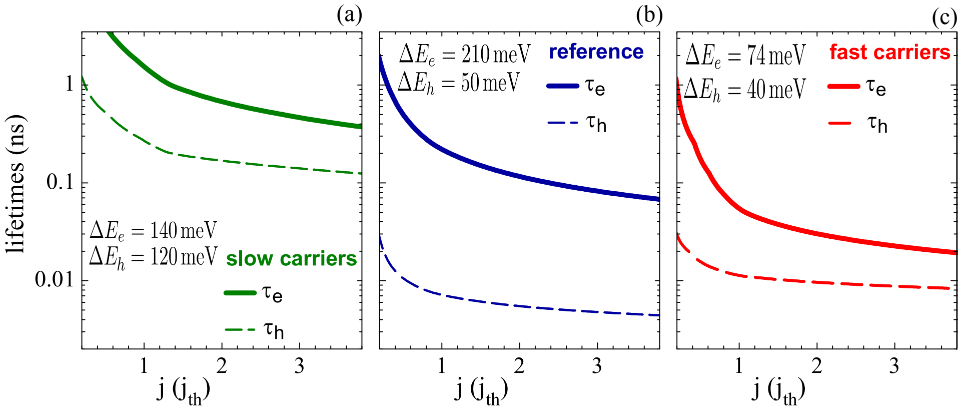

Figure 2.3.: Nonlinear steady state carrier lifetimes τ_e and τ_h for electrons and holes, respectively, as resulting from the microscopically calculated scattering rates calculated microscopically for **(a)**: slow, **(b)**: reference, and **(c)**: fast rates (see Table 2.1). Parameters as in Table 2.2. Modified from [PAU12].

Table 2.1.: Energy differences ΔE_e and ΔE_h between carrier reservoir and QD ground state for the three different sets of scattering rates used for the simulations as well as steady state carrier lifetimes for electrons (τ_e) and holes (τ_h). For a pump current density of $j = 3.5 j_{\mathrm{th}}$. (j_{th} is the pump current density at lasing threshold.)

data set	ΔE_e	ΔE_h	τ_e	τ_h
slow	140 meV	120 meV	0.395 ns	0.129 ns
reference	210 meV	50 meV	0.071 ns	0.005 ns
fast	74 meV	40 meV	0.021 ns	0.01 ns

different sets of confinement energies between QD and carrier reservoir listed in Table 2.1.

By controlling the growth mode during epitaxy, it is possible to create QDs with different size and composition. As such the reference rates plotted in Fig. 2.3(b) result from QDs with a base length of 18 × 18 nm and a ratio of 10 between the effective masses of holes and electrons (as used in [LUE10a]). They are named "reference", because with these rates, good agreement of the QD model with experimental turn-on curves is observed [LUE09]. Figure 2.4 shows the turn-on dynamics of the photon number N_{ph} as measured from experiment (black stars), which is superimposed by the calculated turn-on dynamics for $j = 2.2 j_{\mathrm{th}}$ and $j = 2.7 j_{\mathrm{th}}$ (blue lines), respectively. Typical for QD lasers is the strong suppression of the ROs.

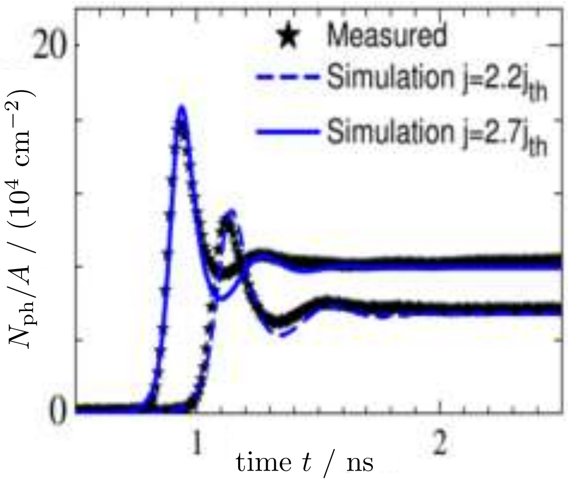

Figure 2.4: QD laser turn-on after the pump current j_{th} is switched on simulated with the reference rates (blue curves) and compared to experimental results (black stars) for $j = 2.2 j_{\mathrm{th}}$ and $j = 2.7 j_{\mathrm{th}}$, respectively. Modified from [LUE09].

Differences in the effective masses (e.g. obtained by changing the QD composition) are expressed in a different ratio between electron and hole confinement energy (see [LUE10]). Fig. 2.3(a) depicts the case of large confinement energies that are similar for electrons and holes, i.e., $\Delta E_e \approx \Delta E_h$, resulting in long Auger scattering lifetimes. Increasing the size of the dots leads to smaller confinement energies (shallow dots with smaller energetic distance between the QD levels and carrier reservoir) and thus to the fast scattering rates (Fig. 2.3(c)). Fit function for the three sets of scattering rates can be found in the Appendix A. All other numerical parameters that were used in the simulation are shown in Table 2.2.

Table 2.2.: Physical parameters used in the simulation of the QD laser model unless stated otherwise.

symbol	value	symbol	value	symbol	value
W	$0.7\,\mathrm{ns}^{-1}$	A	$4\cdot10^{-5}\,\mathrm{cm}^2$	$\mathcal{T}$	$300K$
$\bar{W}$	$0.11\,\mu\mathrm{s}^{-1}$	N_a^{QD}	$0.3\cdot10^{10}\,\mathrm{cm}^{-2}$	L	$1\,\mathrm{mm}$
2κ	$0.1\,\mathrm{ps}^{-1}$	N^{QD}	$1\cdot10^{11}\,\mathrm{cm}^{-2}$	ε_{bg}	14.2
β	$2.2\cdot10^{-3}$	B^S	$540\,\mathrm{ns}^{-1}\,\mathrm{nm}^2$	τ_{in}	$24\,\mathrm{ps}$
a_L	15	Z_a^{QD}	$1.8\cdot10^6$	m_e	$0.043\,m_0$
λ_{opt}	$1.3\,\mu\mathrm{m}$	ν_{las}	$230\,\mathrm{THz}$	m_h	$0.45\,m_0$

2.3. Non-dimensionalized rate equations

For the subsequent study of the dynamical equations (2.1), they are rewritten into a dimensionless form. This has two advantages: on the one hand, the number of independent parameters is reduced by combining them into dimensionless groups, which can be for example time scale ratios. On the other hand, dimensionless equations are better suited for numerical simulations, because very large and very small numbers are avoided [STR94a, FLU11a]. As it is usually done for rate equation models of semiconductor lasers, time is rescaled with respect to the photon lifetime $\tau_{\mathrm{ph}} \equiv (2\kappa)^{-1}$ [ERN10b] by introducing the dimensionless time $t' \equiv 2\kappa t$. Furthermore, dimensionless reservoir populations $W_e \equiv w_e/(2N^{\mathrm{QD}})$ and $W_h \equiv w_h/(2N^{\mathrm{QD}})$ are introduced, which are of order one. The dynamical equations (2.1) then read

$$N'_{\mathrm{ph}} = \rho_{\mathrm{inv}}(\rho_e,\rho_h)N_{\mathrm{ph}} + d\rho_e\rho_h, \tag{2.4a}$$

$$\rho'_e = \gamma\Big[F_e(\rho_e,\rho_h,W_e,W_h) - r_w(\rho_e+\rho_h-1)N_{\mathrm{ph}} - \rho_e\rho_h\Big], \tag{2.4b}$$

$$\rho'_h = \gamma\Big[F_h(\rho_e,\rho_h,W_e,W_h) - r_w(\rho_e+\rho_h-1)N_{\mathrm{ph}} - \rho_e\rho_h\Big], \tag{2.4c}$$

$$W'_e = \gamma\Big[J - F_e(\rho_e,\rho_h,W_e,W_h) - cW_eW_h\Big], \tag{2.4d}$$

$$W'_h = \gamma\Big[J - F_h(\rho_e,\rho_h,W_e,W_h) - cW_eW_h\Big], \tag{2.4e}$$

where $(\,\cdot\,)'$ denotes differentiation with respect to the dimensionless time t'. In Equation (2.4a) a rescaled inversion ρ_{inv} was introduced, which is defined as[1]

$$\rho_{\mathrm{inv}}(\rho_e,\rho_h) \equiv \frac{1}{2}\left[g(\rho_e+\rho_h-1)-1\right]. \tag{2.5}$$

---

[1] For this model, ρ_{inv} is not a very useful coordinate to simplify the calculation of the steady states, because there is no simple expression for the spontaneous emission terms $-\rho_e\rho_h$ in the QD equations (3.12c) and (3.12d) in terms of ρ_{inv}. However, introducing ρ_{inv} permits to directly compare the modeling results with most of the literature on three variable models (R, Ψ, ρ_{inv}) of QW lasers under optical injection, where the rescaled inversion is usually denoted by N or Z. For recent reviews of the literature see for example [WIE05] and [ERN10b].

Since the occupation probabilities ρ_e and ρ_h are restricted to values between zero and one, ρ_{inv} is in turn restricted to

$$-\frac{(g+1)}{2} \leq \rho_{\text{inv}} \leq \frac{g-1}{2}.$$

The functions F_e and F_h contain the contributions of the scattering rates

$$F_e(\rho_e, \rho_h, W_e, W_h) \equiv s_e^{\text{in}}(W_e, W_h)(1-\rho_e) - s_e^{\text{out}}(W_e, W_h)\rho_e, \tag{2.6a}$$

$$F_h(\rho_e, \rho_h, W_e, W_h) \equiv s_h^{\text{in}}(W_e, W_h)(1-\rho_h) - s_h^{\text{out}}(W_e, W_h)\rho_h. \tag{2.6b}$$

Here, dimensionless in-scattering rates (s_e^{in}, s_e^{out}) and out-scattering rates (s_e^{out}, s_h^{out}), dimensionless carrier lifetimes (t_e, t_h), the linear gain coefficient g, the ratio of photon and carrier lifetimes γ, the ratio of the Einstein-factors of induced and spontaneous emission r_w, the dimensionless pump rate J, the spontaneous emission coefficient d, and the coefficient of spontaneous and non-radiative losses in the carrier reservoir c have been introduced as follows

$$\begin{aligned}
s_{e/h}^{\text{in/out}} &\equiv \frac{1}{W} S_{e/h}^{\text{in/out}}, & t_{e/h}^{-1} &\equiv \frac{1}{W}(S_{e/h}^{\text{in}} + S_{e/h}^{\text{in/out}}), & g &\equiv \frac{2a_L \bar{W} A N_a^{\text{QD}}}{2\kappa}, \\
r_w &\equiv \frac{\bar{W}}{W}, & \gamma &\equiv \frac{W}{2\kappa}, & J &\equiv \frac{j}{e_0 2N^{\text{QD}} W}, \\
d &\equiv \beta \frac{W Z_a^{\text{QD}}}{\kappa}, & c &\equiv \frac{B^S 2N^{\text{QD}}}{W}.
\end{aligned} \tag{2.7}$$

The values of the dimensionless parameters g, γ, c, and r_w, which correspond to the physical parameters of Table 2.2, are listed in Table 2.3.

Table 2.3.: Parameter values for the dimensionless dynamical equations for the QD laser (Eqs. (2.4)) that correspond to the physical parameters given in Table 2.2.

Parameters	Value	Meaning
g	3.78	Linear gain parameter
γ	7×10^{-3}	Ratio of photon and carrier lifetime
r_w	1.5×10^{-4}	Ratio of Einstein-factors of induced and spont. emission
c	1.54	Spontaneous and non-radiative losses in QW
d	55.44	Coefficient of spontaneous emission

For the subsequent analysis, it is crucial to note that the carrier equations (2.4b)–(2.4e) are not independent but contain carrier conservation, which can be seen by verifying that

$$\rho_e' + W_e' = \rho_h' + W_h' \tag{2.8}$$

holds. Thus, $\rho_e - \rho_h + W_e - W_h$ is a constant to be determined by the initial conditions. In the absence of doping, this constant is zero and the effect of reservoir doping can be included by choosing a non-zero initial value for one of the reservoir densities, i.e.,

n-doping is described by $W_e \neq 0$ and p-doping by $W_h \neq 0$ [LUE10]. Due to the carrier conservation, one dynamical variable can be eliminated by expressing one carrier type in terms of the others, i.e.,

$$W_h = \rho_e + W_e - \rho_h. \tag{2.9}$$

2.4. Turn-on dynamics

In their dimensionless form, the dynamical equations (2.4) directly reveal the different time scales that determine the dynamics. It has been proposed by Tredicce at al. in [TRE85] that lasers may be classified by the ratio of three important time scales given by the decay of the polarization, of the field in the cavity, and of the carriers:

i In **class C** lasers, these three dynamical variables decay on the same time scale. This leads to complex dynamics, and chaotic behavior may be observed already for the solitary laser.

ii In **class B** lasers, the polarization decays on a much faster time scale (femtoseconds) than the field in the cavity, and may be eliminated adiabatically. Furthermore, a time scale separation exists between the fast photon and the slower carrier subsystem, i.e., the photon lifetime τ_{ph} (tenth of picoseconds) is much smaller than the carrier lifetime τ_c (nonoseconds). This means that the laser is a slow-fast system and thus responds to a perturbation by weakly damped, pronounced oscillations back to equilibrium, which are called relaxation oscillations (ROs) [ERN09]. QW semiconductor lasers are typical class B lasers. Complex and particularly chaotic dynamical behavior only occurs if the laser is subject to an external perturbation, which adds an additional degree of freedom. This perturbation may consist of external optical injection or external optical feedback.

iii In **class A** lasers, the polarization as well as the carriers decay much faster than the field, and both may be eliminated adiabatically. The simple dynamics of class A lasers is well described by one differential equation for the field. External perturbations add one degree of freedom, which makes periodic or quasi periodic behavior possible. Typical representatives of class A lasers are gas lasers. Their cavity consists of highly refractive mirrors, which guarantees a long photon lifetime. Also QD semiconductor lasers can reach the dynamical stability of class A laser [ERN10a], which is discussed in the present and the next Chapter.

In the dynamical equations (2.4) for the QD laser, the polarization has already been eliminated adiabatically. In contrast to QW lasers, the carrier lifetimes τ_e and τ_h of the optically active levels in QD lasers may be tuned by adapting the band structure. If the QD laser behaves like a class B or a class A laser, depends on the scaling of τ_e and τ_h with respect to the photon lifetime $\tau_{\text{ph}} = 2\kappa$. (Note that in the dimensionless equations (2.4) the photon lifetime is unity, i.e., the scaling of the dimensionless carrier lifetimes t_e and t_h with respect to unity has to be discussed.) Figure 2.5(a)–(c) depict the turn-on dynamics of the QD laser for the three different band structures listed in Table 2.1, and additionally the limit of very large scattering rates is depicted in Fig. 2.5(d). For this limit, the in-scattering rates of the shallow dot structure (fast rates) have been multiplied by a factor of $1 \cdot 10^4$.

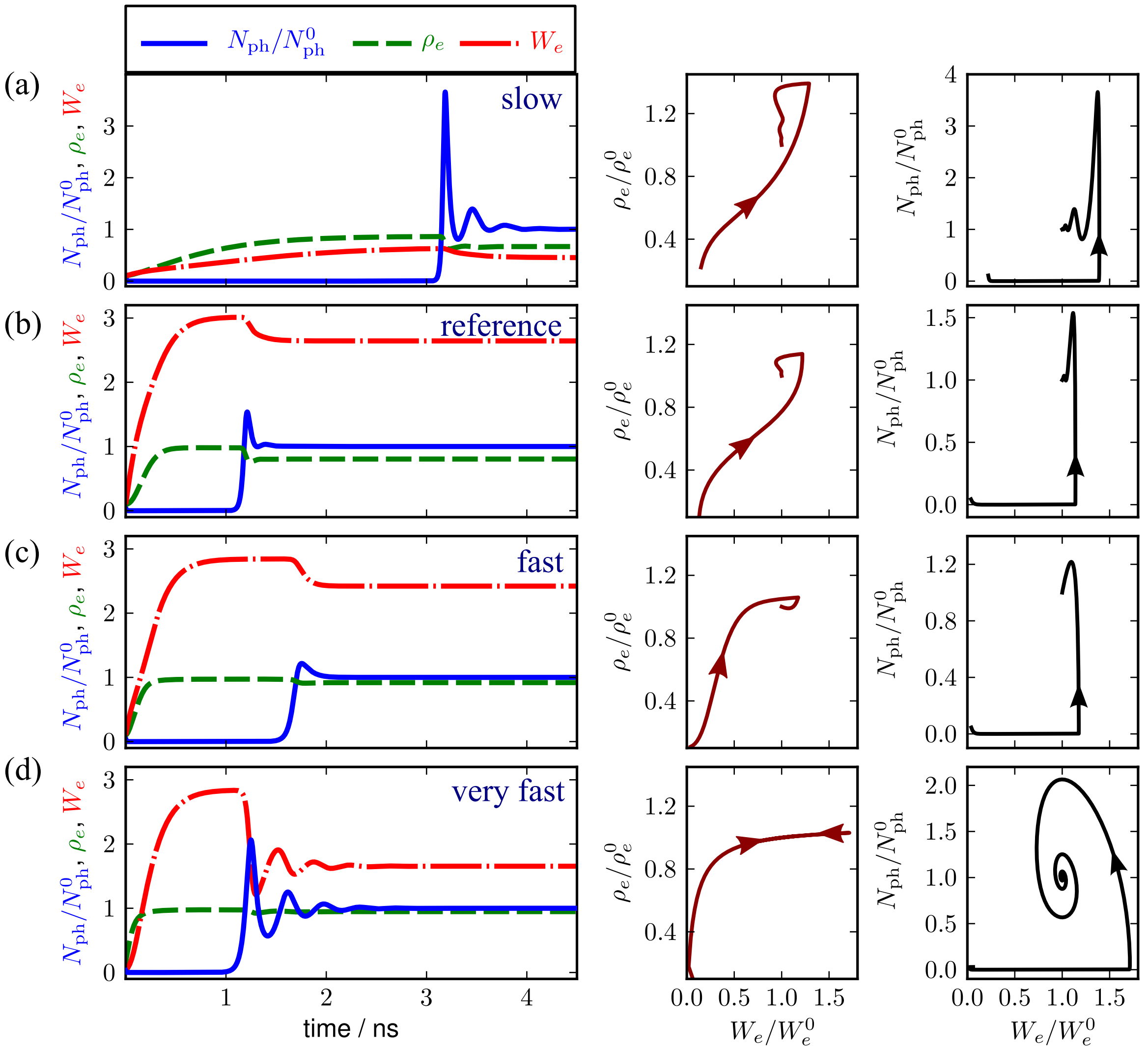

Figure 2.5.: Turn-on dynamics for **(a)**: slow, **(b)**: reference, **(c)**: fast, and **(d)**: very fast sets of scattering rates studied in this work. **Left column**: Time traces of the photon number N_{ph} (normalized to the steady state photon number N^0_{ph}), the electronic occupation probability ρ_e, and the electron density in the carrier reservoir W_e. **Middle column**: Phase space projections of the trajectories onto a plane spanned by W_e and ρ_e (ρ_e^0 and W_e^0 are the steady state values of ρ_e and W_e, respectively). **Right column**: Phase space projections of the trajectories onto a plane spanned by W_e and N_{ph}. Parameters $J = 2.5 \cdot J_{\mathrm{th}}$ and other parameters as in Table 2.2.

The slow rates represent the class B limit of the equations. The carrier equations (2.4b)–(2.4e) are multiplied by the small parameter γ, and the functions F_b ($b = e$ for electrons and $b = h$ for holes), which contain the contributions of the scattering rates, are small enough to guarantee that the product $\gamma F_b \ll 1$ remains small. This means that the equations are of slow-fast type. As a consequence, the time series of the photon number N_{ph} (Fig. 2.5(a) left column) shows pronounced, weakly damped relaxation oscillations. In a linear theory, RO damping and frequency are determined by the eigenvalues of the

Jacobien of Eqs. (2.4). The RO damping Γ_{RO} is determined by the eigenvalue, whose real part has the smallest absolute value, i.e., by the eigenvalue with the smallest decay rate. This eigenvalue is denoted as leading eigenvalue. Usually, the lasing fixed point is a stable focus and has a pair of complex conjugate leading eigenvalues $\tilde{\sigma}_{\pm} = -\Gamma_{\mathrm{RO}} \pm i\omega_{\mathrm{RO}}$. The RO frequency ω_{RO} is then given by the absolute value of the imaginary parts of these eigenvalues. For class B lasers, the damping is much smaller than the frequency ($\Gamma_{\mathrm{RO}} \ll \omega_{\mathrm{RO}}$) and oscillations can be observed. Figures 2.6(a) and (b) depict frequency ω_{RO} and damping Γ_{RO} of the ROs, respectively, for the four different band structures of Fig. 2.5. RO frequency and damping were calculated from the eigenvalues of the linearized dynamical equations.

The fast rates represent the class A limit of the QD equations. Here, the product of γF_b is of order one, and the time scale separation breaks down[2]. As a result, the time series of N_{ph} in Fig. 2.5(c) shows an overdamped, relaxation free turn-on behavior. From Fig. 2.6, it can be seen that for $J < 2.2 J_{\mathrm{th}}$ (J_{th} denotes the pump current at lasing threshold) ω_{RO} and Γ_{RO} are of the same order of magnitude, which makes oscillations impossible. For higher pump currents, the leading eigenvalue is real.

The typical QD laser represented by the reference set of rates lies in between the class A and the class B limit of the equations. A time scale separation still exists, but the RO damping is much higher while the RO frequency is nearly the same as for the slow rates (see Fig. 2.6). This results in strongly suppressed ROs, which are depicted in the time series of Fig. 2.5(b). Lingnau et al. studied RO frequency and damping of the shallow dot structure (energy differences of fast rates) by varying the lifetime of the electrons in the QDs (τ_e) while keeping the ratio of electron and hole lifetime fixed [LIN12, LUE13]. The authors observed that for the deep-dot structure, increasing the electronic lifetime from large values (corresponding to the slow rates) to smaller values first yields an increase of the RO damping. Then, the RO damping reaches a maximum, and eventually decays again. For the shallow-dot structure, the RO oscillations are completely damped out close to the maximum. Furthermore, the authors observed that

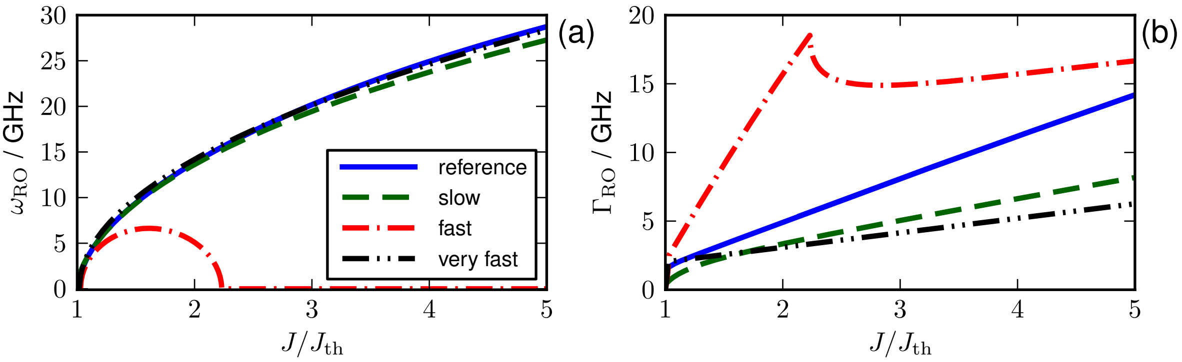

Figure 2.6.: Frequency ω_{RO} **(a)** and damping Γ_{RO} **(b)** of the RO oscillations versus the pump current J (normalized to the pump current at lasing threshold J_{th}) as obtained from the numerically calculated eigenvalues for the four different band structures studied in this work. Parameters as in Table 2.3.

---

[2] In the following, the Landau symbol $\mathcal{O}$ is frequently used to describe the scaling of a quantity, e.g., 'γF_b is of order one' may be written as $\gamma F_b = \mathcal{O}(1)$ [BEN10].

the maximum of the RO damping for the deep dot structure appears when $\omega_{\mathrm{RO}} \sim \tau_e^{-1}$. This corresponds to the observation that in the strongly damped regime, Γ_{RO} and ω_{RO} are of the same order of magnitude, because the analytical formula for the RO damping of the reference rates reveals that the dominant contribution of the RO damping rate is given by the inverse lifetimes of the slower species, i.e.,

$$\Gamma_{\mathrm{RO}} \sim \frac{\tau_e^{-1}}{2} \approx \frac{S_e^{\mathrm{in}}}{2}.$$

This analytic expression for the RO damping was derived in [LUE11] and will also be discussed in detail in Section 2.5.3. Generally, the electrons are slower than the holes, i.e., $\tau_e > \tau_h$, because the energetic distance between carrier reservoir and QD levels is larger for electrons due to their lower effective masses [MAJ10]. Thus, the dominant contribution to the RO damping is always given by the slower carrier type.

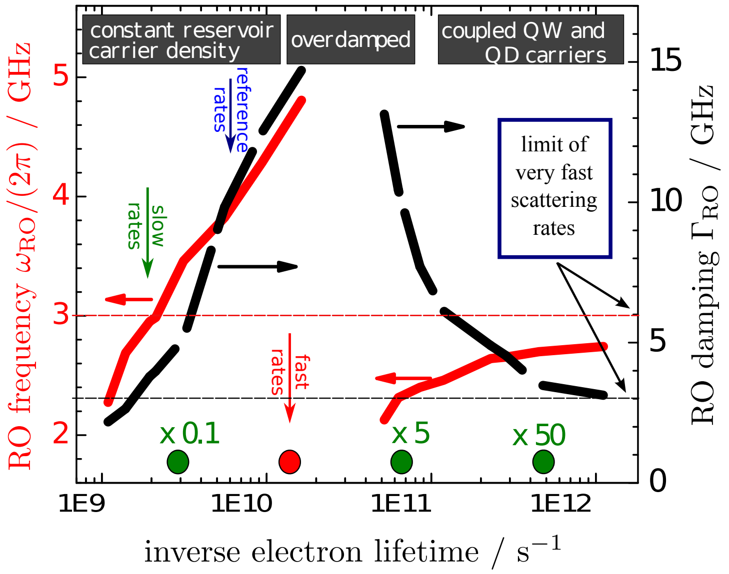

Figure 2.7: RO damping Γ^{RO} and RO frequency ω^{RO} of the QD laser with respect to the inverse electronic carrier lifetime τ_e^{-1}. Electron and hole lifetimes τ_e and τ_h have been varied by multiplying the in-scattering rates $S_{e/h}^{in}$ by constant factors. Black and red dashed lines label asymptotic values of ω_{RO} and Γ^{RO} in the limit of very fast scattering rates ($\tau_{e/h} \to 0$), respectively. Red, green, and blue arrows indicate the values of τ_e for the reference and the fast set of rates, respectively. Parameters: $j = 2 \cdot j_{\mathrm{th}}$ and other parameters as in Table 2.3. Modified from [LUE13].

In Fig. 2.7, RO damping Γ_{RO} (black dashed lines) and RO frequency ω_{RO} (red solid lines) of the shallow-dot QD laser (energy distances of fast set of scattering rates) are plotted with respect to the inverse electronic carrier lifetime τ_e^{-1}. The carrier lifetimes τ_e and τ_h have been varied by multiplying the in-scattering rate $S_{e/h}^{\mathrm{in}}$ with constant factors (indicated by green dots). Meanwhile, the pump current has been adapted to keep a fixed pump level of $J = 2J_{\mathrm{th}}$. The red dot and the red arrow denote the microscopically calculated scattering rates for the shallow dot structure, i.e., the fast set of scattering rates. It is located close to the maximum of the RO damping. Decreasing the scattering rates by multiplying with a factor smaller than unity, yields a strong decrease of the RO damping. Blue and green arrows indicate the inverse electronic lifetimes τ_e^{-1} as obtained from the deep dot structures of the reference rates and the slow rates, respectively. The RO damping decreases from the fast over the reference to the slow set of rates, as depicted in the time series of Figs. 2.5(a)–(c). Increasing the scattering rates by multiplying with a factor larger than unity, i.e., decreasing τ_e^{-1}, leads to a strong decrease of the RO damping, which results in a reappearance of the ROs. For very large values of the scattering rates, RO damping and RO frequency saturate to constant values denoted by the horizontal black dashed line and the horizontal red dashed line, respectively. The turn-on dynamics in the limit of very fast scattering rates is depicted in Fig. 2.5(d).

For slow, reference, and fast scattering rates, the reservoir populations W_e and W_h vary very little above lasing threshold. This can be seen in the time series of Fig. 2.5(a)–(c) (left column) as well as in the phase space projections onto to (W_e,N_{ph})-plane (right column). From the latter, it can be seen that during the turn-on oscillations, W_e remains close to its steady state value above threshold W_e^0. For not too large scattering rates, the reservoir is large enough to be hardly effected by the lasing process. Further, the middle column of Figs. 2.5(a) and (b) reveals that for the slow and the reference rates, the decay of W_e is faster than the decay of ρ_e, which expresses in a nearly vertical section at the end of the trajectory. In contrast, for the fast and very fast rates, ρ_b decay faster than W_b, which expresses in nearly horizontal segment at the end of the trajectory (see middle column of Figs. 2.5(c) and (d)).

In contrast to slow, reference, and fast rates, the variation of the reservoir populations are more pronounced in the limit of very fast scattering rates ($F_b \to \infty$) depicted in Fig. 2.5(d). The oscillations of W_e observed in the time series (left panel) express in a projection of the trajectory onto the (W_e,N_{ph})-plane in a spiraling motion towards the lasing fixed point, which is a stable focus (right panel). The reason is that the large scattering rates induce a carrier exchange fast enough for QD and reservoir carriers to be in quasi-equilibrium, which induces a strong coupling between reservoir and QD levels [LIN12]. The laser system may now be described by dynamical equations for the dynamical variables $N_b^+ \equiv \rho_b + W_b$, which are the sums of the carrier population in the QD levels and in the carrier reservoir. This is discussed in detail in Section 3.7.4. The resulting equations are structurally similar to class B laser equations with a clear time scale separation between the photon and the slow carrier subsystem expressed by the small parameter γ. These findings are consistent with those obtained for a three variable rate equation model for a QD laser in [ERN07a].

2.5. Analytic results

In the last section, it was discussed that the band structure of a QD laser has a strong impact on the damping of the ROs. In this section, analytical approximations of RO frequency and damping are introduced and compared to the corresponding expressions for a QW laser. Therefore, at first, a standard rate equation model for a conventional QW laser is discussed in Subsection 2.5.1. Then, in Subsection 2.5.2, the steady states of the QD laser are studied, before discussing the analytical expressions for RO frequency and damping in the limit of the reference and the slow sets of scattering rates (cf. Table 2.1) in Subsections 2.5.3 and 2.5.4, respectively. Furthermore, in Subsection 2.5.5 a reduced set of equations is derived that is valid in the limit of vanishing carrier lifetimes τ_e and τ_h, i.e., in the limit of very fast scattering rates. Expressions for RO frequency and damping are then derived from the reduced set of equations, and compared to the QW laser. Table 2.4 summarizes the main results of this section. The analytical expressions for frequency ω^{RO} and RO damping Γ^{RO} are expressed with respect to dimensionless

Table 2.4.: Analytic expressions for RO frequency ω^{RO} and RO damping Γ^{RO} with respect to dimensionless time $t' \equiv 2\kappa t$ as obtained for reference, slow, and very fast rates as well as for the QW laser, respectively.

rates/laser	RO frequency (ω^{RO})	RO damping (Γ^{RO})
reference	$\omega^{\mathrm{ref}} \equiv \sqrt{\gamma r_w N_{\mathrm{ph}}^0}$	$\Gamma^{\mathrm{ref}} \equiv \frac{\gamma}{2}\left[r_w N_{\mathrm{ph}}^0\left(\frac{t_h}{\gamma}+1\right)+t_e^{-1}+\rho_h^0\right]$
slow	$\omega^{\mathrm{S}} \equiv \sqrt{2\gamma r_w N_{\mathrm{ph}}^0}$	$\Gamma^{\mathrm{S}} \equiv \Gamma^{\mathrm{S,QW}}+\frac{\gamma}{2}\left[g^{-1}+\frac{(t_e^{-1}+t_h^{-1})}{2}\right]$ with $\Gamma^{\mathrm{S,QW}} \equiv \frac{\gamma}{2}(1+2r_w N_{\mathrm{ph}}^0)$
very fast	$\omega^{\mathrm{vf}} \equiv \sqrt{\gamma r_w N_{\mathrm{ph}}^0\left(\frac{2+z_e+z_h}{(1+z_e)(1+z_h)}\right)}$	$\Gamma^{\mathrm{vf}} \equiv \frac{\gamma r_w N_{\mathrm{ph}}^0}{2(1+z_e)(1+z_h)}\begin{bmatrix} 2+z_h+z_e \\ +\rho_h^0(1+z_h)+\rho_e^0(1+z_e) \\ +c\begin{bmatrix} W_e^0 z_h(1+z_e) \\ +W_h^0 z_e(1+z_h)\end{bmatrix}\end{bmatrix}$
QW laser	$\omega^{\mathrm{QW}} \equiv \sqrt{2\gamma^{\mathrm{QW}} r^{\mathrm{QW}} N_{\mathrm{ph}}^0}$	$\Gamma^{\mathrm{QW}} \equiv \gamma^{\mathrm{QW}}\frac{(1+2r^{\mathrm{QW}}N_{\mathrm{ph}}^0)}{2}$

time $t' = 2\kappa t$, which permits best to compare the expressions obtained for the reference rates (ω^{ref} and Γ^{ref}), for the slow rates (ω^{S} and Γ^{S}), the limit of very fast rates (ω^{vf} and Γ^{vf}), and for the QW model discussed in the next section (ω^{QW} and Γ^{QW}).

2.5.1. Quantum well laser

In this section, analytical expressions for RO frequency and damping for a rate equation model for a conventional, single-mode, class B QW laser model [MOR92, OTT11] are derived. The QW rate equations are given by

$$\frac{d\mathcal{E}}{dt} = \frac{1}{2}\left[G_n(n-n_{\mathrm{tr}})-\frac{1}{\tau_{\mathrm{ph}}}\right]\mathcal{E}, \tag{2.10a}$$

$$\frac{dn}{dt} = \frac{j}{e_0}-\frac{n}{\tau_c}-G_n(n-n_{\mathrm{tr}})(\mathcal{E})^2. \tag{2.10b}$$

Here, $\mathcal{E}$ is the slowly varying amplitude of the electrical field, which is normalized such that $\mathcal{E}^2 = N_{\mathrm{ph}}$, and n is the carrier density. The linear gain coefficient is denoted by G_N, n_{tr} is the transparency density of carriers, j is the pumping current density, e_0 the elementary charge, and τ_{ph} and τ_c are the photon and carrier lifetimes, respectively. Equating the left hand sides of Eqs. (2.10) to zero, the non-zero intensity steady state ($N_{\mathrm{ph}} \neq 0$) is

$$n^0 = n_{\mathrm{tr}}+\frac{1}{G_n\tau_{\mathrm{ph}}}, \tag{2.11}$$

$$(\mathcal{E}^0)^2 = \frac{1}{G_n(n^0-n_{\mathrm{tr}})}\left(\frac{j}{e_0}-\frac{n^0}{\tau_c}\right), \tag{2.12}$$

where the superscript $(\,\cdot\,)^0$ is used to mark steady state values. From the linearized equations, the characteristic equation for the growth rate $\tilde{\sigma}$ is the determined as

$$\tilde{\sigma}^2 + \left(\frac{1}{\tau_c} + G_n(\mathcal{E}^0)^2\right)\tilde{\sigma} + \frac{1}{\tau_{\mathrm{ph}}}G_n(\mathcal{E}^0)^2 = 0. \tag{2.13}$$

In order to properly define the RO frequency and its damping rate, we take advantage of the fact that $\tau_{\mathrm{ph}} << \tau_c$, i.e., that the photon subsystem is much faster than the one of the carriers. The roots of the quadratic equation then take the form

$$\tilde{\sigma} = -\Gamma_{\mathrm{RO}}^{\mathrm{QW}} \pm i\omega_{\mathrm{RO}}^{\mathrm{QW}}, \tag{2.14}$$

where

$$\Gamma_{\mathrm{RO}}^{\mathrm{QW}} \equiv \frac{1}{2}\left(\frac{1}{\tau_s} + G_n(\mathcal{E}^0)^2\right), \tag{2.15}$$

$$\omega_{\mathrm{RO}}^{\mathrm{QW}} \equiv \sqrt{\frac{G_n}{\tau_{\mathrm{ph}}}(\mathcal{E}^0)^2 - \left(\Gamma_{\mathrm{RO}}^{\mathrm{QW}}\right)^2} \approx \sqrt{\frac{G_n}{\tau_{\mathrm{ph}}}N_{\mathrm{ph}}^0} \tag{2.16}$$

are defined as the RO damping rate and RO frequency of the solitary laser, respectively. They are the main quantities of a laser that can be easily measured experimentally.

In order to determine asymptotic approximations, the rate equations have to be reformulated in dimensionless form. The simplest way is to measure time in units of the photon lifetime by introducing

$$t' \equiv t/\tau_{\mathrm{ph}}. \tag{2.17}$$

Furthermore, introducing the new dimensionless dependent inversion ρ_{inv} defined by

$$\rho_{\mathrm{inv}} \equiv \frac{1}{2}\left[G_n(n - n_{\mathrm{tr}})\tau_{\mathrm{ph}} - 1\right] \tag{2.18}$$

allows to reduce the number of parameters.

Inserting Eqs. (2.17) and (2.18) into Eqs. (2.10a) and (2.10b), yields

$$\frac{d\mathcal{E}}{dt'} = \rho_{\mathrm{inv}}\mathcal{E}, \tag{2.19a}$$

$$\frac{d\rho_{\mathrm{inv}}}{dt'} = \gamma^{\mathrm{QW}}\left[P - \rho_{\mathrm{inv}} - r^{\mathrm{QW}}(1 + 2\rho_{\mathrm{inv}})\mathcal{E}^2\right], \tag{2.19b}$$

where the time scale separation γ^{QW}, the pump P, and r^{QW}[3] are defined by

$$\gamma^{\mathrm{QW}} \equiv \frac{\tau_{\mathrm{ph}}}{\tau_c}, \; P \equiv \frac{G_n\tau_{\mathrm{ph}}\tau_c}{2e_0}(j - j_{\mathrm{th}}), \quad \text{where} \quad j_{\mathrm{th}} \equiv e_0\left(\frac{n_{\mathrm{tr}}}{\tau_c} + \frac{1}{G_n\tau_{\mathrm{ph}}\tau_c}\right)$$
$$\text{and} \quad r^{\mathrm{QW}} \equiv \frac{\tau_c G_n}{2}. \tag{2.20}$$

---

[3] Note that often in the literature (cf. [TAR95a, TAR98a, WIE05, ERN10b]) a rescaled field amplitude $R \equiv \sqrt{r^{\mathrm{QW}}}\mathcal{E}$ is introduced, such that the rescaled intensity $I \equiv R^2$ is of $\mathcal{O}(1)$. However, to compare the findings of this section with those derived for the QD model in the next sections, $\mathcal{E}^2 = N_{\mathrm{ph}}$ is used.

The non-zero intensity steady state is given by

$$\rho_{\mathrm{inv}}^0 = 0 \text{ and } N_{\mathrm{ph}}^0 \equiv (\mathcal{E}^0)^2 = P/r^{\mathrm{QW}}. \tag{2.21}$$

The rescaled inversion ρ_{inv}^0 is zero above lasing threshold, which is known as gain-clamping [PET91], and N_{ph}^0 increases linearly with the pump $P \sim j - j_{\mathrm{th}}$. The characteristic equation for the growth rate σ is given by

$$\sigma^2 + \gamma^{\mathrm{QW}}(1 + 2r^{\mathrm{QW}} N_{\mathrm{ph}}^0)\sigma + 2\gamma^{\mathrm{QW}} r^{\mathrm{QW}} N_{\mathrm{ph}}^0 = 0. \tag{2.22}$$

Provided γ^{QW} is sufficiently small, the roots of Eq. (2.22) are complex conjugate. The dimensionless RO damping rate and the RO frequency (in units of time t') are then defined from the imaginary and real part of these roots. We obtain

$$\Gamma^{\mathrm{QW}} \equiv \gamma^{\mathrm{QW}} \frac{(1 + 2r^{\mathrm{QW}} N_{\mathrm{ph}}^0)}{2} = \gamma^{\mathrm{QW}} \frac{(1+2P)}{2}, \tag{2.23a}$$

$$\omega^{\mathrm{QW}} \equiv \sqrt{2\gamma^{\mathrm{QW}} r^{\mathrm{QW}} N_{\mathrm{ph}}^0 - (\Gamma^{\mathrm{QW}})^2} \approx \sqrt{2\gamma^{\mathrm{QW}} r^{\mathrm{QW}} N_{\mathrm{ph}}^0} \text{ as } \gamma^{\mathrm{QW}} \to 0. \tag{2.23b}$$

Note that the RO damping scales like γ^{QW} and is thus much smaller than the RO frequency, which scales like $\sqrt{\gamma^{\mathrm{QW}}}$. This is the reason for the pronounced relaxation oscillations observed in class B lasers.

The same dimensionless time $t' \equiv t/\tau_{\mathrm{ph}}$ is used in the analysis of the QD rate equations of the solitary laser discussed in the remainder of this section as well as in the analysis of the QD laser under optical injection (Chapter 3) and the analysis of the QD laser subject to optical feedback (Chapter 4). Furthermore, the dynamic equations are formulated such that a small time scale separation parameter γ multiplies the right hand side of the carrier equations (cf. Eqs. (2.4)).

2.5.2. Steady states of solitary QD laser

Now, the solitary QD laser equations (2.4) are analyzed starting with the steady states. For the subsequent analysis, the spontaneous emission in the field equation (2.4) is neglected by setting $d = 0$. Equating to zero the right hand sides of Eqs. (2.4), yields the steady state relations

$$0 = \rho_{\mathrm{inv}}^0 N_{\mathrm{ph}}^0, \tag{2.24a}$$

$$0 = \gamma\Big[F_e(\rho_e^0, \rho_h^0, W_e^0, W_h^0) - r_w(\rho_e^0 + \rho_h^0 - 1)N_{\mathrm{ph}}^0 - \rho_e^0\rho_h^0\Big], \tag{2.24b}$$

$$0 = \gamma\Big[F_h(\rho_e^0, \rho_h^0, W_e^0, W_h^0) - r_w(\rho_e^0 + \rho_h^0 - 1)N_{\mathrm{ph}}^0 - \rho_e^0\rho_h^0\Big], \tag{2.24c}$$

$$0 = \gamma\Big[J - F_e(\rho_e^0, \rho_h^0, W_e^0, W_h^0) - cW_e^0 W_h^0\Big], \tag{2.24d}$$

$$0 = \gamma\Big[J - F_h(\rho_e^0, \rho_h^0, W_e^0, W_h^0) - cW_e^0 W_h^0\Big], \tag{2.24e}$$

where steady state values of dynamical variables are denoted by superscript $(\,\cdot\,)^0$. Equation (3.18) shows that above threshold ($N_{\mathrm{ph}} \neq 0$) the inversion is clamped to zero

$$\rho_{\mathrm{inv}}^0 \equiv \frac{1}{2}\left[g(\rho_e^0 + \rho_h^0 - 1) - 1\right] = 0, \tag{2.25}$$

which is known as gain-clamping [TAR95a]. Next, the steady state of the photon number may be expressed in terms of the carrier populations and the pump current, by inserting Eq. (2.24d) into Eq. (2.24b)

$$N_{\mathrm{ph}}^0 = \frac{g}{r_w}\left(J - cW_e^0 W_h^0 - \rho_e^0\rho_h^0\right) \approx \frac{g}{r_w}\left(J - J_{\mathrm{th}}\right) = \frac{g}{r_w}\left(\frac{J}{J_{\mathrm{th}}} - 1\right) J_{\mathrm{th}}. \tag{2.26}$$

Here, the gain-clamping of Eq. (2.25) has been used to write $\rho_e^0 + \rho_h^0 - 1 = g^{-1}$. The approximation in the last equality of Eq. (2.26) is based on the assumption that the product of the carrier densities does not vary significantly above threshold, which permits to introduce the threshold current of the solitary laser as

$$J_{\mathrm{th}} \equiv cW_e^{\mathrm{th}} W_h^{\mathrm{th}} - \rho_e^{\mathrm{th}}\rho_h^{\mathrm{th}}, \tag{2.27}$$

where quantities with superscript $(\,\cdot\,)^{\mathrm{th}}$ are taken at the lasing threshold of the solitary laser. Equation (2.26) expresses the linear increase of the photon number with the current observed above threshold [COL95, HAK83a].

Further, with the help of the carrier conservation relation of Eq. (2.9), expressions of ρ_e^0 and ρ_h^0 in terms of the reservoir populations W_e^0 and W_h^0 are obtained from Eq. (2.25), which read

$$\rho_e^0 = \frac{1}{2}\left[\frac{1+g}{g} + W_h^0 - W_e^0\right] \quad \text{and} \quad \rho_h^0 = \frac{1}{2}\left[\frac{1+g}{g} - W_h^0 + W_e^0\right]. \tag{2.28}$$

Eventually, the steady states of the reservoir populations W_e^0 and W_h^0 can be calculated by inserting Eqs. (3.31) into Eqs. (2.24d) and (2.24e), and the solving self-consistently for W_e^0 and W_h^0. This has to be done numerically, because F_e and F_h are nonlinear functions of W_e^0 and W_h^0 (see Eqs. (2.6)).

2.5.3. QD laser – RO frequency and damping for the reference rates

In the limit of the reference and the slow set of scattering rates (cf. Table 2.1), analytical expression for RO frequency and damping of the QD laser have been derived by Lüdge et al. in Ref. [LUE11]. In this and the next subsection, the resulting expression are discussed for the slow and the reference rates, respectively. The asymptotic methods needed to derive these expression are introduced in Section 3.6 of Chapter 3, and eventually the formulas for RO damping and frequency (cf. Table 2.4) are retrieved from the eigenvalues of the laser under optical injection in Section 3.8.

With respect to the dimensionless time $t' \equiv (2\kappa)^{-1}t$, RO frequency and damping of the solitary laser are given for the set of reference scattering rates by

$$\omega^{\mathrm{ref}} \equiv \sqrt{\gamma r_w N_{\mathrm{ph}}^0} \approx \sqrt{\gamma g (J - J_{\mathrm{th}})} \quad \text{and} \tag{2.29a}$$

$$\begin{aligned} \Gamma^{\mathrm{ref}} &\equiv \frac{\gamma}{2}\left[r_w N_{\mathrm{ph}}^0 \left(\frac{t_h}{\gamma} + 1\right) + t_e^{-1} + \rho_h^0\right] \\ &\approx \frac{\gamma}{2}\left[g(J - J_{\mathrm{th}})\left(\frac{t_h}{\gamma} + 1\right) + t_e^{-1} + \rho_h^0\right], \end{aligned} \tag{2.29b}$$

respectively. In the approximations of Eqs. (2.29), a linear dependence of N^0_{ph} on the pump current was assumed (see Eq. (2.26)). Eventually, we obtain for the RO frequency $\omega^{\mathrm{ref}}_{\mathrm{RO}} \equiv 2\kappa\omega^{\mathrm{ref}}$ and damping $\Gamma^{\mathrm{ref}}_{\mathrm{RO}} \equiv 2\kappa\Gamma^{\mathrm{ref}}$ in terms of physical time t

$$\omega^{\mathrm{ref}}_{\mathrm{RO}} = 2\kappa\sqrt{\gamma r_w N^0_{\mathrm{ph}}} \approx 2\kappa\sqrt{\gamma g(J - J_{\mathrm{th}})}, \tag{2.30a}$$

$$\begin{aligned}\Gamma^{\mathrm{ref}}_{\mathrm{RO}} &= \kappa\gamma\left[2r_w N^0_{\mathrm{ph}}\left(\frac{W\tau_h}{\gamma} + \frac{1}{2}\right) + \frac{1}{W\tau_e} + \rho^0_h\right] \\ &\approx \kappa\gamma\left[2g(J - J_{\mathrm{th}})\left(\frac{W\tau_h}{\gamma} + \frac{1}{2}\right) + \frac{1}{W\tau_e} + \rho^0_h\right].\end{aligned} \tag{2.30b}$$

Figures 2.8**(a)** and **(b)** depict RO frequency and damping as obtained from the numerically calculated eigenvalues of the full system (full black lines) and from the analytical approximations (2.30) (blue dashed lines). The RO frequency clearly shows the square-root like scaling with the pump current as predicted by Eq. (2.30a), and $\Gamma^{\mathrm{ref}}_{\mathrm{RO}}$ scales in very good approximation linearly with the pump current. Further, for low pump currents, the $\kappa\gamma/(W\tau_e)$-term (green dashed line in Fig. 2.8(b)) constitutes the dominant contribution to the RO damping. This permits to conclude that for low pump currents the slower carrier type, i.e., the electrons, dominate the turn-on damping [LUE11], while, for pump currents high above threshold, the first two terms in the rectangular brackets of Eq. (2.30b) become more important. Next, the expression (2.29a) for the RO frequency of the QD laser is compared to the corresponding expression (2.23b) for the QW laser. It can be seen that the RO frequency of the QD laser is by a factor $1/\sqrt{2}$ lower than for the QW laser if for QD and QW the same time scale separation ($\gamma^{\mathrm{QW}} = \gamma$), the same ratio of the Einstein factors ($r^{\mathrm{QW}} = r_w$), and the same steady state photon number N^0_{ph} are assumed.

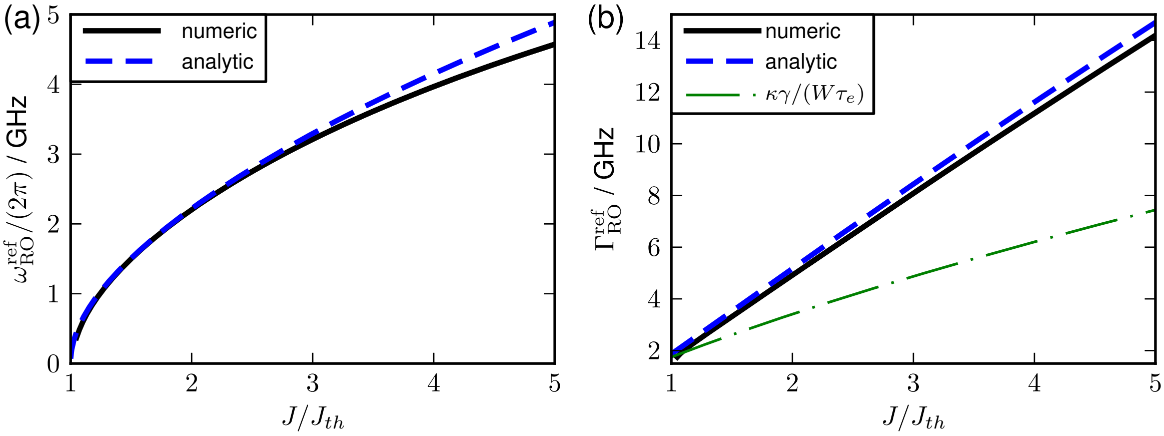

Figure 2.8.: Comparison of RO frequency $\omega^{\mathrm{ref}}_{\mathrm{RO}}$ **(a)** and RO damping $\Gamma^{\mathrm{ref}}_{\mathrm{RO}}$ **(b)** calculated numerically from the eigenvalues of the full system (black solid lines) with their analytical approximations of Eqs. (2.30a) and (2.30b) (blue dashed lines). The thin dash-dotted green line marks the dominant contribution $\kappa\gamma/(W\tau_e)$ of the RO damping. Parameters: reference rates and other parameters as in Table 2.3.

2.5.4. QD laser – RO frequency and damping for the slow rates

For the slow set of scattering rates of Table 2.1, RO frequency and damping read in units of time $t' = (2\kappa)^{-1}t$

$$\omega^{\mathrm{S}} \equiv \sqrt{2\gamma r_w N^0_{\mathrm{ph}}} \approx \sqrt{2\gamma g(J - J_{\mathrm{th}})}, \tag{2.31a}$$

$$\Gamma^{\mathrm{S}} \equiv \Gamma^{\mathrm{S,QW}} + \frac{\gamma}{2}\left[g^{-1} + \frac{(t_e^{-1} + t_h^{-1})}{2}\right], \tag{2.31b}$$

where we have introduced

$$\Gamma^{\mathrm{S,QW}} \equiv \frac{\gamma}{2}(1 + 2r_w N^0_{\mathrm{ph}}) \approx \frac{\gamma}{2}\left[1 + 2g(J - J_{\mathrm{th}})\right], \tag{2.32}$$

The contribution $\Gamma^{\mathrm{S,QW}}$ corresponds to the RO damping of the QW laser (cf. Eq. (2.23a)) for $\gamma^{\mathrm{QW}} = \gamma$ and $r^{\mathrm{QW}} = r_w$. Furthermore, the linear dependence of $N^0_{\mathrm{ph}} \approx g/(r_w)(J - J_{\mathrm{th}})$ on the pump current J (see Eq. (2.26)) was used. Finally, in units of the physical time $t = 2\kappa t'$ the damping rate reads

$$\omega^{\mathrm{S}}_{\mathrm{RO}} \equiv 2\kappa\sqrt{2\gamma r_w N^0_{\mathrm{ph}}} \approx 2\kappa\sqrt{2\gamma g(J - J_{\mathrm{th}})}, \tag{2.33a}$$

$$\Gamma^{\mathrm{S}}_{\mathrm{RO}} \equiv \Gamma^{\mathrm{S,QW}}_{\mathrm{RO}} + \kappa\gamma\left[g^{-1} + \frac{1}{W}\left(\frac{\tau_e^{-1} + \tau_h{-1}}{2}\right)\right], \tag{2.33b}$$

where the QW contribution to the damping rate $\Gamma^{\mathrm{S,QW}}_{\mathrm{RO}}$ is given by

$$\Gamma^{\mathrm{S,QW}}_{\mathrm{RO}} \equiv \kappa\gamma\left[1 + 2r_w N^0_{\mathrm{ph}}\right] \approx \kappa\gamma\left[1 + 2g(J - J_{\mathrm{th}})\right]. \tag{2.34}$$

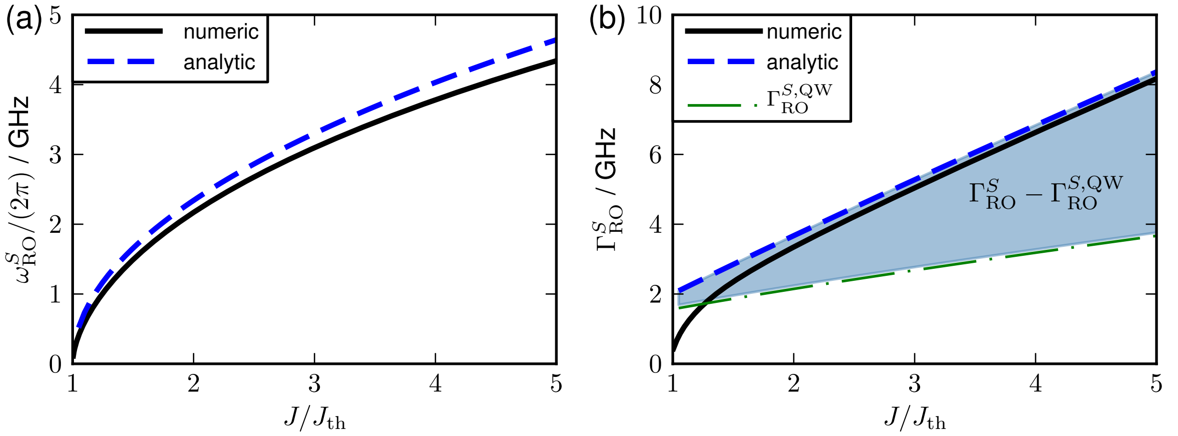

Figure 2.9.: Comparison of RO frequency $\omega^{\mathrm{S}}_{\mathrm{RO}}$ **(a)** and RO damping $\Gamma^{\mathrm{S}}_{\mathrm{RO}}$ **(b)** as obtained numerically form the eigenvalues of the full system (black lines) with their analytical approximations of Eqs. (2.33a) and (2.33b) (blue dash dotted lines). The QW contribution $\Gamma^{\mathrm{S,QW}}_{\mathrm{RO}}$ of Eq. (2.34) is marked by a green dash-dotted line, and the blue shaded region marks the difference of $\Gamma^{\mathrm{S}}_{\mathrm{RO}}$ and $\Gamma^{\mathrm{S,QW}}_{\mathrm{RO}}$. Parameters: slow rates and other parameters as in Table 2.3.

Figures 2.9**(a)** and **(b)** depict RO frequency and damping as obtained from the eigenvalues of the full system (full black lines) and from the analytical approximations (2.33) (dashed blue lines), respectively. As in the limit of the reference rates, the RO frequency clearly shows the square-root like scaling with the pump current as predicted by Eq. (2.33a). The RO damping $\Gamma_{\mathrm{RO}}^{\mathrm{S}}$ (see Eq. (2.33b)) scales for $J \gtrsim 2J_{\mathrm{th}}$ linearly with the pump current. For the QW contribution $\Gamma_{\mathrm{RO}}^{\mathrm{S,QW}}$, this can be seen directly from Eq. (2.34), and the term in the rectangular brackets in Eq. (2.33b) scales nearly linearly with the pump current, because the constant term proportional to g^{-1} is negligible, and the inverse carrier lifetimes τ_e^{-1} and τ_h^{-1} increase nearly linearly with J. To see this, note that for the slow set of scattering rates, the in- and out-scattering rates $S_{e/h}^{\mathrm{in/out}}$ for both, electrons and holes, are similar to the electronic scattering rates for the reference set of rates. The latter are depicted in Fig. 2.2(a) and (b), respectively. From Fig. 2.2(b), we see that the out-scattering rates are negligible, which yields $\tau_{e,h}^{-1} \approx S_{e/h}^{in}$, and from Fig. 2.2(a), we note that well above threshold, i.e., to the right of the gray dashed line denoting the steady state of w_e for $J = 1.5J_{\mathrm{th}}$, the in-scattering rates scale nearly linearly with the pump current.

The RO frequency is exactly the same as for a QW laser (cf. Eq. (2.23b)) with the same time scale separation ($\gamma^{\mathrm{QW}} = \gamma$) and the same ratio of the Einstein factors ($r^{\mathrm{QW}} = r_w$). It would thus be by a factor $\sqrt{2}$ higher than in the limit of the reference rates (see Eq. (2.30b)) if both lasers had the same steady state photon number N_{ph}^0 at the same pump level J/J_{th} (see last equality in Eq. (2.26)). However, comparing the pump dependence of $\omega_{\mathrm{RO}}^{\mathrm{S}}$ in Fig. 2.9(a) with the pump dependence of $\omega_{\mathrm{RO}}^{\mathrm{ref}}$ in Fig. 2.8, we see that the higher photon number in the case of the reference rates overcompensates the factor $\sqrt{2}$, and consequently, $\omega_{\mathrm{RO}}^{\mathrm{ref}}$ is even slightly higher than $\omega_{\mathrm{RO}}^{\mathrm{S}}$.

As already discussed in the introductory Section 2.2, the damping is much higher in the limit of the reference rates than in the limit of the slow rates, which may be seen by comparing Fig. 2.8(b) with Fig. 2.9(b). The formula (2.33b) for the damping of the slow rates contains two contributions. The first term $\Gamma_{\mathrm{RO}}^{\mathrm{S,QW}}$ corresponds to the damping rate of a QW laser having the same time scale separation ($\gamma^{\mathrm{QW}} = \gamma$), the same ratio of the Einstein factors ($r^{\mathrm{QW}} = r_w$), and the same steady state photon number (see Eq. (2.23a)). The second term contains the contribution of the carrier lifetimes τ_e and τ_h in the QD levels and thus describes the impact of the band structure on the RO damping. Since electron and hole lifetimes are similar for the set of slow rates (see Table 2.1), they enter symmetrically into the expression (2.33b). Further, from Table 2.1, it can be seen that τ_e and τ_h are now similar to the electronic lifetime in the limit of the reference rates. This is why they contribute in the same way to $\Gamma_{\mathrm{RO}}^{\mathrm{S}}$ (see Eq. (2.33b)) than the electronic lifetime τ_e contributes to $\Gamma_{\mathrm{RO}}^{\mathrm{ref}}$ (see Eq. (2.30b)). The bluish shaded region in Fig. 2.9 marks the difference between the full damping rate $\Gamma_{\mathrm{RO}}^{\mathrm{S}}$ and its QW contribution $\Gamma_{\mathrm{RO}}^{\mathrm{S,QW}}$. Thus, it describes the impact of the band structure. The difference increases with the pump current, because τ_e^{-1} and τ_h^{-1} increase faster with the pump current (cf. Fig. 2.3) than the steady state of the photon number N_{ph}^0.

2.5.5. QD laser – limit of very fast scattering rates

The limit of very fast scattering rates is described by the limit $F_b \to \infty$ ($b = e$ for electrons and $b = h$ for holes) of the dynamical equations (2.4). In this regime, the carrier lifetimes τ_b in the QD levels vanish, and the carrier exchange is fast enough to ensure that QDs and carrier reservoir remain in quasi-equilibrium during the turn-on process. This results in an enhanced coupling between reservoir and QD variables, which is best taken into account by introducing the new variables N_b^+ and N_b^-

$$N_b^+ \equiv \rho_b + W_b \quad \text{and} \quad N_b^- \equiv \rho_b - W_b. \tag{2.35}$$

Rewriting ρ_b and W_b in terms of the new variables, yields

$$\rho_b = \frac{N_b^+ + N_b^-}{2} \quad \text{and} \quad W_b = \frac{N_b^+ - N_b^-}{2}. \tag{2.36}$$

Further, for the subsequent analysis, it is convenient that the dynamical variables are all $\mathcal{O}(1)$, which simplifies their comparison to the small parameter γ describing the time scale separation. Therefore, we rescale the photon number N_{ph}[4] with respect to its steady state value N_{ph}^0 (see Eq. (2.26)) by introducing $N_{\text{ph}} = N_{\text{ph}}^0 R^2$, where R is $\mathcal{O}(1)$. The dynamical equations (2.4) then read in the new coordinates

$$R' = \rho_{\text{inv}} R, \tag{2.37a}$$

$$(N_e^+)' = (N_h^+)' = \gamma\Big[J - r_{\text{ph}}(\rho_e + \rho_h - 1)R^2 - \rho_e\rho_h - cW_eW_h\Big], \tag{2.37b}$$

$$(N_e^-)' = \gamma\Big[-J + 2F_e - r_{\text{ph}}(\rho_e + \rho_h - 1)R^2 - \rho_e\rho_h + cW_eW_h\Big], \tag{2.37c}$$

$$(N_h^-)' = \gamma\Big[-J + 2F_h - r_{\text{ph}}(\rho_e + \rho_h - 1)R^2 - \rho_e\rho_h + cW_eW_h\Big], \tag{2.37d}$$

where $r_{\text{ph}} \equiv r_w N_{\text{ph}}^0$ has been introduced. Due to the carrier conservation (2.8), which reads in these coordinates as $(N_e^+)' = (N_h^+)'$, the dynamical variables N_e^+ and N_h^+ have the same dynamics, and additionally one carrier variable may be eliminated, i.e, expressed in terms of the others. For the set of very fast scattering rates, we may assume that the terms $F_b \equiv s_b^{\text{in}} - (s_b^{\text{in}} + s_b^{\text{out}})\rho_b$ expressing the impact of the Coulomb scattering rates are at least $\mathcal{O}(\gamma^{-2})$ large, which justifies an adiabatic elimination of N_e^- and N_h^-, i.e, to assume $(N_e^-)' = (N_h^-)' = 0$. Equating to zero the right hand sides of Eqs. (2.37c) and (2.37d), and employing the definitions of the F_b's, the QD populations can be expressed as

$$\rho_b = s_b^{\text{in}} t_b - \frac{t_b}{2}\{J + r_{\text{ph}}(\rho_e + \rho_h - 1)R^2 + \rho_e\rho_h - cW_eW_h\},$$

where we have used the dimensionless carrier lifetimes $t_b \equiv (s_b^{\text{in}} + s_b^{\text{out}})^{-1}$, which are at least $\mathcal{O}(\gamma^2)$ small. Since the terms in the curly brackets are all $\mathcal{O}(1)$, they constitute only a small correction to the first term, and the above equation can be written as

$$\rho_b = t_b s_b^{\text{in}} + \mathcal{O}(\gamma^2). \tag{2.38}$$

In- and out-scattering rates are related by the detailed balance relation (2.2) [LUE09], which reads in its dimensionless form (see also Appendix A)

$$s_b^{\text{out}} = s_b^{\text{in}} e^{-\frac{\Delta E_b}{k_{\text{bo}} T}} \left[e^{c_b W_b} - 1\right]^{-1}, \tag{2.39}$$

---

[4] Typically, $N_{\text{ph}} = \mathcal{O}(10^4)$, which implies that the product of $r_w N_{\text{ph}}^0$ is a $\mathcal{O}(1)$.

where the coefficients $c_b \equiv 2N^{\mathrm{QD}}/(D_b k_{\mathrm{bo}}\mathcal{T})$ were introduced. Inserting Eq. (2.39) into Eq. (2.38), the ρ_b's can be expressed in terms of the reservoir populations W_b as

$$\rho_b(W_b) = t_b s_b^{\mathrm{in}} = \frac{1}{1 + s_b^{\mathrm{out}}/s_b^{\mathrm{in}}} = \left(1 + e^{-\frac{\Delta E_b}{k_{\mathrm{bo}}\mathcal{T}}}\left[e^{c_b W_b} - 1\right]^{-1}\right)^{-1}, \tag{2.40}$$

which is valid up to $\mathcal{O}(\gamma^2)$. From the above formula, we see that in leading order ρ_e is only a function of W_e, and that the same holds for the holes. Thus, the coupling to the other carrier type is at least $\mathcal{O}(\gamma^2)$ small, and may be neglected. This permits to express the reservoir populations W_b in terms of ρ_b by inverting Eq. (2.40)

$$W_b(\rho_b) = \frac{1}{c_b}\ln\left(1 + e^{-\frac{\Delta E_b}{k_{\mathrm{bo}}\mathcal{T}}}\frac{\rho_b}{1-\rho_b}\right). \tag{2.41}$$

Instead of expressing the right hand sides of the dynamical equations (2.37a) and (2.37b) in terms of the $N_b^{\pm}$s, we can use Eq. (2.41) to write $N_e^+ = \rho_e + W_e(\rho_e)$ as a function of ρ_e. This permits to formulate the right hand side of Eq. (2.37b) as

$$(N_e^+)' = \frac{d}{dt'}\left(\rho_e + W_e(\rho_e)\right) = (1 + \partial_{\rho_e} W_e)\rho_e'. \tag{2.42}$$

Employing the above equation, the dynamical equations (2.4) simplify in the limit of very large scattering rates ($F_b \to \infty$) as

$$R' = \rho_{\mathrm{inv}} R, \tag{2.43a}$$

$$\rho_e' = \frac{\gamma}{1+z_e}\left[J - r_{\mathrm{ph}}(\rho_e + \rho_h - 1)R^2 - \rho_e\rho_h - cW_eW_h\right], \tag{2.43b}$$

where the abbreviations

$$z_b \equiv \partial_{\rho_b}\big|_{\rho_b^0} W_b = \left[c_b(1-\rho_b)\left(e^{\frac{\Delta E_b}{k_{\mathrm{bo}}\mathcal{T}}}(1-\rho_b) + \rho_b\right)\right]^{-1} \tag{2.44}$$

have been introduced. In Eqs. (2.43) the hole populations ρ_h and $W_h(\rho_h)$ are functions of ρ_e. For a given value of ρ_e, the electronic population in the reservoir W_e can be calculated from Eq. (2.41) for $b = e$. Furthermore, the occupation probability of the hole level ρ_h can be calculated by inserting Eq. (2.41) for $b = h$ into the carrier conservation (2.9), which yields

$$\rho_h + W_h(\rho_h) = \rho_e + W_e(\rho_e). \tag{2.45}$$

The above equation can then be solved for ρ_h, and eventually, W_h can be calculated from Eq. (2.41) for $b = h$.

The dynamical equations (2.43) describe a typical slow-fast system consisting of a fast optical subsystem (Eq. (2.43a)) and a slow carrier subsystem (Eq. (2.43b)). The time scale separation is expressed by the small parameter γ. (Note that z_e and the terms in the brackets in Eq. (2.43b) are all $\mathcal{O}(1)$.) Thus, from Eqs. (2.43), we would expect the turn-on dynamics of the QD laser to be similar to the one of a class B QW laser. That this is actually the case can be seen from the time series in Fig. 2.5(d), which shows pronounced, weakly damped ROs that are typical for class B QW lasers.

In the remainder of this section, at first, the steady states of Eqs. (2.43) are discussed, and then analytical expression for frequency and damping of the ROs are derived.

Steady states

The steady states are calculated from Eqs. (2.43) by equating to zero their right hand sides, which yields

$$0 = \rho_{\text{inv}} R^0, \tag{2.46a}$$

$$0 = \frac{\gamma}{1+z_e}\left[J - r_{\text{ph}}(\rho_e + \rho_h - 1)\left(R^0\right)^2 - \rho_e\rho_h - cW_eW_h\right]. \tag{2.46b}$$

By definition, the steady state of R above leasing threshold is given by $R^0 = 1$. Since the optical steady state equation (2.46a) is the same as for the full system (see Eq. (2.4a)) with R^0 replaced by N^0_{ph}, the gain-clamping relation $\rho^0_{\text{inv}} = 0$ remains valid (see Eq. (2.25)). From the carrier Eq. (2.46b), we then see that also the expression (2.26) for N^0_{ph} as a function of the carrier populations remains valid. The steady state ρ^0_e of ρ_e may be obtained by at first calculating the steady state ρ^0_h of ρ_h as a function of ρ^0_e from Eq. (2.45), inserting then the resulting expression for $\rho^0_h = \rho_h(\rho^0_e)$ into Eq. (2.25), and then solving for ρ^0_e. Subsequently, ρ^0_h is calculated by inserting ρ^0_e back into Eq. (2.45), and eventually, the steady states of the reservoir populations W^0_e and W^0_h can be calculated from Eqs. (2.41).

RO frequency and damping in the limit of very fast scattering rates

For the linearization of the dynamical equations (2.43), the partial derivatives of ρ_h and W_h with respect to ρ_e have to be calculated. Employing the carrier conservation relation (2.45), they can be calculated as

$$\partial_{\rho_e}\big|_{\rho^0_e}\rho_h = \partial_{\rho_e}\big|_{\rho^0_e}(\rho_e + W_e - W_h) = 1 + z_e - (\partial_{\rho_e}\big|_{\rho^0_e}\rho_h)z_h$$

$$\Leftrightarrow \quad \partial_{\rho_e}\big|_{\rho^0_e}\rho_h = \frac{1+z_e}{1+z_h}, \tag{2.47a}$$

$$\partial_{\rho_e}\big|_{\rho^0_e}W_h = z_h\frac{1+z_e}{1+z_h}, \tag{2.47b}$$

where the derivative has been taken at the steady state value ρ^0_e of the solitary laser. Linearizing Eqs. (2.43) around the lasing steady state $(N^0_{\text{ph}}, \rho^0_e)$, yields the following characteristic equations for the growth rate σ

$$\det\begin{bmatrix} -\sigma & \frac{gR^0}{2}\left(1 + \frac{1+z_e}{1+z_h}\right) \\ -\frac{\gamma 2 r_{\text{ph}} R^0}{(1+z_e)g} & -\gamma\begin{bmatrix} r_{\text{ph}}(R^0)^2\left(\frac{1}{1+z_e} + \frac{1}{1+z_h}\right) \\ +\frac{\rho^0_h}{1+z_e} + \frac{\rho^0_e}{1+z_h} + c\left(\frac{W^0_e z_h}{1+z_h} + \frac{W^0_h z_e}{1+z_e}\right)\end{bmatrix} - \sigma \end{bmatrix} = 0, \tag{2.48}$$

where the gain-clamping $\rho^0_{\text{inv}} = 0$ has been used. Solving for σ, yields two complex conjugate solutions

$$\sigma_\pm = -\gamma\Gamma^{\text{vf}}_1 \pm i\sqrt{\gamma r_{\text{ph}}(R^0)^2\frac{c_z}{1+z_e} - \gamma^2(\Gamma^{\text{vf}}_1)^2} = -\gamma\Gamma^{\text{vf}}_1 \pm i\sqrt{\gamma}\,\omega^{\text{vf}}_{1/2} + \mathcal{O}(\gamma^2), \tag{2.49}$$

where we have introduced

$$c_z \equiv \left(1 + \frac{1+z_e}{1+z_h}\right) \tag{2.50}$$

as well as

$$\Gamma_1^{\mathrm{vf}} \equiv \frac{1}{2}\left[\frac{r_w N_{\mathrm{ph}}^0}{(1+z_e)(1+z_h)}\begin{pmatrix} 2+z_h+z_e+\rho_h^0(1+z_h)+\rho_e^0(1+z_e) \\ +c\left(W_e^0 z_h(1+z_e)+W_h^0 z_e(1+z_h)\right)\end{pmatrix}\right], \tag{2.51a}$$

$$\omega_{1/2}^{\mathrm{vf}} \equiv \sqrt{r_{\mathrm{ph}}(R^0)^2\frac{c_z}{1+z_e}} = \sqrt{r_w N_{\mathrm{ph}}^0\left(\frac{2+z_e+z_h}{(1+z_e)(1+z_h)}\right)}. \tag{2.51b}$$

Damping and frequency of the ROs are then given in terms of the dimensionless time t' by

$$\Gamma^{\mathrm{vf}} \equiv \gamma\Gamma_1^{\mathrm{vf}} \quad \text{and} \quad \omega^{\mathrm{vf}} \equiv \sqrt{\gamma}\omega_{1/2}^{\mathrm{vf}}, \tag{2.52}$$

respectively. In terms of the physical time t, RO damping and frequency read[5]

$$\Gamma_{\mathrm{RO}}^{\mathrm{vf}} \equiv \kappa\gamma\left[\frac{(\bar{W}/W)N_{\mathrm{ph}}^0}{(1+z_e)(1+z_h)}\begin{pmatrix} 2+z_h+z_e+\rho_h^0(1+z_h)+\rho_e^0(1+z_e) \\ +\frac{B^S 2N^{\mathrm{QD}}}{W}\left(W_e^0 z_h(1+z_e)+W_h^0 z_e(1+z_h)\right)\end{pmatrix}\right], \tag{2.53a}$$

$$\omega_{\mathrm{RO}}^{\mathrm{vf}} \equiv 2\kappa\sqrt{\gamma(\bar{W}/W)N_{\mathrm{ph}}^0\left(\frac{2+z_e+z_h}{(1+z_e)(1+z_h)}\right)}, \tag{2.53b}$$

where z_b is given as a function of the carrier densities in the reservoir w_b:

$$z_b = \partial_{\rho_b}\big|_{\rho_e^0} W_b = \frac{1}{2N^{\mathrm{QD}}}\partial_{\rho_b}\big|_{\rho_e^0} w_b.$$

Note that the damping scales like γ and is thus small compared to the frequency, which

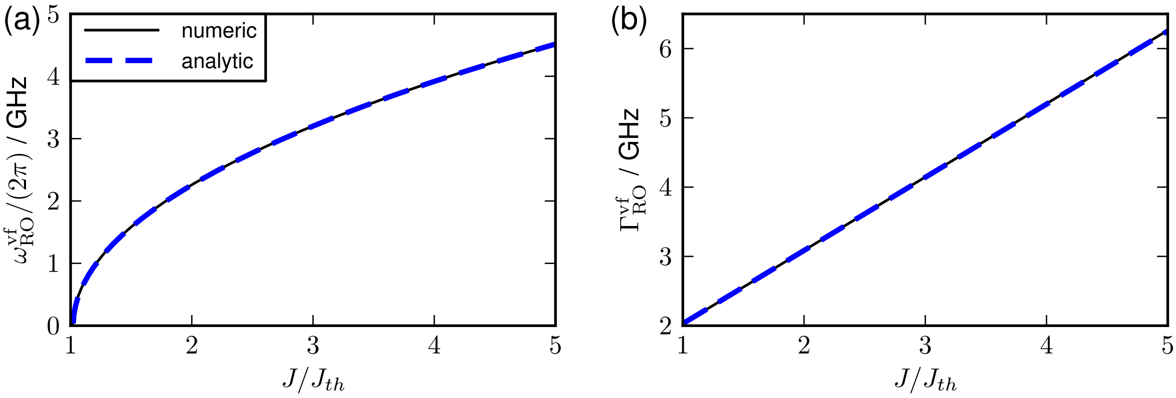

Figure 2.10.: Comparison of RO frequency $\omega_{\mathrm{RO}}^{\mathrm{S}}$ **(a)** and RO damping $\Gamma_{\mathrm{RO}}^{\mathrm{S}}$ **(b)** as obtained numerically form the eigenvalues of the full system (black lines) with their analytical approximations of Eqs. (2.53) (blue dash dotted lines). Parameters: Very fast scattering rates and other parameters as in Table 2.3.

scales like $\sqrt{\gamma}$. This is well known from class B semiconductor lasers [ERN10b] (see also

---

[5] Note that $\Gamma_{\mathrm{RO}}^{\mathrm{vf}}$ and $\omega_{\mathrm{RO}}^{\mathrm{vf}}$ are given by $\Gamma_{\mathrm{RO}}^{\mathrm{vf}} = 2\kappa\gamma\Gamma_1^{\mathrm{vf}}$ and $\omega_{\mathrm{RO}}^{\mathrm{vf}} = 2\kappa\sqrt{\gamma}\omega_{1/2}^{\mathrm{vf}}$, respectively.

Section 2.5.1). In Figure 2.10, RO frequencies (Fig. 2.10(a)) and damping (Fig. 2.10(b)) obtained numerically from the eigenvalues of the full equations (3.12) (solid black lines) are compared to the analytical approximations of Eqs. (2.53) (blue dashed lines). The analytical approximation agree perfectly with the numerical results. The square-root like increase of $\omega_{\mathrm{RO}}^{\mathrm{vf}}$ and the linear increase of $\Gamma_{\mathrm{RO}}^{\mathrm{vf}}$ with the pump current can be attributed to the linear dependence of N_{ph}^{0} on the pump current (see Eq. (2.26)).

Comparison to QW laser

Next, the expressions for RO damping and frequency of Eqs. (2.52) are compared to the expressions obtained for the standard rate equation model for a class B laser derived in Section 2.5.1 (see Eqs. (2.23)). The limit of $z_e \to 0$ of Eqs. (2.52) corresponds to a decoupling of the QD levels from the carrier reservoir $\omega^{\mathrm{vf}} \to \omega^{\mathrm{QW}}$. If we additionally assume that both lasers have the same time scale separation ($\gamma^{\mathrm{QW}} = \gamma$), the same ratio of the Einstein factors of spontaneous and induced emission ($r^{\mathrm{QW}} = r_w$), and the same steady state photon number N_{ph}^{0}, the RO frequency of the QD laser converges to the one of the QW laser $\omega^{\mathrm{vf}} \to \omega^{\mathrm{QW}}$. Further, employing the limit $z_e \to 0$, we obtain for the RO damping of the QD laser Γ^{vf} (see Eqs. (2.52))

$$\Gamma^{\mathrm{vf}} = \frac{\gamma}{2}\left[2r_w N_{\mathrm{ph}}^{0} + r_w N_{\mathrm{ph}}^{0}\left(1+\frac{1}{g}\right)\right], \quad \text{for } z_e \to 0. \tag{2.54}$$

The above expression shows that Γ^{vf} has in the limit $z_e \to 0$ the same linear dependence on $N_{\mathrm{ph}}^{0} \sim J - J_{\mathrm{th}}$ and thus on the pump current J as RO damping for the QW laser Γ^{QW} (cf. Eq. (2.23a)). However, since $r_w N_{\mathrm{ph}}^{0} > 1$ and $g > 0$, the damping is in the limit $z_e \to 0$ larger than for the QW laser. Note however that the reduced dynamical equations (2.43) derived in the limit of very fast scattering rates are valid for strong coupling between carrier reservoir and QD levels, which is expressed by $z_e = \mathcal{O}(1)$.

2.6. Summary

In this chapter, a rate equation model for a QD laser has been introduced, in which the carrier exchange between discrete QD levels and the surrounding quantum well acting as a carrier reservoir is mediated by microscopically calculated Coulomb scattering rates. The latter yield carrier lifetimes τ_e and τ_h of electrons and holes in the QD levels, which depend on the band structure, i.e., on the material composition and the growth conditions of the QDs. Further, τ_e and τ_h constitute additional time scales, which are responsible for the strongly suppressed ROs of QD lasers [ERN07a, LUE11]. The turn-on dynamics has been discussed for three different band structures as well as in the limit of vanishing carrier lifetimes, which has revealed that band structure engineering permits to strongly influence the turn-on of the laser. Subsequently, analytical expressions for RO frequency and damping of the QD laser for different band structures have been presented and compared to the corresponding expressions for a conventional class B QW laser model. These expressions have revealed how the carrier lifetimes τ_e and τ_h, i.e., the band structure, increases the turn-on damping of QD lasers if compared to the turn-on damping of QW lasers.

CHAPTER

THREE

QUANTUM DOT LASER UNDER OPTICAL INJECTION

3.1. Introduction

In this chapter, the complex dynamics of QD lasers under optical injection is discussed. In the typical injection setup sketched in Fig. 3.1, the light of a laser (the master laser) is injected into a second laser (the slave laser). Here, the slave laser is the QD semiconductor laser discussed in Chapter 2. For sufficiently large injection strength K and small input frequency detuning $\Delta\nu_{\mathrm{inj}} \equiv \nu_{\mathrm{inj}} - \nu_{\mathrm{th}}$ between the optical frequency of the injecting master laser ν_{inj} and the optical frequency of the free running slave laser ν_{th}, the slave phase-locks to the master laser. This means the master laser imposes its spectral properties onto the slave, which then displays stable continuous wave (cw) operation at the frequency of the master laser [ERN10b]. The phase-locking region forms an Arnold's tongue [ARN03] in the $(K, \Delta\nu_{\mathrm{inj}})$-plane, which is depicted by the yellow region in Fig 3.1. This injection setup is frequently used to injection lock a high power slave laser to a master laser with lower power but a higher frequency stability. Thus, optical injection permits chirp reduction [OLS85], reduction of relative intensity noise [SCH86g, YAB00],

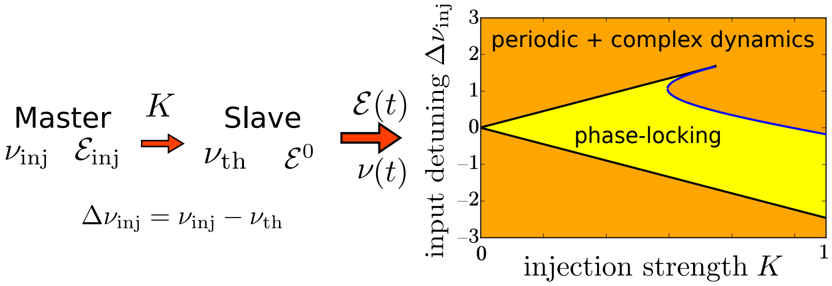

Figure 3.1.: Sketch of the injection setup. The master laser injects light with optical frequency ν_{inj} into the slave laser, and the carrier frequency of the free running slave laser is ν_{th}. Under injection, its output frequency $\nu(t)$ depends on the injection strength K and input frequency detuning $\Delta\nu_{\mathrm{inj}} = \nu_{\mathrm{inj}} - \nu_{\mathrm{th}}$ between master and slave. For small $\Delta\nu_{\mathrm{inj}}$, phase-locking is observed (yellow region), i.e., stable cw operation of the slave on the frequency of the master ν_{inj}, and for larger injection, periodic or more complex waveforms are found (orange region). $\mathcal{E}_{\mathrm{inj}}$ and $\mathcal{E}$ denote the slowly varying field amplitudes of the master and slave under injection, respectively.

and enhanced side-mode suppression [IWA82]. Further, the RO frequency of the slave laser can be enhanced under optical injection, which permits a larger bandwidth under direct electrical modulation [JIN06, LAU09a] and the generation of microwave signals [SEO01, CHA07].

Outside the phase-locking tongue, the slave laser may display a rich variety of dynamical responses reaching from strictly periodic waveforms over quasi-periodic to chaotic outputs. (See [WIE05] for a comprehensive review of the complex bifurcation scenario.) The chaotic output has been used for secure communication [MUR02, YU07, WAN09b].

Due to their small phase-amplitude coupling and strongly suppressed relaxation oscillations, QD lasers under optical injection show smaller chaotic regions and less complicated trajectories compared to semiconductor QW lasers devices [ERN10a, KEL11a, KEL11c]. Based on experimental studies on QD lasers [GOU07, KEL09, ERN10a], simple rate equation approaches have been used to model their optical response under optical injection and to investigate the stability regions and bifurcation scenarios [ERN10a, OLE10]. Further, models based on the standard rate equation approach [PET91] that take into account the gain material and excited state filling typical for QD based devices by an effective gain compression parameter have been proposed [SU05]. They have proven to successfully model the modulation response of quantum dash lasers subject to optical injection [NAD09]. In these models, the gain compression parameter is obtained by fitting the nonlinear dependence of the relaxation oscillation (RO) frequency on the output intensity [GRI08] permitting to model non-constant α-factors that depend nonlinearly on the pump current [GRI08a]. More sophisticated modeling approaches reveal that for QD lasers the α-factor is problematic [LIN12b], because it cannot account for the independent dynamics of resonant charge carries in the QDs and nonresonant charge carriers of the surrounding carrier reservoir [MEL06, LIN12a] and eventually neglects a degree of freedom of the dynamics. It was, however, shown that QD laser models based on a constant α-parameter still yield reliable results as long as only the transition between stable and unstable behavior, i.e., saddle-node and Hopf bifurcations, are considered [LIN12a, LIN12b, LIN13]. In this chapter, we focus on an analytical study of the bifurcations of the stable lasing fixed point at the borders of the phase-locking region. Therefore, for the sake of simplicity, a rate equation approach with a constant α-factor is chosen. Further, more complex modeling approaches reveal that the dynamics of QD lasers is rather more stable than described by models with constant α-factor [LIN13]. In the framework of the present, simple modeling approach a low constant α-factor is used.

The focus of this chapter lies on the distinguishing properties of QD lasers, and on understanding the interplay between epitaxial structure and optical properties by linking the dynamics of the QD laser under injection directly to the carrier exchange dynamics between the QD and carrier reservoir without the need of fit parameters. Therefore, in the next section, the microscopically based QD laser rate equation model that was described in Chapter 2.1 is extended to model optical injection. Then, the impact of α-factor, band structure and pump current on the laser under optical injection is discussed in Section 3.2 before focusing on bistabilities of locked solutions in Section 3.4. From Section 3.5 to Section 3.8, analytic expressions for the steady states of the dynamical equations as well as expressions for the saddle-node and Hopf bifurcation lines limiting the locking-tongue are derived. The bifurcation lines are then compared to results of numerical path continuation in Section 3.9. In Section 3.10, the influence of the injection on the damping of the QD laser is discussed, and in Section 3.11, concluding remarks are given.

3.2. Model of QD laser under optical injection

In this section, a field equation appropriate to describe external optical injection from a master laser is introduced, and combined with the QD material model that was introduced in Chapter 2. Further, the implementation of the equations into path continuation software is discussed in Subsection 3.2.1.

A semiclassical, single mode approach is chosen to model the interaction of the field in the cavity with the injected light field, which has been proven to be adequate for the description of semiconductor lasers subject to external optical injection [TAR95a]. In this approach, the electromagnetic field in the cavity is dealt with classically, using the Maxwell equations, while the amplifying medium inside the cavity is treated quantum mechanically [HAK81]. The electric field in the cavity of the QD slave laser E as well as the electromagnetic field of the injecting master laser E_{inj} are treated in the slowly varying envelope approximation, by assuming that the fields can be split into a product of a slowly varying envelope function and a fast oscillating plane wave

$$E(t) \equiv \mathcal{E}(t)e^{i\omega_{\text{th}}t} + \text{c. c.} \quad \text{and} \quad E_{\text{inj}}(t) \equiv \mathcal{E}_{\text{inj}}e^{i\omega_{\text{inj}}t} + \text{c. c.}, \tag{3.1}$$

where c. c. denotes the complex conjugate. The slowly varying and complex field amplitude of the slave laser and the constant real amplitude of the injected field are denoted by $\mathcal{E}$ and $\mathcal{E}_{\text{inj}}$, respectively, and ω_{th} and ω_{inj} are the carrier frequencies of slave and master, respectively. The emission frequency of the slave laser at lasing threshold ω_{th} is chosen as its carrier frequency. The carrier frequencies are in the THz-regime (optical wavelengths), while $\mathcal{E}$ varies on the time scale of the ROs (GHz), which is studied in the following. The carrier frequency of the slave laser refers to an optical wavelength of $\lambda_{\text{opt}} = c/(\omega_{\text{th}}) = 1.3\,\mu\text{m}$.

The field amplitude $\mathcal{E}$ is scaled such that $\mathcal{E} \equiv \sqrt{N_{\text{ph}}}e^{i\phi}$, where ϕ is the phase of the field. Thus, the instantaneous emission frequency of the slave laser is given by

$$\omega_{\text{las}} \equiv \left(\omega_{\text{th}} + \frac{d\phi}{dt}\right). \tag{3.2}$$

The stochastic differential equation for the slowly varying field amplitude $\mathcal{E}$ of the slave laser, i.e, the QD laser, subject to optical injection reads

$$\frac{d\mathcal{E}}{dt} = \frac{1+i\alpha}{2}\Big[2\bar{W}Z_a^{\text{QD}}(\rho_e+\rho_h-1) - 2\kappa\Big]\mathcal{E} + \sqrt{\beta\frac{R_{\text{sp}}(\rho_e,\rho_h)}{2}}\xi(t) + \frac{K}{\tau_{\text{in}}}\big|\mathcal{E}^0\big|e^{i\Delta\omega_{\text{inj}}t}, \tag{3.3}$$

where the linewidth enhancement factor α has been introduced. It models the phase-amplitude coupling by assuming a linear variation of the absorption and the refractive index with the carrier density. Since refractive index and absorption are described by real and imaginary part of the complex electronic susceptibility, this corresponds to the assumption of a linear dependence of the electronic susceptibility on the carrier density. See [LIN13] for a detailed discussion of the validity of this approach. In the semiclassical approach of Eq. (3.3), the spontaneous emission is modeled by a complex Gaussian white noise term $\xi(t)$ [HEN82], i.e.,

$$\begin{aligned} \xi(t) = \xi_1(t) + i\xi_2(t), \quad \langle \xi_i(t) \rangle = 0, \\ \langle \xi_i(t)\xi_j(\tilde{t}) \rangle = \delta_{i,j}\delta(t-\tilde{t}), \quad \text{for} \quad \xi_i(t) \in \mathbb{R},\, i \in \{1,2\}, \end{aligned}$$

and the rate of the spontaneous emission reads

$$R_{\text{sp}}(\rho_e, \rho_h) \equiv 2Z_a^{\text{QD}} W \rho_e \rho_h. \tag{3.4}$$

It has been determined by rewriting the stochastic differential equation (3.3) for the solitary laser ($K = 0$) in polar coordinates (N_{ph},ϕ) by means of an Ito transformation [GAR02, FLU07]. A comparison with the deterministic term for the spontaneous emission in the dynamical equation for the photon number of the solitary laser (Eq. (2.1a)), which was obtained by a fully quantum mechanical approach [CHO99], then yields the correct expression for R_{sp}.

The last term in Eq. (3.3) models the external injection. Here, K is the strength of the injected light

$$K \equiv (1-r)\frac{|\mathcal{E}_{\text{inj}}|}{|\mathcal{E}^0|}, \tag{3.5}$$

where the slowly varying field amplitudes of the solitary slave laser, and the injecting laser (master laser) are denoted by $\mathcal{E}^0$ and $\mathcal{E}_{\text{inj}}$, respectively. The transmission coefficient of the facet of the slave laser, through which the light of the master laser is injected, is given by $1-r$, where r is the reflection coefficient for the field amplitude that is assumed to be real. Beside K, the frequency detuning $\Delta\omega_{\text{inj}} \equiv \omega_{\text{inj}} - \omega_{\text{th}}$ between the carrier frequency of the master laser ω_{inj} and the frequency of the slave laser at lasing threshold ω_{th} is used as a bifurcation parameter throughout this chapter. To derive the field equation (3.3), it has to be assumed that $\mathcal{E}$ varies little during the roundtrip time of the light in the cavity. This is why the injection rate K is measured in units of the cavity roundrip time τ_{in} [WIE05, TAR95a].

To derive scaling laws for the dynamical variables needed for the asymptotic analysis of the following sections, it is convenient to rewrite the field equation (3.3) in a dimensionless form by rescaling time with respect to the photon lifetime $(2\kappa)^{-1}$ as already discussed for the solitary laser in Section 2.3. Introducing the new time $t' \equiv 2\kappa t$, the rescaled field equation reads

$$\mathcal{E}' = \frac{1+i\alpha}{2}\Big[g(\rho_e+\rho_h-1)-1\Big]\mathcal{E} + \sqrt{\beta\frac{r_{\text{sp}}(\rho_e,\rho_h)}{2}}\xi(t) + \frac{K}{2\kappa\tau_{\text{in}}}|\mathcal{E}^0|e^{i\delta\omega t}. \tag{3.6}$$

Here, $(\,\cdot\,)'$ denotes the differentiation with respect to t', and additionally to the dimensionless groups from Eq. (2.7), the dimensionless rate of the spontaneous emission r_{sp}, and the dimensionless bifurcation parameter $\delta\omega$ determining the input detuning between master and free running slave laser have been introduced as

$$r_{\mathrm{sp}}(\rho_e, \rho_h) \equiv \frac{R_{\mathrm{sp}}}{2\kappa} = \frac{WZ_a^{\mathrm{QD}}}{\kappa}\rho_e\rho_h \quad \text{and} \quad \delta\omega \equiv \frac{\Delta\omega_{\mathrm{inj}}}{2\kappa}. \tag{3.7}$$

In the subsequent calculation, the stochastic term is neglected by setting $\beta = 0$. Furthermore, we note that equation (3.6) is non-autonomous. However, for the analytical considerations it is convenient to treat rotating wave solutions with non-zero $\delta\omega$ but constant photon number and carrier densities as fixed points. Therefore, a coordinate transformation onto a frame rotating with the frequency distance between master and slave $\delta\omega$ is performed, by introducing $\mathcal{E} = \tilde{\mathcal{E}}e^{i\delta\omega t'}$, where $\tilde{\mathcal{E}}$ is the amplitude of the field in the rotating frame. In the new coordinates, the field equation (3.6) reads

$$\tilde{\mathcal{E}}' = \left(\frac{1+i\alpha}{2}\Big[g(\rho_e + \rho_h - 1) - 1\Big] - i\delta\omega\right)\tilde{\mathcal{E}} + \frac{K}{2\kappa\tau_{\mathrm{in}}}|\tilde{\mathcal{E}}^0| \tag{3.8}$$

Since only the modulus of the electrical field $\tilde{\mathcal{E}}$ enters into the carrier equations (2.4b)–(2.4e), they remain unchanged with $N_{\mathrm{ph}} = |\tilde{\mathcal{E}}|^2$.

Further, it is convenient to rewrite the complex field amplitude in polar coordinates $\tilde{\mathcal{E}} = \sqrt{N_{\mathrm{ph}}}e^{i\Psi}$, where Ψ is the phase of the field amplitude in the rotating frame, which yields two real equations for the photon number N_{ph} and the phase Ψ, respectively[1],

$$N_{\mathrm{ph}}' = \Big[g(\rho_e + \rho_h - 1) - 1\Big]N_{\mathrm{ph}} + \frac{2K}{2\kappa\tau_{\mathrm{in}}}\sqrt{N_{\mathrm{ph}}^0 N_{\mathrm{ph}}}\cos(\Psi), \tag{3.9a}$$

$$\Psi' = -\delta\omega + \frac{\alpha}{2}\left[g(\rho_e + \rho_h - 1) - 1\right] - \frac{K}{2\kappa\tau_{\mathrm{in}}}\sqrt{\frac{N_{\mathrm{ph}}^0}{N_{\mathrm{ph}}}}\sin(\Psi). \tag{3.9b}$$

By first writing $\mathcal{E}$ as $\mathcal{E} = \sqrt{N_{\mathrm{ph}}}e^{i\phi}$ and, second, noting that it can also be written as $\mathcal{E} = \tilde{\mathcal{E}}e^{i\delta\omega t'} = \sqrt{N_{\mathrm{ph}}}e^{i(\Psi+\delta\omega t)}$, we see that ϕ can be expressed in terms of Ψ and $\delta\omega$ as

$$\phi = \Psi + \delta\omega t'. \tag{3.10}$$

From Eq. (3.10), we see that $\Psi = \phi - \delta\omega t'$ is the phase difference between the phase ϕ of the slave and the phase $\delta\omega t'$ of the master laser. The dynamics of ϕ is expressed by

$$\phi' = \frac{\alpha}{2}\left[g(\rho_e + \rho_h - 1) - 1\right] - \frac{K}{2\kappa\tau_{\mathrm{in}}}\sqrt{\frac{N_{\mathrm{ph}}^0}{N_{\mathrm{ph}}}}\sin(\phi - \delta\omega t') \tag{3.11}$$

and decouples from the set of dynamical equations, which consists of the field equations (3.9) and the carrier equations (2.4b)–(2.4e).

For the asymptotic analysis presented later in Subsection 3.7.4, it is convenient that the dynamical variables are all $\mathcal{O}(1)$, which simplifies their comparison to the small parameter γ describing the time scale separation. Therefore, we rescale the photon

---

[1] Alternatively, we can directly plug the ansatz $\mathcal{E} \equiv \sqrt{N_{\mathrm{ph}}}e^{i(\Psi+\delta\omega t')}$ in the field equation (3.6).

number N_{ph}[2] with respect to its value for the solitary laser N_{ph}^0 by introducing $N_{\mathrm{ph}} = N_{\mathrm{ph}}^0 R^2$, where R is $\mathcal{O}(1)$. In terms of R, the dynamical equations read[3]

$$R' = \rho_{\mathrm{inv}} R + \tilde{k}\cos(\Psi), \tag{3.12a}$$

$$\Psi' = -\delta\omega + \alpha\rho_{\mathrm{inv}} - \frac{\tilde{k}}{R}\sin(\Psi), \tag{3.12b}$$

$$\rho_e' = \gamma\Big[F_e - r_{\mathrm{ph}}(\rho_e + \rho_h - 1)R^2 - \rho_e\rho_h\Big], \tag{3.12c}$$

$$\rho_h' = \gamma\Big[F_h - r_{\mathrm{ph}}(\rho_e + \rho_h - 1)R^2 - \rho_e\rho_h\Big], \tag{3.12d}$$

$$W_e' = \gamma\Big[J - F_e - cW_eW_h\Big], \tag{3.12e}$$

$$W_h' = \gamma\Big[J - F_h - cW_eW_h\Big], \tag{3.12f}$$

where a rescaled injection strength $\tilde{k}$ and the ratio r_{ph} were introduced as

$$\tilde{k} \equiv \frac{K}{2\kappa\tau_{\mathrm{in}}} \quad \text{and} \quad r_{\mathrm{ph}} \equiv r_w N_{\mathrm{ph}}^0, \tag{3.13}$$

which are both $\mathcal{O}(1)$. The phase equation (3.12b) is of Adler's type [ADL73]. For low injection strengths, the degrees of freedom of the inversion and the photon number N_{ph}^0 may be neglected. The system is then effectively one dimensional, and the phase-locking dynamics of the laser can be described only by the phase equation (3.12b) [ERN10b].

3.2.1. Preparing the equations for numerical path continuation

Numerical path continuation allows to compute, continue, and analyze the stability of steady state solutions and periodic solutions. Moreover, homoclinic and heteroclinic orbits can be computed. The basic idea of numerical path continuation is to find an object of interest and then follow it in a suitable parameter space. Compared to direct numerical integration, it has the advantage that also unstable objects, i.e., unstable fixed points and periodic orbits, and their bifurcations can be tracked. This permits to obtain a more complete picture of the underlying dynamics of the system under consideration. Mathematically, continuation is set up in such a way that there are $L-1$ equations for L unknown variables, so that the solution space is geometrically a one-dimensional curve in $\mathbb{R}^L$ [KRA05a]. The inverse function theorem guarantees that once a first point on this solution curve (branch of solutions) is found, then it is possible to continue it in parameter space [KUZ95]. This is usually done with the method called pseudo-arclength continuation involving a prediction step in the direction tangent to the curve and a Newton correction step in the space perpendicular to this tangent. During the computation, the stepsize along the branch is adapted in response to the success of the Newton correction [KRA07]. The idea of continuation can be used to follow branches of many implicitly defined problems. Most important, since local bifurcations are marked

---

[2] Typically, $N_{\mathrm{ph}} = \mathcal{O}(10^4)$, which implies that the product of $r_w N_{\mathrm{ph}}^0$ is a $\mathcal{O}(1)$.

[3] As a shortcut, we can directly plug the ansatz $\mathcal{E} \equiv \sqrt{N_{\mathrm{ph}}^0} R e^{i(\Psi + \Delta\omega t)}$ in the field equation (3.3).

by changes of stability of fixed points and periodic orbits [GLE94], they may be followed in parameter space. To analyse the stability of steady state solutions, approximations are computed to the rightmost, stability determining roots of the characteristic equation. Similarly, the stability of periodic solutions is determined by calculating approximations to their Floquet multipliers. Periodic solutions are represented by a suitable boundary value problem, which is solved by a piecewise polynomial representation of the solution (orthogonal collocation). In Chapter 4, it will be discussed that the laser under optical feedback is described by a delay differential equation (DDE) for the complex slowly varying envelope of the electric field $\mathcal{E}$. The characteristic equation of a DDE is transcendental so that it has infinitely many solutions. However, it can be shown that for each $\epsilon < 0$, there is always only a finite number of eigenvalues with real parts larger than ϵ [DIE95]. Thus, it is sufficient to calculate the finite number of eigenvalues with real parts larger than zero to determine the stability of a system of DDEs. This permits to extend the methods that have been developed for numerical path continuation of ordinary differential equations to DDEs [ENG01, ENG02, KRA05a, GLO11]. A comprehensive review of numerical path continuation methods for ordinary and delay differential equations is given in Ref. [KRA07].

So far, the optical equations (3.9) were discussed in polar coordinates (N_{ph}, Ψ). For the numerical path continuation, the representation in polar coordinates is not a good choice, because it introduces the symmetry $\Psi \mapsto \Psi + 2\pi$. As a consequence, there is a topological difference between a limit cycle with a bounded phase, i.e., a phase that remains within the interval $(-\pi, \pi]$ and a limit cycle with unbounded phase (running phase solution) [WIE05]. However, the transition from a bounded to an unbounded phase is not a bifurcation, but an "artifact" of the representation in polar coordinates, which is not present in Cartesian coordinates $\tilde{\mathcal{E}} = \tilde{\mathcal{E}}_x + i\tilde{\mathcal{E}}_y$. Therefore, Cartesian coordinates are more convenient for numerical path continuation. In Cartesian coordinates, the optical equations (3.9) read

$$\tilde{\mathcal{E}}_x' = \frac{1}{2}\Big[g(\rho_e + \rho_h - 1) - 1\Big](E_x - \alpha E_y) + \delta\omega E_y + \tilde{k}, \tag{3.14}$$

$$\tilde{\mathcal{E}}_y' = \frac{1}{2}\Big[g(\rho_e + \rho_h - 1) - 1\Big](E_y + \alpha E_x) - \delta\omega E_x. \tag{3.15}$$

3.3. Dynamics of optically injected laser

In this section, the dynamics of the optically injected QD laser modeled by equations (3.12) is discussed. In this and in the next section, the dynamics is studied in dependence of the frequency detuning $\Delta\nu_{\text{inj}}$ (measured in GHz) and the injection strength K that varies between 0 and 1, instead of the corresponding dimensionless quantities $\delta\omega$ and $\tilde{k}$[4] to simplify the comparison with other publications and experimental results.

In the first part of this section, the dynamics of a typical QD laser is modeled by using a small α-factor of $\alpha = 0.9$ and by a band structure that is described by the reference scattering rates (cf. Table 2.1). Then the influence of the α-factor and of

---

[4] Note that $\Delta\nu_{\text{inj}}$ and K are related to the dimensionless quantities $\delta\omega$ and $\tilde{k}$ defined in the previous section by $\Delta\nu_{\text{inj}} = \kappa\delta\omega/\pi$ and $K = 2\kappa\tau_{\text{in}}\tilde{k}$, respectively.

the band structure on the dynamics is studied in Subsections 3.3.1 and 3.3.2, respectively, and eventually the dependence of the dynamics on the pump level is discussed in Subsection 3.3.3.

Figure 3.2.: Two-parameter bifurcation diagram for small $\alpha = 0.9$ in dependence of injection strength K and input frequency detuning $\Delta\nu_{\mathrm{inj}}$. The color code marks the number of local extrema, i.e., the number of maxima and minima, of the photon number N_{ph}. The light yellow area (phase-locking tongue) marks the average frequency locking with steady state photon number, i.e., cw-lasing. The yellow-orange hatched area shows periodic modulations of N_{ph}, i.e., motion on a limit cycle with a locked average frequency. Blue, black, and white lines indicate period doubling (PD), Hopf and saddle-node (SN) bifurcation lines, respectively. Solid and dashed lines indicate super and subcritical bifurcations, respectively. Red diamonds and gray circles mark codimension-2 zero-Hopf (fold-Hopf) points (ZH_1 and ZH_2) and cusp points (C), respectively. Parameters: $J = 3.5J_{\mathrm{th}}$, reference rates, and other parameters as in Table 2.3. Modified from [PAU12].

The contour plot in Figure 3.2 depicts the dynamics of the laser under optical injection in the (K,$\Delta\nu_{\mathrm{inj}}$)-plane. For each pair of ($K, \Delta\nu_{\mathrm{inj}}$)-values, the system was integrated until transient effects had died out, and then the number of local extrema of different height has been extracted from the time series of the photon number N_{ph}. Color coded is the number of local extrema of different height. (For periodic waveforms, this corresponds to the number of local extrema per period.) Further, in order to obtain a clear picture of the bifurcations, path continuation was performed with the software tool MATCONT [DHO03]. The complete bifurcation scenario of an injected class B laser is very complex [WIE99, WIE05]. (A concise review is given in [WIE05a].) Here, the focus lies on the saddle-node (SN) (white lines) and Hopf bifurcation lines (black lines), for which analytic approximation are derived at the end of this chapter. Furthermore, period doubling (PD) bifurcation lines (blue lines) have been continued to study the dependence of the regions with complex dynamics from α-factor, band structure, and pump current. Bifurcations of stable objects are of special interest for the comparison with experiments, because they can be observed experimentally. Following the notation of [WIE99], bifurcations of stable objects, e.g., fixed points, limit cycles, and tori, in which another stable object is created, are called *supercritical*, while bifurcations, in which no attractors are created, are called *subcritical* throughout this work[5]. For example, a Hopf bifurcation of a stable fixed point is called supercritical if a stable limit cycle is created in this bifurcation. It is called subcritical if an unstable limit cycle coexists with the stable fixed point before the bifurcation point, and the fixed point is destabilized by the limit cycle at the bifurcation point. In the bifurcation diagram of Fig. 3.2, super- and subcritical bifurcation lines are depicted by solid and dashed lines, respectively. Although not directly visible in experiments, subcritical bifurcation lines are necessary to obtain an overall and consistent picture of the bifurcation scenario. Furthermore, subcritical bifurcation curves may change their stability and become supercritical when laser parameter as for example the α-factor are changed [WIE99].

Figures 3.3(a)–(d) depict one parameter bifurcation diagrams of local extrema of N_{ph} as a function of the input frequency detuning $\Delta\nu_{\mathrm{inj}}$ for four values of the injection strength K. In these diagrams, a single point indicates continuous wave operation, while two points (maxima and minima) indicate periodic pulsing marked by light shading. Furthermore, Figs. 3.3(e)–(h) depict the resulting frequency difference $\nu_{\mathrm{inj}} - \nu$ (output detuning) of the optical frequency of the master laser ν_{inj} to the instantaneous frequency of the slave laser ν as a function of the input frequency detuning $\Delta\nu_{\mathrm{inj}}$. From Eq. (3.2), it can be seen that the instantaneous frequency of the slave laser is given by $\nu \equiv \omega_{\mathrm{las}}/(2\pi) = \omega_{\mathrm{th}} + \frac{d\phi}{dt}$. Figures 3.3 thus correspond to vertical sections of Fig. 3.2. Further, figures 3.4(a)–(d) depict time series of N_{ph} (left column), projections of the attractors onto the complex $\tilde{\mathcal{E}}$-plane (middle column), and the power spectral densities (PSD) $S_{\tilde{\mathcal{E}}}$ of $\tilde{\mathcal{E}}$ as a function of the output frequency detuning $\nu_{\mathrm{inj}} - \nu$ (right column) for four points in the $(K, \Delta\nu_{\mathrm{inj}})$-plane, labeled by (a)–(d) in Fig. 3.2. The power spectral density reveals the frequency contributions of the signal. It will called power spectrum in the following (see Appendix D.3 for its definition).

Phase-locking occurs when a stable equilibrium exists for the phase difference Ψ of master and slave lasers. From the relation (3.10) of Ψ to the phase of the slave laser ϕ, it can be seen that phase-locking, i.e., $\Psi' = 0$, implies $\phi' = \delta\omega = \Delta\omega_{\mathrm{inj}}/(2\kappa)$. The instantaneous frequency ν of the slave laser is then given by

$$\nu = \frac{\omega_{\mathrm{las}}}{2\pi} = \frac{1}{2\pi}\left(\omega_{\mathrm{th}} + \frac{d\phi}{dt}\right) = \frac{1}{2\pi}\left(\omega_{\mathrm{th}} + 2\kappa\phi'\right) = \frac{\omega_{\mathrm{th}} - \Delta\omega_{\mathrm{inj}}}{2\pi} = \nu_{\mathrm{inj}}. \tag{3.16}$$

---

[5] Note that for Hopf bifurcations there exists a different definition of super- and subcritical. For the two-dimensional Hopf normal form, a supercritical Hopf bifurcation takes place when a stable limit-cycle is created that destabilized the stable fixed point, while in subcritical Hopf bifurcation, an unstable limit-cycle destabilizes the stable fixed-point. This definition can be generalized to higher dimensional systems by defining that in a supercritical Hopf bifurcation, the dimension of the unstable manifold of the fixed point is increased by two, while the limit-cycle gains a pair of complex conjugate Floquet-multipliers $\sigma_{\pm}$ with $|\sigma_{\pm}| < 1$. In a subcritical Hopf bifurcation, the unstable dimension of the fixed point increases by two, and a complex conjugate pair of Floquet-multipliers of the limit-cycle leaves the unit-cycle. In the two dimensional center-manifold of a Hopf bifurcation, the high-dimensional then reduces to the generic two dimensional case of the Hopf normal form [KUZ95]. In this work, we call in the high dimensional case only those Hopf bifurcation supercritical, in which a stable limit cycle is created.

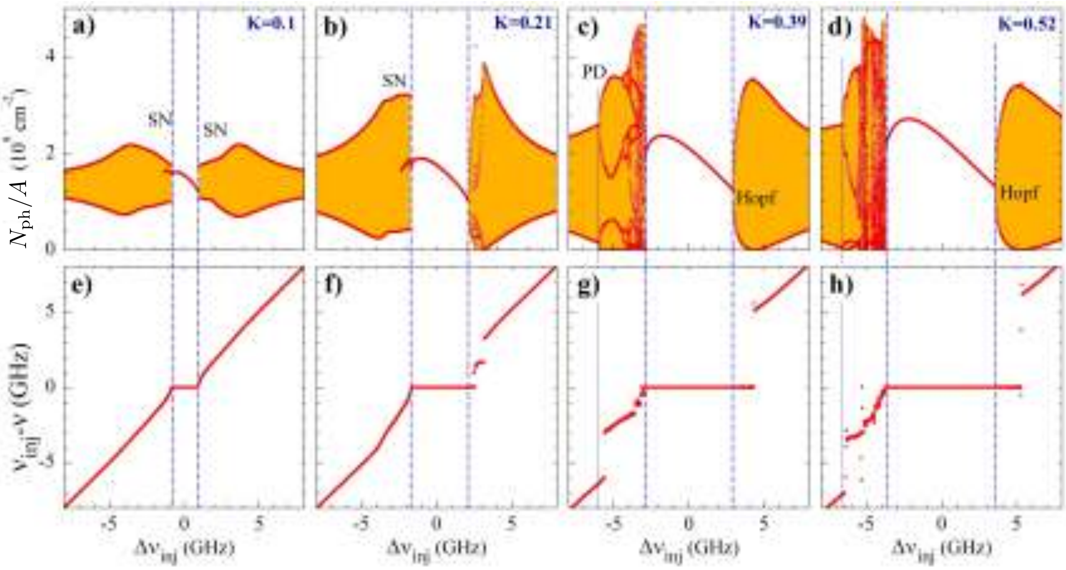

Figure 3.3.: **(a)–(d)**: One-parameter bifurcation diagrams showing maxima and minima of the photon number N_{ph} (normalized to the area of the laser's cross section A) as a function of the input detuning $\Delta\nu_{\mathrm{inj}} \equiv \nu_{\mathrm{inj}} - \nu_{\mathrm{th}}$. **(e)–(h)**: Output detuning $\nu_{\mathrm{inj}} - \nu$ in terms of input detuning $\Delta\nu_{\mathrm{inj}}$. The injection strengths are (**(a)** and **(e)**): $K = 0.1$, (**(b)** and **(f)**): $K = 0.21$, (**(c)** and **(g)**): $K = 0.39$, and (**(d)** and **(h)**): $K = 0.52$. Blue dashed lines indicate the interval of input detunings $\Delta\nu_{\mathrm{inj}}$, where operation is found, light shadings mark periodic, quasiperiodic, or chaotic pulsing. Labels SN, PD, and Hopf indicate saddle-node, period-doubling, and Hopf bifurcations, respectively. Parameters: $\alpha = 0.9$, $J = 3.5J_{\mathrm{th}}$, and other parameters as in Table 2.3. Modified from [PAU12].

This means that phase-locking implies frequency locking. In the phase-locking region of the $(K, \Delta\nu_{\mathrm{inj}})$-plane, stable cw operation of the slave laser on the frequency of the master laser ν_{inj} is observed, i.e., only one extrema of the photon number is detected. In Figure 3.2, phase-locking occurs within the yellow tongue-like structure centered around zero detuning $\Delta\nu_{\mathrm{inj}} = 0$. The width of this locking-tongue increases with the injection strength K. For zero α-factor, the locking-tongue is symmetric with respect to the line $\Delta\nu_{\mathrm{inj}} = 0$, and its asymmetry increases with the α-factor. For low values of K, the locking boundary is given by a saddle-node bifurcation. In this bifurcation, the lasing fixed point, which is a stable focus, collides with an unstable fixed point, which is a saddle-focus, and the fixed points annihilate. In the one parameter bifurcation diagrams of Figs. 3.3(a)–(d), the phase-locking expresses in a steady state of N_{ph} (only one extremum) bordered by the vertical blue dashed lines indicating the saddle-node bifurcations. The output frequency detuning $\nu_{\mathrm{inj}} - \nu$ is zero indicating that the frequency of the slave laser is entrained by the one of the master (cf. power spectrum in Fig. 3.2(a)). For most values of K, the saddle-node bifurcations, which border the locking tongue, take place on a stable invariant cycle. This global bifurcation is called saddle-node on a limit cycle, saddle-node infinite period (SNIPER), or saddle-node on an invariant cycle (SNIC) bifurcation [KUZ95, SCH00, HIZ08b, AUS09].

Outside the locking region, the slowly varying field amplitude $\tilde{\mathcal{E}}$ of the slave laser oscillates with a frequency close to the input detuning $\Delta\nu_{\mathrm{inj}}$ resulting in a periodic modulation of N_{ph} with one maximum and one minimum (orange regions in Fig. 3.2).

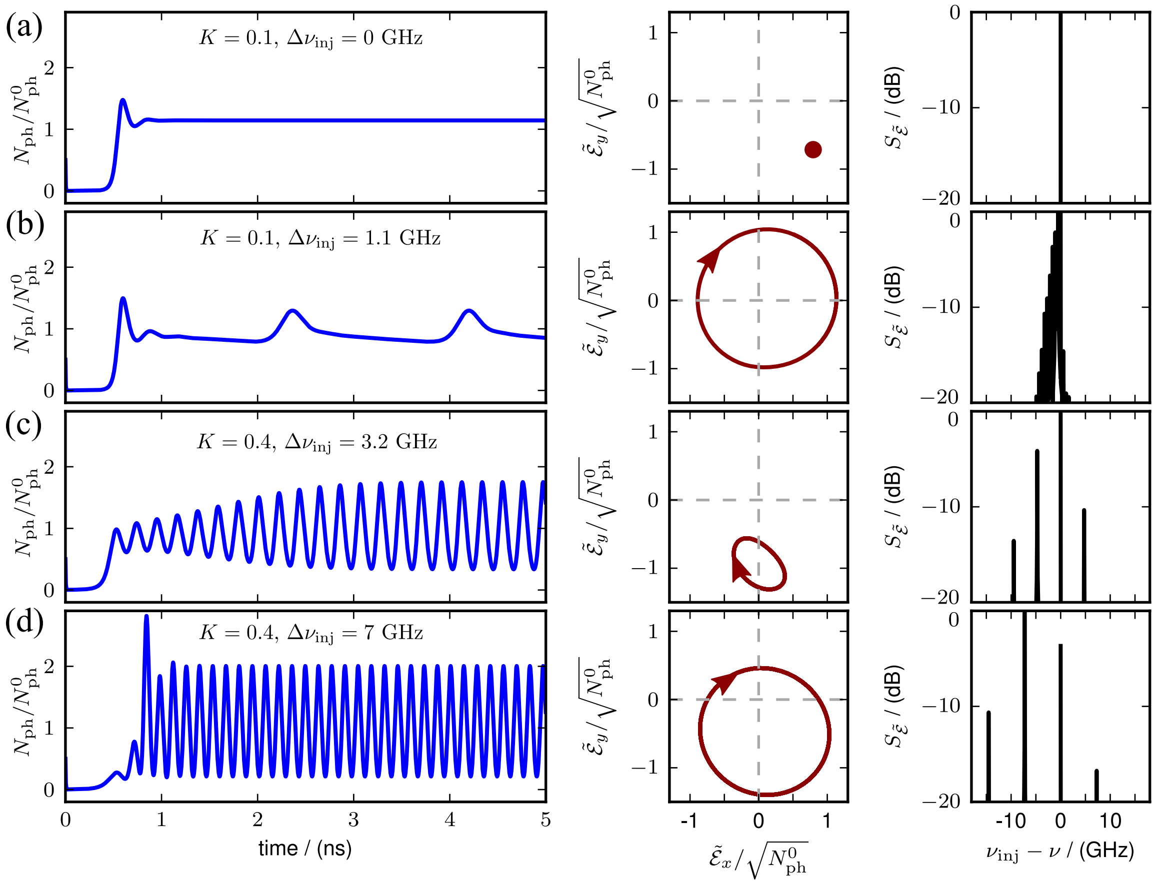

Figure 3.4.: **Left column**: Time-series of the photon number $N_{\rm ph}$ (normalized to the steady state value of the solitary laser $N_{\rm ph}^0$). **Middle column**: Projections of the trajectory onto a plane spanned by the components $\tilde{\mathcal{E}}_x$ and $\tilde{\mathcal{E}}_y$ of the complex field amplitude $\tilde{\mathcal{E}}$. **Right column**: Power spectral density $S_{\tilde{\mathcal{E}}}$. **(a)**: Stable continuous wave operation for zero input frequency detuning $\Delta\nu_{\rm inj} = 0$ and injection strength $K = 0.1$. **(b)**: Limit cycle close to saddle-node bifurcation $\Delta\nu_{\rm inj} = 1.1\,$GHz and $K = 0.1$. **(c)**: Limit cycle with bounded phase close to Hopf bifurcation for $\Delta\nu_{\rm inj} = 3.2\,$GHz and $K = 0.39$. **(d)**: Limit cycle with unbounded phase for $\Delta\nu_{\rm inj} = 7\,$GHz and $K = 0.39$. Parameters: $\alpha = 0.9$, $J = 3.5J_{\rm th}$, and other parameters as in Table 2.3.

Approaching the saddle-node line from the outside of the locking tongue for small K, the flow on the stable limit cycle slows down near the point, where the saddle-node bifurcation will appear and then makes a quick excursion along the other part of the periodic orbit. Figure 3.4(b) depicts the dynamics close to the SNIPER bifurcation. The time series now displays regular pulsing of N_{ph}, and the projection onto the complex $\tilde{\mathcal{E}}$-plane shows the limit-cycle. The quick excursion corresponds to the pulses in the time series. At the SN line, a stable nose and an unstable saddle-focus appear, and the laser locks to the stable node. This kind of phase-locking can be described by the dynamical equation (3.12b) for Ψ only by neglecting the degrees of freedom of N_{ph} and the carrier variables. This means that the system is effectively one dimensional. An equation of this type was firstly derived by Adler to describe phase locking in externally driven radiofrequency oscillators [ADL73]. This is why this type of locking is also known as Adler's type locking. Further, approaching the SNIPER bifurcation line from the interior of the locking tongue, the laser subject to spontaneous emission noise becomes excitable. A superthreshold perturbation away from the stable fixed point then leads to a large excursion of the trajectory in the phase space along the "ghost" of the limit cycle, which was previously annihilated in the SNIPER bifurcation. As a result, the laser emits an intensity spike. Further, in the excitable regime coherence resonance may be observed [OLE10, ZIE13]. Coherence resonance is the effect that an increase of the noise can lead to an increase of the regularity of the spikes [HU93a, PIK97], which will be discussed in detail in Section 4.8.

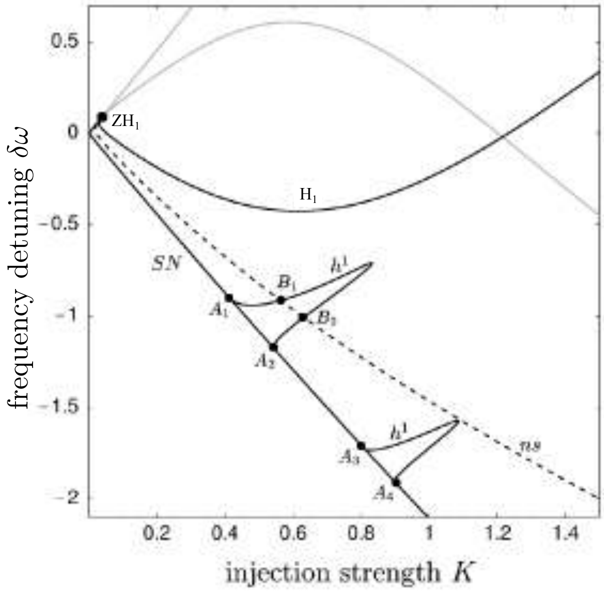

Figure 3.5: Bifurcation lines in a plane spanned by injection strength K and frequency detuning $\delta\omega$. The homoclinic bifurcation line is denoted by h^1 and the supercritical saddle-node and Hopf bifurcation lines are labeled by SN and H_1, respectively. The codimension-2 zero-Hopf point for positive detuning is labeled by ZH_1. Black and gray lines denote supercritical and subcritical bifurcation lines, respectively. The h^1-line touches the SN line in four codimension-2 bifurcation points A_i for $i \in \{1, 2, 3, 4\}$ forming two homoclinic teeth. The line, along which the saddle is neutral, is denoted by ns. It intersects with h^1 in two codimension-2 Belyakov points B_1 and B_2. Modified from [WIE02].

Wieczorek et al. showed in [WIE02] that for semiconductor class B lasers the saddle-node bifurcation does not always take place on a limit cycle, i.e., in a SNIPER bifurcation, due to the additional degrees of freedom of field amplitude and carrier inversion. As shown in Fig. 3.5, at special codimension-2 bifurcation points (non-central homoclinic saddle-node bifurcation points) labeled by A_1 and A_2, a homoclinic curve h^1 touches the saddle-node (SN) line. Consequently, between A_1 and A_2 the saddle-node bifurcation does not take place on a limit cycle. The homoclinic line bends into the interior of the locking tongue forming a so-called homoclinic tooth. The same is true between A_3 and A_4 and at many more homoclinic teeth that become smaller for increasing injection strength. Within the homoclinic teeth, the stable node created in the saddle-node bifurcation, i.e., the lasing fixed point, coexists with the limit cycle, which renders the system bistable. The limit cycle is then annihilated in the homoclinic bifurcation at h^1 in a collision with a saddle-point. Closely beyond h^1, the system is excitable, and noise induced dynamics, for instance, irregular spiking can be observed [OLE10, KEL11a]. The larger homoclinic tooth in Fig. 3.5 intersects with the dashed curve ns, where the saddle created in the saddle-node bifurcation is neutral. This neutral case is reached when the absolute value of the real parts of a real eigenvalue and the real parts of the complex conjugate eigenvalues are equal. Below the ns line, the homoclinic orbit bifurcates at h_1 into an attractive periodic orbit, i.e., a stable limit-cycle, and we obtain the bistability discussed above. This is known as simple Shil'nikov case [KUZ95]. Above ns, the bifurcating limit cycle is no longer stable, which is known as chaotic Shil'nikov case. Breaking the homoclinic orbit at h^1 at any point above ns leads to the creation of n-homoclinic orbits for any $n \in \mathbb{N}$. While the ns line is not a bifurcation line, its intersection points with the homoclinic line h^1 labeled by B_1 and B_2 are codimension-2 bifurcation points known as Belyakov points. They mark the transition between the simple and the chaotic Shil'nikov case. Above these points the laser exhibits complex multi-pulse excitability close to h^1, which was studied in detail in [WIE02, WIE05a] (see [WIE07] for a comprehensive review on this topic). Excitability and coherence resonance of a topologically identical phase space configuration found in semiconductor lasers subject to external optical feedback will be discussed in detail in Section 4.8.

For increasing K, the injection becomes strong enough to undamp the ROs of the slave laser. This is why the phase-locking region is bounded for high injection strength by supercritical Hopf bifurcations (solid black lines in Fig. 3.2). This means that at the bifurcation line, a stable limit-cycle is born, and the lasing fixed point is destabilized. The one dimensional bifurcation diagrams of N_{ph} in Figs. 3.3(c) and (d) reveal a square-root like scaling of the photon number for positive detuning, which is the fingerprint of a supercritical Hopf bifurcation [STR94a]. Figure 3.4(c) depicts time-series, phase space projection, and power spectrum for $K = 0.4$ and a detuning of $\Delta\nu_{\mathrm{inj}} = 3.2\,\mathrm{GHz}$ closely beyond the supercritical Hopf bifurcation line for positive detuning (see label (c) in Fig. 3.2). The time series shows a periodic modulation of $\tilde{\mathcal{E}}$, and the power spectrum reveals that the frequency of the modulation is 5 GHz , which is close to the RO frequency of the solitary laser (cf. Fig. 2.6). Thus, the Hopf bifurcation has indeed undamped the ROs. In projection onto the complex $\mathcal{E}$-plane (Fig. 3.2(d) (middle panel)), the exchange of energy between the electric field and the inversion expresses in a motion on a limit-cycle. This implies that Ψ is no longer constant but remains bounded, because the limit-cycle does not cross the origin of the complex plane. Thus, the average frequency $\bar{\nu} \equiv (\langle \omega_{\mathrm{th}} + \frac{d\phi}{dt} \rangle_T)/(2\pi)$ of the slave laser, which is obtained by averaging ν over the period T of the limit cycle, remains locked. This can also be seen from the power spectrum, which has its dominant frequency still at zero output detuning. Thus, while phase-locking implies frequency locking, the opposite is not true. This can be seen from Figs. 3.3(g) and (h) by noting that the output detuning $\nu_{\mathrm{inj}} - \nu$ remains zero even after the occurrence of the supercritical Hopf bifurcation for positive detuning marked by the rightmost blue dashed lines in Figs. 3.3(g) and (h). The parameter regions, at which frequency-locking without phase-locking occurs, are indicated by yellow hatched areas in Fig. 3.2. Recently, frequency-locking without phase-locking has been observed experimentally in a dual-frequency solid state laser [THE11].

Going away from the Hopf bifurcation line, the limit cycle of Fig. 3.4(d) (middle panel) increases until it touches the origin of the complex $\tilde{\mathcal{E}}$-plane, and the phase becomes unbounded. Figure 3.4(d) depicts the dynamics for $K = 0.4$ and a large detuning of $\Delta\nu_{\mathrm{inj}} = 7\,\mathrm{GHz}$, i.e., beyond the regime of a bounded phase (see label (d) in Fig. 3.2). In the complex $\tilde{\mathcal{E}}$-plane, the limit cycle now encircles the origin, which yields a drift in the phase. The laser oscillates with a frequency corresponding to the frequency of the free running laser ν_{th} shifted according to the new average value of the inversion. These fast oscillations are modulated by the slow frequency of $7\,\mathrm{GHz}$, which corresponds to the input detuning $\Delta\nu_{\mathrm{inj}}$ between master and slave laser. Thus, a beating between ν_{th} and ν_{inj} is observed, which appears as the highest peak in the power spectrum of the slowly varying field amplitude $\tilde{\mathcal{E}}$, is at $-7\,\mathrm{GHz}$. The injected field appears at zero together with an additional phase-conjugate peak at $-14\,\mathrm{GHz}$ characteristic for nonlinear oscillations (see Fig. 3.4(d) right). This effect is called four wave-mixing [WIE05a, MAJ12].

The points in parameter space, where a saddle-node line and a Hopf line become tangent, are called zero-Hopf points (also referred to as saddle-node Hopf or fold-Hopf points). The codimension of these points is two. The zero-Hopf point for positive detuning is labeled by ZH_1, the one for negative detuning is labeled by ZH_2, and both are marked by red diamonds in Fig. 3.2. These codimension-2 bifurcation points are known to generate complex dynamics in their vicinity [WIE99]. Indeed, in Fig. 3.2 close to each of the zero-Hopf points, regions of complex dynamics (dark red, gray, and white regions) are found. Both regions are limited by period doubling (PD) bifurcations, which lead to a motion onto a two-folded limit cycle in phase space. Within the large period doubling loop for negative detuning, complex dynamics is observed (gray and white regions). In the two white regions of Fig. 3.2, a cascade of period doubling bifurcations leads to chaotic pulsations of the photon number [SCH89c]. Depicted in Fig. 3.2 are only the first two bifurcation lines of the cascade, which lead to a periodic motion on two- and four-fold limit cycles in phase-space, respectively.

At a zero-Hopf point, the saddle-node line changes from super- to subcritical, and depending on the normal form coefficients, the Hopf line may change from super to subcritical, and a torus bifurcation (also known as Neimark-Sacker bifurcation) line may appear [KUZ95, GUC83]. Here, the Hopf line changes at ZH_1 and ZH_2 from super- to subcritical (see Fig. 3.2), and supercritical torus lines appear (not shown). One branch of the torus line connects ZH_1 and ZH_2. Close to ZH_2, it intersects in a $1:2$ resonance with the period doubling line closest to ZH_2. This is why the latter changes from super- to subcritical. An analytic approximation of the torus line connecting ZH_1 and ZH_2 was found for a single mode, class B QW rate equation model in [NIZ99]. Further, the other branch of the torus line leaving from ZH_1 intersects with the period-doubling line closely above ZH_1, in a $1:2$ resonance. For the QW rate equation model mentioned above, the torus lines were studied analytically using averaging methods in [NIZ01, ERN10b]. For injection strength $K > K^{\mathrm{ZH},2}$ (where $K^{\mathrm{ZH},2}$ is the injection strength of the ZH_2 point), bistability between stable fixed points may occur in a triangle formed by the supercritical saddle-node and the Hopf line leaving from the ZH_2 point and the saddle-node line coming from the origin. This will be discussed in detail in Subsection 3.4. Within the locking tongue, the RO damping is smaller for positive detuning than for negative detuning, [KEL12a], which will be discussed in detail in Section 3.10. This is the reason why for negative detuning the ROs are easier undamped than for negative detuning, and the zero-Hopf point for positive detuning ZH_1 is located at a lower injection strength K than the zero-Hopf point at negative detuning ZH_2.

Summing up, the position of the zero Hopf points is crucial for the injection dynamics of the laser. For positive detuning, the slave laser locks to the master in a supercritical Hopf bifurcation for $K > K^{\mathrm{ZH},1}$ and in a saddle-node bifurcation for $K < K^{\mathrm{ZH},1}$ ($K^{\mathrm{ZH},1}$ is the injection strength of the ZH_1 point). For negative detuning and $K > K^{\mathrm{ZH},2}$, bistability between fixed points may be observed. Moreover, both zero-Hopf points are located in the vicinity of regions of complex dynamics, to which they are connected in torus bifurcations. This is the reason why they are called organizing centers, and analytic approximations for the upper zero-Hopf point ZH_1 are discussed in Subsection 3.8.6.

3.3.1. Impact of the phase-amplitude coupling (α-factor)

In the last section, an overview of the dynamics in the $(K, \Delta\nu_{\mathrm{inj}})$-plane was given. Now, the impact of the phase-amplitude coupling on the dynamics of the injected laser is analyzed. In the introduction of this chapter, it was discussed that in models, in which the phase-amplitude coupling is described by a constant α-factor, the dynamics of QD lasers is best approximated by small values of α, while QW lasers typically have large α-factors [KAN05]. In Figure 3.6, the dynamics of the injected laser with small $\alpha = 0.9$ (Fig. 3.6(a)) is compared to its dynamics with large $\alpha = 3.2$ (Fig. 3.6(b)). The dynamics for a small α-factor was already discussed in the previous section. (Figure 3.6(a) is identical to Fig. 3.2.) With increasing α, the phase-locking range shrinks, because the upper supercritical Hopf bifurcation line bends towards zero input detuning. Thus, pulsating behavior of the photon number is found for $\Delta\nu_{\mathrm{inj}} = 0$ at high injection strengths. This was observed experimentally in QW lasers [WIE02a, SIM03, WIE05a], but not in QD lasers, which at zero detuning remain stable for arbitrary injection strengths [ERN10a]. For QD lasers, the locking tongue remains nearly symmetrical with respect to $\Delta\nu_{\mathrm{inj}}$ [KEL11c]. This permits to conclude that QD lasers have indeed a smaller phase-amplitude coupling than QW lasers, which is supported by more complex modeling approaches [LIN12b, LIN13]. For QD models, in which the phase-amplitude coupling is simply described by a constant α-factor, this may be modeled by using small values for α, i.e. $\alpha \lesssim 2$. Such a choice of α avoids that the upper supercritical Hopf bifurcation line crosses the zero detuning line.

Further, the region with complex dynamics close to the upper codimension-2 zero-Hopf point ZH_1 increases for large α-factor and moves to the interior of the saddle-node lines that emerge from the origin of the $(K,\Delta\nu_{\mathrm{inj}})$-plane. For negative detuning, one now finds large regions of multistability between periodic (dark-red) as well as quasiperiodic and chaotic motion (purple and white regions) with the lasing fixed point. To see this, note that the thick blue lines, which indicate supercritical period-doubling bifurcations, now extend deeply into the yellow region that indicates the existence of a stable fixed

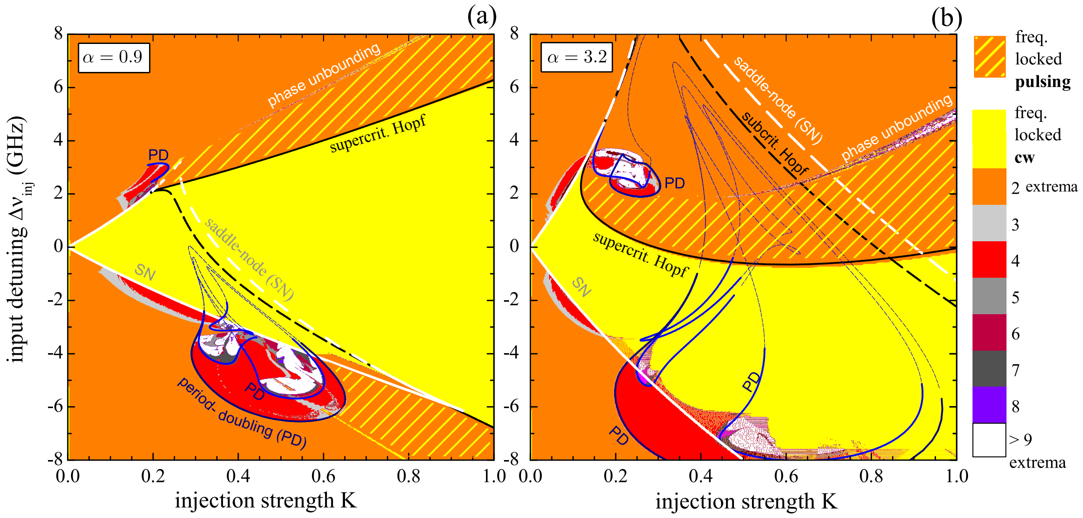

Figure 3.6.: Two-parameter bifurcation diagram in dependence of injection strength K and input frequency detuning $\Delta\nu_{\text{inj}}$ for **(a)**: small $\alpha = 0.9$ and **(b)**: large $\alpha = 3.2$. The color code marks the number of local extrema, i.e., the number of maxima and minima, of the photon number N_{ph}. The light yellow area (locking tongue) marks the average frequency locking with steady state photon number, i.e., cw-lasing. The yellow-orange hatched area shows periodical modulations of N_{ph}, i.e., motion on a limit cycle with a locked average frequency. Blue, black, and white lines indicate period doubling (PD), Hopf and saddle-node (SN) bifurcation lines, respectively. Solid and dashed lines indicate super and subcritical bifurcations, respectively. Red diamonds and gray circles mark codimension-2 zero-Hopf (fold-Hopf) points (ZH_1 and ZH_2) and cusp points (C), respectively. Parameters: $J = 3.5J_{\text{th}}$, reference rates, and other parameters as in Table 2.3. Modified from [PAU12].

point. The color code shown in the Fig. 3.6 was obtained by up-sweeping the value of the injection strength K, and thus parts of the stable limit cycle operation show up inside the yellow area of cw operation. Down-sweeping K instead, reveals only stable cw operation up to the saddle-node line for negative detunings. In experiments, up- and down-sweeping indicate the directions, in which the injection strength is changed. For instance, starting with zero injection and increasing it slowly can lead to different dynamic scenarios than starting with high injection strength and decreasing it slowly. In the simulations, this is done by choosing the last value of the time series as initial conditions for the next simulation.

Qualitatively, the results agree well with results for QD lasers that are modeled with equal and constant lifetimes for electrons and holes [OLE10, KEL11a]. However, in the modeling approach discussed in this chapter, the lifetimes are no fitted parameters, but nonlinear functions of the carrier density in the reservoir that are given by the band structure. Thus, changes concerning the operation point of the device, e.g. changing the pump current, can be studied without re-adjusting parameters.

Summing up, with increasing α-factor, the dynamics of the slave laser becomes more complex, and the region of phase-locking, in which the slave laser provides stable cw operation on the frequency ν_{inj} of the injected light, is decreased.

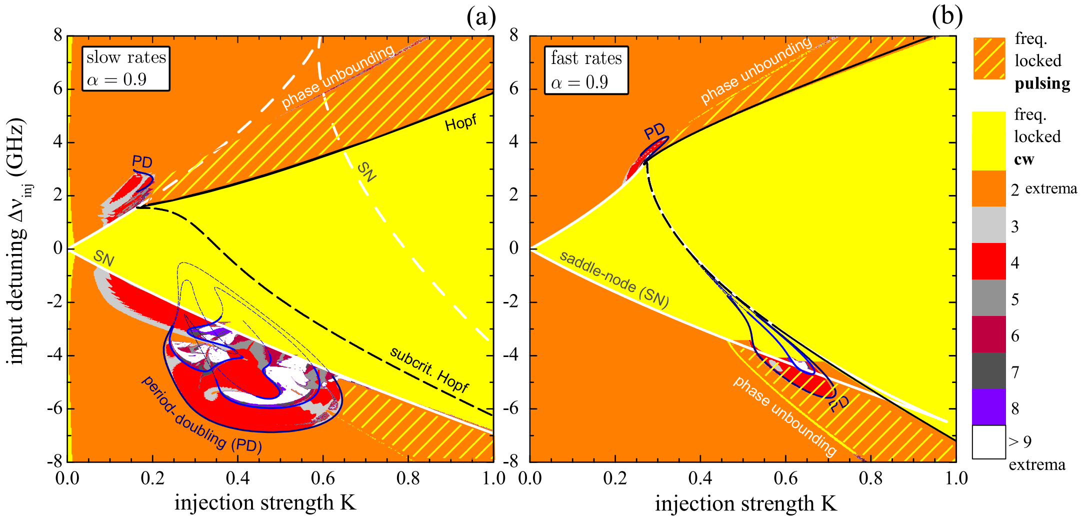

Figure 3.7.: Two-parameter bifurcation diagram in dependence of injection strength K and input frequency detuning $\Delta\nu_{\text{inj}}$ for small $\alpha = 0.9$ and slow scattering rates **(a)** as well as fast scattering rates **(b)**. The color code marks the number of local extrema, i.e., the number of maxima and minima, of the photon number N_{ph}. The light yellow area (locking tongue) marks the average frequency locking with steady state photon number, i.e., cw-lasing. The yellow-orange hatched area shows periodical modulations of N_{ph}, i.e., motion on a limit cycle with a locked average frequency. Blue, black, and white lines indicate period doubling (PD), Hopf and saddle-node (SN) bifurcation lines, respectively. Solid and dashed lines indicate super- and subcritical bifurcations, respectively. Red diamonds and gray circles mark codimension-2 zero-Hopf (fold-Hopf) points (ZH_1 and ZH_2) and cusp points (C), respectively. Parameters: $J = 3.5J_{\text{th}}$, and other parameters as in Table 2.3. Modified from [PAU12].

3.3.2. Impact of the band structure

So far, the reference rates (see Table 2.1) have been used in the simulations. They exhibit a long electronic lifetime τ_e in the QD level that mainly determines the RO damping of the solitary QD laser [LUE09, LUE11]. The damping is a crucial parameter for the understanding of the dynamics of the QD laser under optical injection. Both, the band structure and the pump current effect the RO damping via the carrier lifetimes τ_e and τ_h in the QD levels and the steady state photon number N^0_{ph}. Analytically, this dependence was discussed for the solitary laser in [LUE11]. In this and the following subsections, an overview of the dynamics of a QD laser under optical injection in dependence on the band structure and on the pump current is given, before presenting a detailed analytic study in Sections 3.5–3.10.

As discussed in Section 2.2, different carrier lifetimes τ_e and τ_h can be implemented into the simulations by using scattering rates that have been calculated for different QD sizes and thus different band structures (cf. Fig. 2.3). The different carrier lifetimes influence the size of the phase-locking region in the $(\Delta\nu_{\text{inj}}, K)$-plane. Figure 3.7(a) and (b) depict the locking-dynamics for slow and fast scattering rates, respectively, as introduced in Table 2.1. The α-factor is $\alpha = 0.9$, and a pump current of $J = 3.5J_{\text{th}}$ has been chosen. Thus, Figs. 3.7 correspond to Fig. 3.2 that was obtained for the reference rates. From the turn-on dynamics of the solitary laser (see Fig. 2.4) and the RO damping presented in Fig. 2.6 it can be seen that a deep-dot structure modeled by the set of slow Coulomb scattering rates results in a low RO damping. The RO damping increases for the reference rates, and a shallow-dot structure modeled by the set of fast Coulomb scattering rates eventually has the highest RO damping.

By comparing Fig. 3.7(a) (slow rates) with Fig. 3.2 (reference rates) and Fig. 3.7(b) (fast rates), it can be seen that the zero-Hopf point for positive detuning ZH_1 shifts to higher K, and the size of the yellow-orange hatched area indicating mean frequency locking on a limit cycle decreases. The shift of ZH_1 towards higher K can be directly attributed to the increase of the RO damping, because for higher values of the damping, a larger injection strength K is needed to undamp the ROs. In contrast, the zero-Hopf point for negative detuning ZH_2 shifts to lower values of K, which increases the region in phase space, in which bistability of fixed-points is observed (see Subsection 3.4).

A second crucial effect of the lifetimes on the bifurcation diagram can be found at the negative detuning side of the locking range. For large lifetimes and thus small damping, the range of sustained multipulse emission with complex pulse shape is large, and the lower PD bifurcation line is found already for small values of K (Fig. 3.7(a)). Further, chaotic transients and complex bifurcations are found outside the locking range for negative detunings. In contrast, the bifurcation diagram plotted in Fig. 3.7(b) for the strongly damped QD laser shows a large range of frequency locked cw operation. A very small area with more complex pulse shape is found near the zero-Hopf point for positive detuning, and for $K > 0.5$, a small region limited by a PD bifurcation line is found at the negative detuning side close to ZH_2. It is interesting to note that the period-two oscillations within the PD area have a bounded phase and thus show mean frequency locking as indicated by hatching. The complete suppression of complex pulsforms (multipulses) generated in PD bifurcation was also reported for a class A QD semiconductor laser [KEL11a]. These lasers can be approximately described by a single rate equation for the complex electric field amplitude and thus, as a two-variable system, cannot show chaos.

It can be concluded that a stronger damping of the turn-on dynamics leads to a reduction of the areas with complex dynamics and enlarges the range of stable frequency locked cw operation. This relation between turn-on damping and locking behavior should be interesting for experimentalists, as the knowledge of the α-factor and the small-signal modulation response should be sufficient to predict and optimize the locking behavior of a laser.

3.3.3. Impact of the pump current

Having discussed the impact of the α-factor and the band structure on the dynamics of the QD laser under optical injection, we now focus on the impact of the pump current. The pump current affects many characteristics of the QD laser, e.g., with increasing pump current the photon number and electron and hole densities in the carrier reservoir increase (see [LUE10]). This, in turn, influences the scattering rates, i.e., the carrier lifetimes τ_e and τ_h, that have a strong impact on the RO damping. Figures 3.8(a) and (b) show the two-parameter bifurcation diagrams for current densities of $J = 2.1 J_{\mathrm{th}}$ and $J = 4.9 J_{\mathrm{th}}$, respectively. The α-factor is $\alpha = 0.9$, and the figures thus correspond to Fig. 3.2, where a pump level of $J = 3.5 J_{\mathrm{th}}$ was chosen. The figures show that the codimension-2 saddle-node-Hopf-point for positive detuning, at which the upper subcritical Hopf

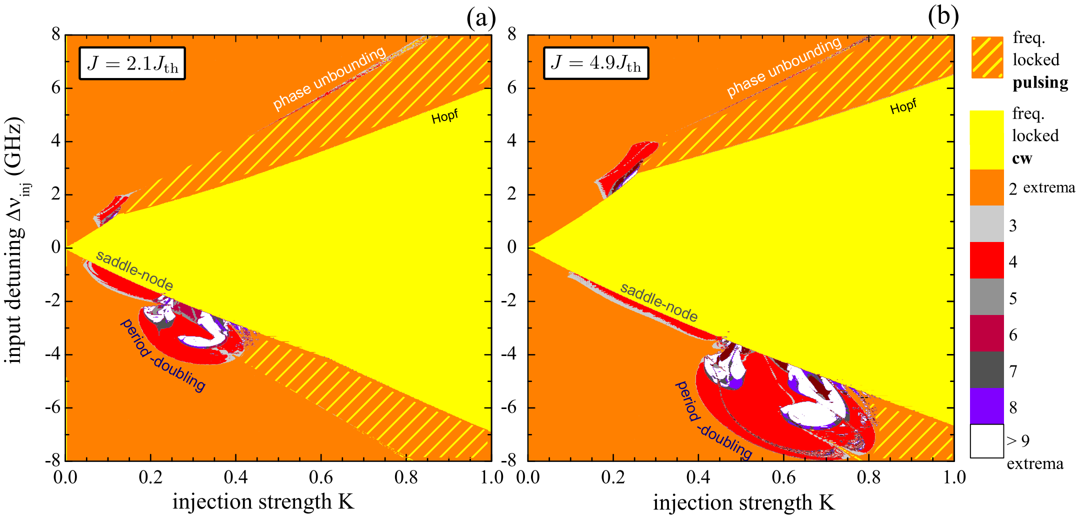

Figure 3.8.: Two-parameter bifurcation diagram for $\alpha = 0.9$ for injected current densities of **(a)**: $J = 2.1J_{\mathrm{th}}$ and **(b)**: $J = 4.9J_{\mathrm{th}}$. The light yellow area indicates the locking region at cw operation, the yellow-orange hatched area indicates the region of frequency locking on a limit cycle. The color code indicates the number of extrema per period of the photon density. Saddle-node, period-doubling, and Hopf bifurcation lines are indicated. Parameters: Reference scattering rates and other parameters as in Table 2.3. From [PAU12].

bifurcation line changes to a supercritical one, shifts towards higher injection strengths K and higher input detunings $\Delta\nu_{\mathrm{inj}}$ with increasing pump current. For $J = 2.1J_{\mathrm{th}}$, the upper zero-Hopf point ZH_1 is located at $K^{\mathrm{ZH},1} = 0.14$ (see Fig. 3.8(a)), for $J = 3.5J_{\mathrm{th}}$, it is located at $K^{\mathrm{ZH},1} = 0.22$ (see Fig. 3.2), and for the high pump level of $J = 4.9J_{\mathrm{th}}$, it is eventually located at $K^{\mathrm{ZH},1} = 0.27$ (see Fig. 3.8(b)). Further, the period-doubling (PD) bifurcation lines for negative detuning shift to higher values of K.

Note that, if the lifetimes τ_e and τ_h are chosen to be constant, the locking range is invariant under changes of the pump current. Thus, the changes in the locking behavior with the pump current can be attributed to the nonlinearity of the carrier lifetimes, which makes them a crucial ingredient for a quantitative modeling of QD lasers under optical injection. High current densities lead to high electron and hole densities in the carrier reservoir, which lead to short carrier lifetimes of electrons and holes, τ_e and τ_h, respectively, and thus to a higher RO damping.

Concluding, it can be assessed that changing the band structure in the previous subsection leads to changes in the locking behavior that have a similar tendency as found in this chapter for the lifetime variations. A shallow-dot band structure with large Coulomb scattering rates has a similar effect as a high current density, and a deep-dot structure with small Coulomb scattering rates has a similar effect as low current density. The reason is that both, band structure and pump current effect the carrier lifetimes in the QD levels, which in terms have a strong influence on the RO damping. The RO damping increases if the carrier lifetimes in the QD levels τ_e and τ_h decrease. Thus, high RO damping can be achieved by either choosing shallow-dots or high pump current densities (cf. Fig. 2.3).

3.4. Bistabilities of locked solutions for high injection strength

In this section, the bistability of stable fixed points observed for high values of the injection strengths K and negative input detuning $\Delta\nu_{\text{inj}}$ are discussed. Bistable optical systems are of special interest, due to their potential use as optical switches needed for all-optical implementations of logical operations and all-optical memory. So far, these applications have been demonstrated for bistable semiconductor ring and micro-disk lasers [HIL04, LI08a]. Particularly, bistability of fixed points is of interest for applications, because it guarantees stable cw emission of the laser in both operation modes. Bistability of fixed points in injection locked Fabry-Perot semiconductor QD lasers was first mentioned in [GOU07] and was then studied in detail experimentally and described theoretically in [ERN10a, KEL11c]. For their analytic investigations, the authors used a rate equation model consisting of dynamical equations for the complex amplitude of the electric field, the carrier density in the carrier reservoir, and an additional equation for the inversion in the QDs. The latter permits to take into account the special carrier scattering dynamics in the QDs. For the in-scattering rates, a linear dependence of the carrier density on the reservoir and constant out-scattering rates were assumed [OBR04, ERN07a]. The authors showed that small phase amplitude coupling and strong RO damping are the main laser parameters that are responsible for the higher dynamical stability of QD lasers. In [KEL11c], the dynamics of the QD laser under injection was directly compared to the dynamics of a class A laser model consisting of only one equation for the complex field amplitude [MAY02]. This revealed that the injection locked dynamics of a QD laser is very similar to a class A laser. Indeed, the bifurcation diagram the authors obtained in the $(K,\Delta\nu_{\text{inj}})$-plane looked similar to the one of Fig. 3.7(b) for the set of fast scattering rates (shallow-dots) and small $\alpha = 0.9$. Both, class A and QD lasers have a nearly symmetric phase-locking tongue with respect to the input frequency detuning $\Delta\nu_{\text{inj}}$, and the upper supercritical Hopf line bends towards large detunings such that the phase-locking range increases for high values of K. In contrast, the phase-locking range of QW lasers with high α-factors (cf. Fig. 3.6(b)) decreases for increasing K, because the upper supercritical Hopf line bends towards zero detuning. Furthermore, for negative input detuning bistability between fixed points becomes possible in a triangle formed by two supercritical saddle-node lines and a supercritical Hopf line. The dynamics inside this triangle is now discussed in more detail.

3.4.1. Bistability for fast scattering rates

Figure 3.9 depicts the saddle-node (gray) and Hopf (red) bifurcation lines for the set of fast rates (see Table 2.1) and small $\alpha = 0.9$ in the $(K,\Delta\nu_{\text{inj}})$-plane. Supercritical and subcritical bifuractions are denoted by solid, thick and thin, dashed lines, respectively. In the following, we want to focus on the triangle formed by the supercritical saddle-node lines labeled by SN_1 and SN_2 and the lower supercritical Hopf line labeled by H_2. Codimension-2 zero-Hopf (ZH_1 and ZH_2) and cusp points (C) are labeled by red diamonds and gray circles, respectively. Within the locking tongue, three fixed points are involved into the bifurcation scenario [WIE99]. Figures 3.9(b)–(d) depict the photon

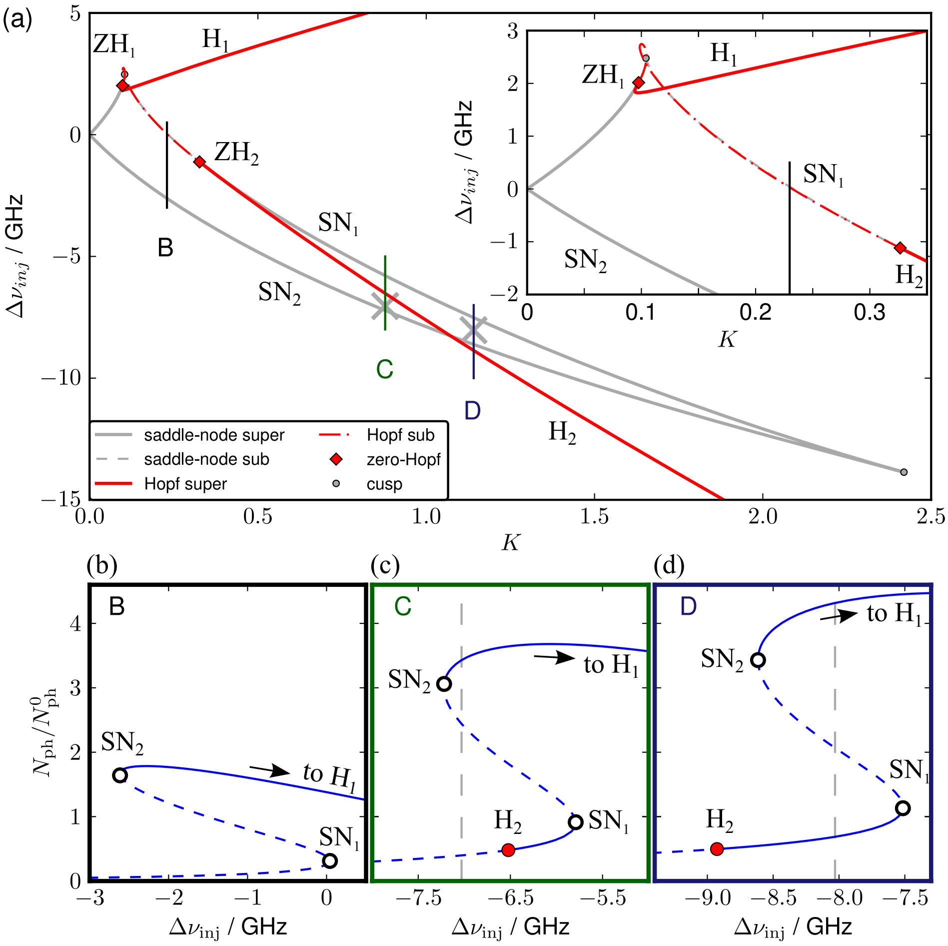

Figure 3.9.: **(a)**: Saddle-node (gray lines labeled by SN_1 and SN_2) and Hopf (red lines labeled by H_1 and H_2) bifurcation lines as functions of injection strengths K and frequency input detuning $\Delta\nu_{\mathrm{inj}}$ for the set of fast scattering rates and small $\alpha = 0.9$. Super- and subcritical bifurcation lines are plotted by thick, solid and thin, dashed lines, respectively. Codimension-2 zero-Hopf (fold-Hopf) points (ZH_1 and ZH_2) and cusp points are labeled by red diamonds and gray circles, respectively. **(b)**, **(c)**, and **(d)**: Steady states of the photon number N_{ph} (normalized to the photon number of the solitary laser N^0_{ph}) as functions of $\Delta\nu_{\mathrm{inj}}$. The figures correspond to vertical sections of **(a)** marked by lines labeled by B, C, and D, respectively. Stable and unstable fixed points are depicted by solid and dashed lines, respectively, and saddle-node and Hopf bifurcation points are labeled by open black and red circles, respectively. Gray crosses in **(a)** and gray dashed lines in **(c)** and **(d)** denote the parameter values of the time-series depicted in Fig. 3.10. Parameters: $J = 1.5J_{\mathrm{th}}$ and other parameters as in Table 2.3.

number N_{ph} of these three branches of fixed points as functions of the detuning $\Delta\nu_{\mathrm{inj}}$ for three values of K. Stable and unstable fixed points are denoted by solid and dashed blue lines, respectively. For $K < K^{\mathrm{ZH},2}$ ($K^{\mathrm{ZH},2}$ is the injection strength of the ZH_2-point), bistability of fixed points is not possible. This can be seen in Fig. 3.9(b) that corresponds to a vertical section of Fig. 3.9(a) along the solid black line labeled B. The upper stable branch, i.e., the lasing branch of fixed points, gains its stability in an inverse supercritical Hopf bifurcation when crossing the H_1-line. At the lower saddle-node line (SN_2), the lasing fixed point collides with a saddle (open black circle labeled SN_1 in Fig. 3.9(b)). This saddle then collides with an other coexisting saddle at the saddle-node line SN_1, which is subcritical (open black circle labeled SN_1 in Fig. 3.9(b)). This means that at the SN_1-point a saddle with a one-dimensional unstable manifold collides with a saddle with a two-dimensional unstable manifold. Thus, two saddles coexist between SN_1 and SN_2. Bistability can occur if one of them is stabilized in an additional bifurcation. This is what happens beyond the zero-Hopf point ZH_2, in which the Hopf line (H_2) (and also SN_1) change from sub- to supercritical. The H_2-line is then located between SN_2 and SN_1, and stabilizes the lower saddle. This is shown in Fig. 3.9(c), which corresponds to a section along the vertical green line labeled C in Fig. 3.9. On the right hand side of the H_2 point (red point), bistability between fixed points is observed, while on the left hand side, bistability of the upper steady state and the stable limit cycle (not shown) occurs between H_2 and SN_2. The H_2 line eventually crosses the SN_2 line at $K = 1.12$. Beyond this point, bistability of fixed points can be observed in the whole $\Delta\nu_{\mathrm{inj}}$-interval between the saddle-node lines SN_2 and SN_1. This is shown in Fig. 3.9(d), which corresponds to a vertical section in Fig. 3.9(a) along the solid blue line labeled by D.

Time series in the bistability region with spontaneous emission noise, i.e., $\beta \neq 0$, are depicted in Fig. 3.10. Fig. 3.10(a) shows a time series for $K = 0.88$ and $\Delta\nu_{\mathrm{inj}} = -7\,\mathrm{GHz}$.

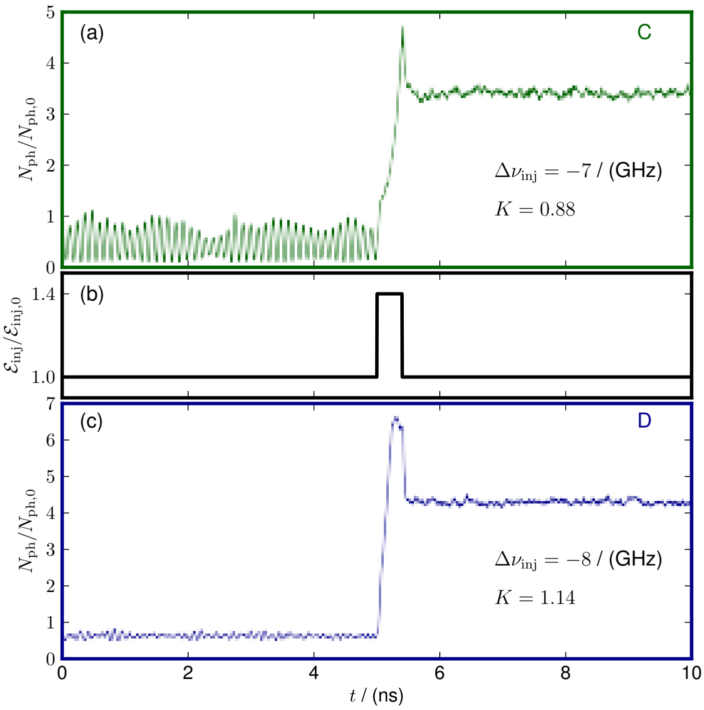

Figure 3.10: Bistability of attractors within the locking tongue. The switching is induced by a rectangular increase of the injection strength with a duration of 400 ps. **(a)**: Switching from stable limit cycle to fixed point for $\Delta\nu_{\mathrm{inj}} = -7\,\mathrm{GHz}$ and $K = 0.88$. **(b)**: Current pulse. **(c)**: Switching between stable fixed points for $\Delta\nu_{\mathrm{inj}} = -8\,\mathrm{GHz}$ and $K = 1.14$. Parameters: fast rates, $\alpha = 2$, $J = 1.5J_{\mathrm{th}}$, $\beta = 1.1 \cdot 10^{-3}$, and other parameters as in Table 2.3.

This point is marked by a gray cross on the green vertical line labeled by C in Fig. 3.9(a) and by the gray dashed line in Fig. 3.9(c). Initially, the laser evolves on the stable limit cycle that was born at the H_2 point (red dot in Fig. 3.9(c)). The limit cycle is deformed by the spontaneous emission noise. At $t = 4.5\,\mathrm{ns}$ a short, rectangular pulse with a duration of $400\,\mathrm{ps}$ and a height of $\mathcal{E}_{\mathrm{inj}} = 1.4\,\mathcal{E}_{\mathrm{inj},0}$ is superimposed to the constant injection with $\mathcal{E}_{\mathrm{inj},0}$, which is depicted in Fig. 3.10(b). (Note that the relation of K and $\mathcal{E}_{\mathrm{inj},0}$ is given by Eq. (3.5).) This pulse excites the system, which then relaxes to the stable fixed point. A switching process into the opposite direction is also possible by reducing the injection strength for a short time. Figure 3.10(c) depicts the bistability of fixed points for $\Delta\nu_{\mathrm{inj}} = 8\,\mathrm{GHz}$ and $K = 1.14$, which is marked by a gray cross on the blue vertical line labeled by D in Fig. 3.9(a) and by the gray dashed line in Fig. 3.9(d). Initially, the system rests in the fixed point with the lower photon number. At $t = 4.5\,\mathrm{ns}$, the current pulse provokes a switching to the stable fixed point with the higher photon number.

Both, the bistability of a periodic orbit and a fixed point as well as the bistability of two fixed points have been observed experimentally in a QD laser under optical injection [ERN10a, KEL11c]. However, in this experiment the spontaneous emission noise showed out to be strong enough to induce the switching processes. At least for the set of fast scattering rates discussed so far, this is only possible very close to the bifurcation points. For applications, it would be advantageous to design the band structure such that the intensity difference between the steady state intensities of the stable fixed points is large enough to prevent noise induced switching processes. Our simulations suggest that this should be possible for shallow-dot band structures. In the next subsection, the dependence of the bistability region on the band structure is discussed.

3.4.2. Dependence of bistability region on band structure

Figures 3.11(a)–(d) depict saddle-node (gray) and Hopf bifurcation (red) lines in the (K,$\Delta\nu_{\mathrm{inj}}$)-plane for slow, reference, fast, and very fast Coulomb scattering rates, respectively. The slow, reference, and fast rates describe the band structures summarized in Table 2.1, and the very fast rates are obtained by multiplying the in-scattering rates of the fast set by the factor $1 \cdot 10^4$ (see Section 2.2). The triangles, in which bistability between fixed points is possible, are blue shaded. For the slow rates, the supercritical part of the Hopf line H_2 has nearly the same slope than the saddle-node line S_1. Furthermore, the lower zero-Hopf point ZH_2 (red diamond), beyond which bistability of fixed points is possible, is located at a very high injection strength $K = 2.1$ close to the lower corner of the triangle, which is given by the lower cusp point C (gray circle). As a result, the surface of the triangle is so small that bistability of fixed points should not be observable experimentally. In Section 2.3, it was discussed that the dynamics of solitary laser for the slow set of rates is similar to the dynamics of QW lasers. The slow carrier exchange between carrier reservoir and QD levels ensures a clear timescale separation between the fast photon- and the slow carrier-subsystems, which is expressed by the small factor γ multiplying the right hand sides of the carrier equations (see Eqs. (2.4)). Similar to a typical class B QW laser, this QD laser is a slow-fast system, showing the characteristic, weakly damped and thus pronounced ROs. The smallness of the bistability region agrees

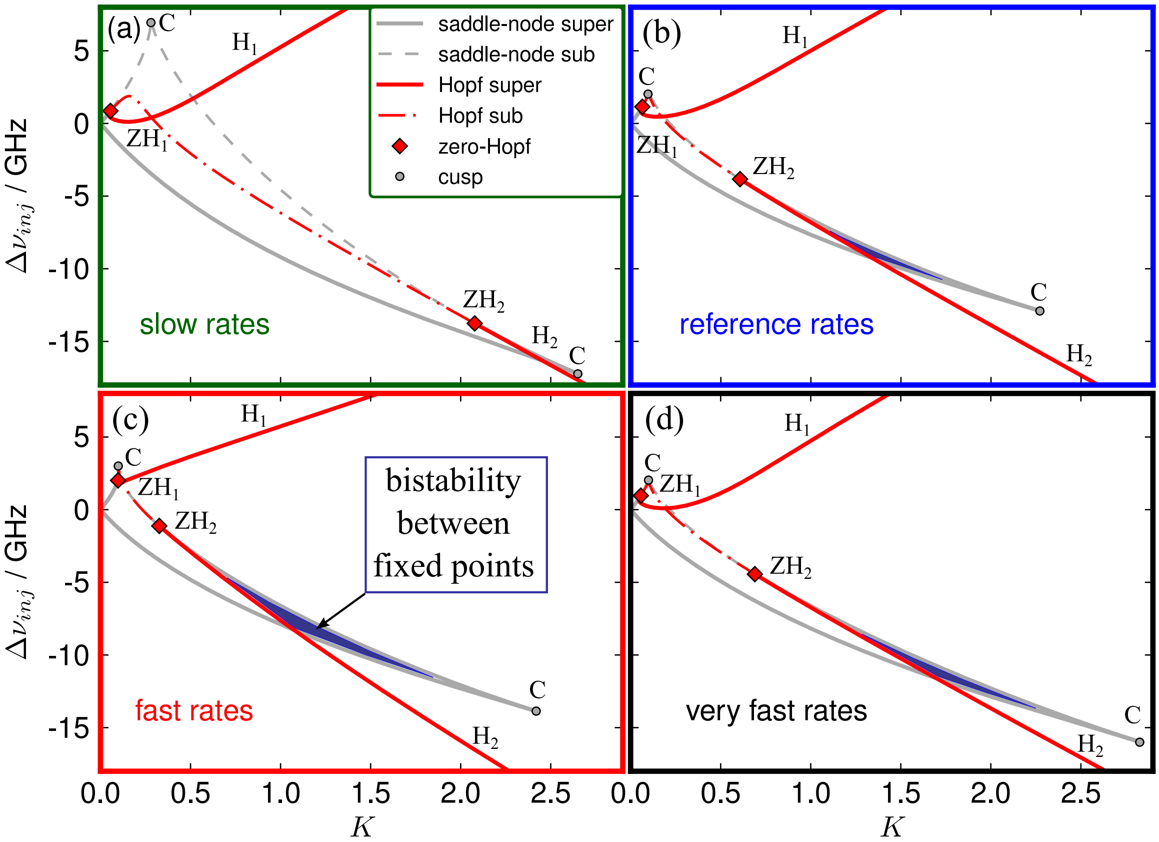

Figure 3.11.: Locking tongues in a plane spanned by injection strength K and frequency detuning $\Delta\nu_{\mathrm{inj}}$ for slow rates **(a)**, reference rates **(b)**, fast rates **(c)**, and very fast rates **(d)**. Red and gray lines denote Hopf (H_1 and H_2) and saddle-node bifurcations, respectively. Solid thick and dashed thin lines mark sub- and supercritical bifurcation lines. Zero-Hopf (ZH_1 and ZH_2) and cusp (C) points are marked by red diamonds and gray dots, respectively. In the blue shaded regions bistability between phase-locked steady states occurs. Parameters: $J = 1.5J_{\mathrm{th}}$ and other parameters as in Table 2.3.

well with experimental findings for QW lasers, where bistability of fixed points was not observed [WIE02a, SIM03].

Going from the slow set of rates (Fig. 3.11(a)) over the reference set of scattering rates (Fig. 3.11(b)) to the fast set of rates (Fig. 3.11(c)), the ZH_2-point shifts strongly towards lower values of the injection strengths. Meanwhile, the cusp point C shifts only weakly. This results in a successive increase of the triangle in phase space (blue shading), in which bistability of fixed points is observed. Comparing the bifurcation diagram for the fast rates to the one of the very fast rates depicted in Fig. 3.11(d), both, ZH_2-point and lower cusp point C shift toward higher values of K, but still the bistability region remains larger than for the reference rates. Note that for the very fast rates, the bistability region is still much larger than for the slow rates, although both have similar RO damping. This indicates that the special Coulomb scattering dynamics of QD laser can not be described completely by its influence on the linear laser characteristics, i.e., RO frequency and damping.

Concluding, our analysis suggests that a shallow-dot band structure formed by large QDs is advantageous to increase the region, in which bistability of fixed points is observed in phase space. This might be a hint that quantum dash semiconductor lasers, in which the active region consist of large, elongated QD like structures, could be well suited to realize all-optical switches.

3.5. Analytic expressions for steady states

In the last section, an overview of the complex dynamics of QD semiconductor lasers under optical injection was given. Starting from this section the focus lies on analytic solutions. At first, the steady states of the dynamical equations are discussed in this section, before expressions for saddle-node and Hopf bifurcation lines are discussed in the next sections. To alleviate the notation, no new symbols are introduced for the steady states of the dynamical variables. Equating to zero the left hand sides of the dynamical equations (3.12), we obtain

$$0 = \rho_{\mathrm{inv}} R + \tilde{k}\cos(\Psi), \tag{3.17a}$$

$$0 = -\delta\omega + \alpha\rho_{\mathrm{inv}} - \frac{\tilde{k}}{R}\sin(\Psi), \tag{3.17b}$$

$$0 = F_e - r_{\mathrm{ph}}(\rho_e + \rho_h - 1)R^2 - \rho_e\rho_h, \tag{3.17c}$$

$$0 = F_h - r_{\mathrm{ph}}(\rho_e + \rho_h - 1)R^2 - \rho_e\rho_h, \tag{3.17d}$$

$$0 = J - F_e - cW_eW_h, \tag{3.17e}$$

$$0 = J - F_h - cW_eW_h. \tag{3.17f}$$

Assuming lasing conditions ($R \neq 0$), Eq. (3.17a) yields an expression for the inversion in terms of the injection strength $\tilde{k}$ and the phase difference between master and slave Ψ

$$\rho_{\mathrm{inv}} = -\frac{\tilde{k}}{R}\cos(\Psi). \tag{3.18}$$

For the solitary laser ($\tilde{k} = 0$), the expression (2.25) for the gain-clamping ($\rho^0_{\mathrm{inv}} = 0$) is retrieved from Eq. (3.18).

Next, we would like to determine the width of the phase-locking tongue, which is given by the condition $\Psi' = 0$. Furthermore, explicit expressions are derived for the saddle-node lines bordering the phase-locking tongue for low injection strength. Therefore, Eq. (3.18) is inserted into Eq. (3.17b), which yields an implicit equation for the steady states of Ψ and R in dependence of the input detuning $\delta\omega$

$$\delta\omega = -\frac{\tilde{k}}{R}\Big(\alpha\cos(\Psi) + \sin(\Psi)\Big) = -\frac{\tilde{k}}{R}\sqrt{1+\alpha^2}\sin\Big(\Psi + \arctan(\alpha)\Big), \tag{3.19}$$

where some trigonometric relations[6] have been used for the second equality. From Eq. (3.19), two solutions for the phase difference between master and slave Ψ are obtained

$$\Psi^1 \equiv -\arcsin\left(\frac{\delta\omega R}{\tilde{k}\sqrt{1+\alpha^2}}\right) - \arctan(\alpha), \tag{3.21a}$$

$$\Psi^2 \equiv (2n+1)\pi + \arcsin\left(\frac{\delta\omega R}{\tilde{k}\sqrt{1+\alpha^2}}\right) - \arctan(\alpha), \quad \text{for} \quad n \in \mathbb{Z}. \tag{3.21b}$$

As discussed in the previous section, inside the phase-locking region always one of the solutions (3.21) is stable, which is known as phase-locking or Adler's type locking [ADL73].

Equation (3.19) admits solutions for Ψ only if the condition

$$\left|\frac{\delta\omega R}{\tilde{k}\sqrt{1+\alpha^2}}\right| \leq 1$$

is fulfilled, which defines the boundaries of the phase-locking tongue. At these boundaries pairs of solutions are created in saddle-node bifurcations. The detuning at the saddle-node bifurcation lines is given in dependence of $\tilde{k}$, R, and α by

$$\delta\omega^{\text{sn}}_{\pm}(\tilde{k}, R, \alpha) \equiv \pm\frac{\tilde{k}\sqrt{1+\alpha^2}}{R}. \tag{3.22}$$

The above equation permits to determine the width of the locking tongue as

$$2|\delta\omega^{\text{sn}}_{\pm}| = 2\tilde{k}\frac{\sqrt{1+\alpha^2}}{R}, \tag{3.23}$$

which reveals that the width of the locking tongue increases with α. Further, the saddle-node points (limit-points) in the ($\delta\omega$,ρ_{inv})-plane can be calculated by first inserting Eq. (3.22) into Eqs. (3.21), and then plugging the expressions for $\Psi^{1/2}$ into Eq. (3.18), which yields

$$(\delta\omega^{\text{sn}}_{\pm}, \rho^{\text{sn}}_{\text{inv}}) \equiv \pm\frac{\tilde{k}}{R}\left(\sqrt{1+\alpha^2}, \frac{\alpha}{\sqrt{1+\alpha^2}}\right), \tag{3.24}$$

where the signs are the same as in Eq. (3.22) and are independent of the choice of the phases Ψ^1 and Ψ^2.

---

[6] The following trigonometric relations are needed

$$\cos(\arctan(\alpha)) = \frac{1}{\sqrt{1+\alpha^2}}, \qquad \sin(\arctan(\alpha)) = \frac{\alpha}{\sqrt{1+\alpha^2}}, \tag{3.20a}$$

$$\sin(x \pm y) = \sin(x)\cos(y) \pm \cos(x)\sin(y), \qquad \cos(x \pm y) = \cos(x)\cos(y) \mp \sin(x)\sin(y). \tag{3.20b}$$

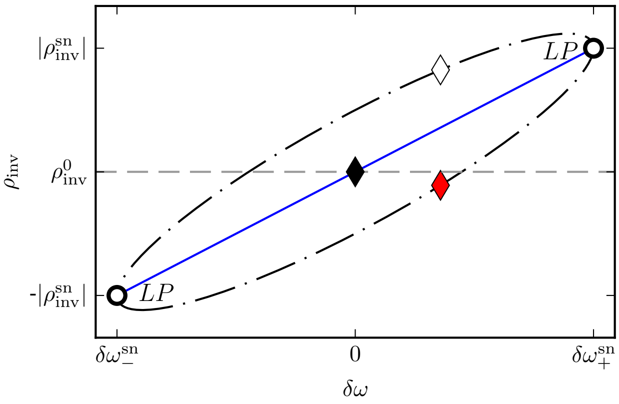

Figure 3.12: Steady state solutions in a plane spanned by frequency detuning $\delta\omega$ and inversion ρ_{inv}. The fixed points lie on an ellipse (black dash-dotted line). Stable and unstable fixed points are denoted by open and filled red diamonds, respectively. The locking-boundary is given by the two intersection points of the ellipse and the saddle-node line (blue line) located at $\left(\delta\omega_{-}^{\mathrm{sn}}, -|\rho_{\mathrm{inv}}^{\mathrm{sn}}|\right)$ and $\left(\delta\omega_{+}^{\mathrm{sn}}, |\rho_{\mathrm{inv}}^{\mathrm{sn}}|\right)$, respectively (black circles labeled by LP). The lasing fixed point (stable node) of the solitary laser is denoted by a filled black diamond. Parameters: $\alpha = 2.0$, $R = 2$, $\tilde{k} = 0.5$, and $\delta\omega = 0.2$.

Geometrically, the locked solutions, i.e., the solutions of equations (3.17), lie on an ellipse in the $(\delta\omega, \rho_{\mathrm{inv}})$-plane. This can be seen by noting that equations (3.18) and (3.19) are a parametric representation of an ellipse with the phase difference Ψ acting as a curve parameter. Figure 3.12 depicts the ellipse by a black dash-dotted line. For nonzero α-factors, it is tilted with respect to the $\delta\omega$-axis. Another expression for the ellipse that will become important in the subsequent sections can be obtained by inserting the square of Eq. (3.18) into the square of Eq. (3.19) and employing $1 = \sin^2(x) + \cos^2(x)$, which yields

$$\tilde{k}^2 = R^2 \left[\rho_{\mathrm{inv}}^2 + (\alpha\rho_{\mathrm{inv}} - \delta\omega)^2\right]. \tag{3.25}$$

Solving for the inversion, we obtain two branches of solutions

$$\rho_{\mathrm{inv}} = \frac{1}{1+\alpha^2}\left(\delta\omega\alpha \pm \sqrt{\frac{(1+\alpha^2)\tilde{k}^2}{R^2} - \delta\omega^2}\right). \tag{3.26}$$

Plus and minus branch correspond to different fixed points of the system. Usually, the fixed point with the lower carrier inversion is stable within the phase-locking region. Since the term under the square-root in Eq. (3.26) remains real within the phase-locking region, it follows that the minus branch has the lower inversion. In Fig. 3.12, the stable and the unstable fixed points are denoted by a filled red diamond, and an open black diamond, respectively. Note that these two fixed points are, in contrast to the black ellipse, obtained for fixed bifurcation parameters $\tilde{k}$, $\delta\omega$, and α. For given bifurcation parameters the phase differences Ψ^1 and Ψ^2 can be calculated from Eqs. (3.21). The corresponding steady states of the inversion ρ_{inv} may then be calculated by inserting $\Psi^{1/2}$ into Eq. (3.17a). The unstable fixed point (plus sign in Eq. (3.26)) is obtained from Ψ^1, and the stable fixed point (minus sign in Eq. (3.26)) is obtained from Ψ^2. Equivalently, the inversion ρ_{inv} of stable and unstable fixed points may be calculated directly by inserting $\tilde{k}$, $\delta\omega$, and α into Eq. (3.26). At the end of this section, it will be shown how $R = R(\tilde{k}, \delta\omega, \alpha)$ needed in Eqs. (3.21) and (3.26) can be calculated for given bifurcation parameters $\tilde{k}$, $\delta\omega$, and α. (In the sketch of Fig. 3.12 R has been set to $R = 2$.)

Demanding that the saddle-node condition of Eq. (3.22) is fulfilled, the square root in Eq. (3.26) vanishes, and we obtain

$$\rho_{\text{inv}}(\delta\omega, \alpha) = \frac{\delta\omega\alpha}{1+\alpha^2}, \tag{3.27}$$

which is depicted by a blue line in Fig. 3.12. The locking boundary given by the limit points (saddle-node bifurcation points) of Eq. (3.24) is geometrically described by the intersection points of the ellipse (3.25) with the line (3.27) (black open circles labeled by LP). The solution with the lower inversion (minus sign in Eq. (3.26)) is stable and lies below the saddle-node line (3.27) (filled red diamond). The other solution (plus sign in Eq. (3.26)) lies above this line and is unstable (open black diamond). Depending on the bifurcation parameters $\tilde{k}$, $\delta\omega$, and α the stable solution can have a lower or a higher inversion than the solitary laser (ρ^0_{inv} depicted by a horizontal gray dashed line). A lower inversion corresponds to constructive interference of master and slave and a higher inversion to destructive interference. The lasing fixed point of the solitary laser is denoted by a filled black diamond in Fig. 3.12.

Next, the steady state of R^2 (or alternatively of $N_{\text{ph}} = N^0_{\text{ph}}R^2$) may be expressed in terms of the carrier populations and the pump current by inserting Eq. (3.17e) into Eq. (3.17c)

$$\begin{aligned} N_{\text{ph}} &= \frac{1}{r_w(\rho_e+\rho_h-1)}\left(J - cW_eW_h - \rho_e\rho_h\right) \\ &\overset{(2.5)}{=} \frac{g}{r_w(2\rho_{\text{inv}}+1)}\left(J - cW_eW_h - \rho_e\rho_h\right) \overset{(2.27)}{\approx} \frac{g\left(J-J_{\text{th}}\right)}{r_w(2\rho_{\text{inv}}+1)}, \end{aligned} \tag{3.28}$$

where in the second equality the definition (2.5), of the rescaled inversion ρ_{inv} was used, and in the approximation in the last line of Eq. (3.28) the definition of the threshold current J_{th} of Eq. (2.27) was employed.

To find an expression for ρ_e and ρ_h in terms of W_e and W_h, and of the parameters $\tilde{k}$ and $\delta\omega$, α, and J, the expression for the steady state of R^2 obtained from the last equality in Eq. (2.26)

$$R^2 = \frac{g(J-J_{\text{th}})}{r_{\text{ph}}(2\rho_{\text{inv}}+1)}, \tag{3.29}$$

is, at first, inserted into Eq. (3.25), which is then solved for ρ_{inv} yielding

$$\begin{aligned} \rho_{\text{inv}} = {} & \frac{\tilde{k}^2 r_{\text{ph}} + \delta\omega g\alpha(J-J_{\text{th}})}{g(1+\alpha^2)(J-J_{\text{th}})} \\ & \pm \frac{1}{g(1+\alpha^2)(J-J_{\text{th}})}\left[\begin{array}{c} \left(\tilde{k}^2 r_{\text{ph}} + \delta\omega g\alpha(J-J_{\text{th}})\right)^2 \\ +g(J-J_{\text{th}})(1+\alpha^2)\left(\tilde{k}^2 r_{\text{ph}} - \delta\omega^2 g(J-J_{\text{th}})\right) \end{array}\right]^{\frac{1}{2}}. \end{aligned} \tag{3.30}$$

The expressions for the steady states of ρ_e and ρ_h are then obtained by inserting the carrier conservation relation (2.9) into the definition (2.5) of ρ_{inv}

$$\rho_e = \frac{1}{2}\left[\frac{2\rho_{\text{inv}}+1+g}{g} + W_h - W_e\right], \tag{3.31a}$$

$$\rho_h = \frac{1}{2}\left[\frac{2\rho_{\text{inv}}+1+g}{g} - W_h + W_e\right]. \tag{3.31b}$$

To sum up, for given parameters $\tilde{k}$, $\delta\omega$, α, and J the steady state values of the dynamical variables can be calculated as follows: at first, the expression (3.30) for ρ_{inv} are inserted into Eqs. (3.31) for ρ_e and ρ_h. This permits to obtain W_e and W_h by inserting the resulting expressions into Eqs. (3.17e) and (3.17f), and solving self-consistently for W_e, and W_h, which has to be done numerically, because the scattering rates are nonlinear function of W_e and W_h. Then ρ_e and ρ_h can be calculated from Eqs. (3.31). Further, R^2 (N_{ph}) may be obtained by inserting the resulting expressions into Eqs. (3.29) and (2.26), respectively, which eventually permits to calculate the phases Ψ^1 and Ψ^2 from Eqs. (3.21).

3.6. Asymptotic approximations

In the following, analytic expressions for the saddle-node and Hopf bifurcation lines that border the phase-locking region of the QD laser under optical injection are discussed. These local bifurcations can be found by analyzing the eigenvalues of the linearization [STR94a]. The QD laser system introduced in Eqs. (3.9) and (3.12c)–(3.12f) is too complex to obtain analytic expressions for its eigenvalues by directly linearizing the full set of equations. Moreover, the small parameter γ describing the time scale separation multiplies the complete right hand sides of the carrier equations (3.12c)–(3.12f), which implies that the limit $\gamma \to 0$ is singular. Thus, one cannot take advantage of the smallness of γ to simplify the equations by firstly expanding the equations in a power-series with respect to γ and then neglecting higher order contributions.

Singular means that $\gamma = 0$ leads to a qualitatively different solution than finite $\gamma \ll 1$ [HIN95, BEN10]. Setting $\gamma = 0$, equations (3.12c)–(3.12f) reduce to $\rho_e' = \rho_h' = W_e' = W_h' = 0$. The carrier populations are constant and thus the photon number N_{ph} of the solitary laser ($\tilde{k} = 0$, $\delta\omega = 0$) increases or decreases exponentially (see Eq. (3.9a)). In contrast, for finite γ stable steady state lasing is observed. Perturbations from this equilibrium decay either exponentially to the lasing steady state in the overdamped limit of the fast scattering rates or damped ROs are observed for the slow, reference, and very fast rates, respectively (cf. Fig. 2.5). Thus, for γ small, we would expect that the leading order problem in γ is conservative, and the damping is introduced by the higher order contributions [LUE11]. In the following, a coordinate transformation is discussed that removes the singularity at $\gamma = 0$ [LUE11] and has been successfully used for rate equations of conventionally class B QW lasers [ERN10b]. Further, this change of coordinates reveals that the dynamical equations for the reservoir populations follow in the limits of the reference, the slow, and the fast rates nearly passively the QD variables and may thus be neglected. This permits an analytic treatment of the reduced equations. In the limit of vanishing carrier lifetimes $\tau_{e/h}$, i.e., for very fast rates, the dynamical variables of the reservoir population cannot be neglected due to the strong coupling of QDs and carrier reservoir. Therefore, a reduced set of dynamical equations is discussed in Subsection 3.7.4, which is an extension of the dynamical equations (2.43) that have been derived for the solitary laser in Section 2.5.5 to the case of optical injection. This reduced set of equations permits to obtain expressions for saddle-node and Hopf bifurcation lines by direct linearization.

3.6.1. Resolving the singularity at $\gamma = 0$

The key observation is that the frequency of the ROs scales like $\sqrt{\gamma}$. Rescaling time with respect to the time scale of the ROs permits to resolve the singularity [LUE11]. The scalings of the deviations from the steady states of the carrier variables are then obtained by balancing the dynamical equations. A derivation of this change of coordinates for the solitary laser from scaling arguments may be found in Appendix B. The new time s and the deviations (y, u_e, u_e, v_e, v_h) from the lasing steady state of the solitary laser $(N^0_{\text{ph}}, \rho^0_e, \rho^0_h, W^0_e, W^0_h)$ are introduced by

$$s \equiv \sqrt{\gamma}\omega t', \qquad N_{\text{ph}} = N^0_{\text{ph}}(1+y), \tag{3.32a}$$

$$\rho_{e/h} = \rho^0_{e/h} + \sqrt{\gamma}\omega g^{-1} u_{e/h}, \qquad W_{e/h} = W^0_{e/h} + \gamma\omega g^{-1} v_{e/h}. \tag{3.32b}$$

Inserting this ansatz into the set of dynamical equations (3.9) and (3.12c)–(3.12f), yields

$$\dot{y} = (1+y)(u_e+u_h) + \frac{2K}{2\kappa\tau_{\text{in}}}\frac{1}{\sqrt{\gamma}\omega}\sqrt{1+y}\cos(\Psi), \tag{3.33a}$$

$$\dot{\Psi} = -\frac{\delta\omega}{\sqrt{\gamma}\omega} + \frac{\alpha}{2}(u_e+u_h) - \frac{K}{2\kappa\tau_{\text{in}}}\frac{1}{\sqrt{\gamma}\omega}\frac{1}{\sqrt{1+y}}\sin(\Psi), \tag{3.33b}$$

$$\omega^2\dot{u}_e = -r_w N^0_{\text{ph}} y - \left[\begin{array}{c}\sqrt{\gamma}\omega\left(t_e^{-1}u_e + r_w N^0_{\text{ph}}(u_e+u_h)(1+y) + u_e\rho^0_h + u_h\rho^0_e\right)\\ +\gamma g^{-1}\omega^2 u_e u_h\end{array}\right], \tag{3.33c}$$

$$\omega^2\dot{u}_h = -r_w N^0_{\text{ph}} y - \left[\begin{array}{c}\sqrt{\gamma}\omega\left(t_h^{-1}u_h + r_w N^0_{\text{ph}}(u_e+u_h)(1+y) + u_e\rho^0_h + u_h\rho^0_e\right)\\ +\gamma g^{-1}\omega^2 u_e u_h\end{array}\right], \tag{3.33d}$$

$$\omega\dot{v}_e = t_e^{-1}u_e - c\sqrt{\gamma}(v_h W^0_e + v_e W^0_h) + c\gamma^{3/2}g^{-1}\omega v_e v_h, \tag{3.33e}$$

$$\omega\dot{v}_h = t_h^{-1}u_h - c\sqrt{\gamma}(v_h W^0_e + v_e W^0_h) + c\gamma^{3/2}g^{-1}\omega v_e v_h, \tag{3.33f}$$

where the contributions of the scattering rates are taken into account by the dimensionless carrier lifetimes $t_{e/h} = (s^{\text{in}}_{e/h} + s^{\text{out}}_{r/h})^{-1}$ in the QD levels. From the scaling laws (3.32), it follows that the scattering rates $s^{\text{in/out}}_{e/h}(W_e, W_h)$ depend only in order $\mathcal{O}(\gamma)$ upon the deviations $v_{e/h}$ from the steady states of the reservoir densities $W^0_{e/h}$. Thus, it follows from (3.33e) and (3.33f) that up to order $\mathcal{O}(\sqrt{\gamma})$, v_e and v_h follow passively the deviations u_e and u_h of the steady states of the QD occupation probabilities ρ^0_e and ρ^0_h. Taking into account only contributions up to $\mathcal{O}(\sqrt{\gamma})$ in the Eqs. (3.33), the dynamical equations of v_e and v_h decouple, and only equations (3.33a)–(3.33d) have to be examined. Further, the leading order problem may be simplified by choosing

$$\omega^2 \equiv 2 r_w N^0_{\text{ph}}. \tag{3.34}$$

A study of the dynamical equations for the solitary laser reveals that $\sqrt{2\gamma r_w N^0_{\text{ph}}}$ is proportional to its RO frequency (measured in units of time t') [LUE11]. Thus, by introducing $s = \sqrt{\gamma}\omega t'$, time was indeed rescaled with respect to the time scale of the ROs. The reduced equations then read

$$\dot{y} = (1+y)(u_e + u_h) + \frac{2K}{2\kappa\tau_{\text{in}}}\frac{1}{\sqrt{\gamma}\omega}\sqrt{1+y}\cos(\Psi), \tag{3.35a}$$

$$\dot{\Psi} = -\frac{\delta\omega}{\sqrt{\gamma}\omega} + \frac{\alpha}{2}(u_e + u_h) - \frac{K}{2\kappa\tau_{\text{in}}}\frac{1}{\sqrt{\gamma}\omega}\frac{1}{\sqrt{1+y}}\sin(\Psi), \tag{3.35b}$$

$$\dot{u}_e = -\frac{y}{2} - bu_e - \sqrt{\gamma}\left[\frac{\omega}{2}(u_e + u_h)(1+y) + \omega^{-1}(u_e\rho_h^0 + u_h\rho_e^0)\right] + \mathcal{O}(\gamma), \tag{3.35c}$$

$$\dot{u}_h = -\frac{y}{2} - au_h - \sqrt{\gamma}\left[\frac{\omega}{2}(u_e + u_h)(1+y) + \omega^{-1}(u_e\rho_h^0 + u_h\rho_e^0)\right] + \mathcal{O}(\gamma), \tag{3.35d}$$

where we have introduced

$$b \equiv \sqrt{\gamma}\omega^{-1}t_e^{-1} = \sqrt{\gamma}\omega^{-1}(s_e^{\text{in}} + s_e^{\text{out}}) \quad \text{and} \quad a \equiv \sqrt{\gamma}\omega^{-1}t_h^{-1} = \sqrt{\gamma}\omega^{-1}(s_h^{\text{in}} + s_h^{\text{out}}), \tag{3.36}$$

which express the impact of the scattering rates onto the dynamics of the QD laser. In Table 3.1 values of ω^{-1}, b, and a are given for the three different sets of scattering rates of Table 2.1 as obtained for a low pump current $J = 1.5J_{\text{th}}$ and for a high pump current $J = 3.5J_{\text{th}}$, respectively. The limit of very fast scattering rates a and b diverge ($a, b \to \infty$), because ω remains $\mathcal{O}(1)$ and $t_{e/h} \to 0$.

Table 3.1.: Values of the parameters ω^{-1}, b, and a for the three sets of scattering rates introduced in Table 2.1 as obtained for a low pump current of $J = 1.5J_{\text{th}}$ and a high pump current of $J = 3.5J_{\text{th}}$, respectively. J_{th} is the dimensionless pump rate at lasing threshold.

set	J/J_{th}	ω^{-1}	b	a
slow rates	1.5	1.35188	0.251138	0.987608
	3.5	2.88049	1.106390	3.08090
reference rates	1.5	1.64994	1.0476	26.7352
	3.5	4.03402	5.43577	85.3158
fast rates	1.5	3.11534	11.9771	30.1707
	3.5	7.07921	45.1732	87.9423

In the following sections, different analytic limits of the reduced problem (3.35) are discussed that permit to find analytic expression for the saddle-node and Hopf bifurcation lines for the set of reference rates as well as for the slow rates. First, a sequence of problems is derived that is ordered in powers of the order parameter γ. Starting from the equations obtained in the lowest order, these problems have to be solved subsequently. Therefore, at first, scaling laws for the steady states of the dynamical variables y, Ψ, u_e, and u_h with respect to γ have to be derived from their steady state relations. Then, the different scalings of b and a with respect to γ in the limit of the reference and of the slow rates are taken into account (see Table 3.1). For the solitary laser, these limits have already been discussed in [LUE11]. For the injection problem, additionally, K and $\delta\omega$ have to be scaled with respect to γ. Therefore, we note that for reference, slow, and in the limit of very fast rates RO damping and RO frequency scale like $\mathcal{O}(\gamma)$ and $\mathcal{O}(\sqrt{\gamma})$, respectively, as discussed in Section 2.5 (see Table 2.4). This suggest that $\Delta\nu_{\mathrm{inj}}$ and K have to scale like $\mathcal{O}(\gamma)$ to obtain a good analytical approximation for a Hopf bifurcation, in which the injection undamps the relaxation oscillations as it is the case for the upper supercritical Hopf line close to the ZH_1 point (cf. Fig. 3.2). This is referred to as *weak* injection in the following. In Section 3.5, it was discussed that the ZH_2-point, at which the Hopf bifurcation line becomes supercritical for negative detuning, appears for $\alpha \gtrsim 0.5$ at a considerably higher injection strength than the ZH_1-point. This suggests to study also a case in which $\Delta\nu_{\mathrm{inj}}$ and K scale like $\mathcal{O}(\sqrt{\gamma})$. This is denoted as *strong* injection in the following.

The main results of the next sections are analytic expressions for the saddle-node and Hopf bifurcation lines in the $(\tilde{k}, \delta\omega)$-plane in the limits of weak and strong injection. Further, formulas are derived for the ZH_1-point and the critical injection strength, below which no Hopf bifurcation can occurs. The most important analytic results are summarized in Table 3.2. For reference, slow, and in the limit of very fast scattering rates the same analytic expressions are obtained. Only the RO damping Γ^{RO} and the RO frequency ω^{RO} frequency change for each set of scattering rates (see Table 2.4).

It is possible to skip the next rather technical sections and to continue directly with Section 3.9, where the bifurcation lines obtained by numerical path continuation are compared with their analytical approximations.

Table 3.2.: Analytic expressions for the frequency detuning of the saddle-node ($\delta\omega_{\pm}^{\mathrm{sn}}$) and the Hopf ($\delta\omega_H$) bifurcation lines as well as for the zero-Hopf point for positive detuning ($\tilde{k}^{\mathrm{ZH},1}, \delta\omega^{\mathrm{ZH},1}$) and the critical Hopf point ($\tilde{k}_{H,c}, \delta\omega_{H,c}$) in a plane spanned by injection strength $\tilde{k}$ and frequency input detuning $\delta\omega$. Further, the frequency of the limit cycle born in the Hopf bifurcation ω_H is listed. The expressions are written with respect to dimensionless time $t' \equiv 2\kappa t$. They are valid for the reference, the slow, and the limit of very fast scattering rates. For these rates RO frequency ω^{RO} and RO damping Γ^{RO} may be found in Table 2.4.

Type of bifurcation line/point	**strong Injection** $\tilde{k} = \mathcal{O}(\sqrt{\gamma})$ and $\delta\omega = \mathcal{O}(\sqrt{\gamma})$	**weak injection** $\tilde{k} = \mathcal{O}(\gamma)$ and $\delta\omega = \mathcal{O}(\gamma)$
saddle-node	$\delta\omega_{\pm}^{\mathrm{sn}} = \pm\tilde{k}\sqrt{1+\alpha^2}$	$\delta\omega_{\pm}^{\mathrm{sn}} = \pm\tilde{k}\sqrt{1+\alpha^2}$
Hopf	$\delta\omega_H = \pm\frac{\tilde{k}}{2}\frac{\left\lvert 2\tilde{k}^2+(\omega^{\mathrm{RO}})^2(1-\alpha^2)\right\rvert}{\left(\tilde{k}^2\left[\tilde{k}^2+(\omega^{\mathrm{RO}})^2\right]+(1+\alpha^2)\frac{(\omega^{\mathrm{RO}})^4}{4}\right)^{1/2}}$	$\delta\omega_H = \frac{4\alpha\Gamma^{\mathrm{RO}}}{1+\alpha^2} \pm \frac{\lvert\alpha^2-1\rvert}{\sqrt{1+\alpha^2}}\sqrt{\tilde{k}^2 - \frac{4(\Gamma^{\mathrm{RO}})^2}{1+\alpha^2}}$
zero-Hopf point	$(\tilde{k}^{\mathrm{ZH},1}, \delta\omega^{\mathrm{ZH},1}) = (0,0)$	$(\tilde{k}^{\mathrm{ZH},1}, \delta\omega^{\mathrm{ZH},1}) = \frac{\Gamma^{\mathrm{RO}}}{\alpha}\sqrt{1+\alpha^2}\left(1, \sqrt{1+\alpha^2}\right)$
critical Hopf point	$(\tilde{k}_{H,c}, \delta\omega_{H,c}) = (0,0)$	$(\tilde{k}_{H,c}, \delta\omega_{H,c}) = \frac{2\Gamma^{\mathrm{RO}}}{\sqrt{1+\alpha^2}}\left(1, \frac{2\alpha}{\sqrt{1+\alpha^2}}\right)$
Hopf frequency	$\omega_H = \sqrt{\left(\omega^{\mathrm{RO}}\right)^2 + \tilde{k}^2}$	$\omega_H = \omega^{\mathrm{RO}}$

3.7. Derivation of saddle-node and Hopf lines for strong injection

In this section, we concentrate on the derivation of the saddle-node and Hopf bifurcation lines for strong injection. Especially, we aim to find an analytic expression of the supercritical part of the Hopf line for negative detuning close to the ZH_2-point. In Section 3.3.3, it was already discussed that the two zero-Hopf (ZH) points (see Fig. 3.3) act as organizing centers of the bifurcation diagram [WIE99, NIZ01, WIE05, WIE06, ERN10b, KEL12a]. Therefore, it is crucial that the analytic approximations match best in their vicinities. The exact values of detuning $\delta\omega$ and injection strength K of these points can be obtained from the numerical path continuation, which then permits to find the best scaling of $\delta\omega$ and K with respect to γ. For the reference rates, a moderate pump current of $J/J_{\mathrm{th}} = 1.5$ as well as moderate $\alpha = 2.0$, the ZH_2-point is located at $(K^{\mathrm{ZH},2}, \Delta\nu_{\mathrm{inj}}^{\mathrm{ZH},2}) = (0.6075, -3.832\,\mathrm{GHz}\,)$, which suggest the scalings

$$k \equiv \frac{K}{2\kappa\tau_{\mathrm{in}}}\frac{1}{\sqrt{\gamma\omega}}, \qquad\qquad \Delta \equiv \frac{\delta\omega}{\sqrt{\gamma\omega}}, \tag{3.37}$$

where k and Δ are $\mathcal{O}(1)$-quantities[7]. These scalings correspond to the limit of strong injection of Table 3.2. The small parameter of this section is $\epsilon \equiv \sqrt{\gamma}$. Inserting the scaling laws (3.37) into the reduced dynamical equations (3.35), yields the set of equations that is discussed in this section

$$\dot{y} = (1+y)(u_e+u_h) + 2k\sqrt{1+y}\cos(\Psi), \tag{3.38a}$$

$$\dot{\Psi} = -\Delta + \frac{\alpha}{2}(u_e+u_h) - \frac{k}{\sqrt{1+y}}\sin(\Psi), \tag{3.38b}$$

$$\begin{aligned}\dot{u}_e = &-\frac{y}{2} - bu_e - \epsilon\frac{\omega}{2}(u_e+u_h)(1+y)\\ &-\epsilon\omega^{-1}(\rho_e^0 u_h + \rho_h^0 u_e) + \mathcal{O}(\epsilon^2),\end{aligned} \tag{3.38c}$$

$$\begin{aligned}\dot{u}_h = &-\frac{y}{2} - au_h - \epsilon\frac{\omega}{2}(u_e+u_h)(1+y)\\ &-\epsilon\omega^{-1}(\rho_h^0 u_e + \rho_e^0 u_h) + \mathcal{O}(\epsilon^2).\end{aligned} \tag{3.38d}$$

At first, the most general case, where a and b are $\mathcal{O}(1)$, is discussed. It permits to calculate the steady states, and additionally a parametric expression for the saddle-node lines in the $(\tilde{k}, \delta\omega)$-plane may be obtained. But to obtain explicit expressions for saddle-node and Hopf lines, the problem has to be further simplified by introducing scalings for a and b that are appropriate for reference and slow rates, respectively.

---

[7] For the special case mentioned above, we obtain $(k^{\mathrm{ZH},2}, \Delta^{\mathrm{ZH},2}) = (1.83, -1.74)$.

3.7.1. General case: $a = \mathcal{O}(1)$ and $b = \mathcal{O}(1)$

Equating to zero the right hands sides of Eqs. (3.38), the following steady state equations are obtained in lowest order ($\mathcal{O}(1)$)

$$k\cos(\Psi) = -u_+\sqrt{1+y}, \tag{3.39a}$$

$$k\sin(\Psi) = (\alpha u_+ - \Delta)\sqrt{1+y}, \tag{3.39b}$$

$$0 = -\frac{y}{2} - bu_e, \tag{3.39c}$$

$$0 = -\frac{y}{2} - au_h, \tag{3.39d}$$

where we have introduced $u_+ \equiv (u_e + u_h)/2$, which plays the role of the inversion in this section. Adding the square of (3.39a) to the square of (3.39b) leads to

$$k^2 = (1+y)\left[u_+^2 + (\alpha u_+ - \Delta)^2\right], \tag{3.40}$$

which corresponds to Eq. (3.25) obtained from the full set of equations (3.17). Solving Eq. (3.40) for u_+, we obtain two branches of solutions

$$u_+ = \frac{1}{1+\alpha^2}\left(\Delta\alpha \pm \sqrt{\frac{(1+\alpha^2)k^2}{1+y} - \Delta^2}\right). \tag{3.41}$$

Plus and minus branch correspond to two different steady states of the dynamical equations (3.38). Their stability depends on the bifurcation parameters k and Δ and on y. Within the phase-locking tongue the minus branch is stable. This can be seen as follows: above threshold, the deviation of the inversion ρ_{inv} (see Eq. (2.5)) from its steady state value for the solitary laser, i.e., from $\rho_{\text{inv}}^0 = 0$, is given by $2u_+$. This deviation u_+ is smaller for the minus branch than for the plus branch yielding a more efficient carrier suppression and a higher photon number. Equations (3.41) correspond to the expressions (3.26) for the steady states of the inversion ρ_{inv} that was obtained from the full set of equations (3.17).

Equation (3.41) permits real solutions within the phase-locking tongue, where the term under the square-root is positive, i.e.,

$$\left|\frac{k\sqrt{1+\alpha^2}}{\sqrt{1+y}}\right| \leq \Delta.$$

A pair of solutions is created in a saddle-node bifurcation at

$$\Delta_\pm^{\text{sn}} \equiv \pm k\sqrt{\frac{1+\alpha^2}{1+y}}, \tag{3.42}$$

where plus and minus branch correspond to the locking boundary for positive and negative detuning Δ, respectively. From Eq. (3.41), we see that the inversion along the saddle-node lines is given by

$$u_+^{\text{sn}} \equiv \frac{\alpha\Delta_\pm^{\text{sn}}}{1+\alpha^2} = \pm\frac{k\alpha}{\sqrt{(1+y)(1+\alpha)}}. \tag{3.43}$$

Equations (3.42) and (3.43) correspond to the expressions (3.22) and (3.27) that were obtained from the full system of equations.

The generic unlocking scenario is the following: within the locking tongue a stable focus represented by the minus branch of Eq. (3.41) and an unstable focus given by the plus branch of this equation coexist and annihilate at the saddle-node lines, where the square-root of Eq. (3.41) vanishes (cf. Fig. 3.3). Note that for positive detuning and k's larger than the injection strength of the ZH_1-point, the stable fixed point has been already destabilized in the supercritical Hopf bifurcation, and two unstable fixed-points annihilate in a subcritical saddle-node bifurcation.

Equations (3.39c) and (3.39d) permit to express y in terms of u_+

$$y = -c_{ab}u_+, \quad \text{with} \quad c_{ab} \equiv \frac{4ab}{a+b}, \tag{3.44}$$

where the constant $c_{ab} > 0$ describes the impact of the scattering rates. Substituting Eq. (3.44) into Eq. (3.40), yields $k^2 = k^2(u_+)$, which reads

$$k^2 = (1 - c_{ab}u_+)\left[u_+^2 + (\alpha u_+ - \Delta)^2\right]. \tag{3.45}$$

For the special case of zero detuning ($\Delta = 0$), Eq. (3.40) simplifies as

$$k^2 = (1 - c_{ab}u_+)u_+^2(1+\alpha^2), \tag{3.46}$$

which permits the solutions

$$u_+^2 = 0 \quad \wedge \quad u_+ = c_{ab}^{-1} > 0. \tag{3.47}$$

To find out more about the physical interpretation of these solutions, we have to study the steady states of the solitary laser (see Eqs. (3.39) for $k = 0$). From Eq. (3.39a), we find

$$u_+ = 0 \quad \text{and} \quad y \neq -1 \quad \vee \quad y = -1 \quad \text{and} \quad u_+ \neq 0.$$

The solution with $u_+ = 0$ implies $u_e = -u_h$, from which we obtain the equality $-bu_e = au_e$ with the help of Eqs. (3.39c) and (3.39d). Since $a, b > 0$, this means that the double root $u_+ = 0$ corresponds to the lasing fixed point of the solitary laser, where the deviations u_e, u_h, and y from its lasing steady state are zero (see the definitions of Eqs. (3.32)). For $y = -1$, we find from Eqs. (3.39c) and (3.39d)

$$u_e = \frac{b}{2} \quad \text{and} \quad u_h = \frac{a}{2},$$

which yields $u_+ = c_{ab}^{-1}$. This solution corresponds to the non-lasing steady state with zero photon number and an inversion ρ_{inv} that deviates from its clamping-value above lasing threshold $\rho_{\text{inv}}^0 = 0$, because u_e and u_h differ from zero. From $u_+ = 0$ and $u_+ = c_{ab}^{-1}$ at $k = 0$, a Z-shaped branch of solutions emerges in the (k,u_+)-plane as well as in the (k,y)-plane. These branches are depicted in Figs 3.13(a) and (b), respectively. Figure 3.13(a) depicts the inversion u_+ as a function of k as obtained from Eq. (3.45) (read dashed line), and Fig. 3.13(b) shows the deviation y from the steady state photon number of the solitary laser N_{ph}^0 as obtained from Eq. (3.44) (red dashed line).

For finite Δ, the double root at $u_+ = 0$ (y=0) unfolds, and $u_+ = c_{ab}^{-1}$ ($y = -1$) remains the only possible solution for $k = 0$. The solutions of u_+ and y for finite $\Delta = 0.2$ are depicted by blue solid lines in Figs. 3.13(a) and (b), respectively. They exhibit two limit-points, i.e., saddle-node bifurcation points, which are depicted by open black circles labeled by SN_1 and SN_2. The coexistence of fixed points between SN_1 and SN_2, i.e., the hysteresis of the steady state curve, does not necessarily mean that multistability of stable fixed points is observed. Usually, only the branch with the lower inversion and thus the higher photon number (lower branch in Fig. 3.13(a) and upper branch in Fig. 3.13(b)) is stable. An example for bistability between the upper and lower branch was discussed in Section 3.4.

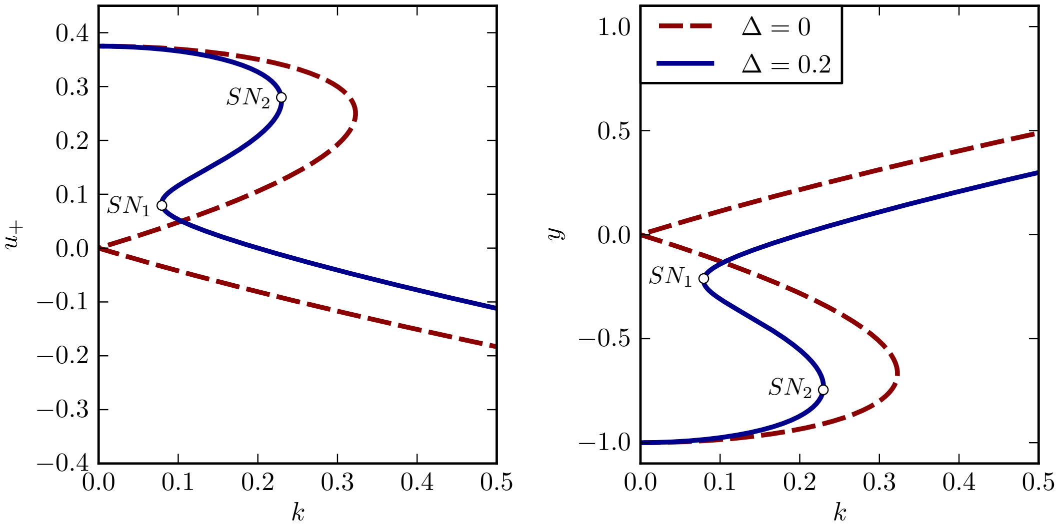

Figure 3.13.: Z-shaped and S-shaped branches of steady states obtained for $\Delta = 0$ (dashed red lines) and $\Delta = 0.2$ (solid blue lines), respectively. Open black circles labeled by SN_1 and SN_2 mark limit-points (saddle-node bifurcation points). **(a)**: Deviation from steady state of the inversion of the solitary laser $u_+ = u_+(k)$ as obtained from Eq. (3.45) **(b)**: Deviation from the steady state of the photon number of the solitary laser $y = y(k)$ as obtained from Eqs. (3.45) and (3.44) for zero detuning $\Delta = 0$ (dashed, red line). Parameters $a = 2$, $b = 1$, and $\alpha = 2$.

The turning points SN_1 and SN_2 of the solid blue steady state curves in Figs. 3.13 obtained for finite Δ are determined by the condition

$$\left.\frac{dk^2}{du_+}\right|_{\mathrm{LP}} = F(\Delta, u_+) = 0, \tag{3.48}$$

where the right hand side is given by

$$F(\Delta, u_+) \equiv -c_{ab}\left[u_+^2 + (\alpha u_+ - \Delta)^2\right] + 2(1 - c_{ab}u_+)\left[u_+ + \alpha(\alpha u_+ - \Delta)\right], \tag{3.49}$$

and $|_{\mathrm{LP}}$ expresses that the derivative is taken at the saddle-node points SN_1 and SN_2. The saddle-node condition (3.48) yields a quadratic equation in $\alpha u_+ - \Delta$. Solving this equation for $\alpha u_+ - \Delta$ for fixed u_+ and then extracting $\Delta = \Delta(u_+)$, yields the detuning at the saddle-node lines as a function of u_+, which reads

$$\Delta_\pm^{\mathrm{sn}}(u_+) \equiv (2u_+ - c_{ab}^{-1})\alpha \pm \sqrt{c_{ab}u_+(2 - 3c_{ab}u_+) + (c_{ab}u_+ - 1)^2\alpha^2}. \tag{3.50}$$

Together with Eq. (3.45) for $k^{\text{sn}} \equiv k(u_+, \Delta^{\text{sn}}_\pm(u_+))$, a parametric solution for the saddle-node lines in the (k, Δ)-plane is obtained.

Stability analysis

Linearizing equations (3.38) around the steady states described by Eqs. (3.39), the following characteristic equation is obtained for the growth rate λ in lowest order ($\mathcal{O}(1)$),

$$\det \begin{bmatrix} u_+ - \lambda & -2(1+y)(\alpha u_+ - \Delta) & 1+y & 1+y \\ \frac{\alpha u_+ - \Delta}{2(1+y)} & u_+ - \lambda & \alpha/2 & \alpha/2 \\ -1/2 & 0 & -b-\lambda & 0 \\ -1/2 & 0 & 0 & -a-\lambda \end{bmatrix} = 0. \tag{3.51}$$

Here, the steady state relations (3.39a) and (3.39b) have been used to eliminate the trigonometric functions. Expanding the determinant, the characteristic equation reads

$$\begin{aligned} 0 = \lambda^4 + \lambda^3 \left[a + b - 2u_+\right] + \lambda^2 \left[1 + y + (\alpha u_+ - \Delta)^2 + u_+^2 - 2u_+(a+b) + ab\right] & \\ + \lambda \begin{bmatrix} (1+y)\left(\frac{(a+b)}{2} + \alpha\Delta - (1+\alpha^2)u_+\right) \\ +(a+b)\left((\alpha u_+ - \Delta)^2 + u_+^2\right) - 2abu_+ \end{bmatrix} & \qquad (3.52) \\ - \frac{(1+y)(a+b)}{2}\left(u_+(1+\alpha^2) - \alpha\Delta\right) + ab\left(u_+^2 + (\alpha u_+ - \Delta)^2\right). & \qquad (3.53) \end{aligned}$$

This fourth order equation is too complex to be solved directly, but it provides a common vantage point for the limits of the reference and the slow rates, which are discussed in the next subsections.

3.7.2. Reference rates: limit $a = \mathcal{O}(\epsilon^{-1})$ and $b = \mathcal{O}(\epsilon)$

The set of reference rates is characterized by fast holes and much slower electrons (cf. Table 3.1), which may be expressed by the following scaling of a and b

$$a = \epsilon^{-1} a_{-1} \quad \text{and} \quad b = \epsilon b_1, \tag{3.54}$$

where a_{-1} and b_1 are $\mathcal{O}(1)$-quantities. Inserting these scalings into the steady state relations of Eqs. (3.38) (cf. Eqs. (3.39)), yields up to $\mathcal{O}(\epsilon)$

$$k\cos(\Psi) = -u_+\sqrt{1+y}, \tag{3.55a}$$

$$k\sin(\Psi) = (\alpha u_+ - \Delta)\sqrt{1+y}, \tag{3.55b}$$

$$0 = -\frac{y}{2} - \epsilon b_1 u_e - \epsilon\frac{\omega}{2}(u_e + u_h)(1+y) - \epsilon\omega^{-1}(\rho_e^0 u_h + \rho_h^0 u_e), \tag{3.55c}$$

$$0 = -\frac{y}{2} - \epsilon^{-1} a_{-1} u_h - \epsilon\frac{\omega}{2}(u_e + u_h)(1+y) - \epsilon\omega^{-1}(\rho_h^0 u_e + \rho_e^0 u_h). \tag{3.55d}$$

The scaling of y, Ψ, u_e, and u_h can now be determined by balancing as many terms as possible in each of Eqs. (3.85). This procedure is known as principle of dominant balance [HIN95, BEN10]. By balancing both sides of Eqs. (3.55a) and (3.55b), we find that $u_+ = (u_e + u_h)/2 = \mathcal{O}(1)$. Thus, either u_e or u_h have to be $\mathcal{O}(1)$. Assuming u_e to be $\mathcal{O}(1)$, and then balancing Eq. (3.55c) reveals that $y = \mathcal{O}(\epsilon)$, which implies $u_h = \mathcal{O}(\epsilon^2)$ from Eq. (3.55d). If we assume $u_h = \mathcal{O}(1)$ instead of $u_e = \mathcal{O}(1)$, we would find from Eq. (3.55d) that $y = \mathcal{O}(\epsilon^{-1})$ and $u_e = \mathcal{O}(\epsilon^{-2})$ holds. This would not permit to balance the leading order ($\mathcal{O}(\epsilon^{-2})$) in Eqs. (3.55a) and (3.55b). Concluding, the following scaling laws for y, u_e, u_h, and u_+ are obtained for the reference rates

$$\begin{aligned} &y = \epsilon Y + \mathcal{O}(\epsilon^2), && u_e = u_e + \mathcal{O}(\epsilon), && u_h = \epsilon^2 U_{h,2} + \mathcal{O}(\epsilon^3), \\ &\Psi = \Psi_0 + \mathcal{O}(\epsilon), && \text{and} \quad u_+ = \frac{u_e}{2} + \mathcal{O}(\epsilon), && \end{aligned} \tag{3.56}$$

where Y, Ψ_0, and $U_{h,2}$ are $\mathcal{O}(1)$-quantities. As we will see in the following subsection, the lowest order approximation for the characteristic equation, which is $\mathcal{O}(\epsilon^{-1})$ for the reference rates, is already a polynomial of order three, and the $\mathcal{O}(1)$-problem is to complex to be solved analytically. It is therefore sufficient to discuss the limit of the reference rates of the equations that were derived from the lowest order approximations (3.39) of the steady states of the general problem (with $a = \mathcal{O}(1)$ and $b = \mathcal{O}(1)$). (This yields the same results as neglecting the terms of order $\mathcal{O}(\epsilon)$ in the steady state relations (3.85).)

Thus, also the general characteristic equation (3.53) may be studied in the limit of the reference rates, i.e., for the scaling of a and b given by Eq. (3.54). For the subsequent calculation, the expression for $k^2(u_+, \Delta)$ of Eq. (3.40) is useful. Inserting the scalings (3.56) of the dynamical variables into Eq. (3.40), it simplifies as

$$k^2 = \left(\frac{u_e}{2}\right)^2 + \left(\alpha\frac{u_e}{2} - \Delta\right)^2. \tag{3.57}$$

The expression (3.41) for the steady state of u_+ simplifies in lowest order to an expression for $u_e/2$

$$\frac{u_e}{2} = \frac{1}{1+\alpha^2}\left(\Delta\alpha \pm \sqrt{(1+\alpha^2)k^2 - \Delta^2}\right), \tag{3.58}$$

and the explicit expression (3.42) for the saddle-node lines now reads

$$\Delta_\pm^{\text{sn}} = \pm k\sqrt{1+\alpha^2}. \tag{3.59}$$

Furthermore, the expression (3.43) for u_+ along the saddle-node lines remains the same with u_+ replaced by $u_e/2$

$$\left(\frac{u_e}{2}\right)^{\text{sn}} \equiv \frac{\alpha\Delta_\pm^{\text{sn}}}{1+\alpha^2} = \pm\frac{k\alpha}{\sqrt{1+\alpha^2}}. \tag{3.60}$$

Stability analysis

Inserting the appropriate scalings of a and b (Eq. (3.54)) and of the dynamical variables (Eq. (3.56)) in the characteristic equation (3.53), its lowest order approximation reads

$$\mathcal{O}(\epsilon^{-1}): \; 0 = \lambda^3 + T_1\lambda^2 + T_2\lambda + T_3, \tag{3.61}$$

where the coefficients are given by

$$\begin{aligned} T_1 &= -2\left(\frac{u_e}{2}\right), \\ T_2 &= \frac{1}{2} + \left(\frac{u_e}{2}\right)^2 + \left(\alpha\frac{u_e}{2} - \Delta\right)^2 = \left(\omega_s^{\mathrm{ref}}\right)^2 + k^2, \\ T_3 &= -\left(\omega_s^{\mathrm{ref}}\right)^2 \left[\frac{u_e}{2}(1+\alpha^2) - \alpha\Delta\right]. \end{aligned} \tag{3.62}$$

To simplify the equation for T_2, the relation (3.57) has been used, and, in addition, the RO frequency of the solitary laser $\omega_s^{\mathrm{ref}} \equiv 1/\sqrt{2}$ (see [LUE11]) has been introduced. The Routh-Hurwitz condition [Pip85] for a stable steady state allows one to determine the bifurcation points from the coefficients T_1, T_2, and T_3 without calculating the eigenvalues λ directly. It reads for a polynomial of order three

$$T_1T_2 - T_3 > 0, \quad T_1 > 0, \quad \text{and} \quad T_3 > 0. \tag{3.63}$$

A steady state can exchange its stability either through a saddle-node bifurcation or a Hopf bifurcation. Since a saddle-node bifurcation is characterized by a zero of a single real eigenvalue, we directly find from Eq. (3.61) that it satisfies the condition

$$T_3 = 0. \tag{3.64}$$

In a Hopf bifurcation, a pair of complex conjugate eigenvalues crosses the imaginary axis. By inserting the ansatz $\lambda = \pm i\omega_{H,s}$ into the characteristic equation (3.61) and subsequently separating real- and imaginary parts, we obtain the conditions

$$-T_1\omega_{H,s}^2 + C_3 = 0 \qquad \wedge \qquad \omega_{H,s}(\mp\omega_{H,s}^2 \pm T_2) = 0. \tag{3.65a}$$

The second condition implies $\omega_{H,s} = 0$ or

$$\omega_{H,s}^2 = T_2 > 0. \tag{3.66}$$

This yields together with the first of Eqs. (3.65a) the conditions for a Hopf bifurcation

$$T_1T_2 - T_3 = 0 \quad \text{and} \quad T_2 > 0. \tag{3.67}$$

Of special interest are bifurcations of stable steady states, because these can be observed experimentally. In the notation of [WIE99] that was already discussed in Section 3.3, bifurcations of stable objects are called *supercritical*, while bifurcations, in which no attractors are created, are called *subcritical*. For a supercritical saddle-node bifurcation, it can be seen from Eq. (3.63) that in addition to the saddle-node-condition (3.64) the conditions

$$T_1T_2 - T_3 > 0 \qquad \text{and} \qquad T_1 > 0 \tag{3.68}$$

have to be fulfilled. Further, for a supercritical Hopf bifurcation, it has to be required that

$$T_1 > 0 \qquad \text{and} \qquad T_3 > 0 \tag{3.69}$$

hold in addition to the Hopf conditions (3.67).

Equation (3.66) has an interesting interpretation from a physical point of view. The coefficient T_2 equals the square of the frequency $\omega_{H,s}^{\mathrm{ref}}$ of the limit-cycle created in the Hopf-bifurcation, i.e.,

$$\omega_{H,s}^{\mathrm{ref}} \equiv \sqrt{\left(\omega_s^{\mathrm{ref}}\right)^2 + k^2} = \sqrt{\frac{1}{2} + k^2}. \tag{3.70}$$

In units of the dimensionless time $t' = 2\kappa t$, the frequency of the Hopf bifurcation reads

$$\omega_H^{\mathrm{ref}} \equiv \sqrt{\left(\omega^{\mathrm{ref}}\right)^2 + k^2} = \sqrt{\gamma r_w N_{\mathrm{ph}}^0 + \tilde{k}^2} = \begin{cases} \omega^{\mathrm{ref}} & \text{for } \tilde{k} \to 0 \\ \tilde{k} & \text{for } \gamma \to 0, \end{cases} \tag{3.71}$$

where $\omega^{\mathrm{ref}} = \sqrt{\gamma r_w N_{\mathrm{ph}}^0}$ is the RO frequency of the solitary laser with respect to time t' (see Table 2.4). Eventually, in units of physical time and injection strength K, Eq. (3.70) reads

$$\omega_{H,t}^{\mathrm{ref}} \equiv \sqrt{\left(\omega_{\mathrm{RO}}^{\mathrm{ref}}\right)^2 + \left(\frac{K}{\tau_{\mathrm{in}}}\right)^2} = 2\kappa\sqrt{\gamma r_w N_{\mathrm{ph}}^0 + \left(\frac{K}{2\kappa\tau_{\mathrm{in}}}\right)^2} = \begin{cases} \omega_{\mathrm{RO}}^{\mathrm{ref}} & \text{for } K \to 0 \\ \frac{K}{\tau_{\mathrm{in}}} & \text{for } \gamma \to 0. \end{cases} \tag{3.72}$$

The RO frequency $\omega_{\mathrm{RO}}^{\mathrm{ref}} = 2\kappa\sqrt{\gamma r_w N_{\mathrm{ph}}^0}$ scales like $\sqrt{\gamma}$. Thus, the Hopf frequency $\omega_{H,t}^{\mathrm{ref}}$ is dominated by the second term that is linear in K if K becomes $\mathcal{O}(1)$. In contrast, for small $K = \mathcal{O}(\sqrt{\gamma})$, the first term under the square-root of Eq. (3.72) dominates, and the Hopf frequency is close to the RO frequency $\omega_{\mathrm{RO}}^{\mathrm{ref}}$ of the solitary laser. Thus, it scales with the square-root of the pump current J

$$\omega_{H,t}^{\mathrm{ref}} \approx \omega_{\mathrm{RO}}^{\mathrm{ref}} \approx 2\kappa\sqrt{\gamma g (J - J_{\mathrm{th}})}. \tag{3.73}$$

In the last approximation, the expression (2.26) for N_{ph}^0 and the gain-clamping above threshold $\rho_{\mathrm{inv}}^0 = 0$ were used. Figure 3.14 depicts the frequency of the limit cycle born in the upper supercritical Hopf bifurcation, which emerges from the ZH_1 point (see for example Fig. 3.6(b)). The black solid line depicts the Hopf frequency calculated numerically from the eigenvalues of the system, and the blue dashed line denotes its analytic approximation of Eq. (3.73). As described by formula (3.73), for low K, the Hopf bifurcation undamps the ROs, i.e., the Hopf frequency $\omega_{H,t}^{\mathrm{ref}}$ is close to the RO frequency of the solitary laser $\omega_{\mathrm{RO}}^{\mathrm{ref}}$, but for high K the Hopf frequency $\omega_{H,t}^{\mathrm{ref}}$ increases linearly with K. This permits to drastically enhance the cutoff frequency of the laser under direct modulation, and thus to increase the modulation bandwidth. The relation (3.70) is well-known for QW lasers and was studied theoretically and verified experimentally in [SIM95, ERN10b]. Further, the linear dependence of $\omega_{H,t}^{\mathrm{ref}}$ on K for high injection strengths (see Eq. (3.72)) was employed to use a semiconductor laser under optical injection as a source for electronic microwave transmission [SEO01]. In simulation, frequencies over six times the RO frequency were proven to be transmitted effectively [CHA07].

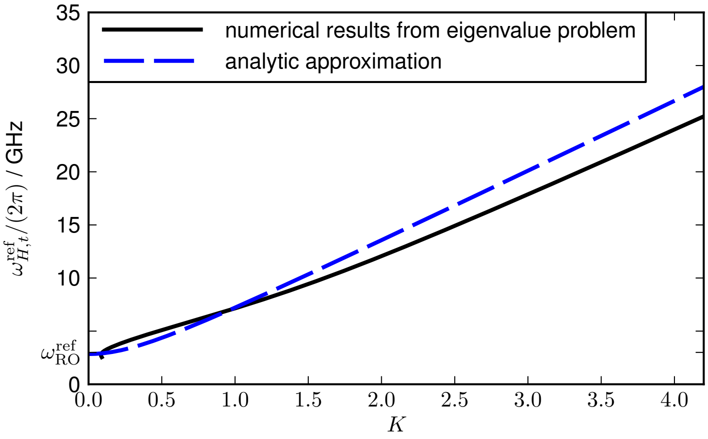

Figure 3.14: Frequency $\omega^{\mathrm{ref}}_{H,t}$ of the limit-cycle created in the supercritical Hopf bifurcation for positive detuning as obtained from the numerically calculated eigenvalues (black solid line) and from the analytic approximation of Eq. (3.73) (blue dashed line), respectively. The RO frequency of the solitary laser is labeled by $\omega^{\mathrm{ref}}_{\mathrm{RO}}$. Parameters: reference rates, $J = 2.5 j_{\mathrm{th}}$, $\alpha = 3$, and other Parameters as in Table 2.3.

Saddle-node lines

Employing the Routh-Hurwitz condition for a saddle-node bifurcation, i.e., $T_3 = 0$ (see Eq. (3.64)), the following parametric expression of the detuning at the saddle-node lines $\Delta^{\mathrm{sn}}_{\pm}(u_e/2) \equiv \Delta(u_e/2)$ are obtained employing the coefficient T_3 of Eq. (3.62)

$$\Delta^{\mathrm{sn}}_{\pm}\left(\frac{u_e}{2}\right) = -\alpha^{-1}\frac{u_e}{2}(1+\alpha^2). \tag{3.74}$$

Here, the detuning depends parametrically on the inversion $u_e/2$. Inserting this into the expression (3.57) for $(k^{\mathrm{sn}})^2 \equiv \left(k\left(u_e/2, \Delta^{\mathrm{sn}}_{\pm}\left(\frac{u_e}{2}\right)\right)\right)^2$, yields

$$k^{\mathrm{sn}}\left(\frac{u_e}{2}\right) = \sqrt{\frac{u_e}{2}\left(\frac{u_e}{2} + \alpha^{-1} + 2\alpha\right)}, \tag{3.75}$$

where k was assumed to be positive. As a quick consistency check, the saddle-node condition (3.48) for the general case $a = \mathcal{O}(1)$ and $b = \mathcal{O}(1)$ can be analyzed in the limit of the reference rates by assuming the scalings of Eqs. (3.54) for a and b, and the scalings of Eqs. (3.56) for u_+ and y. For the constant c_{ab} defined in Eq. (3.44), this yields the relation $c_{ab} = 4\epsilon a_1 + \mathcal{O}(\epsilon^2)$, and the lowest order approximation of the saddle-node condition (3.48) reads

$$\mathcal{O}(1): \quad \left.\frac{dk^2}{d(u_e/2)}\right|_{\mathrm{LP}} = 2\left[\frac{u_e}{2}(1+\alpha^2) - \alpha\Delta\right] = 0, \tag{3.76}$$

which may be also obtained by deriving Eq. (3.57) with respect to $u_e/2$. Comparing $dk^2/d(u_e/2)$ (see Eq. (3.57)) to the coefficient T_3 (Eq. (3.62)), we find that T_3 is antiproportional to the derivative of k^2 with respect to the inversion $u_e/2$

$$T_3 = -\frac{1}{4}\frac{dk^2}{d(u_e/2)}.$$

Thus, it can be seen that the zeros of T_3 correspond to saddle-node bifurcation points of the dynamical equations, which is the Routh-Hurwitz criterion of Eq. (3.64).

By inserting the expression (3.58) for $u_e/2$ into the expression of T_3 of Eq. (3.62) and then employing the limit-point condition (3.64), the explicit expressions (3.59) for the saddle-node lines are retrieved. Thus, the parametric expressions of Eqs. (3.50) and (3.46) yield, in the limit of the reference rates, the same approximation of the saddle-node lines as the explicit expression (3.42), which is valid for small k.

Hopf lines

A parametric solution for the Hopf lines in the (k, Δ)-plane may be obtained by solving the first of the Hopf conditions (3.67), which reads

$$T_1T_2 - T_3 = -2\frac{u_e}{2}(\omega_s^{\text{ref}})^2 + k^2 + (\omega_s^{\text{ref}})^2\left[\frac{u_e}{2}(1+\alpha^2) - \alpha\Delta\right] = 0 \tag{3.77}$$

for $\Delta_H \equiv \Delta(u_e/2, k)$. This yields

$$\Delta_H\left(\frac{u_e}{2}, k\right) = \alpha^{-1}\frac{u_e}{2}\left(\alpha^2 - 1 - \frac{2k^2}{(\omega_s^{\text{ref}})^2}\right) = -\alpha^{-1}\frac{u_e}{2}\left(1 + 4k^2 - \alpha^2\right). \tag{3.78}$$

Inserting Δ_H into the expression for $k_H^2 \equiv k^2(u_e/2, \Delta_H)$ (Eq. (3.57)), and solving for k, we obtain four solutions, of which the two

$$\begin{aligned} k_H\left(\frac{u_e}{2}\right) &\equiv \frac{\left(\omega_s^{\text{ref}}\right)^2}{2\sqrt{2}}\left[\frac{\alpha^2\left(\frac{u_e}{2}\right)^{-2}\left(\omega_s^{\text{ref}}\right)^2}{\pm\alpha\left(\frac{u_e}{2}\right)^{-2}\left(\alpha^2\left(\omega_s^{\text{ref}}\right)^4 - 8\left(\frac{u_e}{2}\right)^2\left[\left(\omega_s^{\text{ref}}\right)^2 + 2\left(\frac{u_e}{2}\right)^2\right]\right)^{1/2} - 4}\right]^{1/2} \\ &= \frac{1}{4\sqrt{2}}\left[\alpha\left(\frac{u_e}{2}\right)^{-2}\left(\frac{\alpha}{2} \pm \sqrt{\frac{\alpha^2}{4} - 8\left(\frac{u_e}{2}\right)^2\left[\frac{1}{2} + 2\left(\frac{u_e}{2}\right)^2\right]}\right) - 4\right]^{1/2} \end{aligned} \tag{3.79}$$

permit non-negative injection strengths at the Hopf line k_H and are thus physically relevant. Equations (3.79) and (3.78) yield the solutions for the Hopf lines in parametric form. For supercritical Hopf lines, additionally the conditions (3.69) have to be fulfilled. It can be seen from Eqs. (3.62) that the first conditions $T_1 > 0$ reads $u_e/2 < 0$, and the second condition $T_3 > 0$ implies the restriction $(u_e/2)(1 + \alpha^2) - \alpha\Delta_H < 0$.

Furthermore, explicit expressions for the detunings at the Hopf lines $\Delta_H = \Delta(k)$ as functions of k may be obtained by inserting the expressions (3.58) for $u_e/2$ into the Hopf condition (3.77) and solving for Δ, which yields

$$\begin{aligned} \Delta_H(k) &= \pm\frac{k}{2}\frac{\left|2k^2 + (\omega_s^{\text{ref}})^2(1-\alpha^2)\right|}{\left(k^2\left[k^2 + \left(\omega_s^{\text{ref}}\right)^2\right] + (1+\alpha^2)\left[\frac{\left(\omega_s^{\text{ref}}\right)^2}{2}\right]^2\right)^{1/2}} \\ &= \pm k\frac{\left|1 + 4k^2 - \alpha^2\right|}{\sqrt{\alpha^2 + (1+4k^2)^2}}. \end{aligned} \tag{3.80}$$

The above equation describes the same approximation of the Hopf lines than the parametric expressions (3.79) and (3.78). In terms of time t', the Hopf condition expresses as

$$\delta\omega_H^{\text{ref}}(\tilde{k}) \equiv \pm\frac{\tilde{k}}{2}\frac{\left|2\tilde{k}^2 + (\omega^{\text{ref}})^2(1-\alpha^2)\right|}{\left(\tilde{k}^2\left[\tilde{k}^2 + \left(\omega^{\text{ref}}\right)^2\right] + (1+\alpha^2)\frac{\left(\omega^{\text{ref}}\right)^4}{4}\right)^{1/2}}. \tag{3.81}$$

Exactly the same expression was obtained by Gavrielides et al. in [GAV97a] for the rate equation model of a conventional class B semiconductor laser discussed in Section 2.5.1[8].

Codimension-2 zero-Hopf point

The approximations for the saddle-node (Eq. (3.59)) and Hopf lines (Eq. (3.80)) only describe one codimension-2 zero-Hopf point, i.e., a tangency of a saddle-node with a Hopf line, which is located at the origin of the (k, Δ)-plane. This can be seen by inserting the expression (3.60) for the inversion at the saddle-node lines into the Hopf condition (3.77). The second term of the Hopf condition then vanishes, and it simplifies as

$$\Delta^{\mathrm{ZH}} \left(\omega_{H,s}^{\mathrm{ref}}\right)^2 \left(k^{\mathrm{ZH}}\right)^2 = 0 \quad \Leftrightarrow \quad \Delta^{\mathrm{ZH}} = 0 \qquad \text{for} \qquad \omega_{H,s}^{\mathrm{ref}} \neq 0. \tag{3.82}$$

From the expression (3.59) for the detuning at the saddle-node lines, it then follows that $\Delta^{\mathrm{ZH}} = 0$ implies $k^{\mathrm{ZH}} = 0$. Thus, the zero-Hopf point for positive detuning (ZH_1-point in Fig. 3.2) shifts to the origin of the $(\tilde{k}, \delta\omega)$-plane

$$(\tilde{k}^{\mathrm{ZH},1}, \delta\omega^{\mathrm{ZH},1}) \equiv (0, 0). \tag{3.83}$$

3.7.3. Slow rates: limit $a = \mathcal{O}(\epsilon)$ and $b = \mathcal{O}(\epsilon)$

For the set of slow scattering rates introduced in Section 2.2, the carrier exchange between carrier reservoir and QD levels is mediated by relatively small Coulomb scattering rates, which results in long carrier lifetimes t_e and t_h in the QD levels. Since the energy spacings between QD and QW (ΔE_e and ΔE_h) are similar for electrons and holes, similar carrier lifetimes are obtained, which translate into comparable values for a and b defined in equations (3.36) (see Table 3.1). This is reflected by the scalings

$$a = \epsilon a_1 \quad \text{and} \quad b = \epsilon b_1, \tag{3.84}$$

where a_1 and b_1 are $\mathcal{O}(1)$. Inserting these scalings into the steady state relations of Eqs. (3.38), yields up to $\mathcal{O}(\epsilon)$

$$k\cos(\Psi) = -u_+\sqrt{1+y}, \tag{3.85a}$$

$$k\sin(\Psi) = (\alpha u_+ - \Delta)\sqrt{1+y}, \tag{3.85b}$$

$$0 = -\frac{y}{2} - \epsilon b_1 u_e - \epsilon\frac{\omega}{2}(u_e + u_h)(1+y) - \epsilon\omega^{-1}(\rho_e^0 u_h + \rho_h^0 u_e), \tag{3.85c}$$

$$0 = -\frac{y}{2} - \epsilon a_1 u_h - \epsilon\frac{\omega}{2}(u_e + u_h)(1+y) - \epsilon\omega^{-1}(\rho_h^0 u_e + \rho_e^0 u_h). \tag{3.85d}$$

Balancing both sides of Eqs. (3.85a) and (3.85b), it can be seen that $u_+ = (u_e + u_h)/2$ is $\mathcal{O}(1)$, and from Eqs. (3.85c) and (3.85d), it follows that both, u_e and u_h, are $\mathcal{O}(1)$, which implies $y = \mathcal{O}(\epsilon)$. Concluding, the following scaling laws for y, u_e,u_h, Ψ, and u_+ are obtained for the slow rates

$$y = \epsilon Y + \mathcal{O}(\epsilon^2),\ u_{e,h} = u_{e,h} + \mathcal{O}(\epsilon),\ \Psi = \Psi_0 + \mathcal{O}(\epsilon),\ \text{and}\ u_+ = u_+ + \mathcal{O}(\epsilon), \tag{3.86}$$

---

[8] To see this, note that in Ref. [GAV97a] the RO frequency is given by $\omega^{\mathrm{RO}} = \sqrt{2\epsilon P}$, where in the notation of Section 2.5.1 $\epsilon = \gamma^{\mathrm{QW}}$, and $P = r^{\mathrm{QW}} N_{\mathrm{ph}}^0$ is the pump parameter (see Eq. (2.23a)). Further, the α-factor was denoted by b in Ref. [GAV97a].

where Y and Ψ_0 are $\mathcal{O}(1)$. Again, the lowest order approximation of the characteristic polynomial, which is now $\mathcal{O}(1)$, permits to obtain expressions for the saddle-node and Hopf bifurcation lines, and the next higher order problem is already to complex to solve. It is therefore sufficient to discuss the limit of the slow rates of the equations that were derived from the lowest order approximations (3.39) of the steady states of the general problem with $a = \mathcal{O}(1)$ and $b = \mathcal{O}(1)$. (This yields the same results as neglecting the terms of order $\mathcal{O}(\epsilon)$ in the steady state relations (3.85).) The expressions derived from the steady states are the same as in the limit of the reference rates if $u_e/2$ is replaced by u_+. Specifically, in the following the steady state relations for $k^2 = k^2(u_+, \Delta)$ of Eq. (3.57) and for $u_+ = u_+(k, \Delta)$ (Eq. (3.58)) are needed. Furthermore, note that the explicit expression (3.42) for the detuning at the saddle-node lines remains valid and the expression for the inversion at the saddle-node lines $(u_+)^{\text{sn}}$ is the same as expression (3.60) for $\left(\frac{u_e}{2}\right)^{\text{sn}}$.

Stability analysis

Inserting the scalings for a and b of Eqs. (3.84) and the scalings of the dynamical variables (Eqs. (3.86)) in the general characteristic equation (3.53), its lowest order approximation reads

$$\mathcal{O}(1): \qquad \lambda\left[\lambda^3 + T_1\lambda^2 + T_2\lambda + T_3\right] = 0. \tag{3.87}$$

This implies that either $\lambda = 0$ or

$$\lambda^3 + T_1\lambda^2 + T_2\lambda + T_3 = 0 \tag{3.88}$$

holds. The coefficients of the characteristic polynomial are given by

$$\begin{aligned}
T_1 &= -2u_+,\\
T_2 &= 1 + (u_+)^2 + (\alpha u_+ - \Delta)^2 = \left(\omega_s^{\text{S}}\right)^2 + k^2,\\
T_3 &= -\left(\omega_s^{\text{S}}\right)^2\left[u_+(1+\alpha^2) - \alpha\Delta\right].
\end{aligned} \tag{3.89}$$

A comparison of the coefficients (Eqs. (3.88)) of the characteristic polynomial in the limit of the slow rates with the expressions for the coefficients obtained for the set of reference rates in Eqs. (3.62) reveals that they have exactly the same form if $u_e/2$ is replaced by u_+, and ω_s^{ref} is replaced by the RO frequency of the solitary laser for the slow rates ω_s^{S}. The latter is given by $\omega_s^{\text{S}} \equiv 1$ [LUE11]. Thus, the expression derived from the characteristic polynomial in the limit of the reference rates in the previous section remains valid for the slow rates. In the following, only the most important expressions for the frequency of the limit-cycle born in the Hopf bifurcation $\omega_{H,s}^{\text{S}}$ and for the Hopf-bifurcation line in the (k,Δ)-plane are discussed. From the coefficient T_2 in Eq. (3.89), the frequency of the Hopf bifurcation is obtained

$$\omega_{H,s}^{\text{S}} \equiv \sqrt{T_2} = \sqrt{\left(\omega_s^{\text{S}}\right)^2 + k^2} = \sqrt{1+k^2}. \tag{3.90}$$

In units of the dimensionless time $t' = 2\kappa t$ normalized to the photon lifetime, it reads

$$\omega_{\text{H}}^{S} \equiv \sqrt{\left(\omega^{\text{S}}\right)^2 + \tilde{k}^2} = \sqrt{2\gamma r_w N_{\text{ph}}^0 + \tilde{k}^2} = \begin{cases} \omega^{\text{S}} & \text{for } \tilde{k} \to 0\\ \tilde{k} & \text{for } \gamma \to 0, \end{cases} \tag{3.91}$$

where $\omega^{\mathrm{S}} = \sqrt{2\gamma r_w N_{\mathrm{ph}}^0}$ is the RO frequency of the solitary laser with respect to time t' (see Table 2.4). Eventually, in units of the physical time t and injection strength K, the RO frequency is given by

$$\omega_{H,t}^{\mathrm{S}} \equiv \sqrt{\left(\omega_{\mathrm{RO}}^{\mathrm{S}}\right)^2 + \left(\frac{K}{\tau_{\mathrm{in}}}\right)^2} = 2\kappa\sqrt{2\gamma r_w N_{\mathrm{ph}}^0 + \left(\frac{K}{2\kappa\tau_{\mathrm{in}}}\right)^2} = \begin{cases} \omega_{\mathrm{RO}}^{\mathrm{S}} & \text{for } K \to 0 \\ \frac{K}{\tau_{\mathrm{in}}} & \text{for } \gamma \to 0, \end{cases} \tag{3.92}$$

where $\omega_{\mathrm{RO}}^{\mathrm{S}} = 2\kappa\sqrt{2\gamma r_w N_{\mathrm{ph}}^0}$ is the RO frequency with respect to the physical time t. From Eq. (3.81), we see that expressing the Hopf lines with respect to time t' yields

$$\delta\omega_H^{\mathrm{S}}(\tilde{k}) \equiv \pm\frac{\tilde{k}}{2}\frac{\left|2\tilde{k}^2 + (\omega^{\mathrm{S}})^2(1-\alpha^2)\right|}{\left(\tilde{k}^2\left[\tilde{k}^2 + \left(\omega^{\mathrm{S}}\right)^2\right] + (1+\alpha^2)\frac{(\omega^{\mathrm{S}})^4}{4}\right)^{1/2}}, \tag{3.93}$$

where $\delta\omega_H^{\mathrm{S}}$ denotes the frequency detuning at the Hopf lines.

3.7.4. Very fast rates: strong coupling between QDs and carrier reservoir

In this subsection, at first, the reduced dynamical equations (2.43) derived in the limit of vanishing carrier lifetimes $t_{e,h} \to 0$ are extended to model the optical injection. Then, the steady states and the linearization of these dynamical equations are discussed, and, eventually, analytical expression for saddle-node and Hopf bifurcations are derived in the limit of strong injection.

In the limit of very fast rates, the optical equations (3.12a) and (3.12b) are the same as for the full set of equations (3.12). Thus, extended by the terms modeling the optical injection the dynamical equations (2.43) read

$$R' = \rho_{\mathrm{inv}} R + \tilde{k}\cos(\Psi), \tag{3.94a}$$

$$\Psi' = -\delta\omega + \alpha\rho_{\mathrm{inv}} - \frac{\tilde{k}}{R}\sin(\Psi), \tag{3.94b}$$

$$\rho_e' = \frac{\gamma}{1+z_e}\left[J - r_{\mathrm{ph}}(\rho_e + \rho_h - 1)R^2 - \rho_e\rho_h - cW_eW_h\right], \tag{3.94c}$$

where the rescaled inversion ρ_{inv} defined in Eq. (2.5) was used to simplify the equations.

Steady states

Equating to zero the right hand sides of equations (3.94), the following steady state relations are obtained

$$\rho_{\mathrm{inv}} R = -\tilde{k}\cos(\Psi), \tag{3.95a}$$

$$\alpha\rho_{\mathrm{inv}} - \delta\omega = \frac{\tilde{k}}{R}\sin(\Psi), \tag{3.95b}$$

$$0 = J - r_{\mathrm{ph}}(\rho_e + \rho_h - 1)R^2 - \rho_e\rho_h - cW_eW_h. \tag{3.95c}$$

Since the field equations for the reduced dynamical equations (3.94) are the same as for the full set of equations (3.12), also the steady state relations (3.95a) and (3.95b) are the same as for the full set of equations (see Eqs. (3.17a) and (3.17b)). This is why the ellipse equation for the injection strength $\tilde{k} = \tilde{k}(\rho_{\text{inv}}, \delta\omega)$ (Eq. (3.25)), for the steady state of the inversion $\rho_{\text{inv}} = \rho_{\text{inv}}(\tilde{k}, \delta\omega)$ (Eq. (3.26)), and the explicit expression for the saddle-node lines in the $(\tilde{k}, \delta\omega)$-plane (Eq. (3.22)) remain unchanged.

Linearization

Linearizing the system of equations (3.94), the following characteristic equation for the growth rate σ is obtained

$$\det \begin{bmatrix} \rho_{\text{inv}} - \sigma & -(\rho_{\text{inv}}\alpha - \delta\omega)R & \frac{gR}{2} c_z \\ \frac{1}{R}(\rho_{\text{inv}}\alpha - \delta\omega) & \rho_{\text{inv}} - \sigma & \frac{\alpha g}{2} c_z \\ -\gamma \frac{2 r_{\text{ph}} R}{1+z_e}\left(\frac{2\rho_{\text{inv}} + g}{g}\right) & 0 & -\gamma 2\Gamma_1 - \sigma \end{bmatrix} = 0, \tag{3.96}$$

where z_e and c_z are given by Eqs. (2.44) and (2.50), respectively. Expanding the characteristic equation, yields a third order polynomial in the growth rate σ

$$\sigma^3 + T_1\sigma^2 + T_2\sigma + T_3 = 0, \tag{3.97a}$$

$$T_1 = 2(\gamma\Gamma_1 - \rho_{\text{inv}}), \tag{3.97b}$$

$$\begin{aligned} T_2 &= \rho_{\text{inv}}^2 + (\alpha\rho_{\text{inv}} - \delta\omega)^2 + \gamma\left[\omega_{1/2}^2 + 2\rho_{\text{inv}}\left(\omega_{1/2}^2 - 2\Gamma_1\right)\right] \\ &= \left(\frac{\tilde{k}}{R}\right)^2 + \gamma\left[\omega_{1/2}^2 + 2\rho_{\text{inv}}\left(\omega_{1/2}^2 - 2\Gamma_1\right)\right], \end{aligned} \tag{3.97c}$$

$$\begin{aligned} T_3 &= \gamma\left[\rho_{\text{inv}}^2 + (\alpha\rho_{\text{inv}} - \delta\omega)^2 - \omega_{1/2}^2(1 + 2\rho_{\text{inv}})\left(\rho_{\text{inv}}(1+\alpha^2) - \alpha\delta\omega\right)\right] \\ &= \gamma\left[\left(\frac{\tilde{k}}{R}\right)^2 - \omega_{1/2}^2(1 + 2\rho_{\text{inv}})\left(\rho_{\text{inv}}(1+\alpha^2) - \alpha\delta\omega\right)\right], \end{aligned} \tag{3.97d}$$

where Γ_1 and $\omega_{1/2}$ denote the first order contribution of the RO damping rate and the $\sqrt{\gamma}$ contribution of the RO frequency $\omega_{1/2}$, respectively. They are defined as

$$\Gamma_1 \equiv \frac{1}{2}\left[\frac{r_{\text{ph}} R^2}{(1+z_e)(1+z_h)}\begin{pmatrix} 2 + z_h + z_e + \rho_h(1+z_h) + \rho_e(1+z_e) \\ +c\left(W_e z_h(1+z_e) + W_h z_e(1+z_h)\right)\end{pmatrix}\right], \tag{3.98a}$$

$$\omega_{1/2} \equiv \sqrt{r_{\text{ph}} R^2 \frac{c_z}{1+z_e}}. \tag{3.98b}$$

Damping rate Γ_1 and frequency $\omega_{1/2}$ are equal to Γ_1^{vf} and $\omega_{1/2}^{\text{vf}}$ obtained for the solitary QD laser (see Eqs. (2.51) if the steady states values R, ρ_b, and W_b of the laser under injection are replaced by the steady state values $R^0 = 1$, ρ_b^0, and W_b^0 of the solitary laser. Further, in the second lines of Eqs. (3.97c) and (3.97c), the ellipse equation for $\tilde{k}^2 = \rho_{\text{inv}}^2 + (\alpha\rho_{\text{inv}} - \delta\omega)^2$ (see Eq. (3.25)) was used to reveal the dependence of T_2 and T_3 on $\tilde{k}$.

The characteristic equation (3.97) is too complicated to directly derive explicit expressions for the Hopf bifurcation lines. Therefore, in the following, approximations for the saddle-node and Hopf lines are derived by scaling the injection parameters $\delta\omega$, $\tilde{k}$, as well as the steady states of the dynamical variables R, Ψ, and ρ_e with respect to the small parameter γ in the limit of strong injection.

Saddle-node and Hopf lines in the limit of strong injection

Strong injection implies that $\tilde{k}$ and $\delta\omega$ scale like $\sqrt{\gamma}$ (cf. Table 3.2). This scaling is motivated by the scaling of the RO frequency of the solitary laser, which is likewise proportional to $\epsilon = \sqrt{\gamma}$ as discussed in Section 3.7.4. Inserting the scalings

$$\tilde{k} = \epsilon \tilde{k}_1 \quad \text{and} \quad \delta\omega = \epsilon \delta\omega_1 \tag{3.99}$$

into the steady state relations (3.95), we see from Eq. (3.95a) that the product of ρ_{inv} and R scales like ϵ, which is fulfilled by the choice $\rho_{\text{inv}} = \mathcal{O}(\epsilon)$ and $R = \mathcal{O}(1)$. The scaling of the inversion $\rho_{\text{inv}} = [g(\rho_e + \rho_h - 1) - 1]/2$ implies that the deviations of ρ_e and ρ_h from their steady state values for the solitary laser ρ_e^0 and ρ_h^0 are at least $\mathcal{O}(\epsilon)$ small. This, in turns, yields that the deviations of W_e and W_h from their steady state values for the solitary laser W_e^0 and W_h^0 are of order $\mathcal{O}(\epsilon)$, which can be seen from the relations (2.41). Summing up, the following scaling laws were derived

$$\begin{aligned} R &= R_0 + \mathcal{O}(\epsilon), & \Psi &= \Psi_0 + \mathcal{O}(\epsilon), & \rho_{\text{inv}} &= \epsilon\rho_{\text{inv},1} + \mathcal{O}(\epsilon^2), \\ \rho_{e,h} &= \rho_{e,h}^0 + \mathcal{O}(\epsilon), & W_{e,h} &= W_{e,h}^0 + \mathcal{O}(\epsilon, \end{aligned} \tag{3.100}$$

where R_0, Ψ_0, and $\rho_{\text{inv},1}$ are $\mathcal{O}(1)$. Lowest order approximations of the saddle-node and Hopf bifurcation lines may be obtained by inserting the scaling laws of Eqs. (3.99) and (3.100) into the characteristic equations (3.97). The coefficients then simplify in lowest order as

$$T_1 = -\epsilon 2\rho_{\text{inv},1}, \tag{3.101a}$$

$$T_2 = \epsilon^2 \left[\left(\frac{\tilde{k}_1}{R_0} \right)^2 + \omega_{1/2}^2 \right], \tag{3.101b}$$

$$T_3 = -\epsilon^3 \omega_{1/2}^2 \left(\rho_{\text{inv},1}(1+\alpha^2) - \alpha\delta\omega_1 \right). \tag{3.101c}$$

The characteristic equation may then be balanced by assuming the scaling

$$\sigma = \epsilon\sigma_1 + \mathcal{O}(\epsilon^2) \tag{3.102}$$

for the growth rate σ. Inserting Eq. (3.102) into the characteristic equation (3.97), it reads in lowest order ($\mathcal{O}(\epsilon^3)$)

$$\sigma_1^3 + T_1\sigma_1^2 + T_2\sigma_1 + T_3 = 0$$

with the coefficients

$$T_1 = -2\rho_{\text{inv},1}, \tag{3.103a}$$

$$T_2 = \omega_{1/2}^2 + \left(\frac{\tilde{k}_1}{R_0} \right)^2, \tag{3.103b}$$

$$T_3 = -\omega_{1/2}^2 \left(\rho_{\text{inv},1}(1+\alpha^2) - \alpha\delta\omega_1 \right). \tag{3.103c}$$

Note that the expressions (3.103) have exactly the same form as the coefficients of the characteristic polynomial for the set of reference rates (Eqs. (3.62)) if ρ_{inv} is replaced by $u_e/2$, $(\tilde{k}_1/R_0)$ is replaced by k, and $\omega_{1/2}$ is replaced by ω_s^{ref}. Thus, the same expressions for the saddle-node and Hopf lines are obtained as in Subsection 3.7.2.

Specifically, from Eq. (3.103b), the frequency of the limit cycle created in the Hopf bifurcation (with respect to time $t' = 2\kappa t$) is given by

$$\omega_H^{\mathrm{vf}} \equiv \epsilon\sqrt{T_2} = \left[\epsilon^2\omega_{1/2}^2 + \left(\frac{\tilde{k}}{R_0}\right)^2\right]^{1/2} \approx \sqrt{\left(\omega^{\mathrm{vf}}\right)^2 + \tilde{k}^2} = \begin{cases}\omega^{\mathrm{vf}} & \text{for } \tilde{k} \to 0\\ \tilde{k} & \text{for } \gamma \to 0,\end{cases} \tag{3.104}$$

where $\epsilon\omega_{1/2}$ has been approximated by the RO frequency of the solitary laser ω^{vf} (see Eq. (2.52)), and R_0 has been replaced by its steady state value for the solitary laser $R^0 = 1$. Eventually, in terms of physical time t, the Hopf frequency $\omega_{H,t}^{\mathrm{vf}}$ is approximated by

$$\omega_{H,t}^{\mathrm{vf}} \approx 2\kappa\sqrt{\left(\omega_{\mathrm{RO}}^{\mathrm{vf}}\right)^2 + \left(\frac{K}{\tau_{\mathrm{in}}}\right)^2} = \begin{cases}\omega_{\mathrm{RO}}^{\mathrm{vf}} & \text{for K } \to 0\\ \frac{K}{\tau_{\mathrm{in}}} & \text{for } \gamma \to 0,\end{cases} \tag{3.105}$$

where $\omega_{\mathrm{RO}}^{\mathrm{vf}}$ denotes the RO frequency of the solitary laser defined in Eq. (2.53b).

Further, applying the Routh-Hurwitz condition (3.64) for a saddle-node bifurcation, i.e., equating $T_3 = 0$ from Eq. (3.103c) to zero, the following approximations for the saddle-node lines in the $(\tilde{k}, \delta\omega)$-plane are obtained

$$\delta\omega_{\pm}^{\mathrm{sn}} = \pm\frac{\tilde{k}\sqrt{1+\alpha^2}}{R^0} \approx \pm\tilde{k}\sqrt{1+\alpha^2}. \tag{3.106}$$

From equation (3.80), it can be seen that the Hopf lines in the $(\tilde{k}, \delta\omega)$-plane read

$$\delta\omega_H^{\mathrm{vf}}(\tilde{k},\alpha) \equiv \pm\frac{\tilde{k}}{2R_0}\frac{|2(\tilde{k}/R_0)^2 + \epsilon^2\omega_{1/2}^2(1-\alpha^2)|}{\sqrt{\tilde{k}^2((\tilde{k}/R_0)^2 + \epsilon^2\omega_{1/2}^2) + (R_0)^2(1+\alpha^2)(\epsilon^2\omega_{1/2}^2/2)^2}} \tag{3.107a}$$

$$\approx \pm\frac{\tilde{k}}{2}\frac{\left|2\tilde{k}^2 + (\omega^{\mathrm{vf}})^2(1-\alpha^2)\right|}{\left(\tilde{k}^2\left[\tilde{k}^2 + (\omega^{\mathrm{vf}})^2\right] + (1+\alpha^2)\frac{\left(\omega^{\mathrm{vf}}\right)^4}{4}\right)^{1/2}}. \tag{3.107b}$$

In the approximations of Eqs. (3.106) and (3.107b), $\epsilon\omega_{1/2}$ and R_0 have again been replaced by ω^{vf} and $R^0 = 1$.

3.7.5. Comparison to numerical path continuation

In this concluding subsection, the analytic approximations for the saddle-node and Hopf bifurcation lines are compared to those obtained from the numerical path continuation. Figure 3.15 depicts saddle-node and Hopf bifurcation lines in the $(K$,$\Delta\nu_{\mathrm{inj}})$-plane for the reference rates (upper row), the slow rates (middle row), and the very fast rates (lower row), respectively. The left column shows the full bifurcation diagram, while the right column depicts detail magnifications close to the zero-Hopf point ZH_1 for positive

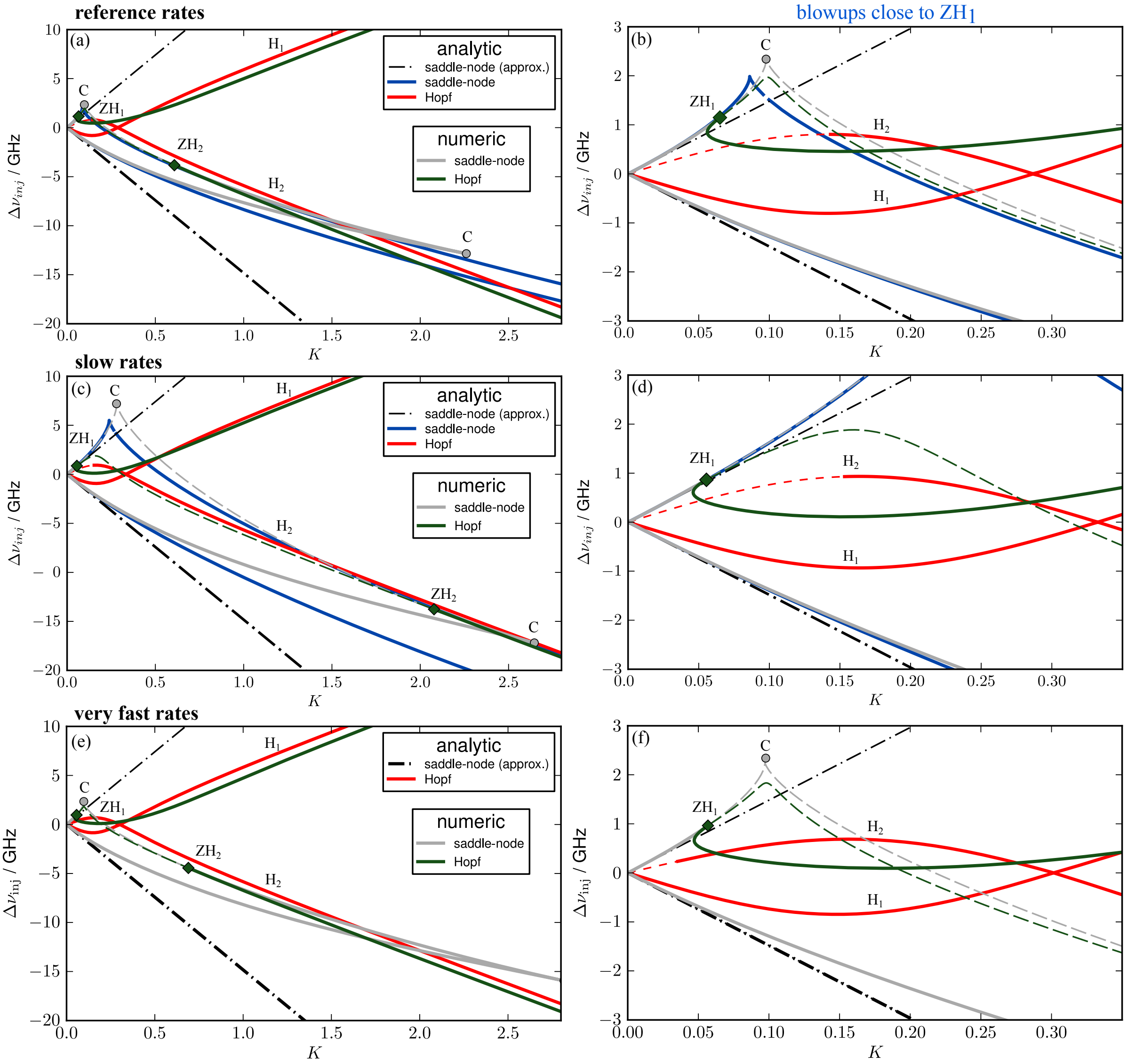

Figure 3.15.: **Left column**: Saddle-node (gray) and Hopf lines (green and labeled by H_1 and H_2) from path continuation and their analytic approximations in a plane spanned by injection strength K and frequency detuning $\Delta\nu_{\text{inj}}$ for reference rates (upper row), slow rates (middle row), and very fast rates (lower row), respectively. Super- and subcritical bifurcation lines are denoted by solid thick and thin dashed lines, respectively. Codimension-2 zero-Hopf (fold-Hopf) points (ZH_1 and ZH_2) and cusp points (C) are labeled by green diamonds and gray circles, respectively. **Analytic expressions:** Blue solid lines denote parametric expressions of Eqs. (3.45) and (3.50) for saddle-node lines. Thick solid and thin dashed red Hopf lines are obtained by Eq. (3.81) (reference rates), Eq. (3.93) (slow rates), and Eq. (3.107b) (very fast rates), respectively. Thick and thin dash-dotted black lines denote supercritical and subcritical saddle-node lines obtained by Eq. (3.59) (reference and slow rates), and Eq. (3.106) (very fast rates), respectively. The supercritical red Hopf and black dash-dotted saddle-node lines were obtained with Routh-Hurwitz criteria of Eq. (3.69) and Eq. (3.68), respectively. **Right column**: Blowups of the left column close to ZH_1-points. Parameters: $\alpha = 0.9$, $J = 1.5J_{\text{th}}$, and other parameters as in Table 2.3.

detuning. Green lines labeled by H_1 and H_2 and gray lines denote numerically calculated Hopf and saddle-node bifurcation lines, respectively. Further, super- and subcritical bifurcations are denoted by thick solid and thin dashed lines, respectively. The blue lines in Figs. 3.15(a)–(d) denote the parametric solutions for the saddle-node lines given by Eqs. (3.45) and (3.50). Here, super- and subcritical parts are not distinguished. The black dash-dotted lines mark the approximations for the saddle-node lines obtained in the limit of reference and slow rates (see Eq. (3.59)) as well as for the very fast rates (see Eq. (3.106)). Here, supercritical lines have been identified by employing the Routh-Hurwitz criterion of Eq. (3.68). Furthermore, red lines denote the analytic expressions for the Hopf lines for reference, slow, and very fast rates as obtained from Eq. (3.81), Eq. (3.93), and Eq. (3.107b), respectively. Super- and subcritical parts of the Hopf lines have been distinguished by the Routh-Hurwitz criterion of Eq. (3.69).

The analytic expressions for the Hopf lines show good agreement with the numerical results for large injection strengths, but deviate for small values of K. In these approximations the zero-Hopf point for positive detuning labeled by ZH_1 shifts to the origin (see Eq. (3.83)). This is why the H_1 line remains supercritical down to $K = 0$. Better analytic expression for the saddle-node lines for low injection strength are obtained in the next Section by assuming a weaker scaling of K and $\Delta\nu_{\text{inj}}$ with respect to γ. The explicit analytic approximations for the saddle-node lines (black dash-dotted line) match well for small values of K, but deviate considerably for high values of K. Further, no explicit expression is found for the saddle-node line connecting the two cusp points (C). This is the reason why no explicit expression for the ZH_2-point was obtained. However, an intersection of the H_2 line with the parametric expression for the saddle-node line (solid blue line) exists, but it is hard to find an explicit analytic expression, because a fourth order problem for the injection strength at the zero-Hopf point has to be solved.

The lowest order approximations for the Hopf lines (see Eqs. (3.81), (3.93), and (3.107b)) do not depend on the damping of the ROs. Since, for high injection strengths, they approximate well the Hopf lines obtained numerically, it may be concluded that the Hopf lines are mainly determined by the injection strength and the α-factor in this regime. Therefore, the frequency of the limit cycle created in the Hopf bifurcation becomes proportional to the injection strength for high K (see Eqs. (3.71), (3.91), and (3.105)). Since the analytic expressions for the Hopf lines do not depend on the RO damping, they are also independent on the details of the band structure that determines the scattering rates, i.e., the lowest order approximations for the Hopf lines are independent of a and b. The RO damping – and thus the details of the band structure – become important in the regime of low injection strengths, which will be discussed in the next section.

3.8. Hopf bifurcation lines for weak injection

In the previous section, it was discussed that under the assumption of strong injection, i.e., $K = \mathcal{O}(\sqrt{\gamma})$ and $\Delta\nu_{\text{inj}} = \mathcal{O}(\sqrt{\gamma})$, the zero Hopf point ZH_1 for positive detuning shifts to the origin of the (K,$\Delta\nu_{\text{inj}}$)-plane. Therefore, in this section, the weaker scaling $K = \mathcal{O}(\gamma)$ and $\Delta\nu_{\text{inj}} = \mathcal{O}(\gamma)$ is discussed, which permits to find a better analytical approximation for the ZH_1 point, and to determine a critical injection strength, below which no Hopf bifurcation can occur.

To take into account the weaker scaling of K and $\Delta\nu_{\mathrm{inj}}$ with respect to γ, a rescaled injection strength k_1 and a rescaled frequency detuning Δ_1, which are both $\mathcal{O}(1)$, are introduced by

$$\epsilon k_1 \equiv \frac{K}{2\kappa\tau_{\mathrm{in}}}\frac{1}{\sqrt{\gamma\omega}} \quad \text{and} \quad \epsilon\Delta_1 \equiv \frac{\delta\omega}{\sqrt{\gamma\omega}}. \tag{3.108}$$

Inserting Eqs. (3.108) into the reduced dynamical equations (3.35), the latter express as follows

$$\dot{y} = (1+y)(u_e+u_h) + 2\epsilon k_1\sqrt{1+y}\cos(\Psi), \tag{3.109a}$$

$$\dot{\Psi} = -\epsilon\Delta_1 + \frac{\alpha}{2}(u_e+u_h) - \epsilon k_1\frac{1}{\sqrt{1+y}}\sin(\Psi), \tag{3.109b}$$

$$\dot{u}_e = -\frac{y}{2} - bu_e - \epsilon\frac{\omega}{2}(u_e+u_h)(1+y) - \epsilon\omega^{-1}(\rho_e^0 u_h + \rho_h^0 u_e) + \mathcal{O}(\epsilon^2), \tag{3.109c}$$

$$\dot{u}_h = -\frac{y}{2} - au_h - \epsilon\frac{\omega}{2}(u_e+u_h)(1+y) - \epsilon\omega^{-1}(\rho_h^0 u_e + \rho_e^0 u_h) + \mathcal{O}(\epsilon^2), \tag{3.109d}$$

where the small parameter $\epsilon = \sqrt{\gamma}$ was introduced. Firstly, the steady states and the linearization of Eqs. (3.109) are calculated without any assumptions on the scalings of the rates a and b. Thus, in the general case as before in the case of strong injection, the general formulation of the problem yields a common basis for the limits of the reference and the slow rates that are discussed in the next subsections.

Steady states

Equating to zero the right hand sides of Eqs. (3.109), the following steady state relations are obtained, which are valid up to $\mathcal{O}(\epsilon)$,

$$\epsilon k_1\cos(\Psi) = -u_+\sqrt{1+y}, \tag{3.110a}$$

$$\epsilon k_1\sin(\Psi) = (\alpha u_+ - \epsilon\Delta_1)\sqrt{1+y}, \tag{3.110b}$$

$$0 = -\frac{y}{2} - bu_e - \epsilon\frac{\omega}{2}(u_e+u_h)(1+y) - \epsilon\omega^{-1}(\rho_e^0 u_h + \rho_h^0 u_e), \tag{3.110c}$$

$$0 = -\frac{y}{2} - au_h - \epsilon\frac{\omega}{2}(u_e+u_h)(1+y) - \epsilon\omega^{-1}(\rho_h^0 u_e + \rho_e^0 u_h), \tag{3.110d}$$

where

$$u_+ = \frac{u_e+u_h}{2} \tag{3.111}$$

has been introduced, which plays the role of the inversion in this section.

By adding the square of Eq. (3.110a) to the square of Eq. (3.110b), an ellipse equation permitting to express k_1 in terms of u_+ is obtained

$$\epsilon^2 k_1^2 = \left(u_+^2 + (\alpha u_+ - \epsilon\Delta_1)^2\right)(1+y). \tag{3.112}$$

Further, an explicit expression for the line of saddle-node bifurcations bordering the locking tongue is retrieved by inserting Eq. (3.110a) into Eq. (3.110b) and employing the trigonometric relations of Eqs. 3.20

$$\Delta_1 = \pm k_1 \sqrt{\frac{1+\alpha^2}{1+y}} \sin\big(\Psi + \arctan(\alpha)\big), \tag{3.113}$$

which has solutions for

$$\left|\Delta_1\right| \leq \left| k_1 \sqrt{\frac{1+\alpha^2}{1+y}} \right|.$$

Pairs of solutions are created in saddle-node bifurcations at

$$\Delta_{1,\pm}^{\mathrm{sn}} \equiv \pm k_1 \sqrt{\frac{1+\alpha^2}{1+y}}. \tag{3.114}$$

Linearization

Linearizing the system (3.109) and taking advantage of the steady state relations (3.110a) and (3.110b)) to eliminate the trigonometric terms, the following characteristic equation for the growth rate λ is obtained

$$\det \begin{bmatrix} u_+ - \lambda & -2(1+y)(u_+\alpha - \Delta_1\epsilon) & 1+y & 1+y \\ \frac{\alpha u_+ - \epsilon\Delta_1}{2(1+y)} & u_+ - \lambda & \alpha/2 & \alpha/2 \\ \begin{bmatrix} -1/2 \\ -\epsilon\omega u_+ \end{bmatrix} & 0 & \begin{bmatrix} -b \\ -\epsilon \begin{bmatrix} \omega^{-1}\rho_h^0 \\ +\frac{\omega}{2}(1+y) \end{bmatrix} \\ -\lambda \end{bmatrix} & -\epsilon \begin{bmatrix} \omega^{-1}\rho_e^0 \\ +\frac{\omega}{2}(1+y)) \end{bmatrix} \\ \begin{bmatrix} -1/2 \\ -\epsilon\omega u_+ \end{bmatrix} & 0 & -\epsilon \begin{bmatrix} \omega^{-1}\rho_h^0 \\ +\frac{\omega}{2}(1+y) \end{bmatrix} & \begin{bmatrix} -a \\ -\epsilon \begin{bmatrix} \omega^{-1}\rho_e^0 \\ +\frac{\omega}{2}(1+y) \end{bmatrix} \\ -\lambda \end{bmatrix} \end{bmatrix} = 0. \tag{3.115}$$

The characteristic equation expands as follows

$$\begin{aligned} &\lambda^4 + \lambda^3 \left[a + b - 2u_+ + \epsilon\left(\omega^{-1}(\rho_e^0 + \rho_h^0) + \omega(1+y)\right)\right] \\ &+ \lambda^2 \begin{bmatrix} 1 + y + ab - 2(a+b)u_+ + u_+^2 + (\epsilon\Delta_1 - \alpha u_+)^2 \\ +\epsilon\left[\frac{\omega}{2}(a+b)(1+y) + \omega^{-1}(a\rho_h^0 + b\rho_e^0) - 2\omega^{-1}u_+(\rho_h^0 + \rho_e^0)\right] \end{bmatrix} \\ &+ \lambda \begin{bmatrix} (1+y)\left(\frac{(a+b)}{2} - u_+ - \alpha(u_+\alpha - \epsilon\Delta_1)\right) - 2abu_+ + (a+b)u_+^2 \\ +2(a+b)(u_+\alpha - \epsilon\Delta_1)^2 \\ +\epsilon \begin{bmatrix} (u_+\alpha - \epsilon\Delta_1)^2\left(2\omega^{-1}(\rho_e^0 + \rho_h^0) + 2\omega\right) - 2u_+\omega^{-1}(b\rho_e^0 + a\rho_h^0) \\ +\omega^{-1}(\rho_e^0 + \rho_h^0)u_+^2 - (1+y)\left(\omega u_+^2 + 2\alpha(u_+\alpha - \epsilon\Delta_1)u_+\omega\right) \end{bmatrix} \end{bmatrix} \\ &+ \frac{u_+}{2}(1+\alpha^2)\left(a(2bu_+ - 1 - y) - y(1+y)\right) \\ &+ \epsilon \begin{bmatrix} \omega^{-1}\left(u_+^2(1+\alpha^2)(b\rho_e^0 + a\rho_h^0)\right) + \frac{\alpha\Delta_1}{2}\left((a+b)(1+y)(-4abu_+)\right) \\ -\frac{\omega}{2}\left((1+\alpha^2)(1+y)(a+b)u_+^2\right) \end{bmatrix} \\ &+ \epsilon^2\left[-2\omega^{-1}\Delta_1 u_+\alpha(b\rho_e^0 + a\rho_h^o) + ab\Delta_1^2\right] = 0. \end{aligned} \tag{3.116}$$

3.8.1. General rates: $a = \mathcal{O}(1)$ and $b = \mathcal{O}(1)$

So far, the two lowest order problems for the eigenvalues (3.124) were derived without any assumptions on the scaling of a, b, and of the dynamical variables. Now, it is assumed that the rates a and b are $\mathcal{O}(1)$-quantities. This permits to derive simple scaling laws for the steady states of y, Ψ, u_e, and u_h from Eqs. (3.110) as it has been done for strong injection in Subsection 3.7.2.

Steady states

With the assumption that Ψ is an $\mathcal{O}(1)$-quantity, u_e or u_h have to scale like $\mathcal{O}(\epsilon)$ to balance Eqs. (3.110a) and (3.110b). From the carrier equations (3.110c) and (3.110d) then follows that u_h scales like u_e, and y has to scale in leading order like ϵ. Summing up, this yields the scalings

$$y = \epsilon Y + \mathcal{O}(\epsilon^2),\ \Psi = \Psi_0 + \mathcal{O}(\epsilon),\ u_{e/h} = 0 + \epsilon U_{e/h} + \mathcal{O}(\epsilon^2),\ \text{and}\ u_+ = \epsilon U_+ + \mathcal{O}(\epsilon^2), \tag{3.117}$$

where Y, Ψ_0, $U_{e/h}$, and U_+ are $\mathcal{O}(1)$. Inserting these scalings into the general steady state relations (3.110), the following relations are obtained, which are valid up to $\mathcal{O}(\epsilon)$,

$$k_1 \cos(\Psi_0) = -U_+, \tag{3.118a}$$

$$k_1 \sin(\Psi_0) = \alpha U_+ - \Delta, \tag{3.118b}$$

$$U_e = -\frac{Y}{2b}, \tag{3.118c}$$

$$U_h = -\frac{Y}{2a}. \tag{3.118d}$$

The ellipse equation (3.112) for k_1^2 simplifies as

$$k_1^2 = U_+^2 + (\alpha U_+ - \Delta)^2, \tag{3.119}$$

and the frequency detuning along the lines of saddle-node bifurcations (Eq. (3.114)) now reads

$$\Delta^{\mathrm{sn}}_{1,\pm} = \pm k_1 \sqrt{1+\alpha^2}. \tag{3.120}$$

Equations (3.119) and (3.120) correspond to the expressions (3.25) and (3.22) that were derived from the full set of dynamical equations.

For the subsequent analysis, it is convenient to derive from Eq. (3.119) an expression of U_+ in terms of k_1 and Δ_1, which corresponds to the expression (3.26) for the steady states of the inversion ρ_{inv} of the full set of dynamical equations,

$$U_+ = \frac{1}{1+\alpha^2}\left(\Delta_1 \alpha \pm \sqrt{(1+\alpha^2)k_1^2 - \Delta_1^2}\right). \tag{3.121}$$

Again, plus and minus in the above equation correspond to different branches of fixed points. Within the phase-locking tongue $\Delta_1^2 < (1+\alpha^2)k_1^2$ holds, and the square-root in Eq. (3.121) remains real.

Linearization

Inserting the scalings for the steady states of the dynamical variables of Eqs. (3.126) and taking into account only terms up to $\mathcal{O}(\epsilon)$, the characteristic equation (3.116) simplifies as

$$\lambda\left[\lambda^3+\lambda^2(a+b)+\lambda(1+ab)+\frac{(a+b)}{2}\right]$$
$$+\,\epsilon\left[\begin{array}{c}\lambda^3\left[\omega^{-1}(\rho_e^0+\rho_h^0)-2U_++\omega\right]\\ +\lambda^2\left[\frac{\omega}{2}(a+b)-2U_+(a+b)+\omega^{-1}(b\rho_e^0+a\rho_h^0)+Y\right]\\ +\lambda\left[\frac{(a+b)}{2}Y-U_+(1+2ab+\alpha^2)+\alpha\Delta_1\right]\\ -\frac{(a+b)}{2}\left[U_+(1+\alpha^2)-\alpha\Delta_1\right]\end{array}\right]=0. \tag{3.122}$$

Further, assuming the scaling

$$\lambda=\lambda_0+\epsilon\lambda_1 \tag{3.123}$$

for the eigenvalues and inserting this ansatz into the characteristic equation (3.122), yields the following two problems in $\mathcal{O}(1)$ and $\mathcal{O}(\epsilon)$, respectively,

$$\mathcal{O}(1):\quad \lambda_0\left[\lambda_0^3+\lambda_0^2(a+b)+\lambda_0(1+ab)+\frac{(a+b)}{2}\right]=0, \tag{3.124a}$$

$$\begin{aligned}\mathcal{O}(\epsilon):\quad &\lambda_1\left[\frac{(a+b)}{2}+2(1+ab)\lambda_0+3(a+b)\lambda_0^2+4\lambda_0^3\right]\\ &+\lambda_0^3\left[\omega^{-1}(\rho_e^0+\rho_h^0)-2U_++\omega\right]\\ &+\lambda_0^2\left[\frac{\omega}{2}(a+b)-2U_+(a+b)+\omega^{-1}(b\rho_e^0+a\rho_h^0)+Y\right]\\ &+\lambda_0\left[\frac{(a+b)}{2}Y-U_+\big(1+2ab+\alpha^2\big)+\alpha\Delta_1)\right]\\ &-\frac{(a+b)}{2}\big[U_+(1+\alpha^2)-\alpha\Delta_1)\big]=0.\end{aligned} \tag{3.124b}$$

The above problems reveal that the ansatz (3.123) for the eigenvalues λ permits to balance more than three terms in each of the two lowest order problems allowing complex solutions for λ_0 and λ_1, which in turns permits to find Hopf bifurcation lines. Even the two lowest order problems (3.124a) and (3.124b) are hard to solve directly. This is why in the next two subsections special scalings for the rates a and b are assumed to derive analytical limits for the set of reference and the set of slow rates, respectively.

3.8.2. Reference rates: limit $a=\mathcal{O}(\epsilon^{-1})$ and $b=\mathcal{O}(\epsilon^{1})$

As already discussed in Subsection 3.7.2, for strong injection in the limit of the reference rates, the decay of holes is much faster than the decay of the electrons, which motivates the following scalings for a and b

$$a=\epsilon^{-1}a_{-1}\quad\text{and}\quad b=\epsilon b_1, \tag{3.125}$$

where a_{-1} and b are $\mathcal{O}(1)$. Next, the resulting scalings have to be determined for y, Ψ, and $u_{e/h}$ from the steady state relations (3.110), or from the steady relation of the previous subsection (see Eqs. (3.118)). Assuming $\Psi = \mathcal{O}(1)$, it can be seen from Eqs. (3.118a) and (3.118b) that to balance the injection terms either $u_e = O(\epsilon)$ or $u_h = O(\epsilon)$. Choosing $u_e = O(\epsilon)$, we see from Eq. (3.118c) that $y = O(\epsilon^2)$, which in terms implies $u_h = O(\epsilon^3)$ from Eq. (3.118d). Summing up, the following scaling laws are obtained for y, Ψ, $u_{e/h}$, and $u_+ = (u_e + u_h)/2$

$$\begin{aligned} y &= \epsilon^2 Y_2 + \mathcal{O}(\epsilon^3), & \Psi &= \Psi_0 + \mathcal{O}(\epsilon), & u_e &= \epsilon U_e + \mathcal{O}(\epsilon^2), \\ u_h &= \epsilon^3 U_{h,3} + \mathcal{O}(\epsilon^4), & u_+ &= \epsilon \frac{U_e}{2} + \mathcal{O}(\epsilon^2), & & \end{aligned} \tag{3.126}$$

where Y_2, Ψ_0, U_e, and $U_{h,3}$ are $\mathcal{O}(1)$. Taking into account that in this limit $U_+ = U_e/2 + \mathcal{O}(\epsilon^2)$ holds, equation (3.121) for the inversion U_+ reads in the limit of the reference rates

$$\frac{U_e}{2} = \frac{1}{1+\alpha^2}\left(\Delta_1 \alpha \pm \sqrt{(1+\alpha^2)k_1^2 - \Delta_1^2}\right). \tag{3.127}$$

Stability analysis

Restricting our analysis to the first two orders, which are $\mathcal{O}(\epsilon^{-1})$ and $\mathcal{O}(1)$, it suffices to study Eq. (3.128) instead of the more general expansion (3.116). Inserting the scaling laws for a and b of Eqs. (3.125) and the scalings of the steady states of the dynamical variables of Eqs. (3.124a) into the characteristic equation (3.124a), the first two order problems for the zeros and the first order contributions λ_0 and λ_1 of the growth rate λ read

$$\mathcal{O}(\epsilon^{-1}): \quad \lambda_0 \left[\lambda_0^2 + \frac{1}{2}\right] = 0, \tag{3.128a}$$

$$\begin{aligned} \mathcal{O}(1): \quad & \lambda_1 \left[\frac{1}{2} + 3\lambda_0^2\right] a_{-1} + \lambda_0^4 \\ & + \lambda_0^2 \left[1 + a_{-1}\left(b_1 + \frac{\omega}{2} - 2\frac{U_e}{2} + \omega^{-1}\rho_h^0\right)\right] \\ & - \frac{a_{-1}}{2}\left[\frac{U_e}{2}(1+\alpha^2) - \alpha\Delta_1\right] = 0. \end{aligned} \tag{3.128b}$$

The lowest order problem (3.128a) admits three solutions

$$\lambda_0^r = 0 \qquad \wedge \qquad (\lambda_0^c)^2 = -\frac{1}{2}, \tag{3.129}$$

one of them is real (λ_0^r) and two are purely imaginary λ_0^c. Thus, in leading order, the dynamical equations are conservative, and the RO damping is introduced by the higher order terms [LUE11].

The first order contribution λ_1^r of the real eigenvalue is obtained by inserting λ_0^r into Eq. (3.128b)

$$\lambda_1^r = \left[\frac{U_e}{2}\left(1+\alpha^2\right) - \alpha\Delta_1\right], \tag{3.130}$$

and the complex conjugate eigenvalues express as

$$\lambda_1^c = -\Gamma_1^{\mathrm{ref}} + \frac{1}{2}\left[\frac{U_e}{2}(1-\alpha^2) + \alpha\Delta_1\right], \tag{3.131}$$

where Γ_1^{ref} is the $\mathcal{O}(\epsilon)$ contribution to the RO damping of the solitary laser, which is defined by

$$\Gamma_1^{\mathrm{ref}} \equiv \frac{1}{2a_{-1}}\left[\frac{1}{2} + a_{-1}(b_1 + \frac{\omega}{2} + \omega^{-1}\rho_h^0)\right]. \tag{3.132}$$

Summing up, by taking into account contributions up to the first order in ϵ, the real eigenvalue λ^r and the pair of complex conjugate eigenvalues λ^c are given by

$$\lambda^r \equiv \lambda_0^r + \epsilon\lambda_1^r = \epsilon\left[\frac{U_e}{2}\left(1+\alpha^2\right) - \alpha\Delta_1\right], \tag{3.133a}$$

$$\lambda^c \equiv \lambda_0^c + \epsilon\lambda_1^c = \pm i\omega_0^{\mathrm{ref}} + \epsilon\left(-\Gamma_1^{\mathrm{ref}} + \frac{1}{2}\left[\frac{U_e}{2}(1-\alpha^2) + \alpha\Delta_1\right]\right), \tag{3.133b}$$

where we have introduced the RO frequency of the solitary laser $\omega_s^{\mathrm{ref}} = 1/\sqrt{2}$. Now, the stability of the two fixed points, which are given by the plus ($(U_e/2)_+$) and the minus branch ($(U_e/2)_-$) of the inversion (see Eq. (3.127)), respectively, can be studied. Inserting Eq. (3.127) into the expressions (3.133) for the eigenvalues, we obtain for the plus branch

$$(\lambda^r)_+ \equiv +\epsilon\sqrt{(1+\alpha^2)k_1^2 - \Delta_1^2}, \tag{3.134a}$$

$$(\lambda^c)_+ \equiv \pm i\omega_s^{\mathrm{ref}} + \epsilon\left(-\Gamma_1^{\mathrm{ref}} + \frac{1}{(1+\alpha^2)}\left[2\alpha\Delta_1 + \frac{(1-\alpha^2)}{2}\sqrt{(1+\alpha^2)k_1^2 - \Delta_1^2}\right]\right), \tag{3.134b}$$

and, for the minus branch, we get the following eigenvalues

$$(\lambda^r)_- \equiv -\epsilon\sqrt{(1+\alpha^2)k_1^2 - \Delta_1^2}, \tag{3.135a}$$

$$(\lambda^c)_- \equiv \pm i\omega_s^{\mathrm{ref}} + \epsilon\left(-\Gamma_1^{\mathrm{ref}} + \frac{1}{(1+\alpha^2)}\left[2\alpha\Delta_1 - \frac{(1-\alpha^2)}{2}\sqrt{(1+\alpha^2)k_1^2 - \Delta_1^2}\right]\right), \tag{3.135b}$$

where the notation $(\lambda^{r,c})_\pm \equiv \lambda^{r,c}\left((U_e/2)_\pm\right)$ was introduced.

RO frequency and damping of solitary laser

For the solitary laser ($k_1 = 0$ and $\Delta_1 = 0$), the leading order contribution of the real eigenvalue vanishes, i.e., from Eqs. (3.134a) and (3.135a) we obtain $(\lambda^r)_\pm = 0$. Further, from the expressions for the complex conjugate eigenvalues $(\lambda^c)_\pm$ of Eqs. (3.134b) and (3.135b), we see that for the solitary laser the terms in the rectangular brackets vanish, and their real parts are simply given by $-\epsilon\Gamma_1^{\mathrm{ref}}$. From the imaginary parts of the complex conjugate eigenvalues, we retrieve the RO frequency $\omega_s^{\mathrm{ref}} = 1/\sqrt{2}$. Thus, in terms of the dimensionless time $t' \equiv (2\kappa)^{-1}t$, the expressions (2.29) for RO frequency $\omega^{\mathrm{ref}} = \sqrt{\gamma\omega}\omega_s^{\mathrm{ref}}$ and damping RO damping $\Gamma^{\mathrm{ref}} = \gamma\omega\Gamma_1^{\mathrm{ref}}$ are retrieved that were already discussed in Subsection 2.5.3 (cf. Table 2.4).

Saddle-node bifurcation lines

A saddle-node bifurcation occurs at a zero of the real eigenvalue. Along the saddle-node lines, both fixed points collide and the square roots in Eqs. (3.134a) and (3.135a) vanish. From $(1+\alpha^2)k_1^2 - \Delta_1^2 = 0$, we retrieve the explicit expression (3.42) for the detuning Δ_1 along the saddle-node lines.

3.8.3. Slow rates: limit $a = \mathcal{O}(\epsilon)$ and $b = \mathcal{O}(\epsilon)$

As already discussed in Subsection 3.7.3 in the limit of the slow rates, a and b are small compared to one, which motivates the scalings

$$a = \epsilon a_1, \quad \text{and} \quad b = \epsilon b_1, \tag{3.136}$$

where a_1 and b_1 are $\mathcal{O}(1)$. To find the scalings of y, Ψ, u_e, and u_h in this limit, the steady state relations (3.118) are considered in the limit that b and a are $\mathcal{O}(\epsilon)$ small. The scalings of $u_{e/h}$ and y remain the same, and from the carrier equations (3.118c) and (3.118d), it can be seen that y has to be $\mathcal{O}(\epsilon^2)$. Summing up, the following scaling laws are obtained for the dynamical variables and $u_+ = (u_e + u_h)/2$

$$y = \epsilon^2 Y_2 + \mathcal{O}(\epsilon^3), \; \Psi = \Psi_0 + \mathcal{O}(\epsilon), \; u_{e/h} = \epsilon U_{e/h} + \mathcal{O}(\epsilon^2), \; \text{and} \; u_+ = \epsilon U_+ + \mathcal{O}(\epsilon^2), \tag{3.137}$$

where Y_2, Ψ_0, $U_{e/h}$, and U_+ are $\mathcal{O}(1)$.

Steady states

The steady state relations (3.118a) and (3.118b) are still valid, because only the scaling of y has changed, and the equations are independent of y. This is why also the relation (3.121) for U_+ in terms of k_1 and Δ_1 as well as the expression for $\Delta^{\mathrm{sn}}_{1,\pm} = \Delta_1(k_1, \Delta_1)$ (Eq. (3.42)) remain unchanged. The steady state relations for the carriers that are valid up to order $\mathcal{O}(\epsilon)$ now express as follows

$$U_e = -\frac{Y_2}{2b_1} \quad \text{and} \quad U_h = -\frac{Y_2}{2a_1}.$$

Stability analysis

Restricting the linear stability analysis again to the two lowest orders in γ, it is sufficient to consider the first two order problems (3.124a) and (3.124b) of the characteristic equation (3.122) in the limit that a and b are $\mathcal{O}(\epsilon)$ small. They simplify as

$$\begin{aligned}
\mathcal{O}(1): \quad & \lambda_0^2 \left[1 + \lambda_0^2\right] = 0, && (3.138\text{a})\\
\mathcal{O}(\epsilon): \quad & \lambda_0(4\lambda_0^2 + 2)\lambda_1 \\
& + \lambda_0^3 \left[a_1 + b_1 + \omega^{-1}(\rho_e^0 + \rho_h^0) - 2U_+ + \omega\right] \\
& + \lambda_0 \left[\frac{(a_1 + b_1)}{2} - U_+ - \alpha(U_+\alpha - \Delta_1)\right] = 0. && (3.138\text{b})
\end{aligned}$$

The leading order problem (3.138a) admits a double real root (λ_0^r) and two complex conjugate roots (λ_0^c)

$$(\lambda_0^r)^2 = 0 \quad \wedge \quad \lambda_0^c = \pm i. \tag{3.139}$$

Thus, in leading order, the equation are conservative as in the case of the reference rates. Inserting the real eigenvalue λ_0^r into the $\mathcal{O}(\epsilon)$ problem (3.138b) does not yield new informations, but inserting the complex conjugate eigenvalues λ_0^c provides the solution

$$\begin{aligned} 2\lambda_1^c &= -\left[a_1 + b_1 + \omega^{-1}(\rho_e^0 + \rho_h^0) - 2U_+ + \omega\right] \\ &\quad + \frac{(a_1+b_1)}{2} - U_+ - \alpha(U_+\alpha - \Delta_1) \\ \Leftrightarrow \qquad \lambda_1^c &= -\Gamma^{\mathrm{S}} + \frac{1}{2}\left[U_+(1-\alpha^2) + \alpha\Delta_1\right], \end{aligned} \tag{3.140}$$

where the gain-clamping $\rho_e^0 + \rho_h^0 = 1 + g^{-1}$ of the solitary laser has been used in the last equality. Further, the first order contribution to the damping rate of the solitary laser was introduced as

$$\Gamma_1^{\mathrm{S}} \equiv \Gamma_1^{\mathrm{S,QW}} + \frac{1}{2}\left[\frac{(a_1+b_1)}{2} + \omega^{-1}g^{-1}\right], \quad \text{with} \quad \Gamma_1^{\mathrm{S,QW}} \equiv \frac{1}{2}(\omega^{-1} + \omega). \tag{3.141}$$

Further, the complex conjugate eigenvalues express as

$$\lambda^c = \lambda_0^c + \epsilon\lambda_1^c = \pm i\omega_s^{\mathrm{S}} + \epsilon\left(-\Gamma_1^{\mathrm{S}} + \frac{1}{2}\left[U_+(1-\alpha^2) + \alpha\Delta_1\right]\right), \tag{3.142}$$

where $\omega_s^{\mathrm{S}} = 1$ is the RO frequency of the solitary laser. Next, the stability of the two fixed points, which are given by the plus ($(U_+)_+$) and the minus branch ($(U_+)_-$) of the inversion, respectively, (see Eq. (3.121)) is studied. Inserting Eq. (3.121) into the expressions (3.142) for the eigenvalues, we obtain for plus and minus branches:

$$(\lambda^c)_+ = \pm i\omega_s^{\mathrm{S}} + \epsilon\left(-\Gamma_1^{\mathrm{S}} + \frac{1}{(1+\alpha^2)}\left[2\alpha\Delta_1 + \frac{(1-\alpha^2)}{2}\sqrt{(1+\alpha^2)k_1^2 - \Delta_1^2}\right]\right), \tag{3.143a}$$

$$(\lambda^c)_- = \pm i\omega_s^{\mathrm{S}} + \epsilon\left(-\Gamma_1^{\mathrm{S}} + \frac{1}{(1+\alpha^2)}\left[2\alpha\Delta_1 - \frac{(1-\alpha^2)}{2}\sqrt{(1+\alpha^2)k_1^2 - \Delta_1^2}\right]\right), \tag{3.143b}$$

where the notation $(\lambda^c)_\pm \equiv \lambda^c\left((U_+)_\pm\right)$ was used.

RO frequency and damping of solitary laser

For the solitary laser ($k_1 = 0$ and $\Delta_1 = 0$), the terms in the rectangular brackets of Eqs. (3.143) vanish, and the real parts of the complex conjugate eigenvalues are simply given by $-\epsilon\Gamma_1^{\mathrm{S}}$. Further, the RO frequency ω_s^{S} is retrieved from their imaginary parts. Thus, with respect to dimensionless time $t' \equiv (2\kappa)^{-1}t$, the expressions (2.31) for RO frequency $\omega^{\mathrm{S}} = \sqrt{\gamma}\omega\omega_s^{\mathrm{S}}$ and damping RO damping $\Gamma^{\mathrm{S}} = \gamma\omega\Gamma_1^{\mathrm{S}}$ are obtained that were already discussed in Subsection 2.5.4 (cf. Table 2.4).

3.8.4. Very fast rates

In this subsection, expressions for the saddle-node and Hopf bifurcation lines are derived in the limit of vanishing carrier lifetimes in the QD levels. In this limit, the characteristic polynomial for the linearized dynamical equations of the laser under optical injection was already derived in Subsection 3.7.4 (see Eq. (3.97)).

Here, approximations of this equation in the limit of weak injection are studied. Weak injection implies that $\tilde{k}$ and $\delta\omega$ scale like γ (cf. Table 3.2). Inserting the scalings

$$\tilde{k} = \gamma\tilde{k}_1 \quad \text{and} \quad \delta\omega = \gamma\delta\omega_1 \tag{3.144}$$

into the steady state relations (3.95) (where $\tilde{k}_1$ and $\delta\omega_1$ are $\mathcal{O}(1)$), we see from Eq. (3.95a) that under the assumption $\Psi = \mathcal{O}(1)$ the product of ρ_{inv} and R scales like γ, which is fulfilled by the choice $\rho_{\text{inv}} = \mathcal{O}(\gamma)$ and $R = \mathcal{O}(1)$. Further, $\rho_{\text{inv}} = \mathcal{O}(\gamma)$ implies that also the deviations of ρ_e and ρ_h from their steady state values of the solitary laser ρ_e^0 and ρ_h^0 are at least $\mathcal{O}(\gamma)$ small (cf. Eq. (3.26)). This, in turns, yields that the deviations of W_e and W_h from their steady state values for the solitary laser W_e^0 and W_h^0 are of order $\mathcal{O}(\gamma)$, which can be seen from the relations (2.41). Summing up, the following scaling laws have been derived

$$\begin{aligned} R &= R_0 + \mathcal{O}(\gamma), & \Psi &= \Psi_0 + \mathcal{O}(\gamma), & \rho_{\text{inv}} &= \gamma\rho_{\text{inv},1} + \mathcal{O}(\gamma^2), \\ \rho_{e,h} &= \rho_{e,h}^0 + \mathcal{O}(\gamma), & W_{e,h} &= W_{e,h}^0 + \mathcal{O}(\gamma). \end{aligned} \tag{3.145}$$

Inserting the scalings (3.145) into the expression for the inversion $\rho_{\text{inv}} = \rho_{\text{inv}}(\tilde{k}, \delta\omega)$ of Eq. Eq. (3.26), we obtain

$$\rho_{\text{inv},1} \equiv \frac{1}{1+\alpha^2}\left(\delta\omega_1\alpha \pm \sqrt{\frac{(1+\alpha^2)\tilde{k}_1^2}{(R_0)^2} - \delta\omega_1^2}\right), \tag{3.146}$$

where plus and minus signs again denote two different fixed points.

Lowest order approximations of the saddle-node and Hopf bifurcation lines may be obtained by inserting the scaling laws of Eqs. (3.144) and (3.145) into the characteristic equations (3.97). In lowest order, its coefficients T_1, T_2, and T_3 then simplify to

$$T_1 = 2\gamma(\Gamma_1 - \rho_{\text{inv},1}), \tag{3.147a}$$

$$T_2 = \gamma(\omega_{1/2})^2, \tag{3.147b}$$

$$T_3 = -\gamma^2(\omega_{1/2})^2\left(\rho_{\text{inv},1}(1+\alpha^2) - \alpha\delta\omega_1\right). \tag{3.147c}$$

Saddle-node bifurcation lines

By inserting Eq. (3.146) into the Routh-Hurwitz condition for a saddle-node bifurcation $T_3 = 0$ (see Eq. (3.64)), the explicit expression for the saddle-node lines of Eq. (3.22) is retrieved, which reads

$$\delta\omega_{\pm}^{\text{sn}} = \pm\frac{\tilde{k}\sqrt{1+\alpha^2}}{R_0} \approx \pm\tilde{k}\sqrt{1+\alpha^2}, \tag{3.148}$$

where in the last approximation R_0 was replaced by the steady state $R^0 = 1$ of the solitary laser.

Hopf bifurcation lines

Noting that the frequency of the limit cycle created in the Hopf bifurcation with respect to the dimensionless time $t' = 2\kappa t$ is given by $\omega_H^{\mathrm{vf}} = \sqrt{T_2}$, yields

$$\omega_H^{\mathrm{vf}} \equiv \sqrt{\gamma \left(\omega_{1/2}\right)^2} \approx \omega^{\mathrm{vf}}, \tag{3.149}$$

where in the last approximation $\sqrt{\gamma\omega_{1/2}}$ has been approximated by the RO frequency of the solitary laser ω^{vf} (see Eq. (2.52)) and Table 2.4. Thus, in the limit of weak injection and in lowest order approximation the frequency of the limit cycle created in the Hopf bifurcation is given by the RO frequency of the solitary laser, i.e., the Hopf bifurcation undamps the ROs. This is the low injection limit $\tilde{k} \to 0$ of expression (3.105) obtained under the assumption of strong injection.

Evaluating the first of the Routh-Hurwitz conditions for a Hopf bifurcation $T_1T_2 - T_3 = 0$ (cf. Eqs. (3.67)), the following condition is obtained in lowest order, which is $\mathcal{O}(\gamma^2)$, from the coefficients of Eqs. (3.147)

$$-\Gamma_1 + \frac{1}{2}\left[\rho_{\mathrm{inv},1}(1-\alpha^2) + \alpha\delta\omega_1\right] = 0. \tag{3.150}$$

Inserting the expressions (3.146) for $\rho_{\mathrm{inv},1}$ into the above equations, the Hopf condition reads

$$-\Gamma_1 + \frac{1}{(1+\alpha^2)}\left[2\alpha\delta\omega_1 \pm \frac{(1-\alpha^2)}{2}\sqrt{(1+\alpha^2)\tilde{k}_1^2 - \delta\omega_1^2}\right] = 0. \tag{3.151}$$

Approximating $\gamma\Gamma_1$ by the damping rate Γ^{vf} of the solitary laser (see Eq. (2.52)), and then rewriting Eq. (3.152) in terms of injection strength $\tilde{k}$ and detuning $\delta\omega$, yields the following expression for the Hopf lines

$$-\Gamma^{\mathrm{vf}} + \frac{1}{(1+\alpha^2)}\left[2\alpha\delta\omega \pm \frac{(1-\alpha^2)}{2}\sqrt{(1+\alpha^2)\tilde{k}^2 - \delta\omega^2}\right] = 0. \tag{3.152}$$

3.8.5. Saddle-node and Hopf bifurcation lines

So far, we have discussed the reference, and the slow rates as well as the limit of very fast scattering rates, separately. Now, we derive analytical expressions for the saddle-node bifurcation lines limiting the locking tongue, the Hopf bifurcation line for positive detuning, and the critical injection strength, below which no Hopf bifurcation may occur, which are valid for all three sets of rates.

A common expression for the saddle-node bifurcation lines in the ($\tilde{k}$,$\delta\omega$)-plane is obtained by rewriting equation (3.42) that is valid in the limit of the reference and the slow rates in terms of $\tilde{k}$ and $\delta\omega$, which yields

$$\delta\omega_{\mathrm{sn}}^{\pm} = \pm\tilde{k}\sqrt{1+\alpha^2}. \tag{3.153}$$

The above expression was previously obtained in the limit of the very fast rates in equation (3.148).

To find a common expression for the Hopf bifurcation lines, we note that the expressions for the complex conjugate pair of eigenvalues $(\lambda^c)_\pm$ have the same form for the reference rates and the slow rates (compare Eqs. (3.134b) and (3.135b) to Eqs. (3.143)). In terms of the dimensionless time $t' = (2\kappa)^{-1}t$, the complex conjugate eigenvalues $(\sigma^c)_\pm \equiv \sqrt{\gamma}\omega(\lambda^c)_\pm$ may be expressed as

$$(\sigma^c)_+ \equiv -\Gamma_+^{\mathrm{eff}} \pm i\omega^{\mathrm{RO}} \quad \text{and} \quad (\sigma^c)_- \equiv -\Gamma_-^{\mathrm{eff}} \pm i\omega^{\mathrm{RO}}, \tag{3.154}$$

where the terms

$$\left(\Gamma^{\mathrm{eff}}\right)_\pm \equiv \Gamma^{\mathrm{RO}} - \frac{1}{(1+\alpha^2)}\left[\alpha\delta\omega \pm \frac{(1-\alpha^2)}{2}\sqrt{(1+\alpha^2)\tilde{k}^2 - \delta\omega^2}\right], \tag{3.155}$$

have been introduced. Plus and minus signs again denote the different fixed points. Physically, the second term on the right hand side of the above equation describes how the RO damping of the solitary laser Γ^{RO} is modified by the injection, thus, $\left(\Gamma^{\mathrm{eff}}\right)_\pm$ plays the role of an effective RO damping. The dependence of this effective damping on the frequency detuning inside the phase-locking tongue is discussed in detail in Section 3.10. Here, we concentrate on the Hopf bifurcation lines. A Hopf bifurcation occurs for $\left(\Gamma^{\mathrm{eff}}\right)_\pm = 0$, when the injection expressed by the term in rectangular brackets on the right hand side of Eq. (3.155) is strong enough to compensate the RO damping Γ^{RO} of the solitary laser. Equations (3.152) describing the Hopf conditions in the limit of very fast scattering rates have the same form than the formulas (3.155) for $\left(\Gamma^{\mathrm{eff}}\right)_\pm$. This permits to conclude that close to the Hopf bifurcation lines the effective damping rate for the very fast rates may also be described by Eqs. (3.155). RO damping Γ^{RO} and RO frequency ω^{RO} for reference, slow, and very fast rates are summarized in Table 2.4. To simplify notation, only the minus branch is considered in the following. As discussed in Subsection 3.8.2, it corresponds to the fixed point with the lower inversion that is stable within the locking tongue, i.e., to the stable focus. However, for both branches the same expression for the detuning at the Hopf lines $\delta\omega = \delta\omega_H(\tilde{k},\alpha)$ is obtained.

Solving the Hopf condition $\left(\Gamma^{\mathrm{eff}}\right)_- = 0$ for $\delta\omega$, yields

$$\begin{aligned}\delta\omega_H(\tilde{k},\alpha) &= \frac{1}{1+\alpha^2}\left[4\alpha\Gamma^{\mathrm{RO}} \pm \sqrt{(\alpha^2-1)^2(1+\alpha^2)\left(\tilde{k}^2 - \frac{4(\Gamma^{\mathrm{RO}})^2}{1+\alpha^2}\right)}\right] \\ &= \frac{4\alpha\Gamma^{\mathrm{RO}}}{1+\alpha^2} \pm \frac{|\alpha^2-1|}{\sqrt{1+\alpha^2}}\sqrt{\tilde{k}^2 - \frac{4(\Gamma^{\mathrm{RO}})^2}{1+\alpha^2}}.\end{aligned} \tag{3.156}$$

The Hopf line has two branches, which coincide for $\alpha = 1$. Inverting Eq. (3.156), the feedback strength at the Hopf bifurcation line $\tilde{k}_H = \tilde{k}_H(\delta\omega,\alpha)$ may be expressed in terms of frequency detuning $\delta\omega$ and α-factor as

$$\tilde{k}_H(\delta\omega,\alpha) = \frac{1}{|\alpha^2-1|}\left[(1+\alpha^2)4\left(\Gamma^{\mathrm{RO}}\right)^2 - 2\alpha\Gamma^{\mathrm{RO}}\delta\omega + (1+\alpha^2)\delta\omega^2\right]^{\frac{1}{2}}. \tag{3.157}$$

Exactly the same expression was obtained by Gavrielides et al. in Ref. [GAV97a] for the standard rate equation model for a conventional class B laser[9] (see also [ERN10b]

---

[9] To compare expression (3.157) with the one obtained in Ref. [GAV97a], note that for the QW rate equation model the RO damping is given by $\Gamma^{\mathrm{RO}} = \epsilon(1+2P)/2$, where $\epsilon = \gamma^{\mathrm{QW}}$ and $P = r^{\mathrm{QW}}N_{\mathrm{ph}}^0$ is the pump parameter (see Eq. (2.23a)). Further, the α-factor was denoted by b in Ref. [GAV97a].

for a comprehensive review). The model for the solitary QW laser was discussed in Section 2.5.1.

To obtain real detunings $\delta\omega_H$, we have to impose that the term under the square root in the last line of Eq. (3.156) remains positive, which yields a critical feedback strength, below which no Hopf instability may occur

$$\tilde{k}_{H,c} \equiv \frac{2\Gamma^{\mathrm{RO}}}{\sqrt{1+\alpha^2}}. \tag{3.158}$$

The position of the critical Hopf point in the ($\tilde{k}$,$\delta\omega$)-plane can be obtained by inserting Eq. (3.158) into Eq. (3.156), which yields

$$(\tilde{k}_{H,c}, \delta\omega_{H,c}) \equiv \frac{2\Gamma^{\mathrm{RO}}}{\sqrt{1+\alpha^2}} \left(1, \frac{2\alpha}{\sqrt{1+\alpha^2}}\right), \tag{3.159}$$

where $\delta\omega_{H,c}$ denotes the frequency detuning at this point. Physically, the existence of a boundary, below which no Hopf bifurcation can occur, may be explained as follows: for low injection strengths, the system is effectively one dimensional, and its phase-locking dynamics may be described by the Adler's type phase equation (3.12b) only. Thus, there cannot be a Hopf bifurcation, and the locking boundaries are given by saddle-node bifurcations. However, for higher injection strengths, changes in the photon number and the inversion become more prominent, which renders higher dimensional bifurcations possible [KEL12a]. For instance, Hopf bifurcations become possible for $\tilde{k} \geq \tilde{k}_{H,c}$. From Eqs. (3.154), it can be seen that in lowest order approximation the frequency of the Hopf bifurcation is given by the RO frequency of the solitary laser, showing that close to $\tilde{k}_{H,c}$ the Hopf bifurcation undamps the ROs. Therefore, it does make sense that $\tilde{k}_{H,c}$ increases linearly with the RO damping. Further, the critical injection strength increases for $\alpha \to 0^+$, which yields a dynamically more stable laser. This can be seen from Figs. 3.6(a) and (b), which depict bifurcation diagrams in the $(\tilde{k}, \delta\omega)$-plane[10] for small $\alpha = 0.9$ and for large $\alpha = 3.2$, respectively. For $\alpha > 1$ the lower branch of the Hopf bifurcation is supercritical, and bends towards zero detuning. The bending of the supercritical Hopf line increases with the α-factor, which in terms provokes a decrease of $\tilde{k}_{H,c}$.

The expression (3.158) for $\tilde{k}_{H,c}$ corresponds up to the factor of 2 to the critical feedback strength, below which the QD laser subject to optical feedback from a distant mirror cannot be destabilized in a Hopf bifurcation [OTT11, GLO12]. This is a first hint to the dynamical similarities of a semiconductor laser under optical injection and a semiconductor laser subject to optical feedback that are further employed in Chapter 4.

Recently, Kelleher et al. proposed in Ref. [KEL12a] a novel method to determine the RO damping Γ^{RO} of a single-mode, semiconductor, class B QW laser by taking advantage of expression (3.158) for the critical feedback strengths $\tilde{k}_{H,c}$. At first, the authors determined experimentally the critical injection strengths $\tilde{k}_{H,c}$. Then, they determined the frequency detunings $\delta\omega_{\pm}^{\mathrm{sn}}$ of the phase-locking boundary. At this injection level, the locking boundary is of saddle-node form, and thus given by Eq. (3.153). Inserting the

---

[10] Injection strength K and frequency detuning $\Delta\nu_{\mathrm{inj}}$ may be expressed $\tilde{k}$ and $\delta\omega$ as $K = 2\kappa\tau_{\mathrm{in}}\tilde{k}$ and $\Delta\nu_{\mathrm{inj}} = \kappa\delta\omega/\pi$.

expression (3.158) for $\tilde{k}_{H,c}$ into Eq. (3.153) and then solving for Γ^{RO}, yields a simple expression of the RO damping in terms of the frequency detuning at the saddle-node lines

$$\Gamma^{\mathrm{RO}} = \frac{1}{2}\left|\delta\omega_{\pm}^{\mathrm{sn}}(\tilde{k}_{H,c})\right|. \tag{3.160}$$

Thus, the RO damping of the solitary laser may be determined by subjecting the laser to external optical injection.

3.8.6. Codimension-2 zero-Hopf point

In this subsection, an expression for the zero-Hopf point for positive detuning, i.e, the ZH_1-point in Fig. 3.2, is derived. A zero-Hopf point occurs at a tangency of a Hopf line with a saddle-node line [KUZ95]. Therefore, the injection strengths $\tilde{k}^{\mathrm{ZH}}$, at which a zero-Hopf point occurs, may be found by inserting expression (3.153) into the Hopf condition $\left(\Gamma^{\mathrm{eff}}\right)_{-} = 0$ (see Eq. (3.155)). The term under the square-root in Eq. (3.155) then vanishes, and solving for $\tilde{k}$, yields

$$\tilde{k}^{\mathrm{ZH}} \equiv \frac{\Gamma^{\mathrm{RO}}}{\alpha}\sqrt{1+\alpha^2}, \tag{3.161}$$

where $\tilde{k}^{\mathrm{ZH}}$ was assumed to be positive. Inserting Eq. (3.161) back into the expression (3.153) for the detuning at the saddle-node lines, yields $\delta\omega_{\pm}^{\mathrm{ZH}} = \pm\tilde{k}^{\mathrm{ZH}}\sqrt{1+\alpha^2}$. Only the plus branch fulfills the Hopf condition $\left(\Gamma^{\mathrm{eff}}\right)_{-} = 0$, which yields the ZH_1 point for positive detuning

$$(\tilde{k}^{\mathrm{ZH,1}}, \delta\omega^{\mathrm{ZH,1}}) \equiv \frac{\Gamma^{\mathrm{RO}}}{\alpha}\sqrt{1+\alpha^2}\left(1, \sqrt{1+\alpha^2}\right). \tag{3.162}$$

Figure 3.16(a) depicts the critical injection strengths $K_{H,c} \equiv 2\kappa\tau_{\mathrm{in}}\tilde{k}_{H,c}$ of Eq. (3.159) (blue solid line) and the injection strength of the ZH_1 point $K^{\mathrm{ZH,1}} = 2\kappa\tau_{\mathrm{in}}\tilde{k}^{\mathrm{ZH,1}}$ of Eq. (3.162) (red dashed line) as functions of the α-factor obtained for the reference rates. For $\alpha = 1$, the critical Hopf point and the zero Hopf point coincide. For $\alpha > 1$, the critical injection strength is lower than the injection strength of the ZH_1-point, which can be attributed to the bending of the supercritical part of the Hopf line towards zero detuning (see Fig. 3.6(b)). Both, $K_{H,c}$ and $K^{\mathrm{ZH,1}}$, decrease for increasing α.

From the results of the numerical path continuation plotted in Fig. 3.6(a) it can be seen that for $\alpha < 1$ the upper branch of the Hopf line emerging from the ZH_1 point is supercritical, and the lower branch is subcritical. Since the critical Hopf point is located at the lower branch, the lowest injection strength, above which the lasing fixed point may be destabilized in a Hopf bifurcation, is for $\alpha < 1$ given by $K^{\mathrm{ZH,1}}$. In the analytical approximation of Eq. (3.162), $K^{\mathrm{ZH,1}}$ diverges for $\alpha \to 0^+$, which is not observed in the numerical path continuation. The reason is that for small values of the α-factor $K^{\mathrm{ZH,1}}$ is too large to justify the assumption of weak injection $\mathrm{K} = \mathcal{O}(\gamma)$, and the approximation therefore becomes inaccurate (see blue shaded areas in Figs. 3.16(a) and (b)).

Figure 3.16(b) depicts the frequency detuning of the critical Hopf point $\Delta\nu_{\mathrm{inj}}^{H,c} \equiv \kappa\delta\omega^{H,c}/\pi$ (blue solid line) and the frequency detuning of the zero-Hopf point $\Delta\nu_{\mathrm{inj}}^{\mathrm{ZH,1}} \equiv$

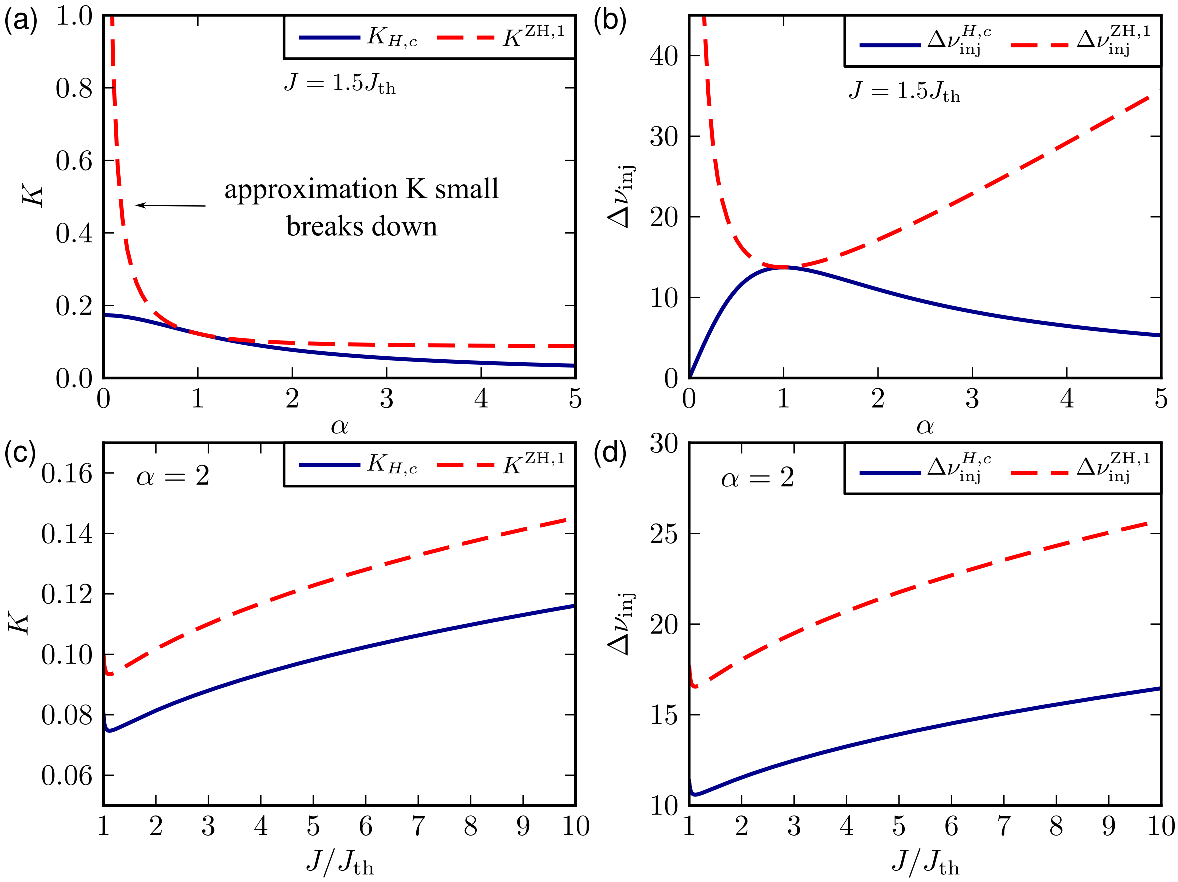

Figure 3.16.: **(a)**: Critical injection strength, below which now Hopf bifurcation can occur $K_{H,c}$ (solid blue line), and injection strength of zero-Hopf point for positive detuning $K^{\mathrm{ZH},1}$ as a function of the α-factor. **(b)**: Frequency detunings at Hopf line for K $_{H,c}$ denoted by $\Delta\nu_{\mathrm{inj}}^{H,c}$ (solid blue line) and frequency detuning at zero-Hopf point labeled by $\Delta\nu_{\mathrm{inj}}^{\mathrm{ZH},1}$ (red dashed line) as a function of α. Blue shaded areas denote α-values at which the analytic approximation for the zero-Hopf point (Eq. (3.162)) breaks down. **(c)** and **(d)**: Same as **(a)** and **(b)**, but for fixed $\alpha = 2.0$ and variable pump current J (normalized to the threshold value of the solitary laser J_{th}). Parameters: reference rates. **(a)** and **(b)**: $J = 1.5J_{\mathrm{th}}$. **(c)** and **(d)**: $\alpha = 2$. Other parameters as in Table 2.3.

$\kappa\delta\omega^{\mathrm{ZH},1}/\pi$ (red dashed line) as functions of the α-factor. Both coincide for $\alpha = 1$. For larger values of the α-factor, $\Delta\nu_{\mathrm{inj}}^{\mathrm{ZH},1}$ increases nearly linearly with α. In contrast, $\Delta\nu_{\mathrm{inj}}^{H,c}$ decreases, which again reflects the progressive bending of the Hopf line towards zero detuning.

Figures 3.16(c) and (d) depict $K_{H,c}$ (blue solid line) and $K^{\mathrm{ZH},1}$ (red dashed line) as well as $\Delta\nu_{\mathrm{inj}}^{H,c}$ (blue solid line) and $\Delta\nu_{\mathrm{inj}}^{\mathrm{ZH},1}$ (red dashed line) for $\alpha = 2$ as functions of the pump current J, which is normalized to the threshold current J_{th}. From Eqs. (3.159) and Eqs. (3.162), it can be seen that all four quantities depend linearly on Γ^{RO}, which explains their nearly linear increase with the pump current. Thus, both, the ZH_1 and the critical Hopf point shift with the pump current to higher values of K and $\Delta\nu_{\mathrm{inj}}$. This yields an increase of the phase-locking region, where stable cw operation of the laser is observed and agrees well with the numerical results of Subsection 3.3.3 (cf. Fig. 3.8).

3.8.7. "Matching" of asymptotic expansions for Hopf lines

To complete the analytic discussion, this subsection points out that the analytical expression (3.81) for the Hopf bifurcation lines for strong injection ($K = \mathcal{O}(\sqrt{\gamma})$ and $\Delta\nu_{\mathrm{inj}} = \mathcal{O}(\sqrt{\gamma})$) that was derived in Section 3.8.5, and the expression (3.156) for the Hopf bifurcation lines derived in this section under the assumption of weak injection ($K = \mathcal{O}(\gamma)$ and $\Delta\nu_{\mathrm{inj}} = \mathcal{O}(\gamma)$) have a common limit.

Under the assumption of strong injection, $\tilde{k}$ scales like the RO frequency $\omega^{\mathrm{RO}} = \mathcal{O}(\sqrt{\gamma})$. Taking the limit of weak injection thus means to study the Hopf bifurcation lines of Eq. (3.81) in the limit $\tilde{k}/\omega^{\mathrm{RO}} \to 0^+$, which yields

$$\delta\omega_H(\tilde{k}) = \pm\frac{\tilde{k}}{2}\frac{\left|2\tilde{k}^2 + (\omega^{\mathrm{RO}})^2(1-\alpha^2)\right|}{\left(\tilde{k}^2\left[\tilde{k}^2 + (\omega^{\mathrm{RO}})^2\right] + (1+\alpha^2)\frac{(\omega^{\mathrm{RO}})^4}{4}\right)^{1/2}} \xrightarrow{\frac{\tilde{k}}{\omega^{\mathrm{RO}}}\to 0^+} \pm\tilde{k}\left(\frac{\alpha^2-1}{\sqrt{\alpha^2+1}}\right). \tag{3.163}$$

Further, under the assumption of weak injection $\tilde{k}$ scales like the RO damping $\Gamma^{\mathrm{RO}} = \mathcal{O}(\gamma)$, and the limit of strong injection is performed by assuming $\Gamma^{\mathrm{RO}}/\tilde{k} \to 0^+$. The Hopf bifurcation lines of Eq. (3.156) simplify as

$$\delta\omega_H(\tilde{k}) = \frac{4\alpha\Gamma^{\mathrm{RO}}}{1+\alpha^2} \pm \frac{|\alpha^2-1|}{\sqrt{1+\alpha^2}}\sqrt{\tilde{k}^2 - \frac{4(\Gamma^{\mathrm{RO}})^2}{1+\alpha^2}} \xrightarrow{\frac{\Gamma^{\mathrm{RO}}}{\tilde{k}}\to 0^+} \pm\tilde{k}\left(\frac{\alpha^2-1}{\sqrt{\alpha^2+1}}\right). \tag{3.164}$$

Both, Eq. (3.163) and Eq. (3.164), yield the same limiting expression. Furthermore, since the injection strength and detuning for the ZH_1 point (Eq. (3.162)) as well as for the critical Hopf point (Eq. (3.159)) scale linearly with Γ^{RO}, both tend to the origin of the ($\tilde{k}$,$\delta\omega$)-plane in the limit of strong injection. This matches well with the observation that under the assumption of strong injection the zero-Hopf point is located at the origin of the ($\tilde{k}$,$\delta\omega$)-plane (cf. Eq. (3.83)). Eventually, the expressions for the frequency of the limit cycle born in the Hopf bifurcation (see Eq. (3.71)) simplifies in the limit of weak injection ($\tilde{k}/\omega^{\mathrm{RO}} \to 0$) to the expression $\omega_H = \omega^{\mathrm{RO}}$ obtained for weak injection (see Table 3.2).

3.9. Comparison to numerical path continuation

The asymptotic approximations for saddle-node and Hopf bifurcation lines as well as for the zero-Hopf and critical Hopf points (see Table 3.2) derived in the last sections are now compared to the results from the numerical path continuation. Figure 3.17 depicts saddle-node and Hopf bifurcation lines in the (K,$\Delta\nu_{\mathrm{inj}}$)-plane for the reference rates (upper row), the slow rates (middle row), and the very fast rates (lower row), respectively. The left column shows the full bifurcation diagram, while the right column depicts detail magnifications close to the zero-Hopf point for positive detuning, which is labeled by ZH_1. Green and gray lines denote numerically calculated Hopf and saddle-node bifurcation lines, respectively, and super- and subcritical lines are denoted by thick solid and thin dashed lines, respectively. The black dash-dotted lines mark the approximations for the saddle-node lines given by Eq. (3.153). Figure 3.17 corresponds to Fig. 3.15 discussed in Subsection 3.7.5, with the difference that now the Hopf lines for small K close to the ZH_1 point are approximated by the analytical expressions of Eqs. (3.156) (thick solid red lines), which were obtained under the assumption of weak injection. In the left panel of Fig. 3.17, only supercritical parts of the analytical Hopf lines are depicted for clarity. In the blowups of the right panel of Fig. 3.17, in addition, the subcritical parts of the Hopf lines are depicted by thin dashed red lines. For high K, the analytical expressions for the Hopf lines of Eq. (3.81), Eq. (3.93), and Eq. (3.107b), have been used, which were obtained for reference, slow, and very fast rates, respectively, under the assumption of strong injection. The different approximations for the Hopf lines were matched at their intersection points.

The limit of weak injection permits to obtain expressions for the ZH_1 point (see Eq. (3.162)) (red diamonds) as well as for the critical Hopf point (see Eq. (3.159)) (vertical dashed red lines in blowups of the right column of Fig. 3.17). The good correspondence of the numerically calculated zero-Hopf points (green diamonds) and critical Hopf points with their analytical approximations permits to conclude that for low injection strengths, the RO damping Γ^{RO} is an important parameter, because both, the ZH_1-point and the critical Hopf point, scale linearly with Γ^{RO}. The RO damping Γ^{RO} is in turns crucially influenced by the band structure as discussed in Subsections 3.8.2 and 3.8.3. Thus, for low injection, the special Coulomb scattering dynamics of QD lasers strongly influences the locking region.

The small mismatch of the numerically calculated ZH_1 points and their analytical approximations mainly results from the deviations of the analytical approximations of the saddle-node lines (black dash-dotted lines) from the numerical saddle-node lines (gray lines). Since the injection strengths of the ZH_1-points $K^{\mathrm{ZH},1}$ increases linearly with Γ^{RO}, the mismatch increases from the very fast (Fig. 3.17(f)) over the slow (Fig. 3.17(d)) to the reference rates (Fig. 3.17(b)). For the same reason, the injection strengths of the critical Hopf point $K_{H,c}$ decreases from reference, over slow to the very fast rates, which can be seen by comparing the red vertical dashed lines labeled $K_{H,c}$ in Figs. 3.17(b), (d), and (f), respectively.

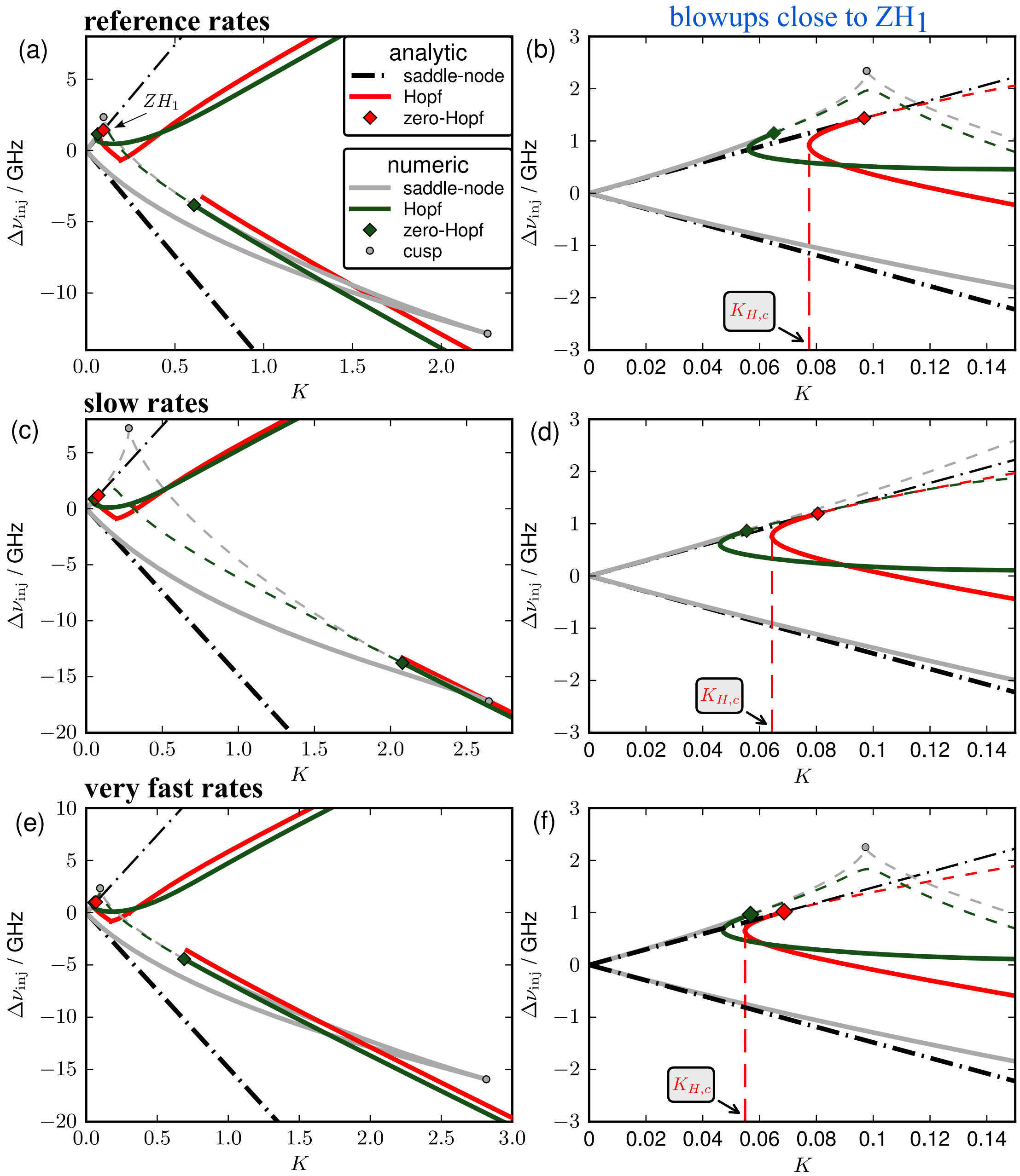

Figure 3.17.: **Left column**: Saddle-node (gray) and Hopf lines (green) from numerical path continuation and their complete analytical approximations that are valid for strong and weak injection (black dash-dotted lines denote saddle-node and red lines denote Hopf bifurcations, respectively) in a plane spanned by injection strength K and frequency detuning $\Delta\nu_{\mathrm{inj}}$ for reference rates (**upper row**), slow rates (**middle row**), and very fast rates (**lower row**), respectively. Super- and subcritical bifurcation lines are denoted by solid thick and thin dashed lines, respectively. For clarity, only supercritical parts of analytical Hopf lines are shown. Numerical and analytical codimension-2 zero-Hopf (fold-Hopf) points are labeled by green and red diamonds, respectively. **Right column**: Blowups close to upper zero-Hopf point labeled ZH_1 in **(a)**, **(d)**, and **(d)**. Here, also the subcritcal parts of the analytical Hopf lines are depicted by thin dashed red lines. Parameters: $\alpha = 0.9$, $J = 1.5J_{\mathrm{th}}$, and other parameters as in Table 2.3.

3.10. Effective damping

In this section, it is discussed how the optical injection influences the effective damping within the phase-locking tongue. Therefore, the injection strength is fixed to its value for the critical Hopf point $K = K_{K,c}$, and the frequency detuning $\Delta\nu_{\mathrm{inj}}$ is varied between the two v-shaped saddle-node bifurcation lines emerging from the origin of the $K, \Delta\nu_{\mathrm{inj}}$-plane. Figure 3.18 depicts the numerically calculated saddle-node and Hopf bifurcation lines and their analytical approximations in the $(K, \Delta\nu_{\mathrm{inj}})$-plane for the reference rates and for weak injection (see Fig. 3.17(b)). The injection strengths of the numerically calculated critical Hopf point $K = K_{H,c}^{\mathrm{num}}$ and its analytical approximation of Eq. (3.158) $K = K_{H,c}$ are indicated by a vertical dashed green line and a vertical dashed red line, respectively. At first, the turn-on dynamics of the laser under optical injection is discussed along the line $K = K_{H,c}^{\mathrm{num}}$ for four different values of the frequency detuning $\Delta\nu_{\mathrm{inj}}$ labeled by **(a)**–**(d)** in Fig. 3.18. Therefore, time-series of the photon number N_{ph} (left column) and projections onto the complex $\tilde{\mathcal{E}}$-plane (right column) are depicted in Fig. 3.19. Stable fixed points are denoted by dots in the phase portraits. Figure 3.19(a) depicts the turn-on dynamics close to the saddle-node point for positive detuning LP_1^{num}. The turn-on damping is strongly reduced compared to the solitary laser (gray dash-dotted lines). At the critical Hopf point labeled by a green dot in Fig. 3.18, the RO damping Γ^{RO} is compensated by the injection and the trajectory decays to a stable limit cycle, which is indicated by a black dashed line in the phase space projection of Fig. 3.19(b). Going from the critical Hopf point down to negative values of the detuning $\Delta\nu_{\mathrm{inj}}$, the effective

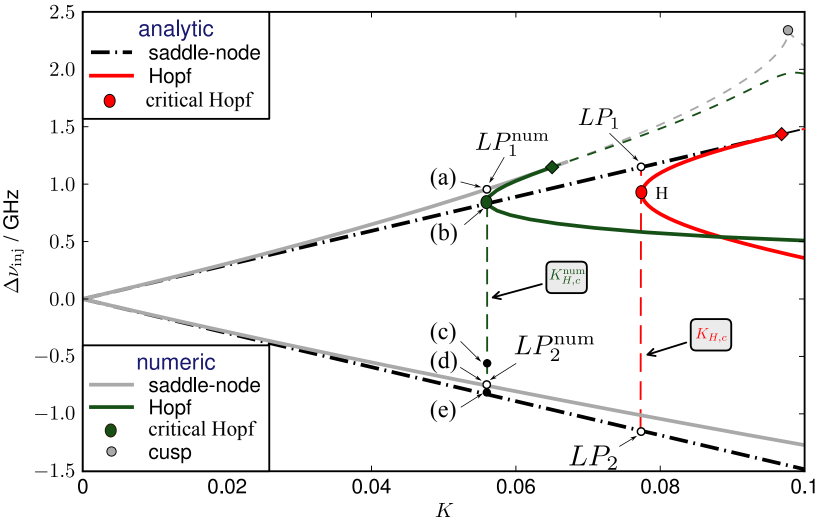

Figure 3.18.: Numerically calculated saddle-node and Hopf bifurcation lines and their analytical approximations in the $(K,\Delta\nu_{\mathrm{inj}})$-plane as in Fig. 3.17(b). The injection strengths of the numerically calculated critical Hopf point (green dot) and its analytical approximation (red dot) are indicated by a vertical dashed green line labeled $K_{H,c}^{\mathrm{num}}$ and vertical dashed red lines labeled $K_{H,c}$, respectively. Numerically calculated limit-points (saddle-node bifurcation points) (open circles) for $K = K_{H,c}^{\mathrm{num}}$ are labeled by LP_1^{num} and LP_2^{num}, and their analytic approximations for $K = K_{H,c}$ are labeled by LP_1 and LP_2. Labels **(a)**–**(e)** indicate values of $\Delta\nu_{\mathrm{inj}}$, at which time series and phase-space projections are shown in Fig. 3.19. Parameters: reference rates, $\alpha = 2$, $J/J_{\mathrm{th}} = 1.5$, and other parameters as in Table 2.3.

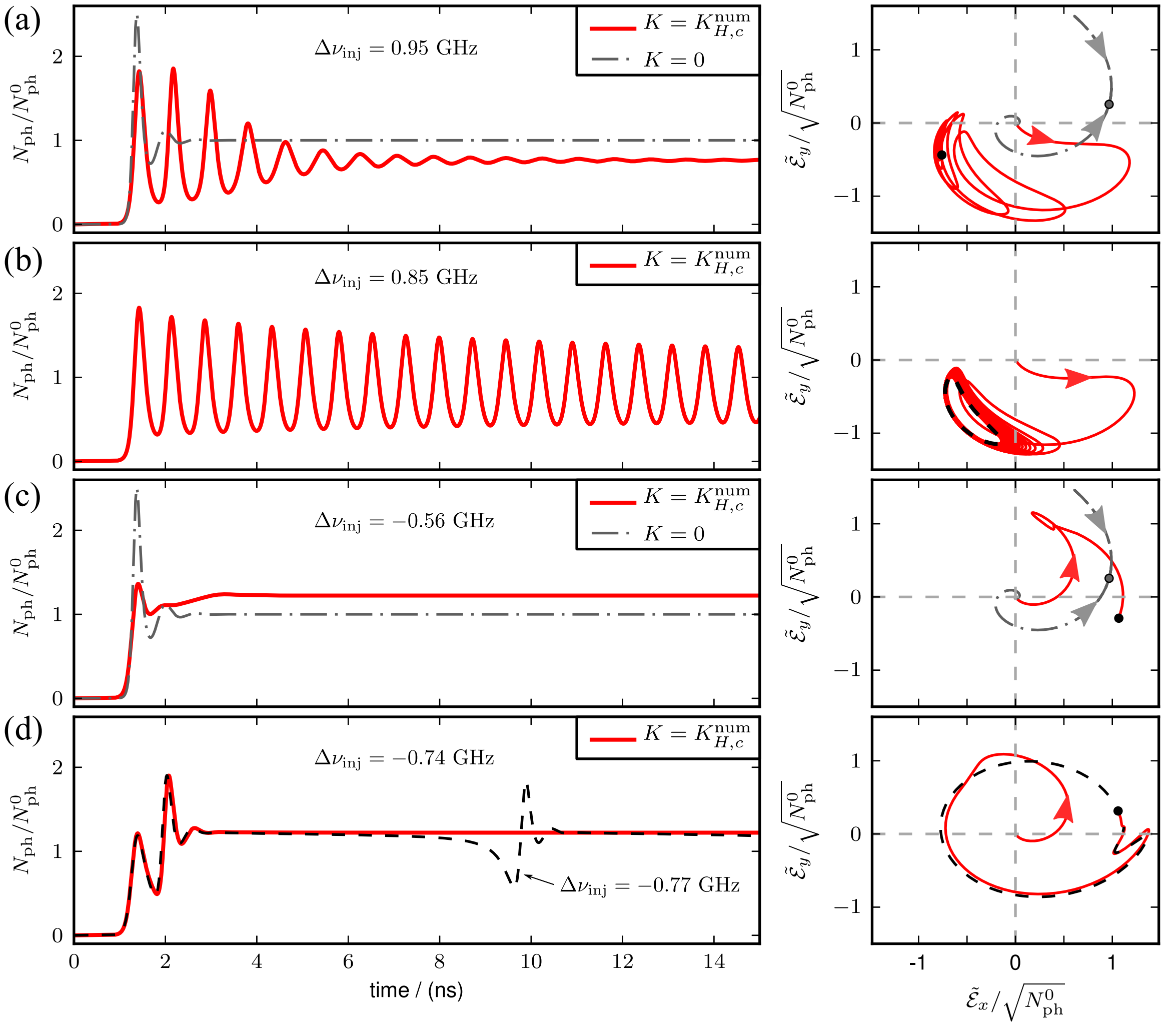

Figure 3.19.: Time series of the photon number N_{ph} (normalized to the steady state value of the solitary laser N^0_{ph}) for injection strength of the numerically calculated critical Hopf point $K = K^{\mathrm{num}}_{H,c}$ (**left column**) and projections of the trajectory onto a plane spanned by the components $\tilde{\mathcal{E}}_x$ and $\tilde{\mathcal{E}}_y$ of the complex field amplitude $\tilde{\mathcal{E}}$ (**right column**). Stable steady states are denoted by dots in the phase space projections. Gray dash-dotted lines in **(a)** and **(c)** indicate the turn-on of the solitary laser ($K = 0$). **(a)**: Turn-on close to saddle-node line for positive detuning $\Delta\nu_{\mathrm{inj}} = 0.95\,\mathrm{GHz}$. **(b)**: Turn-on close to critical Hopf point for $\Delta\nu^{\mathrm{ZH},1}_{\mathrm{inj}} = 0.85\,\mathrm{GHz}$. The black dashed line denoted the stable limit cycle. **(c)**: Turn-on for maximal effective RO damping at $\Delta\nu_{\mathrm{inj}} = -0.74\,\mathrm{GHz}$. **(d)**: Turn-on close to saddle-node line for negative detuning $\Delta\nu_{\mathrm{inj}} = -0.74\,\mathrm{GHz}$. The black dashed lines depict the stable limit cycle beyond the saddle-node line for $\Delta\nu_{\mathrm{inj}} = -0.77\,\mathrm{GHz}$. Parameters: reference rates, $\alpha = 2.0$, $J = 1.5J_{\mathrm{th}}$, $K = K_{H,c}$, and other parameters as in Table 2.3.

damping increases and eventually reaches a maximum at the point labeled by **(c)** in Fig. 3.18. From Fig. 3.19(c), it can be seen that this yields a stronger RO damping in the time trace of N_{ph} and a deformation of the trajectory in phase space compared to the solitary laser (gray dash-dotted line). Eventually, in Fig. 3.19(d), the turn-on process close to the saddle node point for negative detuning (LP_2^{num}) is depicted (see label (d) in Fig. 3.18). The turn-on damping is decreased with respect to Fig. 3.19(c), but it is still higher than for the solitary laser. Time series and phase space projection reveal the ghost of the limit cycle, which is born in a saddle-node infinite period bifurcation at the saddle-node line. The limit cycle close to the saddle-node line (see label (e) in Fig. 3.18) is depicted by black dashed lines in Fig. 3.19(d).

Next, we discuss the expression for the effective turn-on damping $\left(\Gamma^{\mathrm{eff}}\right)_-$ given by Eq. (3.155). To derive an expression for Γ^{eff} at the saddle-node lines, Eq. (3.155) is rewritten as

$$\left(\Gamma^{\mathrm{eff}}\right)_- \overset{\delta\omega\neq 0}{=} \Gamma^{\mathrm{RO}} - \frac{\alpha\delta\omega}{1+\alpha^2}\left[1 \pm \frac{(1-\alpha^2)}{2\alpha\delta\omega}\sqrt{(1+\alpha^2)\tilde{k}^2 - \delta\omega^2}\right], \tag{3.165}$$

where $\delta\omega \neq 0$ was assumed in the equality. At the saddle-node bifurcation lines, the square root in Eq. (3.165) vanishes, and the effective damping reads

$$\left(\Gamma^{\mathrm{eff}}\right)_-^{\mathrm{sn}} \equiv \Gamma^{\mathrm{RO}} - \frac{\alpha\delta\omega_{\mathrm{sn},\pm}}{1+\alpha^2} = \Gamma^{\mathrm{RO}} \mp \frac{\alpha\tilde{k}}{\sqrt{1+\alpha^2}}, \tag{3.166}$$

where in the last equality the expression (3.153) for the detuning at the saddle-node lines $\delta\omega_{\mathrm{sn},\pm}$ was used. The above equation reveals that the effective RO damping is smaller than the RO damping of the solitary laser Γ^{RO} at the upper saddle-node line, and that it is larger at the lower saddle-node line. This is in agreement with the numerical turn-on behavior depicted in Figs. 3.19(a) and (d), and with experimental results for semiconductor class B QW lasers [JIN06, LAU09a, KEL12a].

However, formula (3.165) cannot explain why the turn-on damping is larger for $\Delta\nu_{\mathrm{inj}} = -0.56\,\mathrm{GHz}$ (see Fig. 3.19(c) and label **(c)** in Fig. 3.18) than directly at the saddle-node line (see Fig. 3.19(d) and label **(d)** in Fig. 3.18). To understand this, remember that for the reference rates, in addition to the complex conjugate eigenvalues, a third real eigenvalue has a non-zero contribution in $\mathcal{O}(\epsilon)$ (see Subsection 3.8.1). This real eigenvalue influences the turn-on process, which will be discussed in the following. For the lasing fixed point, i.e., for the stable focus, the real eigenvalue is given by (see Eq. (3.135))

$$(\sigma^r)_- \equiv -\sqrt{(1+\alpha^2)\tilde{k}^2 - \delta\omega^2}. \tag{3.167}$$

From the above equation, it can be seen that for the solitary laser ($\tilde{k} = 0$ and $\delta\omega = 0$) the real eigenvalue is zero, and the effective damping is thus determined only by the RO damping Γ^{RO}. Further, the saddle-node lines are determined by a zero of the real eigenvalue, thus also the expressions (3.166) for the damping at the saddle-node lines $\left(\Gamma^{\mathrm{eff}}\right)_-^{\mathrm{sn}}$ are exact. Further, we found in Subsection 3.8.3 that for the slow rates the real eigenvalue is, also under injection, zero in $\mathcal{O}(\epsilon)$, and the effective RO damping is thus approximated analytically by $\left(\Gamma^{\mathrm{eff}}\right)_-$.

However, in the case of the reference rates, the real eigenvalue influences the effective RO damping. If this eigenvalue is much larger than the real parts of the complex conjugate eigenvalues, the trajectory rapidly decays towards the plane spanned by the eigenvectors of the complex conjugate eigenvalues, where it spirals towards the lasing fixed points. The spiraling motion in the eigenspace of the complex conjugate eigenvalues translates into the damped ROs of the time trace of N_{ph}, and the damping is well described by $\left(\Gamma^{\mathrm{eff}}\right)_{-}$. However, if the real eigenvalue has the same order of magnitude than the real parts of the complex conjugate eigenvalues, the spiraling motion takes place in a hyper-plane spanned by the eigenvectors of all three eigenvalues. In the time trace of N_{ph}, this yields the stronger turn-on damping, and the "crawling" to the lasing fixed point observed in Fig. 3.19(c).

The frequency detunings $\delta\omega_{\pm}^{\mathrm{int}}$, at which the real eigenvalue and the real parts of the complex conjugate eigenvalues have the same magnitude, may be calculated by equating the absolute value of the right-hand side of Eq. (3.167) to the expression of $\left(\Gamma^{\mathrm{eff}}\right)_{-}$ of Eq. (3.165), which yields

$$\delta\omega_{\pm}^{\mathrm{int}} \equiv \frac{4\alpha\Gamma^{\mathrm{ref}}}{1+9\alpha^2} \pm \left(1+3\alpha^2\right)\left[\tilde{k}^2 + 9\tilde{k}^2\alpha^2 - 4\left(\Gamma^{\mathrm{RO}}\right)^2\right]^{\frac{1}{2}}. \qquad (3.168)$$

Figure 3.19(c) depicts time trace and phase space projection at this point.

To see how good the analytic expressions for the eigenvalues approximate the eigenvalues of the full system, the dependence of the eigenvalues on the frequency detuning $\Delta\nu_{\mathrm{inj}}$ within the phase-locking tongue is depicted in Fig 3.20. The numerical eigenvalues were calculated along $K = K_{H,c}^{\mathrm{num}}$, i.e., along the vertical green dashed line in Fig. 3.18, and their analytical approximations are evaluated for $K = K_{H,c}$, i.e., along the vertical red dashed line in Fig. 3.18. Figures. 3.20(a) and (b) depict real and imaginary parts of the eigenvalues, respectively, for the reference rates, and Figs. 3.20(c) and (d) depict real and imaginary parts of the eigenvalues for the slow rates, respectively. The eigenvalues are depicted with respect to physical time t. Thus, the analytical expressions for the real eigenvalue and the complex conjugate eigenvalues are given by $(\tilde{\sigma}^r)_{-} \equiv 2\kappa(\sigma^r)_{-}$ (see Eq. (3.167)) and $(\tilde{\sigma}^c)_{-} \equiv -\Gamma_{\mathrm{RO}}^{\mathrm{eff}} \pm i\omega_{\mathrm{RO}}^{\mathrm{ref}}$ with $\Gamma_{\mathrm{RO}}^{\mathrm{eff}} \equiv 2\kappa\Gamma^{\mathrm{eff}}$ (see Eq. (3.154)), respectively. Thick solid red lines and thick green dash-dotted lines denote the analytically calculated real eigenvalues and the complex conjugate eigenvalues, respectively, while thin lines denote the numerically calculated eigenvalues. The full set of dynamical equations (3.12) has five dimension. (The carrier conservation (2.9) reduces its dimensionality by one.) Depicted are only four eigenvalues denoted by $\tilde{\sigma}_i$ for $i \in \{1,2,3,4\}$, because the real part of the fifth eigenvalue is much larger, and does not influence the damping. Analytically calculated saddle-node points (LP_1 and LP_2) and the critical Hopf points (H) are denoted by black open circles red dots, respectively. The numerically calculated saddle-node points are labeled by LP_1^{num} and LP_2^{num}, and the numerically calculated critical Hopf points are not shown, because they nearly coincide with their analytic approximations. The analytic approximation for the width of the locking tongue, which is given by the distance of LP_1 and LP_2, is larger than the numerically calculated widths (distance between LP_1^{num} and LP_2^{num}), because the analytically calculated critical injection strengths $K_{H,c}$ is higher than the numerical one (see distance between vertical dashed lines in Fig. 3.18), and the width of the locking tongue increases with K. For

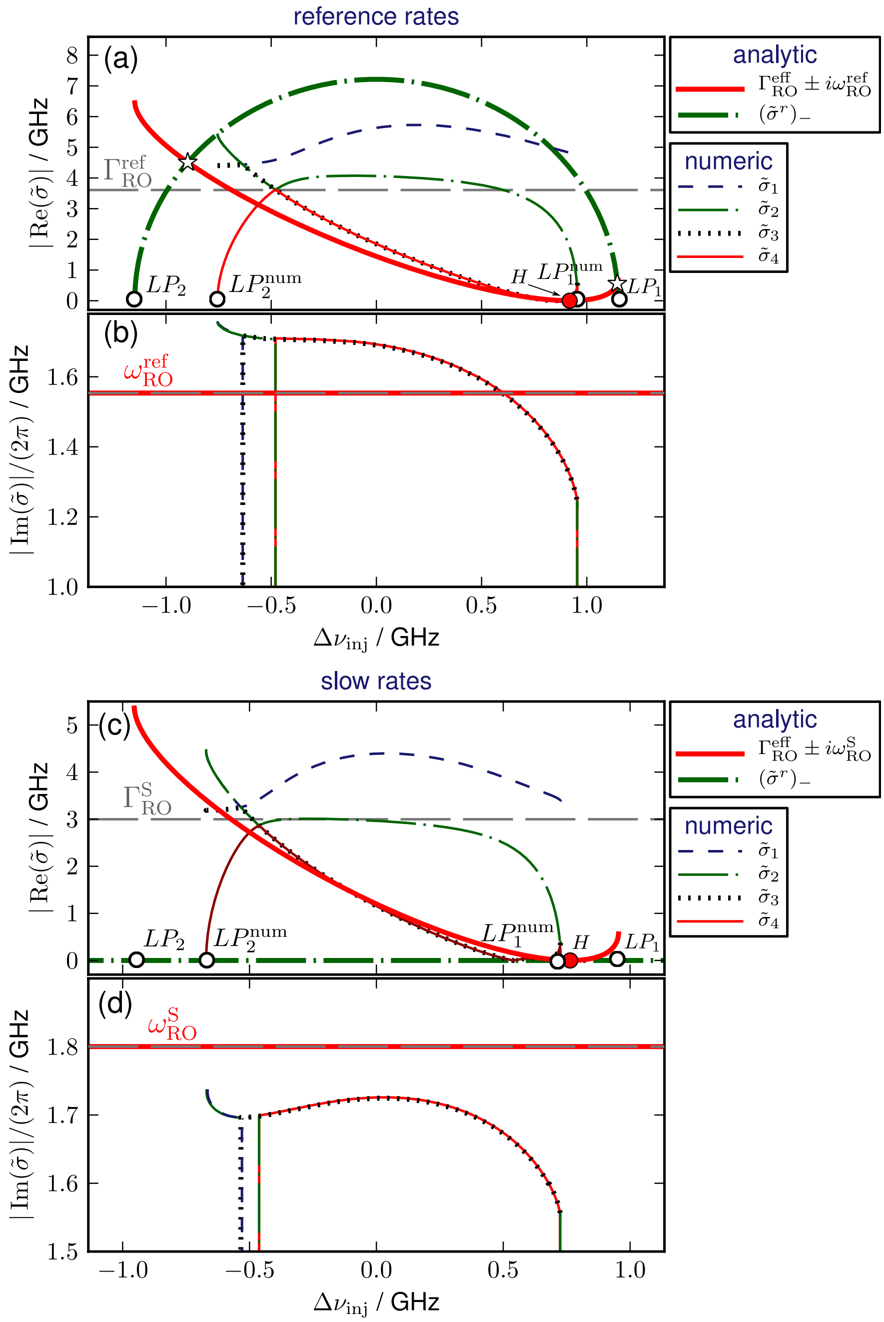

Figure 3.20.: Real parts **(a)** and imaginary parts **(b)** of the eigenvalues vs. detuning $\Delta\nu_{inj}$ as obtained for the reference rates. Thick lines denote the analytic approximations of the eigenvalues, while thin lines mark the eigenvalues of the full system labeled $\tilde{\sigma}_i$ for $i \in \{1, 2, 3, 4\}$. Same colors denote same eigenvalues. The analytically calculated critical Hopf point and limit-points (saddle-node bifurcation points) are labeled by H and LP_1 and LP_2, respectively. Numerically calculated limit-points are labeled LP_1^{num} and LP_2^{num}. Stars mark intersection points of the analytical expressions for the real eigenvalue $\tilde{\sigma}^r$ and the real parts of the complex conjugate eigenvalues $-\Gamma_{RO}^{eff}$ (see Eq. (3.168)). The gray dashed line labeled Γ_{RO}^{ref} marks the damping of the solitary laser. **(c)**–**(d)**: Same as **(a)**–**(b)** but for the slow set of scattering rates. Parameters: $\alpha = 2$, $J/J_{th} = 1.5$, $K = K_{H,c}$, and other parameters as in Table 2.3.

the reference and the slow rates, the analytical expression (3.165) for $\left(\Gamma^{\text{eff}}\right)_{-}$ (thick red lines) agrees well with the real parts of the numerically calculated eigenvalues (thin red lines). In contrast, the analytical approximations for the imaginary parts of the complex conjugate eigenvalues yield only the constant RO frequencies $\omega_{\text{RO}}^{\text{ref}}$ and $\omega_{\text{RO}}^{\text{S}}$ of the solitary laser for reference and slow rates, respectively. They do not permit to describe the increase of the RO frequency with the distance from the critical Hopf point (see Fig. 3.20(b) and (d)). For the reference rates, the absolute value of the real eigenvalues is overestimated (thick dash-dotted green line), and it is zero for the slow rates. In Fig. 3.20(a) the points, at which real and complex conjugate eigenvalues have the same real parts, are labeled by white stars.

In summary, for the slow rates, the effective damping of the QD laser under injection is well described by the expression (3.165) for $\left(\Gamma^{\text{eff}}\right)_{-}$. It reveals that the RO damping of the solitary laser Γ^{RO} is diminished by the injection close to the upper phase-locking boundary and enhanced close to the lower phase-locking boundary. This is in good agreement with earlier observations for class B QW lasers [JIN06, LAU09a, KEL12a]. Furthermore, the increase off Γ^{eff} across the locking-tongue explains why the subcritical part of the Hopf line in Fig. 3.2 bends towards higher injection strengths. (The Hopf line marks the points in phase-space where $\Gamma^{\text{eff}} = 0$.) For the reference rates and frequency detunings close to the lower phase-locking boundary, the turn-on of the QD laser under injection is additionally influenced by the real eigenvalue.

3.11. Conclusion

In the beginning of this chapter the rich dynamics of QD lasers subject to optical injection has been investigated by direct numerical integration and path continuation techniques. Codimension-two zero-Hopf points have been identified as organizing centers of the dynamics [WIE99, WIE05a, ERN10b]. Furthermore, it has been observed that regions with complex dynamics are suppressed by small phase-amplitude coupling (low α-factors), fast carrier exchange between the QDs and the carrier reservoir, and high-pump currents. From Chapter 2, we know that fast carrier scattering as well as high pump current enhance the RO damping of the laser. The asymptotic analysis of this chapter reveals that α-factor and RO damping are the main parameters that determine the saddle-node and Hopf lines limiting the locking tongue as well as the position of the zero-Hopf point for positive detuning and the critical injection strength, below which no Hopf bifurcation can occur. This explains why QD lasers with a low phase-amplitude coupling and strongly suppressed ROs have a higher dynamical stability under optical injection than QW lasers [ERN10a, KEL11c, PAU12].

CHAPTER

FOUR

QUANTUM DOT LASER WITH EXTERNAL FEEDBACK

4.1. Introduction

One particularity of semiconductor lasers is their low tolerance to optical feedback, which can be of disadvantage for technological applications. For example, to use semiconductor lasers as transmitters in optical networks, expensive optical isolators are needed to avoid back reflections that can lead to temporal instabilities of the lasers (coherence collapse). However, there are also several applications that take advantage of the rich dynamics induced by optical feedback. For instance, feedback induced chaos can be used for secure chaos communication and chaos key distribution [FIS00, HEI02a, VIC04, ARG05, VIK07, KIN10]. Furthermore, short optical feedback in an integrated multi-section laser has been used to significantly improve the modulation bandwidth of a directly modulated laser [RAD07].

Moreover, from a dynamical system point of view, semiconductor lasers subject to optical feedback are of high interest, because the optical feedback introduces a delay into the system. The delay in turn induces a high dimensionality, which results in a rich phenomenology, ranging from multistability, bursting, intermittency, irregular intensity dropouts (low-frequency fluctuations LFFs), and fully developed chaos. A review focusing on laser instabilities is given in [TAR98a]. Semiconductor lasers have also been employed to demonstrate the stabilization of steady states (cw emission) or periodic oscillations (self pulsations) by non-invasive time delayed feedback control [SCH06a, FLU07, DAH07, DAH08b, FIE08, DAH10] (see [SCH07, SCH09a] for an overview). Further, delay synchronization of coupled lasers [HIC11], and networks of delay coupled lasers [DAH11b, DAH12] as well as bubbling in coupled lasers [FLU09, FLU10] have been investigated. A recent review summarizing the dynamics and the applications of delay coupled lasers is given in [SOR13].

QD lasers display a higher dynamical stability with respect to optical feedback [SU03, HUY04, OBR03a, CAR06a, CAR05] than conventional QW semiconductor lasers. This allows QD laser transmitters to operate without expensive optical isolators [CAR06a]. Furthermore, due to their increased dynamical stability, the route to chaos can be observed in QD lasers more clearly. The improved performance of QDs under optical feedback has been linked to an increased RO damping and a reduced phase-amplitude coupling [HUY04, OTT10, OTT12a, GLO12].

In this chapter, the QD model described in Chapter 2 is extended to take into account optical feedback from a distant reflector. Therefore, a semiclassical field equation of Lang-Kobayashi (LK) type [LAN80b] is combined with the microscopically based material model described in Section 2.2. The LK-model is widely used for a simplified theoretical description of semiconductor lasers optically coupled with a distant reflector (see [KAN05] for a review). The basic setup is sketched in Fig. 4.1. The field in the laser is modeled by a single complex equation for the slowly varying field amplitude $\mathcal{E}(t)$. A part of the emitted light is reflected from the distant mirror and coupled back into the laser with feedback strength K, rotated by the feedback phase C, and delayed by the roundtrip time of the light in the external cavity τ. Multiple reflections of the light in the external cavity are neglected, which restricts the validity of the model to low feedback strengths [TAR95a]. Further, the laser is treated as a point emitter with no spatial extensions, i.e., the roundtrip time of the light in the laser τ_{in} is neglected. Therefore, the model is only valid for delay times τ that are long compared to τ_{in}. As a consequence, for high injection strengths and very short optical feedback, as it is the case for integrated multi-sections devices, finite-difference traveling wave models are better suited to obtain a quantitative agreement with experiments [KAN05, RAD07]. Further, in this LK-models the phase-amplitude coupling is modeled by a constant α-factor. More sophisticated modeling approaches reveal that for QD lasers the α-factor is problematic [LIN12b], because it cannot account for the independent dynamics of resonant charge carries in the QDs and non-resonant charge carriers in the carrier reservoir [MEL06, LIN12a] and eventually neglects a degree of freedom of the dynamics. It was, however, shown that QD laser models based on a constant α-parameter still yield reliable results as long as only the transition between stable and unstable behavior, i.e., saddle-node and Hopf bifurcations are considered [LIN12a, LIN12b]. Further, more complex modeling approaches reveal that the dynamics of QD lasers is rather more stable than described by models with constant α-factor [LIN13]. In the framework of the present simple modeling approach, this is taken into account by choosing small values of the α-factor.

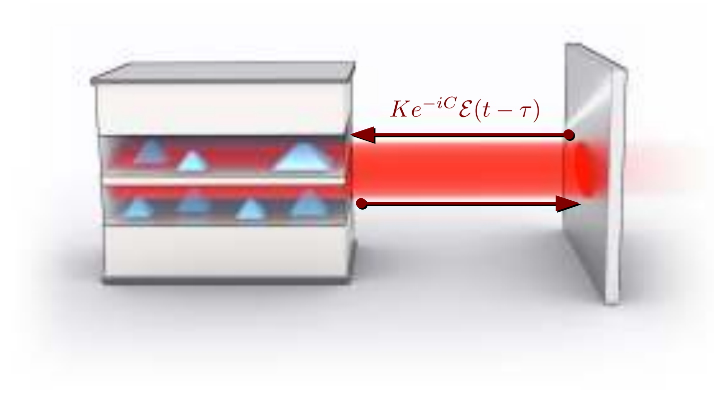

Figure 4.1: Schematic setup of the QD laser device with delayed optical feedback from an external mirror. The electrical field amplitude $\mathcal{E}$ taken at a time $t-\tau$ delayed by the external cavity round trip time τ is coupled back into the laser multiplied with the feedback strength K and rotated by the external cavity phase C.

This modeling approach is, on the one hand, detailed enough to study the impact of the band structure on the instability regions, and, on the other hand, the model is simple enough to permit analytical insight. Thus, an expression for the critical feedback strength, below which the laser is guaranteed to be stable is derived, which directly reveals the impact of the band structure and the phase amplitude coupling on the stability of the laser.

This chapter is organized as follows. After introducing the model in Section 4.2, the structure of basic solutions, which form the "backbone" of the dynamics are discussed in Section 4.3. Then, the impact of the α-factor and the band structure on the dynamics of the laser is studied numerically in Sections 4.4 and 4.5. As mentioned before, the feedback tolerance of the laser is crucial for technological applications. Therefore, in Section 4.6, an analytic formula for the first Hopf bifurcation marking the stability boundary is derived and compared with the results of numerical simulations. In Section 4.8, the excitability of the laser subject to feedback is discussed, and coherence resonance close to a homoclinic bifurcation and close to a crisis of a chaotic attractor is analyzed, before eventually summarizing in Section 4.9.

4.2. Model

Extending the microscopically based rate equation model for the solitary QD laser of Chapter 2 by the terms modeling the delayed optical feedback, the model equations read [OTT10, OTT11, OTT12a]

$$\mathcal{E}'(t') = \frac{1+i\alpha}{2}\Big[g(\rho_e+\rho_h-1)-1\Big]\mathcal{E}(t') + \frac{K}{2\kappa\tau_{\text{in}}}e^{-iC}\mathcal{E}(t'-\tau), \tag{4.1a}$$

$$\rho_e' = \gamma\Big[s_e^{\text{in}}(1-\rho_e) - s_e^{\text{out}}\rho_e - r_w(\rho_e+\rho_h-1)\big|\mathcal{E}\big|^2 - \rho_e\rho_h\Big], \tag{4.1b}$$

$$\rho_h' = \gamma\Big[s_h^{\text{in}}(1-\rho_h) - s_h^{\text{out}}\rho_h - r_w(\rho_e+\rho_h-1)\big|\mathcal{E}\big|^2 - \rho_e\rho_h\Big], \tag{4.1c}$$

$$W_e' = \gamma\Big[J - s_e^{\text{in}}(1-\rho_e) + s_e^{\text{out}}\rho_e - cW_eW_h\Big], \tag{4.1d}$$

$$W_h' = \gamma\Big[J - s_h^{\text{in}}(1-\rho_h) + s_e^{\text{out}}\rho_h - cW_eW_h\Big]. \tag{4.1e}$$

Here, $(\,\cdot\,)'$ denotes the derivative with respect to dimensionless time $t' \equiv 2\kappa t$, and the optical feedback is expressed by the last term of the field equation (4.1a). This corresponds to the well established Lang-Kobayashi model [LAN80b]. The light is coupled back into the device with the dimensionless feedback strength K and the feedback phase is given by $C \equiv \omega_{\text{th}}\tau$, where ω_{th} is the frequency of the solitary laser at lasing threshold. The dimensionless external delay time is denoted by τ (see Fig. 4.1). Although being completely determined by ω_{th} and τ, the feedback phase C is treated as an independent parameter since small variations of the external cavity length cause a variation of the phase C over its full range $[0, 2\pi]$ while the external roundtrip time τ is hardly affected by these fluctuations. This is a well established procedure in the analysis of semiconductor lasers subject to optical feedback [HAE02, HEI03a, GRE09a, OTT12]. Hence, we always consider C as a free parameter throughout this chapter. The equations for the subsystem of the carriers are the same as for the solitary QD laser. In its dimensionless form, it has been introduced in Subsection 2.3. As introduced in Eq. (2.7), the time scale separation between the subsystems of the photons and of the carriers is given by γ, the dimensionless scattering rates are denoted by $s_b^{\text{in/out}}$ ($b = e$ for electrons and $b = h$ for holes), the ratio of the Einstein factors of induced and spontaneous emission is r_w and J and c denote the pump rate and the coefficient of the spontaneous emission in the carrier reservoir, respectively. The parameter values of Table 2.3 have been used unless stated otherwise.

4.3. External cavity modes – structure and symmetries of basic solutions

In this section, the basic solutions of the dynamical equations (4.1) are discussed. They organize the phase space of the system and provide a "backbone" for more complex, e.g., chaotic, dynamics observed in these systems [ROT07]. At first, we note that Eqs. (4.1) are invariant under the continuous symmetry group of all rotations in the complex plane $\mathbb{S}^1 \equiv \{\tilde{c} \in \mathbb{C} \text{ with } \tilde{c}\,\varepsilon\,\mathcal{C}\big|\big|\tilde{c}\big| = 1\}$. This means that the rotation over any angle $\theta = \arg(\tilde{c})$ of the trajectory is again a trajectory. Thus, a solution of the dynamical equations is either $\mathbb{S}^1$ invariant itself, or it is not isolated, but comes as a rotational family parametrized by the elements of $\mathbb{S}^1$. Such a family of solutions

$$\mathbb{S}^1 \circ \Big(\mathcal{E}, \rho_e, \rho_h, W_e, W_h\Big)_{t_0}^{t1} = \Big\{\big(\tilde{c}\mathcal{E}, \rho_e, \rho_h, W_e, W_h\big)_{t_0}^{t1}\Big| \text{ for } c \in \mathbb{S}^1\Big\} \tag{4.2}$$

is called a group orbit. It consists of all images of the trajectory starting at t_0 and ending up at t_1 under all rotations of $\mathbb{S}^1$ [KRA00].

The $\mathbb{S}^1$-symmetry is a consequence of two properties: the linearity of the field equation (4.1a) with respect to $\mathcal{E}$, and the fact that only the modulus $\big|\mathcal{E}\big|$ of the electrical field amplitude enters into the QD carrier equations (4.1b) and (4.1c) through the photon number $N_{\text{ph}} \equiv \big|\mathcal{E}\big|^2$ [KAN05]. The simplest solutions that are $\mathbb{S}^1$ invariant are the external cavity modes (ECMs), which are continuous wave (cw) solutions with constant photon number N_{ph}^{s} and carrier densities $\rho_e^{\text{s}}, \rho_h^{\text{s}}, W_e^{\text{s}}, W_h^{\text{s}}$, and a phase ϕ of the electric field amplitude $\mathcal{E} = |\mathcal{E}|e^{i\phi}$ that varies linearly in time

$$(\mathcal{E}(t'), \rho_e(t'), \rho_h(t'), W_e(t'), W_h(t')) = (\sqrt{N_{\text{ph}}^{\text{s}}}e^{i\delta\omega^{\text{s}}t'}, \rho_e^{\text{s}}, \rho_h^{\text{s}}, W_e^{\text{s}}, W_h^{\text{s}}), \tag{4.3}$$

where the steady states of the dynamic equations (4.1) with feedback are denoted by $(\,\cdot\,)^s$. Due to the slowly varying envelope approximation [HAK83a], only the slowly varying envelope $\mathcal{E}$ of the full electric field

$$E(t) \equiv \frac{1}{2}\left(\mathcal{E}(t)e^{i\omega t} + \mathcal{E}^{\star}(t)e^{-i\omega t}\right)$$

is considered, where $(\,\cdot\,)^{\star}$ denotes the complex conjugate. As a consequence, an ECM oscillates with the deviation $\delta\omega^{\text{s}} \equiv (2\kappa)^{-1}(\omega - \omega_{\text{th}})$ of the lasing frequency ω from the solitary laser threshold frequency ω_{th}. Each ECM is a group orbit of the $\mathbb{S}^1$-symmetry, which means that in a projection on a hyperplane spanned by the photon number N_{ph} and the carrier densities it is just one point. This projection is sometimes called trace of the ECM. That is why ECMs are often referred to as steady state solutions in the literature. A complete discussion of the symmetries for conventional and phase conjugate optical feedback is given in [KRA00a].

Below the lasing threshold, a "trivial" solution with $\mathcal{E} \equiv 0$ is stable. At the lasing threshold, this solution changes its stability, and ECM solutions have to be considered [FIE08].

Inserting the ECM-ansatz of Eq. (4.3) into Eqs. (4.1), we find the following expressions for the non-zero intensity solutions ($N^{\mathrm{s}}_{\mathrm{ph}} \neq 0$)

$$\rho^{\mathrm{s}}_{\mathrm{inv}} = -\tilde{k}\cos(\delta\omega^{\mathrm{s}}\tau + C), \tag{4.4a}$$

$$\delta\omega^{\mathrm{s}} = \alpha\rho^{\mathrm{s}}_{\mathrm{inv}} - \tilde{k}\sin(\delta\omega^{\mathrm{s}}\tau + C), \tag{4.4b}$$

$$0 = s^{\mathrm{in}}_e(W^{\mathrm{s}}_e, W^{\mathrm{s}}_h)(1-\rho^{\mathrm{s}}_e) - s^{\mathrm{out}}_e(W^{\mathrm{s}}_e, W^{\mathrm{s}}_h)\rho^{\mathrm{s}}_e - r_w(\rho^{\mathrm{s}}_e + \rho^{\mathrm{s}}_h - 1)N^{\mathrm{s}}_{\mathrm{ph}} - \rho^{\mathrm{s}}_e\rho^{\mathrm{s}}_h, \tag{4.4c}$$

$$0 = s^{\mathrm{in}}_h(W^{\mathrm{s}}_e, W^{\mathrm{s}}_h)(1-\rho^{\mathrm{s}}_h) - s^{\mathrm{out}}_h(W^{\mathrm{s}}_e, W^{\mathrm{s}}_h)\rho^{\mathrm{s}}_h - r_w(\rho^{\mathrm{s}}_e + \rho^{\mathrm{s}}_h - 1)N^{\mathrm{s}}_{\mathrm{ph}} - \rho^{\mathrm{s}}_e\rho^{\mathrm{s}}_h, \tag{4.4d}$$

$$0 = J - s^{\mathrm{in}}_e(W^{\mathrm{s}}_e, W^{\mathrm{s}}_h)(1-\rho^{\mathrm{s}}_e) + s^{\mathrm{out}}_e(W^{\mathrm{s}}_e, W^{\mathrm{s}}_h)\rho^{\mathrm{s}}_e - cW^{\mathrm{s}}_eW^{\mathrm{s}}_h, \tag{4.4e}$$

$$0 = J - s^{\mathrm{in}}_h(W^{\mathrm{s}}_e, W^{\mathrm{s}}_h)(1-\rho^{\mathrm{s}}_h) + s^{\mathrm{out}}_h(W^{\mathrm{s}}_e, W^{\mathrm{s}}_h)\rho^{\mathrm{s}}_h - cW^{\mathrm{s}}_eW^{\mathrm{s}}_h, \tag{4.4f}$$

where the rescaled feedback strength $\tilde{k} \equiv K/(2\kappa\tau_{\mathrm{in}})$ has been introduced (cf. Eq. (3.13)). Equation (4.4a) describes the impact of the feedback to the rescaled inversion $\rho_{\mathrm{inv}} = \frac{1}{2}\left[g(\rho_e + \rho_h - 1) - 1\right]$ (see definition in Eq. (2.5)). For the solitary laser ($\tilde{k} = 0$), we have $\rho^0_{\mathrm{inv}} = 0$ and, thus, the sum of the electron and hole occupation probabilities in the quantum dots $\rho^0_e + \rho^0_h = (1+g)/g$ is "clamped" to a constant value, which is the well known effect of gain-clamping in semiconductor lasers [TAR95a] (cf. Eq. (2.25)). (Note that the steady states of the solitary laser are marked by $(\,\cdot\,)^0$.)

Taking advantage of the carrier conservation (Eq. (2.8)), we can reformulate Eq. (4.4a) to express ρ^{s}_e and ρ^{s}_h in terms of W^{s}_e and W^{s}_h

$$\rho^{\mathrm{s}}_e = \frac{1}{2}\left[\frac{1+g-2\tilde{k}\cos(\delta\omega^{\mathrm{s}} + C)}{g} + W^{\mathrm{s}}_h - W^{\mathrm{s}}_e\right], \tag{4.5a}$$

$$\rho^{\mathrm{s}}_h = \frac{1}{2}\left[\frac{1+g-2\tilde{k}\cos(\delta\omega^{\mathrm{s}} + C)}{g} + W^{\mathrm{s}}_e - W^{\mathrm{s}}_h\right]. \tag{4.5b}$$

Further, an expression for $N^{\mathrm{s}}_{\mathrm{ph}}$ as a function of the carrier populations can be obtained, by inserting the sum of Eqs. (4.4c) and (4.4d) into the sum of Eqs (4.4e) and (4.4f) and then using Eq. (4.4a) to replace the inversion $\rho^{\mathrm{s}}_e + \rho^{\mathrm{s}}_h - 1 = (2\rho^{\mathrm{s}}_{\mathrm{inv}} + 1)/g$

$$\begin{aligned} N^{\mathrm{s}}_{\mathrm{ph}} &= \frac{g}{r_w\big(1 - 2\tilde{k}\cos(\delta\omega^{\mathrm{s}} + C)\big)}\left[J - \rho^{\mathrm{s}}_e\rho^{\mathrm{s}}_h - cW^{\mathrm{s}}_eW^{\mathrm{s}}_h\right] \\ &\approx \frac{g}{r_w\big(1 - 2\tilde{k}\cos(\delta\omega^{\mathrm{s}} + C)\big)}\left[J - J_{\mathrm{th}}\right], \end{aligned} \tag{4.6}$$

where we have introduced the pump current at lasing threshold J_{th}, which has been defined in Eq. (2.27). Eventually, the steady states of the reservoir populations can be determined by inserting Eqs. (4.5) into Eqs. (4.4e) and (4.4f), and then solving self-consistently for W_e^{s} and W_h^{s}. This has to be done numerically, because the scattering rates $s_{e/h}^{\mathrm{in/out}} = s_{e/h}^{\mathrm{in/out}}(W_e, W_h)$ are nonlinear functions of the reservoir populations W_e and W_h as discussed in Section 2.2 (see also Appendix A.0.1 for fit functions of the scattering rates).

Summing up, for given $\tilde{k}$ and C, at first, the frequency detunings $\delta\omega^{\mathrm{s}}$ of the ECM solutions are calculated by first inserting Eq. (4.4a) into Eq. (4.4b) and then solving the resulting transcendental equation numerically. Together with the steady states of W_e^{s} and W_h^{s} obtained by solving Eqs. (4.4e) and (4.4f) self-consistently, this permits to calculate ρ_e^{s} and ρ_h^{s} from Eqs. (4.5), which eventually yields $N_{\mathrm{ph}}^{\mathrm{s}}$ from Eq. (4.6).

In the next paragraph, expressions for the ellipse, on which the ECMs lie, and the line, at which new pairs of ECMs are created in saddle-node bifurcations, are derived. These expressions are in terms of $\delta\omega^{\mathrm{s}}$ and $\rho_{\mathrm{inv}}^{\mathrm{s}}$ identical to the expressions that have been derived for the LK-model. Detailed discussions of the latter can be found in the review article of [TAR98a] or in [ROT07].

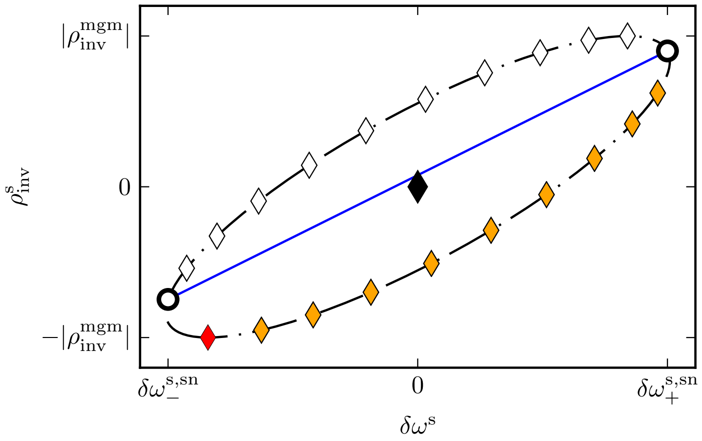

Figure 4.2: Ellipse of ECMs (black dash-dotted line) in ($\delta\omega$,ρ_{inv})-plane as determined from Eqs. (4.4a) and (4.4b). Modes and anti-Modes are marked by filled and open diamonds, respectively. Pairs of ECMs are created in saddle-node bifurcations at intersection points of the ellipse with the blue line (Eq. (4.11)) that are marked by open circles. The black and the red diamond mark the lasing fixed point of the solitary laser and the maximum-gain mode, respectively.

By introducing the curve parameter $\Delta \equiv \delta\omega^{\mathrm{s}}\tau + C$, we see that Eqs. (4.4a) and (4.4b) are a parametric representation of a tilted ellipse in the ($\delta\omega$,ρ_{inv})-plane, which is depicted in Fig. 4.2 with a black dash-dotted line. The tilting is introduced by the argument arctan(α) in the trigonometric functions. This situations is very similar to the one of the injection problem[1]. In the latter, the two fixed points within the locking tongue lie on an ellipse (cf. Fig. 3.12 to Fig. 4.2 and Eqs. (4.4a) and (4.4b) with Eqs. (3.17a) and (3.17b)). The main difference is that for the feedback problem the equation for $\delta\omega^{\mathrm{s}}$ is transcendental permitting infinitely many solutions for suitable $\tilde{k}$, α, and τ. Further, in the injection problem for each value of the injection strength $\tilde{k}$ two solutions, one saddle and one stable node is found, while for the feedback problem only one solution exists below a critical feedback strength $\tilde{k}_{\mathrm{eff}}$. To determine $\tilde{k}_{\mathrm{eff}}$, Eq. (4.4a) is inserted into Eq. (4.4b)

$$\begin{aligned}\delta\omega^{\mathrm{s}} &= -\tilde{k}\left(\alpha\cos(\delta\omega^{\mathrm{s}}\tau + C) + \sin(\delta\omega^{\mathrm{s}}\tau + C)\right)\\ &= -\tilde{k}\sqrt{1+\alpha^2}\sin\left(\delta\omega^{\mathrm{s}}\tau + C + \arctan(\alpha)\right),\end{aligned} \tag{4.7}$$

---

[1] Note that Δ corresponds to the phase Ψ in the injection problem of Chapter 3.

where we have used the trigonometric identities (3.20) in the second equality. The number of ECMs is given by the number of solutions of Eq. (4.7). Geometrically, solutions of Eq. (4.7) are intersection points of the left and the right hand side of Eq. (4.7). Their number increases with $\tilde{k}$, τ and α. New solutions are created pairwise if the slope of both sides of Eq. (4.7) coincides and additionally Eq. (4.7) is fulfilled, i.e.,

$$\frac{df(\delta\omega^{\mathrm{s}})}{d\delta\omega^{\mathrm{s}}} = 0 \;\wedge\; f(\delta\omega^{\mathrm{s}}) = 0, \qquad \text{where } f(\delta\omega^{\mathrm{s}}) \equiv -\tilde{k}\sqrt{1+\alpha^2}\sin\big(\delta\omega^{\mathrm{s}}\tau + C + \arctan(\alpha)\big) - \delta\omega^{\mathrm{s}}. \tag{4.8}$$

Equations (4.8) are the conditions for a saddle-node bifurcation. The first condition evaluates to

$$-\frac{1}{\tilde{k}_{\mathrm{eff}}} = \cos\big(\delta\omega^{\mathrm{s}}\tau + C + \arctan(\alpha)\big), \tag{4.9}$$

where we have defined the effective feedback strength $\tilde{k}_{\mathrm{eff}} \equiv \tilde{k}\sqrt{1+\alpha^2}\tau$ mentioned above. Equation (4.9) has solutions for $\tilde{k}_{\mathrm{eff}} \geq 1$, and for $\tilde{k}_{\mathrm{eff}} = 1$, the first pair of ECMs is created. The critical value $\tilde{k} = 1/(\sqrt{1+\alpha^2}\tau)$ decreases for increasing α, and τ, meaning that for long delay and high α-factors, bi-stability of ECMs occurs at lower feedback levels.

For a geometrical interpretation, it is instructive to derive a saddle-node condition equivalent to Eq. (4.9) by taking the derivative of both sides of the first line of Eq. (4.7) with respect to $\delta\omega^{\mathrm{s}}$

$$-\frac{1}{\tilde{k}\tau} = \cos(\delta\omega^{\mathrm{s}}\tau + C) - \alpha\sin(\delta\omega^{\mathrm{s}}\tau + C). \tag{4.10}$$

Replacing the trigonometric functions in the above equation with the help of Eqs. (4.4a) and (4.4b), we obtain an explicit expressions for the line in the ($\delta\omega$,ρ_{inv})-plane, along which the saddle-node bifurcations take place

$$\rho^{\mathrm{s}}_{\mathrm{inv}}(\delta\omega^{\mathrm{s}}) = \frac{1+\alpha\delta\omega^{\mathrm{s}}\tau}{\tau(1+\alpha^2)}. \tag{4.11}$$

Further, a representation of the ellipse of ECMs may be obtained by adding the square of Eq. (4.4a) to the square of Eq. (4.4b)

$$\tilde{k}^2 = (\rho^{\mathrm{s}}_{\mathrm{inv}})^2 + (\alpha\rho_{\mathrm{inv}} - \delta\omega^{\mathrm{s}})^2. \tag{4.12}$$

Geometrically, ECMs are created in mode-, anti-mode pairs at intersection points (open circles in Fig. 4.2) of the ellipse (4.12) with the line (4.11) (blue line in Fig. 4.2), which are given by

$$(\delta\omega^{\mathrm{s,sn}}_{\pm}, \rho^{\mathrm{s,sn}}_{\mathrm{inv},\pm}) = \left(\pm\frac{1}{\tau}\sqrt{\tilde{k}^2_{\mathrm{eff}} - 1}, \frac{1 \pm \alpha\sqrt{\tilde{k}^2_{\mathrm{eff}} - 1}}{\tau(1+\alpha^2)}\right). \tag{4.13}$$

The anti-modes (saddles) are always unstable due to destructive interference of the laser light with the back-coupled light, while the stability of the modes (nodes) has to be determined by a linear stability analysis. Modes and anti-modes are marked by full and open diamonds in Fig. 4.2, respectively. Note that the ellipse of ECMs (black dash-dotted line) in Fig. 4.2 is obtained by varying the curve parameter $\Delta = \delta\omega^{\mathrm{s}}\tau + C$ in Eqs. (4.4a) and (4.4b), while the frequency detuning $\delta\omega^{\mathrm{s}}$ of modes and anti-modes is obtained for fixed feedback phase C, fixed injection strength $\tilde{k}$, and fixed delay time τ by solving the transcendental Eq. (4.7).

The most stable ECM is the maximum gain-mode (filled red diamond in Fig. 4.2) [LEV95], which profits most from the feedback and thus has the lowest inversion. From Eq. (4.4a), we see that it is given by the condition $C + \delta\omega^{\mathrm{s}}\tau = 0$, which yields

$$(\delta\omega^{\mathrm{s,mgm}}, \rho_{\mathrm{inv}}^{\mathrm{s,mgm}}) = -(\alpha\tilde{k}, \tilde{k}), \text{ and } C^{\mathrm{mgm}} = -\alpha\tilde{k}\tau. \tag{4.14}$$

Next, an expression for the saddle-node lines in the $(C, \tilde{k})$-plane is derived, which provides us with a graphical interpretation of the number of existing ECMs (see Fig. 4.3). Therefore, we note that the saddle-node condition (4.9) implies

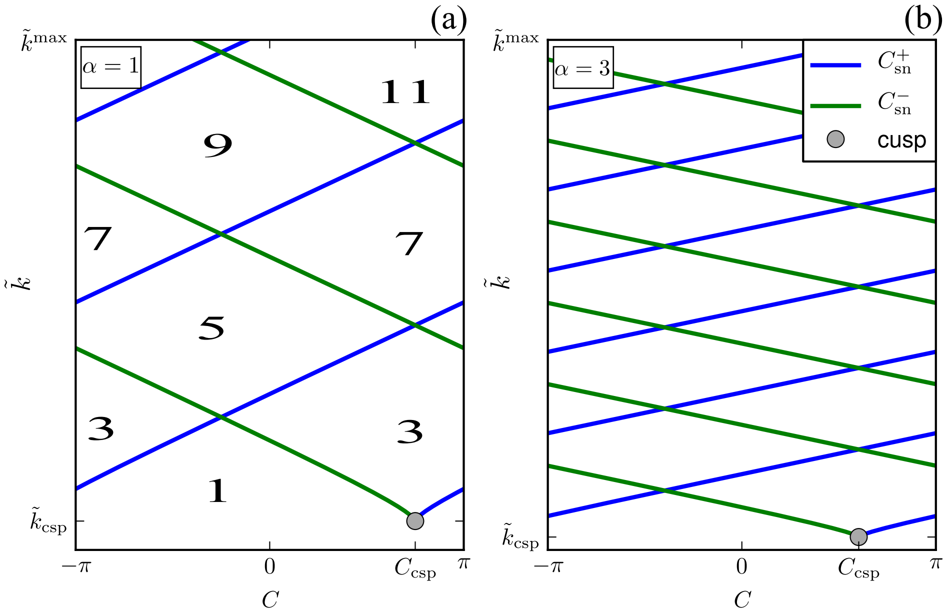

Figure 4.3.: Honey-comb structure of the branches of saddle-node lines (C_{sn}^{+}, C_{sn}^{-}) in the $(C,\tilde{k})$-plane for small $\alpha = 1$ **(a)** and large $\alpha = 3$ **(b)**. Numbers give the number of ECMs in each comb. The cusp point $(C_{\mathrm{csp}},\tilde{k}_{\mathrm{csp}})$ is marked by a gray dot. Parameters: $\tau = 30$, and other parameters as in Table 2.3.

$$\sin\left(\delta\omega^{\mathrm{s}}\tau + C + \arctan(\alpha)\right) = \pm\frac{\sqrt{\tilde{k}_{\mathrm{eff}}^{2} - 1}}{\tilde{k}_{\mathrm{eff}}}, \text{ and} \tag{4.15a}$$

$$\delta\omega^{\mathrm{s}}\tau + C + \arctan(\alpha) = \pm\arccos\left(-\frac{1}{\tilde{k}_{\mathrm{eff}}}\right) + 2n\pi, \tag{4.15b}$$

where the sign in both equations is the same and $n \in \mathbb{Z}$. Inserting Eq. (4.15a) into the second line of the equality (4.4b), we obtain an expression for $\delta\omega^{\mathrm{s}}$ as a function of $\tilde{k}$ that we use to eliminate $\delta\omega^{\mathrm{s}}$ in Eq. (4.15b). Then, solving Eq. (4.15b) for C, provides us with the branches of saddle-node lines $C_{\mathrm{sn}}^{\pm}(\tilde{k})$ in the $(C,\tilde{k})$-plane

$$C_{\mathrm{sn}}^{\pm}(\tilde{k}) = \pm\left[\sqrt{\tilde{k}_{\mathrm{eff}}^{2}(\tilde{k}) - 1} + \arccos\left(-\frac{1}{\tilde{k}_{\mathrm{eff}}(\tilde{k})}\right)\right] - \arctan(\alpha) + 2n\pi. \tag{4.16}$$

Figure 4.3 depicts the honey-comb structure of the branches of saddle-node lines C^{+}_{sn} (blue lines) and C^{-}_{sn} (green lines) in the $(C, \tilde{k})$-plane for small $\alpha = 1$ (Fig. 4.3**(a)**) and large $\alpha = 3$ (Fig. 4.3**(b)**) and $\tau = 30$. For low values of $\tilde{k}$, only the ECM that can be continued out of the solution for the solitary laser exists. Each time one of the saddle-node lines is crossed by varying $\tilde{k}$ or C, a mode- anti-mode pair is created. Numbers in Fig. 4.3 denote the number of ECMs in each honey-comb. The lowest point of the saddle-node curve is a cusp point, where C^{+}_{sn} and C^{-}_{sn} intersect and annihilate (gray dot in Figs. 4.3). This bifurcation point is given by

$$(C_{\mathrm{csp}}, \tilde{k}_{\mathrm{csp}}) = \left(\pi - \arctan(\alpha) + 2n\pi, \frac{1}{\tau\sqrt{1+\alpha^2}}\right). \tag{4.17}$$

4.4. Numerical stability analysis

In this section, we analyze the stability of the ECM solutions (4.3) of the dynamical equations (4.1) and compare our findings with direct numerical simulations as well as results from numerical path continuation methods. For the latter, the $\mathbb{S}^1$-symmetry of the ECMs has to be resolved. Otherwise, the members of the family of solutions with different phases

$$\{\phi = \delta\omega^{\mathrm{s}} t + \phi_0 \mid \phi_0 \in [0, 2\pi]\} \tag{4.18}$$

cannot be distinguished, which is called ϕ-indeterminacy [HAE02, WOL02]. Further, it is convenient to treat the ECMs, which are rotating waves with time-dependent phases, as fixed points. Therefore, a transformation to a rotating frame is performed

$$\Phi : \quad \mathbb{C} \to \mathbb{C} \quad \mathcal{E} \mapsto \mathcal{E} e^{-ibt} = \sqrt{N^{\mathrm{s}}_{\mathrm{ph}}} e^{i(\delta\omega^{\mathrm{s}} - b)t + \phi_0}, \quad \text{for } b \in \mathbb{R}, \tag{4.19}$$

where we have inserted the ECM-ansatz (4.3) in the last equality. Now, it can be seen from Eq. (4.19) that by choosing $b = \delta\omega^{\mathrm{s}}$, the ECMs lose their time dependence. Furthermore, the ϕ-indeterminacy can then be resolved by fixing the phase ϕ_0. A convenient choice is $\phi_0 = 0 \mod 2\pi$, which implies that the ECMs are real. In Cartesian coordinates $\tilde{\mathcal{E}} \equiv \mathcal{E} e^{-ibt} = x + iy$ that are well suited for the numerical implementation, the transformed field equation (4.1a) reads

$$\begin{aligned}
x' &= \frac{1}{2}\Big[g\big[\rho_e + \rho_h - 1\big] - 1\Big]x + by - \frac{\alpha}{2}\Big[g\big[\rho_e + \rho_h - 1\big] - 1\Big]y \\
&\quad + k \cos\big(C + b\tau\big)x(t' - \tau) + k \sin\big(C + b\tau\big)y(t' - \tau), \\
y' &= \frac{1}{2}\Big[g\big[\rho_e + \rho_h - 1\big] - 1\Big]y - bx + \frac{\alpha}{2}\Big[g\big[\rho_e + \rho_h - 1\big] - 1\Big]x \\
&\quad - k \sin\big(C + b\tau\big)x(t' - \tau) + k \cos\big(C + b\tau\big)y(t' - \tau).
\end{aligned} \tag{4.20}$$

The choice of $\phi_0 = 0 \mod 2\pi$ discussed above, which allows one to break the ϕ-indeterminacy, corresponds in Cartesian coordinates to the condition $y(t) = y(t - \tau) = y_s = 0$. Now, one can calculate the ECM solutions as fixed points of Eqs. (4.20) together with the carrier equations (4.1b)–(4.1e) and the additional condition $y_s = 0$. To resolve the symmetry of solutions with a periodic modulated photon number, i.e., of limit-cycles created in Hopf bifurcations, other conditions have to be imposed. These are discussed in detail in [HAE02]. For the numerical path continuation, the packages *DDE-Biftool* [ENG02] and *KNUT* [SZA09] are used.

In this section, we study the most simple bifurcation scenario that is obtained for a small α-factor of $\alpha = 0.9$ and a short external cavity with a length of 2.4 cm, which corresponds to a delay time of $\tau = 16$. This yields an interesting configuration from an experimental point of view, because QD lasers seem to have a smaller phase-amplitude coupling than QW lasers [NEW99a].

Integrated devices consist in the simplest case of an actively pumped, inverted section and a short passive phase-tuning section. They are of experimental interest, because they permit, for example, to strongly enhance the cutoff frequency under small signal modulation [RAD07]. We study the short-cavity regime as introduced by Schunk and Petermann [SCH89h]. The authors define an external cavity as short if the product of the RO frequency and the delay time τ is considerably less than unity. Further, this choice of parameters yields the most simple bifurcation scenario, which will be studied in this section before analyzing the more complex bifurcation scenarios observed for larger α-factors in the next sections with the help of path continuation techniques. Since the optical equation (4.1a) for the electrical field amplitude is a delay differential equations, each mode has infinitely many eigenvalues. Their real parts rise from minus infinity with increasing feedback strength. In Fig. 4.4, the real parts of the eigenvalues of the first ECM (the one that can be followed out of the solution for the solitary laser) are plotted over the feedback strength $\tilde{k}$. The transcendental characteristic equation has been solved numerically. At a critical feedback strength $\tilde{k}_H = 0.041$ (red dash-dotted lines in Fig. 4.4 and in Fig. 4.5), the leading eigenvalue crosses the real axis and the mode becomes unstable in a supercritical Hopf bifurcation leading to a more complex solution with periodically modulated photon number. In the short cavity regime for $\tau = 16$ and for small $\alpha = 0.9$, the laser displays only one instability region in dependence of the feedback strength $\tilde{k}$, which will be discussed in the following.

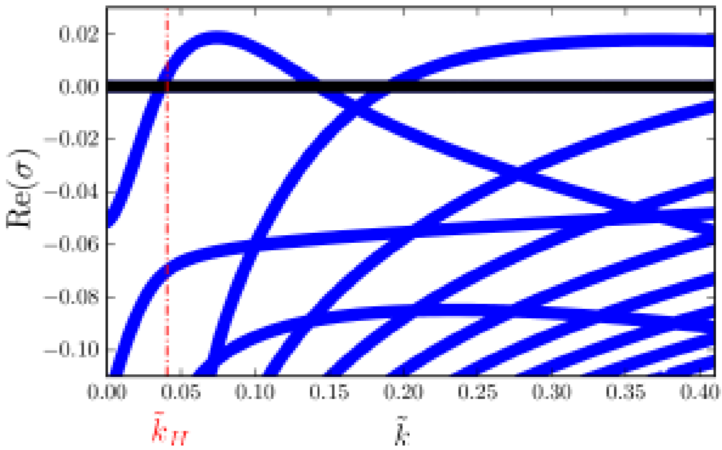

Figure 4.4: Real parts of the Floquet exponents $\mathrm{Re}(\sigma)$ (solid blue lines) of the ECM that can be followed out of the solitary laser solution in dependence of the feedback strength $\tilde{k}$. The horizontal (black) line corresponds to the trivial Floquet-multiplier (Goldstone mode). The vertical red dash-dotted line indicates the feedback strength $\tilde{k}_H$, at which the first supercritical Hopf bifurcation occurs. Parameters: $\alpha = 0.9$, $\tau = 16$, $C = \pi$, other parameters as in Table 2.3. Modified from [OTT12].

In the upper panel of Fig. 4.5, the bifurcation diagram of N_{ph} as a function of $\tilde{k}$ is plotted with red dots. Here, we plot the local extrema of N_{ph} for each value of $\tilde{k}$ after transients died out. Additionally, the photon population $N^{\mathrm{s}}_{\mathrm{ph}}$ of the stable parts of the first and the second ECM given by Eq. (4.6) are indicated by filled circles. The middle panel shows the frequency deviations $\delta\omega^{\mathrm{s}}$ of the ECMs and in the lower panel the carrier inversion ρ_{inv} of the ECMs is plotted as a function of $\tilde{k}$. Stable modes are indicated by filled and unstable modes by open circles. Vertical black dashed lines labeled by (a) to (f) indicate $\tilde{k}$-values, at which time series and phase space projections are presented in Fig. 4.6 and Fig. 4.7, respectively.

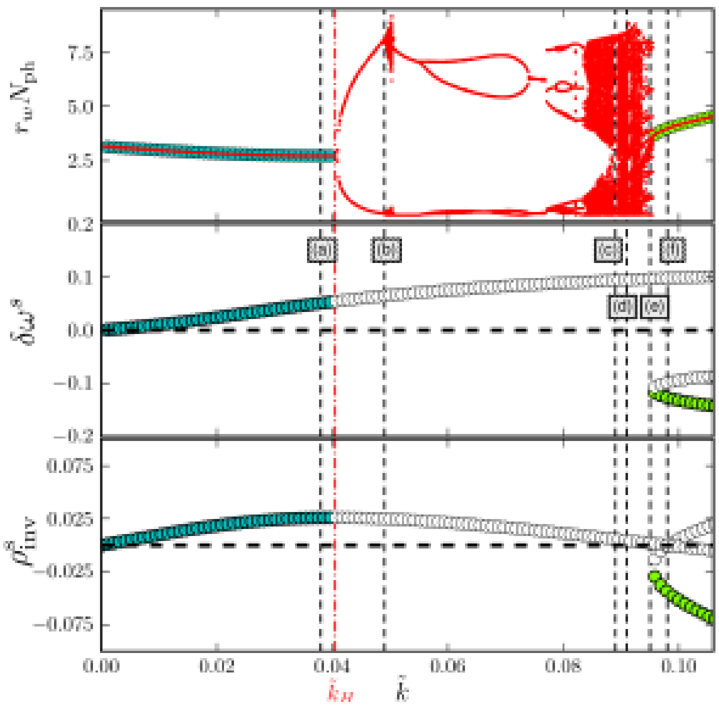

Figure 4.5: **Upper panel**: Bifurcation diagram of the photon number N_{ph} (red points) in dependence of the rescaled feedback strength $\tilde{k}$. Filled circles are steady state values of N_{ph} of the stable ECMs. **Middle and lower panel**: Frequency deviations $\delta\omega^{\mathrm{s}}$ and carrier inversion N_{inv} of the ECMs in dependence of $\tilde{k}$. Stable and unstable ECMs are indicated by filled and open circles, respectively. Vertical black dashed lines labeled (a) to (f) mark $\tilde{k}$-values, at which time series and phase space projections are shown in Fig. 4.6 and Fig. 4.7, respectively. The feedback strength of the first supercritical Hopf bifurcation is labeled $\tilde{k}_H$ (vertical red dash-dotted line). Parameters: Reference rates, $J = 2J_{\mathrm{th}}$, $\alpha = 0.9$, $\tau = 16$, $C = \pi$, and other parameters as in Table 2.3. Modified from [OTT12].

In Fig. 4.7, the trajectory (red solid line) is projected onto a plane spanned by the frequency deviations and the carrier inversion. In this projection, the ECMs appear as points. For more complex solutions with non-constant frequency $\delta\omega^{\mathrm{s}}$, we plot the frequency deviations averaged over one external cavity round trip time τ given by $(\phi - \phi_\tau)/\tau$. The ECMs lie on the ellipse described by Eq. (4.12) (black dashed line in Fig. 4.7). On the blue dash-dotted line in Fig. 4.7, saddle-node bifurcations take place (Eq. (4.11)). Note that the saddle-node line and the ellipse of the ECM are plotted as functions of the curve parameter $\Delta = \delta\omega^{\mathrm{s}}\tau + C$, while the ECMs and the trajectories of more complex solutions are only plotted for the fixed value $C = \pi$ of the feedback phase. For this value of C, the saddle-node bifurcation takes place at a feedback strength $\tilde{k} = 0.08955$ (see Fig. 4.5 middle and lower panel). Also in Fig. 4.7, stable ECMs are indicated by filled circles. The filling color corresponds to the color-code of the stable modes in Fig. 4.5 and Fig. 4.6. Unstable ECMs, modes as well as anti-modes, are indicated by gray open circles.

At $\tilde{k} = 0$, the first ECM is stable. With increasing $\tilde{k}$, its frequency and its carrier inversion shift. This is why in Fig. 4.7(a), the ECM is not located at the origin (see also black dashed line labeled (a) in Fig. 4.5). At $\tilde{k}_H = 0.0041$ (red dash-dotted line in Fig. 4.4 and Fig. 4.5), the first ECM becomes unstable in a super-critical Hopf bifurcation. The

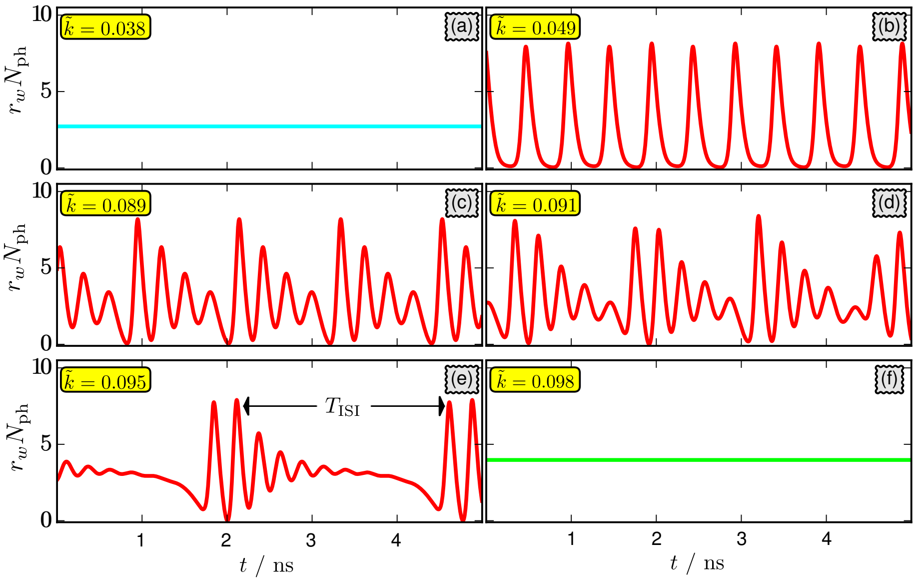

Figure 4.6.: Time series for selected values of the rescaled feedback strength $\tilde{k}$. Feedback strengths in **(a)** to **(f)** correspond to black dashed lines labeled **(a)** to **(f)** in Fig. 4.5. In **(e)**, the time between two consecutive pulse packages is labeled by T_{ISI}. Parameters: Reference rates, $J = 2J_{\mathrm{th}}$, $\alpha = 0.9$, $\tau = 16$, $C = \pi$, other parameters as in Table 2.3. Modified from [OTT12].

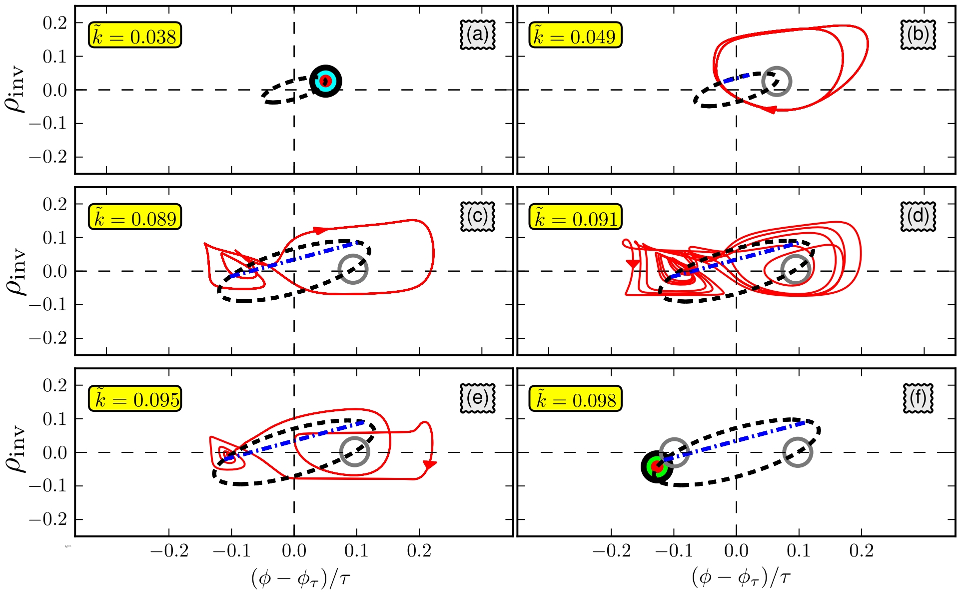

Figure 4.7.: Phase space projections of the trajectory (red solid line) onto planes spanned by the frequency deviation $\delta\omega^{\mathrm{s}}$ and the inversion ρ_{inv} for selected values of the rescaled feedback strength $\tilde{k}$. The stable and unstable ECMs are indicated by filled circles and open gray circles, respectively. The color code of the stable ECMs is the same as in Fig. 4.5. The ECMs lie on the ellipse given by Eq. (4.12) (black dashed line). The blue dash-dotted line is the saddle-node line (Eq. (4.11)). Figures **(a)** to **(f)** correspond to black dashed lines labeled **(a)** to **(f)** in Fig. 4.5. Parameters: Reference rates, $J = 2J_{\mathrm{th}}$, $k = 0.9$, $\tau = 16$, $C = \pi$, and other parameters as in Table 2.3. Modified from [OTT12].

time series displays self-sustained intensity pulsations (see Fig. 4.6(b)) with the frequency of the ROs, as it is expected for higher pump-currents [LYT97]. The bifurcation diagram for $\tilde{k} > \tilde{k}_H$ shows two branches that scale like the square root of the distance from the bifurcation point (Fig. 4.5 upper panel). This is the signature of a Hopf bifurcation [KUZ95]. In phase space, the intensity pulsations correspond to a periodic motion on a delay-induced limit cycle. The Hopf bifurcation is followed by a cascade of period-doubling bifurcations leading to chaos. In Fig. 4.6(b) (black dashed line (b) in Fig. 4.5), we see the time series after the first bifurcation of this cascade has taken place. The time series now consists of two oscillations with slightly different peak heights. The corresponding phase space projection in Fig. 4.7(b) depicts a motion on a two-fold limit cycle. For increasing $\tilde{k}$, the system becomes chaotic. The small chaotic region is followed by a large periodic window ranging from $\tilde{k} = 0.051$ to $\tilde{k} = 0.082$. For larger $\tilde{k}$-values, the laser becomes chaotic again. The chaotic region is interrupted by small windows of frequency locking. Time series and phase-space projection of such a frequency locked solution is depicted in Fig. 4.6(c) and Fig. 4.7(c), respectively (black dashed line (c) in Fig. 4.5). The time series depicts regular intensity pulsations with the RO frequency. In the phase space projection, we note that the attractor has become larger: indeed the trajectory does not only surround the unstable first ECM, as it did at the beginning of the bifurcation cascade (Fig. 4.7(b)), instead it already starts to wind around the point in the phase space, where a new pair of ECMs appears at higher values of $\tilde{k}$ [KRA02b]. The winding in the phase space corresponds to the damped ROs in the time series. In Fig. 4.6(d) and Fig. 4.7(d), we see a time series and a phase space projection in the chaotic region near the end of the bifurcation cascade (dashed line (f) in Fig. 4.5). The time series displays irregular pulse packages. The underlying frequency is again the one of the ROs. In the phase space projection, we recognize the winding mechanism from Fig. 4.7(c).

At $\tilde{k} = 0.0895$, the time series in Fig. 4.6(e) shows strictly regular pulse packages (black dashed line (e) in Fig. 4.5). The long "tail" of the pulse packages in the time series (Fig. 4.6(e)) corresponds to the winding around the point, where the saddle-node bifurcation will take place. At the end of the pulse packages, the trajectory is re-injected into the high gain region ($\rho_{\text{inv}} > 0.1$). A similar re-injection mechanism has previously been observed experimentally and studied theoretically for QW lasers in the short cavity regime [HEI01a, HEI03a, TAB04] and for QW lasers with phase-conjugate feedback [VIR11]. Note that the pulse packages studied by [HEI01a, HEI03a] differ in two ways from the pulse packages described in this paper: At first, their modulation frequency is the external cavity roundtrip time, which can be attributed to the much lower pump current in their studies as discussed in [LYT97]. Second, the pulse packages studied by [HEI01a, HEI03a] are slightly irregular and thus their trajectory does not close up in the phase space to form a limit cycle. We presume that the second difference is due to the higher α-factor of $\alpha = 5.0$ the authors use in their numerical studies. We only find strictly regular pulse packages for $\alpha < 1$ in the short cavity regime. At $\tilde{k} = 0.08955$, a pair of ECMs is created in a saddle-node bifurcation. We can see from Fig. 4.5 (middle and lower panel) that the second ECM mode is stable upon creation, but with the chosen initial conditions its basin of attraction is only accessible for the system after a global bifurcation at $\tilde{k}_{\text{hom}} = 0.096$ that we are going to discuss in the following.

The time between two consecutive pulse packages T_{ISI} (see its definition in Fig. 4.6(e)) scales logarithmically with the distance from the bifurcation point $\tilde{k}_{\mathrm{hom}} = 0.096$, which is depicted in Fig. 4.8 [OTT10]. This behavior is typical for a homoclinic bifurcation of limit cycles with a negative saddle quantity [KUZ95, HIZ08]. The saddle quantity for a saddle-focus is defined as $\sigma_0 \equiv \sigma_s + \mathrm{Re}(\sigma_{u,\pm})$, where σ_s is the positive real eigenvalue and $\mathrm{Re}(\sigma_{u,\pm})$ are the real parts of the complex conjugate leading eigenvalues, respectively. A negative σ_0 results in the birth of a unique stable limit cycle from a homoclinic orbit. Indeed, we find σ_0 to be negative near $\tilde{k}_{\mathrm{hom}}$. The unique limit cycle is the one that is plotted in Fig. 4.7(e) for $\tilde{k} = 0.095$.

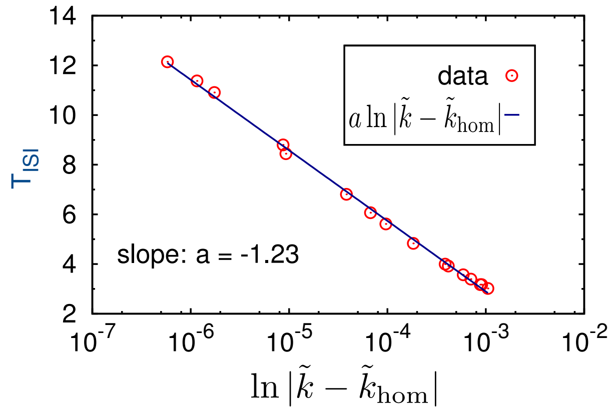

Figure 4.8: Scaling of the inter-spike interval time T_{ISI} as a function of the feedback strength $\tilde{k}$ close to the homoclinic bifurcation at $\tilde{k} = \tilde{k}_{\mathrm{hom}}$. Parameters: Reference rates, $K = 0.227$, $\alpha = 0.9$, $C = \pi$, $\tau = 16$, $J = 2J_{\mathrm{th}}$, and other parameters as in Table 2.3. Modified from [OTT10].

For $\tilde{k}$ slightly smaller than $\tilde{k}_{\mathrm{hom}}$, we find a small range of bistability between the unique limit-cycle and the second ECM mode. For $\tilde{k}$ larger than $\tilde{k}_{\mathrm{hom}}$, the laser performs stable continuous wave emission, as we can see from the time series in Fig. 4.6(f) for $\tilde{k} = 0.098$. The phase-space projection (Fig. 4.7(f)) reveals that now the second ECM is stable (see also black dashed line (g) in Fig. 4.5). In Section 4.8 the excitability of the system near this homoclinic bifurcation will be discussed.

4.4.1. Impact of α-factor on bifurcation scenario

In this section, the impact of the α-factor on the bifurcation scenario is discussed and path continuation techniques are employed to study branches of solutions with time-periodic photon-number, i.e, limit-cycles born in Hopf bifurcations of ECMs.

Therefore, a relatively large α-factor ($\alpha = 3$) is contrasted with small $\alpha = 0.9$ as discussed in the previous section in order to point out the advantages of a small α that QD lasers are supposed to have [NEW99a]. Figure 4.9 shows the one-parameter bifurcation diagrams of the photon number N_{ph} (normalized to $2AN_a^{\mathrm{QD}}$) versus the bifurcation parameter K for $\alpha = 0.9$ in (a) and (c) and $\alpha = 3$ in (b) and (d). In the upper panel (direct numerical integration), local extrema of the photon number are plotted for each K after transients have died out. The differences between gray and black points in Fig. 4.9(a) and (b) result from different choices of the initial conditions in the numerical simulations. The results depicted in gray correspond to solutions, where those values of the photon number and carrier densities were used as initial condition on the delay interval that have been calculated for the lower feedback strength of the previous simulation (upsweep of K). Experimentally, this could be realized by increasing the

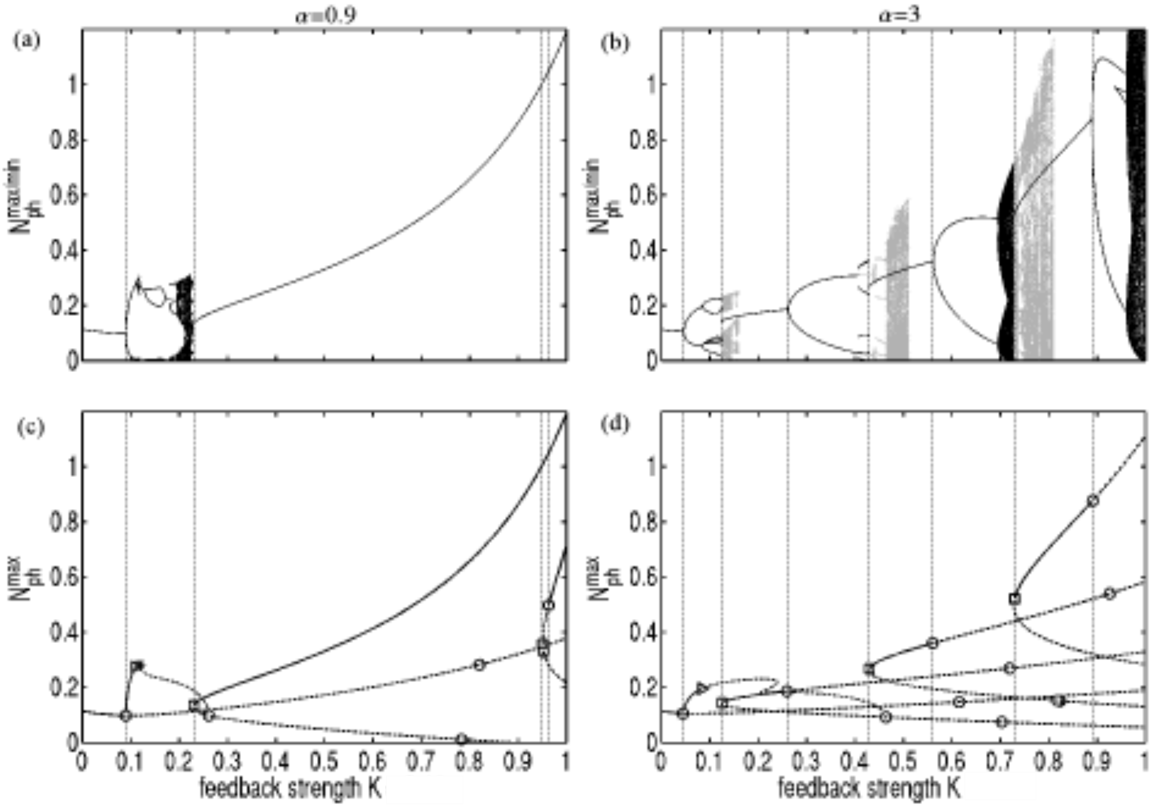

Figure 4.9.: One-parameter bifurcation diagrams of the photon number N_{ph} (normalized to $2AN_a^{\mathrm{QD}}$) vs. feedback strength K for direct numerical integration **(a)**, **(b)**, and path continuation with DDE-Biftool and *KNUT* **(c)**, **(d)**. In the upper panels maxima and minima of the photon density $N_{\mathrm{ph}}^{\mathrm{min/max}}$ (normalized to $2AN_a^{\mathrm{QD}}$) are plotted, in the lower panels only maxima $N_{\mathrm{ph}}^{\mathrm{max}}$ are shown. The α-factor is set to $\alpha = 0.9$ (**left column**) and to $\alpha = 3$ (**right column**). In **(a)**, **(b)** gray points indicate results for an upsweep of K, and black points result from downsweep of K. In **(c)** and **(d)** Hopf, saddle-node, torus, and period doubling bifurcation points are denoted by dots, squares, stars, and triangles, respectively. Stable solutions are printed as solid lines, unstable solutions as dashed lines. Vertical dashed lines facilitate comparison. Parameters: Reference rates, $C = \pi$, $\tau = 16$, $J = 2.5J_{\mathrm{th}}$, and other parameters as in Table 2.3. From [GLO12].

reflectivity of a mirror while the pump current is not switched off. In the same sense, the black points represent the decrease of the feedback strength from $K = 1$ to $K = 0$ (downsweep of K). By distinguishing these two ways of stepwise changing the feedback strength, it is possible to identify hysteresis effects.

The lower panel of Fig. 4.9 shows the bifurcations of the steady state solutions calculated with path continuation methods. For clarity, we plot only the maxima of the photon number $N_{\mathrm{ph}}^{\max}$ (normalized to $2AN_a^{\mathrm{QD}}$). Solid and dashed lines denote stable and unstable ECMs, respectively. Vertical dashed lines facilitate the comparison of Hopf (circles) and saddle-node bifurcation points (squares) in Fig. 4.9(b) and (d) with the bifurcation diagrams in Fig. 4.9(a) and (c). Exemplarily, we discuss the periodic solution that emerges from the Hopf bifurcation of the first ECM for $\alpha = 0.9$ and $\alpha = 3$. Period-doubling and torus bifurcations of these periodic solutions are marked with triangles and stars, respectively.

At first, we note that there exist fewer ECMs for $\alpha = 0.9$ compared to $\alpha = 3$ if K is increased as predicted by the transcendental Eq. (4.7). Secondly, one observes that the solitary solution is initially stable for small values of K before it is destabilized in a Hopf bifurcation (circle). The emerging periodic solution can be clearly identified in the diagrams obtained by direct integration (Fig. 4.9(a), (b)) as well as in the results of path continuation in Fig. 4.9(c) and (d). In Fig. 4.9 (c) and (d), one observes that the periodic solution created in the Hopf bifurcation of the first ECM vanishes in a Hopf bifurcation of the unstable branch (antimode) of the subsequent ECM. These bifurcation bridges between two consecutive ECMs lead to high-frequency oscillations with the frequency difference of both solutions that were also observed experimentally [TAG94]. The bifurcation bridges were suspected for some time by Tager and Petermann [TAG93, TAG94], and later their existence was shown analytically in [ERN00]. Further, their parameter dependence was studied in detail with the help of path continuation techniques in [HAE02]. In the latter paper, the authors suspected that the existence of bifurcation bridges is generic as new modes and anti-modes appear, which is supported by our results.

Focussing on the bifurcation of the ECMs (steady states), it can be seen from Fig. 4.9 (c) and (d) that the next mode- antimode pair of ECMs is born in a saddle-node bifurcation. The stable upper branch, i.e., the mode is again destabilized in a Hopf bifurcation. In general, we note that all the upper branches emerging from a saddle-node bifurcation point are initially stable, and then are destabilized for higher feedback strength K in Hopf bifurcations. The clear difference of upsweep (gray) and downsweep (black) of K in Fig. 4.9 (a) and (b) can be explained directly with the use of the results of the path continuation. For increasing K, each upper ECM branch becomes unstable in a Hopf bifurcation, and the emerging periodic orbit bifurcates via period doubling. When the next pair of ECMs is created in the saddle-node bifurcation, the periodic solution that emerge from the previous ECM does not reach the attractor of the new ECM directly, but needs a further increase of K to do so. Instead, for decreasing K the ECM vanishes in a saddle-node bifurcation and the laser directly jumps to the only stable solution that exists, i.e., a periodic orbit or a chaotic attractor. The consequence of this bistability of a periodic orbit (or chaotic attractor) and an ECM is that the existence of a stable ECM does not necessarily imply that the laser will operate in the cw regime in an experimental setup. This strongly depends on the experimental implementation of the feedback.

4.5. Two-parameter bifurcation diagrams: impact of α-factor and band structure

Now, the bifurcations of the ECMs in the (C, K)-plane are studied, and the impact of the band structure and of the α-factor on these bifurcations are discussed. Therefore, the sets of fast, reference, and slow scattering rates as introduced in Section 2.2 (see Table 2.1) as well as a small α-factor of $\alpha = 0.9$ and a larger α-factor of $\alpha = 3$ are discussed. Numerical path continuation techniques are used to trace the bifurcation lines. The upper panel of Fig. 4.10 shows two-parameter bifurcation diagrams for $\alpha = 0.9$ calculated for the

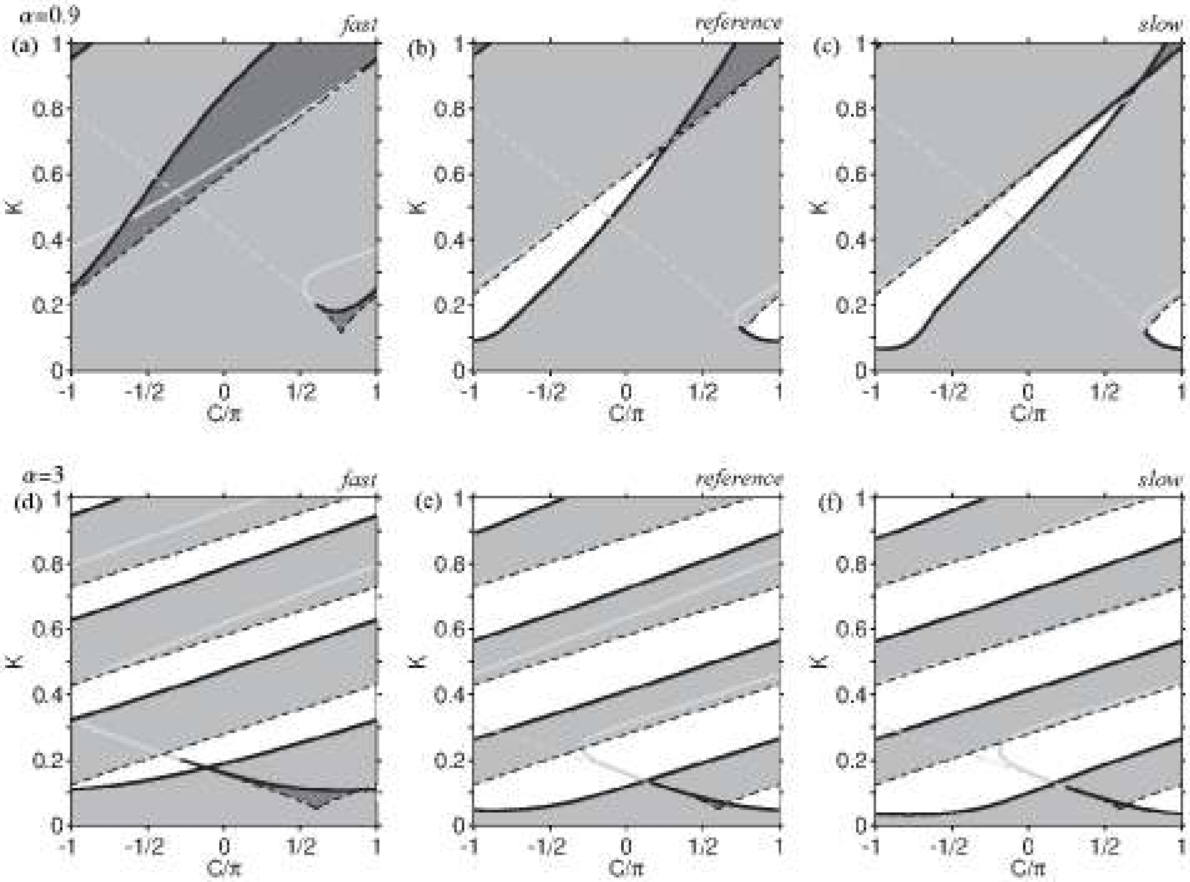

Figure 4.10.: Two-parameter bifurcation diagrams of the ECM solutions in the plane of the feedback phase C versus feedback strength K. **(a)–(c)**: $\alpha = 0.9$, **(d)–(f)** $\alpha = 3$. **(a)** and **(d)** correspond to the set of fast scattering rates, **(b)** and **(e)** to reference rates, and **(c)** and **(f)** to the slow rates. Hopf bifurcation lines are drawn as solid lines, saddle-node bifurcation lines as dashed lines. Bifurcation lines are displayed dark when supercritical and light when subcritical. Shading marks the number of stable ECM solutions. White indicates no stable ECM, light gray marks one stable ECM solution and dark gray denotes bistability of two ECM solutions. Parameters: $2.5J_{\mathrm{th}}$ and $\tau = 16$ and other parameters as in Table 2.3. From [GLO12].

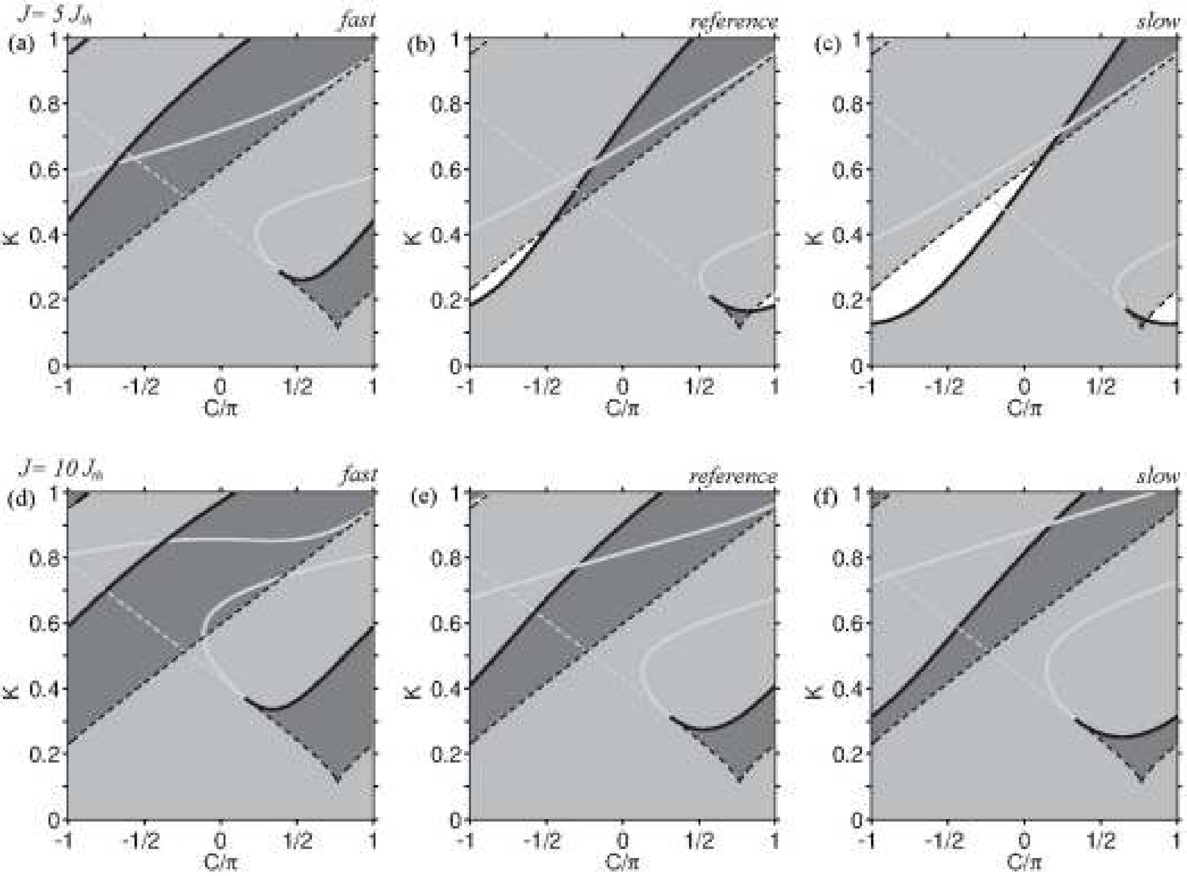

Figure 4.11.: Same as Fig. 4.10 for **(a)-(c)**: $J = 5J_{\mathrm{th}}$ and **(d)-(f)**: $J = 10J_{\mathrm{th}}$. The α-factor is fixed at $\alpha = 0.9$ and other parameters as in Table 2.3. From [GLO12].

implementation of fast (Fig. 4.10(a)), reference (Fig. 4.10(b)), and slow (Fig. 4.10(c)) scattering rates, respectively. The lower panel is organized identically but with larger $\alpha = 3$. Hopf and saddle-node bifurcation lines are depicted as solid and dashed lines, respectively. The bifurcation curves are drawn dark when supercritical, and light when subcritical. The number of stable ECMs is expressed by the shaded areas. White shading indicates no stable ECM, light gray areas correspond to one stable ECM and dark gray labels regions of bistability of two ECMs. The one-parameter bifurcation diagrams we discussed before in Fig. 4.9 correspond to a vertical sections in Figs. 4.10(b) and (e) for $C = \pi$. Beginning our analysis with the upper panel of Fig. 4.10, we note that the solitary solution is stable for all $C \in [-\pi, \pi]$ below a certain feedback strength K. (Note the 2π-periodicity of all bifurcation lines.) The destabilization of the solitary ECM occurs in a Hopf bifurcation for all the three QD energy structures. The important difference between Fig. 4.10(a), (b), and (c) is the position of the destabilizing Hopf bifurcation line with respect to the saddle-node bifurcation line.

As already discussed in Sec. 4.3, the saddle-node bifurcation lines are not affected by changes of the QD band structure or by changes of the pump current, because they do not depend on the carriers (see Eq. (4.16)). Hence, they exhibit the same shape in all the three plots. However, the shape of the Hopf bifurcation lines is drastically different for the three QD structures. In Fig. 4.10(a), the Hopf line always appears above the saddle-node line. Therefore, we can find at least one stable ECM for all $K \in [0, 1]$ and $C \in [-\pi, \pi]$. Thus, the laser never leaves the region of stable cw emission. Figure 4.10(b) shows a quite different situation for the case of the reference rates, where the two white areas indicate the absence of any stable ECM. For $C \in [\pi/2, \pi]$ and low $K < 0.3$, the bistability region of Fig. 4.10(a) disappears, because the Hopf bifurcation line is moved to smaller values of K. The same occurs for the Hopf line at $C \in [\pi, \pi]$ and $K \in [0.1, 0.7]$. Here, the laser is destabilized in a Hopf bifurcation before a new stable ECM exists resulting in oscillatory and chaotic behavior of the photon number. The highest K, for which the ECM that can be followed out of the lasing fixed point of the solitary laser, remains stable in the full range of C is $K_c = 0.1$. An analytical expression for the critical feedback strength K_c, below which the laser is guaranteed to be stable for all C, was first suggested for the LK-model, i.e., for a single mode class B QW laser, in [HEL90b] and it was rigorously derived afterward in [MOR92]. This critical value of the feedback strength is given by

$$K_c \equiv \frac{\tau_{\text{in}} \Gamma_{\text{RO}}}{\sqrt{1 + \alpha^2}}, \tag{4.21}$$

where Γ_{RO} denotes the RO damping. In Section 4.6.6, the above formula will be derived for the QD laser model for the reference and the slow set of scattering rates. It will be shown that K_c is the feedback strength, below which no Hopf instability can occur [OTT11].

Tuning the band structure to slower rates leads to the bifurcation diagram shown in Fig. 4.10(c). The unstable, white regions are even larger than in Fig. 4.10(b) and the $K_c \approx 0.06$ indicates higher sensitivity to optical feedback for this QD structure. This shift of the first Hopf line and thus of the critical feedback strength K_c from formula (4.21) predicting a linear dependence of K_c on the RO damping Γ_{RO}. From

Fig. 2.6(b), we see that the RO damping decreases from high values for the fast rates to much lower values for the slow rates with the reference rates lying in between. This explains the decrease of K_c from fast to the slow rates.

The lower panel of Fig. 4.10 depicts the bifurcation lines for larger $\alpha = 3$. In general, the same conclusions as for the upper panel in Fig. 4.10 may be drawn. The fast QD structure exhibits the highest critical feedback strength K_c and the most extended regions of bistability. Both, K_c and the bistability regions decrease for the reference and slow QD structures. The critical feedback strength K_c decreases in comparison to small α, which is correctly described by the analytic formula (4.21). Due to the increased number of existing ECMs for the higher α-factor, it is no longer possible to guarantee the existence of one stable ECM for the full range of C and K for the fast rates (Fig. 4.10(d)) as it was possible for low $\alpha = 0.9$. However, for the fast QD structure the unstable regions are minimized compared to the reference and the slow scattering rates. Note that the existence of stable ECMs does not imply cw operation of the laser (cf. discussion of Fig. 4.9). If there exists a stable periodic, quasiperiodic, or chaotic solution that was created in a Hopf bifurcation of the last ECM in addition to the now stable ECM, it crucially depends on the initial conditions in a numerical simulation, or the implementation of the feedback in an experiment, which solution is favored by the laser. In order to determine those areas in the $\big(C, K\big)$-plane where the laser is guaranteed to be stable, the bifurcation point connecting the periodic solution with the next ECM has to be found. This is a quite challenging task, which will not be addressed here. Hence, it is important to stress that the light-gray shaded areas label areas in the $\big(C, K\big)$-plane where it is possible to prepare the laser in the cw regime.

In the previous discussion, we observed that the band structure of the QD laser has a large impact on its tolerance to optical feedback. So far, we have fixed the pump current at $2.5J_{\mathrm{th}}$ and analyzed the influence of the scattering rates on the ECM bifurcations. Our next step is to change the pump current to a different, fixed value and compare the bifurcation scenarios with Fig. 4.10. Note that our microscopic modeling of the carrier density dependent scattering rates allows us to change the pump current without adjusting any time scale parameter. Figure 4.11 shows the bifurcation diagrams for $\alpha = 0.9$ and for fast, reference, and slow scattering rates at a pump current of $J = 5J_{\mathrm{th}}$ (upper panel) and $J = 10J_{\mathrm{th}}$ (lower panel). Here, we restrict our numerical analysis to a small α-factor since its value for QD-lasers is expected to be relatively small [NEW99a]. However, it is noted that the general pump current dependent changes that are discussed in the following can be observed for $\alpha = 3$ as well.

Comparing the upper panel of Fig. 4.11 with the upper panel of Fig. 4.10, it may be concluded that the Hopf bifurcation lines are shifted towards higher feedback strength K resulting in more extended regions of stability and bistability, since the saddle-node lines are independent of the scattering rates and, thus, of the pump current (see Eq. (4.16)). Going to even higher currents as shown in the lower panel of Fig. 4.11, it is striking to see that all white regions disappear as the Hopf lines shift above the saddle-node lines for all QD structures. An explanation can again be given by discussing the nonlinear scattering rates.

From Fig. 2.6(b), we know that increasing the pump current leads to a nearly linear increase of the RO damping if the laser is operated high above threshold. This in terms reduces the feedback sensitivity of the laser. Considering the analytical formulas for the RO damping for the reference rates (Eq. (2.30b)) and for the slow rates (Eq. (2.33b)), we see that the linear increase can be attributed on the one hand to an increase of the steady state photon number N_{ph}^{0}, which depends linearly on the pump current (see Eq. (4.6)). On the other hand, the increase of the RO damping is caused by an decrease of the carrier lifetimes. For the reference rates, the electron lifetime τ_e is much larger than the one of the holes τ_h. This means that in Eq. (2.30b) the $1/\tau_e$-contribution to the damping dominates the term proportional to τ_h, i.e, the slower carrier type (electrons), dominates the damping and, thus, the dynamical response of the laser. From Fig. 4.10 and Fig. 4.11, we conclude that it is possible to increase the tolerance of the QD laser to optical feedback by adjusting, both, the pump current and the band structure of the device.

A last interesting remark concerns the shape of the first Hopf bifurcation line in all two-parameter bifurcation diagrams investigated so far. One observes that these lines (light and dark solid lines in Fig. 4.10 and 4.11) appear as a loop in the lower right part of the two-parameter bifurcation diagrams. (The size of this loop drastically increases with the pump current. Compare Fig. 4.11 upper and lower panel.) For $C = \pi$ and low feedback, two distinct Hopf bifurcation points are found in all two-parameter bifurcation diagrams: a supercritical Hopf point for lower feedback strength and a subcritical Hopf point for higher feedback strength. A detailed investigation of the subcritical Hopf point reveals that it coincides with that Hopf bifurcation on the antimode of the subsequent ECM mentioned in the previous subsection. Consequently, the bifurcation bridge that emerges from the supercritical Hopf point disappears in this subcritical Hopf point. If the feedback phase C is now decreased starting with $C = \pi$, the supercritical and subcritical Hopf bifurcation points collide with each other in a generalized Hopf point. This behavior is another indication of the connection between two subsequent ECMs through bifurcation bridges (see Fig. 4.9(c) and (d)) that are created in a supercritical Hopf bifurcation and vanish in a subcritical Hopf bifurcation.

In conclusion, we note that by either tuning the band structure by going from deep QDs (slow rates) to shallow QDs (fast rates), or by increasing the pump level high above threshold, the regions with bistability between ECMs are increased in phase space, because the Hopf bifurcation lines shift to higher feedback strengths. In contrast, the instability regions, where no stable ECMs exists, are decreased. For high pump currents stable cw operation is possible for all three band structures under consideration for the whole range of the feedback strength K and for all values of the feedback phases C.

4.6. Analytical approximation of first Hopf instability

In applications, as for example optical fiber networks, the semiconductor laser may be perturbed by unavoidable optical feedback. It is therefore of major importance, how much feedback the laser can tolerate without being destablized in the so called coherence collapse [TKA86]. This regime of broad linewidth corresponds to the instability regions discussed in this and the previous section. Thus, the stability boundary is marked by the first supercritical Hopf bifurcation of the first ECM. It is therefore from particular interest to find an analytical expression for this stability boundary to reveal its dependence on the laser parameters.

To obtain analytical results, we have to reduce the number of the dynamical equations (4.1). This can be done by noting that the limit $\gamma \to 0$ of the dynamical equations (4.1) is singular, and we thus have to find a coordinate transformation that resolves this singularity. For semiconductor lasers, it has proven to be useful to do this by rescaling time with respect to the RO frequency. This transformation was discussed in detail for the QD laser under optical injection in Section 3.6.1 (see also Appendix B).

The transformed set of rate equations for the phase ϕ of the electric field and the deviations y, u_e, u_h, v_e, and v_h from the steady state values of the dynamical variables of the solitary laser (see Eq. (3.32) for the definitions) read

$$\dot{y} = (u_e + u_h)(1+y) + 2\epsilon k \sqrt{(1+y)(1+y(s-s_c))} \cos\big(C + \phi - \phi(s-s_c)\big), \tag{4.22a}$$

$$\dot{\phi} = \frac{\alpha}{2}(u_e + u_h) - \epsilon k \sqrt{\frac{1+y(s-s_c)}{1+y}} \sin\big(C + \phi - \phi(s-s_c)\big), \tag{4.22b}$$

$$\dot{u}_e = -\frac{y}{2} - b u_e - \epsilon \frac{\omega}{2}(u_e+u_h)(1+y) - \epsilon\omega^{-1}(\rho_e^0 u_h + \rho_h^0 u_e) - \epsilon^4\omega^4 g^{-1} u_e u_h, \tag{4.22c}$$

$$\dot{u}_h = -\frac{y}{2} - a u_h - \epsilon \frac{\omega}{2}(u_e+u_h)(1+y) - \epsilon\omega^{-1}(\rho_h^0 u_e + \rho_e^0 u_h) - \epsilon^4\omega^4 g^{-1} u_e u_h, \tag{4.22d}$$

$$\dot{v}_e = b u_e - c\epsilon^{-1}\epsilon(W_e^0 v_e + v_h W_h^0) + \epsilon^3 c g^{-1} v_e v_h, \tag{4.22e}$$

$$\dot{v}_h = a u_h - \epsilon c \omega^{-1}(W_h^0 v_h + v_e W_e^0) + \epsilon^3 c g^{-1} v_e v_h, \tag{4.22f}$$

where the dot denotes the differentiation with respect to the dimensionless time $s \equiv \epsilon\omega t'$ and

$$\omega \equiv \sqrt{2\gamma r_w N_{\mathrm{ph}}^0} \tag{4.23}$$

is proportional to the RO frequency of the solitary laser. (Equation (4.23) is identical to the RO frequency of the QW laser ω^{QW} given by Eq. (2.23b).) Further, the small parameter ϵ, the new feedback amplitude $k = \mathcal{O}(1)$, and the delay s_c are defined as

$$\epsilon \equiv \sqrt{\gamma}, \quad k \equiv \frac{\tilde{k}}{\epsilon^2\omega}, \text{ and } s_c \equiv \epsilon\omega\tau. \tag{4.24}$$

The scattering rates are expressed by the parameters a and b, which have been defined in Eq. (3.36). Here, we have assumed that $K = \mathcal{O}(\gamma)$. This is motivated by the observation that the first Hopf instability is caused by an undamping of the RO oscillations. Therefore, K has to be of the same order of magnitude than the damping, which is of order γ, as we know from our analytical studies in Chapter 3 (cf. Eqs. (2.29b) and (2.31b)). The scaling $K = \mathcal{O}(\gamma)$ corresponds to the limit of "weak injection" of the injection problem (see Table 3.2). As it was already discussed for the injection problem in Section 3.6.1, the parameters a and b depend on deviation from the steady states W_e^0 and W_h^0 of the reservoir populations $v_{e/b}$ only upon $\mathcal{O}(\epsilon^2)$, which is the reason why in lowest order the dynamical equations for $v_{e/b}$ (Eqs. (4.22e) and (4.22f)) decouple and we only have to deal with Eqs. (4.22a)–(4.22f). In the following, it will be demonstrated that valuable information can be extracted from these equations on the basis of simple scaling assumptions.

4.6.1. External cavity modes

The basic solutions of Eqs. (4.22a)–(4.22d) are ECMs. Analogous to the discussion in Section 4.3, they are defined as solutions with constant deviations from the steady state values of photon number and carrier occupation probabilities, i.e., $y = y_s$, $u_e = u_{e,s}$, $u_h = u_{h,s}$, and a phase that changes linearly in time

$$\phi = \phi_s \equiv \Delta\omega_s s \tag{4.25}$$

with the frequency deviation of the ECM $\Delta\omega_s \equiv \epsilon\omega\delta\omega^{\mathrm{s}}$ from the threshold frequency of the solitary laser. To simplify notation, the index s is omitted in the following. Inserting the ECM ansatz into the dynamical equations (4.22a)- (4.22d), the following set of steady state equations is obtained for $y \neq 0$, i.e., for the non-zero intensity (lasing) steady state, which is valid up to $\mathcal{O}(\epsilon)$

$$0 = u_+ + \epsilon k \cos(\Delta), \tag{4.26a}$$

$$\Delta = C + \alpha u_+ - \epsilon k \sin(\Delta), \tag{4.26b}$$

$$0 = -\frac{y}{2} - b u_e - \epsilon\frac{\omega}{2}(u_e + u_h)(1+y) - \epsilon\omega^{-1}(\rho_e^0 u_h + \rho_h^0 u_e), \tag{4.26c}$$

$$0 = -\frac{y}{2} - a u_h - \epsilon\frac{\omega}{2}(u_e + u_h)(1+y) - \epsilon\omega^{-1}(\rho_e^0 u_h + \rho_h^0 u_e), \tag{4.26d}$$

where we have introduced $u_+ \equiv (u_e + u_h)/2$ and $\Delta \equiv C + \Delta\omega s_c$. From Eqs. (4.26a) and (4.26b), we find that Δ satisfies the following transcendental equation

$$\Delta = C - \epsilon k s_c \left(\alpha\cos(\Delta) + \sin(\Delta)\right), \tag{4.27}$$

which implies that $\Delta \approx C$ as $k \to 0$, i.e., Δ is independent of the feedback strength k in first approximation. From Eq. (4.26a), we also note that u_+ and thus both u_e and u_h are at least $\mathcal{O}(\epsilon)$ small.

4.6.2. Stability

In this section, a linear stability analysis of the dynamical equations (4.22a) - (4.22d) is performed. Therefore, one has to consider the eigenvalues of the linear variational equation [KAN05]

$$M \equiv \lambda - A_1\big|_{\mathrm{ECM}} - A_2\big|_{\mathrm{ECM}} e^{-s_c\lambda} \qquad \text{with}$$

$$A_1\big|_{\mathrm{ECM}} \equiv \frac{\partial G_i}{\partial x_j}\bigg|_{\mathrm{ECM}} \qquad \text{and} \qquad A_2\big|_{\mathrm{ECM}} \equiv \frac{\partial G_i}{\partial x_{j,s_c}}\bigg|_{\mathrm{ECM}} \qquad i,j \in \{1,\dots,4\},$$

where the functions G_i are the right hand sides of Eqs. (4.22a)–(4.22d). Thus, A_1 is just the Jacobien of the system without feedback. The matrix A_2 takes into account that we have to consider the delayed variables $x_{j,s_c} \equiv x_j(s - s_c)$ as independent from the variables x_j, where the state vector $\boldsymbol{x}$ is given by $\boldsymbol{x} \equiv (y, \phi, u_e, u_h)^{\perp}$. The notation $|_{\mathrm{ECM}}$ means that the matrices are evaluated along the circular periodic orbits of the

ECMs, i.e., that Eqs. (4.26a)–(4.26d) are valid. The characteristic equation $\det M = 0$ determines the following condition for the growth rate λ

$$\det \begin{vmatrix} \begin{bmatrix} -\epsilon k\cos(\Delta)F \\ -\lambda \end{bmatrix} & \begin{bmatrix} -2\epsilon k(1+y) \\ \times\sin(\Delta)F \end{bmatrix} & 1+y & 1+y \\ \epsilon k\frac{\sin(\Delta)}{2(1+y)}F & \begin{bmatrix} -\epsilon k\cos(\Delta)F \\ -\lambda \end{bmatrix} & \frac{\alpha}{2} & \frac{\alpha}{2} \\ \begin{bmatrix} -1/2 \\ -\epsilon\omega u_+ \end{bmatrix} & 0 & \begin{bmatrix} -b \\ -\epsilon\begin{bmatrix} \omega^{-1}\rho_h^0 \\ +\frac{\omega}{2}(1+y) \end{bmatrix} \\ -\lambda \end{bmatrix} & -\epsilon\begin{bmatrix} \omega^{-1}\rho_e^0 \\ +\frac{\omega}{2}(1+y)) \end{bmatrix} \\ \begin{bmatrix} -1/2 \\ -\epsilon\omega u_+ \end{bmatrix} & 0 & -\epsilon\begin{bmatrix} \omega^{-1}\rho_h^0 \\ +\frac{\omega}{2}(1+y) \end{bmatrix} & \begin{bmatrix} -a \\ -\epsilon\begin{bmatrix} \omega^{-1}\rho_e^0 \\ +\frac{\omega}{2}(1+y) \end{bmatrix} \\ -\lambda \end{bmatrix} \end{vmatrix} = 0, \tag{4.28}$$

where

$$F \equiv 1 - e^{-\lambda s_c}. \tag{4.29}$$

Expanding the determinant, we obtain

$$\begin{aligned} &\lambda^4 + \lambda^3\left[a + b + \epsilon\big(1 + g^{-1} + \omega(1+y) + 2k\cos(\Delta)F\big)\right] \\ &+ \lambda^2\begin{bmatrix} 1 + y + ab + \epsilon\left[\omega^{-1}(a\rho_h^0 + b\rho_e^0) + \omega(1+y)\left(2u_+ + \frac{(a+b)}{2}\right) + 2k\cos(\Delta)F\,(a+b)\right] \\ +\epsilon^2\left[2k\cos(\Delta)F\,(\omega^{-1}(1+g^{-1}) + (1+y)\omega) + F^2k^2\right] \end{bmatrix} \\ &+ \lambda\begin{bmatrix} (1+y)\frac{(a+b)}{2} \\ +\epsilon\left[\omega u_+(1+y)(a+b) + kF\left[(1+y)\left(\cos(\Delta) - \alpha\sin(\Delta)\right) - 2ab\cos(\Delta)\right]\right] \\ +\epsilon^2 kF\begin{bmatrix} (2\omega^{-1} + kF\cos(\Delta))\cos(\Delta)(a+b) \\ +(1+y)\left[\omega\cos(\Delta)(a+b) + 2u_+\omega\big(\cos(\Delta) - \alpha\sin(\Delta)\big)\right] \\ +kF\sin^2(\Delta)(a+b) \end{bmatrix} \\ +\epsilon^3\left[k^2F^2\left(\omega^{-1}(1+g^{-1}) + \omega(1+y)\right)\right] \end{bmatrix} \\ &+ \epsilon\left[kF\frac{(a+b)}{2}(1+y)\big(\cos(\Delta) - \alpha\sin(\Delta)\big)\right] \\ &+ \epsilon^2 kF\left[kFab + (a+b)(1+y)u_+\omega\big(\cos(\Delta) - \alpha\sin(\Delta)\big)\right] \\ &+ \epsilon^3k^2F^2\left[\omega^{-1}(a\rho_h^0 + b\rho_e^0) + \omega(1+y)\frac{(a+b)}{2}\right] = 0, \end{aligned} \tag{4.30}$$

where we haven taken advantage of the gain-clamping of the solitary laser above threshold $\rho_{\text{inv}}^0 = 0$ (cp. Eq. (4.4a)), which may be rewritten as $\rho_e^0 + \rho_h^0 = 1 + g^{-1}$.

4.6.3. General rates: $a = \mathcal{O}(1)$ and $b = \mathcal{O}(1)$

In this subsection, it is assumes that a and b are $\mathcal{O}(1)$. From the steady state equations (4.26c) and (4.26d), we see that y then is $\mathcal{O}(\epsilon)$ small. Remembering the scalings for u_e, u_h, and Δ that were discussed in Subsection 4.6.1, we obtain the following scaling laws for the dynamical variables

$$y = \epsilon Y + \mathcal{O}(\epsilon^2), \text{ and } u_{e/h} = \epsilon U_{e/h} + \mathcal{O}(\epsilon^2), \tag{4.31}$$

where Y and $U_{e/h}$ are $\mathcal{O}(1)$. Further, the scaling laws for u_e and u_h imply that u_+ scales like $u_+ = \epsilon U_+ + \mathcal{O}(\epsilon^2)$. The ansatz

$$\lambda = \lambda_0 + \epsilon\lambda_1 + \dots \tag{4.32}$$

for the scaling of the growth rate λ permits to balance enough terms in the second lowest order problem to obtain complex growth rates. Inserting Eq. (4.32) and (4.31) into the characteristic equation (4.30), yields the following two problems for λ_0 and λ_1

$$\mathcal{O}(1): \quad \lambda_0 \left[\lambda_0^3 + \lambda_0^2(a+b) + \lambda_0(1+ab) + \frac{(a+b)}{2}\right] = 0, \tag{4.33a}$$

$$\begin{aligned}\mathcal{O}(\epsilon): \quad & \lambda_1 \left[\frac{(a+b)}{2} + 2(1+ab)\lambda_0 + 3(a+b)\lambda_0^2 + 4\lambda_0^3\right] \\ & + \lambda_0^3 \left[\omega^{-1}(1+g^{-1}) + 2F_0 k\cos(\Delta) + \omega\right] \\ & + \lambda_0^2 \left[\frac{\omega}{2}(a+b) + \omega^{-1}(b\rho_e^0 + a\rho_h^0) + 2k\cos(\Delta)F_0(a+b) + Y\right] \\ & + \lambda_0 \left[\frac{(a+b)}{2}Y + kF_0\left(\big[\cos(\Delta) - \alpha\sin(\Delta)\big] + 2ab\cos(\Delta)\right)\right] \\ & + \frac{kF_0(a+b)}{2}\left[\cos(\Delta) - \alpha\sin(\Delta)\right] = 0,\end{aligned} \tag{4.33b}$$

where we have introduced

$$F_0 \equiv 1 - e^{-\lambda_0 s_c}. \tag{4.34}$$

The problems (4.33) are a bit too "bulky" to be solved analytically, but simplified problems can be derived for the reference as well as for the slow rates and will be discussed in the following subsections.

4.6.4. Reference rates: limit $a = \mathcal{O}(\epsilon^{-1})$ and $b = \mathcal{O}(\epsilon^1)$

For the reference rates, the following scalings are assumed for a and b

$$a = \epsilon^{-1}a_{-1} \quad \text{and} \quad b = \epsilon b_1, \tag{4.35}$$

where a_{-1} and b_1 are $\mathcal{O}(1)$. From the electron equation (4.26c), we find that y now is $\mathcal{O}(\epsilon^2)$ small, and the hole equation indicates that u_h then is $\mathcal{O}(\epsilon^3)$ small. Summing up, we obtain the scaling laws

$$y = \epsilon^2 Y_2 + \mathcal{O}(\epsilon^3), \quad u_e = \epsilon U_e + \mathcal{O}(\epsilon^2), \text{ and } u_h = \epsilon^3 U_{h,3} + \mathcal{O}(\epsilon^4), \tag{4.36}$$

where Y_2, U_e, and $U_{h,3}$ are $\mathcal{O}(1)$. With the help of the scaling laws (4.35) and (4.36), the two lowest order problems (4.33) simplify as follows

$$\mathcal{O}(\epsilon^{-1}): \quad \lambda_0 \left[\lambda_0^2 + \frac{1}{2}\right] = 0, \tag{4.37a}$$

$$\begin{aligned}\mathcal{O}(1): \quad & \lambda_1 \left[\frac{1}{2} + 3\lambda_0^2\right] a_{-1} + \lambda_0^4 \\ & + \lambda_0^2 \left[1 + a_{-1}\left(b_1 + \frac{\omega}{2} + \omega^{-1}\rho_h^0 + 2k\cos(\Delta)F_0\right)\right] \\ & + \frac{a_{-1}kF_0}{2}\left[\cos(\Delta) - \alpha\sin(\Delta)\right] = 0.\end{aligned} \tag{4.37b}$$

The lowest order problem (4.37a) admits three solutions

$$\lambda_0^r = 0 \qquad \wedge \qquad (\lambda_0^c)^2 = -\frac{1}{2}, \tag{4.38}$$

one of them is real (λ_0^r) and two are purely imaginary (λ_0^c). The first order contribution λ_1^r of the real eigenvalue is obtained by inserting λ_0^r into Eq. (4.37b), which yields $\lambda_1^r = 0$. Further, the first order contribution of the complex conjugate eigenvalues is obtained by inserting $(\lambda_0^c)^2 = -1/2$ into Eq. (4.37b)

$$\lambda_1^c = -\Gamma_1^{\mathrm{ref}} - \frac{kF_0}{2}\left[\cos(\Delta) + \alpha\sin(\Delta)\right]. \tag{4.39}$$

The eigenvalue λ_1^c has two contributions: one is the damping of the solitary laser Γ_1^{ref} (see Eq. (3.132)), which may be compensated by the second term on the right hand side of Eq. (4.39) describing the impact of the feedback.

Summing up, by taking into account contributions up to the first order in ϵ the real eigenvalue λ^r and the pair of complex conjugate eigenvalues λ^c are given by

$$\lambda^r \equiv \lambda_0^r + \epsilon\lambda_1^r = 0, \tag{4.40a}$$

$$\lambda^c \equiv \lambda_0^c + \epsilon\lambda_1^c = \pm i\omega_s^{\mathrm{ref}} - \epsilon\left(\Gamma_1^{\mathrm{ref}} + \frac{kF_0}{2}\left[\cos(\Delta) + \alpha\sin(\Delta)\right]\right), \tag{4.40b}$$

where we have introduced the RO frequency of the solitary laser $\omega_s^{\mathrm{ref}} \equiv 1/\sqrt{2}$.

4.6.5. Slow rates: limit $a = \mathcal{O}(\epsilon)$ and $b = \mathcal{O}(\epsilon)$

For the slow rates, we assume the scalings

$$a = \epsilon a_1 \quad \text{and} \quad b = \epsilon b_1, \tag{4.41}$$

where a_1 and b_1 are $\mathcal{O}(1)$. From the steady states of the carrier equations, we find that y is $\mathcal{O}(\epsilon^2)$ small, and Δ, u_e, and u_h scale as discussed in Subsection 4.6.2. To sum up, the following scaling laws are obtained for the dynamical variables

$$y = \epsilon^2 Y_2 + \mathcal{O}(\epsilon^3), \text{ and } u_{e/h} = \epsilon U_{e/h} + \mathcal{O}(\epsilon^2), \tag{4.42}$$

where Y_2 and $U_{e/h}$ are $\mathcal{O}(1)$. Inserting the scaling laws for the rates a and b and for the dynamical variables into the first two lowest order problems (4.33), they simplify as

$$\mathcal{O}(1): \quad \lambda_0^2\left[1 + \lambda_0^2\right] = 0, \tag{4.43a}$$

$$\mathcal{O}(\epsilon): \quad \lambda_0 \left[\begin{array}{c} 2(2\lambda_0^2 + 1)\lambda_1 \\ +\lambda_0^2\left[a_1 + b_1 + \omega^{-1}(\rho_e^0 + \rho_h^0) + \omega - 2kF_0\cos(\Delta)\right] \\ +\frac{(a_1+b_1)}{2} + kF_0\big(\cos(\Delta) - \alpha\sin(\Delta)\big) \end{array}\right] = 0. \tag{4.43b}$$

The leading order problem (4.43a) admits a double real root (λ_0^r) and two complex conjugate (λ_0^c) roots

$$(\lambda_0^r)^2 = 0 \quad \text{and} \quad (\lambda_0^c) = \pm i. \tag{4.44}$$

Thus, in leading order the equation are conservative as in the case of the reference rates. The first order contribution of the real eigenvalues evaluates to zero $\lambda_1^r = 0$, while the first order contribution of the complex conjugate eigenvalues yields the same formula as for the reference rates (see Eq. (4.39)) with Γ_1^{ref} replaced by Γ_1^{S} given by Eq. (3.141). Summing up, we obtain the following expressions for the eigenvalues

$$\lambda^r \equiv \lambda_0^r + \epsilon\lambda_1^r = 0, \tag{4.45a}$$

$$\lambda^c \equiv \lambda_0^c + \epsilon\lambda_1^c = \pm i\omega_s^{\mathrm{S}} - \epsilon\left(\Gamma_1^{\mathrm{S}} + \frac{kF_0}{2}\left[\cos(\Delta) + \alpha\sin(\Delta)\right]\right), \tag{4.45b}$$

where we have introduced the RO frequency of the solitary laser $\omega_s^{\mathrm{S}} \equiv 1$.

4.6.6. Feedback strength of first Hopf instability

In this subsection, an analytical expression is derived for the feedback strength, at which the first Hopf bifurcation occurs. This is then compared to expression used throughout the literature before comparing it with numerical results from the path continuation. Therefore, we firstly reformulate the expressions for the complex conjugate pair of eigenvalues (Eqs. (4.40b) and (4.45b)) by rewriting them in terms of time t'. The complex conjugate eigenvalues $\sigma^c \equiv \sqrt{\gamma}\omega\lambda^c$ then read[2]

$$\sigma^c = \pm i\omega^{\mathrm{RO}} - \left(\Gamma^{\mathrm{RO}} + \frac{\tilde{k}F_0}{2}\left[\cos(\Delta) + \alpha\sin(\Delta)\right]\right) \tag{4.47a}$$

$$\begin{aligned} &= -\left(\Gamma^{\mathrm{RO}} + \frac{\tilde{k}}{2}\big(1-\cos(\omega^{\mathrm{RO}}\tau)\big)\sqrt{1+\alpha^2}\cos\big(\Delta - \arctan(\alpha)\big)\right) \\ &\quad \pm i\left(\omega^{\mathrm{RO}} - \sin(\omega^{\mathrm{RO}}\tau)\frac{\tilde{k}}{2}\big(1-\cos(\omega^{\mathrm{RO}}\tau)\big)\sqrt{1+\alpha^2}\cos\big(\Delta - \arctan(\alpha)\big)\right). \end{aligned} \tag{4.47b}$$

Frequency ω^{RO} and damping Γ^{RO} of the ROs are given by Eqs. (2.29) for the reference rates and by Eqs. (2.31) for the slow rates (cf. Table 2.4), and Δ reads in these coordinates $\Delta = C + \delta\omega^{\mathrm{s}}\tau$.

A Hopf bifurcation occurs when the pair of complex conjugate eigenvalues crosses the imaginary axis, i.e., when the real parts of these eigenvalues vanish $\mathrm{Re}(\sigma^c) = 0$. Imposing this condition on Eq. (4.47b), we obtain the following expressions for the

---

[2] Additionally to the trigonometric relation in Eqs. (3.20),

$$\cos(x)\cos(y) = \frac{1}{2}\left[\cos(x-y) + \cos(x+y)\right], \quad \sin(x)\sin(y) = \frac{1}{2}\left[\sin(x-y) + \sin(x+y)\right], \tag{4.46a}$$

$$\sin^2(x) = \frac{1}{2}\left[1 - \cos(2x)\right]. \tag{4.46b}$$

are used to derive Eq. (4.47b)

feedback strength $\tilde{k}_H$, at which the Hopf instability occurs and for the frequency ω_H of the limit-cycle close to the Hopf point

$$\tilde{k}_H \equiv \frac{-2\Gamma^{\mathrm{RO}}}{\left(1-\cos(\omega^{\mathrm{RO}}\tau)\right)\sqrt{1+\alpha^2}\cos\left(C+\delta\omega^{\mathrm{s}}\tau-\arctan(\alpha)\right)}, \tag{4.48a}$$

$$\omega_H \equiv \omega^{\mathrm{RO}} + \Gamma^{\mathrm{RO}}\sin(\omega^{\mathrm{RO}}\tau) = \omega^{\mathrm{RO}} + \mathcal{O}(\gamma). \tag{4.48b}$$

The expression (4.48a) is the same as for the well-known LK-model describing a single mode QW laser subject to external feedback and has been first derived by Ritter and Haug in [RIT93]. In [LEV95], the role of the factor $\cos(\Delta - \arctan(\alpha))$, which describes the impact of the different ECMs, has been discussed. Approximations of the Hopf line that are better suited to describe short external cavities and larger feedback rates have been discussed by Erneux and by Wolfrum and Tuarev in [ERN95, ERN00a] and [WOL02], respectively. Keeping in mind that Γ^{RO} is $\mathcal{O}(\gamma)$ small, we see from Eq. (4.48b) that the frequency of the Hopf instability is close to the RO frequency, i.e., this Hopf bifurcation undamps the ROs.

4.6.7. Critical feedback strength

Stabilizing the feedback phase C in experiments is a difficult task, because the setup has to be mounted on a heat sink to minimize temperature fluctuations [HEI01a]. Further, if we want to study different ECMs, C has to be tuned, which implies that the position of the mirror has to be varied on the sub-wavelength scale. For short delay, only view ECMs exist. The dynamics is therefore simpler than for long delay and it is easier to realize stable cw lasing on one ECM by tuning the feedback phase C, because larger fluctuations, i.e., phase noise, are needed to hop from one mode to the neighboring mode on the ellipse of ECMs (cf. Fig. 4.2). It has been demonstrated by Heil et al. that it is experimentally possible to control the feedback phase in the short feedback regime [HEI01, HEI03a]. Further, in integrated multi-section devices consisting of an actively pumped, inverted section and a passive section, the phase can be controlled by applying a current to the passive section [RAD07]. However, for long feedback and for applications, e.g., optical fiber networks, the phase cannot be controlled, thus the stability boundary is given by the least stable ECM. From Eq. (4.48a), we find that this is the ECM with $\Delta_{\mathrm{min}} \equiv (\pi + \arctan(\alpha)) \mod 2\pi$[3]. Assuming the "worst case" $\omega^{\mathrm{RO}}\tau = \pi \mod 2\pi$, we obtain the following critical feedback strength, below which the laser is guaranteed to be stable

$$\tilde{k}_H \leq \tilde{k}_c \equiv \frac{\Gamma^{\mathrm{RO}}}{\sqrt{1+\alpha^2}}. \tag{4.49}$$

This is the expression (4.21) that was already employed in Section 4.5 to discuss the impact of band structure and pump current on the stability boundary of the laser subject to optical feedback.

In Fig. 4.12, $\tilde{k}_H$ obtained by numerical path continuation (solid black lines) is depicted as a function of α for a long external cavity with $\tau = 80$ (Fig. 4.12(a)) and for a short external cavity with $\tau = 16$ (Fig. 4.12(b)), respectively. The feedback phase has been

---

[3] Here we used Eq. (4.27) revealing that $\Delta \approx C$ holds for $\epsilon \to 0$.

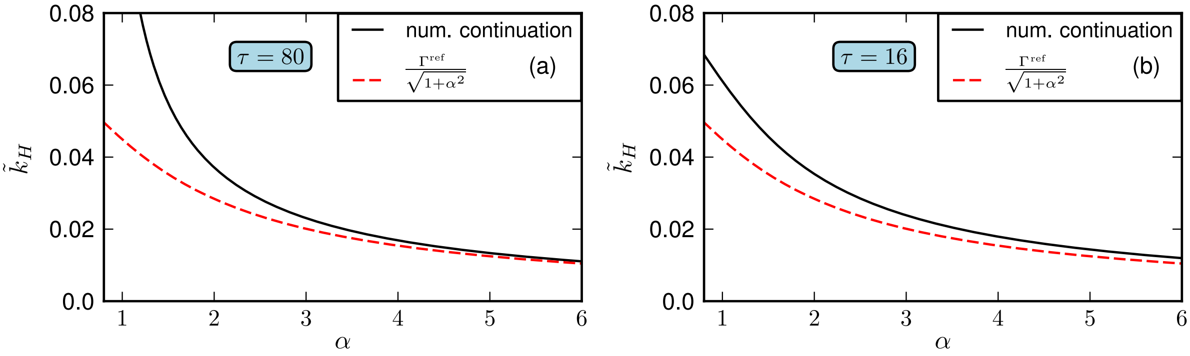

Figure 4.12.: First Hopf bifurcation for the feedback phase $C_{\min} \equiv \pi + \arctan(\alpha) \mod 2\pi$ $(n \in \mathbb{Z})$ in dependence of the linewidth enhancement factor α in the long cavity regime for $\tau = 80$ **(a)** and in the short cavity regime for $\tau = 16$ **(b)**. The black solid lines are obtained by numerical path continuation, and the red dashed lines are analytical approximations. Parameters: Reference rates and other parameters as in Table 2.3. Modified from [OTT12].

fixed to $C_{\min} \equiv \pi + \arctan(\alpha) \mod 2\pi$, which minimizes $\tilde{k}_H$ with respect to $\Delta_{\min}$ within the validity of the approximation $\Delta = C + \mathcal{O}(\epsilon)$ (cf. Eq. (4.27)). The numerical results are compared to the critical feedback strength $\tilde{k}_c$ given by Eq. (4.49) (red dashed lines).

For a long cavity, we find very good correspondence for $\alpha \gtrsim 3$ as depicted in Fig. 4.12(a). For smaller values of the α-factor, the feedback strength $\tilde{k}_H$ becomes so large that the assumption $\tilde{k}_H = \mathcal{O}(\gamma)$, for which Eq. (4.49) is valid, does not hold any longer. That is the reason why the analytic approximation underestimates $\tilde{k}_H$ for small values of α. The same reasoning holds for the short cavity regime $\tau = 16$ (Fig. 4.12 (b)), although the deviations of the analytical and the numerical value for $\tilde{k}_H$ are less pronounced for $\alpha \lesssim 3$, because the feedback strength remains smaller. However, in both cases and for all α-factors in the studied range ($\alpha \in [0.8, 6]$), the analytical formula provides a reliable approximation for the lower bound of $\tilde{k}_H$, i.e., for the critical feedback strength $\tilde{k}_c$, below which our analysis predicts stable cw operation.

The stability condition of Eq. (4.49) was derived for the LK model by Mork et al. in [MOR92]. As noted by the authors, Eq. (4.49) was previously suggested by Helms and Petermann [HEL90b] as a simple analytical criterion for tolerance with respect to optical feedback. Helms and Petermann [HEL90b] evaluated the validity of Eq. (4.49) by analyzing numerically the stability of the minimum linewidth mode. They noted that this approximation gives a good description of the critical feedback level as long as the linewidth enhancement factor α is significantly larger than unity. They then proposed an empirical law given by

$$\tilde{k}_c^{\mathrm{emp}} \equiv \Gamma^{\mathrm{RO}} \frac{\sqrt{1+\alpha^2}}{\alpha^2}. \tag{4.50}$$

The minimum linewidth mode is the most stable ECM in a "thermodynamic" potential model based on neglecting power fluctuations [LEN91, TAR95a], i.e., the minimum linewidth mode is the mode with the deepest potential well. It was supposed to be the most stable ECM for quite some time [SCH88l], despite it was shown that the minimum linewidth mode could be destabilized already at moderate values of the feedback strength [RIT93]. The minimum linewidth mode is determined by the condition $\Delta_{\mathrm{mlm}} \equiv -\arctan(\alpha) \mod 2\pi$ [LEV95] and thus differs from the maximum gain mode $\Delta_{\mathrm{mgm}} = 0 \mod 2\pi$ (cf. Eq. (4.14)) for non-zero α-factors. Inserting Δ_{mlm} into Eq. (4.48a) and assuming the "worst case" $\omega^{\mathrm{RO}}\tau = \pi \mod 2\pi$, we find that the critical feedback strength for the minimum linewidth mode is given by

$$\tilde{k}_c^{\mathrm{mlm}} \equiv \Gamma^{\mathrm{RO}} \frac{\sqrt{1+\alpha^2}}{\alpha^2 - 1}. \tag{4.51}$$

The denominator in Eq. (4.51) is different from the denominator of Eq. (4.50), which explains the numerically observed singularity as $\alpha \to 1^+$ [HEL90b]. Both, Eqs. (4.49) and (4.50) are used in current experimental studies of QD lasers subject to optical feedback. Specifically, Eq. (4.51) is used in Refs. [GIO08, GRI13] and Eq. (4.50) is used in Refs. [OBR03a, GRI08, AZO09, GRI13].

As mentioned in Section 4.4, the α-factor is a problematic quantity for QD lasers due to their more complicated carrier dynamics, but more sophisticated modeling approaches that take into account the polarization and thus avoid the assumptions of a constant α-factor [LIN12a, LIN12b] reveal that the dynamics of QD lasers is even more stable than described by models with constant α [LIN13]. In the framework of the present simplified modeling approach, this would express in small α-factors close to unity. Therefore, using Eq. (4.50) instead of Eq. (4.51) may lead to wrong results, especially for QD lasers.

It is instructive to study the critical feedback phase for the maximum gain mode yielding together with the "worst case" assumption $\omega^{\mathrm{RO}}\tau = \pi \mod 2\pi$

$$\tilde{k}_c^{\mathrm{mlm}} \equiv -\Gamma^{\mathrm{RO}} < 0, \tag{4.52}$$

which indicates that the maximum gain mode cannot be destabilized in a Hopf bifurcation. Indeed, modes with $-\arctan(1/\alpha) < \Delta \leq \Delta_{\mathrm{mgm}} = 0$ cannot be destabilized by increasing feedback [LEV95], but they may be inaccessible to the system due to the presence of a chaotic attractor. The laser then exhibits chaotic behavior in the form of low frequency fluctuations [TAR95b] instead of stable cw operation on a single ECM.

4.6.8. Hopf bifurcation line in the (C,K)-plane

Next, the analytical approximation for $\tilde{k}_H$ given in Eq. (4.48a) is compared with results from path continuation in a projection onto the plane spanned by feedback phase C and injection strength K. Therefore, Eq. (4.48) is solved for $\Delta = C + \delta\omega^{\mathrm{s}}\tau$, which yields

$$\Delta = \arctan(\alpha) \pm \arccos\left(-\frac{\mathcal{G}}{\tilde{k}_{\mathrm{eff}}^{H}}\right) + 2n\pi, \tag{4.53}$$

where we have introduced

$$\mathcal{G} \equiv \frac{2\Gamma^{\mathrm{RO}}\tau}{1-\cos\left(\omega^{\mathrm{RO}}\tau\right)}, \quad \text{and} \quad \tilde{k}_{\mathrm{eff}}^{H} \equiv \tilde{k}_H \tau\sqrt{1+\alpha^2}, \tag{4.54}$$

and $n \in \mathbb{Z}$. Taking advantage that $\Delta = C + \mathcal{O}(\epsilon)$ equals in leading order the external cavity phase C (cf. Eq. (4.27)), the lowest order approximations for the Hopf lines in the (C,K)-plane read

$$C_n^{H,\mathrm{approx}}(k) \equiv \arctan(\alpha) \pm \arccos\left(\frac{-G}{\tilde{k}_{\mathrm{eff}}^{H}}\right) + 2n\pi.$$

Further, an expression for the Hopf lines, which takes into account $\mathcal{O}(\epsilon)$-corrections to Eq. (4.53) can be derived [LEV95]

$$C_n^H(k) = \arctan(\alpha) \pm \arccos\left(\frac{-\mathcal{G}}{\tilde{k}_{\mathrm{eff}}^H}\right) - \frac{2\alpha\mathcal{G}}{1+\alpha^2} \pm \frac{1-\alpha^2}{1+\alpha^2}\sqrt{(\tilde{k}_{\mathrm{eff}}^H)^2 - \mathcal{G}^2} + 2n\pi. \quad (4.55)$$

The details of the derivation are given in Appendix C.

In Figure 4.13(a) and (b), the analytic approximation of the Hopf bifurcation lines given by Eq. (4.55) (dashed lines) is compared to numerical results obtained by path continuation techniques (solid lines) for the reference rates and the slow rates, respectively. Since the preceding discussion showed a better significance of the analytic results for larger α and small τ, a large α-factor of $\alpha = 3$ and a short delay time of $\tau = 16$ were chosen. For the numerical results, we distinguish between supercritical Hopf bifurcations of stable ECMs (modes) depicted by solid black lines and subcritical Hopf bifurcations of unstable ECMs (anti-modes) depicted by solid light lines. For clarity, the bifurcation lines are plotted in the truncated interval $K = 2\kappa\tau_{\mathrm{in}}\tilde{k} \in [0, 0.25]$. In the small feedback regime $K \lesssim 0.2$, we find good agreement between the two bifurcation lines. For C in the vicinity of $\pm\pi$, the shape as well as the position of the analytically obtained bifurcation line compares well with the numerically calculated one. The agreement of the two curves becomes worse for C close to zero, because the critical feedback strength moves to higher values of K. However, even in this regime, the analytical solution reproduces the shape of supercritical, numerical solution but underestimates the feedback strength of the Hopf bifurcation. Thus, it may be used for a conservative estimate of the feedback strength, below which stable cw operation can be guaranteed. The good agreement of

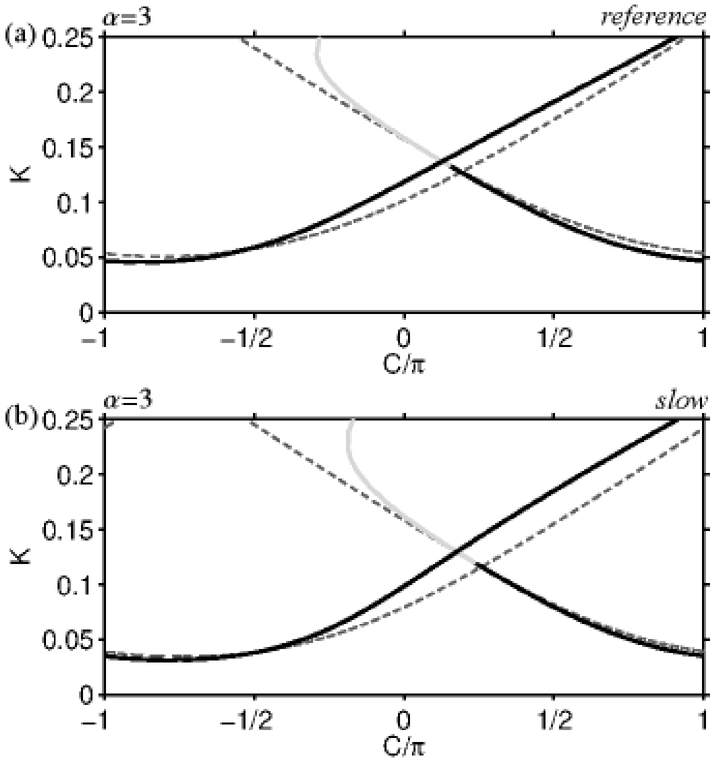

Figure 4.13: Comparison of the analytic approximation for the first Hopf bifurcation line (dashed) with Hopf lines calculated by numerical path continuation (solid) in a plane spanned by the feedback phase C and the feedback strength K for the reference set of scattering rates **(a)** and the slow set of scattering rates **(b)**. Solid black and gray lines denote super- and subcritical Hopf bifurcation lines, respectively. Parameters: $J = 2.5J_{\mathrm{th}}$, $\alpha = 3$, $\tau = 16$, and other parameters as in Table 2.3. From [GLO12].

analytical and numerical Hopf lines reveals that the RO damping and the α-factor are the main parameters that describe the feedback sensitivity of QD lasers.

From Eq. (2.31b), we see that even for the slow rates, which represent the band structure with the lowest damping, the RO damping of a QD laser is higher than for its QW counterpart. (In the next section, it will be discussed how to compare QW and QD lasers.) This gives an explanation for the reduced feedback-sensitivity of QD lasers compared to QW lasers [HUY04]. The formulas for the RO damping (see Eqs. (2.29b) and (2.31b)) reveal that to control the damping and thus the feedback sensitivity one has to control the carrier lifetimes $\tau_{e/h}$ and thus the band structure. This can be done by tuning the material composition and the size of the QDs [BIM99].

4.7. Comparison to bifurcation scenario of quantum well laser

In this section, we compare the dynamic response to optical feedback of a QD laser and a QW laser. For the QD laser, the reference scattering rates (see Table 2.1) are used. Therefore, we have to discuss how to choose the parameters of the QW laser to make it comparable to the QD laser. Best suited for a comparison are the dynamical equations in their dimensionless form given by Eqs. (2.19) and Eqs. (4.1) for QW and QD laser, respectively, because they exhibit a reduced number of free parameters that has to be discussed. A natural choice is to assume the same internal losses κ for both lasers, which fixes the photon lifetime of the QW laser to $\tau_{\text{ph}} = (2\kappa)^{-1}$. Further, we demand that both lasers have the same steady state photon density N_{ph}^{0}. From the dynamical equations (2.19) of the QW laser, it can be seen that we still have to choose the value of the parameter $\gamma^{\text{QW}} = \tau_{\text{ph}}/\tau_c$ describing the time scale separation and the value of the pump rate P. Assuming the same time scale separation for both lasers, i.e., choosing $\gamma^{\text{QW}} = \gamma$, implies $\tau_c = W^{-1}$. Further, from the steady state relations (2.21), we see that choosing the same ratio of the Einstein factors for the induced and the spontaneous emission for both lasers $r^{\text{QW}} = r_w = \bar{W}/W$ permits to determine $P = N_{\text{ph}}^{0}/r^{\text{QW}}$ and the linear gain coefficient as $G_n = 2\bar{W}$.

Figure 4.14 depicts the response of a QW laser (red dashed line) and of a QD laser (blue full line) to a rectangular current pulse (black dash-dotted line) of 6 ns width and a peak-height of $J = 2.5J_{\text{th}}$. For the QW laser, the parameter values discussed above have been used. The QW laser displays pronounced ROs that are weakly damped compared to the ROs of the QD laser. This turn-on behavior is expected from experiments [KUN02] and theoretical works [LUE09, LUE10a], which indicates that this choice of parameters yields realistic results and is therefore well suited for a comparison of both types of lasers.

For the QD laser, the RO damping of the slow set of scattering rates Γ^{S} is smaller than the damping of the reference rates Γ^{ref} (see Fig. 2.6). Equation (2.31b) reveals that the RO damping can be split into two parts $\Gamma^{\text{S}} = \Gamma^{\text{QW}} +$ 'additional terms', where $\Gamma^{\text{QW}} = \sqrt{2\gamma r_w N_{\text{ph}}^{0}}$ is the damping rate of the QW laser for the parameters chosen above, and the additional terms are due to the special carrier scattering dynamics of QD lasers.

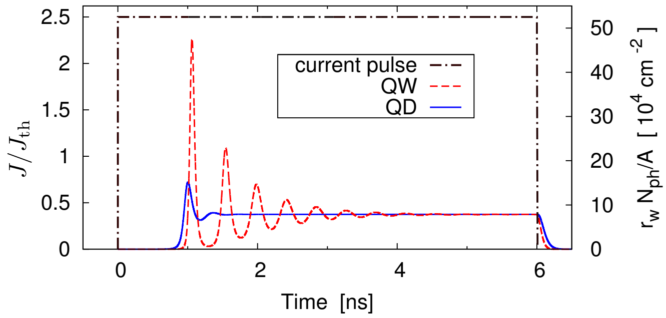

Figure 4.14: Response of photon number $N_{\rm ph}$ to a rectangular current pulse $J(t)$ of 6 ns width and $J = 2.5J_{\rm th}$ (black dash-dotted line) for a QD laser (solid blue line) and a QW laser (red dashed line) without feedback ($K = 0$). Parameters: For QD laser see Table 2.3 and for QW laser $\gamma^{\rm QW} = \gamma$ and $P = N^0_{\rm ph}/r_w$. Modified from [OTT10].

Since $\Gamma^{\rm S} < \Gamma^{\rm ref}$ holds, we see that the analytic expressions for the damping correctly describe the weaker RO damping of the QW laser observed numerically (cf. Fig 4.14) [LUE11].

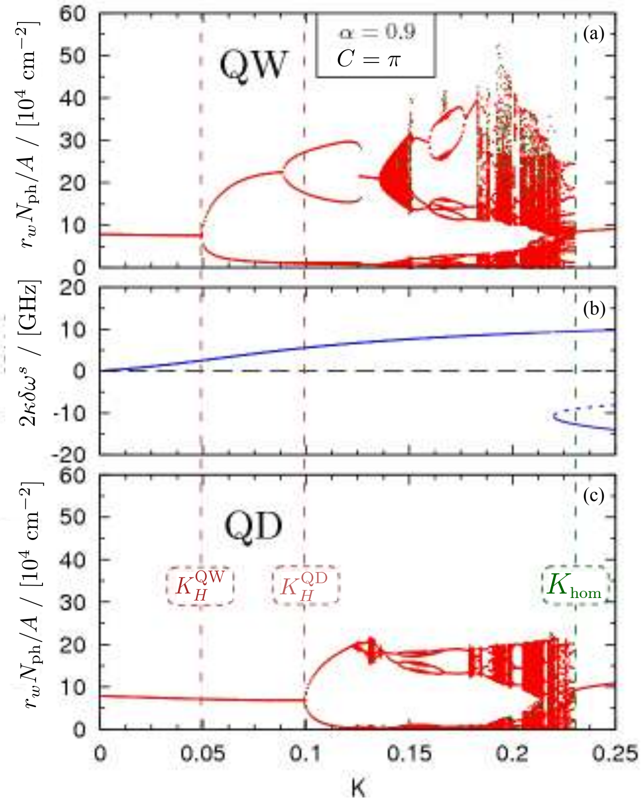

Figure 4.15: Bifurcation diagrams of local maxima of the photon number $N_{\rm ph}$ vs. feedback strength K for a QW laser **(a)** and for as QD laser **(c)** for stepwise increasing K (green dots) and stepwise decreasing K (red dots). The first Hopf instability of QW and QD lasers are marked by $K_H^{\rm QW}$ and $K_H^{\rm QD}$ (vertical brown dashed lines), respectively. The homoclinic bifurcation at the end of the bifurcation cascade is labeled by $K_{\rm hom}$ (green dashed line). **(b)**: Frequency deviations $\delta\omega^{\rm s}$ of the ECMs of the system. Blue solid and dashed lines mark modes and anti-modes, respectively. Parameters: $\alpha = 0.9$, $C = \pi$, and $J = 2.5J_{\rm th}$. For QD the reference rates and the parameters of Table 2.3 were used. For QW laser $\gamma^{\rm QW} = \gamma$ and $P = r_w N^0_{\rm ph}$ were used.

To further compare the dynamics of both lasers, we use bifurcation diagrams depicting local extrema of $N_{\rm ph}$ as a function of K. Figures 4.15(a) and (c) depict bifurcation diagrams for QW and QD lasers, respectively, for a low α-factor of $\alpha = 0.9$ and $C = \pi$. For this choice of parameters, only one bifurcation cascade is found by varying K over its whole range $K \in [0, 1]$ (cf. Fig. 4.9(a)). To catch bistabilities, the feedback strength K has been increased (green dots) and decreased (red dots) stepwise taking for each run the last τ-interval of the previous run as initial condition. The cascade of the QD laser has already been studied in detail in Section 4.4.

Figure 4.15(b) depicts the frequency deviations $\delta\omega^{\rm s}$ of the ECMs as a functions of K. Modes and anti-modes are denoted by solid and dashed lines, respectively. The structure of the solutions is the same for both lasers, because the transcendental equation (4.4b) determining the ECMs is independent of the carrier variables and thus of the band structure. QW and QD laser become unstable in a supercritical Hopf bifurcation at K_H^{QW} and K_H^{QD}, respectively. As predicted by the analytical formula for the critical feedback strength $K_c \equiv 2\kappa\tau_{\mathrm{in}}\tilde{k}_c$ (Eq. (4.49)), below which the laser is guaranteed to be stable, we have $K_H^{\mathrm{QW}} < K_H^{\mathrm{QD}}$, because of the lower RO damping of the QW laser. Increasing K further, both lasers undergo a period-doubling cascade evolving into chaos, which has been studied for the QD laser in detail in [OTT10]. The cascade for the QD laser is more compact (smaller absolute maxima of N_{ph} for fixed K), which corresponds to smaller sizes of the periodic orbits and the chaotic attractor in phase space. This is due to the higher RO damping of the QD laser and its internal carrier dynamics. Further, the K-values of the period doubling bifurcation point, the periodic windows, and the K-values for the onset of chaos are different for both lasers, which could be attributed either to their different linear properties, i.e., to different RO frequency and damping, or to the more complex carrier dynamics of the QD laser. This question will be addressed at the end of the section. Eventually, at the end of the bifurcation cascade, the chaotic attractor collapses onto a stable periodic orbit. Both lasers now emit regular pulse packages as those shown in Figs. 4.6(e) and 4.7(e). For both lasers, this periodic orbit collides with the anti-mode of the 2nd ECM-pair in a homoclinic bifurcation at K_{hom}. This leads to stable cw operation on the 2nd ECM, which is for $K > K_{\mathrm{hom}}$ the sole attractor of the system. Our simulations reveal that K_{hom} is independent of the RO damping, which is the reason why the homoclinic bifurcation takes place for both lasers at the same value of the feedback strength K. Since $K_H^{\mathrm{QW}} < K_H^{\mathrm{QD}}$, the range of K-values, for which no stable ECM exists and thus no stable cw operation is possible, is larger for the QW laser.

In the bifurcation diagrams of Fig. 4.16, the dynamics of QW (Fig. 4.16(a)) and QD (Fig. 4.16(c)) lasers are compared for the same set of parameters used in Fig. 4.15 but for a larger α-factor of $\alpha = 3.2$. The number of ECMs (see Fig. 4.16(b)) increases with the α-factor as discussed in Sec. 4.3 (see Eq. (4.4b)). This is the reason why now four bifurcation cascades are observed. Blowups of the first bifurcation cascades for QW and QD lasers are shown in Figs. 4.16(d) and (f), respectively. The magnification region is marked by a black rectangle in Fig. 4.16(a). For this larger value of α, the lasers return to stable cw emission at the ends of the bifurcation cascades in boundary crises of the chaotic attractors instead of homoclinic bifurcations. (In Figs. 4.16(d)–(f) the bifurcation points of the crises are marked by $K_{\mathrm{cris}}^{\mathrm{QW}}$ and $K_{\mathrm{cris}}^{\mathrm{QD}}$ for the QW and the QD laser, respectively.) This results in larger bistability regions, because for up-sweeping K (green dots) the trajectories remain trapped in the chaotic attractor up to $K = K_{\mathrm{cris}}^{\mathrm{QW}}$ and $K = K_{\mathrm{cris}}^{\mathrm{QD}}$ for QW and QD lasers, respectively, while for down-sweeping K (red dots) the 2nd ECMs of both lasers remain stable upon their annihilation in saddle-node bifurcations at $K = 0.115$, and then the trajectories hop to the remaining attractors. For the QW laser, the remaining attractor is a chaotic attractor, while it is a period-4 orbit for the QD laser. In contrast to the homoclinic bifurcations observed for small $\alpha = 0.9$ that were independent of the RO damping, the K-values of the crises of the chaotic attractors increase with the RO damping. This can be seen in Figs. 4.16(d) and

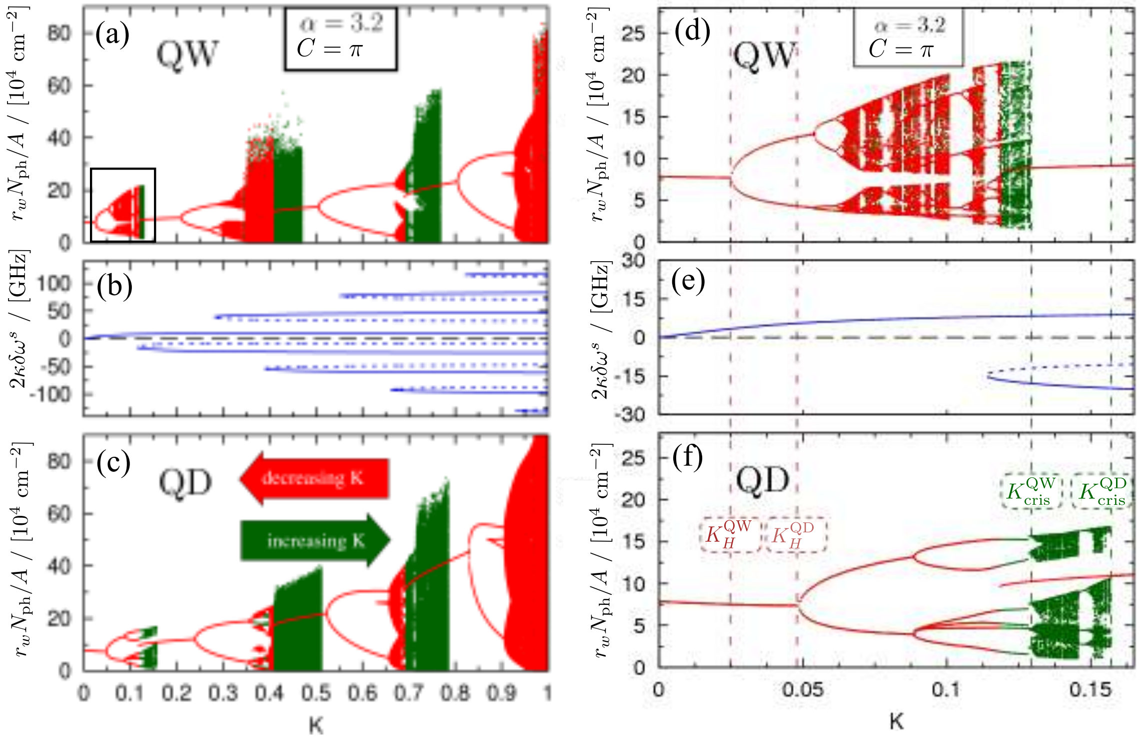

Figure 4.16.: Bifurcation diagrams of local maxima of the photon number $N_{\rm ph}$ vs. feedback strength K for a QW laser **(a)** and a QD laser **(c)** for stepwise increasing K (green dots) as well as stepwise decreasing K (red dots). The first Hopf bifurcation of QW and QD lasers are marked by $K_H^{\rm QW}$ and $K_H^{\rm QD}$ (vertical brown dashed lines), respectively. The K values of the boundary crises of the chaotic attractors marking the ends of the bifurcation cascades are denoted by $K_{\rm cris}^{\rm QW}$ and $K_{\rm cris}^{\rm QD}$ (green, dashed lines) for the QW and the QD laser, respectively. **(b)**: Frequency deviations $\delta\omega^{\rm s}$ of the ECMs of the system. Blue solid and dashed lines mark modes and anti-modes, respectively. **(d)**–**(f)**: Blowups of **(a)**–**(c)**. The magnification region is marked by a black rectangle in **(a)**. Parameters: $\alpha = 3.2$, $C = \pi$, and $J = 2.5J_{\rm th}$. For QD the reference rates and the parameters of Table 2.3 were used. For QW laser $\gamma^{\rm QW} = \gamma$ and $P = r_w N_{\rm ph}^0$ were used.

(f), where $K_{\text{cris}}^{\text{QW}} < K_{\text{cris}}^{\text{QD}}$. As a result, the bistability region at the end of the bifurcation cascade is larger for the QD than for the QW laser.

Further, the injection strengths, at which the first Hopf bifurcations take place, increase linearly with the RO damping as discussed in Subsection 4.6.6, i.e., $K_H^{\text{QW}} < K_H^{\text{QD}}$. (In Figs. 4.16(d)–(f) the Hopf bifurcation points marking the beginnings of the bifurcation cascades are marked by vertical brown dashed lines labeled K_H^{QW} and K_H^{QD} for QW and QD lasers, respectively.) Thus, for up-sweeping K the instability regions of the bifurcation cascades $[K_H^{\text{QW}}, K_{\text{cris}}^{\text{QW}}]$ for the QW laser and $[K_H^{\text{QD}}, K_{\text{cris}}^{\text{QD}}]$ for the QD laser span about the same range of K values.

In the last part of this section, we want to separate the effect of the linear laser parameters, i.e., RO frequency and damping, from the effect of the special carrier scattering dynamics of the QD laser. Therefore, we demand the QW laser to have the same RO frequency and the same damping as the QD laser additionally to the same photon lifetime τ_{ph} and photon density N_{ph}^0, i.e., we demand that

$$\omega^{\text{RO}} = \omega^{\text{QW}} = \sqrt{2\gamma^{\text{QW}}\Gamma^{\text{QW}}N_{\text{ph}}^0}, \quad \text{and} \tag{4.56a}$$

$$\Gamma^{\text{RO}} = \Gamma^{\text{QW}} = \frac{\gamma^{\text{QW}}}{2}\left(1 + 2r^{\text{QW}}N_{\text{ph}}^0\right) \tag{4.56b}$$

hold. Here, ω^{RO} and Γ^{RO} denote frequency and damping of the QD laser, respectively, (cf. Table 2.4). From the dynamical equations describing the QW laser (Eqs. (2.19)), we see that the time scale separation parameter γ^{QW} and r^{QW} have to be determined from Eqs. (4.56). (It then follows from the steady state equation (2.21) that the pump P is given by $P = N_{\text{ph}}^0/\gamma^{\text{QW}}$.) Solving Eq. (4.56a) for γ^{QW}, yields

$$\gamma^{\text{QW}} = \frac{\left(\omega^{\text{RO}}\right)^2}{2r^{\text{QW}}N_{\text{ph}}^0}. \tag{4.57}$$

Inserting this into Eq. (4.56b), solving for r^{QW}, and then plugging the expression obtained for r^{QW} back into Eq. (4.57), yields

$$r^{\text{QW}} = \frac{\left(\omega^{\text{RO}}\right)^2}{2N_{\text{ph}}^0\left(2\Gamma^{\text{RO}} - (\omega^{\text{RO}})^2\right)}, \quad \text{and} \quad \gamma^{\text{QW}} = 2\Gamma^{\text{RO}} - \left(\omega^{\text{RO}}\right)^2. \tag{4.58}$$

The turn-on dynamics of QW and QD laser with this choice of parameters is depicted in Figure 4.17(a). The QW laser (red dashed line) has a smaller turn-on delay then the QD laser (blue full line), but by superimposing both time series, we see that RO frequency and damping of both lasers match exactly (see inset in Fig. 4.17(a)). Figure 4.17(b) depicts bifurcation diagrams of the photon density of the QW laser (red dots) and the QD laser (blue dots) for small $\alpha = 0.9$ and $C = \pi$. The diagram thus corresponds to Fig. 4.15. For both lasers the first Hopf bifurcation takes place at the same value of the feedback strength K_H marked by a vertical brown dash-dot-dotted line. This was expected from the analytic expression for the feedback strength of the first Hopf bifurcation (Eq. (4.48a)), which only depends on RO damping and α-factor. Further, both lasers recover stable cw operation after a homoclinic bifurcation at K_{hom} (green

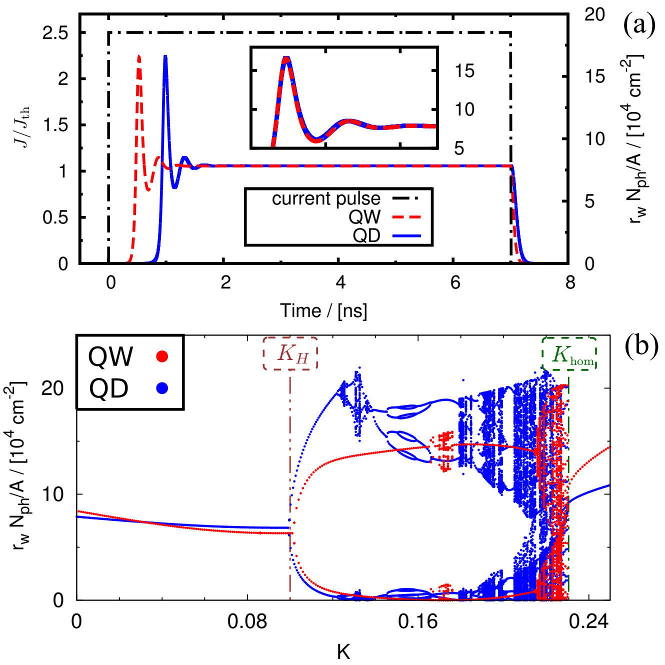

Figure 4.17: **(a)**: Response of photon number to a rectangular current pulse $J(t)$ of 7 ns width and height $J = 2.5J_{\rm th}$ (black dash-dotted line) for a QD laser with the reference set of rates (solid blue line) and a QW laser (dashed red line) without feedback ($K = 0$). The laser parameters are such that both lasers have the RO damping and steady state photon number (cf. Eqs. (4.58)). **(b)**: Bifurcation diagram of local maxima of the photon number $N_{\rm ph}$ vs. feedback strength K for a QW laser (red dots) and a QD laser (blue dots). The α-factor is $\alpha = 0.9$ and the feedback phase $C = \pi$. The first Hopf instability and the homoclinic bifurcation at the end of the bifurcation cascade are marked by K_H and $K_{\rm hom}$, respectively. Other Parameters: For QD laser see Table 2.3. For QW laser $P = r^{\rm QW} N^0_{\rm ph}$, and $\gamma^{\rm QW}$ and $r^{\rm QW}$ are given by Eqs. (4.58).

dash-dot-dotted line). However, the K-values of the period-doubling bifurcations leading into chaos are different for both lasers. The QW laser is more stable than the QD laser, because it undergoes the first period-doubling cascade into chaos at $K = 0.165$ compared to $K = 0.123$ for the QD laser. Both lasers display large periodic windows (frequency locking). The QW laser displays a large period-2 window ranging from $K = 0.175$ to $K = 0.22$, while the QD laser displays several periodic windows. In the larger one, the system undergoes two additional period-doubling bifurcations.

Summing up, we can well describe the first Hopf bifurcation point by Eq. (4.48a), which shows that it depends only on the RO damping and the α-factor. Since the loci of the saddle-node bifurcation lines, which are determined by the transcendental Eq. (4.7)), do not depend on the carrier equations, we conclude that more generally spoken the bifurcations of the ECMs depend on the internal carrier dynamics only via the RO damping (cf. Table 2.4). However, the internal carrier dynamics directly influences the loci of bifurcations of the periodic orbits, which are created in Hopf bifurcations of ECMs. Thus, the special internal carrier dynamics of QD lasers, which is described by nonlinear scattering rates in our modeling approach, determines the structure of the bifurcation cascade.

4.8. Excitability and coherence resonance close to a SNIPER or a homoclinic bifurcation

In this section, excitability and coherence resonance in QD lasers subject to short optical feedback are studied in dependence of pump current and band structure. Well-known examples for excitable systems are spiking neurons [HOD48], cardiac dynamics [MUR93], and nonlinear chemical reactions [ZAI70]. Excitability in laser systems received considerable interest in the last years. It was observed experimentally [GOU07, KEL09, KEL11a] and studied theoretically [WIE02, WIE05] in lasers with optical injection. Furthermore, excitability was found in lasers with short optical feedback [WUE02, USH07] as well as in lasers with a long external cavity [GIU97], and it was investigated theoretically in lasers with saturable absorbers [DUB99, DUB99a].

An excitable optical unit may be used as optical switch that reacts only for sufficiently high optical input signals and could thus be useful for all-optical-signal processing [TRO08a]. Moreover, it can be used for optical telecommunication applications to reduce noise [KRA03a]: a noisy input pulse triggers a "clean" output pulse.

The effect that an increase of the noise can lead to an increase of correlation, e.g., to an increase of the regularity of the spikes observed in the excitable regime, is known as coherence resonance [HU93a, PIK97]. This effect will be discussed in detail below. Coherence resonance was shown theoretically in QW lasers with saturable absorber [DUB99], and it was discussed in QD lasers under optical injection [ZIE13]. Moreover, it was studied experimentally and theoretically in lasers subject to long optical feedback in [GIA00] and in [KRA03a], respectively, and has been investigated in semiconductor superlattices [HIZ06]. It has also been found in systems below a subcritical Hopf bifurcation [USH05, ZAK10a, ZAK13]. The coherence resonance can be controlled by delayed optical feedback, which has been shown for neural systems in the framework of the FitzHugh-Nagumo model (type-II excitability) [JAN04, BAL04]. Moreover, for type-I excitable systems, delay control of coherence resonance has been discussed in [HIZ08b, AUS09].

4.8.1. Excitability

For a system to be excitable, three conditions have to be fulfilled [MUR93]:

i The unperturbed system is at a stable steady state.

ii An excitability threshold exists. This means that a subthreshold perturbation decays rapidly to the stable steady state, while a superthreshold perturbation triggers a large excursion in phase space (a spike).

iii There exists a refractory phase of duration t_r, which the system needs to settle back to the stable steady state after an excitation. During this refractory phase, the system cannot be excited again.

In the different laser systems mentioned above, type-I excitability is found, which takes place either close to a SNIPER bifurcation (in the laser under injection and in the laser with saturable absorber) or close to a homoclinic bifurcation (in the laser subject to optical feedback). Figure 4.18 depicts these two phase space configurations, where type-I excitability is observed [KRA03a]. In Fig. 4.18(a), the two branches of the unstable manifold of the saddle (open circle) form a smooth invariant closed curve, on which the stable node (closed circle) lies. This is the phase portrait of an excitable system close to a SNIPER, which occurs when the two fixed points collide and the unstable manifold of the saddle forms a homoclinic orbit. Figure 4.18(b) depicts a phase space configuration,

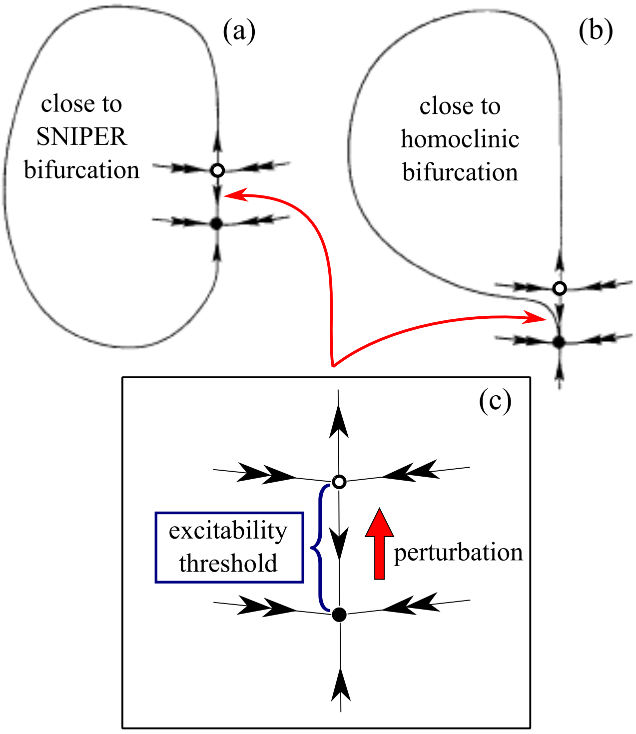

Figure 4.18: The topological configuration leading to type-I excitability: close to a SNIPER bifurcation, the two branches of the unstable manifold of the saddle (open circle) form a smooth invariant closed curve **(a)**, or close to a homoclinic bifurcation, they end on the "same side" of the attractor (filled circle) with respect to its stable manifold **(b)**. **(c)**: Detail enlargement of **(a)** and **(b)**. The short unstable manifold of the saddle acts as excitability threshold.

where both branches of the unstable manifold of the saddle come back to the "same side" of the stable manifold of the stable node. A homoclinic bifurcation occurs when the upper branch of the unstable manifold of the saddle becomes parallel to the left branch of the stable manifold forming a homoclinic loop. Both configurations have in common that a threshold exists, which is given by the short unstable manifold of the saddle. If the system is in the stable steady state (lasing fixed point), to excite the system, the projection of a perturbation onto the eigendirection of the short unstable manifold (red arrow in Fig. 4.18(c)) has to be large enough to push the trajectory above the stable manifold of the saddle. Therefore, in parts of the literature (cf. [DUB99, DUB99a, KRA03a]), the stable manifold of the saddle is denoted as excitability threshold.

The existence of an excitability threshold distinguishes the phase space configurations of Fig. 4.18 from type-II excitable systems, where a clear-cut threshold is absent [GER02]. Subthreshold perturbations from the stable node decay rapidly back to this steady state, while superthreshold perturbations lead to a large excursion of the trajectory in phase space close to the upper branch of the unstable manifold of the saddle. Characteristic for this type of excitability is a logarithmic scaling of the refractory time with the distance of the bifurcation point [KUZ95], i.e., with the distance of saddle and node in phase space. Both phase space configurations of Fig. 4.18 are topologically equivalent. They both depict the phase portrait close to a codimension-2 bifurcation point (non-central saddle-node homoclinic bifurcation point), which acts as an organizing center for type-I excitability in laser systems. A detailed discussion of the bifurcation structure near this codimension-2 bifurcation point can be found in [KRA03a, WIE07]. The configuration of Fig. 4.18(a) is observed in injected semiconductor lasers close to the locking boundary when Adler's type locking occurs [ZIE13, OLE10] (see locking tongues in Chapter 3).

However, if a homoclinic tooth is formed (see Fig. 3.5 and discussion in Section 3.3), the phase portrait is similar to Fig. 4.18(b) with one difference: Figure 4.18(b) depicts the most simple phase portrait for a real saddle. To describe the situation in a semiconductor laser, the saddle has to be replaced by a saddle-focus. The upper branch of the unstable manifold of the saddle-focus then winds around the lower branch (short unstable manifold) that directly connects both fixed points. The time series of trajectories close to the upper branch of the unstable manifold then consist of a large pulse with an oscillating tail [GOU07]. Furthermore, the homoclinic loop can be folded n-times, which leads to n-pulse excitability [WIE02, WIE05a]. Also in semiconductor lasers with saturable absorber [DUB99, DUB99a] and short optical feedback, the phase portrait looks like in Fig. 4.18(b) with the saddle replaced by a saddle-focus [KRA03a].

Experimentally, the laser can be excited by spontaneous emission noise [GOU07, KEL09, KEL11a], by short external optical pulses [WUE02], or by charge carrier variations introduced by a modulation of the pump current [GIU97]. From a dynamical system point of view, the first two methods are a perturbation in phase space, while the latter represents a change of the pump parameter.

It is relatively simple to realize a modulation of the pump current experimentally, but this method has the disadvantage to shift the bifurcation lines. Thus, one has to be careful that the modulation is short enough to avoid that the laser follows adiabatically this change of parameters [KRA03a]. To observe coherence resonance, the strength of the noise has to be tuned, which can be realized experimentally by superimposing broad band Gaussian noise to a constant pump current [GIA00]. In our simulations, we vary the strength of the spontaneous emission and expect that this method yields similar results as applying the noise to the pump current.

To model the spontaneous emission noise, the dynamical equation (4.1a) for the slowly varying complex field amplitude $\mathcal{E}$ is extended by a stochastic term. With respect to the dimensionless time $t' = 2\kappa t$, it reads

$$\mathcal{E}'(t') = \frac{1+i\alpha}{2}\Big[g(\rho_e+\rho_h-1)-1\Big]\mathcal{E}(t') + \tilde{k}e^{iC}\mathcal{E}(t'-\tau) + \sqrt{\beta\frac{r_{\mathrm{sp}}(\rho_e,\rho_h)}{2}}\,\xi(t'), \quad (4.59)$$

where $\xi(t')$ denotes the complex Gaussian white noise term $\xi(t')$, i.e.,

$$\begin{gathered}\xi(t') = \xi_1(t') + i\xi_2(t'), \quad \langle\xi_i(t')\rangle = 0,\\ \langle\xi_i(t')\xi_j(\tilde{t}')\rangle = \delta_{i,j}\delta(t-\tilde{t}'), \quad \text{for} \quad \xi_i(t')\in\mathbb{R},\, i\in\{1,2\}.\end{gathered}$$

The spontaneous emission is modeled by bi-molecular recombinations

$$r_{\mathrm{sp}}(\rho_e,\rho_h) \equiv \frac{Z_a^{\mathrm{QD}}W}{\kappa}\rho_e\rho_h, \quad Z_a^{\mathrm{QD}} \equiv a_L A N_a^{\mathrm{QD}}, \quad (4.60)$$

and the rate for the spontaneous emission r_{sp} can be determined by calculating the coherent interaction of a two-level system, i.e., a single QD, with all resonator modes in the framework of the second quantization [CHO99] (see discussion in Section 3.2).

Figure 4.19(a) and (c) depict bifurcation diagrams of the local maxima of N_{ph} versus the feedback strength K for the reference rates, a short delay time of $\tau = 16$, $C = \pi$, and a pump current of $J = 2J_{\mathrm{th}}$. The bifurcation cascade is thus the same as discussed in

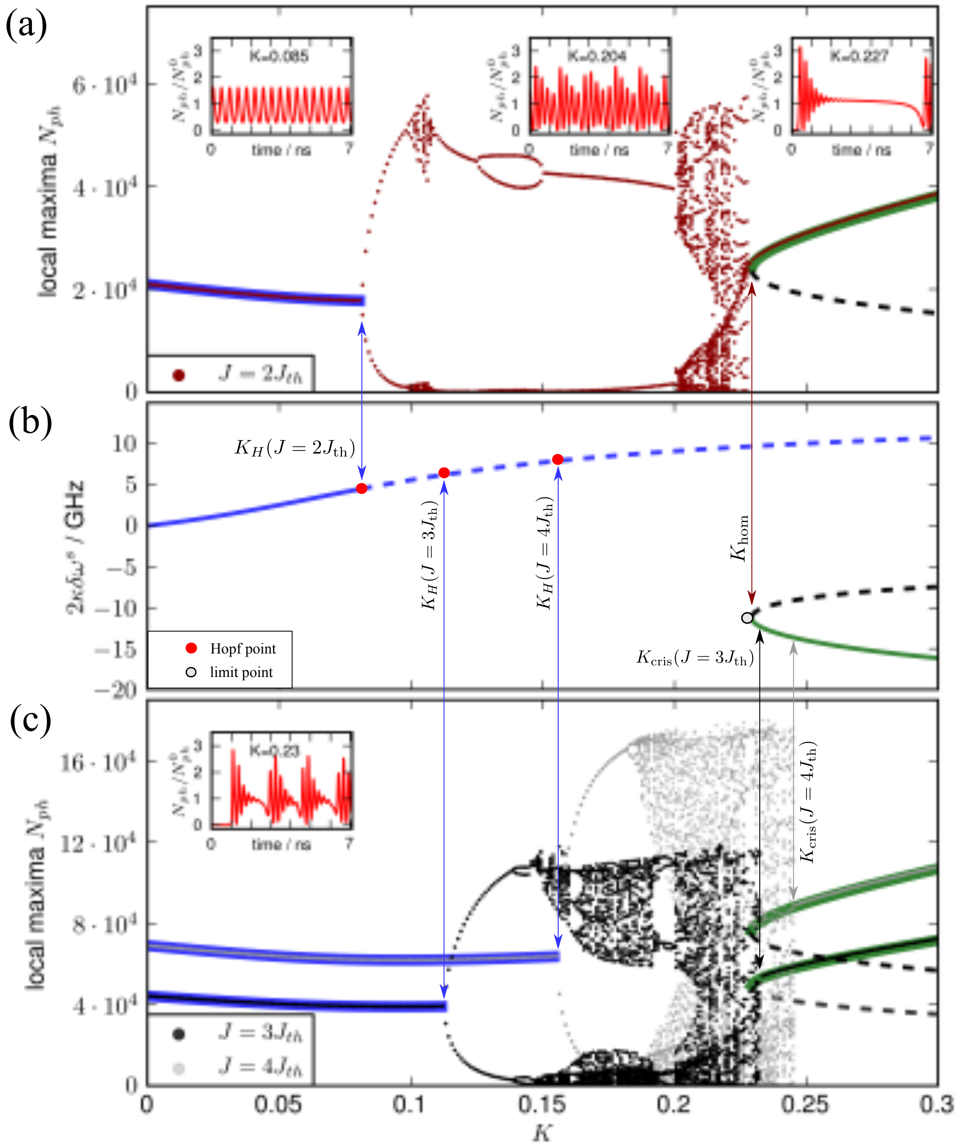

Figure 4.19.: **(a)**: Bifurcation diagram of the local maxima of the photon number N_{ph} versus feedback strength K for pump current $J = 2J_{\mathrm{th}}$ (brown dots). The thick blue and the thick green line denote the steady state photon numbers $N^{\mathrm{s}}_{\mathrm{ph}}$ of the stable parts of the first and the second ECM, respectively, and the black dashed line denotes $N^{\mathrm{s}}_{\mathrm{ph}}$ of the unstable antimode. Insets show time traces of N_{ph} for fixed K. **(b)**: Frequency deviations $\delta\omega^{\mathrm{s}}$ of the ECMs. Solid and dashed lines denote stable and unstable solutions, respectively. Hopf and limit points are denoted by red dots and open black circles, respectively. Blue, red, and black (gray) arrows indicate the feedback strengths of the Hopf points (K_H), the homoclinic bifurcation (K_{hom}), and the boundary crisis (K_{cris}), respectively. **(c)**: Same as **(a)** but for higher $J = 3J_{\mathrm{th}}$ (black dots) and $J = 4J_{\mathrm{th}}$ (gray dots). Parameters: Reference rates, small $\alpha = 0.9$, short $\tau = 16$, $C = \pi$, and other parameters as in Table 2.3.

Section 4.4 (cf. Fig. 4.5 (upper panel)). Insets in Fig. 4.19(a) depict time traces of N_{ph}. With increasing K, at first, a periodic modulation of N_{ph} after the first Hopf bifurcation is shown followed by a time trace within the chaotic attractor, and eventually strictly periodic pulse packages close to the homoclinic bifurcation are depicted in the rightmost inset.

Figure 4.19(c) depicts the bifurcation cascade for larger $J = 3J_{\mathrm{th}}$ (black dots) and for $J = 4J_{\mathrm{th}}$ (gray dots). The bifurcation diagrams have been obtained by increasing K stepwise using in each step the last τ-interval of the time series of the previous run as initial condition. Figure 4.19(b) shows the frequency deviation $\delta\omega^{\mathrm{s}}$ of the ECMs. Solid and dashed lines indicate stable and unstable solutions, respectively. Initially, for low K, only one ECM (blue line) exists, before a new pair of ECMs is created at $K_{\mathrm{sn}} = 0.2290$ in a saddle-node bifurcation (limit point) indicated by an open black circle. The stable 2nd ECM is depicted by a green and the unstable anti-mode by a black dashed line. The photon number $N^{\mathrm{s}}_{\mathrm{ph}}$ of the stable parts of the first and the 2nd ECM and of the unstable anti-mode are plotted in Figs. 4.19(a) and (c), by thick blue, thick green, and black dashed lines, respectively. Initially, the first ECM is stable, before it is destabilized in a supercritical Hopf bifurcation at K_H as discussed in Section 4.6.6. Since the RO damping increases with the pump current (cf. Eq. (2.30b) and Fig. 2.6), the Hopf bifurcation points (red dots and blue arrows) shift toward higher K-values as expected from the analytical expression (4.48a) for $K_H = 2\kappa\tau_{\mathrm{in}}\tilde{k}_H$. For $J = 2J_{\mathrm{th}}$ (Fig. 4.19(a)), the system evolves on a periodic orbit at the end of the bifurcation cascade, which is destroyed in a homoclinic bifurcation at $K_{\mathrm{hom}} = 0.2292$ (brown vertical arrow).

For $K > K_{\mathrm{hom}}$, the laser emits in stable cw operation on the 2nd ECM. For pump currents larger than $J > 2.8J_{\mathrm{th}}$, the end of the bifurcation cascade is not marked by a homoclinic bifurcation, but by a boundary crisis [GRE83a] of the chaotic attractor that collides at K_{cris} with the saddle (anti-mode) of the pair of ECMs created at $K = 0.229$. In contrast to the homoclinic bifurcation that is found to be nearly independent of the pump current for $J \in [J_{\mathrm{th}}, 2.8J_{\mathrm{th}}]$, the feedback strength K_{cris}, at which the boundary crisis occurs, depends on the RO damping, and it increases nearly linearly with the pump current (see dark and light arrow in Fig. 4.19(c) and formula (2.30b)). The inset in Fig. 4.19(c) shows chaotic pulse packages close to the boundary crisis of the chaotic attractor.

The laser system is excitable for values of the feedback strength that are slightly larger than K_{hom} for $J < 2.8J_{\mathrm{th}}$ and analogously for K-values slightly above K_{cris} for $J > 2.8$. In both cases, we have a phase space configuration similar to the one depicted in Fig. 4.18(b) with the short unstable manifold of the anti-mode acting as perturbation threshold. The response of the system to a superthreshold perturbation is a large excursion of the trajectory in phase space close to the "ghost" of the limit-cycle that is destroyed in the homoclinic bifurcation. For the larger values of J depicted in Fig. 4.19(c), the excursion in phase space is guided by the ruin of the chaotic attractor that collapses at K_{cris}. In Figures 4.19(a) and (c), the threshold is given by the difference of the photon numbers $N^{\mathrm{s}}_{\mathrm{ph}}$ of the 2nd ECM (thick green line) and of the anti-mode (black dashed line). We see that the threshold is very low for $K = K_{\mathrm{hom}}$ and increases with K. This implies that for $J > 2.8$, when the system restabilizes in a boundary crisis, the threshold can be tuned by varying the pump current and with it $K_{\mathrm{cris}} = K_{\mathrm{cris}}(J)$.

For a better understanding of the difference between the excitable behavior close to the homoclinic bifurcation for $J = 2J_{\mathrm{th}}$ as well as close to the boundary crisis for $J = 3$, now, the dynamics in phase space is discussed. Figure 4.20(a)–(b) depict time series and phase space projections onto the (N_{ph}, W_e)-plane for $K = 0.2290$, i.e., just below K_{hom}, where the periodic orbit still exists. A subthreshold perturbation of the system from the stable 2^{nd} ECM, i.e, the lasing fixed point, (green line) decays rapidly back to this steady state, while a superthreshold perturbation (blue line) yields strictly periodic pulse package, i.e., a motion along the periodic orbit. The green and the blue triangle denote the starting point of the trajectories and the photon number of the anti-mode is plotted as a black line (see inset in Fig. 4.20(a)). The inter-pulse interval time T_{ISI} scales logarithmically with the distance from the bifurcation point, i.e., $T_{\mathrm{ISI}} \sim \ln|K - K_{\mathrm{hom}}|$, as it is expected close to a homoclinic bifurcation [KUZ95] (cf. Fig. 4.8 and discussion in Section 4.6.2). Note that close to a SNIPER bifurcation, T_{ISI} reveals the characteristic scaling $T_{\mathrm{ISI}} \sim |K - \mathrm{K}_{\mathrm{sn}}|^{-1/2}$ [HIZ07], where K_{sn} denotes the feedback strength, at which the SNIPER bifurcation takes place.

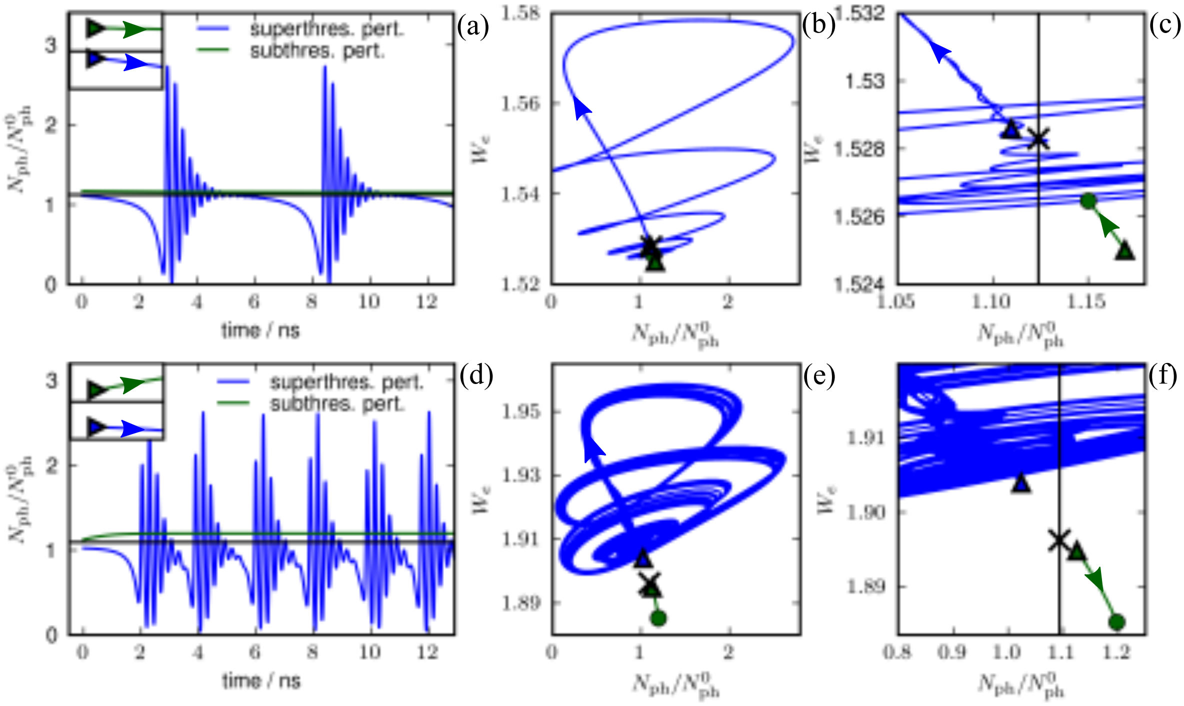

Figure 4.20.: Subthreshold (green lines) and superthreshold (blue lines) excitations **(a)**–**(c)**: Close to a homoclinic bifurcation for $K = 0.229$ and $J = 2J_{\mathrm{th}}$, and **(d)**–**(f)**: Close to a boundary crisis of the chaotic attractor for $K = 0.23$ and $J = 3J_{\mathrm{th}}$. Blue and green triangles mark the starting points of the perturbed trajectories for super- and subthreshold perturbations, respectively. Black lines denote the steady state photon number of the unstable anti-mode of the second ECM-pair. **(a)** and **(d)**: Time series of the perturbed trajectories. **(b)** and **(e)**: Projections of the trajectories onto the (N_{ph}, W_e)-plane. Green dots and black crosses indicate the position of the stable second ECM-mode and the unstable ECM-anti-mode in phase space, respectively. **(c)** and **(f)**: Blowups of **(b)** and **(e)** close to initial points of trajectories. Parameters: Reference rates, small $\alpha = 0.9$, short delay time $\tau = 16$, $C = \pi$, and other parameters as in Table 2.3.

In the phase space projection (Fig. 4.20)(b)), it can be seen that after a power dropout at the end of each pulse package (nearly vertical part of the trajectory), the trajectory at first performs pronounced damped oscillations spiraling around the point in phase space, where the 2^{nd} pair of ECMs has been created at the nearby saddle-node bifurcation, before it is reinjected into the high gain region during the power dropout. The position of the 2^{nd} ECM pair can be seen best in Figure 4.20(c) depicting a detail enlargement of the phase space close to the center of the spiral. Mode and anti-mode are denoted by a green dot and a black cross, respectively.

The lower panel of Fig. 4.20 depicts the excitability of the laser close to the boundary crisis for $K = 0.23$, which is a little below $K_{\text{cris}}(J = 3)$. A superthreshold perturbation (blue line in Fig. 4.20(d)) yields rather regular pulse packages, although they are not strictly periodic as the one observed close to the homoclinic bifurcation. Furthermore, the inter-spike interval time does not obey a specific scaling law as the pulse packages described before. From the phase space projection in Fig. 4.20(b), we see that the trajectory has essentially the same shape observed close to the homoclinic bifurcation, but does not close up, which yields a certain width of the chaotic attractor in phase space. Note that these regular pulse packages are similar to those observed by Heil et al. in a QW laser with short optical feedback [HEI01a, HEI03a]. They also correspond to the low frequency fluctuations (LFF) found in semiconductor lasers subject to moderate optical feedback from a long external cavity, which will be discussed in-depth below. In comparison to the phase space configuration in Fig. 4.20(a)–(c) close to the homoclinic bifurcation, the excitability threshold is much larger. This can be seen best in the detail enlargements of Figs. 4.20(c) and (f) by comparing the distance of the 2^{nd} ECM marked by the green dot to the vertical line indicating the steady state photon number of the anti-mode. (Please note the larger scale of the N_{ph}-axis in Fig. 4.20(f).)

Excitability close to a homoclinic bifurcation as well as close to a boundary crisis of a chaotic attractor was observed experimentally in [WUE02] and [USH07], respectively. In these studies, a two-section integrated QW laser design consisting of an actively pumped gain-section and a passive phase-tuning section was investigated. Such a device yields very short and strong optical feedback. The lasers were excited by short external optical pulses.

4.8.2. Coherence resonance

In this section, we show that the regularity of the pulse packages in the excitable regimes discussed in the last section first increases with the noise strength β, reaches a maximum, and eventually decays. This counterintuitive effect that more noise can increase the coherence of the system is known as coherence resonance [HU93a, PIK97].

To characterize the regularity of the pulse packages quantitatively, three measures are used in the literature [PIK97]. One measure is the correlation time of a stationary stochastic process y that was introduced by Stratonovich [STR63] as

$$t_{\text{cor}} \equiv \int_{\mathbb{R}_0^+} |\Psi_y(s)| ds, \text{ where } \Psi_y \equiv \frac{1}{\sigma_y^2} \langle (y(t-s) - \langle y \rangle)(y(t) - \langle y \rangle) \rangle, \tag{4.61}$$

where $\langle \cdot \rangle$ denotes the ensemble average, the variance is given by $\sigma_y^2 \equiv \Psi_y(0) = \langle (y(t) - \langle y \rangle)^2 \rangle$, and the normalized autocorrelation function of y is denoted by Ψ_y. Using the Wiener-Khinchin theorem, which states that power spectral density and autocorrelation function are a Fourier-pair [GAR02, POM05a, POM07], we calculate Ψ_y from the ensemble averaged power spectral density (PSD) (see Appendix D.3 for details). Here, we take the photon number as stochastic process, i.e., $y = N_{\mathrm{ph}}$. Another measure for the regularity of the spikes is the normalized standard deviation of the inter-spike interval time T_{ISI} [JAN03, HIZ06, BRA09]

$$R_T \equiv \frac{\sqrt{\langle T_{\mathrm{ISI}}^2 \rangle - \langle T_{\mathrm{ISI}} \rangle^2}}{\langle T_{\mathrm{ISI}} \rangle}, \tag{4.62}$$

which is also known as normalized fluctuations [PIK97, BEA08]. A third measure is the signal-to-noise ratio [HU93a], which is the ratio of the height of the power spectral peak h and its normalized width $\Delta\omega/\omega_0$, where ω_0 is the frequency of the peak maximum and $\Delta\omega$ is the full width at $h_1 \equiv e^{-1/2}h$. Figure 4.21(d) depicts t_{cor} (red triangles, right y-axis) and R_T (blue dots, left y-axis) as functions of the noise strength β close to the homoclinic bifurcation for $K = 0.2292$ and $J = 2J_{\mathrm{th}}$. Furthermore, t_{cor} is shown close to the crisis of the chaotic attractor for $K = 0.2314$ and $J = 3J_{\mathrm{th}}$ (black stars, right y-achsis) as well as for $K = 0.24056$ and $J = 4J_{\mathrm{th}}$ (gray hexagons, right y-achsis). Figures 4.21(a)–(c) and Figs. 4.21(e)–(g) depict time traces of the system close to the homoclinic bifurcation for $J = 2J_{\mathrm{th}}$ and close to the boundary crisis for $J = 3J_{\mathrm{th}}$, respectively, at β-values indicated by gray dashed vertical lines in Fig. 4.21(d). At first, the coherence close to the homoclinic bifurcation is discussed. Generally, the time between two excitations T_{ISI} can be decomposed into the time needed to activate the system t_a and the refractory time t_r, which the system needs to settle back to the rest state. In our system, the rest state is the stable 2nd ECM, and the refractory time is given by the time the system needs to spiral back to the 2nd ECM after one excitation. This means that t_r is fixed by the internal dynamics of the system, while t_a depends on the noise strength β. For low values of β, the activation time t_a is long compared to t_r (see Fig. 4.21(a)). Increasing β, it becomes easier for the system to overcome the excitation threshold and the pulse packages arise more regularly (see Fig. 4.21(b)). This is indicated by an increase of t_{cor} and a decrease of R_T. Increasing β further, pulse packages are excited more often, but the regularity of their appearance decreases and they are additionally deformed by the noise (see Fig. 4.21(c)). This leads to a decrease of t_{cor} and an increase of R_T. The maximum of t_{cor} does not coincide exactly with the minimum of R_T. This is expected, because t_{cor} accounts for coherence in periodicity of the pulse packages as well as coherence in amplitude fluctuations, while R_T only measures the periodicity of the pulse packages.

Higher pump currents of $J = 3J_{\mathrm{th}}$ and $J = 4J_{\mathrm{th}}$ lead to higher excitability thresholds (see Fig. 4.19(c)). Thus, as far as coherence resonance is discussed, a maximum of the correlation is therefore expected at a higher level of the noise. This is the reason why the maximum of t_{cor} shifts to higher values of the noise strength β with increasing β (see black stars and gray hexagons in Fig. 4.21(d) for $J = 3J_{\mathrm{th}}$ and $J = 4J_{\mathrm{th}}$, respectively). By comparing the time traces taken at the maxima of t_{cor} for $J = 2J_{\mathrm{th}}$ and $J = 3J_{\mathrm{th}}$, which are depicted in Fig. 4.21(b) and (f), respectively, two effects are prominent. On the one hand, the higher noise level in Fig. 4.21(f) becomes obvious, and, on the other hand, we see that the peak heights of the pulse package are varying more strongly in Fig. 4.21(f) than in Fig. 4.21(b), i.e., the amplitude jitter of the pulse packages is larger. The variation of the heights of the pulse maxima is the reason why the measure R_T fails at higher values of the noise strength and has not been depicted for $J = 3J_{\mathrm{th}}$ and $J = 4J_{\mathrm{th}}$. For $J = 3J_{\mathrm{th}}$ and $J = 4J_{\mathrm{th}}$, the dynamics beyond the coherence maximum is dominated by the noise, which can be seen in Fig. 4.21(g) depicting for $J = 3J_{\mathrm{th}}$ a time trace right to the maximum of t_{cor}.

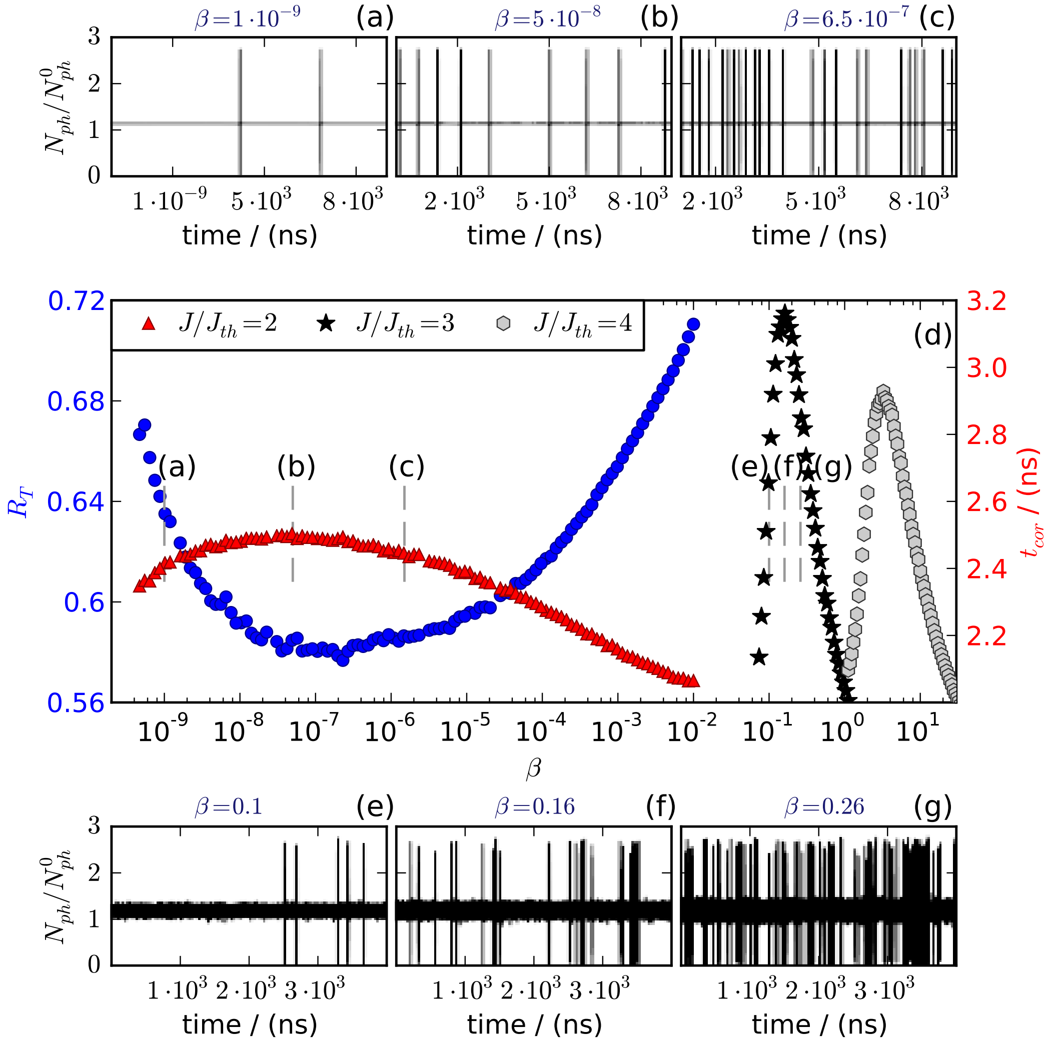

Figure 4.21.: **(a)**–**(c)**: Time series for $J = 2J_{\mathrm{th}}$ and $K = 0.2292$ for different β indicated by gray dashed lines in **(d)**. Central panel **(d)**: Normalized standard deviation of inter-spike interval R_T (blue dots) for $J = 2J_{\mathrm{th}}$ and coherence time t_{cor} versus noise strength β for $J = 2J_{\mathrm{th}}$ (red triangles), $J = 3J_{\mathrm{th}}$ (black stars), and $J = 4J_{\mathrm{th}}$ (gray hexagons). The feedback strength is x K $= 0.22920$ for $J = 2J_{\mathrm{th}}$, $K = 0.23140$ for $J = 3J_{\mathrm{th}}$ and $K = 0.24506$ for $J = 4J_{\mathrm{th}}$, respectively. **(e)**–**(g)**: Time series for $J = 3J_{\mathrm{th}}$ and $K = 0.2314$ for different β indicated by gray dashed lines in **(d)**. Parameters: Small $\alpha = 0.9$, $\tau = 16$, $C = \pi$, and other parameters as in Table 2.3.

Coherence resonance has already been observed experimentally in QW lasers subject to long external feedback by Giacomelli et al. [GIA00] close to a LFF-chaotic attractor. The LFF regime is characterized by chaotic intensity oscillations on a short time scale (10–100 GHz) overlayed by sudden intensity dropouts, which occur on a much longer time scale (1–10 ms). These are known as power dropouts [FIS96] and they are chaotic meaning that the time between power dropouts is pseudo-randomly distributed [SUK99, FLU11a]. The LFF dynamics is deterministic and can be understood as follows [SAN94, TAR95b, FIS96]: in between the intensity dropouts, the trajectory displays chaotic itinerancy wandering around many attractor ruins with a general drift to the maximum gain mode (see ellipse in Fig. 4.2). This drift leads to a power build-up. Before reaching the maximum gain mode, it collides with an anti-mode in a crises, and a power dropout takes place. For short feedback, we only have a few (in our case even only one) attractor ruins formed by the chaotic saddles of the unstable modes. Thus, the time needed for the trajectory to wander around in phase space is much shorter (0.1–10 ns) than in the LFF regime [HEI01a, HEI03a, TAB04]. Further, the pulse packages are more regular than the chaotic intensity pulsation between the power dropouts observed in the LFF regime, and for lower pump level even completely regular pulse packages are possible as discussed above and in Section 4.4.

The small number of ECMs for short feedback is also the reason for the dependence of the dynamics on the feedback phase C in this regime. Intuitively, this can be understood as follows: geometrically, variations of C change the positions of the ECMs on the ellipse in Fig. 4.2. Previous to a change in C the laser emits on the most stable ECM. After a change in C, the lasing takes place at the ECM that is most stable for the new value of C. For short feedback, this ECM can have a considerably different inversion ρ_{inv}, which results in changes of the laser intensity. Further, it is also possible that for the new value of C none of the ECMs is stable (see for example Figs. 4.7(b)-(e)), then the intensity of the laser is periodically modulated, quasiperiodic, or even chaotic. In contrast, for long delay, hundreds of ECMs exist on the ellipse. Thus, the ECM that is most stable after the change in C has a similar inversion – and a similar intensity – than the ECM, on which the laser emitted previous to the change in C.

The phase dependence in the short cavity regime permits to shift the bifurcation cascade and, thus, the excitability region, which is located close to the homoclinic bifurcation at K_{hom} for $J \leq 2.8J_{\text{th}}$ and close to the crisis of the chaotic attractor at $K_{\text{cris}} = K_{\text{cris}}(J)$ for $J > 2.8J_{\text{th}}$ (see Fig. 4.19), into a range that is well accessible in experiments. Further, the current dependence of K_{cris} permits to shift the excitability threshold, and with it the maximum of the coherence to a noise level, which is well accessible in experimental investigations.

4.8.3. Impact of band structure

In this subsection, the dependence of the coherence resonance on the band structure is discussed. Therefore, we fix the pump current to $J = 2J_{\text{th}}$ and keep the other parameters as in the previous section. Figure 4.22(a) and (b) depict the correlation time t_{cor} (red triangles) in dependence of the noise strength β for the slow and the fast set of scattering rates, respectively. For the slow scattering rates, the system is excitable and close to

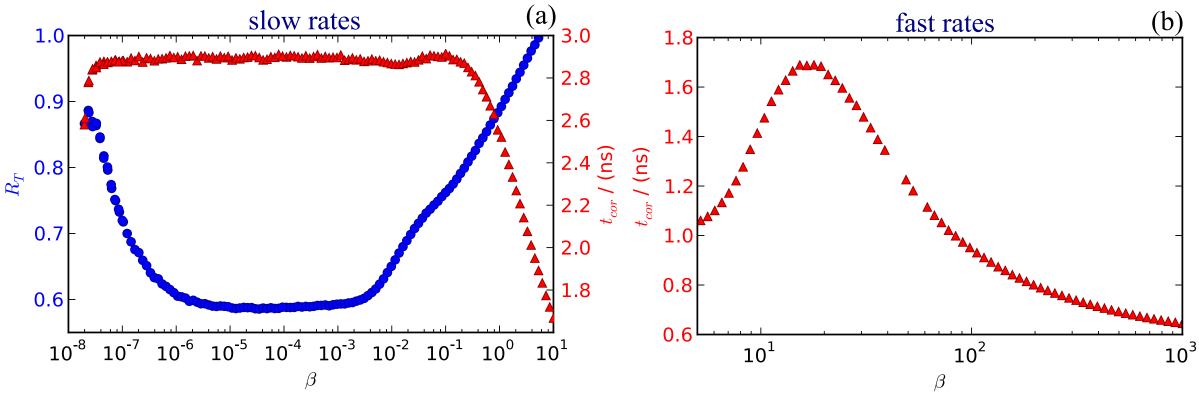

Figure 4.22.: Normalized standard deviation of inter-spike interval R_T and coherence time t_{cor} for small $\alpha = 0.9$ and short $\tau = 16$. **(a)**: Slow carrier scattering rates and $K = 0.2292$. **(b)**: Fast carrier scattering rates and $K = 0.2610$. Parameters: $J = 2J_{\text{th}}$, $C = \pi$, and other parameters as in Table 2.3.

a homoclinic bifurcation, which takes place at the same value $K_{\text{hom}} = 0.229$ as for the reference rates (cf. Fig. 4.19). This is why the coherence maximum is also found at very small value of the noise strength β. Here, additional to t_{cor}, the normalized standard deviation of the inter-spike interval time R_T can be used as a measure for coherence (blue dots in Fig. 4.22(a)). In comparison to the reference rates (compare to leftmost resonance curves in Fig. 4.21(d)), t_{cor} and R_T show a strongly broadened maximum and minimum, respectively.

For the fast scattering rates the chaotic attractor collapses in a boundary crisis at $J = 2J_{\text{th}}$, in contrast to the slow and the reference, where a homoclinic bifurcation takes places. Since $K_{\text{cris}} = 0.26 > K_{\text{hom}}$, the threshold is larger than for the slow and the reference rates and the maximum of t_{cor} is found at large values of the noise strength. At these high noise strengths, it is not possible to measure R_T, because of the high amplitude variations.

4.9. Summary

In this chapter, the microscopically based rate equation model for a QD laser of Chapter 2 has been extended by a Lang-Kobayashi-type field equation to take into account delayed optical feedback. At first, the structure of the basic rotating wave solutions, i.e., external cavity modes (ECMs), of the dynamic equations was studied analytically, and it has then been compared to the structure of solutions of the QD laser under injection. The ECMs yield cw emission of the laser, and they form the "backbone" for more complex dynamics. This has been investigated for the example of the regular pulse packages observed for short delay times. These are the analogon of the low frequency fluctuations (LFFs) found in the long cavity regime. In general, semiconductor lasers subject to delayed feedback show a rich phenomenology of complex dynamics. Here, the routes to chaos and the dependence of the instability regions on the band structure, the pump current, and the phase-amplitude coupling have been studied in detail. As a result, it can be stated that the stability of the laser increases with enhanced RO damping, which may in QD lasers be achieved by shallow QDs, i.e., a fast carrier exchange between QDs and surrounding carrier reservoir.

From particular interest is the Hopf instability of the first ECM limiting the parameter region, where stable cw emission of the QD laser can be guaranteed. A formula for the first Hopf bifurcation line has been derived, and it has then been discussed for particular ECMs. This analysis reveals that the region of stable cw emission on the one hand increases linearly with the RO damping, and that on the other hand a small phase-amplitude coupling is favorable for stable cw operation. A comparison with the Lang-Kobayashi-model for a conventional QW laser has shown that this scattering dynamics has a strong impact on the structure of the bifurcation cascades in the instability regions.

In a second part of this chapter, it has been discussed how a QD laser subject to feedback may be employed as an excitable optical unit. At their creation in a saddle-node bifurcations, the mode solutions of the ECM pairs are always stable. Thus, in the regions with complex dynamics the creation of an ECM pair yields bistability between the newly created ECM and the more complex periodic or chaotic attractor. Increasing the feedback strength K, the periodic or chaotic attractor collapses in a homoclinic bifurcation or a boundary crises. Little above this bifurcation, the laser is excitable, because a superthreshold perturbation provokes an excursion of the trajectory along the ghost of the complex attractor and coherence resonance occurs. It has been found that the feedback strengths, at which the boundary crisis takes place, increases with the RO damping, and thus with the pump current. This permits to shift the excitability threshold and, consequently, the maximum of the coherence, which could facilitate an experimental investigation of the coherence resonance.

Part II.

Mode-locked laser

CHAPTER

FIVE

MODE-LOCKED LASER

5.1. Introduction

Passively mode-locked (ML) semiconductor lasers are of broad interest as sources of ultrashort picosecond and sub-picosecond optical pulses with high repetition rates. These sources are, among other applications, needed for data-communication, optical clocking, high speed optical sampling, all-optical clock recovery, and microscopy [AVR00, LEL07, LUE11b]. Compared to actively [SCH91c] and hybrid ML lasers, they are simpler to fabricate and to handle. However, their major drawback is their relatively large timing jitter due to the absence of an external reference clock [LIN10c]. Since timing fluctuations degrade the performance of the laser, a lot of efforts have been made to reduce them. An efficient and inexpensive method for timing jitter reduction based on the use of all-optical feedback from an external cavity is discussed in this chapter.

One basic timescale of the passively ML laser is the inter-spike interval time $T_{\mathrm{ISI},0}$, which is the inverse of the pulse repetition frequency. The optical feedback introduces an additional timescale into the system, namely the roundtrip time of the light in the external cavity τ. The experimental setup we aim to model is sketched in Fig. 5.1. The laser has an actively pumped gain section (gain) and saturable absorber (SA). A part of the emitted light is reflected back into the laser diode from a distant mirror forming an passive, external cavity with delay time τ. The inter-spike interval T_{ISI}, i.e., the temporal distance of subsequent pulses, can slightly differ from the inter-spike interval of the solitary laser $T_{\mathrm{ISI},0}$.

By measuring the radio frequency (rf)-linewidth of a passively ML quantum well lasers as done already in 1993 by Solgaard and Lau [SOL93], it was shown that optical feedback can have a stabilizing or a de-stabilizing effect on the laser dynamics depending on the ratio of τ and $T_{\mathrm{ISI},0}$. Further, the authors observed a pulling of the repetition rate of the pulses by variation of τ. Both effects have been recently observed in experiments with quantum dot lasers [MER09, BRE10, LIN10e, LIN11d]. In addition, the dependence of the timing jitter on the pump current and the feedback strength has been studied for a fixed ratio of τ and $T_{\mathrm{ISI},0}$ [BRE10, LIN11f] and for variable τ [FIO11].

In contrast to the wealth of experimental results, only few theoretical works have been published on this subject. The bifurcation scenarios of a free-running quantum dot

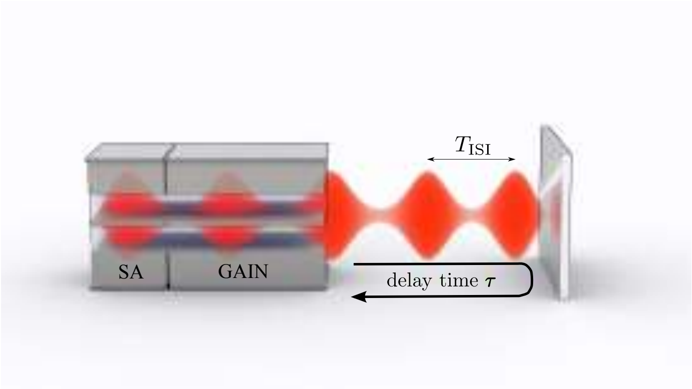

Figure 5.1: Sketch of a linear-cavity Fabry-Perot mode-locked two-section laser subject to external optical feedback from a distant mirror. Saturable absorber and gain section are denoted by SA and GAIN, respectively. T_{ISI} is the inter-spike interval time of the laser subject to feedback with delay time τ.

laser with optical feedback have been studied in [OTT10, OTT12, GLO12] as discussed in detail in Chapter 4. In [MUL06] the authors study the amplitude and timing jitter of a quantum dot ML laser subject to optical feedback with $\tau = 5\,T_{\mathrm{ISI},0}$ (intermediate feedback delay time). In [AVR09] the authors discuss the impact of a variation of the ratio $\tau/T_{\mathrm{ISI},0}$ on the dynamics of a ML quantum well laser for τ-values ranging from $\tau \approx 0.3\,T_{\mathrm{ISI},0}$ to $\tau \approx 3.1\,T_{\mathrm{ISI},0}$ (short feedback delay time). They identify different dynamical regimes of ML laser operation: main resonances are found when τ is an integer multiple of $T_{\mathrm{ISI},0}$, higher order resonances take place when $\tau/T_{\mathrm{ISI},0}$ is a rational number, and non-resonant regimes are detected for values of $\tau/T_{\mathrm{ISI},0}$ in between two resonant regimes. The dynamics in each regime will be discussed in detail in Section 5.4 of this chapter. For a short external cavity, the impact of different ratios of $\tau/T_{\mathrm{ISI},0}$ on the pulse characteristics of a quantum dot ML laser model has recently been studied in [SIM12a].

In the theoretical studies mentioned above, finite-difference traveling wave models have been used. Here a delay differential equations (DDE) model for a passively mode-locking laser is studied. This model generalizes the model of Haus [HAU75, HAU00] to the case of large gain and loss per cavity roundtrip, which is typical for semiconductor ML lasers. The model has been extended to take into account a quantum dot material model [VIK06, VLA10], hybrid mode-locking [VLA10a, FIO10], and external optical injection [REB11]. Further, for a quantum dot model with ground- and excited state lasing, a multi-section modification of the DDE model was proposed, which permits to take into account more symmetric cavity designs and tapered waveguides [ROS11e, ROS11d, XU12] (see also Ref. [VLA09], where a multi-section model for a linear-cavity ML laser was developed). The DDE model has the advantage of a strongly reduced computational cost. On the one hand this permits us to study the regime of longer external cavities with τ up to $70\,T_{\mathrm{ISI},0}$. This is of experimental interest, because long fiber based cavities are experimentally easier to handle than shorter external cavities consisting of external mirrors. Thus, long fiber based cavities they are frequently considered in experiments [SOL93, LIN10e, LIN11d, LIN11f, BRE10, FIO11, ROS12b]. On the other hand, the DDE approach permits to study the dependence of the timing jitter on feedback strength and delay time over the whole $T_{\mathrm{ISI},0}$-interval between two subsequent main resonances and not only for the exact main resonances discussed in [MUL06].

The chapter is organized as follows: at first, the DDE model with optical feedback is derived in Section 5.2. Then, the mode-locking dynamics of the free running laser is studied in Section 5.3, before discussing in Section 5.4 the resonance structure of inter-spike interval time $T_{\mathrm{ISI},0}$ and delay time τ for the ML laser subject to optical feedback in the regimes of intermediate and long delays. Further, additional effects introduced by a nonzero amplitude-phase coupling are addressed in Section 5.5. Afterward, different methods to measure the timing jitter are discussed in Section 5.6, and the impact of the resonances of $T_{\mathrm{ISI},0}$ and τ on the timing jitter are investigated in Section 5.7, before concluding in Section 6.

5.2. Model

In this section the derivation of the DDE model for a model locked laser (MLL) introduced in [VLA05] is reviewed, and an extension of the model that permits to study external optical feedback is discussed. Further, the assumptions made in the derivation of the DDE model are reviewed.

5.2.1. Derivation of the DDE model with feedback

To derive the dynamical equations we consider a standard traveling wave model for a quantum well semiconductor laser [SCH88j, SCH90b, TRO94, BAN01][1]

$$\pm\partial_z\mathcal{E}_r^{\pm}(t',z)+\frac{1}{v}\partial_{t'}\mathcal{E}_r^{\pm}(t',z)=\frac{g_r\Gamma_r}{2}(1-i\alpha_r)[n_r(t',z)-n_r^{\mathrm{tr}}]\mathcal{E}_r^{\pm}(t',z), \tag{5.1a}$$

$$\partial_{t'}n_r(t',z)=j_r(t)-\gamma_r n_r(t',z)-vg_r\Gamma_r[n_r(t',z)-n_r^{\mathrm{tr}}]\sum_{\pm}\left|\mathcal{E}_r^{\pm}(t',z)\right|^2. \tag{5.1b}$$

In this model, the longitudinal spatial dependence of the electric field

$$E(t',z)\equiv\left(\mathcal{E}_r^{+}(t',z)e^{-ikz}+\mathcal{E}_r^{-}(t',z)e^{+ikz}\right)e^{i\Omega_0 t'} \tag{5.2}$$

is expressed as a superposition of two counter-propagating waves in slowly varying envelope approximation, where $\mathcal{E}_r^{+}$ and $\mathcal{E}_r^{-}$ denote the dimensionless slowly varying amplitudes of the forward and the backward traveling waves, respectively. The field is scaled such that $n_{\mathrm{ph}}=|\mathcal{E}^{\pm}|^2$ is the photon density.

The partial derivatives with respect to the (longitudinal) z-coordinate and time t' are denoted by ∂_z and $\partial_{t'}$, respectively. The index $r\in\{g,q,p\}$ labels gain section (g), saturable absorber (q), and passive section (p), respectively. The reference propagation constant fulfills the linear dispersion relation $k\equiv\Omega_0/v$ with the (optical) carrier frequency Ω_0 and the group velocity v. The latter is assumed to be the same in all sections. The linear gain (loss) coefficients are denoted by g_r, Γ_r are the transverse confinement factors, γ_r are denote the relaxation rates of the carrier densities, and α_r are the linewidth enhancement factors. The carrier densities are denoted by n_r, and n_r^{tr} are

---

[1] Note that N_r, g_r, v, γ_r, j_r, and $|\mathcal{E}|^2$ have the following dimensions [TRO94]: $[N_r]=\mathrm{Length}^{-3}$, $[g_r]=\mathrm{Length}^2$, $[v]=\mathrm{Length/Time}$, $[\gamma_r]=\mathrm{Time}^{-1}$, $[j_r]=\mathrm{Time}^{-1}\times\mathrm{Length}^{-3}$, $\left[|\mathcal{E}|^2\right]=\mathrm{Length}^{-3}$.

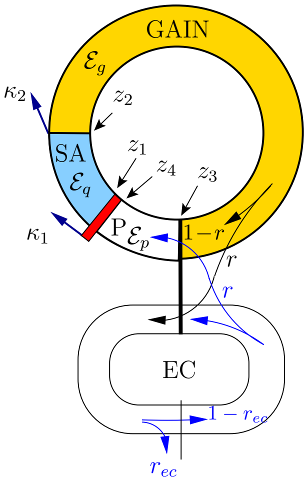

Figure 5.2: Sketch of the ring cavity laser with external optical feedback used for the derivation of the DDE model. The laser consists of five sections: a saturable absorber section (SA), a gain section (GAIN), an external cavity (EC), a passive section (P), and a Lorentzian filter (red bar). The field amplitudes in the saturable absorber, in the gain section, and in the passive section are denoted by $\mathcal{E}_q$, $\mathcal{E}_g$ and $\mathcal{E}_p$, respectively. The facets between the sections are located at z_i for $i = 1, \ldots, 4$. κ_1 and κ_2 are non-resonant and out-coupling losses located at z_1 and z_2, respectively. r and r_{ec} are intensity transmission and reflection coefficients at the interface between gain section and external cavity and at the interface in the external cavity, respectively.

the transparency densities of the corresponding sections. The pump parameters j_r are proportional to the pump current densities, where only the gain section is electrically pumped, i.e., $j_r = 0$ for $r \in \{q, p\}$.

One main assumption of the DDE model is that the light propagates only in one direction, and the other direction is suppressed (unidirectional lasing). Without loss of generality, a clockwise propagation is assumed, i.e., $\mathcal{E}_r \equiv \mathcal{E}_r^+$ and $\mathcal{E}_r^- \equiv 0$. The ring cavity design implies a periodic boundary condition

$$\mathcal{E}_r(t', z) = \mathcal{E}_r(t', z + L), \tag{5.3}$$

where L is the length of the laser. This boundary condition fixes the possible propagation constants of the cavity modes and the frequency of the carrier wave to

$$k \equiv n\frac{2\pi}{L}, \quad \text{and} \quad \Omega_0 \equiv n\frac{2\pi}{T} \quad \text{for :} \quad n = \pm 1, \pm 2, \ldots,$$

where we have introduced the cold-cavity roundtrip time $T \equiv L/v$, which is the roundtrip time of the light in the cavity without lasing activity. Non-resonant and out-coupling losses at the interface between gain and absorber section ($z = z_2$) are taken into account by the boundary condition

$$\mathcal{E}_g(t', z_2) = \sqrt{\kappa_2}\mathcal{E}_q(t', z_2). \tag{5.4}$$

To simulate for example a linear Fabry-Perot laser of length L_{FP} and intensity reflectivities r_1 and r_2 at the facets, one may take into account the internal losses α_i and the mirror losses r_1 and r_2 at the facets of the Fabry-Perot laser by $\kappa_1 \equiv r_1 r_2 \exp(-\alpha_i L_{\mathrm{FP}})$. The length of the corresponding ring laser is $L = 2L_{\mathrm{FP}}$ [ROS11d].

Figure 5.3 sketches the optical spectrum of a free running MLL consisting of a comb of evenly spaced lines having a frequency spacing of $\Delta\nu \equiv 1/T$. Which of these modes lase and take part at the mode-locking process is determined by the shape of the gain spectrum of the semiconductor material (gray envelope). In the DDE model, the finite gain spectral bandwidth is taken into account in a lumped element approach [RAF11] by a bandwidth-limiting element, i.e., a filtering function that is located between z_1 and z_4.

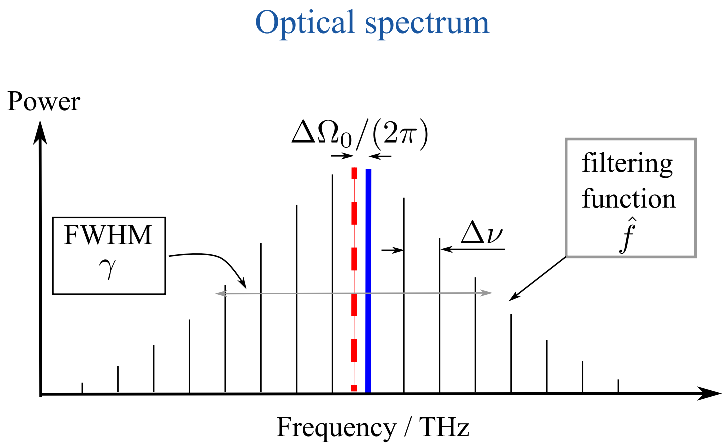

Figure 5.3: Sketch of an optical spectrum of a ML laser. The frequency spacing of the cavity modes (black vertical lines) is $\Delta\nu$, the frequency detuning between the frequency, at which the filtering function $\hat{f}$ has its maximum (thick red dashed line), and the frequency of the carrier wave (thick blue line) is marked by $\Delta\Omega$. The FWHM of $\hat{f}$ is denoted by γ.

In the following the filter is assumed to be infinitely thin, i.e., $z_1 = z_4$. In the frequency domain the filter can be expressed as

$$\hat{\mathcal{E}}_q(\omega, z_1 + L) = \sqrt{\kappa_1}\hat{f}(\omega)\hat{\mathcal{E}}_p(\omega, z_1 + L) = \sqrt{\kappa_1}\hat{f}(\omega)\hat{\mathcal{E}}_p(\omega, z_4), \tag{5.5}$$

where $\hat{\mathcal{E}}_{q,p}$ denote the Fourier transformed field amplitudes[2], out-coupling losses at the facet $z = z_1$ are taken into account by κ_1, and $\hat{f}$ is the filtering function in the frequency domain (see Fig. 5.3). Further, in the last equality of Eq. (5.5) the periodic boundary condition of Eq. (5.3) has been employed. In this derivation a Lorentzian shaped filtering function is chosen, which delivers an analytical derivation of an DDE for the field amplitude. It reads in a frame of reference rotating with the frequency Ω_0 of the carrier wave

$$\hat{f}(\omega) \equiv \frac{\gamma}{\gamma + i(\omega - \Delta\Omega)}, \tag{5.7}$$

where γ is the full-width at half maximum (FWHM), and $\Delta\Omega \equiv \Omega_{\text{max}} - \Omega_0$ is the detuning of the frequency of the maximum of the gain spectrum Ω_{max} (thick dashed read line in Fig. 5.3) from the frequency of the carrier wave Ω_0 (thick blue line in Fig. 5.3). With increasing γ more modes can lock and shorter pulses are obtained.

In each roundtrip of the light in the internal cavity, a part of the light is coupled out at the facet $z = z_3$ into an external ring cavity (see Fig. 5.2), which is assumed to be a passive section, i.e., in this section we have $n = n^{\text{tr}}$, and the right hand side of Eq. (5.1a) vanishes. The external cavity has an additional facet, where a part of the light is coupled out, which permits to model the losses in the external cavity. In the coordinates (t', z), the boundary condition for the field at the facet $z = z_3$ reads

$$E_p(t', z_3) = \sqrt{1-r}\left\{E_g(t', z_3) + \sum_{l=1}^{\infty} K_l E_g(t' - l\tau, z_3)\right\}, \tag{5.8}$$

---

[2] The Fourier transform $\mathcal{F}_{t\to\omega}$ and its inverse $\mathcal{F}^{-1}_{\omega\to t}$ are defined by

$$\hat{f}(\omega) = \mathcal{F}_{t\to\omega}[f(t)] = \int_{\mathbb{R}} f(t)e^{-i\omega t}dt \text{ and } f(t) = \mathcal{F}^{-1}_{\omega\to t}[\hat{f}(\omega)] = \frac{1}{2\pi}\int_{\mathbb{R}} \hat{f}(\omega)e^{i\omega t}d\omega, \tag{5.6}$$

respectively, where $\omega = 2\pi\nu$.

here we have introduced the intensity reflection coefficient r at $z = z_3$, r_{ec} is the intensity reflection coefficient at the facet of the external cavity, and τ is the roundtrip time of the light in the external cavity. Further, the feedback strengths $K_l \equiv r(1-r_{\text{ec}})^{l/2}(1-r)^{l/2-1}$ of order l for $l = 1, 2, \dots$ have been introduced. The first term of Eq. (5.8) represents the amplitude of the field E_g that is directly transmitted through the facet at $z = z_3$, while the sum takes into account the contributions of E_g after $l = 1, 2, \dots$ roundtrips in the external cavity. In terms of the slowly varying amplitudes $\mathcal{E}_p$ and $\mathcal{E}_g$, this can be rewritten as

$$\mathcal{E}_p(t', z_3) = \sqrt{1-r}\left\{\mathcal{E}_g(t', z_3) + \sum_{l=1}^{\infty} K_l \mathcal{E}_g(t' - l\tau, z_3)e^{-ilC}\right\}, \tag{5.9}$$

where we have introduced the phase of the light in the external cavity $C \equiv \Omega_0\tau$.

The wave equation for the field amplitudes (Eq. (5.1a)) is solved by every function that depends only on the reduced coordinate $t \equiv t' - z/v$, which motivates the following change of coordinates to a co-moving frame[3]

$$\Sigma : \mathbb{R}^2 \to \mathbb{R}^2 \quad (t', z) \mapsto (t, \zeta) \equiv (t' - \frac{z}{v}, \frac{z}{v}). \tag{5.10}$$

Rewriting Eqs. (5.1a) - (5.1b) in the coordinates (t, ζ), we obtain the following set of ordinary differential equations

$$\partial_\zeta A_r(t, \zeta) = \frac{1}{2}(1 - i\alpha_r)N_r(t, \zeta)A_r(t, \zeta), \tag{5.11a}$$

$$\partial_t N_g(t, \zeta) = \mathcal{J}_g(t) - \gamma_g N_g(t, \zeta) - N_g(t, \zeta)\left|A_g(t, \zeta)\right|^2, \tag{5.11b}$$

$$\partial_t N_q(t, \zeta) = -\mathcal{J}_q(t) - \gamma_q N_q(t, \zeta) - \tilde{r}_s N_q(t, \zeta)\left|A_q(t, \zeta)\right|^2, \tag{5.11c}$$

where we have introduced the rescaled amplitudes of the electric field $A_r \equiv \sqrt{v g_g \Gamma_g}\mathcal{E}_r$, rescaled carrier densities $N_r \equiv v g_r \Gamma_r [n_r - n_r^{\text{tr}}]$ that are proportional to the carrier inversion in the corresponding section, and rescaled pump rates $\mathcal{J}_g \equiv v g_g \Gamma_g (j_g - \gamma_g n_g^{\text{tr}})$ and $\mathcal{J}_q \equiv v g_q \gamma_q \Gamma_q n_q^{\text{tr}}$[4]. Further, $\tilde{r}_s \equiv g_q\Gamma_q / g_g\Gamma_g = E_{\text{sat,g}}/E_{\text{sat,q}}$ is the ratio of the saturation energies of gain and absorber section, where $E_{\text{sat,g}} \equiv (v\Gamma_g g_g)^{-1}$ and $E_{\text{sat},q} \equiv (v\Gamma_q g_q)^{-1}$ define the saturation energies of gain and absorber section, respectively, ϵ_0 is the vacuum permittivity, and ϵ_{bg} is the background permittivity.

---

[3] The Jacobian of the transformation Σ is given by

$$D\Sigma = \begin{pmatrix} 1 & -\frac{1}{v} \\ 0 & \frac{1}{v} \end{pmatrix}.$$

Thus, the differentials transform like

$$\partial_{t'} = \left(\frac{d\Sigma_1}{dt'}\right)\partial_t + \left(\frac{d\Sigma_2}{dt'}\right)\partial_\zeta = \partial_t, \qquad \partial_z = \left(\frac{d\Sigma_1}{dz}\right)\partial_t + \left(\frac{d\Sigma_2}{dz}\right)\partial_\zeta = -\frac{1}{v}(\partial_t - \partial_z),$$

where Σ_1 and Σ_2) are the components of Σ.

[4] Note that A_r, N_r, and $J_{g,q}$ have the following dimensions: $[A_r] = (\text{Time} \times \text{Length})^{-3/2}$, $[N_r] = \text{Time}^{-1}$, $[J_{g,q}] = \text{Time}^{-2}$.

The saturation energy is the energy of a short pulse that decreases the inversion to $1/e$ of its initial value [YAM93, HAU93, HAU00, KAE98]. This can be seen from Eqs. (5.11b) and (5.11c) as follows: under the assumption that the pulse duration τ_p is much smaller than the carrier relaxation times γ_g^{-1} and γ_q^{-1} and the pump rates $\mathcal{J}_g$ and $\mathcal{J}_q$, the first two terms on the right hand sides of Eqs. (5.11b) and (5.11c) can be neglected. Integrating the equations for fixed $\zeta = \zeta_0$ with respect to local time t over one cavity roundtrip, yields an exponential decay of N_r with the saturation energies $E_{\mathrm{sat},r}$ as decay constants

$$N_r, (t, \zeta_0) = N_r(t-T, \zeta_0) e^{-v\Gamma_r g_r \int_{t-T}^{t} |\mathcal{E}_r(s)|^2 ds} = N_r(-T, \zeta_0) e^{-\frac{\int_{t-T}^{t} |\mathcal{E}_r(s)|^2 ds}{E_{\mathrm{sat},r}}}, \tag{5.12}$$

for $r = g$ and $r = q$, respectively.

The evolution of the field in the gain and absorber sections is obtained by integrating Eq. (5.11a) over these sections

$$A_g(t, \zeta_3) = e^{\frac{1}{2}(1-i\alpha_g)G(t)} A_g(t, \zeta_2), \quad A_q(t, \zeta_2) = e^{-\frac{1}{2}(1-i\alpha_q)Q(t)} A_q(t, \zeta_1), \tag{5.13}$$

where dimensionless carrier densities

$$G(t) \equiv \int_{\zeta_2}^{\zeta_3} N_g(t, \zeta) d\zeta \qquad \text{and} \qquad Q(t) \equiv -\int_{\zeta_1}^{\zeta_2} N_q(t, \zeta) d\zeta, \tag{5.14}$$

have been introduced that are integrated over gain and absorber sections, respectively. The passive section is transparent to the laser light resulting in $N_p \equiv 0$. Thus, integrating Eq. (5.11a) over the passive section, yields

$$A_p(t, \zeta_4) = A_p(t, \zeta_3). \tag{5.15}$$

To derive differential equations for G and Q, Eqs. (5.11b) and (5.11c) are integrated with respect to ζ over gain and absorber section, respectively,

$$\partial_t G(t) = J_g(t) - \gamma_g G(t) - \int_{\zeta_2}^{\zeta_3} N_g(\zeta) |A_g(t, \zeta)|^2 d\zeta, \tag{5.16a}$$

$$\partial_t Q(t) = J_q(t) - \gamma_q Q(t) + \tilde{r}_s \int_{\zeta_1}^{\zeta_2} N_q(\zeta) |A_q(t, \zeta)|^2 d\zeta, \tag{5.16b}$$

where we have introduced the spatially averaged pump parameters

$$J_g \equiv \int_{\zeta_2}^{\zeta_3} \mathcal{J}_g(\zeta) d\zeta, \quad \text{and } J_q \equiv \int_{\zeta_1}^{\zeta_2} \mathcal{J}_q(\zeta) d\zeta.$$

By multiplying Eq. (5.11a) by the complex conjugate field amplitude A_r^* and the complex conjugate of Eq. (5.11a) by A_r and then adding up the resulting equations, one obtains

$$\partial_\zeta \left| A_r(t, \zeta) \right|^2 = N_r(t, \zeta) \left| A_r(t, \zeta) \right|^2, \quad \text{for} \quad r \in \{g, q\}. \tag{5.17}$$

Integrating Eq. (5.17) over gain and absorber sections, respectively, yields

$$\int_{\zeta_1, \zeta_2}^{\zeta_2, \zeta_3} N_{q,g}(t, \zeta) \left| A_{q,g}(t, \zeta) \right|^2 d\zeta = \left| A_{q,g}(t, \zeta_{2,3}) \right|^2 - \left| A_{q,g}(t, \zeta_{1,2}) \right|^2, \tag{5.18}$$

which permits to replace the integral terms in the dynamical equations for G and Q (Eqs. (5.16)) in terms of the field intensities at the facets. By inserting Eqs. (5.13) into Eq. (5.18), the carrier equations (Eqs. (5.11b) - (5.11c)) can be rewritten in terms of G and Q

$$\partial_t G(t) = J_g - \gamma_g G(t) - \kappa_2 e^{-Q(t)} \left(e^{G(t)} - 1\right) \left|A(t)\right|^2, \tag{5.19a}$$

$$\partial_t Q(t) = J_q - \gamma_q Q(t) - \tilde{r}_s e^{-Q(t)} \left(e^{Q(t)} - 1\right) \left|A(t)\right|^2, \tag{5.19b}$$

where we have introduced $A(t) \equiv A_q(t, \zeta_1)$.

Next, an integral equation for the evolution of the field amplitude during one roundtrip in the internal cavity is derived. Rewriting Eq. (5.5) in the time domain, we obtain from its right hand side a convolution product ($\star$) of the filtering function in the time domain f and $\mathcal{E}_p$

$$\mathcal{E}_q(t', z_1 + L) = \sqrt{\kappa_1}\Big(f \star \mathcal{E}_p\Big)(t', z_1 + L) = \sqrt{\kappa_1}\Big(f \star \mathcal{E}_p\Big)(t', z_4). \tag{5.20}$$

Applying the coordinate transformation of Eq. (5.10), we can rewrite Eq. (5.20) in terms of (t, ζ) and the rescaled field amplitudes A_q and A_p

$$A_q(t - T, \zeta_1 + T) = \sqrt{\kappa_1} \int_{-\infty}^{t-T} f(t - T - \Theta) A_p(\Theta, \zeta_4) d\Theta, \tag{5.21}$$

where we have assumed that $A_q(\Theta, \zeta_4) = 0$ holds for $\Theta > t - T$ to preserve causality. This is why we obtain $t-T$ instead of infinity as upper limit of the integration. The field amplitude $A_p(\Theta, \zeta_4)$ on the right hand side of Eq. (5.21) can be expressed in terms of $A(t) \equiv A_q(t, \zeta_1)$ by employing the boundary conditions of Eqs. (5.4) and (5.9) thathave to be rewritten in terms of the coordinates (t, ζ) and by using the evolution of the field given by Eqs. (5.13), which yields

$$A(\Theta, \zeta_4) = R(\Theta) A(t). \tag{5.22}$$

Where the R-term that describes the evolution of the field equation during one roundtrip in the internal cavity is given by

$$R(\Theta) \equiv \sqrt{\kappa} e^{\frac{1}{2}(1 - i\alpha_g) G(\Theta) - \frac{1}{2}(1 - i\alpha_q) Q(\Theta)} \quad \text{and} \quad \kappa \equiv (1 - r)\kappa_1 \kappa_2. \tag{5.23}$$

The right hand side of Eq. (5.21) can also be rewritten in terms of $A(t)$ by employing the periodic boundary condition of Eq. (5.3), which expressed in terms of the coordinates (t, ζ) reads

$$A_q(t, \zeta_1) = A_q(t - T, \zeta_1 + T). \tag{5.24}$$

To see this, at first, we introduce the notation $\tilde{\mathcal{E}}(t, \zeta) \equiv \mathcal{E} \circ \Sigma^{-1}(t, \zeta)$ and $\mathcal{E}(t', z) = \tilde{\mathcal{E}} \circ \Sigma(t, z)$ to stress that $\mathcal{E} = \mathcal{E}(t', z)$ and $\tilde{\mathcal{E}} = \tilde{\mathcal{E}}(t, \zeta)$ are different functions that are connected by the isomorphisms Σ and Σ^{-1}, i.e., by the coordinate transformation of Eq. (5.10) and its inverse Σ^{-1}, respectively. Employing that Σ implies $t \equiv t' - z_1/v$ and $\zeta_1 \equiv z_1/v$, yields the following relations

$$\mathcal{E}(t', z_1) = \tilde{\mathcal{E}} \circ \Sigma(t', z_1) = \tilde{\mathcal{E}}(t' - \frac{z_1}{v}, \frac{z_1}{v}) = \tilde{\mathcal{E}}(t, \zeta_1), \tag{5.25a}$$

$$\mathcal{E}(t, z_1 + L) = \tilde{\mathcal{E}} \circ \Sigma(t, z_1 + L) = \tilde{\mathcal{E}}(t' - \frac{z_1}{v} - T, \frac{z_1}{v} + T) = \tilde{\mathcal{E}}(t - T, \zeta_1 + T). \tag{5.25b}$$

The first terms of Eq. (5.25a) and Eq. (5.25b) are equal due to the periodic boundary condition of Eq. (5.3). This implies equality of the last terms. Rewriting the latter in terms of $A_q = A_q(t, \zeta_1)$, then yields the relation (5.24). With the help of Eqs. (5.22) and (5.24), Eq. (5.21) can be rewritten as

$$\begin{aligned} A(t) = &\int_{-\infty}^{t-T} f(t-T-\Theta)R(\Theta)A(\Theta)d\Theta \\ &+\sum_{l=1}^{\infty} K_l e^{-ilC} \int_{-\infty}^{t-T} f(t-T-\Theta)R(\Theta-l\tau)A(\Theta-l\tau)d\Theta. \end{aligned} \tag{5.26}$$

By applying coordinate transformations $\Theta \to \Theta + l\tau$ for each l, the integrals in the second term of Eq. (5.26) can be expressed as convolution integrals similar to the first term of Eq. (5.26), but with $t - T - \tau$ as upper limit for the integration. For the Lorentzian filter function of Eq. (5.7) that reads in the time domain

$$f(t) \equiv \gamma e^{(-\gamma + i\Delta\Omega)t},$$

a DDE can be derived by differentiating Eq. (5.26) with respect to time t [YOU99, VLA05], which yields

$$\dot{A}(t)+(\gamma-i\Delta\Omega)A(t) = \gamma R(t-T)A(t-T)+\gamma\sum_{l=1}^{\infty} K_l e^{-ilC} R(t-T-l\tau)A(t-T-l\tau). \tag{5.27}$$

Here, $(\dot{\cdot})$ denotes the derivative with respect to time t. Transforming Eq. (5.27) to a co-moving frame by introducing $A(t) \equiv \frac{1}{\sqrt{\kappa_2}}\mathcal{E}(t)e^{i\Delta\Omega t}$, the dynamical equations take the form

$$\begin{aligned} \gamma^{-1}\dot{\mathcal{E}}(t) + \mathcal{E}(t) = &R(t-T)e^{-i\Delta\Omega T}\mathcal{E}(t-T) \\ &+\sum_{l=1}^{\infty} K_l e^{-ilC} R(t-T-l\tau)e^{-i\Delta\Omega(T+l\tau)}\mathcal{E}(t-T-l\tau) + \sqrt{R_{\mathrm{sp}}}\xi(t), \end{aligned} \tag{5.28a}$$

$$\dot{G}(t) = J_g - \gamma_g G(t) - e^{-Q(t)}\left(e^{G(t)} - 1\right)\left|\mathcal{E}(t)\right|^2, \tag{5.28b}$$

$$\dot{Q}(t) = J_q - \gamma_q Q(t) - r_s e^{-Q(t)}\left(e^{Q(t)} - 1\right)\left|\mathcal{E}(t)\right|^2, \tag{5.28c}$$

where the rescaled ratio of saturation intensities in gain and absorber section $r_s \equiv \tilde{r}_s/\kappa_2$ has been introduced [VLA11]. Further, to model spontaneous emission noise a complex Gaussian white noise term $\xi(t)$ was added to the field equation (5.28a), i.e.,

$$\begin{aligned} \xi(t) = \xi_1(t) + i\xi_2(t), \quad \langle \xi_i(t) \rangle = 0, \\ \langle \xi_i(t)\xi_j(t') \rangle = \delta_{i,j}\delta(t-t'), \quad \text{for} \quad \xi_i(t) \in \mathbb{R},\, i \in \{1,2\}, \end{aligned}$$

and R_{sp} is the rate of the spontaneous emission.

5.2.2. Dimensionless formulation for numerical integration

To study the dynamical equations numerically, it is convenient to introduce a dimensionless time variable by rescaling time with respect to one important time scale in the system. Here we choose the cold cavity roundtrip time of the light T^* as reference time scale. Since we aim to model a laser with a repetition rate of $40\,\mathrm{GHz}$, T^* is set to $T^* = 25\,\mathrm{ps}$. In terms of the dimensionless time $s \equiv t/T^*$, the dynamical equations (Eqs. (5.28)) take the form[5]

$$\begin{aligned}\gamma_s^{-1} a'(s) + a(s) = {}& R(s-S)e^{-i\Delta\omega S}a(s-S) \\ &+ \sum_{l=1}^{\infty} K^l e^{-ilC} R(s-S-lS_{\text{ec}})e^{-i\Delta\omega(S+lS_{\text{ec}})}a(s-S-lS_{\text{ec}}) + \sqrt{r_{\text{sp}}}\xi(s),\end{aligned} \tag{5.29a}$$

$$G'(s) = G_0 - \gamma_{s,g}G(s) - e^{-Q(s)}\left(e^{G(s)}-1\right)\left|a(s)\right|^2, \tag{5.29b}$$

$$Q'(s) = Q_0 - \gamma_{s,q}Q(s) - r_s e^{-Q(s)}\left(e^{Q(s)}-1\right)\left|a(s)\right|^2, \tag{5.29c}$$

where

$$R(s) \equiv \sqrt{\kappa}e^{\frac{1}{2}(1-i\alpha_g)G(s)-\frac{1}{2}(1-i\alpha_q)Q(s)}, \tag{5.30}$$

and $(\,\cdot\,)'$ denotes the derivative with respect to dimensionless time s.

Here, we have introduced a rescaled filter width γ_s, rescaled carrier decay rates $\gamma_{s,g}$ and $\gamma_{s,q}$, a rescaled field amplitude a, rescaled pump and absorption rates G_0 and Q_0, the dimensionless optical frequency of the laser light $\Delta\omega$, the dimensionless cold-cavity roundtrip time S, the dimensionless delay-time S_{ec}, and the dimensionless rate of the spontaneous emission r_{sp} as follows:

$$\begin{aligned}\gamma_s &\equiv \gamma T^*, & \gamma_{s,g} &\equiv \gamma_g T^*, & \gamma_{s,q} &\equiv \gamma_q T^*,\\ a &\equiv \sqrt{T^*}\mathcal{E}, & G_0 &\equiv T^* J_g, & Q_0 &\equiv T^* J_q,\\ \Delta\omega &\equiv T^*\Delta\Omega, & \omega_0 &\equiv T^*\Omega_0, & S &\equiv \frac{T}{T^*},\\ S_{\text{ec}} &\equiv \frac{\tau}{T^*}, & r_{\text{sp}} &\equiv T^* R_{\text{sp}}.\end{aligned} \tag{5.31}$$

5.3. Dynamics of free running mode-locked laser

At first, we concentrate on the dynamics of the laser without feedback ($K = 0$) and without noise ($R_{\text{sp}} = 0$). The parameters used in the simulations are given in Table 5.1 unless

---

[5] More formally, we introduce a coordinate transformation

$$\Phi : t \mapsto s \equiv t/T^*.$$

For a function $F : t \mapsto F(t)$ the derivative with respect to t then reads in the new coordinates according to the chain rule

$$\frac{d}{dt}F(t) = \frac{d}{dt}\underbrace{F\circ\Phi^{-1}}_{=\tilde{F}}\circ\Phi(t) = \frac{d\Phi}{dt}\frac{d}{d\Phi}\tilde{F}(s) = \frac{1}{T^*}\frac{d}{ds}\tilde{F}(s),$$

where we have introduced $\tilde{F}(s) \equiv F\circ\Phi^{-1}(s)$ and the linear operator $\frac{d}{ds} \equiv \frac{d}{d(\Phi(t))}$.

stated otherwise. For an easier comparison with experiments, all results are expressed with respect to physical time t, i.e., the dynamical equations (5.28) are discussed.

The carrier dynamics in the gain section is described by the saturable gain $G(t) \propto \int_{\zeta_2}^{\zeta 3}[n_g(t) - n_g^{\mathrm{tr}}]d\zeta$, which is proportional to the difference of the spatially averaged concentration of electron hole-pairs in the gain section and their spatially averaged concentration at transparency, i.e., G is proportional to the inversion in the gain section. The carrier dynamics in the slow saturable absorber is expressed by the saturable loss $Q(t) \propto \int_{\zeta_1}^{\zeta_2}[n_q^{\mathrm{tr}} - n_q(t)]d\zeta$, which contrary to G decreases for increasing spatially averaged carrier concentration. The term "saturable" is used in this context to describe that G and Q are strongly varied during one roundtrip of the pulse in the cavity due to light-matter interactions. The gain section is actively pumped meaning that this section is inverted and to the saturable absorber an inverse voltage is applied depleting the electron hole pairs generated by the light-matter interaction. Thus, the concentration of electron-hole pairs in the absorber is far below their transparency concentration. At the arrival of a pulse, the gain G is depleted, because the induced emission is the dominating process in the inverted gain section. Simultaneously, the absorption Q is decreased, because electron-hole pairs are generated by the induced absorption, which is the dominating process in the absorber. The absorber is driven towards transparency, i.e., the absorber is bleached.

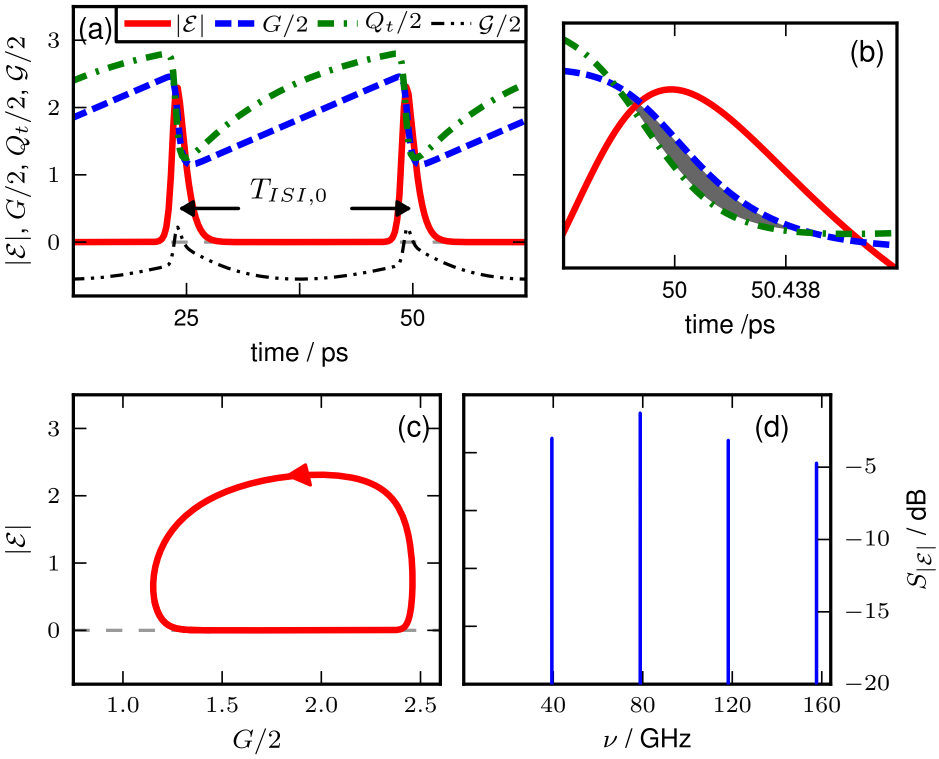

Figure 5.4.: Dynamics of the mode-locked laser without feedback ($K = 0$). **(a)**: time traces of the absolute value of the amplitude $|\mathcal{E}|$, gain G, total loss Q_t, and net gain $\mathcal{G}$. $T_{\mathrm{ISI},0}$ is the inter-spike interval time. **(b)**: blowup of black rectangle in **(a)**. The net gain window where $\mathcal{G} > 0$ is highlighted in gray. **(c)**: projection of trajectory onto the (G,$|\mathcal{E}|$)-plane. **(d)**: power spectrum. Parameter values are as in Table 5.1.

In a passively ML laser, the interplay of G and Q leads to a fixed phase relation, i.e., phase locking, of many cavity modes resulting in narrow pulses with large intensity. The number of locked modes can be roughly estimated by the ratio of the bandwidth of the spectral filter γ and the frequency spacing of the cavity modes $\Delta\nu = 1/T$. This means that the number of modes participating in the ML process usually increases with γ. Since the pulse width $\tau_p \propto \gamma^{-1}$ is anti-proportional to γ, an increase of γ results in a shorter pulse width [VLA05]. If γ is large compared to the decay times of gain and loss media γ_g and γ_q, respectively, the dynamics of the electrical field amplitude $\mathcal{E}$ is much faster than the dynamics of the carriers (Eq. (5.28b)-(5.28c)) due to the presence of the small factor $\gamma^{-1} \ll 1$ on the left hand side of Eq. (5.28a). Thus, the ML laser acts in this regime as a typical slow-fast system [ERN10b]. In the ML regime, a regular pulse train is obtained. The width τ_p of the pulses is short compared to the inter-spike interval time $T_{\mathrm{ISI},0} \approx T + O(\gamma^{-1})$ [VLA04], which is close to the cold-cavity roundtrip time T. Figure 5.4(a) shows time traces of the absolute value of the amplitude $|\mathcal{E}|$ (red solid line), the saturable gain G (blue dashed line), the total loss $Q_t \equiv Q + |\ln\kappa|$ (green dash-dotted line), which is the sum of saturable and non-resonant losses per cavity roundtrip, and the net gain $\mathcal{G} \equiv G - Q_t$ (thin black dash-dot-dotted line). The latter is the difference of the overall gain and total loss per cavity roundtrip. It is illustrative to calculate the net gain for a continuous wave (cw) solution of the model equations (5.28) in the simplest case of a real valued field equation, i.e., for $\alpha_g = \alpha_q = 0$. Inserting the ansatz $(\mathcal{E}(t), G(t), Q(t)) = (\mathcal{E}_s, G_s, Q_s)$ with $|\mathcal{E}_s| \neq 0$ into Eqs. (5.28), we see from Eq. (5.28a) that above the linear laser threshold $\mathcal{G}_s \equiv G_s - (Q_s + |\ln\kappa|) = 0$ holds. Thus, $\mathcal{G} = 0$ corresponds to the gain-clamping above threshold observed in single-mode one-section laser models with only one carrier type [KAN05]. A bifurcation analysis of the rotating wave solutions of Eqs. (5.28) (cw emission) with complex $\mathcal{E}$, i.e, nonzero α-factors, and $K = 0$ was performed in [BAN06]. In the ML regime, the system evolves on a stable limit cycle in phase space as it can be see in Fig. 5.4(c) in a projection onto the $(G,|\mathcal{E}|)$-plane. From the power spectrum in Fig. 5.4(d), we see that this set of parameters leads to a pulse repetition rate $\nu_{\mathrm{rep},0} \equiv 1/T_{\mathrm{ISI},0}$ close to 40 GHz, which is realized in recent experiments [FIO11, FIO11a]. Figures 5.4(a) and (c) illustrate that the dynamics can be divided into a slow evolution close to the slow manifold $\mathcal{E} \equiv 0$ in between the pulses (slow stage) and a fast and short excursion through the phase space during the pulse (fast stage). In each of the two stages, approximate analytic solutions for the dynamical system (Eqs. (5.28a)–(5.28c)) can be found [VLA05]. During the slow stage G and Q recover after the passage of the previous pulse. Throughout the recovery process, the total losses predominate the gain, thus $\mathcal{G}$ is negative. This can be seen in Fig. 5.4(a), where $Q_t > G$ holds in the slow stage. The pulses have stable background, i.e., the pulse train remains stable with respect to perturbations, as long as the perturbations are too weak to open a net gain window during the slow stage, which means that New's stability criterion [NEW74] is fulfilled [VLA05]. The leading edge of each pulse depletes G and Q on the fast timescales of the light-matter interaction given by vg_g and vg_q for gain and absorber section, respectively, where g_g and g_q are the linear gain coefficients for gain and absorber sections, respectively. For $r_s > 1$, the depletion of Q is faster than the depletion of G, which leads to a short net gain window with $\mathcal{G} > 0$ triggering the pulse (gray shaded region in Fig. 5.4(b)). The condition $r_s > 1$ means that the saturation energy of the absorber section is smaller than the one of the gain section (see Section 5.2.1 for details), thus the absorber bleaches first opening the net gain window. The faster decay of Q can also be seen from Eqs. (5.28b) and (5.28c). In the fast stage the linear terms $J_g - \gamma_g G$ and $J_q - \gamma_q Q$ can be neglected [VLA05]. Since $r_s > 1$ and $Q > G > 0$ hold at the beginning of the fast stage, the saturation term in Eq. (5.28c) that is proportional to $|\mathcal{E}|^2$ is larger than the corresponding term in Eq. (5.28b). During the net gain window the center part of the pulse is amplified.

Table 5.1.: Parameter values used in numerical simulations unless states otherwise. The values of the parameters are given with respect to physical time t as well as with respect to dimensionless time $s = t/T^*$, where $T^* = 25\,\mathrm{ps}$.

Parameter		Value		Meaning
time t	time s	time t	time s	Physical time (t) and dimensionless time (s)
γ	γ_s	$2.66\,\mathrm{ps}^{-1}$	66.5	Pulse width
γ_g	$\gamma_{s,g}$	$1\,\mathrm{ns}^{-1}$	0.025	Carrier relaxation rate in gain section
γ_q	$\gamma_{s,q}$	$75\,\mathrm{ns}^{-1}$	1.875	Carrier relaxation rate in absorber section
r_s		25		Ratio of saturation energies
J_g	G_0	$0.12\,\mathrm{ps}^{-1}$	3	Pump rate in gain section
J_q	Q_0	$0.3\,\mathrm{ps}^{-1}$	7.5	Pump rate in absorber section
κ		0.1		Cavity intensity loss-rate
T	S	$25\,\mathrm{ps}$	1	Ringcavity roundtrip time
$T_{\mathrm{ISI},0}$	$S_{\mathrm{ISI},0}$	$1.015T$	$1.015S$	Free running laser inter-spike interval time
α_g		0		Alpha factor in gain section
α_q		0		Alpha factor in absorber section
τ	S_{ec}	variable		External cavity roundtrip time
K		variable		Feedback strength
C		0		External cavity phase
$\Delta\Omega$	$\Delta\omega$	0		Detuning carrier frequency – filter maximum
R_{sp}	r_{sp}	0		Rate of spontaneous emission

5.4. Dynamics of mode-locked laser subject to optical feedback

In the previous section, we have seen that an important time scale of the solitary ML laser is the inter-spike interval time $T_{\mathrm{ISI},0}$. By including external feedback, a new time scale is introduced namely the delay time τ. The facet between the ring laser and the external cavity splits the pulse-stream into two parts: one part propagating in the ring laser and another part propagating through the external cavity. The latter is, after one roundtrip in the delay line, coupled back into the internal cavity multiplied by the feedback strength $K < 1$ and a phase shift e^{-iC}. The external cavity phase $C \equiv \Omega_0 \tau$ describes the phase shift of the light due to the finite delay time. Since the optical frequency Ω_0 is large (THz), a tiny variation of τ causes a variation of C over its full range $[0, 2\pi]$, while the variation of τ in the delayed terms $R(t-T-l\tau)$ and $\mathcal{E}(t-T-l\tau)$ in Eq. (5.28a) has only a negligible effect on the solution for $\mathcal{E}(t)$. Therefore, we consider in the following C and τ as independent parameters.

Delay time τ and phase C determine the relative temporal position and the phase relation of the pulses coupled back from the external cavity to the pulses in the laser. In this subsection, we describe the resonances of the system for the case $C = 0$ before discussing the influence of C on the dynamics in the next subsection. Throughout this section we concentrate on the case $\alpha_g = \alpha_q = 0$, which shows the clearest resonance structure. In combination with the assumption $\Delta\Omega = 0$, this yields a real valued field equation. For simplicity, we use constant initial conditions $\mathrm{Re}\left(\mathcal{E}(t)\right) = 0.4$, $\mathrm{Im}\left(\mathcal{E}(t)\right) = 0$, $G(t) = 4$, and $Q(t) = 1$ for $t \in [-\tau, 0]$ unless stated otherwise. Here Re and Im denote real and imaginary parts, respectively.

Synchronization effects can be observed if an integer multiple of τ matches an integer multiple of $T_{\mathrm{ISI},0}$, i.e.,

$$p\tau = qT_{\mathrm{ISI},0}, \quad \text{for} \quad p, q \in \mathbb{N}, \tag{5.32}$$

where the relation $p < q$ holds in the regimes of intermediate and long delays discussed here. The resonances described by Eq. (5.32) can be further sub-classified into main and higher order resonances. In the main resonances ($p = 1$), the pulses traveling in the external cavity match perfectly with the pulses in the laser cavity, and only one pulse travels in the internal cavity. In the higher order resonances ($p > 1$), p pulses may travel in the cavity, i.e., p pulses are found in an interval of length $T_{\mathrm{ISI},0}$: one main pulse stemming from the solitary laser and $p-1$ secondary pulses with smaller amplitudes that are induced by the feedback. Later on, we compare our results with the theoretical work of Avrutin et al. [AVR09]. The authors discussed a finite difference traveling wave model for a monolithic passively ML laser in the short cavity regime ($\tau \sim 3T_{\mathrm{ISI},0}$). Note that Avrutin et al. referred to main and higher order resonances as integer and fractional resonant case, respectively. Here, the notion of main and higher order resonances is preferred to emphasize the ordering of the corresponding fractions p/q in a Farey tree, which will be discussed in Subsection 5.4.5.

The maximum number of pulses in the cavity is limited by the cold cavity roundtrip time T and the width of the pulses, which is determined by γ. The longer the cavity and the smaller the pulse width, the larger is the number of pulses that can fit into the cavity. For the set of parameter values given in Table 5.1, we find up to five pulses in the cavity, i.e, $p \leq 5$. At the exact resonances, the main pulses and the feedback induced pulses are well separated by low values of the intensity. Furthermore, the pulses are almost evenly spaced over the inter-spike interval. This means, if we have p pulses and the main pulse is located at $t = 0$, the $p-1$ feedback induced pulses are located close to $lT_{\mathrm{ISI},0}/p$ for $l = 1, \dots, p-1$. Figure 5.5(a)-(d) depicts time traces of $|\mathcal{E}|$, G, Q_t and $\mathcal{G}$ (left column), phase space projections onto the (G,$|\mathcal{E}|$)-plane (middle column), and power spectra of $|\mathcal{E}|^2$ (right column) for $p = 1$ to $p = 4$ pulses in the cavity and small feedback strength

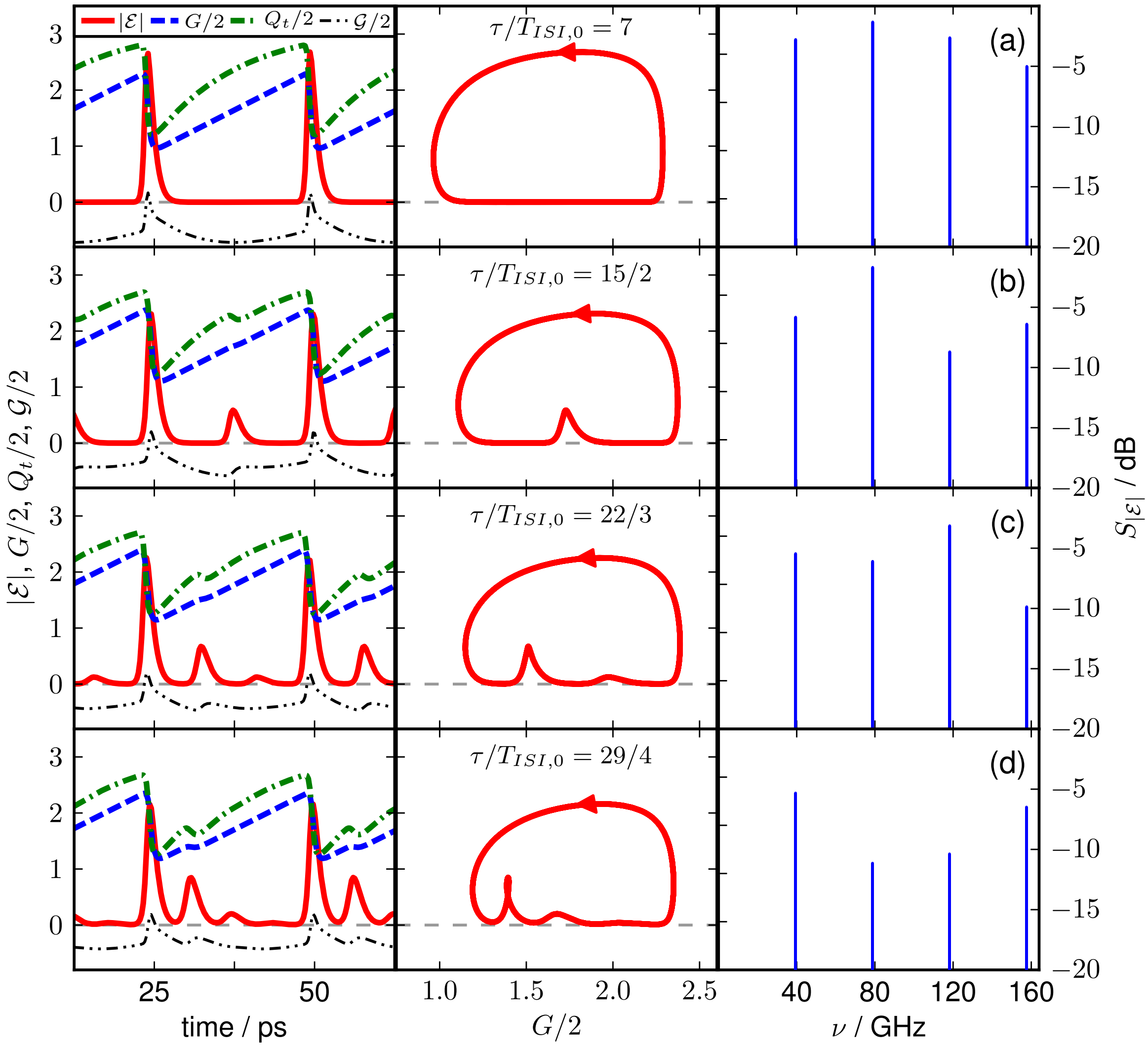

Figure 5.5.: Feedback induced deformations of the periodic orbit for a small feedback strength of $K=0.12$. The ratios of the delay time τ to the inter-spike interval $T_{\mathrm{ISI},0}$ are chosen to fulfill the resonance condition of Eq. (5.32) for $p/q=1/7$, $p/q=2/15$, $p/q=3/23$ and $p/q=4/29$ from panel (a) to (d), respectively. **Left column**: Time traces of absolute value of the amplitude $|\mathcal{E}|$ (red solid line), saturable gain G (blue dashed line), total loss Q_t (green dash-dotted line), and net gain $\mathcal{G}$ (black dash-dot-doted line). **Middle column**: Phase space projection onto the ($|\mathcal{E}|$,G)-plane. **Right column**: Power spectra. Other parameter values are as in Table 5.1.

$K = 0.12$. Periodic pulse trains with $p = 5$ different pulses have also been found, but the intensities of the smallest pulses are too low to be visible in the scale of Fig. 5.5. In the main resonances, the feedback reduces the width of the pulses and increases their peak intensities. This can be seen by comparing the peak values of $|\mathcal{E}|$ for $\tau/T_{\mathrm{ISI}} = 7$ (corresponding to $p/q = 1/7$) in Fig. 5.5(a) (left) with the ones for the solitary laser in Fig. 5.4(a) (see also Fig. 5.8 in Subsection 5.4.2). In simulations with spontaneous emission noise ($R_{\mathrm{sp}} \neq 0$), we found an enhanced stability of the pulse train with respect to noise in the main resonances. This is discussed in detail in Section 5.6. At the higher order resonances, the peak intensities of the dominant pulses decrease in the presence of delay, because the total energy of the pulse stream is now divided between the p pulses in the cavity.

5.4.1. Dependence on external cavity phase

In this subsection, we discuss the influence of the external cavity phase C on the dynamics of the ML laser for exact resonant optical feedback. In the presence of resonant optical feedback, the pulses in the external cavity interfere coherently with the pulses traveling in the internal cavity. Thus, intuitively, one could expect that the dynamics of the ML laser with resonant feedback is similar to the dynamics of a single mode laser subject to external optical feedback [AVR09]. Indeed, we find several parallels between both systems to be discussed in this section and in Section 5.5. In Fig. 5.6, the dependence of the dynamics on K and C is depicted for three different regimes of the delay time τ: short delay ($\tau = 3\,T_{\mathrm{ISI},0}$) models monolithically integrated devices as it has been done in [AVR09] (upper panel in Fig. 5.6), intermediate delay ($\tau = 7\,T_{\mathrm{ISI},0}$) models short external cavities (middle panel in Fig. 5.6), and long delay ($\tau = 67\,T_{\mathrm{ISI},0}$) describes long, fiber based external cavities that are frequently used in experiments [SOL93, LIN10e, LIN11d, LIN11f, BRE10, FIO11, ROS12b] (lower panel in Fig. 5.6). In simulations with long delay times, the system has to be integrated for many roundtrips of the light in the external cavity to exclude transient dynamics, which results in long simulations times. Therefore, long delays can be studied best with simple DDE models, which can be integrated more efficiently than partial differential equations described by finite difference traveling wave models.

Figure 5.6(a) depicts a one-parameter bifurcation diagram of the local maxima of the time trace of $|\mathcal{E}(t)|$ for short, exactly resonant optical feedback ($\tau = 3\,T_{\mathrm{ISI},0}$) in terms of K and $C = \pi$ fixed. For each K-value, the dynamic equations (5.28a)–(5.28c) have been integrated over $5 \cdot 10^4$ time units to avoid transient effects and then the local maxima of the time trace of $|\mathcal{E}|$ were collected for 100 time units. The bifurcation diagram has been obtained by up-sweeping (orange dots) and down-sweeping (black dots) K taking the last τ-interval of the previous run as initial conditions. (For the first runs of each sweep-direction the constant initial condition mentioned in the previous Section were chosen.) At a critical feedback strength $K_H = 0.14$, the fundamental mode-locked (FML) solution is destabilized in a secondary Hopf-bifurcation (or Neimark-Sacker bifurcation [KUZ95]) introducing an additional frequency into the system that is incommensurate to the pulse repetition frequency $\nu_{\mathrm{rep},0} = 1/T_{\mathrm{ISI},0}$. This leads to a quasiperiodic (QP) motion of the trajectory on a torus in phase-space. For increasing K, a cascade of bifurcation takes

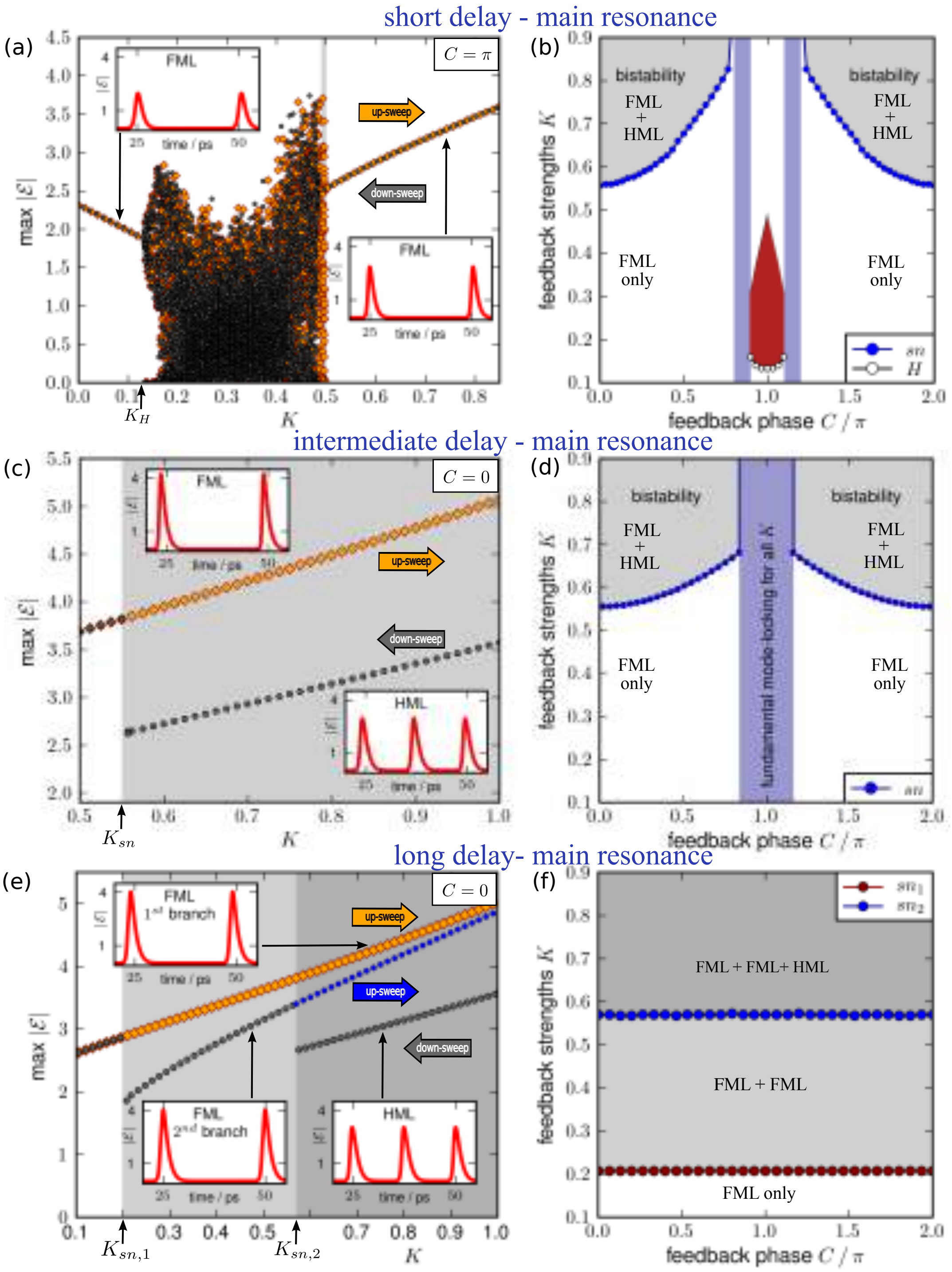

Figure 5.6.: **Left column**: One-parameter bifurcation diagrams of the maxima of $|\mathcal{E}|$ versus feedback strength K for stepwise increase (up-sweep, orange diamonds and blue circles) and decrease of K (down-sweep, black circles) in the exact main resonance and fixed feedback phase C. **Right Column**: Saddle-node bifurcation lines ($\mathrm{sn}, \mathrm{sn}_2$, blue circles, sn_1 red circles) and Hopf (H, open circles) bifurcation lines in (C, K)-plane. **Upper panel**: Short delay time $\tau = 3\,T_{\mathrm{ISI},0}$ and $C = \pi$ in **(a)**. **Middle panel**: Intermediate delay time $\tau = 7\,T_{\mathrm{ISI},0}$ and $C = 0$ in **(c)**. **Lower panel**: Long delay time $\tau = 67\,T_{\mathrm{ISI},0}$ and $C = 0$ in **(e)**. Light (dark) gray shaded area for $K > K^{\mathrm{sn}}, K^{\mathrm{sn},1}$ $(K > K^{\mathrm{sn},2})$ marks region of bistability (tristability) between fundamental mode-locking (FML) and harmonic mode-locking (HML), and $K^{\mathrm{sn}}, K^{\mathrm{sn},1}, K^{\mathrm{sn},2}$ and K_H mark K values of saddle-node and Hopf-points respectively. Insets show time traces of $|\mathcal{E}|$ for the FML and the HML branches, respectively. Red shading in **(b)** marks an instability region. Other parameters as in Table 5.1.

place leading to chaotic motion, before the laser is re-stabilized on a FML solution at $K = 0.48$. For this value of $C = \pi$, only a small region of bistability between the chaotic dynamic and the FML solution is observed by up- and down-sweep of τ (gray shaded region). Lower and upper insets in Fig. 5.6(a) depict time traces of $|\mathcal{E}(t)|$ for the FML solution before ($K = 0.1$) and after ($K = 0.75$) the bifurcation cascade, respectively. This bifurcation scenario is similar to the one observed for single mode semiconductor lasers in the short cavity regime [HEI01a, HEI03a, OTT10] (see discussion in Section 4.4). Figure 5.6(b) depicts the dependence of the saddle-node and secondary Hopf bifurcation lines on the external cavity phase C and feedback strength K as observed by down-sweeping K starting with constant initial conditions from $K = 1$. Figure 5.6(b) reveals that the system is 2π-symmetric with respect to C, which can be seen directly from the field Eq. (5.28a). The secondary Hopf-bifurcation (H, open circles) takes place in a small interval symmetric around $C = 0$ leading to the instability region discussed above (red shaded region). The minimum of the Hopf-line and the largest extension of the instability region is found for $C = 0$. Adjacent to the instability region, two thin intervals are observed, for which the system remains stable on the FML solution for all K (blue shaded regions). These findings are in agreement with the observations of Avrutin et al. [AVR09]. In a broad symmetric interval around $C = 0$, a saddle-node bifurcation line of limit-cycles (fold bifurcation [KUZ95]) (sn, blue circles) creates a new pair of solutions: a stable branch of node-solutions and an unstable saddle branch. The node-solution is a harmonically mode-locked solution (HML) with a repetition frequency of $\nu_{\mathrm{rep}} = 2\nu_{\mathrm{rep},0}$. In the (C, K)-plane, the sn-line forms a parabola symmetric around $C = 0$ with a minimum at $C = 0$. For K values above the sn-bifurcation line, bistability is observed between FML and HML solutions (gray shaded regions labeled FML+HML).

Figures 5.6(c) and (d) correspond to Figs 5.6(a) and (b), but depict the dynamics for intermediate delay times. In this regime, the laser remains in the fundamental mode-locked regime for all K if $C = \pi$. Therefore, in contrast to Fig. 5.6(a), the phase $C = 0$ has been chosen in Fig. 5.6(c) to reveal bistability between a branch of FML and a branch of HML solutions. To focus on the bistability region, additionally, a different K-range has been chosen in Fig. 5.6(c) than in Fig. 5.6(a). At the critical feedback strength $K^{\mathrm{sn}} = 0.55$, a new mode anti-mode pair of solutions becomes available to the system in a fold bifurcation. The mode solution is stable and yields HML with $\nu_{\mathrm{rep}} = 2\nu_{\mathrm{rep},0}$. The creation of new mode anti-mode pairs in fold bifurcations is also observed in single mode lasers subject to feedback as discussed in Section 4.6.1. This underlines the assumption of Avrutin at al. [AVR09] that the structure of solutions with time periodic intensity of a ML laser subject to resonant optical feedback is similar to the structure of rotating wave solution (external cavity modes) of a single mode laser subject to feedback. For $K > K^{\mathrm{sn}}$, the laser is bistable (gray shaded region). For up-sweeping K, the system remains in the FML regime with period $T_{\mathrm{ISI},0}$. The upper inset in Fig. 5.6(c) shows a time trace of $|\mathcal{E}(t)|$ in this regime for $K = 0.8$. However, for the constant initial conditions and the highest possible K-value of $K = 1$, the system exhibits harmonic mode-locking. For down-sweeping K, the HML branch of solutions remains stable until $K = K^{\mathrm{sn}}$, where the HML solution is annihilated in a fold bifurcation, and the system abruptly jumps back to the FML branch. The lower inset in Fig. 5.6(a) depicts a time trace of $|\mathcal{E}(t)|$ for the HML solution and $K = 0.8$. Figure 5.6(d) depicts the dependence of the feedback strength of the fold bifurcation line K^{sn} on the feedback phase C as observed by down-sweeping K starting with constant initial conditions from $K = 1$. The lowest value of K^{sn} is observed for $C = 0$, and K^{sn} increases strongly with C. In a symmetrical interval around $C = \pi$, the system remains in the FML regime and no bistability is observed (blue shaded region).

A bifurcation diagram of the maxima of $|\mathcal{E}|$ as in Fig. 5.6(c), but for long delay ($\tau = 67\,T_{\mathrm{ISI},0}$), is depicted in Fig. 5.6(e). By up-sweeping K from $K = 0$, the laser remains in the FML state for all K. For down-sweeping K, the system remains in a HML state down to $K^{\mathrm{sn},2} = 0.56$ and then abruptly jumps to a second FML branch before jumping back to the first FML branch at $K^{\mathrm{sn},1} = 0.2$. By up-sweeping K starting at the second FML branch, we find that this branch remains stable up to the highest value of K (blue dots). In terms of bifurcation theory, bistability is induced into the system by a first fold bifurcation at $K^{\mathrm{sn},1}$ (light shaded area), and a second fold bifurcation at $K^{\mathrm{sn},2}$ induces tristability into the system (dark shaded area). This means that in contrast to short and intermediate delay, an additional stable solution becomes available to the system for long delay in the first fold bifurcation at K^{sn}. This scenario is well known from delay differential equations with long delay, where with increasing delay more solutions become available to the system leading to more complex dynamics [YAN04, YAN06, WOL10, YAN10]. The two fold bifurcation lines sn_1 (red circles) and sn_2 (blue circles) in the (C, K)-plane reveal that there is no dependence on the external cavity phase C. Also in Lang-Kobayashi type single-mode lasers, one finds that in the limit of long delay the dynamics is independent of the external cavity phase C [KAN05].

In conclusion, comparing the three bifurcation diagrams in the (C, K)-plane (right column of Fig. 5.6), one sees that the minimum of the fold bifurcation line (blue dots labeled by sn in Fig. 5.6(b) and (d) and sn_2 in Fig. 5.6(e)) occurs for $C = 0$. Further, it is independent of the delay time τ. However, the range of phases C, for which we observe bistability between FML and HML solutions broadens with increasing τ until the fold bifurcations become independent of C for long delay. For short delay, more complex dynamics is induced by a secondary Hopf-bifurcation in an interval around $C = \pi$, while for long delay tristability is induced by an additional fold bifurcation line sn_1.

5.4.2. Dependence on delay time and feedback strength

To present a more complete picture of the feedback induced dynamics away from the exact resonances, now the dependence of the dynamics of the ML laser subject to feedback on the delay time τ is studied. In this and the following subsections, we concentrate on intermediate delay times modeling a short external cavity. Afterward, the regime of long delays is discussed in Section 5.4.6.

Figure 5.7 depicts the number of pulses in the cavity (color code) as a function of delay time τ and feedback strength K for $C = 0$. For each pair of (τ,K)-values, the system was integrated over $3 \cdot 10^4$ time units, and then the number of maxima with different peak heights is counted for 25 time units. For up-sweeping τ (Fig. 5.7(a)) for each K and the lowest value of τ, the constant initial conditions were chosen that were discussed in the beginning of Section 5.4. Then, τ was increased stepwise from its lowest value taking an interval of length τ from the end of the time series of the previous run as

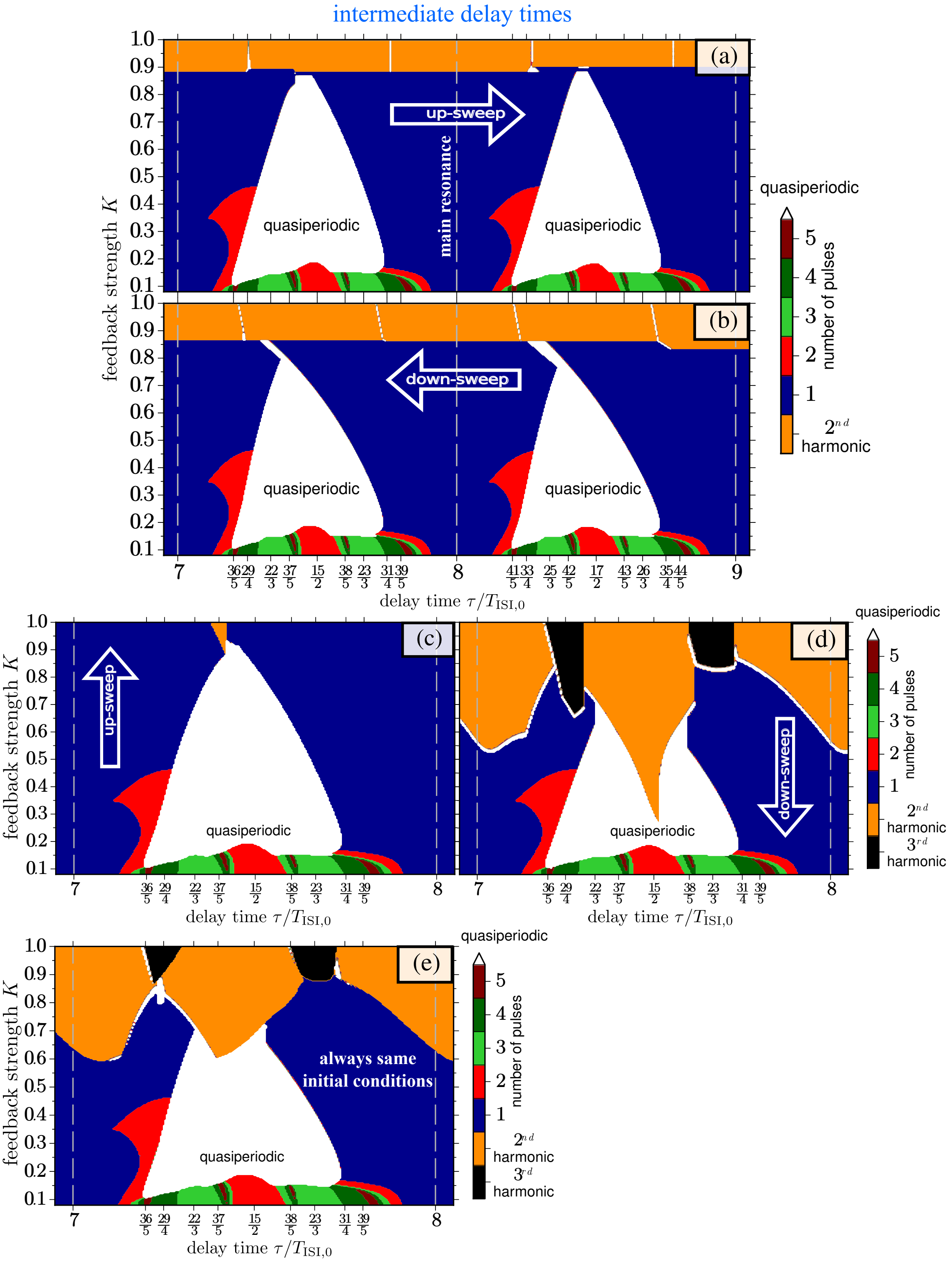

Figure 5.7.: Two-parameter bifurcation diagram of the dynamics of the ML laser subject to external optical feedback in terms of delay time τ (in units of the interspike interval of the solitary laser $T_{\mathrm{ISI},0}$) and feedback strength K in the regime of intermediate delay times obtained by **(a)**: up-sweeping τ, **(b)**: down-sweeping τ, **(c)**: up-sweeping K, **(d)**: down-sweeping K, and **(e)**: always identical, constant initial conditions for each tuple of (τ, K)-values. The color code provides the number of pulses in the cavity. White, orange, and black regions indicate quasiperiodic pulse trains, 2^{nd}, and 3^{rd} order harmonic mode-locking, respectively. Parameters as in Table 5.1.

initial condition in each step. To catch bistabilities, the same procedure was performed by down-sweeping τ from its maximum to its lowest value (Fig. 5.7(b)). To give a more complete picture of the different dynamical regimes also K, instead of τ, was up- and down-swept in Figs. 5.7(c) and (d), respectively. Furthermore, Fig. 5.7(e) depicts the dynamical regimes observed by choosing identical, constant initial conditions for each tuple of (τ, K)-values. The contour plots of Fig. 5.7 are almost periodic in τ. Their periodicity of $T_{\mathrm{ISI},0}$ corresponds to the distance between the vertical white dashed lines within the large cone-like blue areas around the main resonances $\tau = 7\,T_{\mathrm{ISI},0}$, $\tau = 8\,T_{\mathrm{ISI},0}$, and $\tau = 9\,T_{\mathrm{ISI},0}$. Within these blue areas, we find complete synchronization, i.e, only one pulse travels in the cavity. In the following, we call these intervals main resonant regimes. For increasing K, the resonant regimes broaden and the laser synchronizes also for larger deviations from the exact main resonances. The increase of their width is not linear in K, instead a sudden broadening is observed for $K \approx 0.15$, which we interpret as a transition from small to intermediate values of K. Away from the main resonant regimes this transition is marked by the appearance of QP pulse forms (white region) to be discussed in Subsection 5.4.3.

In Fig. 5.8, bifurcation diagrams of the local maxima of $|\mathcal{E}|$ in terms of the delay time τ are depicted for different K. They correspond to one dimensional sections of Fig. 5.7 for small $K = 0.1$ (Fig. 5.8(a)), intermediate $K = 0.4$ (Fig.5.8(b)), large $K = 0.65$ (5.8(c)), and very large $K = 0.9$ (5.8(d)). Thus, Fig. 5.8 provides us with additional information about the height of the pulse maxima in comparison to the ones of the solitary laser (horizontal blue dash-dotted lines) and multistability regions are revealed more clearly than in Fig. 5.7. To catch multistabilities, the local maxima of $|\mathcal{E}|$ are plotted as obtained by up-sweeping τ (large red dots), by down-sweeping τ (gray dots), and by down-sweeping K (small black dots). The local maxima of $|\mathcal{E}|$ obtained by down-sweeping K and by always identical initial conditions do not contribute additional multistabilities for the chosen K-values and are omitted for clarity.

For small K, we find that the periodic orbit is deformed by the feedback in a nonlinear way (see Fig. 5.5 (middle column)). These deformations lead to τ-intervals around the exact higher order resonances (Eq. (5.32) with $2 \leq p \leq 5$), where we find p pulses in the cavity that are well separated by low values of the intensity. They appear as red, light green, dark green, and brown regions in Fig. 5.7, and they are denoted as higher order resonant regimes in the following. For very small values of K and $p = 5$, the smallest pulse cannot be detected numerically. This is why the brown regions indicating the presence of five pulses in the cavity do not reach down to the lowest K-value ($K = 0.08$ for $\tau/T_{\mathrm{ISI},0} = 37/5$ and $\tau/T_{\mathrm{ISI},0} = 38/5$ as well as for $\tau/T_{\mathrm{ISI},0} = 42/5$ and $\tau/T_{\mathrm{ISI},0} = 43/5$). From Fig. 5.8(a), it can be seen that in the main resonant regime the pulse height is increased compared to the pulse height of the solitary laser (compare pulse heights around $\tau = 7\,T_{\mathrm{ISI},0}$ and $\tau = 8, T_{\mathrm{ISI},0}$ with blue dash-dotted line). At the same time, the pulse width is decreased, which results in an enhanced stability of the pulses with respect to perturbations introduced for example by spontaneous emission noise. In Section 5.7, the enhanced stability of the pulse stream in the main resonant regime with respect to timing fluctuations is discussed in the context of the timing jitter. Figures 5.8(b) and (c) show that the increase of the height of the pulses in the main resonant regime becomes more pronounced for higher feedback strengths K leading to an enhancement

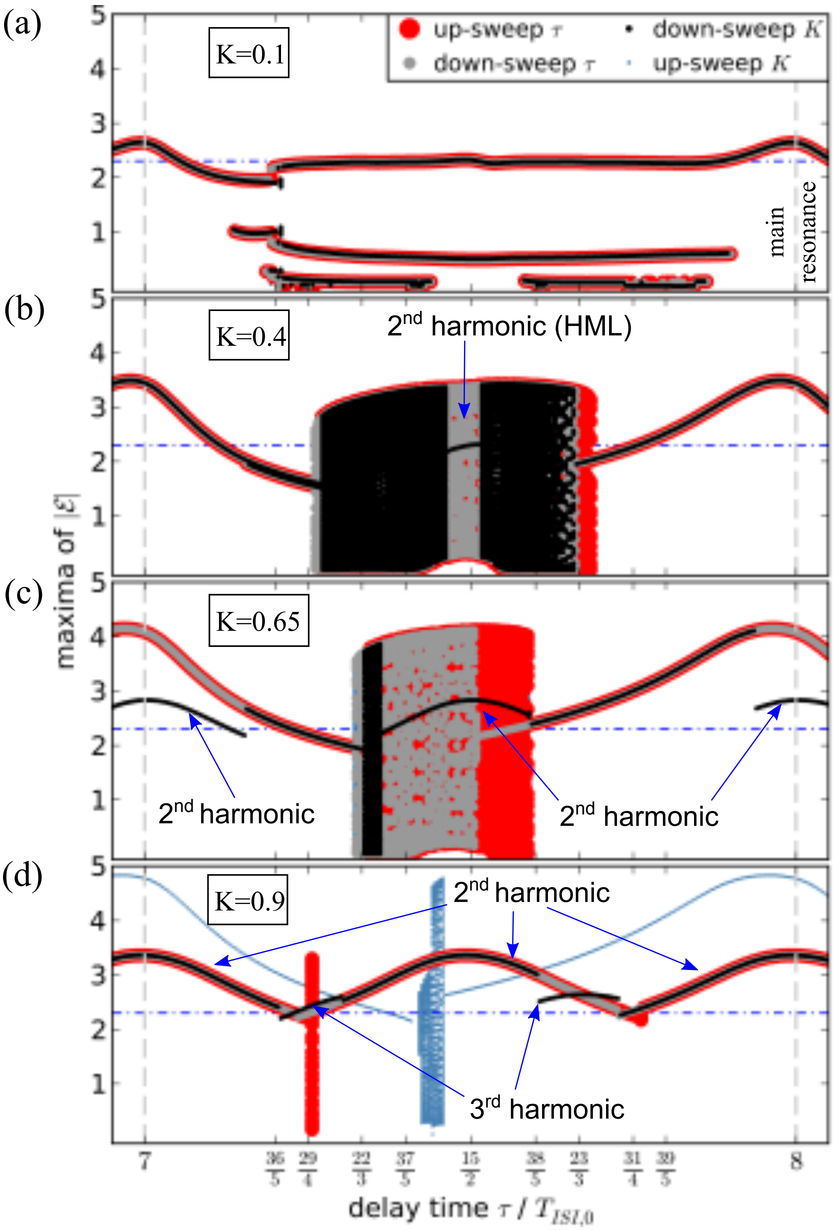

Figure 5.8.: One-parameter bifurcation diagrams of local extrema of the time trace of $|\mathcal{E}|$ in terms of τ (in units of the interspike interval of the solitary laser $T_{\mathrm{ISI},0}$) for intermediate delay times as obtained by up-sweeping τ (large red dots), by down-sweeping τ (gray dots), by down-sweeping K (small black dots), and by up-sweeping K (tiny blue dots) for fixed **(a)**: $K = 0.1$, **(b)**: $K = 0.4$, **(c)**: $K = 0.65$, and **(d)**: $K = 0.9$. The blue dash-dotted lines mark the maxima of the time trace of $|\mathcal{E}|$ of the ML solitary laser. Blue arrows indicate 2^{nd} and 3^{rd} order harmonically mode-locked solutions.

of the temporal stability of the pulses for increasing K. Furthermore, the maximal pulse heights are no longer found at the exact resonances but shift to shorter delay times.

In between the resonant regimes, the mismatch of the two timescales τ and $T_{\mathrm{ISI},0}$ leads to overlapping pulses that are not well separated by low values of the intensity. We find broad (main) pulses that are not unimodal but have one to three side-peaks. In the following, we call these τ-intervals between two adjacent resonant regimes non-resonant regimes. In the non-resonant regime in between the main resonant regime around $\tau/T_{\mathrm{ISI},0} = 7$ and the fifth order resonant regime around $\tau/T_{\mathrm{ISI},0} = 36/5$, a broadened pulse with one to three sidepeaks is observed leading to the regions with two (red), three (light-green), and four maxima (dark-green), respectively. (The same holds for τ values in between the main resonant regimes around $\tau/T_{\mathrm{ISI},0} = 8$ and $\tau/T_{\mathrm{ISI},0} = 9$ and the adjacent fifth order resonant regimes, respectively.) Also between adjacent higher order resonances, non-resonant regimes are observed, which are for example responsible for the light-green ($p = 3$) and dark-green ($p = 4$) colored regions between the second order resonance regimes around $\tau/T_{\mathrm{ISI},0} = 15/2$ and $\tau/T_{\mathrm{ISI},0} = 17/2$ (red) and the adjacent fifth order regimes (brown), respectively.

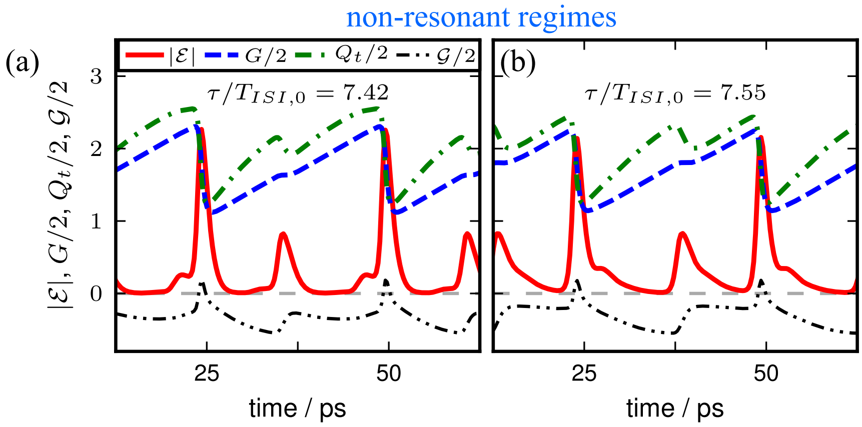

Figure 5.9.: Time traces of absolute value of the amplitude $|\mathcal{E}|$ (red solid line), saturable gain G (blue dashed line), total loss Q_t (green dash-dotted line), and net gain $\mathcal{G}$ (black dash-dot-doted line) in the non-resonant regimes between the second order resonant regime around $\tau/T_{\mathrm{ISI},0} = 15/2$ and the fifth order resonant regimes around $\tau/T_{\mathrm{ISI},0} = 37/5$ **(a)** and $\tau/T_{\mathrm{ISI},0} = 38/5$ **(b)**, respectively. Parameters $K = 0.12$ and other parameters as in Table 5.1.

For $K = 0.12$, Fig. 5.9 shows time traces of $|\mathcal{E}|$, G, Q_t, and $\mathcal{G}$ in the non-resonant regimes to the left (see Fig. 5.9(a)) and to the right (see Fig. 5.9(b)) of the second order resonant regime around $\tau/T_{\mathrm{ISI},0} = 15/2$, respectively. We observe broadened main pulses with shoulders at the leading (see Fig. 5.9(a)) and trailing edge (see Fig. 5.9(b)) of the main pulse, respectively. The pulses in the non-resonant regimes have relatively low peak intensities compared to the pulses in the resonant regimes. This can be seen in Fig. 5.8(a) by comparing the heights of the maxima of $|\mathcal{E}|$ for $\tau = 7\,T_{\mathrm{ISI},0}$ (exact main resonance) and slightly on the left of the fifth order resonance with $\tau = 36/5, T_{\mathrm{ISI},0}$ (off resonant regime) (cf. also Fig. 5.9 and Fig. 5.5(left panel)). In addition, the net gain $\mathcal{G}$ (dash-dot-dotted line) shows a broad shoulder with only slightly negative values between the small pulse and the leading edge of the next larger pulse. This is why the pulses in the non-resonant regimes are more easily destabilized by noise than the pulses in the resonant regimes (see Subsection 5.7).

Comparing Fig. 5.7(a)–(e) for small feedback strengths $K \lesssim 0.15$, one sees that in this regime nearly no multistabilities are observed. In the one dimensional bifurcation diagram of Fig. 5.8(a) depicting the situation for $K = 0.1$, we find only one small bistability interval for τ-values slightly larger than the fifth order resonance with $\tau = 36/5\, T_{\mathrm{ISI},0}$. Further, in this regime of small K, the dynamics is robust against changes of the feedback phase C except for the small bistability interval mentioned before. However, the situation changes for higher values of K. Comparing Fig. 5.8(d) with Fig. 5.8(a)–(c), one observes a bistability between QP motion on a torus in phase space and a 2^{nd} order HML solution in the second order resonant regime for $K > 0.36$. Both, QP and HML solutions are discussed in detail in Subsection 5.4.3 and Subsection 5.4.4, respectively. Furthermore, bistabilities between QP and FML solutions are found at the borders of the QP regions (white cones) (compare Fig. 5.7(a) and Fig. 5.7(b)). This can also be seen in the bifurcation diagram of Fig. 5.8(b) depicting the situation for $K = 0.4$. The HML solution is indicated by the blue arrow labeled 2^{nd} harmonic, and the bistability between QP and FML solutions is revealed by the red and the gray regions at the edges of the instability interval. The interval around the 2^{nd} order resonance, in which the HML solution is found, broadens with K and for $K > 0.53$ also in the main resonant regime 2^{nd} order HML solutions are observed, which are bistable with the FML solution. This can be seen best in the one dimensional bifurcation diagram of Fig. 5.8(c) for $K = 0.65$ close to the vertical gray dashed lines (exact main resonances) by comparing the small black dots denoting the FML solution with the red and gray dots denoting the HML solution. Further, comparing Figs. 5.8(b) and (c) reveals that with increasing K the bistability-interval around the second order resonance ($\tau = 15/2\, T_{\mathrm{ISI},0}$), in which the 2^{nd} order HML solution (black dots) and the QP solution (blue, read, and gray dots) are both stable, broadens.

For very high $K \gtrsim 0.9$, Fig. 5.7(a) and (b) show that 2^{nd} order HML solutions are stable over the whole $T_{\mathrm{ISI},0}$-interval. Further, Fig. 5.7(c) reveals that also FML solutions with only one pulse in the cavity are stable nearly of the whole $T_{\mathrm{ISI},0}$-interval, and from Figs. 5.7(d) and (e), it becomes obvious that also stable 3^{rd} order HML solutions exist in an interval between $\tau = 36/5\, T_{\mathrm{ISI},0}$ and $\tau = 22/3\, T_{\mathrm{ISI},0}$ as well as in the third order resonant regime around $\tau = 23/3\, T_{\mathrm{ISI},0}$. From the one dimensional bifurcation diagram in Fig. 5.8(d), one clearly sees that the 2^{nd} order HML solutions have a periodicity of $T_{\mathrm{ISI},0}/2$ with respect to τ (see red or gray dots). For this high value of K, they are already stable over the whole $T_{\mathrm{ISI},0}/2$ interval and the white stripes in Fig. 5.7(a) and (b) mark the transitions between adjacent 2^{nd} order HML solutions. Further, Fig. 5.8(d) reveals that 2^{nd} order HML branches overlap, i.e., bistability between 2^{nd} order HML solutions is found. This can be seen for example in an interval around the $\tau = 31/4\, T_{\mathrm{ISI},0}$ resonance by comparing the black and the red dots. In a small interval around the forth order resonance with $\tau = 29/4\, T_{\mathrm{ISI},0}$, a 3^{rd} order HML solution coexists with a stable FML solution (tiny blue dots), a stable 2^{nd} order HML solutions (gray dots) as well as with a QP solution (red dots).

Figures 5.7 and 5.8 were obtained for a fixed value of the external cavity phase $C = 0$. For low values of K, the dynamics is only negligible effected by changes of C. But for high values of $K \gtrsim 0.36$, where multistabilities are observed, the trajectory can switch from one attractor to another by changing C.

Summing up, with increasing K, the structure of coexisting stable periodic and QP solutions becomes already quite involved in the simple case of zero α-factors and intermediate delay times. Thus, for high K, Figs. 5.7 and 5.8, which were obtained by direct numerical integration, can only give an overview over the different dynamical regimes, but they cannot provide a complete picture of all coexisting periodic solutions. For long delay times and nonzero α-factors, the structure of solutions becomes more complex, which will be discuss in the Subsections 5.4.6 and 5.5, respectively.

5.4.3. Quasiperiodic motion

Examples for the QP behavior that is observed away from the main resonant regimes for intermediate and high values of K (white regions in Fig. 5.7) are depicted in Fig. 5.10 for $K = 0.25$. Figure 5.10(a) and (b) depict the dynamics at the second and third order resonance with $\tau/T_{\mathrm{ISI},0} = 15/2$ and $\tau/T_{\mathrm{ISI},0} = 22/3$, respectively. We find two and three competing pulse trains, respectively, leading to a periodic modulation of the peak amplitude of the pulses. Like in the periodic regime for small K, the inter-pulse temporal distance is given at the exact resonances by approximately $T_{\mathrm{ISI},0}/2$ and $T_{\mathrm{ISI},0}/3$ resulting in dominant frequencies of $2\nu_{\mathrm{rep},0}$ and $3\nu_{\mathrm{rep},0}$, respectively (see Fig. 5.10 (right panel)). The lowest frequency in the power spectra is the competition frequency ν_c of neighboring pulse trains, which is small ($\sim 1-3\,\mathrm{GHz}$) compared to the pulse repetition frequency $\nu_{\mathrm{rep},0} \equiv 1/T_{\mathrm{ISI},0}$. Thus we plot only the maxima of the competing pulse trains

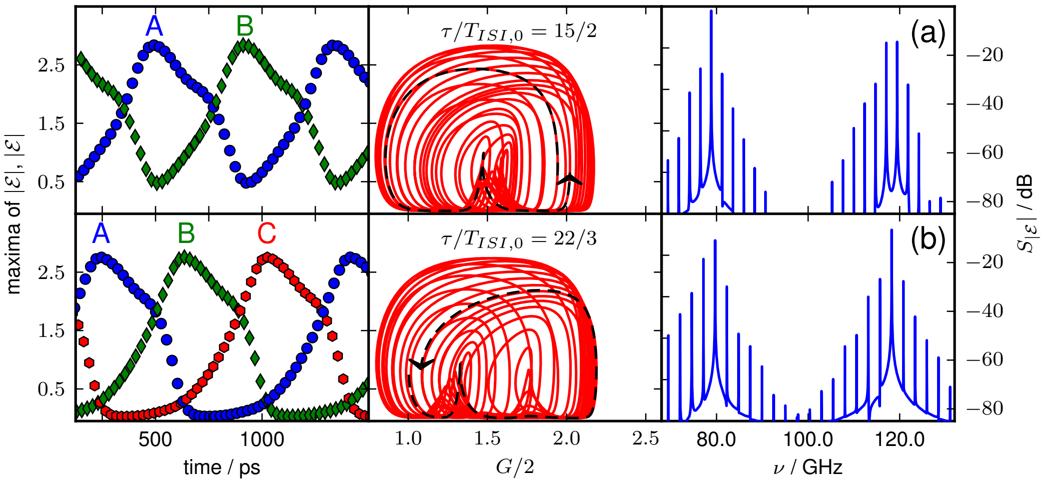

Figure 5.10.: Quasiperiodic pulse trains found in the white regions of Fig. 5.7. **Left column**: Local maxima of the time trace of $|\mathcal{E}|$. Competing pulse trains are labeled by A (blue circles), B (red circles) and C (green diamonds), respectively. **Middle column**: Phase space projections onto the $(G,|\mathcal{E}|)$-plane (red orbit). The black-dashed orbits indicate projections of an $T_{\mathrm{ISI},0}$-interval of the time series ($T_{\mathrm{ISI},0}$ is the inter-spike interval time). **Right column**: Power spectra. **Panel (a)**: Second order resonance $p = 2$ ($\tau/T_{\mathrm{ISI},0} = 15/2$). **Panel (b)**: Third order resonance $p = 3$ ($\tau/T_{\mathrm{ISI},0} = 22/3$). Parameters: $K = 0.25$ and other parameters as in Table 5.1.

in Fig. 5.10(a) and (b) (left column). For the second order resonance (see Fig. 5.10(a)), two competing pulse trains appear that are labeled A and B. Their competition frequency $\nu_c = 2.38\,\mathrm{GHz}$ corresponds to the temporal distance between the largest maximum of pulse train A and the largest maximum of pulse train B. For the third order resonance (Fig. 5.10(b) (left)), we find three competing pulse trains A, B, and C with a competition frequency of $\nu_c = 2.55\,\mathrm{GHz}$. The two (three) competing pulses can also be seen in the phase space projection onto the $(G,|\mathcal{E}|)$-plane in Fig. 5.10(a) (middle) that shows projections of the trajectories for one competition period $T_c \equiv 1/\nu_c$. The black dashed parts of the trajectory are the projection of one $T_{\mathrm{ISI},0}$-interval of the limit cycle.

5.4.4. Harmonic mode-locking in higher order resonances

In this subsection, we take a closer look at the dynamics in the exact second and third order resonances. In Figs. 5.7(d) and (e) and Fig. 5.8(d), we have found stable 2^{nd} and 3^{rd} order HML solutions for high K in the second and the third order resonances, respectively. This is expected from the resonance condition of Eq. (5.32), because the resonance condition for a p-th order resonance of a FML solution with an inter-spike interval time of $T_{\mathrm{ISI}} = T_{\mathrm{ISI},0}$ ($p\tau = qT_{\mathrm{ISI},0}$) is simultaneously the condition for a main resonance of a p^{th} order HML solution with inter-spike interval time $T_{\mathrm{ISI}} = T_{\mathrm{ISI},0}/p$, which reads

$$1\,\tau = \frac{T_{\mathrm{ISI},0}}{p}.$$

Thus, in the second and the third order resonances, we expect that stable 2^{nd} order HML solutions ($T_{\mathrm{ISI}} = T_{\mathrm{ISI},0}/2$) and 3^{rd} order HML solutions ($T_{\mathrm{ISI}} = T_{\mathrm{ISI},0}/3$) can exist.

Figures 5.11(a) and (b) depict one parameter bifurcation diagrams of the local maxima of time traces of $|\mathcal{E}|$ for K varying from 0 to 1 in the second order resonance with $\tau = 15/2\,T_{\mathrm{ISI},0}$ and in the 3^{rd} order resonance with $\tau = 23/3\,T_{\mathrm{ISI},0}$, respectively. The diagrams have been obtained by up-sweeping (large red dots) and down-sweeping (black dots) K as described for Fig. 5.6. For small K, we retrieve the periodic pulse trains with $p = 2$ and $p = 3$ pulses in the cavity (see Figs. 5.5(b) and (c)). Time traces of these pulse trains are also depicted in the leftmost insets of Fig. 5.11(a) and (b) for $K = 0.12$. At feedback strength of $K_H = 0.19$ for the second order resonance and of $K_H = 0.14$ for the third order resonance, a new incommensurate frequency is introduced into the system by a secondary Hopf bifurcation leading to a quasiperiodic motion on a torus in phase space (cf. Fig. 5.10(a)). For the 2^{nd} order resonance and up-sweeping K, the system remains on the QP branch of solutions up to $K = 0.84$, where it eventually stabilizes again onto a FML branch of solutions. Starting with constant initial conditions from the highest possible K-value $K = 1$ and then decreasing K stepwise, a HML branch of solutions is stable down to $K_{\mathrm{crit}} = 0.295$. Thus, for $K \geq K_{\mathrm{crit}}$, bistability of solutions is observed, which is marked by a gray shading in Fig. 5.11. For $K \in [K_{\mathrm{crit}}, 0.83]$, a FML and a QP branch of solutions are bistable, and for $K \in [0.83, 1]$ bistability between the FML and a HML branch of solutions is observed. The middle and the rightmost insets in Fig. 5.11(a) depict time traces of the 2^{nd} order HML and the coexisting FML solutions for $K = 0.9$, respectively.

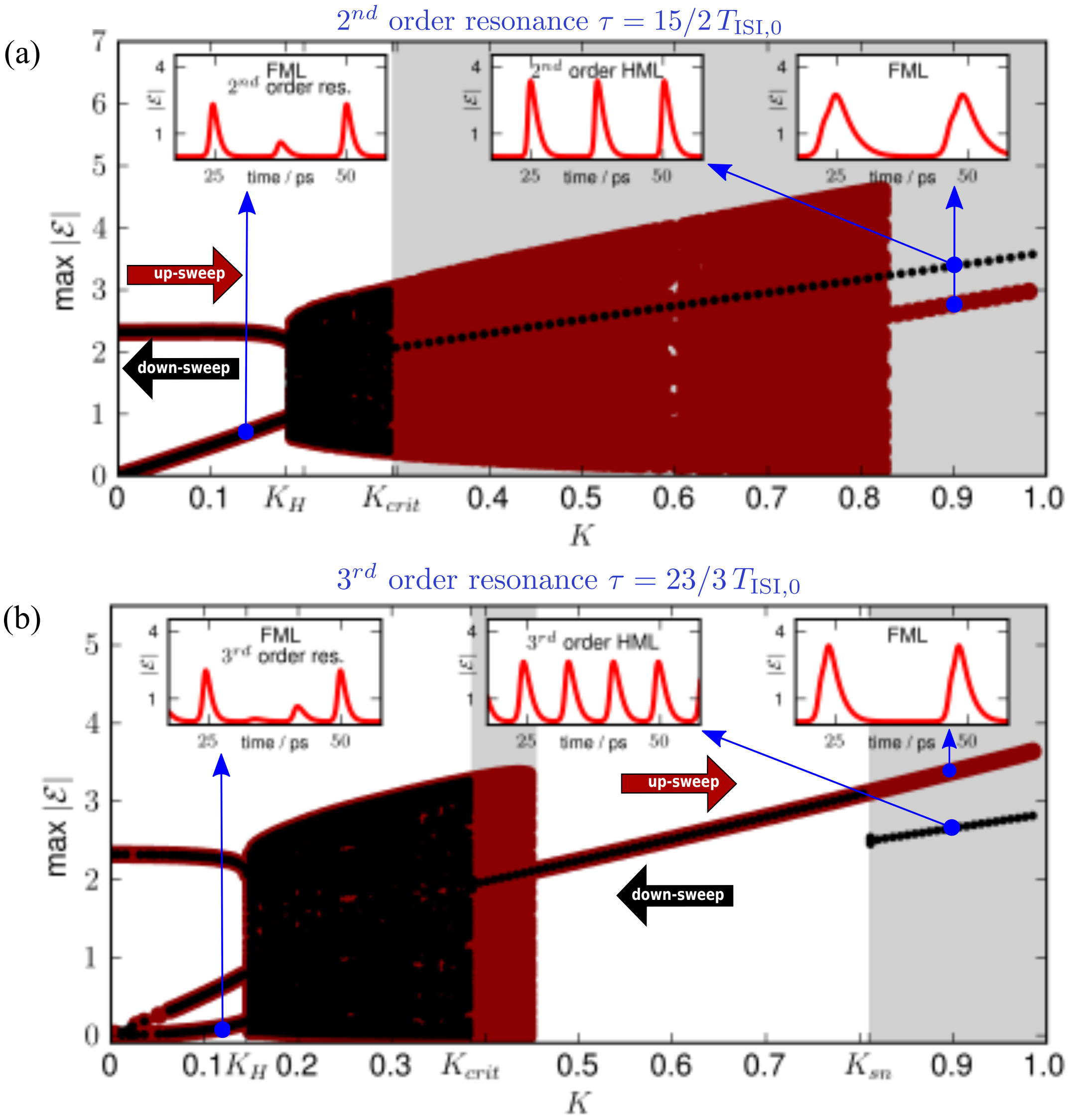

Figure 5.11.: One-parameter bifurcation diagrams showing the amplitude maxima of the pulses as a function of feedback strength K for up-sweeping K (large red dots) and down-sweeping K (black dots), respectively. Gray shadings mark bistability regions. K_H, K_{crit}, and K^{sn} denote the first Neimark-Sacker (secondary Hopf) bifurcation point, the onset of bistability, and the fold (saddle-node of limit-cycles) bifurcation point, respectively. **(a)**: Second order resonance with $\tau = 15/2\,T_{\mathrm{ISI},0}$. Left, middle, and rightmost insets depict time traces of $|\mathcal{E}|$ of the FML solution for $K = 0.12$, of the 2^{nd} order HML solution for $K = 0.9$ (down-sweeping K), and of the FML solution for $K = 0.9$ (up-sweeping K), respectively. **(b)**: Third order resonance with $\tau = 23/3\,T_{\mathrm{ISI},0}$. Left, middle, and rightmost insets depict time traces of $|\mathcal{E}|$ of the FML solution for $K = 0.12$, of the 3^{rd} order HML solution for $K = 0.9$ (down-sweeping K), and of the FML solution for $K = 0.9$ (up-sweeping K), respectively.

In the third order resonance depicted in Fig. 5.11(b), bistability between a QP solution obtained by up-sweeping K and a FML solution obtained by down-sweeping K is induced at $K_{\mathrm{crit}} = 0.38$. Again, bistability regions are marked by gray shadings. At $K = 0.48$, the system hops from the QP branch to the FML branch rendering the system again monostable. At high $K^{\mathrm{sn}} = 0.81$, a fold bifurcation introduces a branch of stable 3rd order HML solutions, which remains stable up to $K = 1$. Middle and rightmost insets in Fig. 5.11(b) depict time traces of $|\mathcal{E}|$ of the coexisting 3rd order HML solution obtained by down-sweeping K and the FML solution obtained by up-sweeping K for $K = 0.9$, respectively.

Comparing the pulse forms of the FML solutions for high K in the rightmost insets of Fig. 5.11(a) and (b) with the HML solutions in the middle insets as well as with the time trace of $|\mathcal{E}|$ of the solitary laser in Fig. 5.4(a), it becomes obvious that the pulses of the FML state are much broader than the pulses of the solitary laser. Thus, we can conclude that for high K the FML branch of solutions is less stable subject to perturbations than the HML branch. As a result, only the HML branch remains stable for high K if the laser is subject to spontaneous emission noise.

5.4.5. Farey tree

The resonances of the inter-spike interval time $T_{\mathrm{ISI},0}$ and the external delay time τ given by Eq. (5.32) may be ordered in a Farey-sequence (or Haros-Farey-sequence) [COB03]. Therefore, we compare the pulse trains found in the ML laser subject to feedback to the locking dynamics of externally driven dynamical systems. A generic example for such a system is the circle map with an external forcing [SCH89c], where the forcing introduces an additional frequency into the system and leads to dynamic evolution on a torus in phase space. We now shortly recall the concept of Farey tree ordering in these systems before we show that this concept can be also applied to the ML laser with delay. In general, the frequency of the external signal and the resulting resonance frequency of the system itself are non-commensurate, which results in a quasiperiodic motion on the surface of a torus. Locking takes place if the ratio of the frequency of the external signal and the resonance frequency of the system is a rational number p/q with $p, q \in \mathbb{N}$. The fractions p/q are called winding numbers and can be ordered in a Farey-tree by applying the Farey-sum operation [SCH01]. This means that the denominators and the numerators of two neighboring fractions p/q and p'/q' are added up separately yielding a new fraction $(p+p')/(q+q')$ in the next higher level of the tree (see Fig. 5.12(a)). With increasing injection strength, the length of the intervals around the exact p/q-resonances, at which locking takes place, increase forming the well-known Arnold's tongues. For fixed injection strength, one finds a hierarchy of the sizes of the locking plateaus according to their ordering in the Farey tree, i.e., the plateau sizes decrease from lower to upper levels resulting in a self similar pattern. This generic type of frequency locking has been found in a wealth of nonlinear dynamical systems, just to mention modulated external cavity semiconductor lasers [BAU89, SAC92a].

In the case of a ML laser, the τ-intervals of the resonant regimes form plateaus with p well separated pulses in the cavity (compare to Fig. 5.5(b)–(d) (left column)), where p defines the level of the plateau in the Farey tree. In the numerical simulations, we

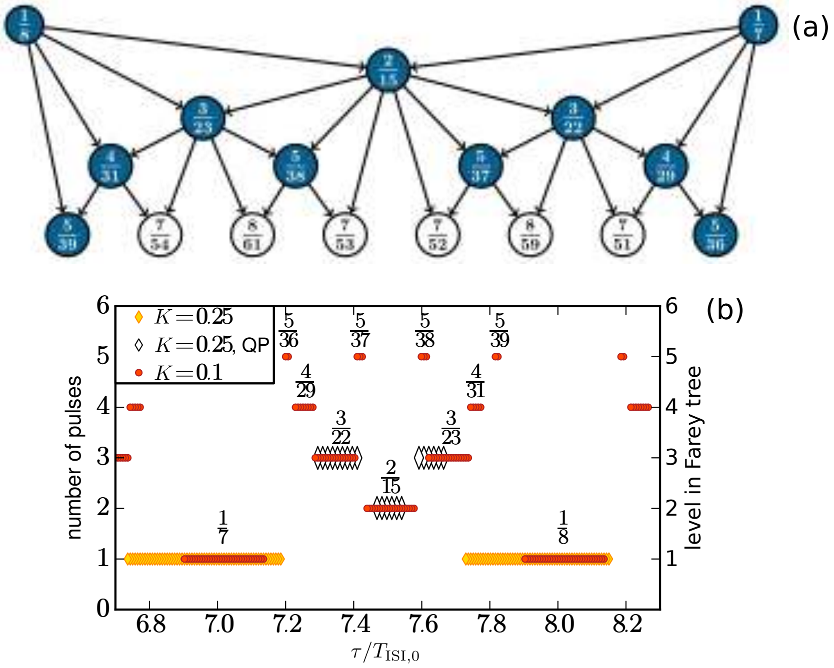

Figure 5.12.: **(a)**: Farey tree. The fractions p/q for $p, q \in \mathbb{N}$ are the resonance conditions for the delay time τ and the inter-spike interval time $T_{\mathrm{ISI},0}$ given by Eq. (5.32). Resonances found in the laser model are highlighted in blue. **(b)**: Plateaus with a given number of well separated pulses (see Subsection 5.4.2) of ML laser for small $K = 0.1$ (red circles) and intermediate $K = 0.25$ feedback strength (open and filled diamonds) as a function of the delay time τ. The fractions denote the resonance condition p/q. Their ordering from bottom to top corresponds to the ordering in the Farey tree. Filled colored symbols depict time periodic solutions, while open black diamonds correspond to quasiperiodic (QP) solutions. Parameters as in Table 5.1. From [OTT12a].

consider two subsequent pulses as well separated if between the pulses a time point $t_{\min}$ exists with $|\mathcal{E}(t_{\min})| < 1 \times 10^{-3}$. Figure 5.12(a) shows a Farey tree, where the resonances present in the ML laser model are highlighted in blue. (Solutions with $p > 5$ pulses in the fifth level of the tree are not found in the laser model, because only up to $p = 5$ well separated pulses can propagate in the cavity as discussed in Subsection 5.4.2.) In Fig. 5.12(b), the number of pulses p is plotted as a function of the delay time τ for small $K = 0.1$ (filled red circles) and intermediate $K = 0.25$ (filled yellow diamonds and open diamonds). It can be seen that plateaus similar to the locking plateaus in the Farey tree form. The width of the plateaus shrinks with increasing number of pulses p, i.e, with increasing tree level, as one would expect from the study of the generic circle map. A similar scenario has also been observed for a pair of delay-coupled oscillators [PAN12].

For a higher feedback strength of $K = 0.25$, the width of the plateaus increases, which is similar to the broadening of the Arnold's tongues for increasing control parameter in the case of externally driven systems. As already discussed in Fig. 5.7 and Fig. 5.10, quasiperiodic motion is observed away from the main resonances for the higher feedback strength ($K = 0.25$). Nevertheless, we still find $p = 2$ and $p = 3$ well separated pulses in the cavity in the second and third order resonant regimes, respectively. They are indicated by the open black diamonds in Fig. 5.12(b).

5.4.6. Long delay

So far, the dynamics of the ML laser subject to optical feedback has been investigated for intermediate delay times. Now, ten times larger delays are studied. As already discussed in the introduction of this chapter, this regime of long delay lines is of particular interest, because in experimental setups optical feedback is often provided by long optical fiber loops [SOL93, LIN10e, LIN11d, LIN11f, BRE10, FIO11, ROS12b]. Figure 5.13 depicts the number of pulses (color code) as a function of the delay time τ and the feedback strength K obtained by up- and down-sweeping τ (Fig. 5.13(a) and Fig. 5.13(b)), up- and down-sweeping K (Fig. 5.13(c)) and Fig. 5.13(d)), and by using identical, constant initial conditions for each (τ, K)-tuple (Fig. 5.13(e)), respectively. Comparing Fig. 5.13 to the corresponding Fig. 5.7 for intermediate delay times τ, one observes that for long delay the main resonant regimes are strongly broadened. For example, already for intermediate $K \gtrsim 0.18$, the main resonant regions are only separated by a very tiny (white) region with quasiperiodic solutions for up- and down-sweeping τ (Fig. 5.13(a) and (b)). Further, by comparing the regions with more than one pulse in the cavity of Fig. 5.13(a)-(d) (red, light-green, dark-green, and brown regions) for $K \lesssim 0.15$, we find that for long delay times the structure of the higher order resonances subsists up to order four ($p = 4$), but the fifth order resonances cannot be clearly assigned. In contrast to intermediate delay times, multistabilities between periodic orbits with different numbers of pulses in the cavity are now already observed for small feedback strengths K. This is the reason why the fifth order resonances are shadowed by the adjacent second and third order resonances, which overlap.

Figure 5.14 depicts the multistabilities for small $K = 0.12$. In Fig. 5.14(a) a bifurcation diagram of the maxima of the time trace of $|\mathcal{E}|$ versus delay time τ (τ ranging from $66.8\,T_{\mathrm{ISI},0}$ to $69.2\,T_{\mathrm{ISI},0}$) is shown, which corresponds to a horizontal section of

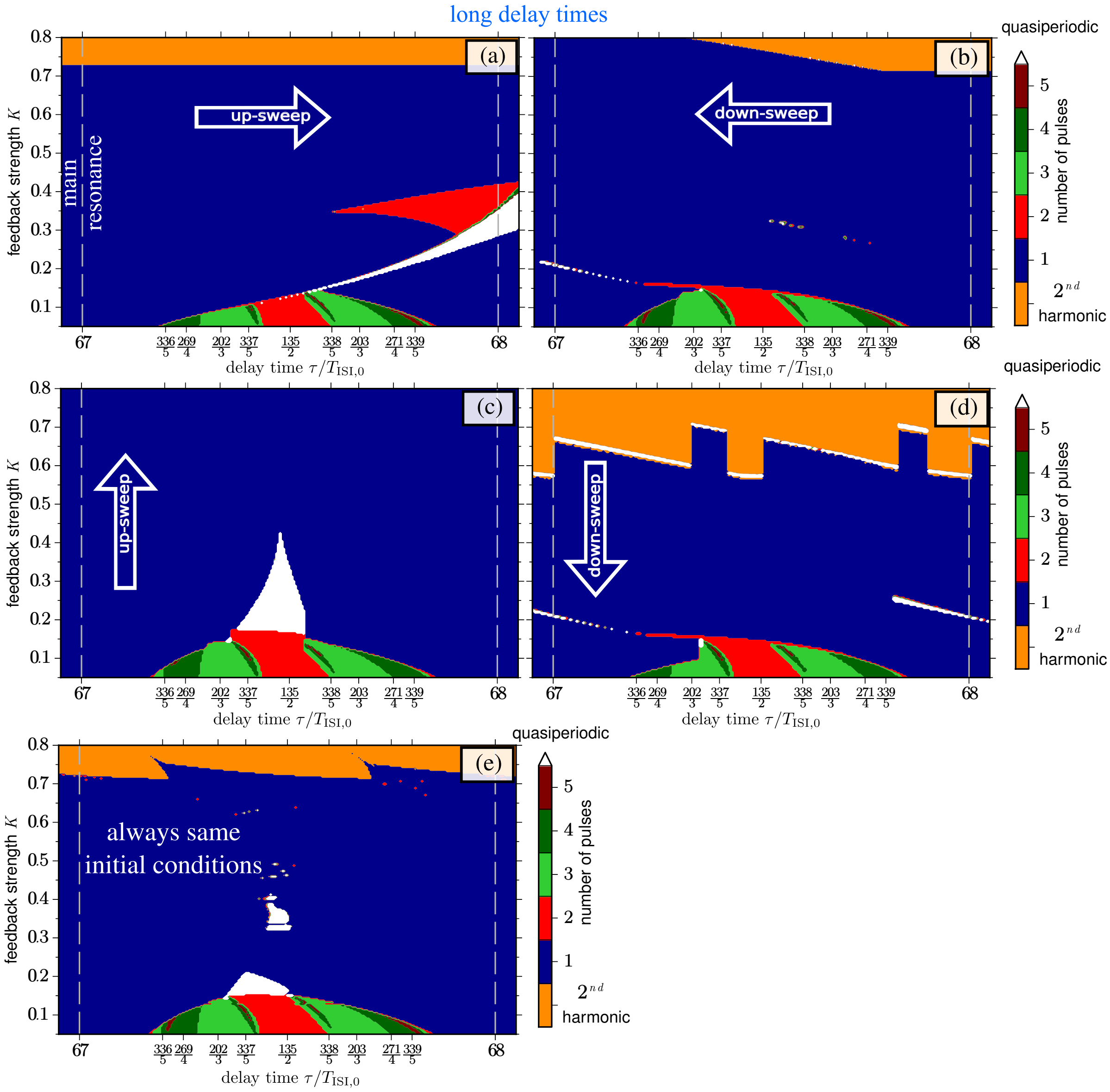

Figure 5.13.: Two-parameter bifurcation diagram of the dynamics of the ML laser subject to external optical feedback in terms of delay time τ (in units of the inter-spike interval of the solitary laser $T_{\mathrm{ISI},0}$) and feedback strength K in the regime of long delay times obtained by **(a)**: up-sweeping τ, **(b)**: down-sweeping τ, **(c)**: up-sweeping K, **(d)**: down-sweeping K, and **(e)**: always identical, constant initial conditions for each tuple of (τ, K)-values. The color code provides the number of pulses in the cavity. White, orange, and black regions indicate quasiperiodic pulse trains and 2^{nd} order harmonic mode-locking, respectively. Parameters as in Table 5.1.

Figs. 5.13(a) and (b). Orange diamonds and black circles depict maxima of the time trace of $|\mathcal{E}|$ for stepwise increasing τ (up-sweep) and stepwise decreasing τ (down-sweep), respectively. The horizontal blue dash-dotted line marks the maxima of the time trace of $|\mathcal{E}|$ for the solitary laser. In the gray shaded parts of the main resonant regimes in Fig. 5.14(a), the peak values of the time trace of $|\mathcal{E}|$ are higher and the pulse width is shorter than for the solitary laser. Simulations with white noise ($R_{\mathrm{sp}} \neq 0$) reveal that in these regions the stability of the pulses with respect to fluctuations is increased. In comparison with the corresponding figure for intermediate delay (Fig. 5.8(a)), the main resonant regimes are, on the one hand, broader than for intermediate delay, and, on the other hand, the increase of the height of the pulses with respect to the solitary laser (blue, dash-dotted horizontal line) is larger than for intermediate delay. This stabilizing effect of resonant optical feedback will be employed in Section 5.7 for timing jitter reduction. In the blue shaded region of Fig. 5.14(a), the multistability of solutions with one pulse in the cavity and solutions with two, three, or four pulses in the cavity mentioned above is found. (For clarity, only bistability between up- and down-sweeping τ are shown and the other sweep-direction are omitted.) In Fig. 5.14(b), exemplary time traces of $|\mathcal{E}|$ are plotted for two periodic orbits that are bistable for $\tau = 67.45\,T_{\mathrm{ISI},0}$ (vertical gray dashed

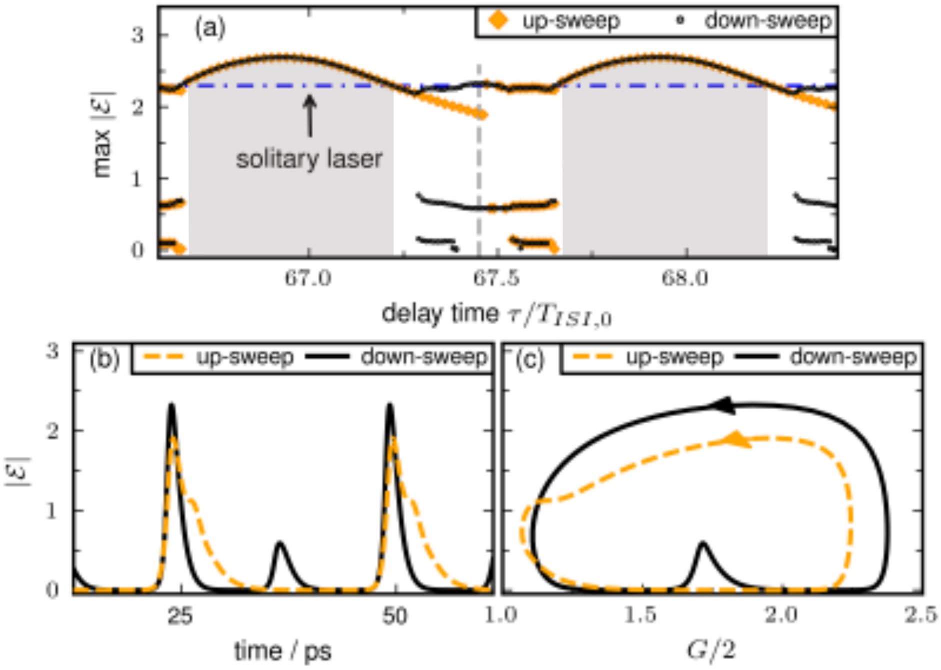

Figure 5.14.: Bistability of periodic orbits for long delay time τ **(a)**: Hysteresis of amplitude maxima of time traces of $|\mathcal{E}|$ versus τ (in units of the inter-spike interval time $T_{\mathrm{ISI},0}$ of the solitary laser) for stepwise increase (up-sweep, orange diamonds) and stepwise decrease of τ (down-sweep, black circles). The blue dash-dotted line marks the maxima of the time trace of $|\mathcal{E}|$ for the solitary laser. In the gray shaded areas the stability of the pulse train with respect to white noise is increased by the feedback. In the blue shaded area bistability is observed. **(b) and (c)**: Bistability of periodic orbits obtained by an up-sweep of τ (orange dashed line) and by a down-sweep of τ (black solid line) for $\tau = 67.45\,T_{\mathrm{ISI},0}$ (vertical gray dashed line in **(a)**); **(b)**: Time traces of $|\mathcal{E}|$; **(c)**: Projections of the trajectories on the (G,$|\mathcal{E}|$)-plane. Parameters: $K = 0.12$ and other parameters as in Table 5.1.

line in Fig. 5.14(a)). By up-sweeping τ, a pulse train with only one pulse traveling in the cavity ($p = 1$) is observed (orange dashed line), while by down-sweeping τ, a pulse train with two pulses in the cavity ($p = 2$) is detected (black solid line). Figure 5.14(c) depicts phase space projections of the trajectories onto the (G,$|\mathcal{E}|$)-plane.

A comparison of the white regions indicating quasiperiodic behavior for intermediate delay (see Fig. 5.7) and long delay (see Fig. 5.13) reveals that the quasiperiodic regime is suppressed for long delay. For intermediate delay, a large cone-like region with QP behavior is found away from the main resonances for every sweep direction as well as for constant, always identical initial conditions. In contrast, for long delay, small cone-like QP-regions are only found for up-sweeping K as well as for constant, always identical initial conditions (see Fig. 5.13(d) and Fig. 5.14(e), respectively). However, the long delay induced additional stripe-like QP regions for the other sweep directions (see Fig. 5.13 (a), (b), and (d)). They stem from transitions from one FML solution to another FML solution as discussed below. But in contrast to intermediate delay, always a stable FML solution with only one pulse in the cavity (main resonant regime) coexists with the QP solution. This could be interesting for applications that need temporal stable pulse streams, e.g., data communication. However, in experiments, noise cannot be completely suppressed, and from the direct numerical simulations of the deterministic system, it is not clear if the FML solutions always remain stable subjected to noise. Indeed, simulations with noise reveal that away from the main resonance, in a cone-like structure similar to the white QP-region in Fig. 5.14(c), the FML solutions can be destabilized already for white noise of moderate strength, i.e., by spontaneous emission noise (see Subsection 5.7).

The larger main resonant regimes (blue regions) observed for long delay do not imply a simplification of the dynamics of the system. In contrast, for long delay, already for small injection strengths K coexisting FML solutions are found in the main resonant regimes, which introduce a larger complexity into the system than for intermediate delay. This higher complexity is "shadowed" by the color code of Fig. 5.13 indicating only the number of pulses in the cavity. Two coexisting FML branches of solutions are depicted in Fig. 5.15, which corresponds to Fig. 5.14 for slightly higher $K = 0.2$. The bifurcation diagram in Fig. 5.15(a) reveals that for all delay times τ at least one FML solution exists with pulses that have larger peak heights than the pulses of the solitary ML laser (blue dash-dotted line). From the above discussion, we know that this yields an enhanced stability of the FML solution with respect to perturbations. However, for τ-values in the interval $[67.2\,T_{\mathrm{ISI},0}, 67.5\,T_{\mathrm{ISI},0}]$, in which the peak heights of both solutions are similar, noise can also lead to 'switching' between both solutions, and thus to unstable pulse trains. Figure 5.15(b) and (c) exemplary show time traces of $|\mathcal{E}|$ and phase space projections of the trajectories of the coexisting FML solutions onto the $(G, |\mathcal{E}|)$-plane for $\tau = 67.45\,T_{\mathrm{ISI},0}$.

Figures. 5.13, 5.14, and 5.15 are plotted for an external cavity phase of $C = 0$. However, in contrast to intermediate delay, the phase C has no impact on the dynamics of the ML laser for long delay. For the special case of the exact main resonances, this was already discussed in Subsection 5.4.1 (cf. Fig. 5.6(f)).

To sum up, with increasing delay time, the main resonant regimes, in which only one pulse travels in the cavity, broaden. In these regimes, the stability of the pulses with

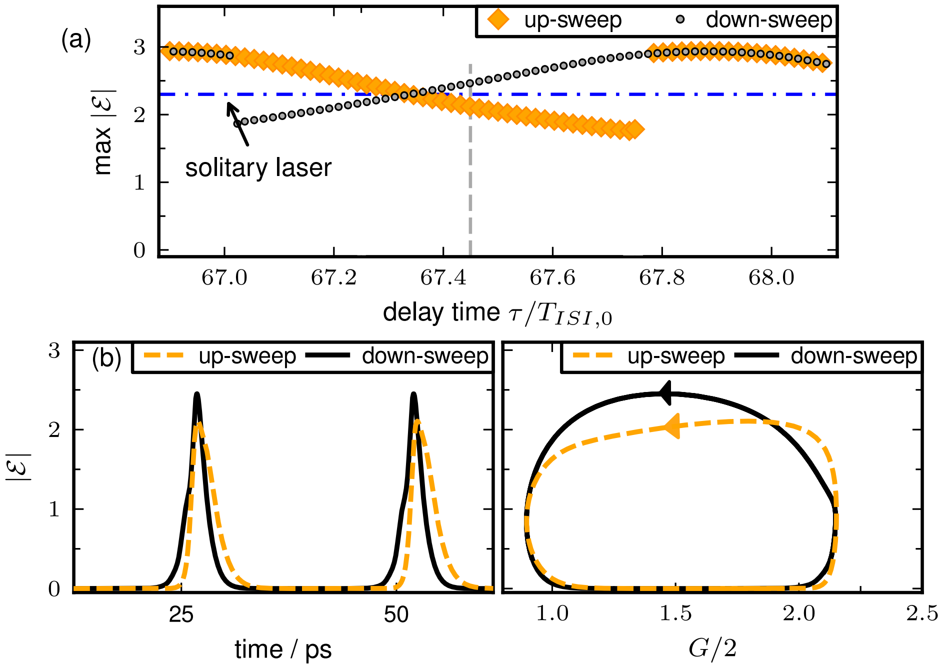

Figure 5.15.: Bistability of periodic orbits for long delay time τ **(a)**: Hysteresis of amplitude maxima of time traces of $|\mathcal{E}|$ versus τ (in units of the inter-spike interval time $T_{\mathrm{ISI},0}$ of the solitary laser) for stepwise increase (up-sweep, orange diamonds) and stepwise decrease of τ (down-sweep, black circles). The blue dash-dotted line marks the maxima of the time trace of $|\mathcal{E}|$ for the solitary laser. **(b)** and **(c)**: Bistability of periodic orbits obtained by an up-sweep of τ (orange-dashed line) and by a down-sweep of τ (black solid line) for $\tau = 67.45\,T_{\mathrm{ISI},0}$ (vertical gray dashed line in (a)); (b): Time traces of $|\mathcal{E}|$; (c): Projections of the trajectories on the $(G,|\mathcal{E}|)$-plane. Parameters: $K = 0.2$, other parameters as in Table 5.1.

respect to perturbation, e.g., spontaneous emission noise, is increased. This increase of stability is more pronounced for long than for intermediate delay. However, in contrast to intermediate delay, multistabilities are already present for long delay in the regime of small feedback strengths K.

5.4.7. Delay induced frequency pulling

In general, the inter-spike interval time T_{ISI} differs for finite K and τ from the inter-spike interval time $T_{\mathrm{ISI},0}$ of the laser without feedback, except for τ-values fulfilling exactly the main resonance condition ($p = 1$ in Eq. (5.32)). This dependence of T_{ISI} on τ results in a delay induced variation of the pulse repetition frequency (center frequency) $\nu_{\mathrm{rep}}(\tau, K) \equiv 1/T_{\mathrm{ISI}}(\tau, K)$, which is known as frequency pulling and has been observed experimentally in QW lasers [SOL93] and more recently in QD lasers [MER09, GRI09, BRE10, LIN10e, FIO11, LIN11d]. Figure 5.16 depicts the deviations

$$\Delta\nu_{\mathrm{rep}}(\tau, K) \equiv \nu_{\mathrm{rep}}(\tau, K) - \nu_{\mathrm{rep},0}$$

of ν_{rep} from the pulse repetition frequency in a laser without feedback $\nu_{\mathrm{rep},0} = 1/T_{\mathrm{ISI},0}$ as a function of the delay time τ for small feedback strength $K = 0.03$ (red circle), intermediate $K = 0.25$ (white diamonds), and strong $K = 0.5$ (orange circles), respectively. We only discuss the frequency pulling in the main resonant regime, where one pulse travels in the cavity (blue regions in Fig. 5.7 and the two largest plateaus in Fig. 5.12(b)).

In this regime, synchronization is observed if the inter-spike interval time T_{ISI} adapts to the external delay time τ according to $q\,T_{\mathrm{ISI}}(q, \tau) = \tau$ leading to a frequency deviation of

$$\Delta\nu^{\mathrm{syn}}_{\mathrm{rep}}(q, \tau) = q/\tau - \nu_{\mathrm{rep},0}. \tag{5.33}$$

From the above equation, we expect that the frequency pulling decreases for increasing delay times τ. This can be seen by splitting $\tau = q\,T_{\mathrm{ISI},0} + \Delta\tau$ into its value at an exact main resonance $q\,T_{\mathrm{ISI},0}$ and a deviation $\Delta\tau$. Inserting this ansatz into Eq. (5.33) and Taylor-expanding up to the first order in τ, yields

$$\Delta\nu^{\mathrm{syn}}_{\mathrm{rep}}(q, \tau) = \underbrace{1/T_{\mathrm{ISI},0}}_{=\nu_{\mathrm{rep},0}} - \frac{q}{\tau^2}\Delta\tau - \nu_{\mathrm{rep},0} + \mathcal{O}((\Delta\tau)^2) = -\frac{q}{\tau^2}\Delta\tau + \mathcal{O}((\Delta\tau)^2). \tag{5.34}$$

Thus, the frequency deviation $\Delta\nu^{\mathrm{syn}}_{\mathrm{rep}}$ decreases in leading order like $1/\tau^2$.

Figures 5.16(a) and (b) show the frequency pulling $\Delta\nu_{\mathrm{rep}}$ in the main resonant regime for intermediate ($q = 7$) and large τ ($q = 67$ to $q = 69$), respectively, together with the synchronization condition of Eq. (5.33) (black dash-dotted lines). For intermediate delay times, we see from Fig. 5.16(a) that the main resonant regimes broaden and the frequency deviations $\Delta\nu_{\mathrm{rep}}$ increase with K (see also Fig. 5.7). For small values of K, the frequency detuning is very small, and a nearly horizontal line is found (red circle) that reaches zero detuning (horizontal gray dashed line) when τ approaches the boarders of the main resonant regime. Instead, for intermediate and large K (white diamonds and orange circles, respectively), $\Delta\nu_{\mathrm{rep}}$ increases nearly linearly with the distance from the exact resonance, but remains below the detuning expected for synchronization (black dash-dotted line).

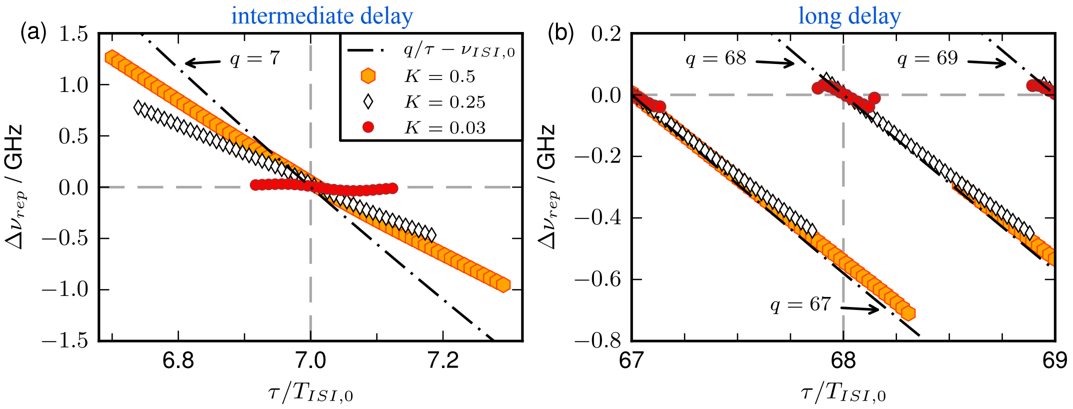

Figure 5.16.: Deviations $\Delta\nu_{\mathrm{rep}}$ of the pulse repetition frequency $\nu_{\mathrm{rep}}(\tau, K)$ of the laser with feedback from its solitary laser value $\nu_{\mathrm{rep},0}$ in terms of delay time τ for three different feedback strengths K. Black dash-dotted lines denote complete frequency locking and vertical gray dashed lines mark exact main resonances. **(a)**: Intermediate delay times τ. **(b)**: Large delay times τ. Other parameters as in Table 5.1.

From Fig. 5.16(b), it can be seen that the width of the main resonant regimes increases for longer delay (note the different scale of the τ-axis in Fig. 5.16(a) and Fig. 5.16(b)). For small values of K (red crosses), we find a similar behavior of $\Delta\nu_{\mathrm{rep}}$ as for intermediate delay. An increase of K (white diamonds), however, leads to a frequency entrainment that stays close to its value for synchronization (see Eq. (5.33)) over nearly the whole interval length of $T_{\mathrm{ISI},0}$ (compare the slope of the white diamonds and the black dash-dotted line). Further, jumps of $\Delta\nu_{\mathrm{rep}}$ take place close to the exact resonance conditions. In Fig. 5.16(b), such a jump is observed at $\tau = 67.85\,T_{\mathrm{ISI},0}$ when the system switches from the main resonant regime with $q = 67$ to the main resonant regime with $q = 68$ at $\tau = 67.9\,T_{\mathrm{ISI},0}$. In between two subsequent main resonant regimes, a short interval with more complex dynamics is found.

Intuitively, Eq. (5.34) gives us an idea why synchronization with the external delay works better for long cavities. Since the frequency deviation for a given distance $\Delta\tau$ from the exact main resonance ($\Delta\nu_{\mathrm{rep}}^{\mathrm{syn}} \propto 1/\tau^2$) is much smaller for long delay, the system can synchronize with the external delay with less effort. The sawtooth like shape of $\Delta\nu_{\mathrm{rep}}$ in terms of τ resulting from synchronization over the full $T_{\mathrm{ISI},0}$-interval observed for long delay (see open diamonds in Fig. 5.16(b) and Eq. (5.33)) corresponds well to the experimental findings for long delay lines [SOL93, LIN10e, FIO11]. Two of these experiments are presented in Fig. 5.17. Figure 5.17(a) depicts the radio frequency (rf) linewidth (left y-axis) and the pulling of the repetition frequency (center frequency) (right y-axis) in terms of changes in the length of the external delay line for a long delay time of $\tau = 3.1\,\mathrm{ns}$ in an early experiment with a $1.3\,\mu\mathrm{m}$ $50\,\mathrm{GHz}$ GaAs, multiple quantum well passively mode-locked laser [SOL93]. Figure 5.17(b) depicts the pulling of the repetition frequency in terms of changes of the delay time in the regime of very long delay times $\tau = 91\,\mathrm{ns}$ as obtained for a $1.3\,\mu\mathrm{m}$ $40\,\mathrm{GHz}$ GaAs quantum dot passively mode-locked laser [FIO11]. Both lasers show a sawtooth like shape of the repetition frequency in terms of τ with a repetition period of the inter-spike interval time $T_{\mathrm{ISI},0}$, which is marked by the blue arrow labeled "MLL Period" in Fig. 5.17(b). The delay

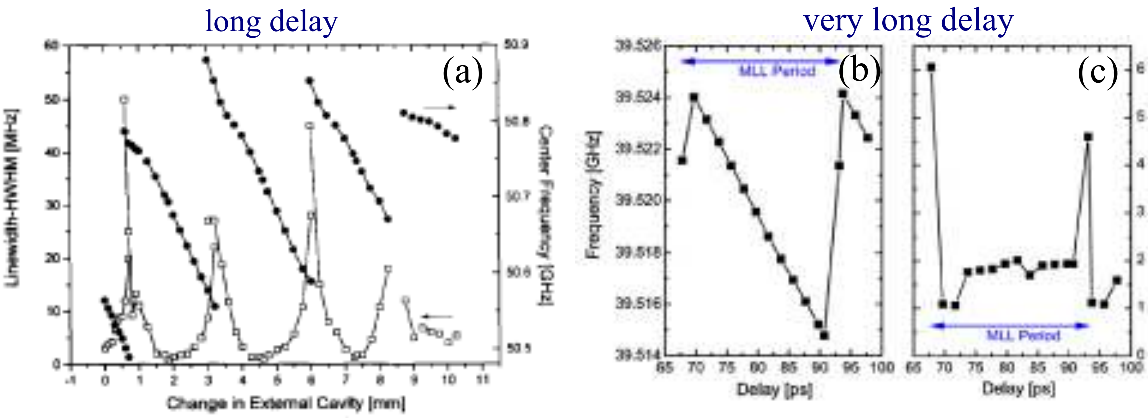

Figure 5.17.: **(a)**: Experimentally measured radio frequency (rf) linewidth and center frequency pulling in terms of changes in the length of the external delay line for long delay time $\tau = 3.1\,\mathrm{ns}$ in a $1.3\,\mu\mathrm{m}$ $50\,\mathrm{GHz}$ GaAs, multiple quantum well passively mode-locked laser. Modified from [SOL93]. **(b)** and **(c)**: Experimentally measured center frequency pulling and root-mean-square (rms) timing jitter in terms of changes of the delay time for very long delay time of $\tau = 1/11\,\mu\mathrm{s}$ in a $1.3\,\mu\mathrm{m}$ $40\,\mathrm{GHz}$ GaAs quantum dot passively mode-locked laser. Blue arrows indicate the repetition frequency of the laser $\nu_{\mathrm{rep}} = 1/T_{\mathrm{ISI},0} = 25$ ps ($T_{\mathrm{ISI},0}$ is the inter-spike interval time of the solitary laser). Modified from [FIO11].

time in Fig. 5.17(a) ($\tau = 3.1\,\mathrm{ns}$) has the same order of magnitude than the long delay discussed in Fig. 5.16(b) ($68\,T_{\mathrm{ISI},0} = 1.7\,\mathrm{ns}$). This is why according to Eq. (5.34) also the deviation of the repetition frequency over one $T_{\mathrm{ISI},0}$-interval $\Delta\nu_{\mathrm{rep}}^{\mathrm{max}} = 0.35\,\mathrm{GHz}$ has the same order of magnitude than the one obtained in our theoretical simulations ($\Delta\nu_{\mathrm{rep}}(K = 0.25) = 0.3\,\mathrm{GHz}$). For the very long delay of Fig. 5.17(b) ($\tau = 91\,\mathrm{ns}$), the deviation of the repetition frequency over one $T_{\mathrm{ISI},0}$-interval is much smaller ($\Delta\nu_{\mathrm{rep}}^{\mathrm{max}} = 9\,\mathrm{KHz}$) as expected from Eq. (5.34). Further, the experimental results of Fig. 5.17(a) and (b) obtained for different types of lasers suggest that the material system has only a negligible effect on the frequency pulling, which justifies the simple DDE modeling approach of this chapter.

Figure 5.17(c) shows that also the root-mean-square (rms) timing jitter exhibits a periodical dependence on $T_{\mathrm{ISI},0}$ for long delay lines, which will be discussed in detail in Subsection 5.7.

Figure 5.16 was obtained by stepwise increasing the τ-values (up-sweep). This explains the asymmetry of $\Delta\nu_{\mathrm{rep}}$ with respect to zero detuning (horizontal gray dashed line) for long delay (Fig. 5.16(b)). For down-sweeping τm qualitatively the same resonance structure is obtained, but in this case the larger absolute values of $\Delta\nu_{\mathrm{rep}}$ are observed for positive detuning. Thus, for intermediate and large K-values, we retrieve the bistability of periodic orbits from neighboring main resonant regimes (here $q = 67$ and $q = 68$) that was already discussed in Subsection 5.4.6. These orbits have the simple shape of the one depicted in Fig. 5.5(a)(left) (only one pulse in the cavity) and a frequency difference of $\Delta\nu = 1/\tau$, which is the vertical distance of neighboring black dash-dotted lines in Fig. 5.16(b). When the length of the delay line is increased even further, these bistabilities become more pronounced and appear at lower values of the feedback strength.

5.5. Additional dynamical regimes for nonzero α-factors

So far, the dynamics of the simplest configuration with a real equation for the amplitude of the electric field $\mathcal{E}$ (see Eq. (5.28a)) was studied to reveal the basic resonance structure of τ and $T_{\mathrm{ISI},0}$. Now, the additional dynamical regimes introduced by a complex field equation are studied. Therefore, the more realistic situation of finite phase-amplitude coupling expressed by nonzero α-factors in the gain section (α_g) and in the saturable absorber (α_q) is discussed. Figure 5.18(a) and (b) depict time traces of $|\mathcal{E}|$ (thick solid lines, left y-axis) and of the net gain $\mathcal{G}$ (thin dashed lines, right y-axis) of the free running ML laser ($K = 0$) for symmetric α-factors and asymmetric α-factors, respectively. Due to the different pump conditions in gain and absorber section, asymmetric α-factors ($\alpha_g > \alpha_q$) are more realistic than symmetric configurations.

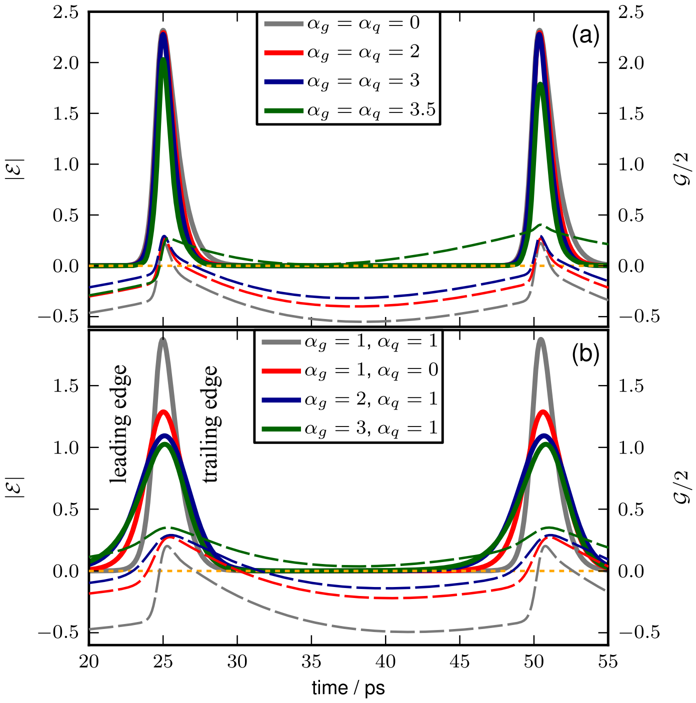

Figure 5.18: Time traces of $|\mathcal{E}|$ (full lines, left y-axis) and of the net gain parameter $\mathcal{G}$ (dashed lines, right y-axis) for different combinations of α-factors in gain (α_g) and absorber (α_q) sections for the free running ML laser ($K = 0$). **(a)**: Symmetric setups $\alpha_g = \alpha_q$, pump parameter $J_g = 0.12\,\mathrm{ps}^{-1}$. **(b)**: Asymmetric setups $\alpha_g > \alpha_q$, pump parameter $J_g = 0.09\,\mathrm{ps}^{-1}$. Other parameters as in Table 5.1.

The gray line in Fig. 5.18(a) depicts the time trace obtained for zero α-factors and the colored lines denote finite α-factors. For small, symmetric α-factors (see red and blue line in Fig. 5.18(a)), the impact on height and width of the pulses is negligible, but the net gain $\mathcal{G}$ in between the pulses reaches less negative values indicating a decreasing stability of the pulse stream with respect to perturbations. At a critical value of the α-factors of $\alpha_g = \alpha_q = 3.06$, the pulse stream is destabilized, and a pulse train with varying heights of the pulses is obtained as depicted in Fig. 5.18(a) for $\alpha_g = \alpha_q = 3.5$ (green line).

In Fig. 5.18(b), asymmetric configurations of the α-factors (colored lines) are compared to the symmetric case of $\alpha_g = \alpha_q = 1$ (gray line). Already, for the configuration with the lowest α-factors ($\alpha_g = 1$ and α_q=0, red lines), a small trailing edge instability opens up, i.e., the net gain window with $\mathcal{G} > 0$ stays open after the decay of the intensity.

As a result, the pulse is easily destabilized by perturbations as for example spontaneous emission noise, and the pulse height strongly decreases.

This trailing edge instability increases for larger α-factors. Note that Figs. 5.18(a) and (b) cannot be compared directly, because different pump rates J_g were chosen. This was necessary, because the ML regime shifts with the pump current, and for the parameters of Table 5.1 no mode-locking is obtained for the asymmetric α-factors of Fig. 5.18(b).

Roughly spoken, an increasing phase-amplitude coupling degrades the quality of the pulse stream. The impact of the phase-amplitude coupling is much smaller for symmetric than for asymmetric configurations. Intuitively, this can be understood as follows [VLA11]: the α-factors for gain and absorber section enter into the R-term of Eq. (5.23), which describes the gain and the losses per cavity roundtrip with different signs. If saturable gain $\mathcal{G}$ and saturable absorption Q had exactly the same dynamics, the terms $-\alpha_g G$ and $\alpha_q Q$ in the denominator of Eq. (5.23) would cancel out, and the same dynamics as for zero α-factors would be observed. Since the recovery of $\mathcal{G}$ and Q is different, the term $-\alpha_g G$ is only partially compensated by the term $\alpha_q Q$. The largest compensation is obtained for symmetric α-factors, which is the reason why the smallest impact of finite α-factors on the dynamics of the ML laser are observed for symmetric α-factors.

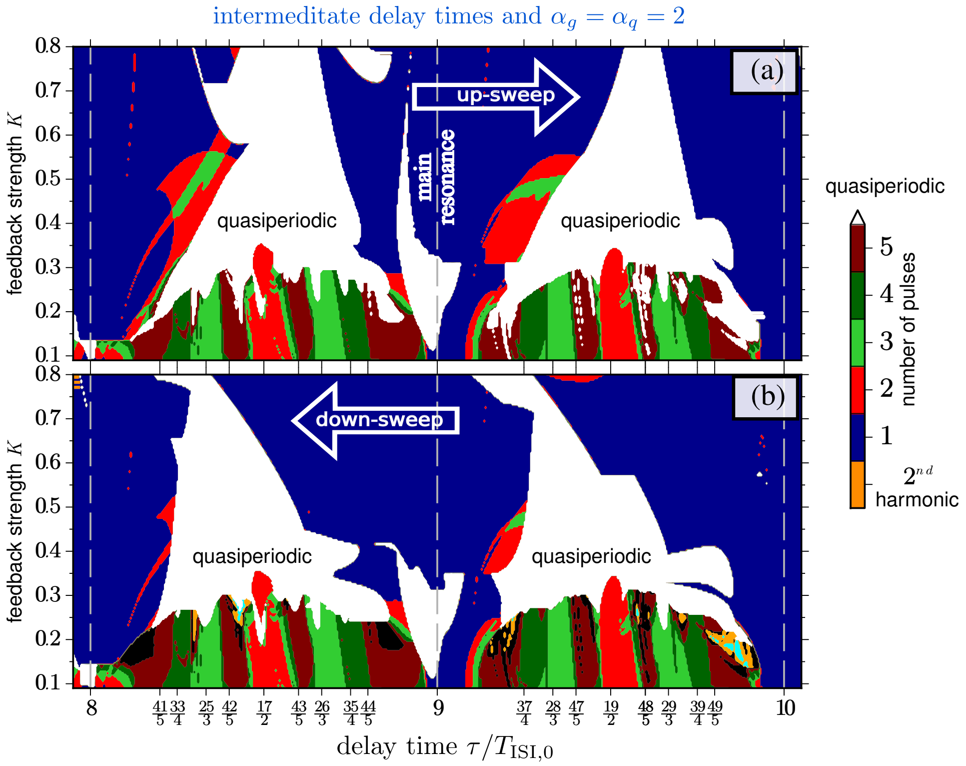

Figure 5.19.: Two-parameter bifurcation diagrams of the dynamics of the ML laser subject to external optical feedback in terms of delay time τ (in units of the inter-spike interval of the solitary laser $T_{\mathrm{ISI},0}$) and feedback strength K for **(a)**: up-sweeping τ and **(b)**: down-sweeping τ. The color code provides the number of pulses in the cavity (compare with Fig. 5.5). White regions indicate quasiperiodic pulse trains as depicted in Fig. 5.10 and orange region depict harmonic mode locking. Parameters: $\alpha_g = \alpha_q = 2.0$ and other parameters as in Table 5.1

Next, the effect of finite α-factors onto the resonance structure of $T_{\mathrm{ISI},0}$ and τ of the ML laser subject to external feedback is studied. Figure 5.19(a) and (b) depict the number of maxima of $|\mathcal{E}|$ of different heights (color code) in dependence of τ and K for up-sweeping K and down-sweeping K, respectively, in the regime of intermediate delay for symmetric $\alpha_g = \alpha_q = 2.0$. Thus, the figure corresponds to Figs. 5.7(a) and (b) that were obtained in the regime of intermediate delays for zero α-factors. Comparing Figs. 5.19 and 5.7, two main differences can be observed. On the one hand, the vertical transitions between the quasiperiodic regimes (white) and the main resonant regime (blue) indicate that the system now has a higher complexity. This results in an increase of the number of multistable solutions. As a consequence, the system cannot any longer be analyzed in detail by up- and down-sweeping K and τ as it has been done for zero α-factors in Section 5.4. On the other hand, the white region around the exact main resonance with $\tau = 9T_{\mathrm{ISI},0}$ for $K \in [0.12, 0.31[$ indicates that instabilities may occur for finite α-factors also in the main resonant regime. These resonant self-pulsations were also observed in experiments [GRI09, LIN10e] and in numerical simulations with a more complex finite-difference traveling wave approach [AVR09]. The authors of the theoretical study supposed that ML lasers subject to resonant optical feedback behave similar as single mode semiconductor lasers coupled to a distant optical reflector, which were discussed in Chapter 4. They observed that above a critical feedback strength the system undergoes a cascade of bifurcations leading to chaos, before it eventually re-stabilizes at high $K = 0.31$. However, a detailed analysis of the route to chaos is still missing. This cascade of bifurcations is analyzed in the following for the exact main resonance with $\tau = 9T_{\mathrm{ISI},0}$. We compare our findings to a bifurcation cascade for a single mode laser subject to feedback studied by Mørk at al. with the LK-model [MOR92].

Figure 5.20(a) depicts the evolution of the trajectory in the phase space spanned by the saturable gain $\mathcal{G}$, the total loss Q_t, and the absolute value of the field amplitude $|\mathcal{E}|$ for $K = 0.15$ (red line), i.e., at the beginning of the bifurcation cascade. The thick blue dashed line marks the limit-cycle of the solitary laser. To reveal the dimensionality of the attractor, Fig. 5.20(b) depicts the intersection points of the trajectory with a transversal plane (Poincaré plane [SCH89c]) that is defined by $Q_t = 2.4$. Notice that only intersection points that result from traversals through the Poincaré plane in direction of increasing Q_t are recorded, i.e., "mirror points" are rejected. In the Poincaré section, the attractor forms a closed curve indicating a quasiperiodic motion on a two dimensional torus performed by the trajectory of the full system. Thus, the system has previously undergone a Neimark-Sacker or secondary Hopf bifurcation [KUZ95], which introduced a new frequency into the system that is incommensurate to the repetition rate of the pulses $\nu_{\mathrm{rep},0} = 1/T_{\mathrm{ISI},0}$. Figure 5.20(c) depicts a second Poincaré section for $G = 4.6$ (see gray dashed line in Fig. 5.20(b)). Plotted is the projection of the attractor onto a plane spanned by $|\mathcal{E}(t)|$ and $|\mathcal{E}(t - T_{\mathrm{ISI},0})|$.

Figures 5.20(d)–(f) are the same as Figs. 5.20(a)–(c), but they were obtained for a higher value of $K = 0.25$. The phase space trajectory in Fig. 5.20(d) reveals that the size of the attractor has increased, and the first Poincaré section in Fig. 5.20(e) shows a broadening of the attractor. This means that the attractor now has an higher dimensionality, and eventually the closed curve in the second Poincaré section (see blowup in Fig. 5.20(f)) reveals that the attractor is a three dimensional torus. Meaning that a sec-

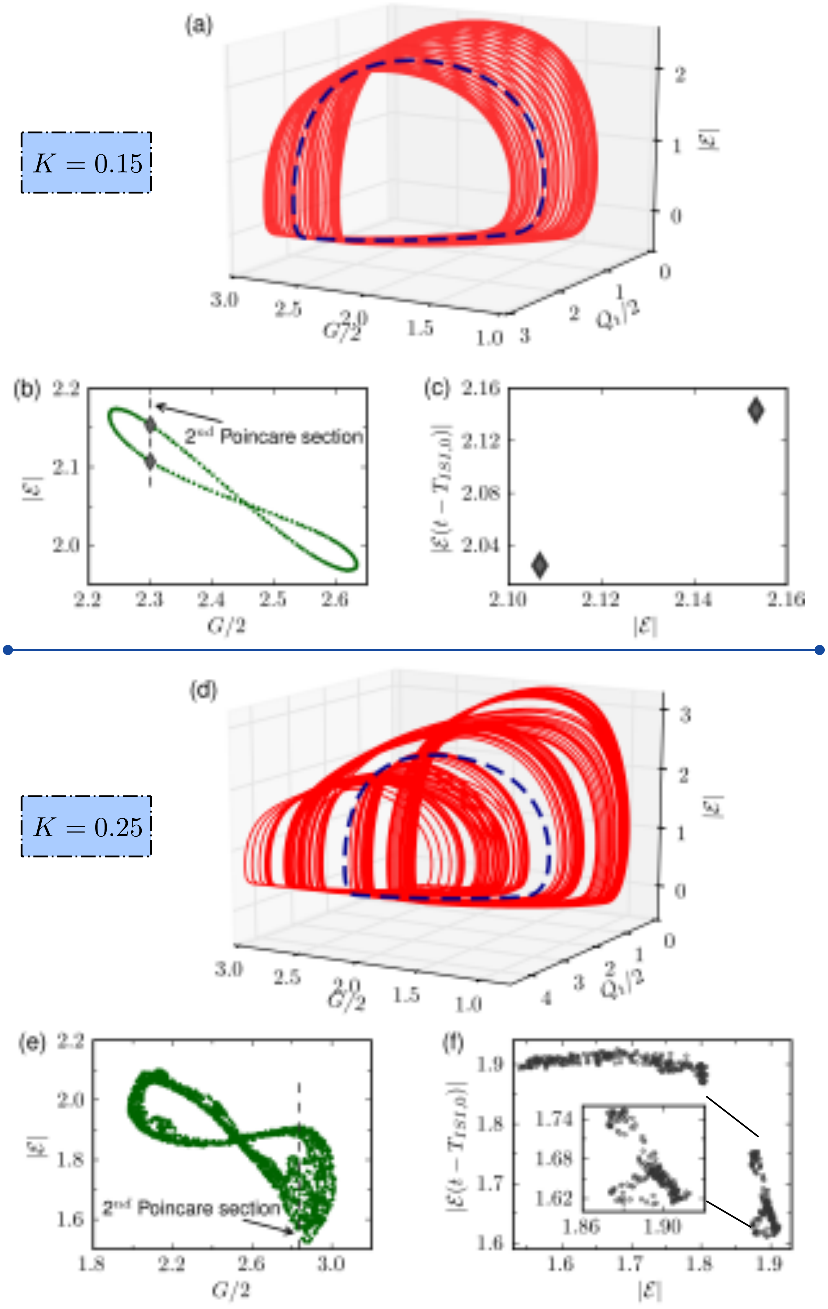

Figure 5.20.: Phase space projections and Poincaré sections for exactly resonant delay time $\tau = 9T_{\mathrm{ISI},0}$ ($T_{\mathrm{ISI},0}$ is the inter-spike interval time of the solitary laser.) **(a)**: Portrait of the trajectory in the phase space spanned by saturable gain G, total loss Q_t, and the absolute value of the complex field amplitude $|\mathcal{E}|$ for a feedback strength of $K = 0.15$. The blue dashed curve indicates the periodic orbit of the free running ML laser. **(b)**: First Poincaré section of **(a)** at $Q_t = 2.4$. **(c)**: Second Poincaré section of **(a)** for $Q_t = 2.4$ and $G = 4.6$ (gray dashed line in **(b)**). **(d)-(f)**: Same as **(a)-(c)** but for higher $K = 0.25$ and second Poincaré section for $G = 5.1$. Parameters: $\alpha_g = \alpha_q = 2$ and other parameters as in Table 5.1.

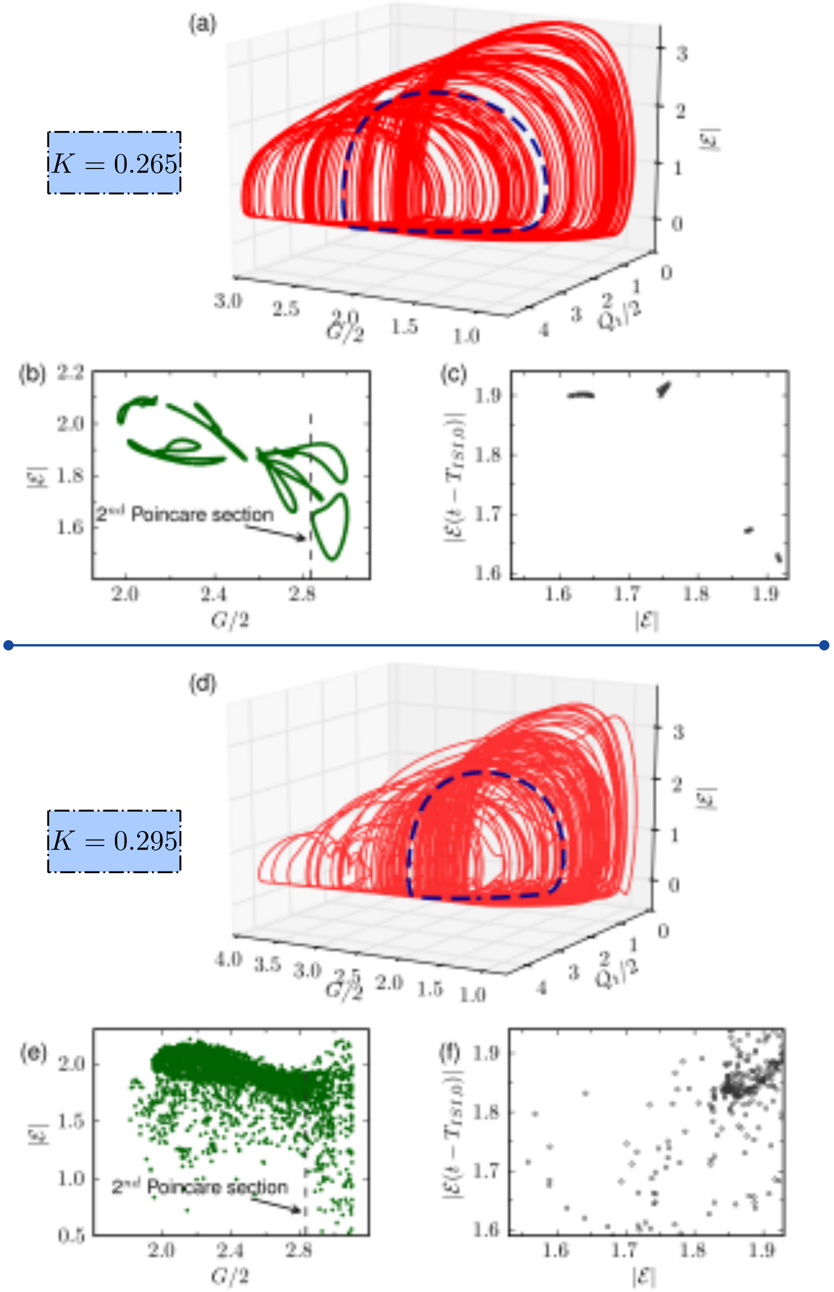

Figure 5.21.: Phase space projections and Poincaré sections for exactly resonant delay time $\tau = 9T_{\text{ISI},0}$ ($T_{\text{ISI},0}$ is the inter-spike interval time of the solitary laser.) **(a)**: Portrait of the trajectory in the phase space spanned by saturable gain G, total loss Q_t, and the absolute value of the complex field amplitude $|\mathcal{E}|$ for a feedback strength of $K = 0.165$. The blue dashed curve indicates the periodic orbit of the free running ML laser. **(b)**: First Poincaré section of **(a)** at $Q_t = 2.4$. **(c)**: Second Poincaré section of **(a)** for $Q_t = 2.4$ and $G = 5.6$ (gray dashed line in **(b)**). **(d)**-**(f)**: Same as **(a)**-**(c)** but for higher $K = 0.265$. Parameters: $\alpha_g = \alpha_q = 2$ and other parameters as in Table 5.1.

ond Neimark-Sacker bifurcation took place, which introduced a third non-commensurate frequency into the system.

Increasing the injection strength further, for $K = 0.265$ (see Fig. 5.21(a)–(c)), locking on a two dimensional torus of order nine is found, which can be seen from the nine closed curves in the first Poincaré section depicted in Fig. 5.21(b). Eventually, the system undergoes a transition to chaos, which is depicted in Figs. 5.21(d)–(f) for $K = 0.295$. Note that the attractor now extends into the region of high gain (large $G \gtrsim 3$), which could be the analogue to the re-injection mechanism observed for the regular pulse packages of the QD single mode laser subject to short optical feedback discussed in Section 4.4. Finally, at $K = 0.31$, the chaotic attractor collapses onto a stable limit-cycle.

Concluding, in the main resonance with $\tau = 9T_{\text{ISI},0}$, the ML laser undergoes a quasiperiodic route to chaos, before it re-stabilizes again for higher feedback strengths. This route to chaos was also observed in single mode lasers subject to optical feedback (LK-model) [MOR92], which substantiates the assumption of Avrutin et al. [AVR09] that a ML laser subject to resonant optical feedback undergoes a similar instability scenario as a single mode laser.

5.6. Timing jitter

As already mentioned in the introduction of this chapter, one major drawback of passively ML lasers is their large timing jitter due to the absence of a reference clock. The timing jitter is a measure for the temporal variations of the inter-spike interval time T_{ISI} of the pulses in the stream, which degrades the performance of the laser. Previous works [HAU93a, ELI97] have shown that spontaneous emission noise is the main source for timing jitter in passively ML lasers. Therefore, in the remainder of this chapter, the timing jitter induced by spontaneous emission noise is studied. The spontaneous emission is modeled by complex Gaussian white noise ($R_{\text{sp}} \neq 0$ in Eqs. (5.28)).

At first, in the next subsection, a method to measure the root-mean-square (rms) timing jitter from the power spectrum that is known as von Linde technique [LIN86] is discussed. It is frequently used for experimental measurements of the timing jitter [KOL86, FIO11, FIO11a, ROS12b], but has the drawback of a large computational effort. Further, it is strictly valid only for stationary stochastic processes (see Appendix D.2). Thus, it can be applied for actively and hybrid ML lasers, where the external voltage applied to the absorber acts as a reference clock. The existence of the external clock provokes that the variance of the timing fluctuations is time independent, i.e., their covariance depends only on time differences. Thus, the timing fluctuations can be modeled by a wide-sense stationary process (see Appendix D). In contrast, in passively mode locked lasers, the variance of the timing fluctuation increases with time, which is the fingerprint of a non-stationary process [GAR02]. Therefore, in Section 5.6.2, an other method to measure the rms timing-jitter is introduced that is computationally more efficient and remains valid for non-stationary processes [HAU93a, MUL06]. Then, in Subsection 5.6.3 with the pulse-to-pulse and the long-term timing jitter, two other measures for the timing jitter are introduced [LEE02c], which are also of relevance for experiments [KEF08, LIN11f]. Moreover, they have a reduced computational effort with respect to the rms timing jitter. Thus, the long-term timing jitter permits to study the dependence of the timing jitter on delay time and feedback strength, which will be done in Section 5.7. Eventually, in Subsection 5.6.4, it will be discussed, under which assumptions the rms timing jitter can be calculated from the long-term jitter. Further, it will be explained how rms and long-term timing jitter can be calculated from the radio-frequency (rf) linewidth of a ML laser [KEF08, LIN11f].

5.6.1. Measuring the timing jitter from the power spectrum

Detailed information about the dominant fluctuations present in a ML laser can be obtained from its power spectral density (PSD) [PAS04, PAS04a, PAS06], which is also denoted as power spectrum (see Appendix D.3 for details). Experimentally, the most exact way to measure the PSD is to record the rf-spectrum of the laser intensity with a fast photodiode, and subsequently analyze it with an electronic spectrum analyzer [KOL86]. The power spectrum of the intensity is often called electrical spectrum to distinguish it from the optical spectrum of the ML laser. From the power spectrum, different types of jitter can be calculated [PAS04, PAS04a]. In the following, we will focus on the dominant contributions of the timing jitter and the amplitude jitter. The latter is a measure for the variation of the amplitudes of the pulses in the stream. The spectrum of an ideal ML semiconductor laser is a comb of δ-distributions located at the multiples $h\nu_{\mathrm{rep}}$ of the repetition frequency ν_{rep}, where $h \in \mathbb{N}$ is the harmonic number. If noise is present in the system, the δ-peaks are broadened. The contribution of the jitter to the spectrum can thus be found by analyzing the sidebands of the peaks. The von Linde technique permits to distinguish the contributions of amplitude and timing jitter in experiments [LIN86]. Von der Linde derived a formula for the PSD of a ML laser under the assumptions of uncorrelated amplitude and timing fluctuations with stationary Gaussian probability distributions. Thus, they assumed that amplitude and timing fluctuations to be driven by independent white noise sources. A sketch of the spectrum of a ML laser is shown in Fig. 5.22. The gray sidebands and the blue Lorentzians centered around the harmonics (black lines) illustrate the contributions of timing and amplitude noises, respectively. Von der Linde derived that the level of the amplitude noise does not depend on the harmonic number h (horizontal blue dotted line), while the level of the timing noise increases proportionally to the square of the

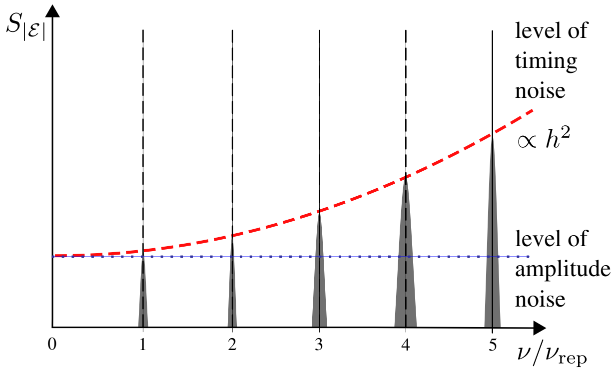

Figure 5.22: Sketch of power spectral density $S_{|\mathcal{E}|}$ of a ML laser with repetition frequency ν_{rep}. Gray sidebands and blue Lorentzians illustrate contributions of timing and amplitude noise, respectively. The red dashed line that is proportional to the square of the harmonic number h and the blue dotted line marks the level of timing and amplitude noise, respectively.

harmonic number h (red dashed line). Figure 5.23 depicts the PSD $S_{|\mathcal{E}|}$ of the free running ML laser as obtained for the DDE model in an interval of ±10 GHz around the center frequencies $h\nu_{\mathrm{rep}}$ of different harmonics in the spectrum. The offset frequency is defined by

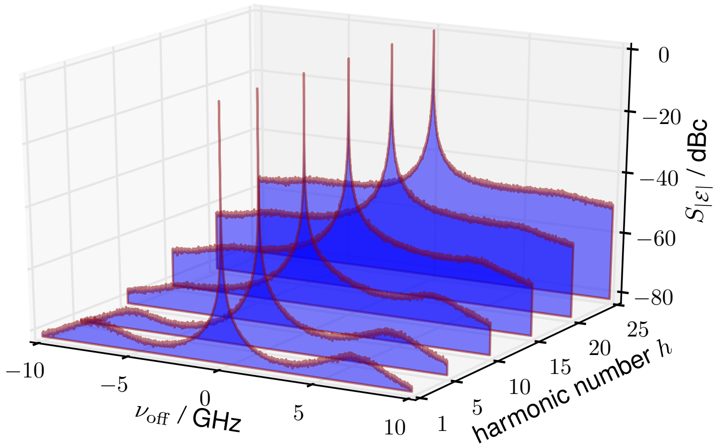

Figure 5.23.: Power spectral density $S_{|\mathcal{E}|}$ of the free running laser as a function of offset frequency ν_{off} and harmonic number h (for each harmonics, $S_{|\mathcal{E}|}$ is normalized to the peak-power (carrier-power) per Hz of this harmonics). Depicted are intervals of $\nu_{\mathrm{off}} \in [-10\,\mathrm{GHz}\,, +10\,\mathrm{GHz}\,]$ around the carrier frequencies $h\nu_{\mathrm{rep}}$ of the harmonics, where ν_{rep} is the repetition frequency of the ML laser. The resolution is 1 MHz. Parameters: $T_{\mathrm{i}} = 4 \cdot 10^4\, T_{\mathrm{ISI},0}$, $R_{\mathrm{sp}} = 1.6\,\mathrm{ns}^{-1}$, and other parameters as in Table 5.1.

$$\nu_{\mathrm{off}}(h) \equiv \nu - h\nu_{\mathrm{rep}}. \tag{5.35}$$

Figure 5.23 clearly reveals the increase of the side bands with the harmonic number. Further, the contributions of the RO frequency at $\nu_{\mathrm{off}} = \pm 7.5\,\mathrm{GHz}$ can be observed.

The increase of the side bands with the harmonic number permits to distinguish the contributions of amplitude and timing jitters: the amplitude jitter can be measured from the sideband of the zeroth frequency component, and the timing jitter can be calculated by integrating over the sidebands of a higher harmonics ($h \geq 1$) in the power spectrum. More precisely, at first, the phase noise spectrum (or phase-noise-to-carrier-power ratio) S_φ of the h-th harmonics is defined as the power spectrum $S_{|\mathcal{E}|}$ of $|\mathcal{E}|$ (or equivalently of the intensity $|\mathcal{E}^2|$) normalized to the power per Hz $P(h)$ of the h-th harmonics [KOL86], i.e.,

$$S_\varphi(\nu, h, T_{\mathrm{i}}) \equiv \frac{S_{|\mathcal{E}|}(\nu, T_{\mathrm{i}})}{P(h)}, \tag{5.36}$$

where T_{i} is the duration of the measurement. Thus, Fig. 5.23 depicts the phase noise spectra for different harmonics. For a non-stationary processes, the phase-noise spectrum S_φ depends on the duration of the measurement T_{i}. For a passively ML laser, this can be understood as follows. For increasing integration time T_{i}, the variance of the timing fluctuation increases, which yields a broadening of the side-bands of the harmonic peaks in the spectrum and thus a different phase-noise spectrum.

How the PSD $S_{|\mathcal{E}|}$ is calculated from a numerically calculated time series is described in detail in Appendix D.4. Here, only the final expression for the phase-noise spectrum is given

$$S_\varphi(\nu, h, \tilde{N}) \equiv \frac{S_{|\mathcal{E}|}(\nu, \tilde{N})}{P(h, \tilde{N})} = T_\mathrm{i}\frac{\langle |F_d[\{|\mathcal{E}|\}](\nu)|^2\rangle_M}{P(h, \tilde{N})}, \tag{5.37}$$

where $P(h, \tilde{N}) \equiv \langle F_d[\{|\mathcal{E}|\}](h\nu_\mathrm{rep})|^2\rangle_M$. In Eq. (5.37), $\{\mathcal{E}\}$ denotes the discrete set of values of the time series of $\mathcal{E}$, and F_d denotes the discrete Fourier transform. Since the simulations can be carried out only for a finite integration time T_i, also for stationary processes an ensemble average $\langle\,\cdot\,\rangle_M$ over $M \in \mathbb{N}$ realizations of the noise has to be performed. This yields a minimal frequency that can be resolved, which is given by $1/T_\mathrm{i}$. In experimental setups, this is the resolution bandwidth of the electrical spectrum analyzer [KOL86]. For non-stationary processes, $S_{|\mathcal{E}|}$ and thus S_φ depend on the measurement (integration) time $T_\mathrm{i} = \tilde{N}dt$ and, thus, on the number of samples $\tilde{N}$ of the time series. (The time step of the integration is denoted by dt, i.e, $1/dt$ is the sampling rate.)

The rms timing jitter is obtained by the phase-noise spectrum by integrating S_φ over one sideband of the h-th harmonic from a minimal positive offset frequency $\nu_\mathrm{off} = \nu_\mathrm{low}$ to a maximal offset frequency of $\nu_\mathrm{off} = \nu_\mathrm{high}$

$$\sigma_\mathrm{rms}(\nu_\mathrm{low}, \nu_\mathrm{high}, \tilde{N}) \equiv \frac{T_C}{2\pi h}\sqrt{\int_{\nu_\mathrm{low}}^{\nu_\mathrm{high}} 2S_\varphi(\nu, \tilde{N}, h)d\nu}. \tag{5.38}$$

For active and hybrid ML lasers, T_C is the repetition period of the external modulation (clocking time), and for passively ML lasers, we choose the average of the inter-spike intervals, i.e.,

$$T_C \equiv \left\langle \frac{1}{N-1}\sum_{n=1}^{N-1} T_\mathrm{ISI,n}\right\rangle_M. \tag{5.39}$$

Note that T_C is obtained by at first averaging over the $N-1$ inter-spike intervals $T_{\mathrm{ISI},n}$ of a single noise realization and subsequently averaging over the M realizations of the noise ($\langle\,\cdot\,\rangle_M$). If von der Linde's theory is valid, i.e., under the assumption of uncorrelated, stationary probability distributions for amplitude and timing fluctuations, $S_\varphi \propto h^2$ holds, and as a consequence, the rms timing jitter defined in Eq. (5.38) is independent of the harmonic number h.

Note that in this section, the definition (5.38) of the rms timing jitter has been motivated by the sidebands of the harmonics of the power spectrum that contain the contributions of the timing fluctuations. In the next subsection, it will be shown that for stationary stochastic processes the rms timing-jitter is indeed proportional to the standard deviation of the timing fluctuations (see also Appendix D.3).

Figure 5.24 depicts the phase noise spectrum divided by the square of the harmonic number S_φ/h^2 for the free running ML laser in a double log plot as a function of positive offset frequencies ν_off for different harmonic numbers h. Beyond a corner frequency of about 2.2 MHz, all power spectra show the typical roll-off with a slope of $1/\nu^2$ (see discussion in next subsection). This is in qualitative agreement with recent experiments on QD passively ML lasers [LIN10c]. Beyond the corner frequency, S_φ/h^2 and thus σ_{rms} (see Eq. (5.38)) are independent of h, i.e., von der Linde's theory is valid. However, the largest contributions to the rms timing jitter are obtained for offset frequencies that are smaller than the corner frequency, where S_φ/h^2 depends on h. In conclusion, Fig. 5.24 suggests that von der Linde's technique is strictly valid for passively ML semiconductor lasers only for large lower offset frequencies of ν_{low} of 2–3 MHz, which is in agreement with recent experiments [LIN11f]. However, in experiments, lower offset frequencies in the kHz-range are frequently used [FIO11, LIN10c]. Then, the measured rms jitter depends on the harmonic number h, which has to be specified for reproducibility.

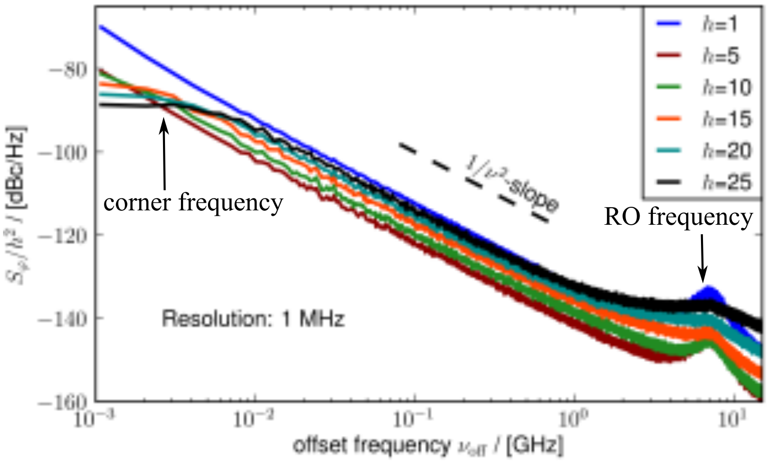

Figure 5.24: Phase noise spectra S_φ divided by the square of the harmonic number h as a function of the offset frequency ν_{off} for different harmonics of the spectrum for the free running laser. $1/\nu^2$ is the slope expected for white noise, and the resolution is 1 MHz. Black arrows mark the corner frequencies and the RO frequency, respectively. Parameters: $T_{\text{i}} = 4 \cdot 10^4\, T_{\text{ISI},0}$, $R_{\text{sp}} = 1.6\,\text{ns}^{-1}$, and other parameters as in Table 5.1.

5.6.2. Pure time-domain method to measure the timing jitter

Measuring the timing jitter from the rf-spectrum has the drawback that, in practice, the contributions of amplitude and timing jitter cannot be completely separated. Further, the required resolution of at least 1MHz leads to large data sets. Therefore, we use in addition a pure time-domain method for timing jitter measurements that was proposed in [MUL06] and is computationally less demanding. The idea for this method goes back to a paper of Haus et al. [HAU93a]. The authors used perturbation theory of the Haus's master equation for ML lasers [HAU75, HAU00] to derive equations of motions for the four orthogonal pulse perturbation parameters: pulse timing, energy, emission frequency, and optical phase [6]. For an analytical application of this technique to the DDE model with external injection see [REB11], and for an application of this technique to an extended version of the model suitable for hybrid mode locked lasers see [VLA10a].

---

[6] In a more mathematical description, the unperturbed pulse train is given by a stable limit-cycle in phase space $\mathcal{E}_0(t)$. Most sensitive to perturbations are the Floquet modes with Floquet multipliers on the unit cycle. These Goldstone modes are determined by the symmetries of the system. For instance, autonomous differential equations have always one Goldstone mode associated with their time-shift symmetry, which is given by $\chi_0 \equiv \frac{d}{dt}\mathcal{E}_0(t)$. Since Floquet modes are orthogonal, projecting the perturbed pulse train onto their adjoints and imposing solvability conditions yields equations of motions for the perturbation in the directions of the Goldstone modes. This yields the orthogonal pulse perturbations [HAU93a].

Here, we focus on a numerical description of the perturbations on the timing position t_n of the pulses, where $n = 1, \dots N$ for $N \in \mathbb{N}$ labels the pulses, and N is the total number of pulses in the stream. The timing positions are detected with the following algorithm: in Section 5.3, we discussed that the main pulses are shaped by a net gain window with $\mathcal{G}(t) > 0$ (see Fig. 5.4). Therefore, at first, a probability density is defined by

$$\rho_n(t) \equiv \frac{\mathcal{G}^2(t)}{\mathcal{G}_n}, \quad \text{with} \quad \mathcal{G}_n \equiv \int_{t_{n,b}}^{t_{n,e}} \mathcal{G}^2(t)dt, \tag{5.40}$$

where $t_{n,b}$ is the first time point, at which the leading edge of the n-th pulse exceeds a threshold $\mathcal{G}(t_{n,b}) > G_{\text{thres}}$, and $t_{n,e}$ is the first time point, at which the trailing edge of the pulse deceeds the threshold value, i.e., $\mathcal{G}(t_{n,e}) < G_{\text{thres}}$[7]. In the numerical simulations, $G_{\text{thres}} = 0.01$ was chosen. The timing position of the n-th pulse is determined by the first moment (mean) of the distribution function $\rho_n(t)$

$$t_n \equiv \int_{t_{n,b}}^{t_{n,e}} \rho_n(t)\, t\, dt, \tag{5.41}$$

higher moments of $\rho_n(t)$ give informations about the shape of the pulse. Note that for asymmetrical pulses, the t_n's do not coincide with the time points of the intensity maxima of the pulses. Further, this pulse detection method does not permit to include the smaller, feedback induced pulses (see Fig. 5.5) directly into the calculation of the timing jitter, as long as they are not large enough to open a net gain window ($\mathcal{G} > 0$). But, as discussed in Sec. 5.4, the feedback induced pulses have much smaller peak intensities. This is why they are expected to have only a negligible effect on the power spectrum of the ML laser subject to feedback. This is confirmed by the good agreement of the rms timing jitter calculated with this technique with the rms timing jitter calculated from the power spectrum of the full system, which will be discussed in Section 5.7.

Further, the main resonant regimes are of particular interest for applications, because in these regimes the largest reduction of the timing jitter is obtained, which will be discussed in Section 5.7. Note that the above method is exact in the main resonant regimes, where only one pulse travels in the cavity.

For each of the M noise realizations, a set of timing fluctuations is obtained

$$\{\Delta t_n \equiv t_n - nT_C\}_{n=1}^{N}, \tag{5.42}$$

which are the temporal deviations of the timing positions of the pulses in a noisy pulse stream $\{t_n\}_{n=1}^{N}$ from the timing positions $\{nT_C\}_{n=1}^{N}$ of the pulses in an ideal, jitter free pulse stream (clock) (see Fig. 5.25). In active and hybrid ML lasers, the clock is given by the modulation frequency of the external electrical signal. In passively ML lasers, we use the average of the inter-spike interval-times

$$\{T_{\text{ISI},n} \equiv t_{n+1} - t_n\}_{n=1}^{N-1} \tag{5.43}$$

---

[7] In the paper of Mulet and Mørk [MUL06], the pulse energy $|\mathcal{E}|^2$ is used instead of the net gain $\mathcal{G}$ to determine the timing positions t_n of the pulses. This has the advantage that the pulse energy jitter can be evaluated in addition to the timing jitter. However, since the additive noise is applied to the field equation, it has a much noisier time trace than the carrier equations, which in turn results in more artifacts for large noise strengths.

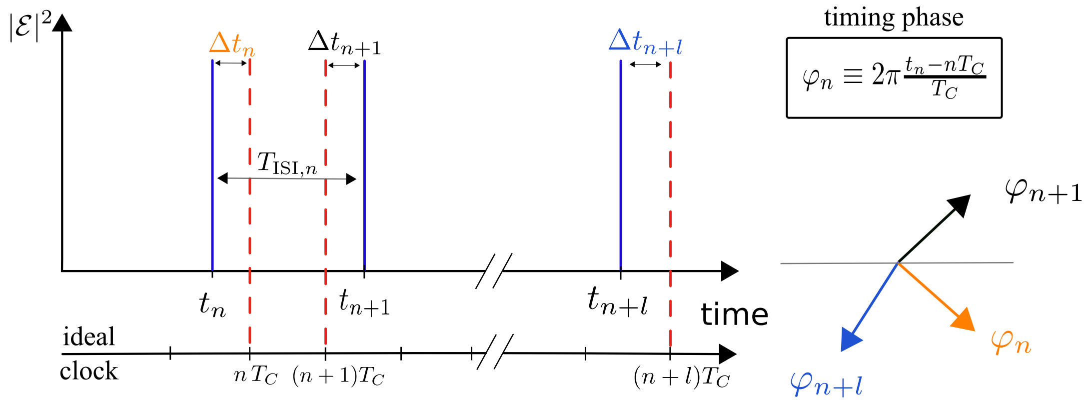

Figure 5.25.: Timing positions $\{t_n\}_{n=1}^N$ of the noisy pulse stream and of an ideal clock $\{nT_C\}_{n=1}^N$ yielding the timing deviations $\{\Delta t_n \equiv t_n - nT_C\}_{n=1}^N$ and a set of inter-spike intervals $\{T_{\mathrm{ISI},n} \equiv t_{n+1} - t_n\}_{n=1}^{N-1}$. N is the number of pulses in the pulse stream, and the average of the inter-spike interval times is used as clocking time T_C. Further, the timing deviations can be expressed as a set of phase fluctuations $\{\varphi_n \equiv 2\pi \Delta t_n / T_C\}_{n=1}^N$.

as timing T_C of the reference clock.

The timing fluctuations can also be expressed as a set of fluctuations φ_n of the (timing) phase φ

$$\left\{ \varphi_n \equiv \frac{2\pi}{T_C} \Delta t_n = 2\pi \frac{t_n - nT_C}{T_C} \right\}_{n=1}^{N} . \tag{5.44}$$

Considering the timing phase as a continuous variable of time $\varphi = \varphi(t)$ with $\varphi(t_k) = \varphi_k$ (see Fig. 5.25), the instantaneous repetition frequency of the pulses ν_{rep} is given by the derivative of φ with respect to time

$$\nu_{\mathrm{rep}}(t) = \frac{d\varphi(t)}{dt}. \tag{5.45}$$

The definitions of the phase fluctuations (5.44) and of the PSD (see Eq. (D.17)) reveal that the power spectra of timing fluctuations and timing phase fluctuations are related by

$$S_\varphi(\nu_{\mathrm{off}}, N) = \left(\frac{2\pi}{T_C} \right)^2 S_{\Delta t}(\nu_{\mathrm{off}}, N), \tag{5.46}$$

where ν_{off} is the offset frequencies from the carrier frequency $1/T_C$. To simplify notation, the subscript "off" is suppressed for the following calculation. For non-stationary stochastic processes, the power spectra depend on the number N of timing fluctuations, i.e., on the length T_{i} of the time series. Experimentally, the noise of the timing phase is obtained by the noise of the lowest harmonics ($h = 1$) of the output of a photodiode measuring the intensity of the ML laser, i.e., from the noise of the photocurrent [KEF08], and corresponds to the phase noise introduced in the previous subsection.

Taking into account that the Fourier transform of the linear operator $\frac{d}{dt}$ yields a multiplication with $\omega = 2\pi\nu$, the PSD of the timing phase can be expressed in terms of the PSD $S_{\nu_{\mathrm{rep}}}$ of the repetition frequency ν_{rep} as

$$S_\varphi(\nu, N) = \frac{1}{\nu^2} S_{\nu_{\mathrm{rep}}}(\nu, N). \tag{5.47}$$

Thus, fluctuations of low (offset) frequencies ν lead to larger accumulated timing deviations, i.e., larger fluctuations of the timing phase. Furthermore, if $S_{\nu_{\mathrm{rep}}}$ is frequency independent, i.e., the noise of ν_{rep} is white, $S_\varphi \propto 1/\nu^2$. From the phase noise spectrum in Fig. 5.24, it can be seen that the white noise added to the dynamical equation (5.28a) of the field amplitude $\mathcal{E}$ translates into an essentially constant (white) PSD of ν_{rep}, which corresponds to the $1/\nu^2$-slope of S_φ. Since this $1/\nu^2$-slope of S_φ is also observed experimentally [LIN10e, LIN11f], we can conclude that the timing jitter is essentially driven by white spontaneous emission noise [HAU93a, ELI97].

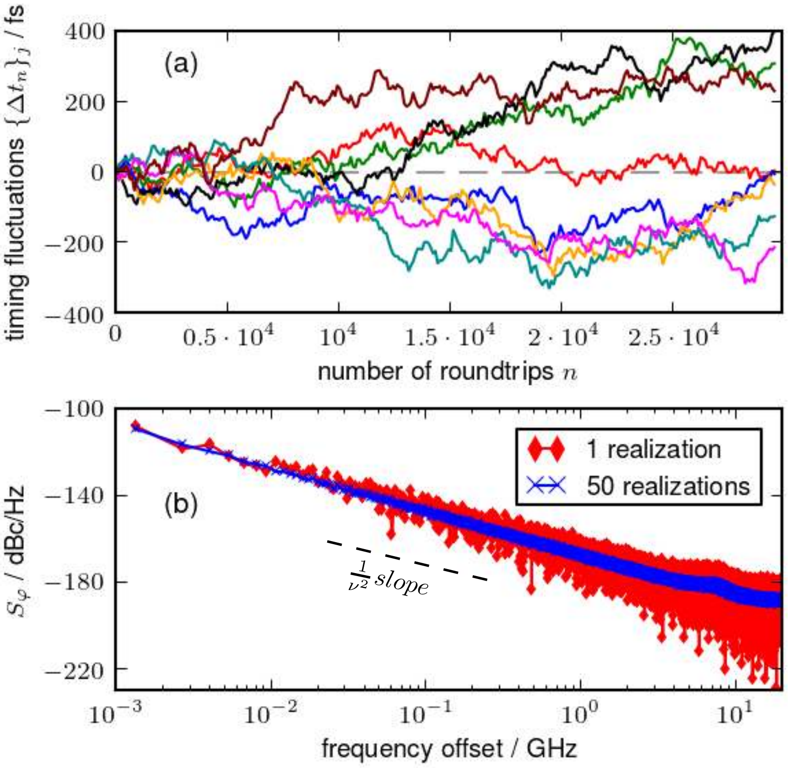

Figure 5.26.: **(a)**: Different realization of the timing fluctuations $\{\Delta t_n\}_j$ for the free running ML laser. The ideal clock is given by the gray dashed horizontal line. **(b)**: Phase-noise spectra S_φ for a single realization (red diamonds) and averaged over 50 realization (blue crosses). The dashed black line marks the $1/\nu^2$-dependence obtained for white noise of the repetition frequency. The resolution is 1.5 MHz. Parameters: $T_{\mathrm{i}} = 3 \cdot 10^4\, T_{\mathrm{ISI},0}$, $R_{\mathrm{sp}} = 0.1\,\mathrm{ns}^{-1}$, and other parameters as in Table 5.1.

In Fig. 5.26(a), different realizations j of the timing fluctuations $\{\Delta t_n\}_j$ are depicted as functions of the number of roundtrips n in the cavity, and the gray dashed horizontal line marks the ideal clock (no fluctuations). For the simulations, pulse trains containing $N = 3 \cdot 10^4$ pulses were used. In Fig. 5.26(b), phase noise spectra calculated by the time-domain method (Eq. (5.46)) are depicted. Red diamonds depict S_φ for a single set of timing fluctuations ($M = 1$), and blue crosses depict the S_φ obtained by averaging over $M = 50$ noise realizations to illustrate that the averaging procedure over multiple realizations of the noise is necessary to obtain a meaningful result. In the log-log plot of Fig. 5.26(b) the spectrum decays linearly over more than three orders of magnitude, which corresponds to a $1/\nu^2$-decay of S_φ (cf. Fig. 5.24). The slight increase of the phase noise at high frequency offsets of about 7.5 GHz stems from the RO frequency of the system.

In Appendix D.3 it is discussed that for wide-sense stationary processes the variance $\mathrm{Var}(x)$ of a stochastic process x with zero mean ($\langle x\rangle = 0$) can be calculated from its PSD S_x as

$$\mathrm{Var}(x) = \frac{1}{2\pi}\int_0^\infty 2S_x(\omega)d\omega = \int_0^\infty 2S_x(\nu)d\nu. \tag{5.48}$$

This motivates the following definition of the rms timing jitter, which is a measure for the standard deviation of the timing fluctuations,

$$\sigma_{\mathrm{rms}}(\nu_{\mathrm{low}}, \nu_{\mathrm{high}}, N) \equiv \sqrt{\int_{\nu_{\mathrm{low}}}^{\nu_{\mathrm{high}}} 2S_{\Delta t}(\nu, N)d\nu} = \frac{T_C}{2\pi}\sqrt{\int_{\nu_{\mathrm{low}}}^{\nu_{\mathrm{high}}} 2S_{\varphi}(\nu, N)d\nu}, \tag{5.49}$$

here ν_{low} and ν_{high} denote the minimal and maximal offset frequency from the carrier frequency $1/T_C$, respectively. Since the PSD of a real stochastic process is symmetric, i.e., $S_x(\nu) = S_x(-\nu)$, it is sufficient to integrate over the side band with positive offset frequencies. This is why the PSDs on the right hand side of Eq. (5.49) are multiplied by a factor of 2[8]

5.6.3. Pulse-to-pulse and long-term jitter

Figure 5.26(a) reveals that the variance of the timing fluctuations $\Delta t_n = t_n - nT_C$ increase with the number n of roundtrips of the light in the cavity, while their mean remains zero ($\langle \Delta t_n\rangle_M = 0$). Thus ,the timing fluctuations Δt_n can be modeled by a non wide-sense stationary random process (see Appendix D.2). The reason is that in contrast to active and hybrid mode-locking, in passively ML lasers there is no external reference clock that suppresses the drift of the timing fluctuations, i.e., the drift of the repetition frequency. Figure 5.27 depicts the variance of the timing fluctuations (divided by the number of roundtrips in the cavity n) versus n for the free running ML laser (red line), as well as for the main resonance with $\tau = 7\,T_{\mathrm{ISI},0}$ (dark-green line), the second order resonance with $2\tau = 15\,T_{\mathrm{ISI},0}$ (dark-blue line), and a non-resonant case with $\tau = 7.22T_{\mathrm{ISI},0}$ (black-line) for small feedback strength $K = 0.1$. The variance was calculated by averaging the timing fluctuations Δt_n for constant n over $M = 200$ realizations of the noise[9], i.e.,

$$\mathrm{Var}(\Delta t_n)(n, \tau) \equiv \langle(\Delta t_n(\tau))^2\rangle_M, \tag{5.50}$$

The variance divided by n ($\mathrm{Var}(\Delta t_n)/n$) decreases strongly for small n, but eventually approaches a constant value for large n ($n \gtrsim 5000$). Thus, for large n, the variance depends linearly on n, i.e.,

$$\mathrm{Var}(\Delta t_n)(n, \tau) = 2\,\mathrm{D}_{\Delta\mathrm{t}}(\tau)n, \tag{5.51}$$

---

[8] Note that in engineering disciplines commonly single sided PSDs are used. They are defined only for non-negative frequencies, and are thus two times higher than the two sided ones to obtain the same norm. This is why the factor of 2 is sometimes absent in the literature.

[9] In simulations with an external feedback loop that is long compared to the inter-spike interval time $T_{\mathrm{ISI},0}$, the integration time has to be long compared to the delay time τ to avoid transient behavior. For intermediate delay $\tau = \mathcal{O}(10T_{\mathrm{ISI},0})$ and long delay $\tau = \mathcal{O}(100T_{\mathrm{ISI},0})$, the system has therefore been integrated for $5\cdot 10^3\,T_{\mathrm{ISI},0}$ and $20\cdot 10^3\,T_{\mathrm{ISI},0}$, respectively, before calculating the timing fluctuations.

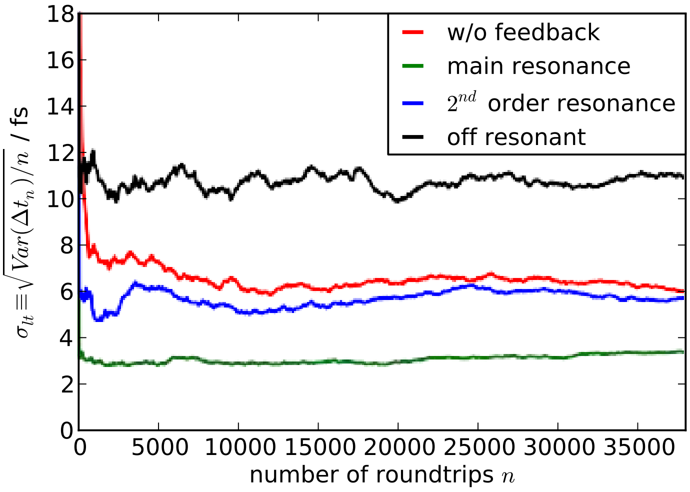

Figure 5.27: Long-term jitter σ_{lt} as a function of the number of roundtrips n of the light in the cavity for the solitary laser (red line), the main resonance with $\tau = 7\,T_{\mathrm{ISI},0}$ (dark-green line), the second order resonance with $2\tau = 15\,T_{\mathrm{ISI},0}$ (dark-blue line), and for a non-resonant case with $\tau = 7.22 T_{\mathrm{ISI},0}$ (black line). Parameters: $R_{\mathrm{sp}} = 1.6\,\mathrm{ns}^{-1}$, $K = 0.1$, and other parameters as in Table 5.1.

where we have introduced the diffusion constant $\mathrm{D}_{\Delta \mathrm{t}}(\tau)$, which depends on the delay time τ. As a result, the timing fluctuations Δt_n for $n \gtrsim 5000$ can be described by a discrete Lévy process with stationary, independent increments, which is better known as discrete Wiener process or random walk [GAR02, JAC10]. The timestep of the process is T_C, and at each timestep the probability distribution of the stochastic, cumulative process Δt_n is Gaussian with zero mean and variance of $\mathrm{D}_{\Delta \mathrm{t}}\, n$

$$\rho(\Delta t_n | \Delta t_1 = 0, n = 1) = \frac{1}{\sqrt{4\pi\,\mathrm{D}_{\Delta \mathrm{t}}\, n}} e^{-\frac{(\Delta t)^2}{2\,\mathrm{D}_{\Delta \mathrm{t}}\, n}}. \tag{5.52}$$

The statistically independent increments of the stochastic process are given by

$$\{j_l(1) \equiv \Delta t_{l+1} - \Delta t_l = t_{l+1} - t_l - T_C = T_{\mathrm{ISI},l} - T_C\}_{l=1}^{N-1}, \tag{5.53}$$

which are just the deviations of the inter-spike interval T_{ISI} from its mean value T_c.

Since for every n, the stochastic variable Δt_n is Gaussian, also the increments have a Gaussian probability distribution [JAC10], and the independence of its increments yields

$$\langle j_{n+l}(1) j_n(1) \rangle_M = \langle (j_n(1))^2 \rangle \delta_{l,0}, \tag{5.54}$$

where δ denotes Kronecker's delta.

The strong decrease of $\mathrm{Var}(\Delta t_n)/n$ for small n could be due to finite correlations times of the Δt_n's for adjacent n, which cause deviations from Eq. (5.51). Intuitively, this can be understood as follows: we know from the discussion in Section 5.3 that the distance between subsequent pulses is fixed by the time the saturable gain G needs to recover until it overcomes the total loss $Q_t = Q + |\ln \kappa|$, and a net gain window $(G - Q_t > 0)$ opens up (cf. Fig. 5.4). Thus, if the n-th pulse has a large negative timing deviation with respect to the clock $(\Delta t_n < 0)$, we expect that also the subsequent pulse arrives previous to the clock $(\Delta t_{n+1} < 0)$.

In summary, equation (5.51) expresses that for an integration time T_{i}, which is longer than the largest correlation time in the system, the effect of the white noise applied to the field equation (5.28a) can, in a projection into the direction of the timing fluctuations, be modeled by a random walk.

Since $\mathrm{Var}(\Delta t_n)/n$ is a constant for large n, it is a good measure for the timing jitter,

$$\sigma_{\mathrm{lt}} \equiv \sqrt{\mathrm{Var}(\Delta t_n)/n} = \sqrt{2\,\mathrm{D}_{\Delta \mathrm{t}}(\tau)}. \tag{5.55}$$

This type of jitter is known as *long-term timing jitter* [LEE02c]. For $n = 1$, the standard deviations of the inter-spike intervals $T_{\mathrm{ISI},n}$ from their average value T_C is obtained. This quantity is known as **pulse-to-pulse**

$$\sigma_{\mathrm{ptp}} = \sqrt{\mathrm{Var}(\Delta t_1)} = \sqrt{\langle (T_{\mathrm{ISI}_1} - T_C)^2 \rangle_M} \tag{5.56}$$

or **cycle-to-cycle jitter** in the physical community [KEF08], and in the electrotechnical community, the name **period jitter** is commonly used [LEE02c]. The pulse-to-pulse jitter σ_{ptp} corresponds (up to the normalization with respect to T_C) to the standard deviation of the inter-spike interval time R_T (see Eq. (4.62)) discussed in the context of the coherence resonance in Section 4.8. If the assumption of independent increments is strictly valid, then $\mathrm{Var}(\Delta t_n)$ needed for the calculation of σ_{lt} in Eq. (5.55) can be calculated from the ensemble of the n-th differences

$$\{ j_l(n) \equiv \Delta t_{l+n} - \Delta t_l = t_{l+n} - t_l - T_C = T_{\mathrm{ISI},l+n} - T_C \}_{l=1}^{N-n} \tag{5.57}$$

of a single noise realization, instead of averaging over M realizations, which speeds up the calculations tremendously. Analogously, the pulse-to-pulse jitter may, under the assumption that the T_{ISI}'s are independent, be calculated from the ensemble of inter-spike intervals of a single noise realization

$$\sigma_{\mathrm{ptp}} = \left[\frac{1}{N-1} \sum_{n=1}^{N-1} \left(T_{\mathrm{ISI},n} - \langle T_{\mathrm{ISI}} \rangle \right)^2 \right]^{\frac{1}{2}}. \tag{5.58}$$

5.6.4. Calculating the root-mean-square timing jitter from the long-term timing jitter

Under the assumption that the timing fluctuations can be modeled by a random walk, the rms timing-jitter may be calculated from the long-term timing jitter, which will be discussed in this subsection. More precisely, the statistical independence of the increments of the timing deviations Δt_n permits to analytically calculate their autocorrelation function, their PSD, and eventually their rms timing jitter from the diffusion constant $\mathrm{D}_{\Delta \mathrm{t}}$, and thus from the long-term jitter (see Eq. (5.55)). For the sake of simplicity, the timing deviations are considered for the remainder of this section as functions Δt of a continuous time variable t, which equals the discrete set of timing fluctuations $\{\Delta t_n\}_{n=1}^{N}$ at the time points nT_C, i.e.,

$$\Delta t(nT_C) \equiv \Delta t_n, \quad \text{for: } 1 \le n \le N \quad \text{and} \quad N \in \mathbb{N}. \tag{5.59}$$

As a consequence, the variance of $\Delta t = \Delta t(t)$ is given by (cf. Eq. (5.51))

$$\mathrm{Var}(\Delta t) = \langle (\Delta t(t))^2 \rangle = 2\,\tilde{\mathrm{D}}_{\Delta \mathrm{t}}\, t, \quad \text{with} \quad \tilde{\mathrm{D}}_{\Delta \mathrm{t}} \equiv \frac{\mathrm{D}_{\Delta \mathrm{t}}}{T_C}. \tag{5.60}$$

Calculating the autocorrelation of the timing deviations $\Psi_{\Delta t}$ from its definition in Eq. (D.11)), yields

$$\Psi_{\Delta_t}(s,T_\mathrm{i}) = \frac{1}{T_\mathrm{i}}\int_0^{T_\mathrm{i}-|s|}\big\langle \Delta t(t+s)\Delta t(t)\big\rangle dt$$
$$= \frac{2\,\tilde{\mathrm{D}}_{\Delta\mathrm{t}}}{T_\mathrm{i}}\int_0^{T_\mathrm{i}-|s|} t\,dt = \tilde{\mathrm{D}}_{\Delta\mathrm{t}}\,T_\mathrm{i}\left(1-\frac{|s|}{T_\mathrm{i}}\right)^2. \tag{5.61}$$

In the first equality of the second line of Eq. (5.61), we have used that Δt is a cumulative stochastic process with independent increments. This means that Δt at a time point $t+s$ can always be split into two statistically independent parts: a part $\Delta t(t)$ that depends only on t and a rest $R_{\Delta t}(s)$ that depends only on s, i.e. $\Delta t(t+s) = \Delta_t(t) + R_{\Delta(t)}(s)$, with $\langle \Delta t(t) R_{\Delta t}(t)\rangle = 0$. Thus, the covariance function simplifies as

$$\langle \Delta(t+s)\Delta(t)\rangle = \langle [\Delta(t) + R_{\Delta t}(s)]\Delta t\rangle = 2\,\tilde{\mathrm{D}}_{\Delta\mathrm{t}}\,t.$$

The Wiener-Khinchin theorem [GAR02] stating that PSD and autocorrelation function form a Fourier-pair (see Eqs. (D.12) in Appendix D.3) permits to calculate the power spectrum of the timing fluctuations from Eq. (5.61)

$$S_{\Delta t}(\omega,T_\mathrm{i}) = 2\int_0^{T_\mathrm{i}}\Psi_{\Delta t}(s,T_\mathrm{i})\cos(\omega s)ds = \frac{4\,\tilde{\mathrm{D}}_{\Delta\mathrm{t}}}{\omega^2}\left[1-\frac{\sin(\omega T_\mathrm{i})}{\omega T_\mathrm{i}}\right] \overset{\omega T_\mathrm{i}\gg 1}{\approx} \frac{4\,\tilde{\mathrm{D}}_{\Delta\mathrm{t}}}{\omega^2}. \tag{5.62}$$

For long integration times T_i and not to small offset frequencies ω, the limit $\omega T_\mathrm{i} \gg 1$ is valid, which permits to neglect the sinc-function in the rectangular brackets. In this limit, we retrieve the $1/\omega^2$-decay of $S_{\Delta t}$. Thus, also the phase noise spectrum S_φ decays like $1/\omega^2$ (see Eq. (5.46)), which was observed in the phase noise spectrum of Fig. 5.24 for offset frequencies larger than $\sim$ 2–3 MHz .

Eventually, the rms-timing jitter can be calculated by inserting Eq. (5.62) into Eq. (5.49), which yields

$$\sigma_\mathrm{rms}(\nu_\mathrm{low},\nu_\mathrm{high},T_\mathrm{i}) = \sqrt{\int_{\nu_\mathrm{low}}^{\nu_\mathrm{high}} 2S_{\Delta t}(\nu,T_\mathrm{i})d\nu} = \frac{1}{\pi}\sqrt{2\,\tilde{\mathrm{D}}_{\Delta\mathrm{t}}\left(\frac{1}{\nu_\mathrm{low}}-\frac{1}{\nu_\mathrm{high}}\right)}$$
$$= \frac{\sigma_\mathrm{lt}}{\pi\sqrt{T_C}}\sqrt{\left(\frac{1}{\nu_\mathrm{low}}-\frac{1}{\nu_\mathrm{high}}\right)} \approx \frac{\sigma_\mathrm{lt}}{\pi\sqrt{T_C}}\frac{1}{\sqrt{\nu_\mathrm{low}}}. \tag{5.63}$$

In the last approximation of Eq. (5.63), the upper integration limit ν_high has been neglected, because ν_high is in the order of GHz and therefore much larger than the lower integration limit, which has to be chosen in the order of MHz to guarantee that the last approximation in Eq. (5.62) remains valid. Equation (5.63) provides us with a method to calculate σ_rms from the long-term jitter σ_lt defined in Eq. (5.55). The latter has the advantage of a much lower computational effort.

The assumption of vanishing correlations between the timing fluctuations used in the calculation of $\Psi_{\Delta t}$ (Eq. (5.61)) can be avoided. In [ELI96, ELI97], the authors have calculated the PSD of the timing fluctuations under the assumption of exponentially decaying correlations

$$\langle \Delta t(t) \Delta t(s) \rangle = \langle \Delta t^2 \rangle e^{-\frac{|t-s|}{\tau_c}}, \tag{5.64}$$

where τ_c denotes the correlation time. Such a stochastic process is known as Ornstein-Uhlenbeck-Process, and its PSD is a Lorentzian [GAR02]. This was employed in [KEF08, LIN11f] to calculate the long-term timing jitter and the rms timing jitter by fitting the experimentally measured phase noise spectrum with a Lorentzian. In the meaningful limit that the lower offset frequency ν_{low} is small compared to the FWHM $\Delta\nu_{\mathrm{rf}}$ of the Lorentzian, a similar expression for the rms timing jitter as in Eq. (5.63) is obtained with σ_{lt} expressed in terms of $\Delta\nu_{\mathrm{rf}}$ [KEF08].

5.7. Impact of the feedback on the timing jitter

Having discussed the different measures for the timing jitter in the last section, we focus now on the impact of the feedback on the timing jitter. Therefore, at first, the impact of the feedback on the power spectrum $S_{|\mathcal{E}|}$ is discussed for intermediate and long delay. In the next subsection, the different methods to measure the rms timing jitter introduced in the last section are compared, and the long-term timing jitter is studied in dependence of τ and K. This permits to retrieve the "resonance cones" discussed for the deterministic system in Section 5.4.2. Eventually, in the last subsection, the dependence of these "resonance cones" is studied for nonzero phase-amplitude coupling.

Figure 5.28 depicts the PSD $S_{|\mathcal{E}|}(\nu_{\mathrm{off}})$ (color code) of the absolute value of the field amplitude as a function of the delay time τ for intermediate delay between the 7th ($\tau = 7T_{\mathrm{ISI},0}$) and the 8th ($\tau = 8T_{\mathrm{ISI},0}$) main resonance and a small feedback strength of $K = 0.1$. Thus, it corresponds to Fig. 5.8 obtained for the pulse maxima of the deterministic system. The power spectrum is depicted in an interval of ± 0.5 GHz around the $h = 25$-th harmonics of the free running ML laser, i.e., the center frequency in Fig. 5.28(a) is $\nu = 25\nu_{\mathrm{rep},0}$. Bright colors indicate high power.

From the discussion of the resonance structure of inter-spike interval time T_{ISI} and delay time τ in Section 5.4, we remember that in the main resonances of the deterministic system the pulse height is increased while the pulse width is decreased, which indicates an increase of the stability of the pulses with respect to the free running laser. Consequently, the main resonant regimes displays the lowest power in the side bands of the spectrum of Fig. 5.28(a) (dark colors), which reveals that in these regimes, the pulse stream has the highest temporal stability. Further, a reduction of the power of the side bands can be observed in the second order resonant regime in an interval around $\tau = 15/2T_{\mathrm{ISI},0}$. The destabilizing effect of non-resonant feedback can be observed best between the main resonance with $\tau = 7T_{\mathrm{ISI},0}$ and the fifth order resonance with $\tau = 36/5T_{\mathrm{ISI},0}$, where broad, high power side bands are observed indicating a high timing jitter. They correspond to the broad pulse forms of the deterministic system depicted in Fig. 5.9 resulting from a mismatch of the main pulses with the feedback induced pulses. Further, the pulling of the repetition frequency in the main resonant regime that was discussed in Section 5.4.7 is clearly observed in Fig. 5.28(a). Also in the second order resonant regime, the repetition frequency depends nearly linearly on the delay time τ.

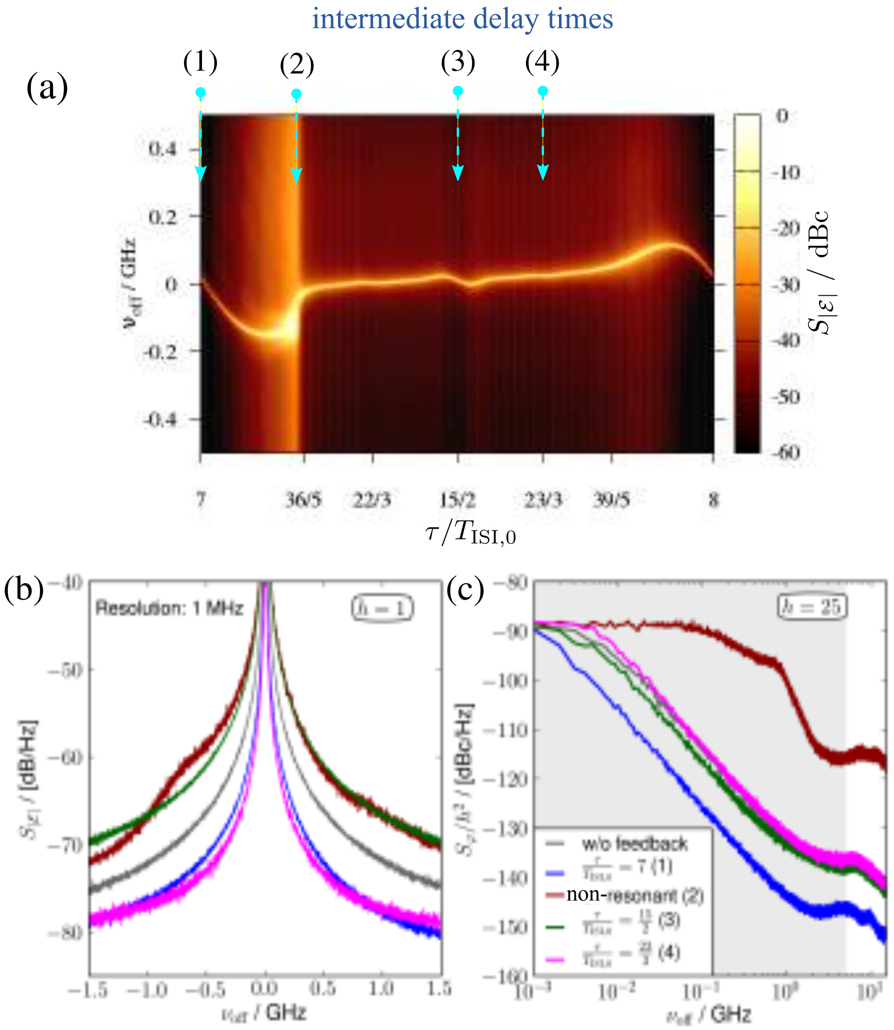

Figure 5.28.: **(a)**: Power spectra (color code) of the absolute value of the field amplitude $|\mathcal{E}|$ versus delay time τ for intermediate delay. ($T_{\mathrm{ISI},0}$ is the inter-spike interval time of the free running laser.) and small feedback strength $K = 0.1$. The spectrum is centered around the $h = 25$-th harmonics, and $\nu_{\mathrm{off}} = \nu - h\nu_{\mathrm{rep}}$ denotes the offset frequency. (ν_{rep} is the repetition rate of the free running laser.) **(b)**: Power spectrum of $|\mathcal{E}|$ centered at the first harmonics ($h = 1$) for τ-values indicated by (1)–(4) in **(a)** as well as for the free running laser (gray). **(c)**: Phase noise spectrum S_φ for positive ν_{off} of the $h = 25$-th harmonics for τ-values indicated by (1)–(4) in **(a)** as well as for the free running laser (gray). Bright shading indicates the range of integration for the calculation of the rms timing jitter. The resolution is 1 MHz. Parameters: $T_{\mathrm{i}} = 4 \cdot 10^4\, T_{\mathrm{ISI},0}$, $R_{\mathrm{sp}} = 1.6\,\mathrm{ns}^{-1}$, $K = 0.1$, and other parameters as in Table 5.1.

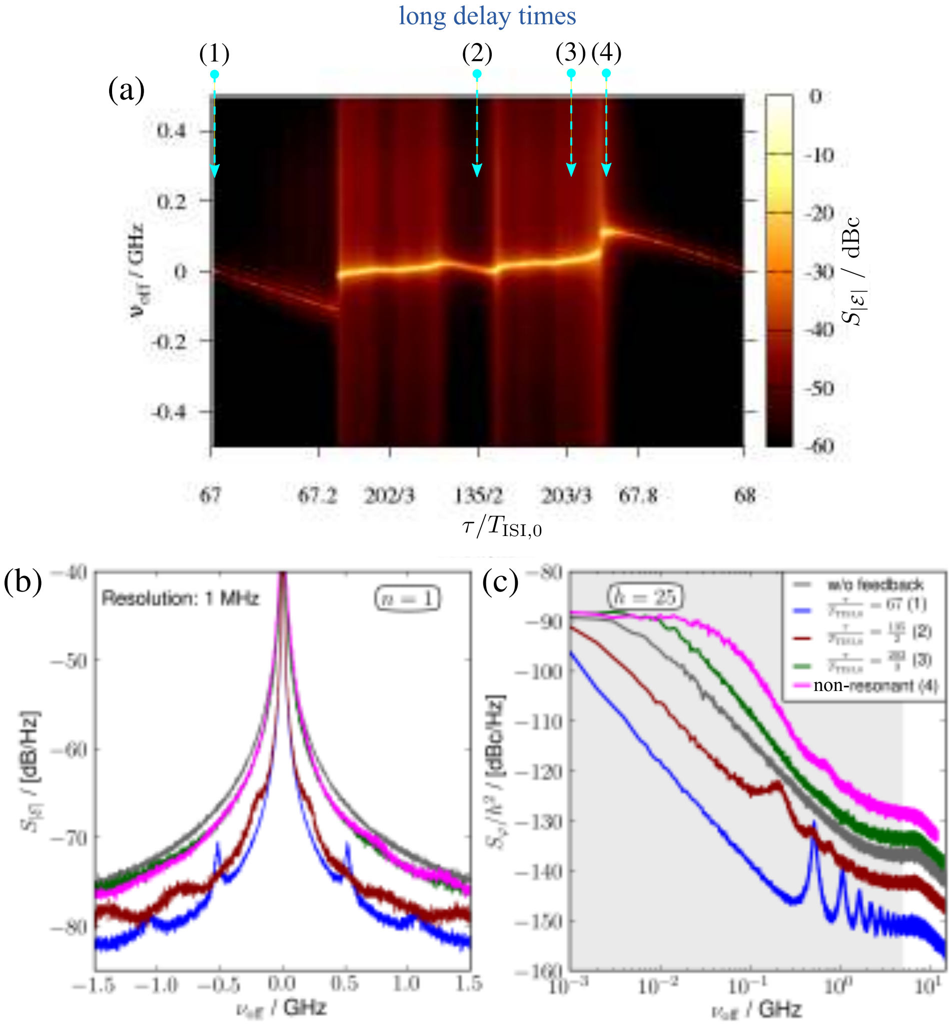

Figure 5.29.: Same as Fig. 5.28 but in the regime of long delay times.

Figure 5.28(b) depicts $S_{|\mathcal{E}|}$ in an interval of $\pm 1.5\,\mathrm{GHz}$ around the first harmonics (center frequency ν_{rep}) for the free running ML laser (gray) as well as for four τ values indicated by blue arrows labeled (1)–(4) in Fig. 5.28(a). It reveals a strong decrease of the rf-linewidth, i.e., the FWHM of $S_{|\mathcal{E}|}$, for resonant optical feedback (blue line) with respect to the free running laser (gray line), while the rf-linewidth is strongly increased for non-resonant optical feedback (brown line). Further, for non-resonant feedback, the $S_{|\mathcal{E}|}$ is asymmetric with respect to the center frequency, which was also observed experimentally [FIO11]. If the timing jitter is calculated by fitting the rf-spectrum with a Lorentzian to extract its FWHM as discussed in Subsection 5.6.4 and applied in [KEF08, LIN11f], the asymmetric lineshape of $S_{|\mathcal{E}|}$ for non-resonant feedback could yield artifacts.

Figure 5.28(c) depicts the phase noise spectrum S_φ as obtained from Eq. (5.37) for the $h = 25$-th harmonics for the free running laser (gray) as well as for the four delay times that are indicated by blue arrows labeled (1)–(4) in Fig. 5.28(a). Thus, Fig. 5.28(c) corresponds to vertical sections of Fig. 5.28(a) along the blue arrows and for positive offset frequencies ν_{off}. The phase noise spectra for the exact main resonance (blue line labeled (1)), the second order resonance (brown line labeled (3)), and the third order resonance (pink line labeled (4)), show, similar to the phase noise spectrum of the free running laser (gray line), a $1/\nu^2$-slope, which indicates a white PSD of the instantaneous frequency ν_{rep}. Thus, we expect that in the resonant regime, the rms timing jitter σ_{rms} can be calculated from the long-term jitter σ_{lt} from Eq. (5.63). However, for off resonant feedback (brown line labeled by (2)), the decay of S_φ with the offset frequency is more complicated.

Figure 5.29 corresponds to Fig. 5.28 in the regime of long delay times. From the power spectrum $S_{|\mathcal{E}|}$ of Fig. 5.29(a), we note that the side band suppression is in the resonant regimes much stronger than for intermediate delay (dark colors) indicating a more efficient temporal stabilization of the pulse stream, i.e., a stronger reduction of the timing jitter. Further, the resonant regimes are strongly broadened with respect to intermediate delay. This corresponds to the broadening of the main resonant regimes of the deterministic system (compare for low feedback strengths Fig. 5.7(e) to Fig. 5.13(e)). Moreover, the pulling of the center frequency in the main resonant regime is smaller for the long delay than for intermediate delay as discussed in Section 5.4.7.

The power spectrum $S_{|\mathcal{E}|}$ in Fig. 5.29(b) reveals that in the main resonances (blue line) and in the second order resonances (brown line), the rf-linewidth is strongly reduced with respect to the free running laser (gray line), which is in agreement with experimental results for ML QW lasers [SOL93], for ML quantum dash lasers [MER09], and for ML QD lasers [LIN10e, MES10, FIO11, LIN11d, ROS12b]. The phase noise spectra S_φ depicted in Fig. 5.29(c) indicate that the phase noise measured from the side band of the $h = 25$-th harmonics is reduced under resonant optical feedback (blue and brown line) with respect to the solitary laser (gray line), but enhanced for non-resonant feedback (pink line), which was observed experimentally in [GRI09]. In the main resonances, the roundtrip frequency of the light in the external cavity $1/\tau \approx 0.58\,\mathrm{GHz}$ can be clearly seen as sidepeaks in the power spectrum of Fig. 5.29(b) (blue line) and as "rippling" in the tail of the phase noise spectrum (blue line inf Fig. 5.29(c)), which is in correspondence with experimental findings [MER09, FIO11, ROS12b].

5.7.1. Feedback dependence of rms timing jitter and long-term timing jitter

In this subsection, it is studied how the delay induced changes of the power spectrum of the ML laser translate to changes of the timing jitter. In Figure 5.30(a), the rms timing jitter σ_{rms} is depicted vs. τ in the regime of intermediate delay and for a small feedback strengths of $K = 0.1$. The figure compares the three different methods to measure σ_{rms} discussed in the last section: the red line depicts σ_{rms} calculated from the $h = 25$-th harmonics of the power spectrum $S_{|\mathcal{E}|}$ (see Eq. (5.38)), the black line indicates σ_{rms} calculated from the timing fluctuations $\{\Delta t_n\}$ (see Eq. (5.49)), and the green line

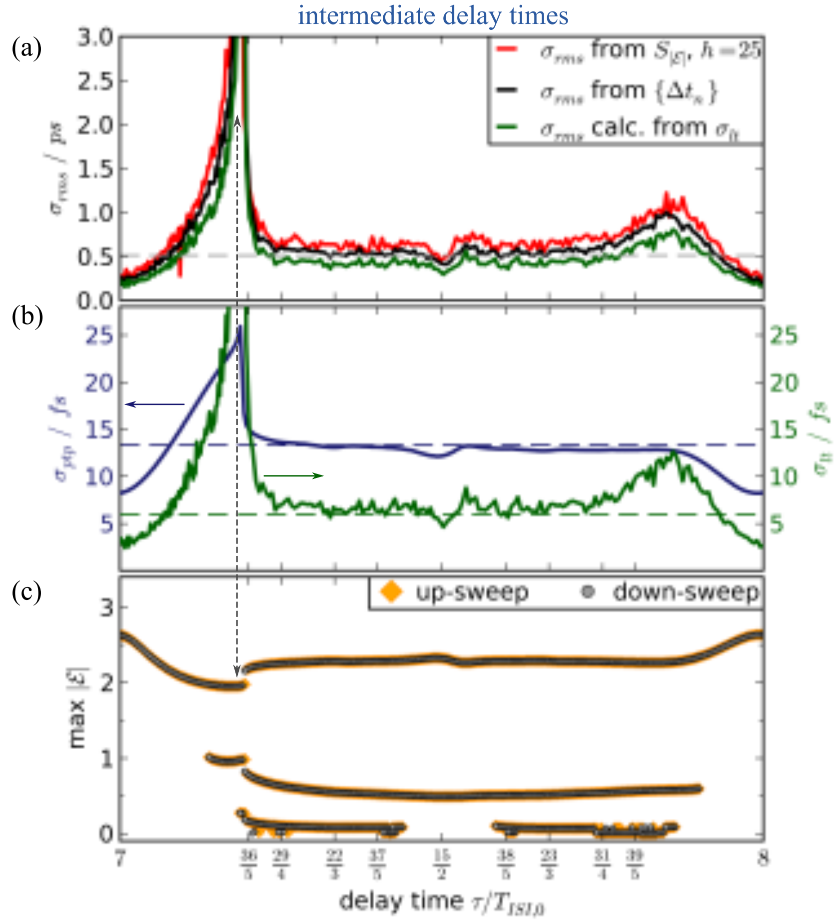

Figure 5.30.: **(a)**: Root-mean-square timing jitter σ_{rms} in dependence of the delay time τ for intermediate delay times and small $K = 0.1$. The red line depicts σ_{rms} calculated from the $h = 25$-th harmonics of the power spectrum $S_{|\mathcal{E}|}$ of the absolute value of the field amplitude $|\mathcal{E}|$ (Eq. (5.38)), the black line indicates σ_{rms} calculated from the timing fluctuations $\{\Delta t_n\}$ (Eq. (5.49)), and the green line depicts σ_{rms} calculated from the long-term jitter σ_{lt} (Eq. (5.63)). The horizontal gray line denotes the rms timing jitter of the free running laser. **(b)**: Dependence of pulse-to-pulse jitter σ_{ptp} (blue line, left y-axis) and long-term jitter σ_{lt} (green line, right y-axis) on τ. Horizontal blue and green dashed lines mark the pulse-to-pulse and the long-term timing jitter of the free running laser, respectively. **(c)**: Bifurcation diagram of maxima of $|\mathcal{E}|$ vs. τ for up-sweeping τ (orange diamonds) and down-sweeping τ (gray dots). Gray shadings indicate a reduction of the jitter with respect to the free running laser. Parameters: $T_{\mathrm{i}} = 4 \cdot 10^4\, T_{\mathrm{ISI},0}$, $R_{\mathrm{sp}} = 1.6\,\mathrm{ns}^{-1}$, $K = 0.1$, and other parameters as in Table 5.1.

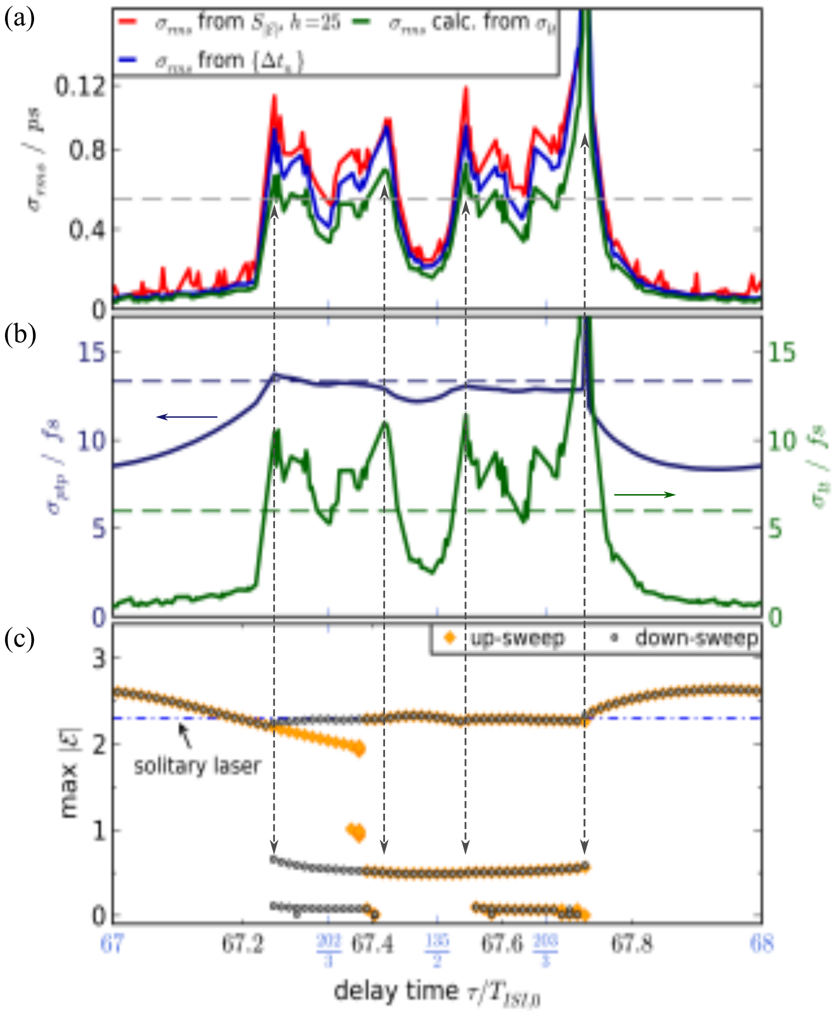

Figure 5.31.: Same as Fig. 5.28 but in the regime of long delay times τ.

depicts σ_{rms} obtained from the long-term jitter σ_{lt} under the assumption that the timing fluctuations can be described by a random walk, i.e., by a cumulative stochastic process with Gaussian probability distribution and statistically independent increments. For the first two methods, the phase noise spectra were integrated from $\nu_{\mathrm{low}} = 1\,\mathrm{MHz}$ to $\nu_{\mathrm{high}} = 5\,\mathrm{GHz}$ (see gray shaded region in Fig. 5.28(c)).

Figure 5.30(b) depicts the dependence of the pulse-to-pulse jitter σ_{ptp} as defined by Eq. (5.58) (blue line, left y-axis) and long-term jitter σ_{lt} as defined by Eq. (5.55) (green line, right y-axis) as functions of τ. Further, Fig. 5.30(c) depicts the amplitude maxima of $|\mathcal{E}|$ of the deterministic system ($R_{\mathrm{sp}} = 0$) for up-sweeping τ (orange diamonds) and down-sweeping τ (gray dots) (see Section 5.4 for details), respectively. Thus, it reveals the resonance structure of the deterministic system (cf. Fig. 5.8(a)).

From Fig. 5.30(a), we note that all three methods to calculate σ_{rms} yield the same dependence on the delay time τ. As expected from the power spectrum in Fig. 5.28(a), the jitter is reduced in the main resonant regimes with respect to the free running laser (gray dashed line), and also in the second order resonant regime around $\tau/T_{\mathrm{ISI},0} = 15/2$ a small dip of σ_{rms} is detected. High values of σ_{rms} are observed in the non-resonant regimes in between the main and the fifth order resonances. The good correspondence of σ_{rms} calculated from the long-term jitter σ_{lt} (green line in Fig. 5.30(a)) with the rms timing jitters obtained from the power spectrum and the timing fluctuations, respectively, (red and black lines in Fig. 5.30(a)) reveals that the timing fluctuations are well approximated by a random walk. However, the shape of σ_{ptp} (blue line in Fig. 5.30(b)) deviates in the non-resonant regimes from the shapes of σ_{lt} (green line in Fig. 5.30(b)) and σ_{rms} (Fig. 5.30(a)). The pulse-to-pulse jitter σ_{ptp} has been calculated under the assumption of independent T_{ISI}'s from the ensemble average over the T_{ISI}'s of a single noise realization (see Eq. (5.58)). Therefore, non-vanishing short term correlations between adjacent T_{ISI}'s could be the reason for these deviations (see discussion in Section 5.6.3). The bifurcation diagram in Fig. 5.30(c) reveals a single bistability region close to $\tau/T_{\mathrm{ISI},0} = 36/5$ indicated by the dashed vertical arrow. If the laser is subject to noise ($R_{\mathrm{sp}} \neq 0$), the laser switches between both solutions close to the bistability of the deterministic system. This results in temporal instabilities of the pulse train, which are responsible for the strong increase of the jitter.

Figure 5.31 corresponds to Fig. 5.30 in the regime of long delay times. All three measures of the timing jitter σ_{rms}, σ_{lt}, and σ_{ptp} reveal that in the main and the second order resonance the timing jitter is decreased more effectively than for intermediate delay as expected from the discussion of the power spectra (cf. Fig. 5.29). The gray shaded regions in Fig. 5.31(a) and (b) indicate a reduction of the timing jitter with respect to the free running laser. Moreover, the main resonances and the second order resonance are strongly broadened. However, the timing-jitter can also be increased for non-resonant feedback. The bifurcation diagram of Fig. 5.31(c) reveals that τ values, for which high values of the timing jitter are observed, correspond to bistabilities of the deterministic system (vertical dashed arrows). In these regions, the noise induces switching processes between solutions with different numbers of pulses in the cavity, which are temporally less stable than the pulse stream obtained in the resonant regimes.

So far, the dependence of the timing jitter was studied for a fixed, small value of the feedback strength ($K = 0.1$). Now, the K-dependence of the long-term timing jitter σ_{lt}

is discussed. Figure 5.32(b) and (d) depict σ_{lt} (color code) as a function of τ and K for intermediate delay and long delay, respectively. The feedback strength ranges from $K = 0.01$ to $K = 0.5$ covering the regimes of very weak feedback up to strong feedback. Blue colors indicate a reduction of σ_{lt} with respect to its value for the free running laser $\sigma_{\mathrm{lt},0}$, red and yellow colors indicate a moderate enhancement of the timing jitter, and in the white regions, the pulse stream is destabilized by the feedback. For every pair of (τ, K)-values, the same constant initial conditions were chosen, such that Figs. 5.32(a) and (b) correspond to Figs. 5.7(a) and 5.13(e), respectively. In Figs. 5.32(a) and (c), σ_{lt} is plotted for several constant values of K. Thus, Figs. 5.32(a) and (c) correspond to horizontal sections of Figs 5.32(b) and (d), respectively. The long-term jitter of the free running laser $\sigma_{\mathrm{lt},0}$ is indicated by a gray dashed line, and gray shading marks a reduction of σ_{lt} with respect to $\sigma_{\mathrm{lt},0}$. As expected from the discussion of the resonance structure of τ and T_{ISI} in Section 5.4, the best suppression of the timing jitter is found in "resonance cones" centered at the exact main resonances $\tau = qT_{\mathrm{ISI},0}$ for $q \in \mathbb{N}$, and the width of the cones increases with the feedback strength. They correspond to the main resonant regimes of the deterministic system (blue regions in Figs. 5.7 and 5.13). From the level curves in Figs. 5.32(b) and (d) or Figs. 5.32(a) and (b), it can be seen that for the long delay the suppression of the jitter in the main resonances is more effective. Further, for high values of the feedback strength, a strong suppression of the jitter over the whole $T_{\mathrm{ISI},0}$-interval is possible. This can be seen best from the green and black lines in Fig. 5.32(c) depicting σ_{lt} for $K = 0.35$ and $K = 0.5$, respectively.

From our findings of this section, the following preliminary conclusion may be drawn: the best suppression of the timing jitter is obtained in the main resonant regimes, i.e., in the blue "resonance cones" of Fig. 5.32(d) and for high values of the feedback strength. However, the next subsection reveals that for more realistic configurations taking into account the phase-amplitude coupling, the scenario becomes more complicated and unstable pulse trains can also be observed close to the exact main resonances.

5.7.2. Timing jitter for nonzero phase-amplitude coupling

In this section, the phase-amplitude coupling is modeled by moderate symmetric α-factors of $\alpha_g = \alpha_q = 2$. These values for the α-factors were used in [FIO10] to model a hybrid ML QD laser and compare the simulation with experimental data. Figures 5.33(b) and (d) depict σ_{lt} in dependence of τ and K in the regime of intermediate and long delay, respectively, and Figs. 5.33(a) and (c) correspond to horizontal sections of Figs. 5.33(b) and (d), respectively. One striking difference to the simpler case of zero α-factors is that now an increase of the long-term timing jitter σ_{lt} can occur close to the exact main resonances (cf. Section 5.5). For instance, σ_{lt} is increased for intermediate delay and low K in the main resonant regime with $\tau = 8T_{\mathrm{ISI},0}$ (see Fig. 5.33(b)) and for long delay and low K in the main resonant regime with $\tau = 68T_{\mathrm{ISI},0}$ (see Fig. 5.33(d)). For small $K = 0.05$, this increase of σ_{lt} can be seen from the red lines in Figs. 5.33(a) and (b) depicting σ_{lt} for intermediate and long delay, respectively. The peaks of σ_{lt} correspond to unstable or chaotic waveforms with low temporal stability. The bifurcation cascade undergone by the deterministic system was discussed in detail in Section 5.5. These resonant self-pulsations were also observed by Avrutin et al. [AVR09] in a finite-difference

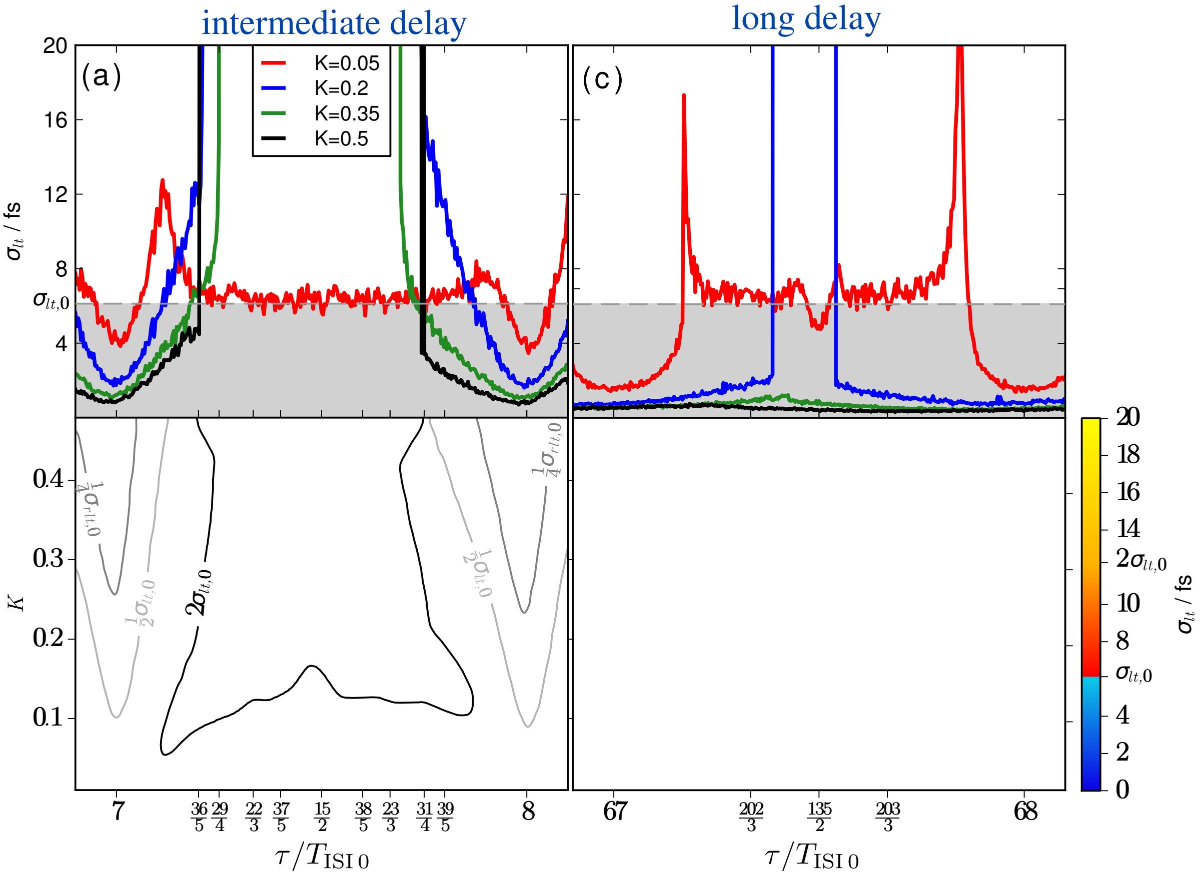

Figure 5.32.: Long-term timing jitter σ_{lt} for $\alpha_g = \alpha_q = 0$ in dependence of delay time τ for intermediate delay times (**(a)** and **(b)**) and long delay times (**(c)** and **(d)**). **(a)** and **(c)**: σ_{lt} for various feedback strengths K. Gray shaded regions indicate a reduction of σ_{lt} with respect to the long-term timing jitter of the free running laser $\sigma_{\mathrm{lt},0}$. **(b)** and **(d)**: Density plot of σ_{lt} (color code) as a function of τ and K. Blue and red colors denote a reduction and an enhancement of σ_{lt} with respect $\sigma_{\mathrm{lt},0}$, respectively, and white regions mark unstable pulse trains. Parameters: $T_{\mathrm{i}} = 4 \cdot 10^4\, T_{\mathrm{ISI},0}$, $R_{\mathrm{sp}} = 1.6\,\mathrm{ns}^{-1}$, and other parameters as in Tab. 5.1.

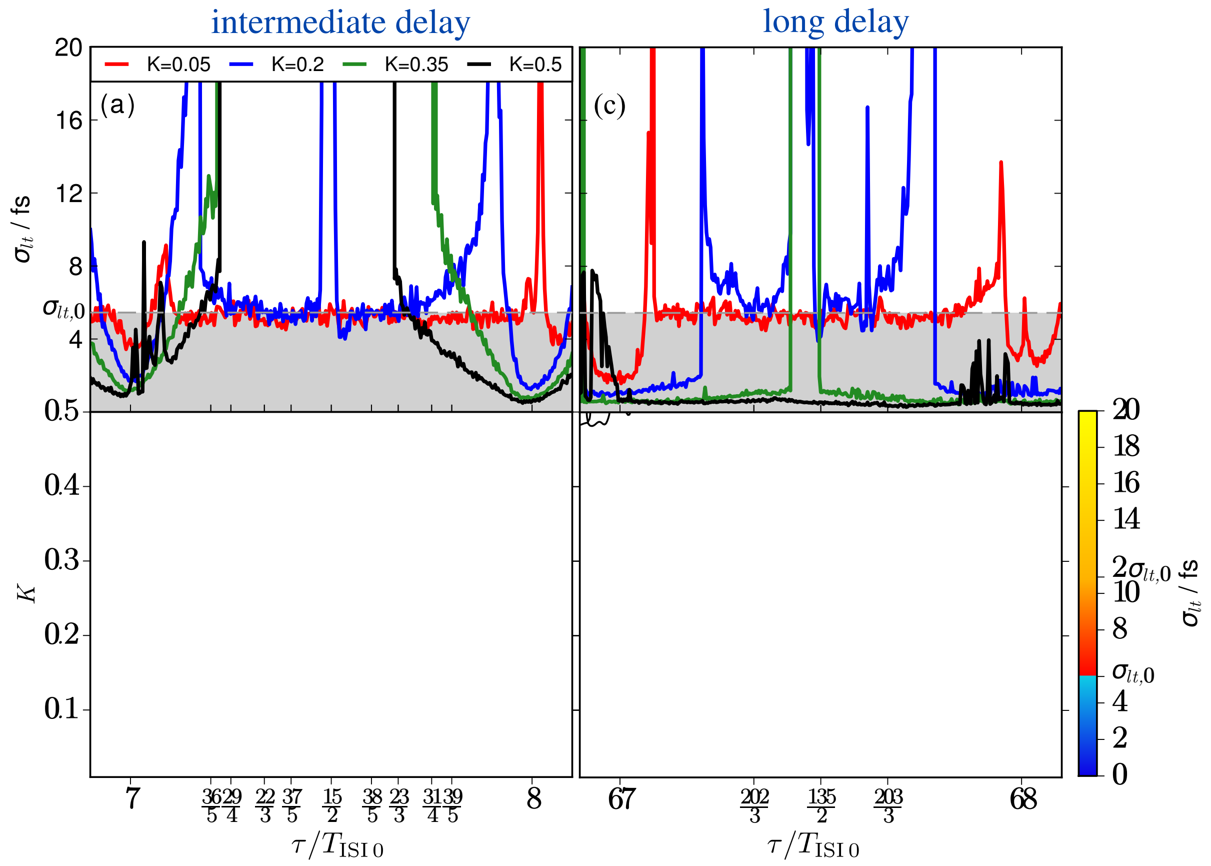

Figure 5.33.: Long-term timing jitter σ_{lt} for finite $\alpha_g = \alpha_q = 2$ in dependence of delay time τ for intermediate delay times (**(a)** and **(b)**) and long delay times (**(c)** and **(d)**). **(a)** and **(c)**: σ_{lt} for various feedback strengths K. Gray shaded regions indicate a reduction of σ_{lt} with respect to the long-term timing jitter of the free running laser $\sigma_{\mathrm{lt},0}$. **(b)** and **(d)**: Density plot of σ_{lt} (color code) as a function of τ and K. Blue and red colors denote a reduction and an enhancement of σ_{lt} with respect $\sigma_{\mathrm{lt},0}$, respectively, and white regions mark unstable pulse trains. Paramters: $T_{\mathrm{i}} = 4 \cdot 10^4\, T_{\mathrm{ISI},0}$, $R_{\mathrm{sp}} = 1.6\,\mathrm{ns}^{-1}$, and other parameters as in Tab. 5.1.

traveling wave model. Further, experimentally, a sudden transition to unstable pulse trains for resonant optical feedback was observed in observed in [LIN10e]. However, also for finite α-factors, especially for long delay, a significant jitter reduction can be achieved for high K away from the exact main resonances (see black line in Fig. 5.33(c) for $K = 0.5$). This is in agreement with various experimental studies [SOL93, BRE10, FIO11].

5.8. Summary

In conclusion, a DDE model for a passively mode-locked semiconductor laser has been extended to study the influence of external optical feedback on the laser dynamics. Resonances between the inter-spike interval time $T_{\mathrm{ISI},0}$ and the delay time τ that follow the ordering of the Farey sequence have been observed. If τ is close to an integer multiple of $T_{\mathrm{ISI},0}$, only one pulse travels in the cavity (main resonant regime), while p pulses are found (higher order resonant regimes) if the ratio of τ and $T_{\mathrm{ISI},0}$ is close to a rational number ($p\tau \approx qT_{\mathrm{ISI},0}$). In between the resonant regimes, the mismatch of τ and $T_{\mathrm{ISI},0}$ leads to pulse trains of broad and less stable pulses (non-resonant regime).

For small feedback strengths, the periodic orbit of the pulse train is deformed in a nonlinear way, but remains stable. For intermediate feedback strengths, the main resonant regimes broaden, while quasiperiodic motion is observed outside of this regime. For high feedback strengths, harmonic mode locking is found in the second order and third order resonant regimes.

By increasing the delay time, on the one hand, a broadening of the width of the main resonant regimes, and, on the other hand, bistability between pulse trains with different numbers of pulses in the cavity is observed for long delay.

Taking into account the amplitude-phase coupling by nonzero α-factors in gain and absorber section, instabilities, i.e., resonant self-pulsations, are observed close to the exact main resonances, which is in agreement with recent experimental studies. A detailed study of the bifurcation cascade reveals that the mode-locked laser undergoes a quasiperiodic route to chaos, which suggests the assumption that mode-locked lasers with resonant optical feedback display similar instabilities than single mode lasers under optical feedback.

Further, it was shown that the pulse repetition frequency is entrained by the external feedback in the main resonant regimes. For long delay and intermediate feedback strengths a sawtooth-like shape of the frequency detuning in dependence of the delay time τ is found as also observed in experiments.

Moreover, the temporal stability of the pulse stream of the passively mode-locked laser subject to Gaussian white noise, which models the spontaneous emission noise, was discussed. The white noise applied to the field equations results in a random walk of the timing fluctuations, which yields a computationally efficient approach to calculate the root-mean-square timing jitter.

The resonance structure observed for the deterministic system subsists under spontaneous emission noise. As a result, the timing jitter can be reduced in the main resonant regime, and the suppression of the timing jitter is more efficient for long delay, because the main "resonance cones" broaden. For finite phase-amplitude coupling, the timing jitter increases close to the exact main resonances due to the resonant self-pulsations found in the deterministic system, which is in agreement with recent experiments.

CHAPTER
SIX

SUMMARY AND OUTLOOK

In this thesis, the complex dynamics of semiconductor laser structures under optical injection and delayed optical feedback has been investigated.

In Part I, the focus has been on the complex dynamics of single mode QD semiconductor lasers. In general, semiconductor lasers are very sensitive to external perturbations, i.e., optical injection and optical feedback due to the relatively low reflectivity of their facets. As a consequence, already small external perturbations can destabilize the laser leading to a wealth of complex dynamical regimes ranging from time periodic output, over quasiperiodic waveforms, and weakly chaotic dynamics (low frequency fluctuations) to fully developed chaos (coherence collapse). However, QD semiconductor lasers display an enhanced dynamical stability under optical injection and optical feedback. To understand this, a simple semiclassical differential equation for the electric field in the cavity has been combined with microscopically based rate equations for the carrier subsystem. The sophisticated material model takes into account the Coulomb scattering processes between the discrete energy levels of the QDs and the surrounding carrier reservoir. This yields carrier lifetimes for electrons and holes in the QDs, which depend nonlinearly on the filling of the carrier reservoir, and thus on the pump current. Furthermore, they are strongly dependent on the energy spacing between QD levels and the band edges of the carrier reservoir, which permits to model different band structures. With this modeling approach, it was possible to attribute the higher damping of the relaxation oscillations of QD lasers to the finite carrier lifetimes in the QDs and to study the dependence of the higher damping of the relaxation oscillations the band structure. Further, the enhanced dynamical stability of QD lasers under external optical injection and optical feedback has been attributed, on the one hand, to their stronger damping of the relaxation oscillations and, on the other hand, to their lower phase-amplitude coupling in comparison to QW lasers.

Despite its microscopic basis, this modeling approach has turned out to be simple enough to deliver analytic insight: for the laser under optical injection analytic expressions for the saddle-node and Hopf bifurcation lines bordering the phase-locking tongue have been derived, and they show a good agreement with the bifurcation lines obtained by numerical path continuation. Moreover, analytic expressions have been derived for the zero-Hopf point for positive detuning, which acts as an organizing center for more complex dynamics, and the critical injection strength, below which no Hopf bifurcation can occur. The latter limits the range of injection strengths, in which the system is effectively one dimensional, and can consequently be described by a single differential equation of Adler's type for the phase difference of master and slave. The analytic expressions reveal a linear increase of the injection strengths of the zero-Hopf point as well as the critical injection strength for the first Hopf instability with the damping of the relaxation oscillations, which explains the higher dynamical stability of strongly damped QD lasers compared to QW lasers. Further, for the laser subject to feedback, an analytic expression for the first Hopf bifurcation has been derived, which represents the lower bound for the transition to the coherence collapse regime. Like the critical injection strength, below which no Hopf instability can occour, it depends linearly on the damping of the relaxation oscillations.

Further, the possibility to use a semiconductor laser subject to optical feedback as an excitable optical unit has been discussed, and coherence resonance has been observed. For low values of the pump current and small α-factors, excitability is found in the vicinity of a saddle-node homoclinic bifurcation, and for higher pump levels and larger α-factors, it is observed close to a boundary crisis of a chaotic attractor. The boundary crisis has the advantage that the feedback strength of the crisis increases with the pump current, which at the same time enhances the excitability threshold. This is of interest for experiments, because for the homoclinic bifurcation the noise level, at which the coherence has its maximum, is very low, and may not be accessible experimentally. In contrast, close to the boundary crisis, the coherence maximum can be shifted to higher noise levels by increasing the pump current.

The second part of this work has been devoted to the study of passively mode-locked semiconductor lasers subject to delayed optical feedback. Therefore, a simple delay differential equation model has been extended to take into account delayed optical feedback. This has permitted to explain the reduction of the timing jitter for resonant optical feedback by the resonance structure of inter-spike interval time and delay time. Further, it has been shown that the suppression of the timing jitter is more effective for long delay, which has been explained by the broadening of the main resonance regimes for increasing delay time. Moreover, resonant self-pulsations have been studied close to the exact main resonances revealing that for resonant optical feedback the mode-locked laser undergoes the same route to chaos than a single mode Lang-Kobayashi-type laser.

Now, I would like to discuss some open questions and directions for future works. QD lasers have lower cutoff frequencies than their QW counterparts due to their enhanced damping of the relaxation oscillations. However, Radziunas et al. demonstrated in Ref. [RAD07] that the cutoff frequency of a semiconductor laser under strong optical feedback from a short integrated cavity can be significantly enhanced by tuning the phase with that the light is coupled back into the gain section. Due to the strong optical feedback, the theoretical analysis was performed by a traveling wave approach. A detailed analysis of the QD laser model with Lang-Kobayashi-type field equation discussed in Chapter 4 would permit to study the enhancement of the cutoff frequency in terms of the external cavity modes analytically and to gain therefore analytical insight into the phase dependence of the cutoff frequency.

Further, in this thesis the resonance structure of inter-spike interval time and delay time was discussed for vanishing and for symmetric α-factors in gain and absorber sections. However, the operation conditions of the gain section and of the saturable absorber are very different: the gain section is strongly pumped to reach carrier inversion, while an inverse voltage is applied to the absorber. Therefore, different α-factors for gain and absorber sections are more realistic. Consequently, for the comparison with experiments a detailed analysis of the timing jitter for non-symmetric α-factors is promising.

Moreover, in this thesis, the simplest scheme for delayed feedback control has been investigated, where the system is controlled by the invasive optical feedback from an external cavity. A different feedback scheme providing non-invasive time-delayed feedback control was proposed by Pyragas [PYR92] to stabilize unstable periodic orbits as well as unstable fixed points. More recently, this control scheme was successfully applied to a single mode QW laser subject to optical feedback [SCH06a, DAH10]. In these experiments stabilization of unstable steady states, chaos control, and the suppression of intensity pulsation has been demonstrated. Therefore, it seems promising to stabilize the pulse stream of a mode-locked laser subject to spontaneous emission noise by non-invasive feedback control and consequently reduce the timing jitter.

Part III.

Appendices

APPENDIX

A

SCATTERING RATES

In this appendix, the fit functions for the microscopically calculated scattering rates are discussed. Due to the principle of detailed balance, the out-scattering rates may be calculated from the in-scattering rates [LUE09, LUE10]. The detailed balance relations read in their dimensionless form with respect to time $t' = 2\kappa t$

$$s_b^{\text{out}} = s_b^{\text{in}} e^{-\frac{\Delta E_b}{k_{\text{bo}}\mathcal{T}}} \left[e^{c_b W_b} - 1\right]^{-1}, \quad \text{for} \quad b \in \{e, h\}, \tag{A.1}$$

where the coefficients $c_b = 2N^{\text{QD}}/(D_b k_{\text{bo}}\mathcal{T})$ were introduced. Here, $D_b = m_b/(\pi\hbar^2)$ are the 2D densities of state in the carrier reservoir with the effective masses m_b. The temperature is denoted by $\mathcal{T}$, and k_{bo} is Boltzmann's constant. Further, $\Delta E_e \equiv E_e^{\text{QW}} - E_e^{\text{QD}}$ and $\Delta E_h \equiv E_h^{\text{QD}} - E_h^{\text{QW}}$ are the energy differences between the QD levels E_e^{QD} and E_h^{QD} and the band edges of the QW E_e^{QW} and E_h^{QW} for electrons and holes, respectively, (see Fig. A.1).

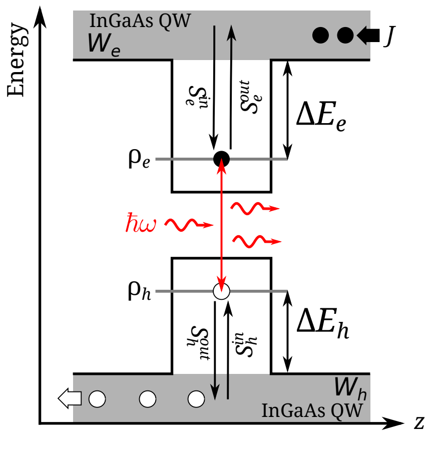

Figure A.1: Energy diagram of the band structure across a QD. The ground state lasing energy is labeled by $\hbar\omega$. The energetic distances of the QD levels from the band edge of the carrier reservoir (QW) for electrons and holes are marked by ΔE_e and ΔE_h, respectively. The Auger in- and out-scattering rates between QD levels and QW are denoted by $S_{e/h}^{\text{in}}$ and $S_{e/h}^{\text{out}}$, respectively. The occupation probabilities of the QDs are denoted by $\rho_{e/h}$, the reservoir carrier densities are labeled by $W_{e/h}$, and J is the pump current density.

In this work, three different sets of microscopically calculated band structures are considered named reference, slow, and fast. They differ in the energy spacings ΔE_e and ΔE_h between QD levels and the band edge of the carrier reservoir (see Table 2.1), which results in different carrier lifetimes $t_b^{-1} = (s_b^{\text{in}} + s_b^{\text{out}})$ as discussed in Section 2.2.

A.0.1. Fit functions for scattering rates

For all three sets of scattering rates, the same functional dependence of s_b^{in} on the reservoir populations are assumed. They are fitted by forth order polynomials in W_e and W_h multiplied by a tanh, which allows for a good agreement with the microscopically calculated rates at low values of the reservoir populations W_e and W_h. The fit functions read

$$s_e^{\text{in}}(W_e, W_h) = \tanh(a_e W_e + b_e) \sum_{i=1}^{4} \left(c_{e,i} W_e^i + d_{e,i} W_h^i\right), \tag{A.2}$$

$$s_h^{\text{in}}(W_e, W_h) = \tanh(a_h W_h + b_h) \sum_{i=1}^{4} \left(c_{h,i} W_e^i + d_{h,i} W_h^i\right), \tag{A.3}$$

where the coefficients $a_{e/h}$, $b_{e/h}$, $c_{e/h,i}$, and d_{e/h_i} for $i \in \{1, 2, 3, 4\}$ are listed in Tables A.1, A.3, and A.5 for reference, slow, and fast sets of scattering rates, respectively. Further, Tables A.2, A.4, and A.6 list the parameter values for $\Delta E_{e/h}$ and $c_{e/h}$ as well as the steady state values of the dynamical variables, the scattering rates and the dimensionless carrier lifetimes for a pump level of $J = 1.5 J_{\text{th}}$ and a pump level of$J = 3.5 J_{\text{th}}$ for reference, slow, and fast sets of scattering rates, respectively.

Table A.1.: Fit parameters for the reference set of carrier scattering rates of Table 2.1 for the QD laser model.

Coefficient	Value	Coefficient	Value
a_e	-1.836×10^{-5}	a_h	3.326×10^{-5}
b_e	-7.89×10^{-6}	b_h	-8.064×10^{-4}
$c_{e,1}$	-298187.0	$c_{h,1}$	-6886.56
$c_{e,2}$	38443.3	$c_{h,2}$	-7191.73
$c_{e,3}$	-3287.08	$c_{h,3}$	1117.15
$c_{e,4}$	112.303	$c_{h,4}$	-43.6502
$d_{e,1}$	53262.5	$d_{h,1}$	-17291.4
$d_{e,2}$	571.696	$d_{h,2}$	-13288.4
$d_{e,3}$	-72.5439	$d_{h,3}$	1000.69
$d_{e,4}$	0.683815	$d_{h,4}$	-52.8802

Table A.2.: Parameters and steady state values of the solitary QD laser with the fast set of carrier scattering rates. Other parameters as in Table 2.2.

Parameters	Value	Meaning
ΔE_e (ΔE_h)	210 (50) meV	Energy separation QW band edges – QD levels
c_e	4.3070×10^{-1}	Constant for el. out-scattering rate
c_h	4.1155×10^{-2}	Constant for hole out-scattering rate
J/J_{th}	1.50 (3.5)	Ratio of current to current at lasing threshold
J_{th}	3.04	Current at lasing threshold
N^0_{ph}	9074.34 (54244.4)	Steady state photon density
W_e	1.33 (2.09)	Steady state electron density in QW
W_h	1.89 (2.52)	Steady state hole density in QW
ρ_e	0.91 (0.84)	Steady state electron population
ρ_h	0.35 (0.42)	Steady state hole population
s_e^{in}	7.58 (16.10)	Steady state of electron in-scattering rates
s_h^{in}	69.42 (108.79)	Steady state of hole in-scattering rates
s_e^{out}	2.9×10^{-3} (3.2×10^{-3})	Steady state electron out-scattering rates
s_h^{out}	124.25 (143.94)	Steady state hole out-scattering rates
t_e	1.3×10^{-1} (6.2×10^{-2})	Electron lifetime
t_h	5.2×10^{-3} (4.0×10^{-3})	Hole lifetime

Table A.3.: Fit parameters for the slow set of carrier scattering rates of Table 2.1 for the QD laser model.

Coefficient	Value	Coefficient	Value
a_e	-2.6612×10^{-5}	a_h	1.94259×10^{-5}
b_e	-1.64753×10^{-6}	b_h	4.74478×10^{-4}
$c_{e,1}$	-363381.0	$c_{h,1}$	-3601.34
$c_{e,2}$	50519.5	$c_{h,2}$	-15193.1
$c_{e,3}$	-4290.71	$c_{h,3}$	1441.14
$c_{e,4}$	146.177	$c_{h,4}$	-47.7236
$d_{e,1}$	69984.1	$d_{h,1}$	-19129.2
$d_{e,2}$	-74.2397	$d_{h,2}$	-5584.61
$d_{e,3}$	-86.6277	$d_{h,3}$	435.245
$d_{e,4}$	1.65736	$d_{h,4}$	-27.6885

Table A.4.: Parameters and steady state values of the solitary QD laser with the slow set of carrier scattering rates. Other parameters as in Table 2.2.

Parameters	Value	Meaning
ΔE_e (ΔE_h)	140 (120) meV	Energy separation QW band edges – QD levels
c_e	4.3070×10^{-1}	Constant for el. out-scattering rate
c_h	4.1155×10^{-2}	Constant for hole out-scattering rate
J/J_{th}	1.50 (3.5)	Ratio of current to current at lasing threshold
J_{th}	0.576	Current at lasing threshold
N_{ph}^0	6091.92 (27657.3)	Steady state photon density
W_e	0.334 (0.555)	Steady state electron density in QW
W_h	0.438 (0.606)	Steady state hole density in QW
ρ_e	0.684 (0.658)	Steady state electron population
ρ_h	0.580 (0.607)	Steady state hole population
s_e^{in}	2.16 (4.52)	Steady state of electron in-scattering rates
s_h^{in}	5.71 (9.25)	Steady state of hole in-scattering rates
s_e^{out}	6.21×10^{-2} (7.44×10^{-2})	Steady state electron out-scattering rates
s_h^{out}	3.03 (3.53)	Steady state hole out-scattering rates
t_e	4.50×10^{-1} (2.18×10^{-1})	Electron lifetime
t_h	1.15×10^{-1} (7.82×10^{-2})	Hole lifetime

Table A.5.: Fit parameters for the fast set of carrier scattering rates of Table 2.1 for the QD laser model.

Coefficient	Value	Coefficient	Value
a_e	-1.18454×10^{-5}	a_h	0.542381
b_e	-1.12055×10^{-5}	b_h	−7.51954
$c_{e,1}$	-1.67918×10^{-5}	$c_{h,1}$	6.93691
$c_{e,2}$	246065	$c_{h,2}$	−3.05438
$c_{e,3}$	−20090.5	$c_{h,3}$	0.436126
$c_{e,4}$	666.063	$c_{h,4}$	−0.021217
$d_{e,1}$	305994	$d_{h,1}$	−10.1779
$d_{e,2}$	1224.67	$d_{h,2}$	−2.57347
$d_{e,3}$	−758.135	$d_{h,3}$	0.159026
$d_{e,4}$	21.2669	$d_{h,4}$	−0.00408522

Table A.6.: Parameters and steady state values of the solitary QD laser with the fast set of carrier scattering rates. Other parameters as in Table 2.2.

Parameters	Value	Meaning
ΔE_e (ΔE_h)	74 (40) meV	Energy separation QW band edges – QD levels
c_e	4.3070×10^{-1}	Constant for el. out-scattering rate
c_h	4.1155×10^{-2}	Constant for hole out-scattering rate
J/J_{th}	1.50 (3.5)	Ratio of current to current at lasing threshold
J_{th}	6.78947	Current at lasing threshold
N_{ph}^0	39532.1 (191311)	Steady state photon density
W_e	2.040 (2.946)	Steady state el. for $k = 0$
W_h	2.639 (3.486)	Steady state hole density for $k = 0$
ρ_e	0.932 (0.903)	Steady state electron population
ρ_h	0.333 (0.362)	Steady state hole population
s_e^{in}	62.15 (102.43)	Steady state of electron in-scattering rates
s_h^{in}	37.28 (57.14)	Steady state of hole in-scattering rates
s_e^{out}	2.52 (2.29)	Steady state electron out-scattering rates
s_h^{out}	69.16 (78.83)	Steady state hole out-scattering rates
t_e	1.55×10^{-2} (9.55×10^{-2})	Electron lifetime
t_h	9.39×10^{-3} (7.35×10^{-3})	Hole lifetime

APPENDIX

B

RESOLVING THE SINGULARITY AT $\gamma \to 0$

In this appendix, it is discussed how the singularity of the dynamical equations (2.4) for $\gamma \to 0$ can be resolved by rescaling the dimensionless time t' as well as the dynamical variables N_{ph}, ρ_e, ρ_h, W_e, and W_h. The initial set of ordinary differential equations reads

$$N'_{\text{ph}} = \Big[g(\rho_e + \rho_h - 1) - 1\Big] N_{\text{ph}}, \tag{B.1a}$$

$$\rho'_e = \gamma\Big[s_e^{\text{in}}(1-\rho_e) - s_e^{\text{out}}\rho_e - r_w(\rho_e + \rho_h - 1)N_{\text{ph}} - \rho_e\rho_h\Big], \tag{B.1b}$$

$$\rho'_h = \gamma\Big[s_h^{\text{in}}(1-\rho_h) - s_h^{\text{out}}\rho_h - r_w(\rho_e + \rho_h - 1)N_{\text{ph}} - \rho_e\rho_h\Big], \tag{B.1c}$$

$$W'_e = \gamma\Big[J - s_e^{\text{in}}(1-\rho_e) + s_e^{\text{out}}\rho_e - cW_eW_h\Big], \tag{B.1d}$$

$$W'_h = \gamma\Big[J - s_h^{\text{in}}(1-\rho_h) + s_h^{\text{out}}\rho_h - cW_eW_h\Big], \tag{B.1e}$$

where the spontaneous emission in Eq. (B.1) has been neglected ($d = 0$). First note that the limit $\gamma \to 0$ is indeed singular. Singular means that $\gamma = 0$ leads to a qualitatively different solution than finite $\gamma \ll 1$ [HIN95, BEN10]. Setting $\gamma = 0$, yields $\rho'_e = \rho'_h = W'_e = W'_h = 0$, which results in constant carrier populations and thus in an exponential increase or decrease of N_{ph}. In contrast, for finite γ, stable steady state lasing is observed in the numerical simulations. Perturbations from this equilibrium decay either exponentially in the overdamped limit of the set of fast scattering rates or for small values of γ, damped ROs are observed for the slow, reference, and very fast rates (cf. Fig. 2.5). Thus, for γ small, we would expect that the leading order problem in γ is conservative and the damping is introduced by the higher order contributions [LUE11]. Therefore, we try to find a coordinate transformation that resolves the singularity at $\gamma = 0$. Generally, singular perturbation problems are difficult to solve, because no systematic technique exists. For the present problem, the singularity can be removed by a change of variables that is known from rate equations of conventional semiconductor QW lasers [ERN10b]. The key observation is that the frequency of the ROs scales like $\sqrt{\gamma}$. Rescaling time with respect to the time scale of the ROs permits to resolve the singularity [LUE11]. The scalings of the deviations from the steady states of the carrier variables are then obtained by balancing the dynamical equations.

At first, deviations (y, u_e, u_e, v_e, v_h) from the lasing steady state $(N_{\mathrm{ph}}^0, \rho_e^0, \rho_h^0, W_e^0, W_h^0)$ and a new time s are introduced by

$$y \equiv \frac{N_{\mathrm{ph}} - N_{\mathrm{ph}}^0}{a_{\mathrm{ph}}}, \qquad u_b \equiv \frac{\rho_b - \rho_b^0}{a_b}, \qquad v_b \equiv \frac{W_b - W_b^0}{b_b}, \qquad \text{and} \qquad s \equiv \eta t', \tag{B.2}$$

where $b = e$ and $b = h$ denote electrons and holes, respectively. The coefficients a_{ph}, a_b, v_b, and η are functions of γ, and their scalings have to be determined in the following. Inserting the ansatz (B.2) into Eqs. (B.1), yields

$$\dot{y} = \frac{1}{\eta}\left[\left(\frac{N_{\mathrm{ph}}^0}{a_{\mathrm{ph}}} + y\right) g(a_e u_e + a_h u_h)\right], \tag{B.3a}$$

$$\dot{u}_e = -\frac{\gamma}{\eta a_e}\left[\begin{array}{c} a_e t_e^{-1} u_e + a_{\mathrm{ph}} y r_w(\rho_e^0 + \rho_h^0 - 1 + a_e u_e + a_h u_h) \\ + r_w N_{\mathrm{ph}}^0 (a_e u_e + a_h u_h) + a_e u_e \rho_h^0 + a_h u_h \rho_e^0 + a_e a_h u_e u_h \end{array}\right], \tag{B.3b}$$

$$\dot{u}_h = -\frac{\gamma}{\eta a_h}\left[\begin{array}{c} a_h t_h^{-1} u_h + a_{\mathrm{ph}} y r_w(\rho_e^0 + \rho_h^0 - 1 + a_e u_e + a_h u_h) \\ + r_w N_{\mathrm{ph}}^0 (a_e u_e + a_h u_h) + a_e u_e \rho_h^0 + a_h u_h \rho_e^0 + a_e a_h u_e u_h \end{array}\right], \tag{B.3c}$$

$$\dot{v}_e = \frac{\gamma}{\eta b_e}\left[a_e t_e^{-1} u_e - c(b_h v_h W_e^0 + b_e v_e W_h^0 + b_e b_h v_e v_h)\right], \tag{B.3d}$$

$$\dot{v}_h = \frac{\gamma}{\eta b_h}\left[a_h t_h^{-1} u_h - c(b_h v_h W_e^0 + b_e v_e W_h^0 + b_e b_h v_e v_h)\right], \tag{B.3e}$$

where the gain-clamping relation (2.25) was used to simplify the photon equation (B.3a), and $t_b^{-1} \equiv s_e^{\mathrm{in}} + s_e^{\mathrm{out}}$ was introduced. Furthermore, the carrier equations (B.3b)–(B.3e) have been simplified by using steady state relations, which were obtained by equating to zero the right hand sides of Eqs. (B.1b)–(B.1e).

In a next step, scaling laws for the coefficients are derived under the conditions that in the rescaled equations [STR94a]

i The time scale separation γ does not multiply the complete right hand sides of the carrier equations (B.3b)–(B.3e) to resolve the singularity at $\gamma = 0$.

ii The number of independent parameters is reduced by regrouping them into dimensionless groups.

To balance the photon equation (B.3a), a_e and a_h have to scale like η, because the derivative of y with respect to the slow time s is assumed to be of order $\mathcal{O}(1)$. Thus, the choice $a_e = \mathcal{O}(\eta)$ and $a_h = \mathcal{O}(\eta)$ permits to balance all the terms on the right hand side of the equation if we additionally assume the $a_{\mathrm{ph}} = \mathcal{O}(N_{\mathrm{ph}}^0)$. The concept to balance as many terms as possible is known as principle of dominant balance [BEN10]. As mentioned above, the corresponding transformation for conventional class B semiconductor lasers [ERN10b] suggests that $\eta = \mathcal{O}(\sqrt{\gamma})$. This choice additionally prevents that γ multiplies the full right hand sides of Eqs. (B.3b) and (B.3c). A simple choice to reduce the number of the independent parameters is to set equal a_e and a_h, i.e., to introduce $a \equiv a_e = a_h$. Moreover, the photon equation (B.3a) may be simplified by choosing $a_{\mathrm{ph}} = N_{\mathrm{ph}}^0$ and setting the dimensionless group ga/η equal to unity, which yields

$$\frac{ga}{\eta} = 1 \quad \Leftrightarrow \quad a = g^{-1}\eta = g^{-1}\sqrt{\gamma}\omega, \tag{B.4}$$

where $\eta = \sqrt{\gamma}\omega$ with $\omega = \mathcal{O}(1)$ has been used in the last equality. Inserting these scaling laws into the dynamical equations (B.3), they simplify as

$$\dot{y} = (u_e + u_h)(1 + y)\,, \tag{B.5a}$$

$$\omega^2 \dot{u}_e = -r_w N^0_{\text{ph}} y - \begin{bmatrix} \sqrt{\gamma}\omega \left(t_e^{-1} u_e + r_w N^0_{\text{ph}} (u_e + u_h)(1+y) + u_e \rho_h^0 + u_h \rho_e^0\right) \\ +\gamma g^{-1} \omega^2 u_e u_h \end{bmatrix}, \tag{B.5b}$$

$$\omega^2 \dot{u}_h = -r_w N^0_{\text{ph}} y - \begin{bmatrix} \sqrt{\gamma}\omega \left(t_h^{-1} u_h + r_w N^0_{\text{ph}} (u_e + u_h)(1+y) + u_e \rho_h^0 + u_h \rho_e^0\right) \\ +\gamma g^{-1} \omega^2 u_e u_h \end{bmatrix}, \tag{B.5c}$$

$$\omega \dot{v}_e = \frac{\sqrt{\gamma}}{b_e}\left[\sqrt{\gamma} g^{-1} \omega t_e^{-1} u_e - c(b_h v_h W_e^0 + b_e v_e W_h^0 + b_e b_h v_e v_h)\right], \tag{B.5d}$$

$$\omega \dot{v}_h = \frac{\sqrt{\gamma}}{b_h}\left[\sqrt{\gamma} g^{-1} \omega t_h^{-1} u_h - c(b_h v_h W_e^0 + b_e v_e W_h^0 + b_e b_h v_e v_h)\right], \tag{B.5e}$$

where the gain-clamping relation (2.25) was employed to simplify Eqs. (B.5b) and (B.5c). In Section 2.2, it was discussed that the scattering rates have a crucial impact on the damping of the ROs, which in terms influences the tolerance of the laser subject to optical injection and optical feedback. Therefore, the coefficients b_e and b_h in Eqs. (B.5d) and (B.5e) are chosen such that the first terms in the brackets on the right hand sides of the equations, which are proportional to the carrier lifetimes t_e and t_h, constitute the leading order terms of these equations. A simple choice for b_e and b_h that simplifies the leading order problem is $b \equiv b_e = b_h = g^{-1}\gamma\omega$. Inserting b into Eqs. (B.5d) and (B.5e), yields the final set of equations

$$\dot{y} = (u_e + u_h)(1 + y)\,, \tag{B.6a}$$

$$\omega^2 \dot{u}_e = -r_w N^0_{\text{ph}} y - \begin{bmatrix} \sqrt{\gamma}\omega \left(t_e^{-1} u_e + r_w N^0_{\text{ph}} (u_e + u_h)(1+y) + u_e \rho_h^0 + u_h \rho_e^0\right) \\ +\gamma g^{-1} \omega^2 u_e u_h \end{bmatrix}, \tag{B.6b}$$

$$\omega^2 \dot{u}_h = -r_w N^0_{\text{ph}} y - \begin{bmatrix} \sqrt{\gamma}\omega \left(t_h^{-1} u_h + r_w N^0_{\text{ph}} (u_e + u_h)(1+y) + u_e \rho_h^0 + u_h \rho_e^0\right) \\ +\gamma g^{-1} \omega^2 u_e u_h \end{bmatrix}, \tag{B.6c}$$

$$\omega \dot{v}_e = t_e^{-1} u_e - c\sqrt{\gamma}(v_h W_e^0 + v_e W_h^0) + c\gamma^{3/2} g^{-1} \omega v_e v_h, \tag{B.6d}$$

$$\omega \dot{v}_h = t_h^{-1} u_h - c\sqrt{\gamma}(v_h W_e^0 + v_e W_h^0) + c\gamma^{3/2} g^{-1} \omega v_e v_h. \tag{B.6e}$$

APPENDIX

C

LOCI OF HOPF BIFURCATIONS IN (C,K)-PLANE

In this appendix, the loci of the Hopf bifurcation lines for the single mode laser subject to feedback in the plane spanned by the feedback phase C and the feedback strength K are derived. From Eq. (4.53), we obtain

$$\delta\omega^{\mathrm{s}}\tau = \arctan(\alpha) - C \pm \arccos\Big(-\frac{\mathcal{G}}{\tilde{k}^H_{\mathrm{eff}}}\Big) + 2n\pi, \tag{C.1}$$

Further, rewriting the transcendental Eq. (4.7) in the same way, yields

$$\delta\omega^{\mathrm{s}}\tau = -\tilde{k}^H_{\mathrm{eff}} \sin\big(C + \delta\omega^{\mathrm{s}}\tau + \arctan(\alpha)\big). \tag{C.2}$$

Inserting Eq. (C.1) into Eq. (C.2) permits to eliminate $\delta\omega^{\mathrm{s}}\tau$

$$\begin{aligned} C =& \arctan(\alpha) \pm \arccos\Big(-\frac{\mathcal{G}}{\tilde{k}^H_{\mathrm{eff}}}\Big) \\ &+ \tilde{k}^H_{\mathrm{eff}} \sin\Big(2\arctan(\alpha) \pm \arccos\Big(-\frac{\mathcal{G}}{\tilde{k}^H_{\mathrm{eff}}}\Big)\Big) + 2n\pi. \end{aligned} \tag{C.3}$$

With the help of some trigonometric identities[1] Eq. (C.3) can be expanded as

$$\begin{aligned} \sin\Big(2\arctan(\alpha) \pm \arccos\Big(-\frac{\mathcal{G}}{\tilde{k}^H_{\mathrm{eff}}}\Big)\Big) \overset{(C.4)}{=} & \sin\Big(2\arctan(\alpha)\Big)\cos\Big(\arccos\Big(-\frac{\mathcal{G}}{\tilde{k}^H_{\mathrm{eff}}}\Big)\Big) \\ & \pm \cos\Big(2\arctan(\alpha)\Big)\sin\Big(\arccos\Big(-\frac{\mathcal{G}}{\tilde{k}^H_{\mathrm{eff}}}\Big)\Big). \end{aligned}$$

---

[1] In order to simplify Eq. (C.3), several trigonometric identities are employed for resolving the sine

$$\sin(x \pm y) = \sin(x)\cos(y) \pm \sin(y)\cos(x), \tag{C.4}$$

$$\cos(x \pm y) = \cos(x)\cos(y) \mp \sin(y)\sin(x), \tag{C.5}$$

$$\sin\big(\arctan(x)\big) = \frac{x}{\sqrt{1+x^2}}, \tag{C.6}$$

$$\cos\big(\arctan(x)\big) = \frac{1}{\sqrt{1+x^2}}, \tag{C.7}$$

$$\sin\big(\arccos(x)\big) = \sqrt{1-x^2}., \tag{C.8}$$

Using

$$\sin\Big(2\arctan(\alpha)\Big) \overset{(C.4)}{=} 2\sin\Big(\arctan(\alpha)\Big)\cos\Big(\arctan(\alpha)\Big) \overset{(C.6),(C.7)}{=} \frac{2\alpha}{1+\alpha^2}$$

and

$$\cos\Big(2\arctan(\alpha)\Big) \overset{(C.5)}{=} \cos^2\Big(\arctan(\alpha)\Big) - \sin^2\Big(\arctan(\alpha)\Big) \overset{(C.6),(C.7)}{=} \frac{1-\alpha^2}{1+\alpha^2},$$

one obtains

$$\begin{aligned}
&\sin\Big(2\arctan(\alpha) \pm \arccos\Big(-\frac{\mathcal{G}}{\tilde{k}^H_{\text{eff}}}\Big)\Big)\\
&\quad= -\frac{2\alpha\mathcal{G}}{\tilde{k}^H_{\text{eff}}\big(1+\alpha^2\big)} \pm \frac{1-\alpha^2}{1+\alpha^2}\sin\Big(\arccos\Big(-\frac{\mathcal{G}}{\tilde{k}^H_{\text{eff}}}\Big)\Big)\\
&\quad\overset{(C.8)}{=} -\frac{2\alpha\mathcal{G}}{\tilde{k}^H_{\text{eff}}\big(1+\alpha^2\big)} \pm \frac{1-\alpha^2}{1+\alpha^2}\sqrt{1-\frac{\mathcal{G}^2}{(\tilde{k}^H_{\text{eff}})^2}} = \frac{1}{\tilde{k}^H_{\text{eff}}}\Big\{-\frac{2\alpha\mathcal{G}}{1+\alpha^2} \pm \frac{1-\alpha^2}{1+\alpha^2}\sqrt{(\tilde{k}^H_{\text{eff}})^2-\mathcal{G}^2}\Big\}.
\end{aligned}$$

Inserting this result into equation Eq. (C.3), yields the final expression for the loci of Hopf-bifurcations in the $(C, \tilde{k})$-plane [LEV95]

$$C^H_n(k) = \arctan(\alpha) \pm \arccos\Big(\frac{-\mathcal{G}}{\tilde{k}^H_{\text{eff}}}\Big) - \frac{2\alpha\mathcal{G}}{1+\alpha^2} \pm \frac{1-\alpha^2}{1+\alpha^2}\sqrt{(\tilde{k}^H_{\text{eff}})^2-\mathcal{G}^2} + 2n\pi. \tag{C.9}$$

APPENDIX

D

STOCHASTIC METHODS

In this appendix, the basic mathematical methods to characterize stochastic processes are discussed.

D.1. Time average vs. ensemble average

A stochastic process $x(t)$ is given by a random variable, which is a function of time, and is thus only statistically characterized. A single event $x(t_1)$ at the time point t_1 only gives us one of the possible state of the system, which in general depends on t_1 and on the realization of the stochastic process, i.e., on its sample path. Therefore, only averaged quantities can be discussed. There are two different averaging procedures: on the one hand, an average can be performed over an ensemble $\{x^{(1)}(t_1), x^{(2)}(t_1), \dots, x^{(N)}(t_1)\}$ of $N \in \mathbb{N}$ realizations of the stochastic process at a fixed point in time t_1, which is called *ensemble average*. On the other hand, one single realization $x^{(n)}(t)$ of the stochastic process can be averaged over a certain time interval, which is called *time average*. Both averaging procedures are illustrated in Fig. D.1. The graph of a single realization $x^{(n)}(t)$ as a function of time is called a sample path of the stochastic process.

The first order time-average of a stochastic process is defined by

$$\overline{x^{(n)}} \equiv \lim_{T_\mathrm{i} \nearrow \infty} \frac{1}{T_\mathrm{i}} \int_0^{T_\mathrm{i}} x^{(n)}(t')dt', \tag{D.1}$$

where the integration time is denoted by T_i. Further, the correlations of the stochastic process at different time points are described by its autocorrelation function [STR63, GAR02, HOR84, JAC10]

$$\Psi_x(s) \equiv \lim_{T_\mathrm{i} \nearrow \infty} \frac{1}{T_\mathrm{i}} \int_0^{T_\mathrm{i}} x^{(n)}(t')x^{(n)}(t'+s)dt'. \tag{D.2}$$

The first order ensemble average at a time point t_1 is defined by

$$\langle x(t_1) \rangle \equiv \lim_{N \nearrow \infty} \sum_{i=1}^{N} x^{(n)}(t_1) = \int_{\mathbb{R}} x_1 \rho_1(x_1, t_1) dx_1, \tag{D.3}$$

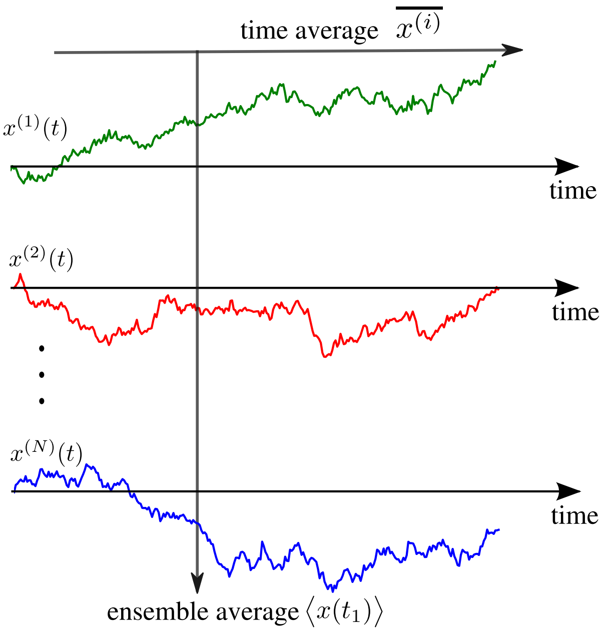

Figure D.1: Illustration of time and ensemble average. The different sample paths are denoted by $x^{(i)}(t)$ for $i \in \{1, \dots, N\}$. The time average $\overline{x^{(i)}}$ is performed over one sample path i, while the ensemble average $\langle x(t_1)\rangle$ is performed over the whole ensemble of sample path at a fixed point in time t_1.

where $\rho_1(x_1, t_1)$ is the probability density of the stochastic process. The correlation of the stochastic process at two different time points t_1 and t_2 averaged over an ensemble of realizations is given by its covariance

$$\langle x(t_1)x(t_2)\rangle \equiv \lim_{N\nearrow\infty} \sum_{i=1}^{N} x^{(n)}(t_1)x^{(n)}(t_2) = \int_{\mathbb{R}} x_1 x_2 \rho_2(x_2, t_2; x_1, t_1)dx_1 dx_2, \tag{D.4}$$

where we have introduced $x_1 \equiv x(t_1)$ and $x_2 \equiv x(t_2)$ as well as the first order probability density function $\rho_1(x_1, t_1)$ and the second order joint probability density function $\rho_2(x_2, t_2; x_1, t_1)$[1]. The ensemble average is thus given by the first moment of the probability function ρ_1, and the second moment reads

$$\langle x^2(t_1)\rangle \equiv \int_{\mathbb{R}} x_1^2 \rho_1(x_1, t_1)dx_1. \tag{D.5}$$

The ensemble average is a convenient concept for the theoretical treatment of a physical systems, since it is directly related to the systems probability density function, which can be generally obtained from the theoretical analysis of the system. However, from an experimental point of view, time-averaging is the more natural procedure since one cannot experimentally prepare an infinite number of identical systems. In the next subsection, we will address the question, under which conditions both averaging procedures are equivalent.

---

[1] The probability that x is found in the interval $[x_1, x_1 + dx_1]$ is given by $\rho_1(x_1, t_1)dx_1$, and the probability that x is found in $[x_1, x_1 + dx_1]$ at t_1 and in $[x_2, x_2 + dx_2]$ at a (different) time point t_2 is given by $\rho_2(x_2, t_2; x_1, t_1)dx_1 dx_2$.

D.2. Statistically stationary vs. non-stationary random processes

A process is called ergodic in the mean if its time-average (D.1) equals its ensemble average (D.3). Since the time-average (D.1) does not depend on the time point t_1, also the ensemble average has to be stationary (time-independent). Further, a process is called ergodic in the autocorrelation if additionally its autocorrelation function (D.2) equals its covariance (D.4), which implies that the covariance depends only on the time differences $s \equiv t_2 - t_1$ of the considered time points t_1 and t_2, and the second moment (D.5) is independent of time, i.e., stationary.

Processes with constant ensemble average and a covariance that depends only on time differences s are called weakly stationary or wide-sense stationary. From the above considerations, we see that a process, which is ergodic in the autocorrelation is also wide-sense stationary, thus ergodicity implies stationarity, but the inverse is not true [GAR02]. Since the time averaged quantities are obtained by averaging only over one sample function, for an ergodic (and thus a wide-sense stationary) process one sample function is sufficient to obtain all statistical information about the process. For non-stationary processes, the limes $T_\mathrm{i} \nearrow \infty$ does not exist, which means that its time average and its autocorrelation function depend on the integration time T_i. In practice, this is not a disadvantage, because experimental measurements are always carried out for a finite time. The concept of the ensemble average can be employed as before under the assumption that all member functions of the ensemble, i.e., all sample paths have the same probability density function.

D.3. Power spectral density and Wiener-Khinchin theorem

In this section, we will discuss the power spectral density (PSD) or power spectrum, which reveals the frequency content of a stochastic process and is therefore the most universal tool to characterize the typical time scales of the process. Further, the Wiener-Khinchin theorem will be discussed, which states that PSD and autocorrelation function (D.2) of a wide-sense stationary process form a Fourier-pair.

First, we have to introduce the Fourier transform of a stochastic process. Here, we run into the problem that stationary stochastic processes are not integrable, i.e., their $\mathbb{L}^1$-norm $\|\cdot\|_1$ is not finite. This means that they do not belong to the Banach space

$$\mathbb{L}^1 \equiv \left\{ f : \mathbb{R} \longrightarrow \mathbb{C}, \text{ with } \|f\|_1 \equiv \int_\mathbb{R} |f(x)| dx < \infty \right\}$$

of measurable functions f. However, every real measurement always has a finite integration time T_i, therefore the Fourier transform can be defined on the Banach space of the gated stochastic processes x_{T_i} [BUC83], defined by

$$x_{T_\mathrm{i}}(t) \equiv \begin{cases} x(t) & \text{for } t \leq T_\mathrm{i}, \\ 0 & \text{else.} \end{cases}$$

The Fourier transform $\mathcal{F}$ and its inverse $\mathcal{F}^{-1}$ of a stochastic process $x_{T_\mathrm{i}}(t)$ is then simply defined by the Fourier transforms of its realizations $x_{T_\mathrm{i}}^{(n)}$ for $n \in \{1, \dots, N\}$ and $N \in \mathbb{N}$

$$\hat{x}_{T_\mathrm{i}}^{(n)}(\omega) \equiv \mathcal{F}[x_{T_\mathrm{i}}^{(n)}](\omega) \equiv \int_{\mathbb{R}} x_{T_\mathrm{i}}^{(n)}(t) e^{-i\omega t} dt, \tag{D.6a}$$

$$x_{T_\mathrm{i}}^{(n)}(t) = \mathcal{F}^{-1}[\hat{x}_{T_\mathrm{i}}^{(n)}](t) \equiv \frac{1}{2\pi} \int_{\mathbb{R}} \hat{x}_{T_\mathrm{i}}^{(n)}(\omega) e^{i\omega t} d\omega, \tag{D.6b}$$

where $\hat{x}_{T_\mathrm{i}}^{(n)}$ denotes the Fourier transform of the realization $x_{T_\mathrm{i}}^{(n)}$.

With the help of the time-shift property of the Fourier transform $\mathcal{F}[x(t+s)] = \hat{x}(\omega)e^{i\omega s}$, the following relation is obtained

$$\int_{\mathbb{R}} x_{T_\mathrm{i}}^{(n)}(t+s) \big(x_{T_\mathrm{i}}^{(n)}\big)^{*}(t) dt = \frac{1}{2\pi} \int_{\mathbb{R}} \left| \hat{x}_{T_\mathrm{i}}^{(n)}(\omega) \right|^2 e^{i\omega s} d\omega, \tag{D.7}$$

where $()^{\star}$ denotes the complex conjugate. Taking for $s = 0$, the norm of both sides of Eq. (D.7) yields the Plancherel theorem [RED80]

$$\int_{\mathbb{R}} \left| x_{T_\mathrm{i}}^{(n)} \right|^2 dt = \frac{1}{2\pi} \int_{\mathbb{R}} \left| \hat{x}_{T_\mathrm{i}}^{(n)}(\omega) \right| d\omega. \tag{D.8}$$

It has the physical interpretation that the energy of a signal is the same for the signal itself and for the Fourier transform of the signal, which is sometimes denoted as energy theorem. This means that $|\hat{x}^{(n)}(\omega)|^2$ is the energy density of the harmonic component $e^{i\omega t}$ in units of energy per Hz. For a real non-stationary process x_{T_i}, the energy of the signal will depend on the realization n of the stochastic process. Therefore, to define the time averaged power of the process meaningfully, we have to take the ensemble average (D.3) of both sides of Eq. (D.7) and additionally divide both sides of Eq. (D.7) by the integration time T_i

$$\frac{1}{T_\mathrm{i}} \int_{\mathbb{R}} \langle x_{T_\mathrm{i}}(t+s) x_{T_\mathrm{i}}(t) \rangle dt = \frac{1}{2\pi} \int_{\mathbb{R}} \frac{\langle |\hat{x}_{T_\mathrm{i}}(\omega)|^2 \rangle}{T_\mathrm{i}} e^{i\omega s} d\omega = \mathcal{F}^{-1} \left[\frac{\langle |\hat{x}_{T_\mathrm{i}}(\omega)|^2 \rangle}{T_\mathrm{i}} \right]. \tag{D.9}$$

For $s = 0$, the right hand side of Eq. (D.9) yields the time averaged power of the stochastic process, so it does make sense to interpret

$$S_x(s, T_\mathrm{i}) \equiv \frac{\langle |\hat{x}_{T_\mathrm{i}}(\omega)|^2 \rangle}{T_\mathrm{i}} \tag{D.10}$$

as power spectral density. Further, the right hand side of Eq. (D.9) can be interpreted as ensemble averaged autocorrelation function (see Eq. (D.2))

$$\Psi_x(s, T_\mathrm{i}) \equiv \frac{1}{T_\mathrm{i}} \int_{\mathbb{R}} \langle x_{T_\mathrm{i}}(t+s) x_{T_\mathrm{i}}(t) \rangle dt = \frac{1}{T_\mathrm{i}} \int_0^{T_\mathrm{i} - |s|} \langle x(t+s) x(t) \rangle dt. \tag{D.11}$$

Equation (D.9) is the Wiener-Khinchin theorem for a non-stationary stochastic processes, which states that $\Psi_x(s, T_\mathrm{i})$ and $S_x(s, T_\mathrm{i})$ form a Fourier-pair. Since for every real function x_T the corresponding PSD is an even function of frequency [GAR02], i.e., $S_x(\omega, T_\mathrm{i}) = S_x(-\omega, T_\mathrm{i})$, the Fourier-pair can be rewritten as

$$\Psi_x(s, T_\mathrm{i}) = \frac{1}{\pi} \int_0^\infty S_x(\omega, T_\mathrm{i}) \cos(\omega s) d\omega, \tag{D.12a}$$

$$S_x(\omega, T_\mathrm{i}) = 2 \int_0^\infty \Psi_x(s, T_\mathrm{i}) \cos(\omega s) ds. \tag{D.12b}$$

As discussed in Subsection D.2 for wide-sense stationary stochastic processes, each realization contains its full statistic information, and the limit $T_\mathrm{i} \nearrow \infty$ does exist. In this case, we can apply, instead of the ensemble average $\langle \cdot \rangle$, the limit $T \nearrow \infty$ to both sides of Eq. (D.9). We then find the Wiener-Khinchin theorem for wide-sense stationary processes [DRA67]

$$S_x(\omega) \equiv \mathcal{F}[\Psi_x(s)], \quad \text{and} \quad \Psi_x(s) = \mathcal{F}^{-1}[S_x(\omega)], \tag{D.13}$$

where $\Psi_x(s)$ is the autocorrelation function as defined in Eq. (D.2) and the PSD is defined by

$$S_x(\omega) \equiv |\mathcal{F}[x(t)]|^2 = \lim_{T_\mathrm{i} \nearrow \infty} \frac{1}{2\pi T_\mathrm{i}} \left| \int_0^{T_\mathrm{i}} x(t) e^{-i\omega t} dt \right|^2, \tag{D.14}$$

as commonly used throughout the literature [POM05, POM07, PAS04].

For the calculation of the timing jitter in Section 5.6, it is important to note that Eq. (D.13) permits us to calculate the variance $\mathrm{Var}(x) \equiv \langle x^2 \rangle - \langle x \rangle^2$ of a real stochastic process $x(t)$ with zero mean $\langle x \rangle = 0$ from the PSD

$$\mathrm{Var}(x) = \langle x^2 \rangle = \Psi_x(0) \overset{(\mathrm{D.12a})}{=} \frac{1}{2\pi} \int_\mathbb{R} S_x(\omega) d\omega \overset{x(t)\in\mathbb{R}}{=} \frac{1}{\pi} \int_0^\infty S_x(\omega) d\omega, \tag{D.15}$$

where the second equality holds due the equivalence of covariance (D.4) and autocorrelation function (D.2) for stationary stochastic processes, in the third equality Eq. (D.12a) in the limit $T_\mathrm{i} \nearrow \infty$ has been employed, and eventually the last equality holds due to the symmetry of S_x for real $x(t)$ with zero mean ($\langle x \rangle = 0$).

D.4. Numerical calculation of power spectral density

In this section, it is briefly discussed how to obtain the PSD from numerical simulations. In numerical simulations, we obtain a finite set $\{x\} \equiv \{x_1, \ldots, x_N\}$ of samples x_n of the continuous function $x(t)$ with $x_n \equiv x(nT_s)$ and $n \in [1, \ldots, N]$, where T_s is the sampling time of the signal. We have to replace the continuous Fourier transform $\mathcal{F}$ and its inverse $\mathcal{F}^{-1}$ by a discrete-time Fourier transform F_d and its inverse, respectively,

$$F_d[\{x\}](\nu) \equiv \left\{ \frac{1}{N} \sum_{n=1}^{N} x_n e^{-i2\pi n\nu T_s} \right\}, \quad F_d^{-1}[\{\hat{x}\}](t) \equiv \left\{ \frac{1}{N} \sum_{k=1}^{N} \hat{x}_k e^{i2\pi k t \nu_s} \right\}. \tag{D.16}$$

Here, $\{\hat{x}\} \equiv \{\hat{x}_1, \ldots, \hat{x}_N\}$ is the finite set of samples of $\hat{x}$ with $\hat{x}_n \equiv \hat{x}(n\nu_s)$ and the sampling frequency $\nu_s \equiv 1/T_s$. In simulation, the system can only be integrated for finite times $T_{\mathrm{i}} = NT_s$. Therefore the observables, i.e., Fourier transform, power spectrum, and autocorrelation function depend on the realization of the stochastic process. Therefore, also for wide sense stationary stochastic processes, one has to average over an ensemble of $M \in \mathbb{N}$ realizations, which is denoted by $\langle \cdot \rangle_M$. The power spectrum $S_x(\nu, N)$ of $\{x\}$ is then defined as follows

$$S_x(\nu, N) \equiv T_{\mathrm{i}} \langle |F_d[\{x\}]|^2 \rangle_M = \frac{T_{\mathrm{i}}}{M} \sum_{m=1}^{M} \left| \left\{ \frac{1}{N} \sum_{n=1}^{N} x_n e^{-i2\pi n \nu T_s} \right\}_m \right|^2 . \tag{D.17}$$

For non wide-sense stationary processes, $S_x(\nu, N)$ depends on the length T_{i} of the time-series x, i.e., on the number of samples N. For wide-sense stationary processes and T_{i} sufficiently large, the observables are independent of N. The factor of T_{i} is introduced in Eq. (D.17), because the discrete Fourier tranform of x has the dimension $[x]/\,\mathrm{Hz}$ [PAS04], thus $|F_d[\{x\}]|^2$ has the dimension $[x]^2/\,\mathrm{Hz}^2$. The PSDs defined in Eqs. (D.10) and (D.14) have the units $[x]^2/\,\mathrm{Hz}$. The factor T_{i} ensures that the discrete PSD has the same dimension than the continuous one. Physically, it takes into account the finite resolution bandwidth $1/T_{\mathrm{i}}$ of the measuring instrument, i.e., of the electrical spectrum analyzer [KOL86].

PUBLICATIONS

LUE13 K. Lüdge, B. Lingnau, C. Otto, and E. Schöll: *Understanding electrical and optical modulation properties of semiconductor quantum-dot lasers in terms of their turn-on dynamics*, Nonlinear Phenom. Complex Syst. **15**, 350–359 (2012).

OTT12a C. Otto, K. Lüdge, A. G. Vladimirov, M. Wolfrum, and E. Schöll: *Delay induced dynamics and jitter reduction of passively mode-locked semiconductor laser subject to optical feedback*, New J. Phys. **14**, 113033 (2012).

OTT12 C. Otto, B. Globisch, K. Lüdge, E. Schöll, and T. Erneux: *Complex dynamics of semiconductor quantum dot lasers subject to delayed optical feedback*, Int. J. Bif. Chaos **22**, 1250246 (2012).

GLO12 B. Globisch, C. Otto, E. Schöll, and K. Lüdge: *Influence of carrier lifetimes on the dynamical behavior of quantum-dot lasers subject to optical feedback*, Phys. Rev. E **86**, 046201 (2012).

PAU12 J. Pausch, C. Otto, E. Tylaite, N. Majer, E. Schöll, and K. Lüdge: *Optically injected quantum dot lasers - impact of nonlinear carrier lifetimes on frequency locking dynamics*, New J. Phys. **14**, 053018 (2012).

OTT11 C. Otto, K. Lüdge, E. A. Viktorov, and T. Erneux: *Quantum dot laser tolerance to optical feedback*, in *Nonlinear Laser Dynamics - From Quantum Dots to Cryptography*, edited by K. Lüdge (WILEY-VCH, Weinheim, 2012), chapter 6, pp. 141–162.

OTT10 C. Otto, K. Lüdge, and E. Schöll: *Modeling quantum dot lasers with optical feedback: sensitivity of bifurcation scenarios*, phys. stat. sol. (b) **247**, 829–845 (2010).

BIBLIOGRAPHY

[ADL73] R. Adler: *A study of locking phenomena in oscillators*, Proc. IEEE **61**, 1380–1385 (1973). (Cited on pages 40, 46 and 60.)

[ALF69] Z. I. Alferov, A. D. Andreev, V. I. Korolkov, E. L. Portnoi, and D. N. Tretyako: *Injection properties of N-AlxGa1-XAs-P-GaAs heterojunctions.*, Soviet Physics Semiconductors-USSR **2**, 843 (1969). (Cited on page 1.)

[ARA82] Y. Arakawa and H. Sakaki: *Multidimensional quantum well laser and temperature dependence of its threshold current*, Appl. Phys. Lett. **40**, 939 (1982). (Cited on page 1.)

[ARG05] A. Argyris, D. Syvridis, L. Larger, V. Annovazzi-Lodi, P. Colet, I. Fischer, J. García-Ojalvo, C. R. Mirasso, L. Pesquera, and K. A. Shore: *Chaos-based communications at high bit rates using commercial fibre-optic links*, Nature **438**, 343–346 (2005). (Cited on page 109.)

[ARN03] L. Arnold: *Random Dynamical Systems*, Springer Monographs in Mathematics (Springer, Berlin, 2003). (Cited on page 35.)

[ASA86a] M. Asada, Y. Miyamoto, and Y. Suematsu: *Gain and the threshold of three-dimensional quantum-box lasers*, IEEE J. Quantum Electron. **22**, 1915–1921 (1986). (Cited on page 1.)

[AUS09] R. Aust, P. Hövel, J. Hizanidis, and E. Schöll: *Delay control of coherence resonance in type-I excitable dynamics*, Eur. Phys. J. ST **187**, 77–85 (2010). (Cited on pages 44 and 146.)

[AVR00] E. A. Avrutin, J. H. Marsh, and E. L. Portnoi: *Monolithic and multi-gigahertz mode-locked semiconductor lasers: Constructions, experiments, models and applications*, IEE Proc. Optoelectron. **147**, 251 (2000). (Cited on page 161.)

[AVR09] E. A. Avrutin and B. M. Russell: *Dynamics and spectra of monolithic mode-locked laser diodes under external optical feedback*, IEEE J. Quantum Electron. **45**, 1456 (2009). (Cited on pages 3, 162, 174, 176, 178, 200, 203 and 222.)

[AZO09] S. Azouigui, B. Dagens, F. Lelarge, J. G. Provost, D. Make, O. Le Gouezigou, A. Accard, A. Martinez, K. Merghem, F. Grillot, O. Dehaese, R. Piron, S. Loualiche, Q. Zou, and A. Ramdane: *Optical feedback tolerance of quantum-dot- and quantum-dash-based semiconductor lasers operating at* $1.55\mu m$, IEEE J. Sel. Topics Quantum Electron. **15**, 764–773 (2009). (Cited on page 138.)

[BAL04] A. G. Balanov, N. B. Janson, and E. Schöll: *Control of noise-induced oscillations by delayed feedback*, Physica D **199**, 1–12 (2004). (Cited on page 146.)

[BAN01] U. Bandelow, M. Radziunas, J. Sieber, and M. Wolfrum: *Impact of gain dispersion on the spatio-temporal dynamics of multisection lasers*, IEEE J. Quantum Electron. **37**, 183 (2001). (Cited on page 163.)

[BAN06] U. Bandelow, M. Radziunas, A. G. Vladimirov, B. Hüttl, and R. Kaiser: *40GHz mode locked semiconductor lasers: Theory, simulation and experiments*, Optical and Quantum Electronics **38**, 495 (2006). (Cited on page 172.)

[BAU89] D. Baums, W. Elsäßer, and E. O. Göbel: *Farey tree and devil's staircase of a modulated external-cavity semiconductor laser*, Phys. Rev. Lett. **63**, 155 (1989). (Cited on page 188.)

[BEA08] V. Beato, I. Sendiña Nadal, I. Gerdes, and H. Engel: *Coherence resonance in a chemical excitable system driven by coloured noise*, Phil. Trans. R. Soc. A **366**, 381–395 (2008). (Cited on page 153.)

[BEN10] C. M. Bender and S. A. Orszag: *Advanced mathematical methods for scientists and engineers*, vol. 1 (Springer, 2010). (Cited on pages 19, 63, 72, 239 and 240.)

[BIM95] D. Bimberg, M. Grundmann, N. N. Ledentsov, S. S. Ruvimov, P. Werner, U. Richter, J. Heydenreich, V. M. Ustinov, P. S. Kop'ev, and Z. I. Alferov: *Self-organization processes in mbe-grown quantum dot structures*, Thin Solid Films **267**, 32–36 (1995). (Cited on page 2.)

[BIM99] D. Bimberg, M. Grundmann, and N. N. Ledentsov: *Quantum Dot Heterostructures* (John Wiley & Sons Ltd., New York, 1999). (Cited on pages 1, 9, 13 and 140.)

[BIM08] D. Bimberg: *Quantum dot based nanophotonics and nanoelectronics*, Electron. Lett. **44**, 168 (2008). (Cited on page 1.)

[BRA09] S. A. Brandstetter, M. A. Dahlem, and E. Schöll: *Interplay of time-delayed feedback control and temporally correlated noise in excitable systems*, Phil. Trans. R. Soc. A **368**, 391 (2010). (Cited on page 153.)

[BRE10] S. Breuer, W. Elsäßer, J. G. McInerney, K. Yvind, J. Pozo, E. A. J. M. Bente, M. Yousefi, A. Villafranca, N. Vogiatzis, and J. Rorison: *Investigations of repetition rate stability of a mode-locked quantum dot semiconductor laser in* *an auxiliary optical fiber cavity*, IEEE J. Quantum Electron. **46**, 150 (2010). (Cited on pages 3, 161, 162, 176, 190, 195 and 225.)

[BUC83] M. J. Buckingham: *Noise in electronic devices and systems*, Electrical and electronic engineering (Wiley, 1983). (Cited on page 247.)

[CAR05] O. Carroll, S. P. Hegarty, G. Huyet, and B. Corbett: *Length dependence of feedback sensitivity of InAs/GaAs quantum dot lasers*, Electron. Lett. **41**, 39–40 (2005). (Cited on pages 2 and 109.)

[CAR06a] O. Carroll, I. O'Driscoll, S. P. Hegarty, G. Huyet, J. Houlihan, E. A. Viktorov, and P. Mandel: *Feedback induced instabilities in a quantum dot semiconductor laser*, Opt. Express **14**, 10831–10837 (2006). (Cited on pages 2 and 109.)

[CHA07] S. C. Chan, S. K. Hwang, and J. M. Liu: *Period-one oscillation for photonic microwave transmission using an optically injected semiconductor laser*, Opt. Express **15**, 14921–14935 (2007). (Cited on pages 3, 36 and 75.)

[CHO99] W. W. Chow and S. W. Koch: *Semiconductor-Laser Fundamentals* (Springer, Berlin, 1999). (Cited on pages 1, 9, 11, 38 and 148.)

[CHO05] W. W. Chow and S. W. Koch: *Theory of semiconductor quantum-dot laser dynamics*, IEEE J. Quantum Electron. **41**, 495–505 (2005). (Cited on page 10.)

[COB03] C. Cobeli and A. Zaharescu: *The Haros-Farey sequence at two hundred years. a survey.*, Acta Universitatis Apulensis. Mathematics - Informatics **5**, 1–38 (2003). (Cited on page 188.)

[COL95] L. A. Coldren and S. W. Corzine: *Diode Lasers and Photonic Integrated Circuits* (John Wiley and Sons, New York, 1995). (Cited on page 25.)

[COL12] J. J. Coleman: *The development of the semiconductor laser diode after the first demonstration in 1962*, Semicond. Sci. Technol. **27**, 090207 (2012). (Cited on page 1.)

[DAH07] T. Dahms, P. Hövel, and E. Schöll: *Control of unstable steady states by extended time-delayed feedback*, Phys. Rev. E **76**, 056201 (2007). (Cited on pages 3 and 109.)

[DAH08b] T. Dahms, P. Hövel, and E. Schöll: *Stabilizing continuous-wave output in semiconductor lasers by time-delayed feedback*, Phys. Rev. E **78**, 056213 (2008). (Cited on pages 3 and 109.)

[DAH10] T. Dahms, V. Flunkert, F. Henneberger, P. Hövel, S. Schikora, E. Schöll, and H. J. Wünsche: *Noninvasive optical control of complex semiconductor laser dynamics*, Eur. Phys. J. ST **191**, 71 (2010). (Cited on pages 3, 109 and 229.)

[DAH11b] T. Dahms: *Synchronization in Delay-Coupled Laser Networks*, Ph.D. thesis, Technische Universität Berlin (2011). (Cited on pages 3 and 109.)

[DAH12] T. Dahms, J. Lehnert, and E. Schöll: *Cluster and group synchronization in delay-coupled networks*, Phys. Rev. E **86**, 016202 (2012). (Cited on pages 3 and 109.)

[DHO03] A. Dhooge, W. Govaerts, and Y. A. Kuznetsov: *matcont: A matlab package for numerical bifurcation analysis of ODEs*, ACM TOMS **29**, 141 (2003). (Cited on page 42.)

[DIE95] O. Diekmann, S. A. van Gils, S. M. Verduyn Lunel, and H. O. Walther: *Delay Equations* (Springer-Verlag, New York, 1995). (Cited on page 41.)

[DIN76] R. Dingle and C. H. Henry: *Quantum effects in heterostructure lasers*. United States Patent No. 3982207 (1976). (Cited on page 1.)

[DRA67] A. W. Drake: *Fundamentals of applied probability theory*, Porbability and Statistics (McGraw-Hill, 1967). (Cited on page 249.)

[DUB99a] J. L. A. Dubbeldam and B. Krauskopf: *Self-pulsations of lasers with saturable absorber: dynamics and bifurcations*, Opt. Commun. **159**, 325–338 (1999). (Cited on pages 146, 147 and 148.)

[DUB99] J. L. A. Dubbeldam, B. Krauskopf, and D. Lenstra: *Excitability and coherence resonance in lasers with saturable absorber*, Phys. Rev. E **60**, 6580 (1999). (Cited on pages 146, 147 and 148.)

[ELI96] D. Eliyahu, R. A. Salvatore, and A. Yariv: *Noise characterization of a pulse train generated by actively mode-locked lasers*, J. Opt. Soc. Am. B **13**, 1619 (1996). (Cited on page 214.)

[ELI97] D. Eliyahu, R. A. Salvatore, and A. Yariv: *Effect of noise on the power spectrum of passively mode-locked lasers*, J. Opt. Soc. Am. B **14**, 167 (1997). (Cited on pages 203, 210 and 214.)

[ENG01] K. Engelborghs, T. Luzyanina, and G. Samaey: *DDE-BIFTOOL v. 2.00: a matlab package for bifurcation analysis of delay differential equations*, Tech. Rep. TW-330, Department of Computer Science, K.U.Leuven, Belgium (2001). (Cited on page 41.)

[ENG02] K. Engelborghs, T. Luzyanina, and D. Roose: *Numerical bifurcation analysis of delay differential equations using DDE-Biftool*, ACM Transactions on Mathematical Software **28**, 1–21 (2002). (Cited on pages 41 and 118.)

[ERN95] U. Ernst, K. Pawelzik, and T. Geisel: *Synchronization induced by temporal delays in pulse-coupled oscillators*, Phys. Rev. Lett. **74**, 1570–1573 (1995). (Cited on page 136.)

[ERN00a] T. Erneux: *Asymptotic methods applied to semiconductor laser models*, Proc. SPIE **3944**, 588–601 (2000). (Cited on page 136.)

[ERN00] T. Erneux, F. Rogister, A. Gavrielides, and V. Kovanis: *Bifurcation to mixed external cavity mode solutions for semiconductor lasers subject to optical feedback*, Opt. Commun. **183**, 467–477 (2000). (Cited on page 124.)

[ERN07a] T. Erneux, E. A. Viktorov, and P. Mandel: *Time scales and relaxation dynamics in quantum-dot lasers*, Phys. Rev. A **76**, 023819 (2007). (Cited on pages 2, 9, 21, 33 and 54.)

[ERN09] T. Erneux: *Applied delay differential equations* (Springer, 2009). (Cited on page 17.)

[ERN10b] T. Erneux and P. Glorieux: *Laser Dynamics* (Cambridge University Press, UK, 2010). (Cited on pages 2, 15, 23, 32, 35, 40, 48, 63, 68, 75, 96, 108, 172, 239 and 240.)

[ERN10a] T. Erneux, E. A. Viktorov, B. Kelleher, D. Goulding, S. P. Hegarty, and G. Huyet: *Optically injected quantum-dot lasers*, Opt. Lett. **35**, 070937 (2010). (Cited on pages 2, 9, 17, 36, 49, 54, 57 and 108.)

[FIE08] B. Fiedler, S. Yanchuk, V. Flunkert, P. Hövel, H. J. Wünsche, and E. Schöll: *Delay stabilization of rotating waves near fold bifurcation and application to all-optical control of a semiconductor laser*, Phys. Rev. E **77**, 066207 (2008). (Cited on pages 3, 109 and 113.)

[FIO10] G. Fiol, D. Arsenijević, D. Bimberg, A. G. Vladimirov, M. Wolfrum, E. A. Viktorov, and P. Mandel: *Hybrid mode-locking in a 40 GHz monolithic quantum dot laser*, Appl. Phys. Lett. **96**, 011104 (2010). (Cited on pages 162 and 222.)

[FIO11a] G. Fiol: *1.3μm monolithic mode-locked quantum-dot semiconductor lasers*, (2011). (Cited on pages 172 and 203.)

[FIO11] G. Fiol, M. Kleinert, D. Arsenijević, and D. Bimberg: *1.3μm range 40 GHz quantum-dot mode-locked laser under external continuous wave light injection or optical feedback*, Semicond. Sci. Technol. **26**, 014006 (2011). (Cited on pages 3, 161, 162, 172, 176, 190, 195, 196, 197, 203, 207, 218 and 225.)

[FIS96] I. Fischer, G. H. M. van Tartwijk, A. M. Levine, W. Elsäßer, E. O. Göbel, and D. Lenstra: *Fast pulsing and chaotic itinerancy with a drift in the coherence collapse of semiconductor lasers*, Phys. Rev. Lett. **76**, 220 (1996). (Cited on page 155.)

[FIS00] I. Fischer, Y. Liu, and P. Davis: *Synchronization of chaotic semiconductor laser dynamics on subnanosecond time scales and its potential for chaos communication*, Phys. Rev. A **62**, 011801 (2000). (Cited on page 109.)

[FLU07] V. Flunkert and E. Schöll: *Suppressing noise-induced intensity pulsations in semiconductor lasers by means of time-delayed feedback*, Phys. Rev. E **76**, 066202 (2007). (Cited on pages 3, 38 and 109.)

[FLU09] V. Flunkert, O. D'Huys, J. Danckaert, I. Fischer, and E. Schöll: *Bubbling in delay-coupled lasers*, Phys. Rev. E **79**, 065201 (R) (2009). (Cited on pages 3 and 109.)

[FLU10] V. Flunkert: *Delayed complex systems and applications to lasers*, Ph.D. thesis, TU-Berlin (2010). (Cited on pages 3 and 109.)

[FLU11a] V. Flunkert: *Delay-Coupled Complex Systems*, Springer Theses (Springer, Heidelberg, 2011). (Cited on pages 15 and 155.)

[GAR02] C. W. Gardiner: *Handbook of Stochastic Methods for Physics, Chemistry and the Natural Sciences* (Springer, Berlin, 2002). (Cited on pages 38, 153, 203, 212, 214, 215, 245, 247 and 249.)

[GAV97a] A. Gavrielides, V. Kovanis, and T. Erneux: *Analytical stability boundaries for a semiconductor laser subject to optical injection*, Opt. Commun. **136**, 253–256 (1997). (Cited on pages 78 and 96.)

[GOM09] J. Gomis-Bresco, S. Dommers, V. V. Temnov, U. Woggon, J. Martinez-Pastor, M. Lämmlin, and D. Bimberg: *InGaAs quantum dots coupled to a reservoir of nonequilibrium free carriers*, IEEE J. Quantum Electron. **45**, 1121–1128 (2009). (Cited on page 10.)

[GER02] W. Gerstner and W. Kistler: *Spiking neuron models* (Cambridge University Press, Cambridge, 2002). (Cited on page 147.)

[GIA00] G. Giacomelli, M. Giudici, S. Balle, and J. R. Tredicce: *Experimental evidence of coherence resonance in an optical system*, Phys. Rev. Lett. **84**, 3298 (2000). (Cited on pages 146, 148 and 155.)

[GIE07] C. Gies, J. Wiersig, M. Lorke, and F. Jahnke: *Semiconductor model for quantum-dot-based microcavity lasers*, Phys. Rev. A **75**, 013803 (2007). (Cited on page 9.)

[GIO08] M. Gioannini, G. A. P. The, and I. Montrosset: *Multi-population rate equation simulation of quantum dot semiconductor lasers with feedback*, in *Numerical Simulation of Optoelectronic Devices, 2008. NUSOD '08. International Conference on*, edited by 2008), pp. 101–102. (Cited on page 138.)

[GIU97] M. Giudici, C. Green, G. Giacomelli, U. Nespolo, and J. R. Tredicce: *Andronov bifurcation and excitability in semiconductor lasers with optical feedback*, Phys. Rev. E **55**, 6414–6418 (1997). (Cited on pages 146 and 148.)

[GLE94] P. Glendinning: *Stability, instability and chaos* (Cambridge University Press, Cambridge, 1994). (Cited on page 41.)

[GLO11] B. Globisch: *Bifurkationsanalyse von Quantenpunktlasern mit optischer Rückkopplung*, Master's thesis, TU Berlin (2011). (Cited on page 41.)

[GLO12] B. Globisch, C. Otto, E. Schöll, and K. Lüdge: *Influence of carrier lifetimes on the dynamical behavior of quantum-dot lasers subject to optical feedback*, Phys. Rev. E **86**, 046201 (2012). (Cited on pages 2, 11, 97, 110, 123, 125, 126, 139 and 162.)

[GOU07] D. Goulding, S. P. Hegarty, O. Rasskazov, S. Melnik, M. Hartnett, G. Greene, J. G. McInerney, D. Rachinskii, and G. Huyet: *Excitability in a quantum dot semiconductor laser with optical injection*, Phys. Rev. Lett. **98**, 153903 (2007). (Cited on pages 9, 36, 54, 146 and 148.)

[GRE83a] C. Grebogi, E. Ott, and J. A. Yorke: *Crises, sudden changes in chaotic attractors, and transient chaos*, Physica D **7**, 181–200 (1983). (Cited on page 150.)

[GRE09a] K. Green: *Stability near threshold in a semiconductor laser subject to optical feedback: A bifurcation analysis of the Lang-Kobayashi equations*, Phys. Rev. E **79**, 036210 (2009). (Cited on page 111.)

[GRI08a] F. Grillot, B. Dagens, J. G. Provost, H. Su, and L. F. Lester: *Gain compression and above-threshold linewidth enhancement factor in*$1.3\mu m$ *InAs/GaAs quantum-dot lasers*, IEEE J. Quantum Electron. **44**, 946–951 (2008). (Cited on page 36.)

[GRI08] F. Grillot, N. A. Naderi, M. Pochet, C. Y. Lin, and L. F. Lester: *Variation of the feedback sensitivity in a* $1.55\mu m$ *InAs/InP quantum-dash fabry–perot semiconductor laser*, Appl. Phys. Lett. **93**, 191108 (2008). (Cited on pages 36 and 138.)

[GRI09] F. Grillot, C. Y. Lin, N. A. Naderi, M. Pochet, and L. F. Lester: *Optical feedback instabilities in a monolithic InAs/GaAs quantum dot passively mode-locked laser*, Appl. Phys. Lett. **94**, 153503 (2009). (Cited on pages 195, 200 and 218.)

[GRI13] F. Grillot, C. Wang, N. Naderi, and J. Even: *Modulation properties of self-injected quantum dot semiconductor diode lasers*, IEEE J. Quantum Electron. **PP**, 1 (2013). (Cited on page 138.)

[GUC83] J. Guckenheimer and P. Holme: *Nonlinear Oscillations, Dynamical Systems, and Bifurcations of Vector Fields*, Applied mathematical sciences 42 (Springer, Berlin, 1983). (Cited on page 48.)

[HAE02] B. Haegeman, K. Engelborghs, D. Roose, D. Pieroux, and T. Erneux: *Stability and rupture of bifurcation bridges in semiconductor lasers subject to optical feedback*, Phys. Rev. E **66**, 046216 (2002). (Cited on pages 111, 117, 118 and 124.)

[HAK81] H. Haken: *Licht und Materie 2* (Bibiographisches Institut, 1981). (Cited on page 37.)

[HAK83a] H. Haken: *Laser Theory* (Springer, 1983). (Cited on pages 13, 25 and 112.)

[HAL62] R. N. Hall, G. E. Fenner, J. D. Kingsley, T. J. Soltys, and R. O. Carlson: *Coherent light emission from GaAs junctions*, Phys. Rev. Lett. **9**, 366–368 (1962). (Cited on page 1.)

[HAU75] H. Haus: *A theory of forced mode locking*, IEEE J. Quantum Electron. **11**, 323–330 (1975). (Cited on pages 162 and 207.)

[HAU93] H. Haug and S. W. Koch: *Quantum Theory of the Optical and Electronic Properties of Semiconductors* (World Scientific, Singapore, 2 edition, 1993). (Cited on page 167.)

[HAU93a] H. A. Haus and A. Mecozzi: *Noise of mode-locked lasers*, IEEE J. Quantum Electron. **29**, 983 (1993). (Cited on pages 203, 207 and 210.)

[HAU00] H. Haus: *Mode-locking of lasers*, IEEE J. Sel. Top. Quantum Electron. **6**, 1173–1185 (2000). (Cited on pages 3, 162, 167 and 207.)

[HEI01a] T. Heil, I. Fischer, W. Elsäßer, and A. Gavrielides: *Dynamics of semiconductor lasers subject to delayed optical feedback: The short cavity regime*, Phys. Rev. Lett. **87**, 243901 (2001). (Cited on pages 121, 136, 152, 155 and 178.)

[HEI01] R. Heitz, H. Born, F. Guffarth, O. Stier, A. Schliwa, A. Hoffmann, and D. Bimberg: *Existence of a phonon bottleneck for excitons in quantum dots*, Phys. Rev. B **64**, 241305(R) (2001). (Cited on page 136.)

[HEI02a] T. Heil, J. Mulet, I. Fischer, C. R. Mirasso, M. Peil, P. Colet, and W. Elsäßer: *On/off phase shift keying for chaos-encrypted communication using external-cavity semiconductor lasers*, IEEE J. Quantum Electron. **38**, 1162–1170 (2002). (Cited on page 109.)

[HEI03a] T. Heil, I. Fischer, W. Elsäßer, B. Krauskopf, K. Green, and A. Gavrielides: *Delay dynamics of semiconductor lasers with short external cavities: Bifurcation scenarios and mechanisms*, Phys. Rev. E **67**, 066214 (2003). (Cited on pages 111, 121, 136, 152, 155 and 178.)

[HEL90b] J. Helms and K. Petermann: *A simple analytic expression for the stable operation range of laser diodes with optical feedback*, IEEE J. Quantum. Electron. **26**, 833 (1990). (Cited on pages 127, 137 and 138.)

[HEN82] C. H. Henry: *Theory of the linewidth of semiconductor lasers*, IEEE J. Quantum Electron. **18**, 259–264 (1982). (Cited on page 38.)

[HIC11] K. Hicke, O. D'Huys, V. Flunkert, E. Schöll, J. Danckaert, and I. Fischer: *Mismatch and synchronization: Influence of asymmetries in systems of two delay-coupled lasers*, Phys. Rev. E **83**, 056211 (2011). (Cited on pages 3 and 109.)

[HIL04] M. T. Hill, H. J. S. Dorren, T. de Vries, X. J. M. Leijtens, J. H. den Besten, B. Smalbrugge, Y.-S. Oei, H. Binsma, G.-D. Khoe, and M. K. Smit: *A fast low-power optical memory based on coupled micro-ring lasers*, Nature **432**, 206–209 (2004). (Cited on page 54.)

[HIN95] E. J. Hinch: *Perturbation Methods*, Cambridge Texts in applied mathematics (Cambridge University Press, 1995). (Cited on pages 63, 72 and 239.)

[HIR94a] H. Hirayama, K. Matsunaga, M. Asada, and Y. Suematsu: *Lasing action of* $Ga_{0.67}In_{0.33}As/GaInAsP/InP$ *tensile-strained quantum-box laser*, Electron. Lett. **30**, 142–143 (1994). (Cited on page 2.)

[HIZ06] J. Hizanidis, A. G. Balanov, A. Amann, and E. Schöll: *Noise-induced front motion: signature of a global bifurcation*, Phys. Rev. Lett. **96**, 244104 (2006). (Cited on pages 146 and 153.)

[HIZ07] J. Hizanidis, R. Aust, and E. Schöll: *Delay-induced multistability near a global bifurcation*, Int. J. Bifur. Chaos **18**, 1759–1765 (2008). (Cited on page 151.)

[HIZ08b] J. Hizanidis and E. Schöll: *Control of coherence resonance in semiconductor superlattices*, Phys. Rev. E **78**, 066205 (2008). (Cited on pages 44 and 146.)

[HIZ08] J. Hizanidis and E. Schöll: *Control of noise-induced spatiotemporal patterns in superlattices*, phys. stat. sol. (c) **5**, 207–210 (2008). (Cited on page 122.)

[HOD48] A. L. Hodgkin: *The local electric changes associated with repetitive action in a medullated axon*, J. Physiol. **107**, 165 (1948). (Cited on page 145.)

[HOR84] W. Horsthemke and R. Lefever: *Noise-Induced Transitions. Theory and Applications in Physics, Chemistry, and Biology* (Springer Verlag, Berlin, 1984). (Cited on page 245.)

[HU93a] G. Hu, T. Ditzinger, C. Z. Ning, and H. Haken: *Stochastic resonance without external periodic force*, Phys. Rev. Lett. **71**, 807 (1993). (Cited on pages 46, 146, 152 and 153.)

[HUA91] D. Huang, E. Swanson, C. Lin, J. Schuman, W. Stinson, W. Chang, M. Hee, T. Flotte, K. Gregory, C. Puliafito, and a. et: *Optical coherence tomography*, Science **254**, 1178–1181 (1991). (Cited on page 1.)

[HUY04] G. Huyet, D. O'Brien, S. P. Hegarty, J. G. McInerney, A. V. Uskov, D. Bimberg, C. Ribbat, V. M. Ustinov, A. E. Zhukov, S. S. Mikhrin, A. R. Kovsh, J. K. White, K. Hinzer, and A. J. SpringThorpe: *Quantum dot semiconductor lasers with optical feedback*, phys. stat. sol. (b) **201**, 345–352 (2004). (Cited on pages 2, 9, 109, 110 and 140.)

[IWA82] K. Iwashita and K. Nakagawa: *Suppression of mode partition noise by laser diode light injection*, IEEE J. Quantum Electron. **18**, 1669–1674 (1982). (Cited on pages 3 and 36.)

[JAC10] K. Jacobs: *Stochastic processes for physicists: understanding noisy systems* (Cambridge Univ Pr, 2010). (Cited on pages 212 and 245.)

[JAN04] N. B. Janson, A. G. Balanov, and E. Schöll: *Delayed feedback as a means of control of noise-induced motion*, Phys. Rev. Lett. **93**, 010601 (2004). (Cited on page 146.)

[JAN03] N. B. Janson, A. G. Balanov, and E. Schöll: *Delayed feedback as a means of control of noise-induced motion*, Phys. Rev. Lett. **93**, 010601 (2004). (Cited on page 153.)

[JIN06] X. Jin and S. L. Chuang: *Bandwidth enhancement of fabry-perot quantum-well lasers by injection-locking*, Solid-State Electron. **50**, 1141–1149 (2006). (Cited on pages 3, 36, 105 and 108.)

[KAE98] F. X. Kärtner, J. A. der Au, and U. Keller: *Mode-locking with slow and fast saturable absorbers-what's the difference?*, Selected Topics in Quantum Electronics, IEEE Journal of **4**, 159 (1998). (Cited on page 167.)

[KAN05] D. M. Kane and K. A. Shore (Editors): *Unlocking Dynamical Diversity: Optical Feedback Effects on Semiconductor Lasers* (Wiley VCH, Weinheim, 2005). (Cited on pages 49, 110, 112, 131, 172 and 179.)

[KEE03] G. A. Keeler, B. E. Nelson, D. Agarwal, C. Debaes, N. C. Helman, A. Bhatnagar, and D. A. B. Miller: *The benefits of ultrashort optical pulses in optically interconnected systems*, IEEE J. Sel. Top. Quantum Electron. **9**, 477–485 (2003). (Cited on page 1.)

[KEF08] F. Kefelian, S. O'Donoghue, M. T. Todaro, J. G. McInerney, and G. Huyet: *RF linewidth in monolithic passively mode-locked semiconductor laser*, IEEE Photon. Technol. Lett. **20**, 1405 (2008). (Cited on pages 204, 209, 213, 215 and 218.)

[KEL09] B. Kelleher, D. Goulding, S. P. Hegarty, G. Huyet, D. Y. Cong, A. Martinez, A. Lemaitre, A. Ramdane, M. Fischer, F. Gerschütz, and J. Koeth: *Excitable phase slips in an injection-locked single-mode quantum-dot laser*, Opt. Lett. **34**, 440–442 (2009). (Cited on pages 36, 146 and 148.)

[KEL11a] B. Kelleher, C. Bonatto, G. Huyet, and S. P. Hegarty: *Excitability in optically injected semiconductor lasers: Contrasting quantum-well- and quantum-dot-based devices*, Phys. Rev. E **83**, 026207 (2011). (Cited on pages 2, 36, 47, 50, 52, 146 and 148.)

[KEL11c] B. Kelleher, D. Goulding, S. P. Hegarty, G. Huyet, E. A. Viktorov, and T. Erneux: *Optically injected single-mode quantum dot lasers* (Springer New York, 2011), vol. 13 of *Lecture Notes in Nanoscale Science and Technology*, chapter 1, pp. 1–22. (Cited on pages 2, 9, 36, 49, 54, 57 and 108.)

[KEL12a] B. Kelleher, S. P. Hegarty, and G. Huyet: *Modified relaxation oscillation parameters in optically injected semiconductor lasers*, J. Opt. Soc. Am. B **29**, 2249–2254 (2012). (Cited on pages 49, 68, 97, 105 and 108.)

[KIN10] W. Kinzel, A. Englert, and I. Kanter: *On chaos synchronization and secure communication*, Phil. Trans. R. Soc. A **368**, 379–389 (2010). (Cited on page 109.)

[KNO00] W. H. Knox: *Ultrafast technology in telecommunications*, IEEE J. Sel. Top. Quantum Electron. **6**, 1273–1278 (2000). (Cited on page 1.)

[KOL86] B. Kolner and D. Bloom: *Electrooptic sampling in GaAs integrated circuits*, IEEE J. Quantum Electron. **22**, 79 (1986). (Cited on pages 203, 204, 205, 206 and 250.)

[KRA00] B. Krauskopf and D. Lenstra (Editors): *Fundamental Issues of Nonlinear Laser Dynamics*, vol. 548 of *AIP Conference Proceedings*, American Institute of Physics, Melville (New York), 2000. (Cited on page 112.)

[KRA00a] B. Krauskopf, G. H. M. van Tartwijk, and G. R. Gray: *Symmetry properties of lasers subject to optical feedback*, Opt. Commun. **177**, 347–353 (2000). (Cited on page 113.)

[KRA02b] B. Krauskopf and S. Wieczorek: *Accumulating regions of winding periodic orbits in optically driven lasers*, Physica D **173**, 97 (2002). (Cited on page 121.)

[KRA03a] B. Krauskopf, K. Schneider, J. Sieber, S. Wieczorek, and M. Wolfrum: *Excitability and self-pulsations near homoclinic bifurcations in semiconductor laser systems*, Opt. Commun. **215**, 367 (2003). (Cited on pages 146, 147 and 148.)

[KRA05a] B. Krauskopf: *Bifurcation analysis of lasers with delay*, in *unlocking dynamical diversity – optical feedback effects on semiconductor lasers*, edited by D. M. Kane and K. A. Shore (Wiley & Sons, Ltd, 2005), book chapter 5, pp. 147–183. (Cited on pages 40 and 41.)

[KRA07] B. Krauskopf: *Numerical Continuation Methods for Dynamical Systems: Path following and boundary value problems* (Springer Verlag, 2007). (Cited on pages 40 and 41.)

[KRO63] H. Kroemer: *A proposed class of hetero-junction injection lasers*, Proc. IEEE **51**, 1782–1783 (1963). (Cited on page 1.)

[KUN02] M. Kuntz, N. N. Ledentsov, D. Bimberg, A. R. Kovsh, V. M. Ustinov, A. E. Zhukov, and Y. M. Shernyakov: *Spectrotemporal response of* 1.3 *μm quantum-dot lasers*, Appl. Phys. Lett. **81**, 3846–3848 (2002). (Cited on pages 2, 9 and 140.)

[KUN05c] M. Kuntz: *Modulated InGaAs/GaAs Quantum Dot Lasers (Ph. D. Thesis)*, Ph.D. thesis, Technische Universität Berlin (2006). (Cited on page 11.)

[KUZ95] Y. A. Kuznetsov: *Elements of Applied Bifurcation Theory* (Springer, New York, 1995). (Cited on pages 40, 43, 44, 47, 48, 98, 121, 122, 147, 151, 176, 178 and 200.)

[LAN80b] R. Lang and K. Kobayashi: *External optical feedback effects on semiconductor injection laser properties*, IEEE J. Quantum Electron. **16**, 347–355 (1980). (Cited on pages 110 and 111.)

[LAU09a] E. K. Lau, L. J. Wong, and M. C. Wu: *Enhanced modulation characteristics of optical injection-locked lasers: A tutorial*, IEEE J. Sel. Top. Quantum Electron. **15**, 618–633 (2009). (Cited on pages 3, 36, 105 and 108.)

[LEE02c] D. C. Lee: *Analysis of jitter in phase-locked loops*, IEEE Trans. Circuits Syst. II **49**, 704 (2002). (Cited on pages 203 and 213.)

[LEL07] F. Lelarge, B. Dagens, J. Renaudier, R. Brenot, A. Accard, F. van Dijk, D. Make, O. L. Gouezigou, J. G. Provost, F. Poingt, J. Landreau, O. Drisse, E. Derouin, B. Rousseau, F. Pommereau, and G. H. Duan: *Recent advances on InAs/InP quantum dash based semiconductor lasers and optical amplifiers operating at* $1.55\mu\ m$, IEEE J. Sel. Top. Quantum Electron. **13**, 111 (2007). (Cited on page 161.)

[LEN91] D. Lenstra: *Statistical-theory of the multistable external-feedback laser*, Opt. Commun. **81**, 209–214 (1991). (Cited on page 137.)

[LEV95] A. M. Levine, G. H. M. van Tartwijk, D. Lenstra, and T. Erneux: *Diode lasers with optical feedback: Stability of the maximum gain mode*, Phys. Rev. A **52**, R3436 (1995), (4 pages). (Cited on pages 116, 136, 138, 139 and 244.)

[LI08a] B. Li, M. Irfan Memon, G. Yuan, Z. Wang, S. Yu, G. Mezosi, and M. Sorel: *All-optical response of semiconductor ring laser bistable to duo optical injections*, in *cs and Laser Science. CLEO/QELS 2008. Conference onLasers and Electro-Optics, 2008 and 2008 Conference on Quantum Electroni*, edited by 2008), pp. 1–2. (Cited on page 54.)

[LIN10c] C. Y. Lin, F. Grillot, Y. Li, R. Raghunathan, and L. F. Lester: *Characterization of timing jitter in a 5 GHz quantum dot passively mode-locked laser*, Opt. Express **18**, 21932 (2010). (Cited on pages 161 and 207.)

[LIN10e] C. Y. Lin, F. Grillot, N. A. Naderi, Y. Li, and L. F. Lester: *rf linewidth reduction in a quantum dot passively mode-locked laser subject to external optical feedback*, Appl. Phys. Lett. **96**, 051118 (2010). (Cited on pages 3, 161, 162, 176, 190, 195, 196, 200, 210, 218 and 225.)

[LIN10a] B. Lingnau, K. Lüdge, E. Schöll, and W. W. Chow: *Dynamic many-body and nonequilibrium effects in a quantum dot microcavity laser*, in *Semiconductor Lasers and Laser Dynamics IV*, edited by K. Panajotov, M. Sciamanna, A. A. Valle, and R. Michalzik (SPIE, 2010), vol. 7720 of *Proceedings of SPIE*, pp. 77201F–77201F–11. (Cited on page 10.)

[LIN10] B. Lingnau, K. Lüdge, E. Schöll, and W. W. Chow: *Many-body and nonequilibrium effects on relaxation oscillations in a quantum-dot microcavity laser*, Appl. Phys. Lett. **97**, 111102 (2010). (Cited on page 10.)

[LIN11f] C. Y. Lin, F. Grillot, and Y. Li: *Microwave characterization and stabilization of timing jitter in a quantum dot passively mode-locked laser via external optical feedback*, IEEE J. Sel. Topics Quantum Electron. **17**, 1311 (2011). (Cited on pages 3, 161, 162, 176, 190, 204, 207, 210, 215 and 218.)

[LIN11d] C. Y. Lin, F. Grillot, N. A. Naderi, Y. Li, J. H. Kim, C. G. Christodoulou, and L. F. Lester: *RF linewidth of a monolithic quantum dot mode-locked laser under resonant feedback*, IET Optoelectron. **5**, 105 (2011). (Cited on pages 3, 161, 162, 176, 190, 195 and 218.)

[LIN12b] B. Lingnau, K. Lüdge, W. W. Chow, and E. Schöll: *Failure of the α-factor in describing dynamical instabilities and chaos in quantum-dot lasers*, Phys. Rev. E **86**, 065201(R) (2012). (Cited on pages 36, 49, 110 and 138.)

[LIN12] B. Lingnau, K. Lüdge, W. W. Chow, and E. Schöll: *Influencing modulation properties of quantum-dot semiconductor lasers by electron lifetime engineering*, Appl. Phys. Lett. **101**, 131107 (2012). (Cited on pages 10, 19 and 21.)

[LIN12a] B. Lingnau, K. Lüdge, W. W. Chow, and E. Schöll: *Many-body effects and self-contained phase dynamics in an optically injected quantum-dot laser*, in *Semiconductor Lasers and Laser Dynamics V, Brussels*, edited by K. Panajotov, M. Sciamanna, A. A. Valle, and R. Michalzik (SPIE, 2012), vol. 8432 of *Proceedings of SPIE*, pp. 84321J–1. (Cited on pages 10, 36, 110 and 138.)

[LIN12t] B. Lingnau, K. Lüdge, W. W. Chow, and E. Schöll: *Many-body effects and self-contained phase dynamics in an optically injected quantum-dot laser*, SPIE Proc. **8432** (2012). (Cited on page 10.)

[LIN13] B. Lingnau, W. W. Chow, E. Schöll, and K. Lüdge: *Nonequilibrium dynamics of quantum-dot lasers under optical injection and feedback*, New J. Phys. **in preparation** (2013). (Cited on pages 36, 38, 49, 110 and 138.)

[LOR06] M. Lorke, T. R. Nielsen, J. Seebeck, P. Gartner, and F. Jahnke: *Influence of carrier-carrier and carrier-phonon correlations on optical absorption and gain in quantum-dot systems*, Phys. Rev. B **73**, 085324 (2006). (Cited on page 11.)

[LUE08] K. Lüdge, M. J. P. Bormann, E. Malić, P. Hövel, M. Kuntz, D. Bimberg, A. Knorr, and E. Schöll: *Turn-on dynamics and modulation response in semiconductor quantum dot lasers*, Phys. Rev. B **78**, 035316 (2008). (Cited on page 9.)

[LUE09] K. Lüdge and E. Schöll: *Quantum-dot lasers – desynchronized nonlinear dynamics of electrons and holes*, IEEE J. Quantum Electron. **45**, 1396–1403 (2009). (Cited on pages 2, 9, 10, 12, 14, 29, 51, 140 and 233.)

[LUE10a] K. Lüdge, R. Aust, G. Fiol, M. Stubenrauch, D. Arsenijević, D. Bimberg, and E. Schöll: *Large signal response of semiconductor quantum-dot lasers*, IEEE J. Quantum Electron. **46**, 1755 –1762 (2010). (Cited on pages 9, 10, 14 and 140.)

[LUE10] K. Lüdge and E. Schöll: *Nonlinear dynamics of doped semiconductor quantum dot lasers*, Eur. Phys. J. D **58**, 167–174 (2010). (Cited on pages 9, 12, 14, 17, 52 and 233.)

[LUE11] K. Lüdge, E. Schöll, E. A. Viktorov, and T. Erneux: *Analytic approach to modulation properties of quantum dot lasers*, J. Appl. Phys. **109**, 103112 (2011). (Cited on pages 11, 20, 25, 26, 33, 51, 63, 64, 65, 74, 79, 90, 141 and 239.)

[LUE11a] K. Lüdge: *Modeling Quantum Dot based Laser Devices*, in *Nonlinear Laser Dynamics - From Quantum Dots to Cryptography*, edited by K. Lüdge (WILEY-VCH Weinheim, Weinheim, 2012), chapter 1, pp. 3–34. (Cited on pages 2 and 9.)

[LUE11b] K. Lüdge: *Nonlinear Laser Dynamics - From Quantum Dots to Cryptography* (Wiley-VCH, Weinheim, 2012). (Cited on page 161.)

[LUE13] K. Lüdge, B. Lingnau, C. Otto, and E. Schöll: *Understanding electrical and optical modulation properties of semiconductor quantum-dot lasers in terms of their turn-on dynamics*, Nonlinear Phenom. Complex Syst. **15**, 350–359 (2012). (Cited on pages 19 and 20.)

[LUE12] K. Lüdge and E. Schöll: *Temperature dependent two-state lasing in quantum dot lasers*, in *Laser Dynamics and Nonlinear Photonics, Fifth Rio De La Plata Workshop 6-9 Dec. 2011*, edited by (IEEE Publishing Services, New York, 2012), IEEE Conf. Proc., pp. 1–6. (Cited on page 11.)

[LYT97] G. Lythe, T. Erneux, A. Gavrielides, and V. Kovanis: *Low pump limit of the bifurcation to periodic intensities in a semiconductor laser subject to external optical feedback*, Phys. Rev. A **55**, 4443–4448 (1997). (Cited on page 121.)

[MAJ10] N. Majer, K. Lüdge, and E. Schöll: *Cascading enables ultrafast gain recovery dynamics of quantum dot semiconductor optical amplifiers*, Phys. Rev. B **82**, 235301 (2010). (Cited on pages 10, 11 and 20.)

[MAJ11] N. Majer, S. Dommers-Völkel, J. Gomis-Bresco, U. Woggon, K. Lüdge, and E. Schöll: *Impact of carrier-carrier scattering and carrier heating on pulse train dynamics of quantum dot semiconductor optical amplifiers*, Appl. Phys. Lett. **99**, 131102 (2011). (Cited on page 10.)

[MAJ11a] N. Majer, K. Lüdge, and E. Schöll: *Maxwell-bloch approach to four-wave mixing in quantum dot semiconductor optical amplifiers*, in 11th Internat. Conf. on Numerical Simulation of Optical Devices (NUSOD), Rome 2011, edited by J. Piprek, IEEE Proc., 153–154 (2011). (Cited on page 10.)

[MAJ12] N. Majer: *Nonlinear Gain Dynamics of Quantum Dot Semiconductor Optical Amplifiers*, Ph.D. thesis (2012). (Cited on page 48.)

[MAL06] E. Malić, K. J. Ahn, M. J. P. Bormann, P. Hövel, E. Schöll, A. Knorr, M. Kuntz, and D. Bimberg: *Theory of relaxation oscillations in semiconductor quantum dot lasers*, Appl. Phys. Lett. **89**, 101107 (2006). (Cited on pages 2, 9 and 11.)

[MAL07] E. Malić, M. J. P. Bormann, P. Hövel, M. Kuntz, D. Bimberg, A. Knorr, and E. Schöll: *Coulomb damped relaxation oscillations in semiconductor quantum dot lasers*, IEEE J. Sel. Top. Quantum Electron. **13**, 1242–1248 (2007). (Cited on pages 9 and 11.)

[MAY02] C. Mayol, R. Toral, C. R. Mirasso, and M. Natiello: *Class-a lasers with injected signal: Bifurcation set and lyapunov-potential function*, Phys. Rev. A **66**, 013808 (2002). (Cited on page 54.)

[MEL06] S. Melnik, G. Huyet, and A. V. Uskov: *The linewidth enhancement factor α of quantum dot semiconductor lasers*, Opt. Express **14**, 2950–2955 (2006). (Cited on pages 36 and 110.)

[MER09] K. Merghem, R. Rosales, S. Azouigui, A. Akrout, A. Martinez, F. Lelarge, G. H. Duan, G. Aubin, and A. Ramdane: *Low noise performance of passively mode locked quantum-dash-based lasers under external optical feedback*, Appl. Phys. Lett. **95**, 131111 (2009). (Cited on pages 3, 161, 195 and 218.)

[MES10] C. Mesaritakis, C. Simos, S. Mikroulis, I. Krestnikov, E. Roditi, and D. Syvridis: *Effect of optical feedback to the ground and excited state emission of a passively mode locked quantum dot laser*, Appl. Phys. Lett. **97**, 061114 (2010). (Cited on page 218.)

[MOR92] J. Mørk, B. Tromborg, and J. Mark: *Chaos in semiconductor lasers with optical feedback-Theory and experiment*, IEEE J. Quantum Electron. **28**, 93–108 (1992). (Cited on pages 22, 127, 137, 200 and 203.)

[MUL06] J. Mulet and J. Mørk: *Analysis of timing jitter in external-cavity mode-locked semiconductor lasers*, IEEE J. Quantum Electron. **42**, 249 (2006). (Cited on pages 3, 162, 203, 207 and 208.)

[MUR93] J. D. Murray: *Mathematical Biology*, vol. 19 of *Biomathematics Texts* (Springer, Berlin Heidelberg, 2nd edition, 1993). (Cited on pages 145 and 146.)

[MUR02] A. Murakami and J. Ohtsubo: *Synchronization of feedback-induced chaos in semiconductor lasers by optical injection*, Phys. Rev. A **65**, 033826 (2002). (Cited on page 36.)

[NAD09] N. A. Naderi, M. Pochet, F. Grillot, N. B. Terry, V. Kovanis, and L. F. Lester: *Modeling the injection-locked behavior of a quantum dash semiconductor laser*, IEEE J. Sel. Top. Quantum Electron. **15**, 563 (2009). (Cited on page 36.)

[NAT62] M. I. Nathan, W. P. Dumke, G. Burns, J. F.H. Dill, and G. Lasher: *Stimulated emission of radiation from GaAs p-n junctions*, Appl. Phys. Lett. **1**, 62–64 (1962). (Cited on page 1.)

[NEW74] G. New: *Pulse evolution in mode-locked quasi-continuous lasers*, IEEE J. Quantum Electron. **10**, 115 (1974). (Cited on page 172.)

[NEW99a] T. C. Newell, D. J. Bossert, A. Stintz, B. Fuchs, K. J. Malloy, and L. F. Lester: *Gain and linewidth enhancement factor in InAs quantum-dot laser diodes*, IEEE Photonics Technol. Lett. **11**, 1527–1529 (1999). (Cited on pages 118, 122 and 128.)

[HOL62] J. N. Holonyak and S. F. Bevacqua: *Coherent (visible) light emission from* $Ga(As_{1-x}P_x)$ *junctions*, Appl. Phys. Lett. **1**, 82–83 (1962). (Cited on page 1.)

[NIE04] T. R. Nielsen, P. Gartner, and F. Jahnke: *Many-body theory of carrier capture and relaxation in semiconductor quantum-dot lasers*, Phys. Rev. B **69**, 235314 (2004). (Cited on page 11.)

[NIL05] H. H. Nilsson, J. Z. Zhang, and I. Galbraith: *Homogeneous broadening in quantum dots due to auger scattering with wetting layer carriers*, Phys. Rev. B **72**, 205331 (2005). (Cited on page 11.)

[NIZ99] M. Nizette, T. Erneux, A. Gavrielides, and V. Kovanis: *Injection-locked semiconductor laser dynamics from large to small detunings*, Proc. SPIE **3625**, 679–689 (1999). (Cited on page 48.)

[NIZ01] M. Nizette, T. Erneux, A. Gavrielides, and V. Kovanis: *Averaged equations for injection locked semiconductor lasers*, Physica D **161**, 220 (2001). (Cited on pages 48 and 68.)

[OBR03a] D. O'Brien, S. P. Hegarty, G. Huyet, J. G. McInerney, T. Kettler, M. Lämmlin, D. Bimberg, V. Ustinov, A. E. Zhukov, S. S. Mikhrin, and A. R. Kovsh: *Feedback sensitivity of 1.3 µm InAs/GaAs quantum dot lasers*, Electronics Letters **39**, 1819–1820 (2003). (Cited on pages 2, 109 and 138.)

[OBR04] D. O'Brien, S. P. Hegarty, G. Huyet, and A. V. Uskov: *Sensitivity of quantum-dot semiconductor lasers to optical feedback*, Opt. Lett. **29**, 1072–1074 (2004). (Cited on pages 9 and 54.)

[OLE10] L. Olejniczak, K. Panajotov, H. Thienpont, and M. Sciamanna: *Self-pulsations and excitability in optically injected quantum-dot lasers: Impact of the excited states and spontaneous emission noise*, Phys. Rev. A **82**, 023807 (2010). (Cited on pages 36, 46, 47, 50 and 147.)

[OLS85] N. A. Olsson, H. Temkin, R. A. Logan, L. F. Johnson, G. J. Dolan, J. P. Van der Ziel, and J. C. Campbell: *Chirp-free transmission over 82.5 km of single mode fibers at 2 Gbit/s with injection locked DFB semiconductor lasers*, J. Lightwave Technol. **3**, 63–67 (1985). (Cited on pages 3 and 35.)

[OTT10] C. Otto, K. Lüdge, and E. Schöll: *Modeling quantum dot lasers with optical feedback: sensitivity of bifurcation scenarios*, phys. stat. sol. (b) **247**, 829–845 (2010). (Cited on pages 110, 111, 122, 141, 142, 162 and 178.)

[OTT12] C. Otto, B. Globisch, K. Lüdge, E. Schöll, and T. Erneux: *Complex dynamics of semiconductor quantum dot lasers subject to delayed optical feedback*, Int. J. Bif. Chaos **22**, 1250246 (2012). (Cited on pages 111, 118, 119, 120, 137 and 162.)

[OTT11] C. Otto, K. Lüdge, E. A. Viktorov, and T. Erneux: *Quantum dot laser tolerance to optical feedback*, in *Nonlinear Laser Dynamics - From Quantum Dots to Cryptography*, edited by K. Lüdge (WILEY-VCH, Weinheim, 2012), chapter 6, pp. 141–162. (Cited on pages 22, 97, 111 and 127.)

[OTT12a] C. Otto, K. Lüdge, A. G. Vladimirov, M. Wolfrum, and E. Schöll: *Delay induced dynamics and jitter reduction of passively mode-locked semiconductor laser subject to optical feedback*, New J. Phys. **14**, 113033 (2012). (Cited on pages 110, 111 and 189.)

[PAN12] A. Panchuk, D. P. Rosin, P. Hövel, and E. Schöll: *Synchronization of coupled neural oscillators with heterogeneous delays*, Int. J. Bif. Chaos (2012), in print (arXiv:1206.0789). (Cited on page 190.)

[PAS04] R. Paschotta: *Noise of mode-locked lasers (part i): numerical model*, Appl. Phys. B: Lasers and Optics **79**, 153–162 (2004). (Cited on pages 204, 249 and 250.)

[PAS04a] R. Paschotta: *Noise of mode-locked lasers (part ii): timing jitter and other fluctuations*, Appl. Phys B: Lasers and Optics **79**, 163–173 (2004). (Cited on page 204.)

[PAS06] R. Paschotta, A. Schlatter, S. C. Zeller, H. R. Telle, and U. Keller: *Optical phase noise and carrier-envelope offset noise of mode-locked lasers*, Appl. Phys. B: Lasers and Optics **82**, 265–273 (2006). (Cited on page 204.)

[PAU12] J. Pausch, C. Otto, E. Tylaite, N. Majer, E. Schöll, and K. Lüdge: *Optically injected quantum dot lasers - impact of nonlinear carrier lifetimes on frequency locking dynamics*, New J. Phys. **14**, 053018 (2012). (Cited on pages 2, 11, 13, 42, 44, 50, 51, 53 and 108.)

[PET91] K. Petermann: *Laser Diode Modulation and Noise* (Kluwer Academic, Boston, 1991). (Cited on pages 24 and 36.)

[PIK97] A. S. Pikovsky and J. Kurths: *Coherence resonance in a noise-driven excitable system*, Phys. Rev. Lett. **78**, 775 (1997). (Cited on pages 46, 146, 152 and 153.)

[Pip85] A. B. Pippard: *Response and stability* (Cambridge University Press, 1985). (Cited on page 74.)

[POM05] J. Pomplun: *Time-delayed feedback control of noise-induced oscillations*, Master's thesis, TU Berlin (2005). (Cited on page 249.)

[POM05a] J. Pomplun, A. Amann, and E. Schöll: *Mean field approximation of time-delayed feedback control of noise-induced oscillations in the Van der Pol system*, Europhys. Lett. **71**, 366 (2005). (Cited on page 153.)

[POM07] J. Pomplun, A. G. Balanov, and E. Schöll: *Long-term correlations in stochastic systems with extended time-delayed feedback*, Phys. Rev. E **75**, 040101(R) (2007). (Cited on pages 153 and 249.)

[PYR92] K. Pyragas: *Continuous control of chaos by self-controlling feedback*, Phys. Lett. A **170**, 421 (1992). (Cited on page 229.)

[QUI62] T. M. Quist, R. H. Rediker, R. J. Keyes, W. E. Krag, B. Lax, A. L. McWhorter, and H. J. Zeigler: *Semiconductor maser of GaAs*, Appl. Phys. Lett. **1**, 91–92 (1962). (Cited on page 1.)

[RAC02] A. Rack, R. Wetzler, A. Wacker, and E. Schöll: *Dynamical bistability in quantum-dot structures: Role of Auger processes*, Phys. Rev. B **66**, 165429 (2002). (Cited on page 11.)

[RAD07] M. Radziunas, A. Glitzky, U. Bandelow, M. Wolfrum, U. Troppenz, J. Kreissl, and W. Rehbein: *Improving the Modulation Bandwidth in Semiconductor Lasers by Passive Feedback*, IEEE J. Sel. Top. Quantum Electron. **13**, 136–142 (2007). (Cited on pages 109, 110, 118, 136 and 228.)

[RAF11] E. U. Rafailov, M. A. Cataluna, and E. A. Avrutin: *Ultrafast Lasers Based on Quantum Dot Structures* (WILEY-VCH, Weinheim, 2011). (Cited on pages 9 and 164.)

[REB11] N. Rebrova, G. Huyet, D. Rachinskii, and A. G. Vladimirov: *Optically injected mode-locked laser*, Phys. Rev. E **83**, 066202 (2011). (Cited on pages 162 and 207.)

[RED80] M. Reed and B. Simon: *Functional analysis*, vol. 1 of *Methods of modern mathematical physics* (Academic Press, 1980). (Cited on page 248.)

[REI99] O. Reimann, D. Huhse, E. Droge, E. H. Bottcher, D. Bimberg, and H. D. Stahlmann: *Electrooptical sampling using* $1.55-\mu;m$ *self-seeded semiconductor laser with soliton pulse compression*, IEEE Photon. Technol. Lett. **11**, 1024–1026 (1999). (Cited on page 1.)

[RIT93] A. Ritter and H. Haug: *Theory of laser diodes with weak optical feedback. I. small-signal analysis and side-mode spectra*, J. Opt. Soc. Am. B **10**, 130–144 (1993). (Cited on pages 136 and 137.)

[ROS11d] M. Rossetti, P. Bardella, and I. Montrosset: *Modeling passive mode-locking in quantum dot lasers: A comparison between a finite- difference traveling-wave model and a delayed differential equation approach*, IEEE J. Quantum Electron. **47**, 569 (2011). (Cited on pages 162 and 164.)

[ROS11e] M. Rossetti, X. Tianhong, P. Bardella, and I. Montrosset: *Impact of gain saturation on passive mode locking regimes in quantum dot lasers with straight and tapered waveguides*, IEEE J. Quantum Electron. **47**, 1404 (2011). (Cited on page 162.)

[ROS12b] R. Rosales, K. Merghem, A. Martinez, A. Akrout, J. P. Tourrenc, A. Accard, F. Lelarge, and A. Ramdane: *InAs/InP quantum-dot passively mode locked lasers for* $1.55\mu m$ *applications*, IEEE J. Sel. Top. Quantum Electron. **17**, 1292–1300 (2012). (Cited on pages 162, 176, 190, 203 and 218.)

[ROT07] V. Rottschäfer and B. Krauskopf: *The ECM-backbone of the Lang-Kobayashi equations: A geometric picture*, Int. J. Bif. Chaos **17**, 1575–1588 (2007). (Cited on pages 112 and 114.)

[SAC92a] J. Sacher, D. Baums, P. Panknin, W. Elsäßer, and E. O. Göbel: *Intensity instabilites of semiconductor lasers under current modulation external light injection, and delayed feedback*, Phys. Rev. A **45**, 1893–1905 (1992). (Cited on page 188.)

[SAN94] T. Sano: *Antimode dynamics and chaotic itinerancy in the coherence collapse of semiconductor lasers with optical feedback*, Phys. Rev. A **50**, 2719–2726 (1994). (Cited on page 155.)

[SCH86g] N. Schunk and K. Petermann: *Noise analysis of injection-locked semiconductor injection lasers*, IEEE J. Quantum Electron. **22**, 642–650 (1986). (Cited on pages 3 and 35.)

[SCH87] E. Schöll: *Nonequilibrium Phase Transitions in Semiconductors* (Springer, Berlin, 1987). (Cited on page 12.)

[SCH88j] E. Schöll: *Dynamic theory of picosecond optical pulse shaping by gain-switched semiconductor laser amplifiers*, IEEE J. Quantum Electron. **24**, 435–442 (1988). (Cited on page 163.)

[SCH88l] N. Schunk and K. Petermann: *Numerical analysis of the feedback regimes for a single-mode semiconductor laser with external feedback*, IEEE J. Quantum Electron. **24**, 1242–1247 (1988). (Cited on page 137.)

[SCH89h] N. Schunk and K. Petermann: *Stability analysis for laser diodes with short external cavities*, IEEE Photonics Technol. Lett. **1**, 49–51 (1989). (Cited on page 118.)

[SCH89c] H. G. Schuster: *Deterministic Chaos* (VCH Verlagsgesellschaft, 1989). (Cited on pages 48, 188 and 200.)

[SCH90b] M. Schell and E. Schöll: *Time-dependent simulation of a semiconductor laser amplifier: Pulse compression in a ring configuration and dynamic optical bistability*, IEEE J. Quantum Electron. **26**, 1005–1003 (1990). (Cited on page 163.)

[SCH91c] M. Schell, A. Weber, E. Schöll, and D. Bimberg: *Fundamental limits of sub-ps pulse generation by active mode locking of semiconductor lasers: The spectral gain width and the facet reflectivities*, IEEE J. Quantum Electron. **27**, 1661 (1991). (Cited on page 161.)

[SCH00] E. Schöll: *Nonlinear spatio-temporal dynamics and chaos in semiconductors* (Cambridge University Press, Cambridge, 2001). (Cited on page 44.)

[SCH01] E. Schöll: *Nonlinear spatio-temporal dynamics and chaos in semiconductors* (Cambridge University Press, Cambridge, 2001), Nonlinear Science Series, Vol. 10. (Cited on page 188.)

[SCH06a] S. Schikora, P. Hövel, H. J. Wünsche, E. Schöll, and F. Henneberger: *All-optical noninvasive control of unstable steady states in a semiconductor laser*, Phys. Rev. Lett. **97**, 213902 (2006). (Cited on pages 3, 109 and 229.)

[SCH07] E. Schöll and H. G. Schuster (Editors): *Handbook of Chaos Control* (Wiley-VCH, Weinheim, 2008), Second completely revised and enlarged edition. (Cited on pages 3 and 109.)

[SCH09a] E. Schöll, P. Hövel, V. Flunkert, and M. A. Dahlem: *Time-delayed feedback control: from simple models to lasers and neural systems*, in *Complex time-delay systems: theory and applications*, edited by F. M. Atay (Springer, Berlin, 2010), pp. 85–150. (Cited on pages 3 and 109.)

[SEO01] Y. K. Seo, A. Kim, J. T. Kim, and W. Y. Choi: *Optical generation of microwave signals using a directly modulated semiconductor laser under modulated light injection*, Microw. Opt. Techn. Lett. **30**, 369–370 (2001). (Cited on pages 3, 36 and 75.)

[SHC99] V. A. Shchukin and D. Bimberg: *Spontaneous ordering of nanostructures on crystal surfaces*, Rev. Mod. Phys. **71**, 1125 (1999). (Cited on page 2.)

[SHC03] V. A. Shchukin, N. N. Ledentsov, and D. Bimberg: *Epitaxy of Nanostructures* (Springer, Berlin, 2004). (Cited on page 2.)

[SHC07] V. A. Shchukin, E. Schöll, and P. Kratzer: *Thermodynamics and kinetics of quantum dot growth*, in *Semiconductor Nanostructures*, edited by D. Bimberg (Springer, Berlin, 2008), pp. 1–39. (Cited on page 2.)

[SIM95] T. B. Simpson, J. M. Liu, A. Gavrielides, V. Kovanis, and P. M. Alsing: *Period-doubling cascades and chaos in a semiconductor laser with optical injection*, Phys. Rev. A **51**, 4181–4185 (1995). (Cited on page 75.)

[SIM03] T. B. Simpson: *Mapping the nonlinear dynamics of a distributed feedback semiconductor laser subject to external optical injection*, Opt.Commun. **215**, 135–151 (2003). (Cited on pages 49 and 59.)

[SIM12a] H. Simos, C. Simos, C. Mesaritakis, and D. Syvridis: *Two-section quantum-dot mode-locked lasers under optical feedback: Pulse broadening and harmonic operation*, IEEE J. Quantum Electron. **48**, 872 (2012). (Cited on page 162.)

[SOL93] O. Solgaard and K. Y. Lau: *Optical feedback stabilization of the intensity oscillations in ultrahigh-frequency passively modelocked monolithic quantum-well lasers*, IEEE Photonics Technol. Lett. **5**, 1264 (1993). (Cited on pages 3, 161, 162, 176, 190, 195, 196, 197, 218 and 225.)

[SOR13] M. C. Soriano, J. García-Ojalvo, C. R. Mirasso, and I. Fischer: *Complex photonics: Dynamics and applications of delay-coupled semiconductors lasers*, Rev. Mod. Phys. **85**, 421–470 (2013). (Cited on pages 3 and 109.)

[STR63] R. L. Stratonovich: *Topics in the Theory of Random Noise*, vol. 1 (Gordon and Breach, New York, 1963). (Cited on pages 152 and 245.)

[STR94a] S. H. Strogatz: *Nonlinear Dynamics and Chaos* (Westview Press, Cambridge, MA, 1994). (Cited on pages 15, 47, 63 and 240.)

[SU03] H. Su, L. Zhang, A. L. Gray, R. Wang, T. C. Newell, K. J. Malloy, and L. F. Lester: *High external feedback resistance of laterally loss-coupled distributed feedback quantum dot semiconductor lasers*, IEEE Photonics Technol. Lett. **15**, 1504–1506 (2003). (Cited on pages 2 and 109.)

[SU05] H. Su, L. Zhang, A. L. Gray, R. Wang, P. M. Varangis, and L. F. Lester: *Gain compression coefficient and above-threshold linewidth enhancement factor in InAs/GaAs quantum dot DFB lasers*, Proc. of SPIE **5722**, 72 (2005). (Cited on page 36.)

[SU10] Y. Su, A. Carmele, M. Richter, K. Lüdge, E. Schöll, D. Bimberg, and A. Knorr: *Theory of single quantum dot lasers: Pauli-blocking enhanced anti-bunching*, Semicond. Sci. Technol. **26**, 014015 (2011). (Cited on page 9.)

[SUG05] M. Sugawara, N. Hatori, M. Ishida, H. Ebe, Y. Arakawa, T. Akiyama, K. Otsubo, T. Yamamoto, and Y. Nakata: *Recent progress in self-assembled quantum-dot optical devices for optical telecommunication: temperature-insensitive 10 Gbs directly modulated lasers and 40 Gbs signal-regenerative amplifiers*, J. Phys. D **38**, 2126–2134 (2005). (Cited on page 3.)

[SUK99] D. W. Sukow, T. Heil, I. Fischer, A. Gavrielides, A. Hohl-AbiChedid, and W. Elsäßer: *Picosecond intensity statistics of semiconductor lasers operating in the low-frequency fluctuation regime*, Phys. Rev. A **60**, 667–673 (1999). (Cited on page 155.)

[SZA09] R. Szalai: *KNUT: A continuation and bifurcation software for delay-differential equations* (2009). (Cited on page 118.)

[TAB04] A. Tabaka, K. Panajotov, I. Veretennicoff, and M. Sciamanna: *Bifurcation study of regular pulse packages in laser diodes subject to optical feedback*, Phys. Rev. E **70**, 036211 (2004). (Cited on pages 121 and 155.)

[TAG93] A. A. Tager and B. B. Elenkrig: *Stability regimes and high-frequency modulation of laser diodes with short external cavity*, IEEE J. Quantum Electron. **29**, 2886–2890 (1993). (Cited on page 124.)

[TAG94] A. A. Tager and K. Petermann: *High-frequency oscillations and self-mode locking in short external-cavity laser diodes*, IEEE J. Quantum Electron. **30**, 1553–1561 (1994). (Cited on page 124.)

[THE11] J. Thévenin, M. Romanelli, M. Vallet, M. Brunel, and T. Erneux: *Resonance assisted synchronization of coupled oscillators: Frequency locking without phase locking*, Phys. Rev. Lett. **107**, 104101 (2011). (Cited on page 48.)

[TKA86] R. Tkach and A. Chraplyvy: *Regimes of feedback effects in* $1.5-\mu m$ *distributed feedback lasers*, J. Lightwave Technol. **4**, 1655–1661 (1986). (Cited on page 129.)

[TRE85] J. R. Tredicce, F. T. Arecchi, G. L. Lippi, and G. P. Puccioni: *Instabilities in lasers with an injected signal*, J. Opt. Soc. Am. B **2**, 173–183 (1985). (Cited on page 17.)

[TRO94] B. Tromborg, H. E. Lassen, and H. Olesen: *Traveling wave analysis of semiconductor lasers: modulation responses, mode stability and quantum mechanical treatment of noise spectra*, IEEE J- Quantum Electron. **30**, 939 (1994). (Cited on page 163.)

[TRO08a] V. Z. Tronciu: *Excitability and coherence resonance of a DFB laser with passive dispersive reflector*, Moldavian Journal of the Physical Sciences **7**, 516 (2008). (Cited on page 146.)

[USH05] O. V. Ushakov, H. J. Wünsche, F. Henneberger, I. A. Khovanov, L. Schimansky-Geier, and M. A. Zaks: *Coherence resonance near a Hopf bifurcation*, Phys. Rev. Lett. **95**, 123903 (2005). (Cited on page 146.)

[USH07] O. Ushakov, N. Korneyev, M. Radziunas, H. J. Wünsche, and F. Henneberger: *Excitability of chaotic transients in a semiconductor laser*, Europhys. Lett. **79** (2007). (Cited on pages 146 and 152.)

[LIN86] D. von der Linde: *Characterization of the noise in continuously operating mode-locked lasers*, Appl. Phys. B **39**, 201 (1986). (Cited on pages 203 and 204.)

[VIC04] R. Vicente, C. R. Mirasso, and I. Fischer: *Simultaneous bidirectional message transmisson in a chaos-based communication scheme*, Opt. Lett. **32**, 403–405 (2007). (Cited on page 109.)

[VIK06] E. A. Viktorov, P. Mandel, A. G. Vladimirov, and U. Bandelow: *Model for mode locking of quantum dot lasers*, Appl. Phys. Lett. **88**, 201102 (2006). (Cited on page 162.)

[VIK07] E. A. Viktorov, P. Mandel, and G. Huyet: *Long-cavity quantum dot laser*, Opt. Lett. **32**, 1268–1270 (2007). (Cited on page 109.)

[VIR11] M. Virte, A. Karsaklian Dal Bosco, D. Wolfersberger, and M. Sciamanna: *Chaos crisis and bistability of self-pulsing dynamics in a laser diode with phase-conjugate feedback*, Phys. Rev. A **84**, 043836 (2011). (Cited on page 121.)

[VLA04] A. G. Vladimirov, D. Turaev, and G. Kozyreff: *Delay differential equations for mode-locked semiconductor lasers*, Opt. Lett. **29**, 1221 (2004). (Cited on pages 3 and 172.)

[VLA05] A. G. Vladimirov and D. Turaev: *Model for passive mode locking in semiconductor lasers*, Phys. Rev. A **72**, 033808 (2005). (Cited on pages 3, 163, 169, 172 and 173.)

[VLA09] A. G. Vladimirov, A. S. Pimenov, and D. Rachinskii: *Numerical study of dynamical regimes in a monolithic passively mode-locked semiconductor laser*, IEEE J. Quantum Electron. **45**, 462–46 (2009). (Cited on page 162.)

[VLA10] A. G. Vladimirov, U. Bandelow, G. Fiol, D. Arsenijević, M. Kleinert, D. Bimberg, A. Pimenov, and D. Rachinskii: *Dynamical regimes in a monolithic passively mode-locked quantum dot laser*, J. Opt. Soc. Am. B **27**, 2102 (2010). (Cited on page 162.)

[VLA10a] A. G. Vladimirov, M. Wolfrum, G. Fiol, D. Arsenijević, D. Bimberg, E. A. Viktorov, P. Mandel, and D. Rachinskii: *Locking characteristics of a 40-GHz hybrid mode-locked monolithic quantum dot laser*, Proc. of SPIE **7720**, 77200Y–1 (2010). (Cited on pages 162 and 207.)

[VLA11] A. G. Vladimirov, D. Rachinskii, and M. Wolfrum: *Modeling of passively mode-locked semiconductor lasers*, in *Nonlinear Laser Dynamics - From Quantum Dots to Cryptography*, edited by K. Lüdge (Wiley-VCH, Weinheim, 2011), Reviews in Nonlinear Dynamics and Complexity, chapter 8, pp. 183–213. (Cited on pages 3, 169 and 199.)

[TAR95a] G. H. M. van Tartwijk and D. Lenstra: *Semiconductor laser with optical injection and feedback*, Quantum Semiclass. Opt. **7**, 87–143 (1995). (Cited on pages 2, 23, 25, 37, 38, 110, 113 and 137.)

[TAR95b] G. H. M. van Tartwijk, A. M. Levine, and D. Lenstra: *Sisyphus effect in semiconductor lasers with optical feedback*, IEEE J. Sel. Topics Quantum Electron. **1**, 466 (1995). (Cited on pages 138 and 155.)

[TAR98a] G. H. M. van Tartwijk and G. P. Agrawal: *Laser instabilities: a modern perspective*, Prog. Quantum Electronics **22**, 43–122 (1998). (Cited on pages 3, 23, 109 and 114.)

[WAN09b] A. B. Wang, Y. C. Wang, and J. F. Wang: *Route to broadband chaos in a chaotic laser diode subject to optical injection*, Opt. Lett. **34**, 1144 (2009). (Cited on page 36.)

[WEG10] M. Wegert, N. Majer, K. Lüdge, S. Dommers-Völkel, J. Gomis-Bresco, A. Knorr, U. Woggon, and E. Schöll: *Nonlinear gain dynamics of quantum dot optical amplifiers*, Semicond. Sci. Technol. **26**, 014008 (2011). (Cited on page 10.)

[WET00] R. Wetzler, A. Wacker, E. Schöll, C. M. A. Kapteyn, R. Heitz, and D. Bimberg: *Capacitance-voltage characteristics of InAs/GaAs quantum dots embedded in a pn structure*, Appl. Phys. Lett. **77**, 1671 (2000). (Cited on page 11.)

[WET04a] R. Wetzler, A. Wacker, and E. Schöll: *Coulomb scattering with remote continuum states in quantum dot devices*, J. Appl. Phys. **95**, 7966 (2004). (Cited on page 11.)

[WET04] R. Wetzler, A. Wacker, and E. Schöll: *Non-local Auger effect in quantum dot devices*, Semicond. Sci. Technol. **19**, S43 (2004). (Cited on page 11.)

[WIE99] S. Wieczorek, B. Krauskopf, and D. Lenstra: *A unifying view of bifurcations in a semiconductor laser subject to optical injection*, Opt. Commun. **172**, 279–295 (1999). (Cited on pages 42, 43, 48, 54, 68, 74 and 108.)

[WIE02] S. Wieczorek, B. Krauskopf, and D. Lenstra: *Multipulse excitability in a semiconductor laser with optical injection*, Phys. Rev. Lett. **88**, 063901 (2002). (Cited on pages 46, 47, 146 and 148.)

[WIE02a] S. Wieczorek, T. B. Simpson, B. Krauskopf, and D. Lenstra: *Global quantitative predictions of complex laser dynamics*, Phys. Rev. E **65**, 045207 (2002). (Cited on pages 49 and 59.)

[WIE05a] S. Wieczorek and B. Krauskopf: *Bifurcations of n-homoclinic orbits in optically injected lasers*, Nonlinearity **18**, 1095 (2005). (Cited on pages 42, 47, 48, 49, 108 and 148.)

[WIE05] S. Wieczorek, B. Krauskopf, T. Simpson, and D. Lenstra: *The dynamical complexity of optically injected semiconductor lasers*, Phys. Rep. **416**, 1–128 (2005). (Cited on pages 15, 23, 36, 38, 41, 42, 68 and 146.)

[WIE06] S. Wieczorek, W. W. Chow, L. Chrostowski, and C. J. Chang-Hasnain: *Improved semiconductor-laser dynamics from induced population pulsation*, IEEE J. Quantum Electron. **42**, 552–562 (2006). (Cited on page 68.)

[WIE07] S. Wieczorek: *Global bifurcation analysis in laser systems*, in *Numerical continuation Methods for Dynamical Systems – Path following and boundary value problems*, edited by B. Krauskopf, H. M. Osinga, and J. Galan-Vioque (Springer, 2007), Understanding Complex Systems, book chapter 6, pp. 177–220. (Cited on pages 47 and 147.)

[WIL12c] S. Wilkinson, B. Lingnau, J. Korn, E. Schöll, and K. Lüdge: *Influence of noise on the signal properties of quantum-dot semiconductor optical amplifiers*, IEEE J. Sel. Top. Quantum Electron. (2012). (Cited on page 10.)

[WOL02] M. Wolfrum and D. Turaev: *Instabilities of lasers with moderately delayed optical feedback*, Opt. Commun. **212**, 127–138 (2002). (Cited on pages 117 and 136.)

[WOL10] M. Wolfrum, S. Yanchuk, P. Hövel, and E. Schöll: *Complex dynamics in delay-differential equations with large delay*, Eur. Phys. J. ST **191**, 91 (2010). (Cited on page 179.)

[WUE02] H. J. Wünsche, O. Brox, M. Radziunas, and F. Henneberger: *Excitability of a semiconductor laser by a two-mode homoclinic bifurcation*, Phys. Rev. Lett. **88**, 023901–023901–4 (2001). (Cited on pages 146, 148 and 152.)

[XU12] T. Xu, M. Rossetti, P. Bardella, and I. Montrosset: *Simulation and analysis of dynamic regimes involving ground and excited state transitions in quantum dot passively mode-locked lasers*, IEEE J. Quantum Electron. **48**, 1193 (2012). (Cited on page 162.)

[YAB00] G. Yabre, H. De Waardt, H. P. A. Van den Boom, and G.-D. Khoe: *Noise characteristics of single-mode semiconductor lasers under external light injection*, IEEE J. Quantum Electron. **36**, 385–393 (2000). (Cited on pages 3 and 35.)

[YAM93] M. Yamada: *A theoretical analysis of self-sustained pulsation phenomena in narrow-stripe semiconductor lasers*, IEEE J. Quantum Electron. **29**, 1330–1336 (1993). (Cited on page 167.)

[YAN04] S. Yanchuk and M. Wolfrum: *Instabilities of stationary states in lasers with long-delay optical feedback*, Report of Weierstraß-Institut for Applied Analysis and Stochastics **962**, 1–16 (2004). (Cited on page 179.)

[YAN06] S. Yanchuk, M. Wolfrum, P. Hövel, and E. Schöll: *Control of unstable steady states by long delay feedback*, Phys. Rev. E **74**, 026201 (2006). (Cited on page 179.)

[YAN10] S. Yanchuk and M. Wolfrum: *A multiple time scale approach to the stability of external cavity modes in the lang–kobayashi system using the limit of large delay*, SIAM Journal on Applied Dynamical Systems **9**, 519 (2010). (Cited on page 179.)

[YU07] L. Yu-Jin, Z. Sheng-Hai, and Q. Xing-Zhong: *Chaos synchronization in injection-locked semiconductor lasers with optical feedback*, Chinese Physics **16**, 463 (2007). (Cited on page 36.)

[YOU99] M. Yousefi and D. Lenstra: *Dynamical behavior of a semiconductor laser with filtered external optical feedback*, IEEE J. Quantum Electron. **35**, 970 (1999). (Cited on page 169.)

[ZAI70] A. N. Zaikin and A. M. Zhabotinsky: *Concentration wave propagation in two-dimensional liquid-phase self-oscillating system*, Nature **225**, 535–537 (1970), 10.1038/225535b0. (Cited on page 146.)

[ZAK10a] A. Zakharova, T. Vadivasova, V. Anishchenko, A. Koseska, and J. Kurths: *Stochastic bifurcations and coherencelike resonance in a self-sustained bistable noisy oscillator*, Phys. Rev. E **81**, 011106 (2010). (Cited on page 146.)

[ZAK13] A. Zakharova, A. Feoktistov, T. Vadivasova, and E. Schöll: *Coherence resonance and stochastic synchronization in a nonlinear circuit near a subcritical hopf bifurcation*, Eur. Phys. J. Spec. Top. (2013), submitted. (Cited on page 146.)

[ZIE13] D. Ziemann, R. Aust, B. Lingnau, E. Schöll, and K. Lüdge: *Optical injection enables coherence resonance in quantum-dot lasers*, EPL **submitted** (2013). (Cited on pages 46, 146 and 147.)

ACKNOWLEDGEMENTS

I would like to thank my supervisor Prof. Dr. Eckehard Schöll, PhD for the chance to work in the interesting field of nonlinear laser dynamics in his group. I very much appreciated his inspiring way to discuss scientific topics. Further, I would like to thank him, on the one hand, for his guidance and, an the other hand, for motivating me and giving me the freedom to study new questions. Further, I am grateful for his constant encouragement to participate at international conferences as well as his support during application procedures.

I would like to thank Priv.–Doz. Dr. Kathy Lüdge for our frequent exchange of scientific ideas and her encouragement to explore new questions. Further, my thanks go to her for organizing the weekly meetings (jours fixes) in an enjoyable atmosphere. Moreover, I would like to thank her for her support and her encouragement during the publication process. Furthermore, I am very grateful for her most helpful suggestions to improve the manuscript.

I am very much indebted to Prof. Dr. Thomas Erneux for the inspiring time I had in his group, and for our numerous instructive discussions on asymptotic analysis. Further, I would like to thank him to assess this thesis as the external reviewer.

I very much appreciated the vivid discussion with Lionel Weicker. Sharing an office with him, was a great pleasure for me. Further, I am grateful for his help in preparing a french article about Art Nouveau.

I would like to thank Dr. Andrei G. Vladimirov and Dr. Matthias Wolfrum for our vivid collaboration and their inspiring thoughts.

Moreover, I would like to thank the present and the former members of the AG Schöll for the great working atmosphere. Especially, I would like to thank Judith Lehnert, Miriam Wegert, Philipp Hövel, Niklas Hübel, Thomas Isele, and Valentin Flunkert. My thanks go to Benjamin Lingnau for reading parts of the manuscript, vivid discussions, and his schematic sketches, which are graphical highlights of the thesis. Further, I would like to thank Björn Globisch for our joint work on the feedback laser, and thanks go to Johannes Pausch and Egle Tylaite for our cooperation on the injection problem. My thanks go to Dr. Niels Majer, who shared an office with me for two years, for our many scientific discussions. Further, I would like to thank Dr. Thomas Dahms for making the emacs editor and minimalistic window managers tempting to me. Moreover, I would like to thank Roland Aust for helping me with my computer problems and for occasional data recovery.

Further, I appreciated the "Bifurkationsklatsch"-meetings with David A. Strehober and Markus Radszuweit, which helped me a lot to get a deeper understanding of bifurcation theory.

I am very grateful to Antje for her love and for her support in all stages of the thesis as well as for her positive way of thinking, which encouraged me a lot. Further, I very much appreciated her careful proofreading of the manuscript. Moreover, I would like to thank my parents for their support and encouragement.

This work was supported by DFG in the framework of GRK 1558.